CENTRAL LASER FACILITY

Making Progress

ANNUAL REPORT 1991

ANNUAL REPORT TO THE LASER FACILITY COMMITTEE 1991

5 April 1990 to 4 April 1991

SERC CENTRAL LASER FACILITY
RUTHERFORD APPLETON LABORATORY
CHILTON
DIDCOT
OXON
OX11 0QX

Telephone 0235 821900
Telefax 0235 445888

Rutherford Appleton Laboratory Report RAL-91-025

Cover designed by
J Houliston & J Mackintosh

Science and Engineering Research Council

"The Science and Engineering Research Council does not accept any responsibility for loss or damage arising from the use of information contained in any of its reports or in any communication about its tests or investigations"

ACKNOWLEDGEMENTS

It is a pleasure for me to acknowledge the skilled work of the team who have produced this report. Particular thanks are due to Chris Ayling and Katharine Higgs in connection with production of text, to Jan Smith for tracing diagrams and to Nic Allen and Chris Reason for the organisation of production.

Chapter and Section editing was undertaken by Abdeslem Djaoui, Chris Edwards, Andrew Langley, Peter Norreys, Tony Parker, Chris Reason, Allan Ridgeley, Steve Rose, Ian Ross, Mick Shaw, Phil Taday, Greg Tallents, Sue Tavender, Bill Toner, Mike Towrie and Edmond Turcu.

Once again, the camera-ready format has been very helpful to the production team and much of the material has been prepared by Facility users in their own Institutes and they too deserve many thanks particularly for, in some cases, meeting very tight deadlines for reports on experiments close to the end of the reporting year.

The document has been produced by RAL Reprographics service with the assistance of Borough Press for the printing of the cover. Winner of the cover design competition was James Houliston and the photograph was obtained from J Scott and B Shorter of Planet Earth Pictures.

M H Key

PREFACE

The year to 31 March 1991, covered by this report, has been highly productive in the volume and quality of scientific research carried out by the UK University and Polytechnic users of our research facilities.

Users of the major high power lasers, Vulcan and Sprite, carried out 17 different experimental campaigns deploying more than 2,300 high power laser shots on a similar number of specially constructed micro-targets. They also carried out extensive theoretical and computational studies related to the experimental research. The multiplicity of smaller lasers of the Laser Support Facility were used in some 60 different experiments of a highly multidisciplinary character spanning chemistry, biology and physics.

Work with the high power lasers covered a broad field ranging from the basic physics to the applications of laser-produced plasmas. Outstanding results were obtained in the application of plasma X-ray sources to measure plasma opacity in the study of the interplay of radiation transport and atomic physics in laser-produced plasmas. Important advances were made in X-ray laser research notably in the demonstration of high gain amplification in a double plasma experiment with the 23 nm Ge XXIII laser which has made it possible to begin to use the XUV laser beam for microscopy. The newly developed KrF-pumped Raman laser beam was used in very novel experiments capitalising on its extreme brightness and pulse contrast ratio to study energy transport and ionisation physics phenomena for very short pulse laser plasma interactions. Amongst the extensive theoretical work, the modelling of the hydrodynamics of non-uniformly driven spherical implosions, produced notable new results.

The work of the Laser Support Facility was further broadened in its scope by the addition of experiments related to elementary particles, physics-based archaeology and astrophysically relevant chemistry, in addition to the more established fields of activity in chemistry, biochemistry, cell biology and atomic physics. Among such a large number of experiments it is difficult to do justice to them all by picking out a few for comment but certainly the induction of cell proliferation by exposure to laser light, extension of co-variance mapping techniques in multiphoton multiple ionisation to three dimensions, and the demonstration of the photo-oxidation of water by triplet ubiquinone are all worthy of mention.

The year was not only scientifically productive but also one of major change and uncertainty regarding the future of the high power laser activity. Vigorous development throughout the year of the new technology of the KrF laser-pumped Raman laser produced exceptionally interesting results, notable among which was the demonstration of extreme brightness in the operation of the Raman beam at pulse lengths in the region of 10 ps. Significant progress was made also in the development of transform-limited pulse generators, the study of the performance of large amplifiers, the demonstration of broadband incoherent irradiation of high uniformity and in the prototyping of components of size appropriate to a future multi-kilojoule KrF laser facility.

The uncertainties arose in connection with developments in SERC's domestic and European policy. The main aim of the KrF development work through the early part of the year had been the verification of concepts related to the krypton-fluoride laser option for a European Laser Facility (ELF) with SERC initially enthusiastically committed to participation in ELF. With the publication of the report of the European Working Group and its subsequent discussion during the year, complications arose both within SERC and among the ELF partners. A perception within SERC of financial difficulties for next year and beyond led to a cost-cutting exercise of which one of the consequences was a decision by SERC Council to suspend for the time being SERC's participation in the ELF initiative.

An abrupt change in the near-term objectives of the KrF programme was therefore produced, with ELF becoming a longer-term goal. Interest was re-focused on the previously recommended provision of a domestically-funded laser system, Supersprite, which could in the future replace the Vulcan laser. Present strategy is to complete a design study for the KrF option (Supersprite) and to evaluate this against the possibilities presented by continued use of glass lasers. The process involves both technical work and extensive consultation with Facility users, and I hope that next year's report will give the results of both the design studies and the decision making process and show a clear way forward for the high power laser programme.

A corollary of the financial problems within SERC has been a total ban on recruitment in SERC, imposed since November 1990. Laser staff have the highest turnover rate within the Rutherford Appleton Laboratory and this ban is proving damaging to our staffing situation through rapid attrition of our numbers. There is difficulty in finding laser experts for redeployment within the Laboratory and we can but hope that this situation will not persist for more than the next financial year for which it is presently in force.

In conclusion, it is a pleasure for me to draw attention to the dedicated work of CLF staff throughout the year and particularly to the efforts of those who have had an increased burden through the under-manning which has resulted from the staff recruitment freeze. I am also impressed by the capacity of staff to continue their work with enthusiasm when there are major uncertainties in the direction of the future programme. Some are working in areas where future development is anticipated, and some in areas which may see closure but it is my expectation that when the future directions are defined staff will redeploy their efforts with enthusiasm to deliver their usual level of excellent service to the Facility users.

The Facility users themselves have been a great source of inspiration to the staff through their boundless energy and enthusiasm during the periods of their various scheduled experiments and it remains as always true that there is no purpose and can be no significant achievement in the Central Laser Facility without their contribution which is most obviously visible in their accounts of their work contained in this report.

Professor M H Key
Head of the Central Laser Facility

ORGANISATION AND MANAGEMENT OF THE CENTRAL LASER FACILITY

W T Toner and S J Rose

The Central Laser Facility (CLF) is funded by the Science Board of the Science and Engineering Research Council and the programme is managed by the Laser Facility Committee (LFC) chaired by Professor R J Donovan FRSE. The LFC delegates responsibility to the Director of the Rutherford Appleton Laboratory for the operations of the facility.

The expenditure of the CLF for the period covered by this report, April 1990 to March 1991 was £3.2M. Fifty six man years of effort were used and the staff costs and overheads amounted to 56% of the allocation. The resources were divided between the three programmes of the Facility as shown in Figure 1, where users' travel and subsistence and provision for administration have been aggregated into the programme costs.

The major facilities provided by the CLF and their principal scientific applications are listed in Table 1. The Nd Glass Laser VULCAN is the main facility for experiments using high-power lasers by UK user groups and their overseas collaborators. The results of this work are contained in Section A of this report.

In the KrF programme, development of a novel KrF-pumped Raman laser is mainly aimed at establishing the basic design for new high power laser facilities for the mid 1990's. The high brightness of the Raman beam is also being exploited for some user experiments. An account of this work is reported in Section B.

The Laser Support Facility provides small lasers and covers all areas of research supported by the Science Board. The experiments are frequently multi-disciplinary in character. Results from the scheduled programme of the LSF make up Section C of this report. Section D contains reports of other research and development work by Facility staff.

An engineering support group including a target preparation service, a small group giving theoretical support by maintaining computer codes and a laser R&D group service all CLF activities. Figure 2 shows the present divisional and group structure of the CLF.

Use of the CLF by UK research workers in Higher Education Institutes (HEI's) is free of charge to those successful in a peer review process. The cost of travel to the facility and some incidental costs of the research are borne by the CLF out of its allocation from the Board. The costs of research assistants and expenditure in HEI laboratories may be sought by application to the SERC for a research grant. The Laser Facility Committee funds users wholly or mainly using the CLF and the subject committees of the Science Board also award grants to users of the Facility.

Grant holders may bid for time on the facilities of the CLF by application to one of the two selection panels: the High Power Laser Panel chaired by Dr T A Hall and the Laser Support

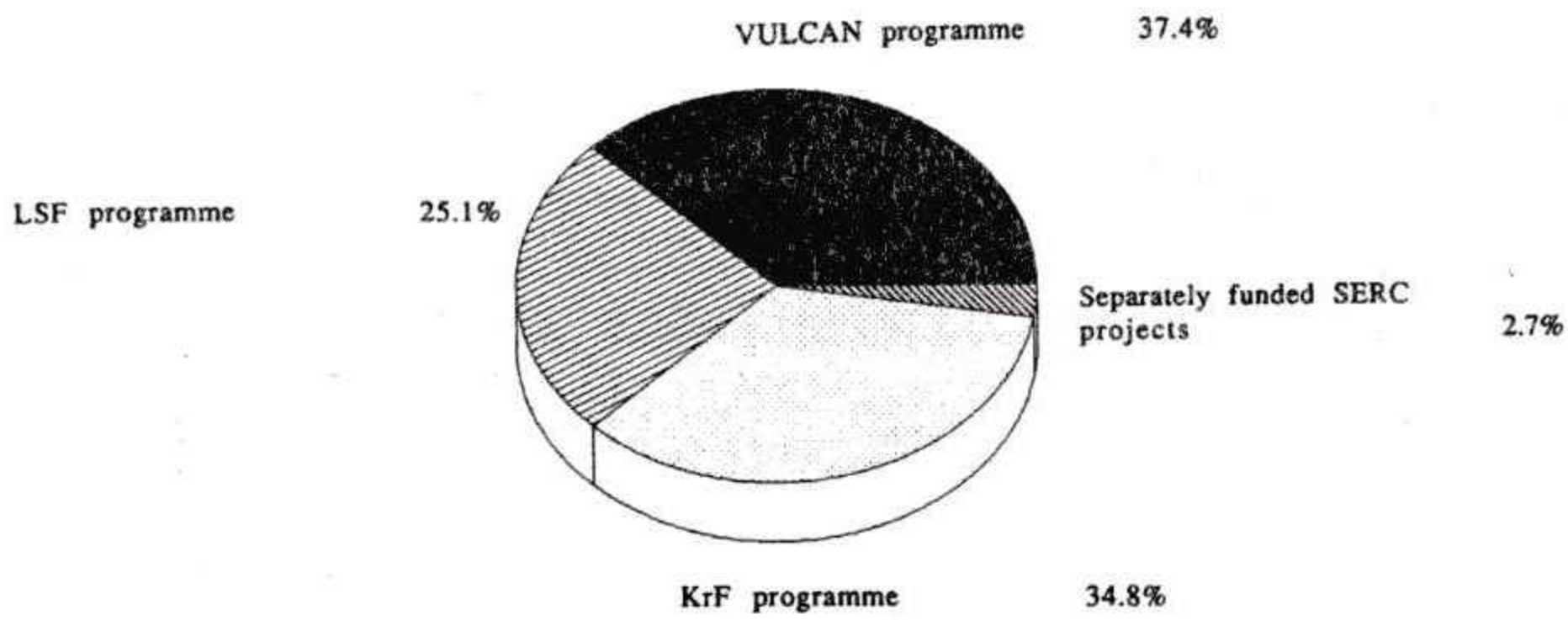

Figure 1. Breakdown of expenditure

TABLE 1: Major Programmes at the CLF

Nd Glass Laser Facility	Laser Support Facility	High Power KrF Lasers
Laser plasma interactions and energy transport	Photochemistry, Photobiology, Nonlinear Optics	Research and development in Raman beam combining and novel architectures for high power lasers. Research and development in large scale KrF amplifiers
Laser compression of matter and dense plasmas	High field atomic physics Laser Loan Pool Raman facility	Short pulse laser-plasma interaction studies
XUV lasers and applications of laser produced plasma sources	Picosecond laser High repetition rate X-ray source	
Engineering Service		
Laser R&D Service		
Theoretical Support Service		

Facility Panel chaired by Dr K Burnett. The panels meet three times a year to determine the relative priority of the bids for time in a specific four month schedule period. A small proportion of the time may be allocated by the Panels to applicants without grant support. Following the recommendation of the Panels as to priority, and taking account of logistical factors, schedules are prepared by CLF staff which are then discussed, modified as necessary and approved by open committees of facility users.

The SERC encourages use of the CLF by industry or other organisations on the basis of payment for the full costs of laser time. Such use is limited to 10% of available laser time.

International collaboration in the research programme is extensive through collaborative participation in approved experiments of UK University groups and through agreements negotiated with the CLF and SERC.

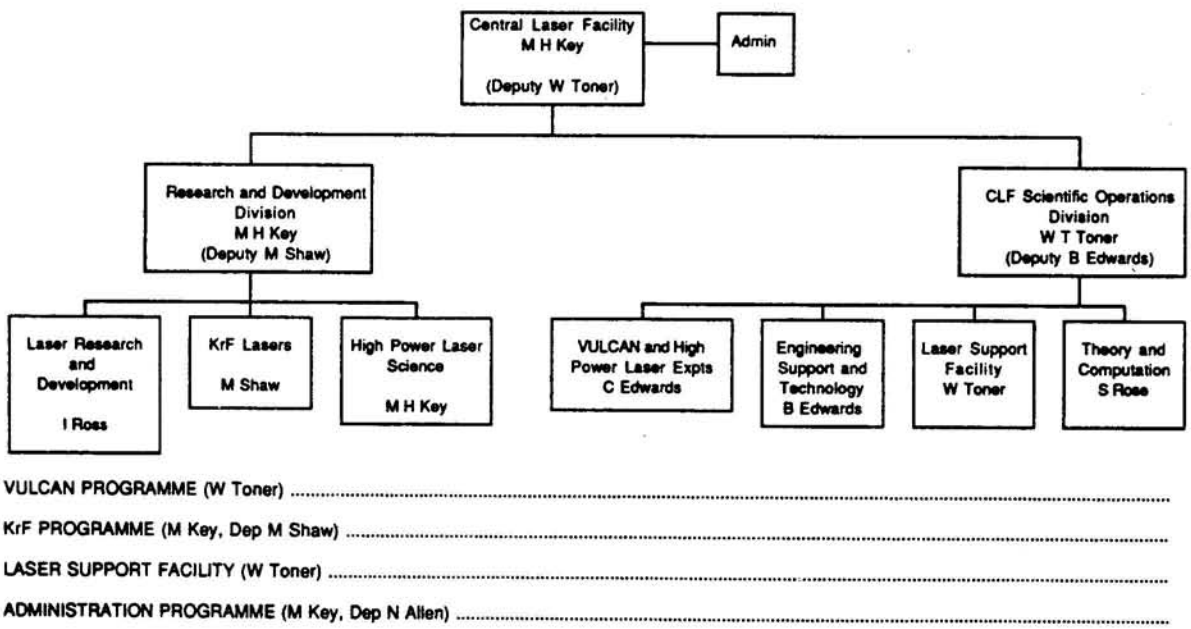

Figure 2: Divisional and Group Structure of the Central Laser Facility and Programme Management

A STUDY OF AN INJECTOR/AMPLIFIER DOUBLE TARGET CONFIGURATION FOR THE NEON LIKE GE X-RAY LASER SCHEME

D Neely[1], CLS Lewis[1], DM O'Neill[1], J Uhomoibhi[1], S A Ramsden[2], GJ Tallents[3]
YA Hadithi[3], MH Key[4], SJ Rose[4] and GJ Pert[5]

1 Department of Pure and Applied Physics, Queen's University, Belfast BT7 INN
2 Department of Applied Physics, University of Hull, Hull HU6 7RX
3 Department of Physics, University of Essex, Colchester CO4 3SQ
4 Rutherford Appleton Laboratory, Chilton, Didcot, Oxon OX11 OQX
5 Department of Physics, University of York, York YO1 5DD

INTRODUCTION

The single target slab Neon like Ge soft X-ray laser has been extensively studied at RAL[1,2,3]. Experiments were carried out using three 1.06μm beams in a single sided illumination configuration. A peak gain of > 4.5 cm^{-1} is available at a target irradiance of > 2.0±0.5 x 10^{13} W cm^{-2}. Above threshold (0.6±0.1 x 10^{13} Wcm^{-2}) the gain production efficiency (gl/P) of the system peaks at a target irradiance of 1.2±0.2 x 10^{13} Wcm^{-2} and then slowly falls such that it is 10% less at irradiances of 2.0 and 0.8 x 10^{13} W cm^{-2}. To achieve saturation i.e a gl product 16-20 would require target lengths of 4.0 cm at gains of 4.5 cm^{-1} (at an irradiance of 2.0 ±0.2 x 10^{13} W cm^{-2}) or 6.5 cm targets at gains of 2.8 cm^{-1} (at an irradiance of 1.2±2.0 x 10^{13} W cm^{-2}). Since the gain production efficiency is not a primary effect, it is best to choose the target lengths to minimise problems associated with uniform intensity illumination and beam refraction.

EXPERIMENTAL

The Vulcan laser delivers its energy to the X-ray laser target chamber in two groups of three beams arriving from opposite directions, East and West. Because we have concentrated on massive targets, as opposed to exploding foil targets (which can have double-sided irradiation), only half of VULCAN's potential pump power can be utilised in heating a plasma column. In practice, the existing line focus geometry limits this column length to 30 mm. In order to use all VULCAN's pump power to generate a longer plasma with a gain-length product large enough to approach saturated outputs, we devised a double target arrangement whose geometry is illustrated in Figures 1 and 2. Two separate targets are irradiated from opposite directions in such a way that ASE from one plasma can couple into the second plasma and amplify further. This scheme has the added benefit of mitigation against deleterious refraction effects which, in a single plasma column, could limit the useful amplifier length. Double targets typically consisted of Ge stripes 14 and 22 mm

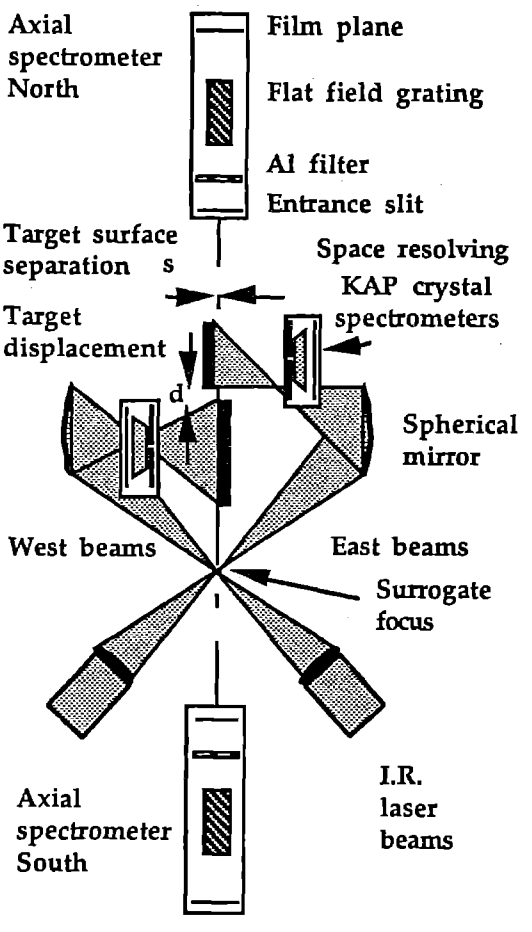

Figure 1 A schematic diagram showing the off-axis mirror line focus geometry and main diagnostics used .

long which emitted ASE beams in the North and South directions respectively. Both targets were irradiated at 2.5 x 10^{13} Wcm^{-2} using 1.05 μm pump light in 620 ps pulses. The 22 mm target was 100 μm wide and the 14 mm target was 150 μm wide. This geometry was initially chosen to maximise the coupling of the 22 mm plasma output into the 14 mm plasma in the vertical plane.

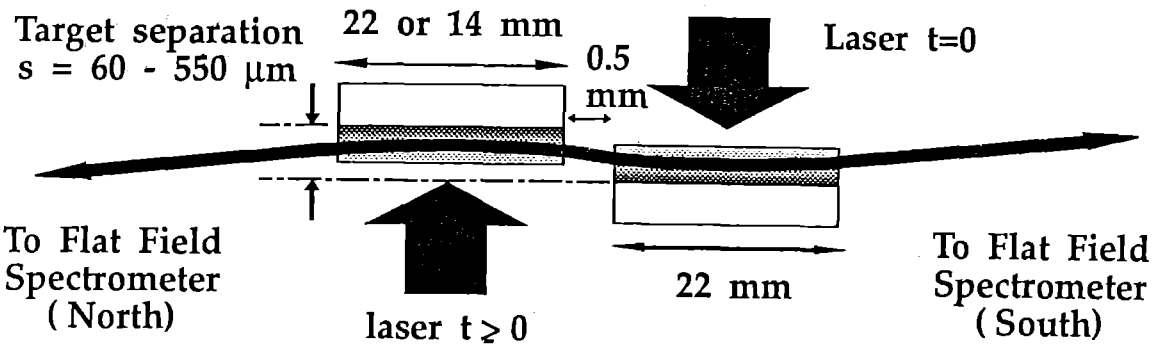

Figure 2 A schematic ray path through a double target amplifier showing how refractive beam bending can be compensated to increase the effective amplifying plasma length.

It was expected that the North beam output would exceed the South beam output. Both beams were monitored with standard flat-field spectrometers fitted with axial fiducial markers in the flat-field planes. The North spectrometer had an 85μm entrance slit at a distance of 10 cm from the plasma end and the South spectrometer had a 200μm entrance slit at a distance of 75 cm from the other plasma end.

A space resolving double crystal spectrometer[4] was also used to monitor the uniformity of illumination along the target length. The crystal spectrometer observed emission in the 9.0-10.5Å region. Using a previous calibration of the Ne/F 3s-2p resonance line ratio, the rms deviation of incident intensity was measured at 22% for a 22mm target and 17% for a 14mm target. The intensities, pointing directions and divergences of the two output lasing beams were measured as a function of the separation of the two opposing target surface planes. From our previous characterisation of single target properties, maximum coupling between the plasmas was expected when this offset distance was of the order of a 150 μm. Based on earlier observation that careful control of target substrate flatness lead to improved reproducibility, we eliminated this quality control problem by using 250 μm thick optically polished glass substrates to support the Ge stripes, although even these targets could be badly mounted if due care was not taken.

The double targets were prealigned relative to each other in a single mount using an alignment jig which allowed us to accurately set the two target surface planes parallel (±1.5 mrad) to each other at a specified separation (±10 μm) and to place the two coated Ge stripes in the same horizontal plane (±5 μm). The composite target was then aligned in the target chamber in the normal manner using a split-field microscope arrangement.

RESULTS

The correlation between the North and South beam peak brightnesses is shown in Figure 3 for the 23.6 nm line, where the only parameter that has been significantly changed is the target surface plane separation. The data is normalised at unity on each axis which corresponds to the average recorded signal in each spectrometer for a number of single 22 mm long target shots. Clearly, and contrary to our initial expectations, the South beam is typically observed to be up to about X10 more intense than the North beam.

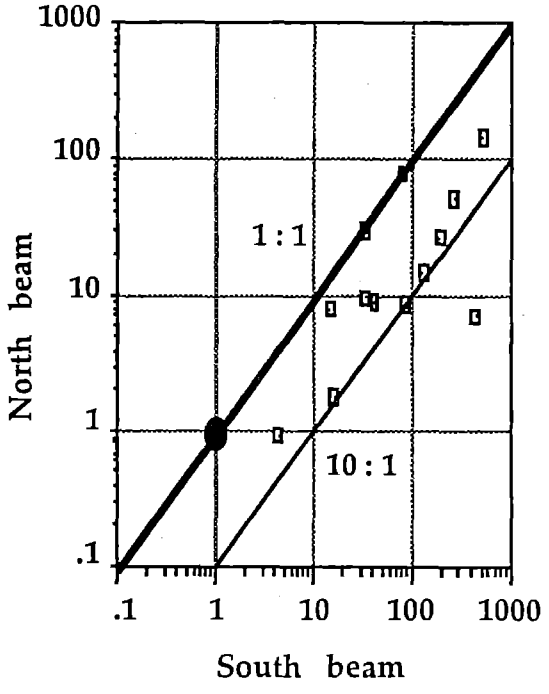

Figure 3 Relative outputs of the beams on different shots. The solid circle refers to normalisation of outputs from 22mm plasmas which are about equal.

This is further illustrated in Figure 4 where the outputs are plotted separately as a function of the target separation. Both beam outputs peak at a separation of 200 μm. Compared to the outputs from a 22 mm single target, the South beam is enhanced by a factor of 100-1000 and the North beam by a factor of 10-100 which implies that, for some shots, the coupling efficiency of radiation from the 14 mm plasma to the 22 mm plasma is approaching 100%. Our best estimates of maximum absolute beam power from film calibration, estimated vertical divergence and streak records indicate that up to

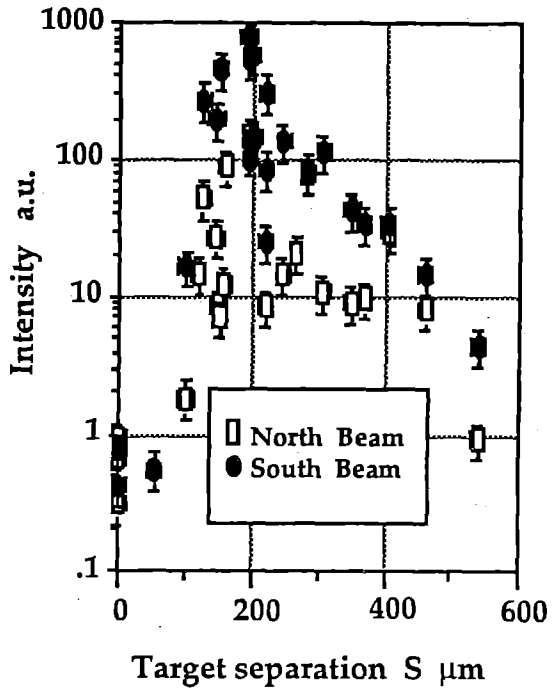

Figure 4 The peak brightness in each direction versus surface plane separation, s. Points at s=0 refer to single 22mm target outputs with 1au corresponding to ≈ 2 KW.

2 megawatts of power was emitted on each of the 23.2 and 23.6 nm lines in the South beam. Aluminium filters of 4 μm thickness were needed in the North spectrometer on these shots to prevent film saturation.

Figure 5 shows how the pointing direction of the two ASE beams (for 23.6 nm) changed with the target surface separation distance. The South output, which is presumably more determined by gain guiding in the longer plasma, is fairly constant in pointing direction at 10 mrad away from the target surface plane. The North beam, on the other hand, varies systematically with the surface separation and can swing either side of the target plane. The maximum intensity output for this beam under the present conditions is emitted along the line focus axis. The observed beam divergences were typically in the range 5-10 mrad (fwhm) with the North beam tending to be slightly narrower. A limited number of shots were taken where both targets were 22 mm long and 100,um wide. The outputs from these 22/22 mm targets were not significantly different from the 14/22 mm targets. This probably indicates that the system was operated close to saturation.

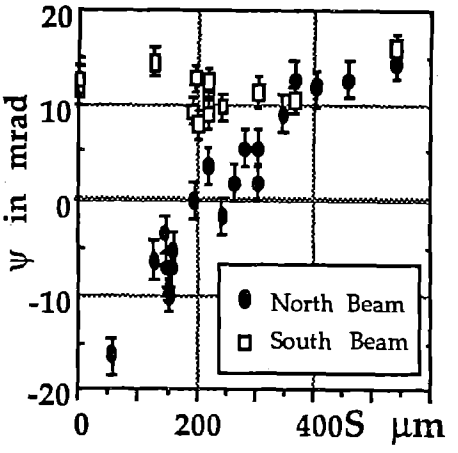

Figure 5 Plot showing the beam pointing direction as a function of target plane separation.

A limited data set of streaks of the 22/22mm target temporal output of the South beams showed some interesting trends. At the optimum surface plane separation 200μm for the J=2-1 23.2 and 23.5nm lines both beams have a temporal duration of 300ps FWHM Figures 6 and 7. The J=1-0 19.6nm line however comes in two 100ps bursts separated by 500ps. These two bursts of the 19.6 nm line are each sufficiently intense that they show coupling between the two plasmas both early and late in time.

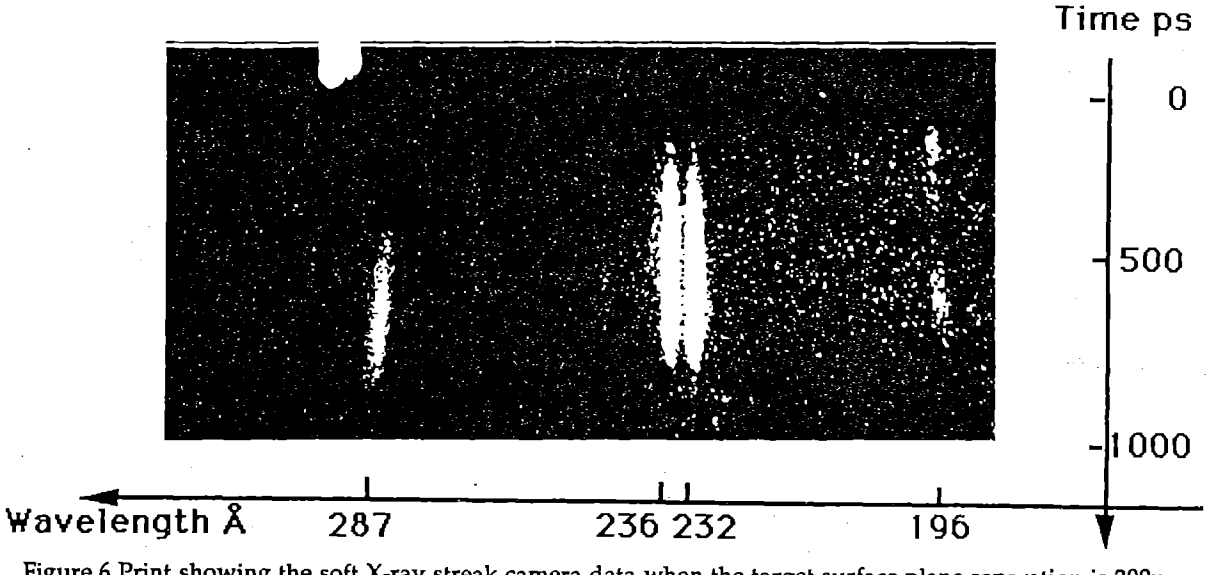

Figure 6 Print showing the soft X-ray streak camera data when the target surface plane separation is 200μm.

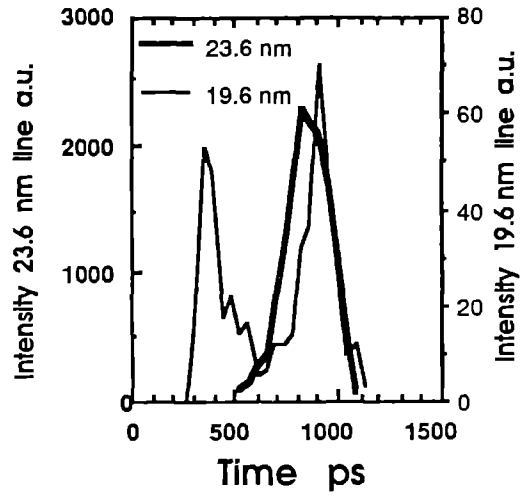

Figure 7 Temporal history of the J=2-1 23.6nm line and the J=1-0 19.6 nm line for a double target at a surface plane separation of 200μm.

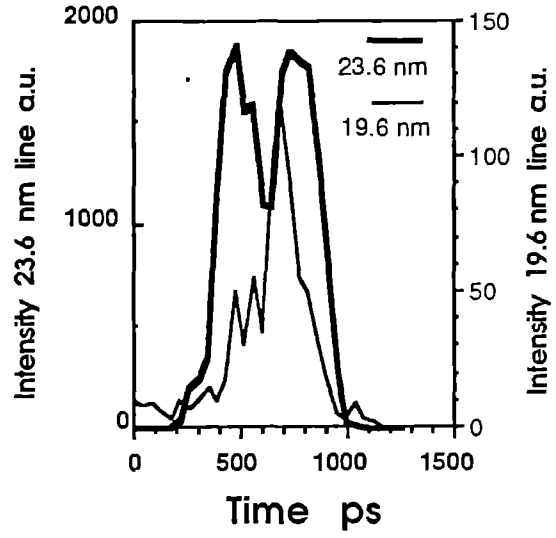

Figure 8 Temporal history of the J=2-1 23.6nm line and the J=1-0 19.6 nm line for a double target at a surface plane separation of 425μm.

With a surface plane separation of 425μm, the J=2-1 lines are observed to develop a similar but less pronounced double peaked structure (Figure 8). The intensity in each peak is again consistent with the ASE coupling and being amplified in each plasma. The J=1-0 line however, now has only a single peak of 100ps FWHM but its intensity shows that strong coupling between the two plasmas has occurred.

CONCLUSION

Massive double target slab geometries are shown to be convenient for producing powerful beams in the XUV spectrum from collisionally excited laser-produced plasmas. We have demonstrated that efficient coupling of an ASE beam from one plasma to another is possible and have reached megawatt power levels in a single line. This technique has the potential to overcome refraction effects and can probably be extended to a zig-zag target arrangement for multiple high power pump beams arriving from opposite directions. In the near future[5] we plan to extend this type of systematic study to more ions; to achieve saturation in Ne like Ge, either using cavities or by increasing our available laser pump power; and to initiate simple application-type experiments. Many of our observations require recourse to detailed modelling (hydrodynamic, atomic and ray tracing) which will be available in the near future.

REFERENCES

1 Neely D, Lewis CLS, Uhomoibhi J, O'Neill DM, Ramsden SA, Key MH, Shiwai B, Tragin N and Tallents GJ 1990 SERC Central Laser Facility, Ann. Rept. to LF RAL90-26 pp 3-7

2 O'Neill DM, Lewis CLS, Neely D, Uhomoibhi J, Key MH, MacPhee A, Tallents GJ,Ramsden SA, Rogoyski A and McLean EA 1990 Opt. Comm. 75406

3 Lewis CLS, Neely D, Uhomoibhi J, O'Neill DM, Ramsden SA, Tallents GJ, Hadithi YA, Key MH, Rose SJ and Pert GJ Proc of the 2nd Colloquium on X-Ray Lasers, York Sep 1990 I.O.P. Publishing Ltd To be published.

4 Hadithi YA, Tallents GJ and Neely D Proc of the 2nd Colloquium on X-Ray Lasers, York Sep 1990 I.O.P. Publishing Ltd To be published.

5 In a recent experimental run we have used the 1MW output beams from this system as a "standard" beam. We have used mirror coupling in an attempt to reach a saturated output and a Schwartzchild / zone plate microscope system to record sub-micron structure of test objects. Detailed analysis of both experiments will be presented in next year's annual report.

TIME AND SPACE RESOLVED CVI GAIN MEASUREMENTS WITH LONG SLAB TARGETS

D M O'Neill,[1] J O Uhomoibhi,[1] D Neely,[1] C L S Lewis,[1] L B da Silva,[2] J Krishnan,[3] L Dwivedi [3] G J Tallents,[3] G J Pert,[4] S A Ramsden,[5] J Jacoby,[6] M H Key,[6] R Kodama,[6] P Norreys,[6] S J Rose,[6] N Tragin.[6]

[1] Queen's University of Belfast
[2] Lawrence Livermore National Laboratory
[3] University of Essex
[4] University of York
[5] University of Hull
[6] Rutherford Appleton Laboratory

INTRODUCTION

The potential efficiency and favourable scaling characteristics of the recombination X-ray laser scheme has attracted much experimental and theoretical effort since it's first proposal.

Evidence for the production of gain in recombining laser-produced plasmas has been obtained over a wide range of wavelengths, from 20 to 4nm, using a variety of different target configurations and often under vastly disparate irradiation conditions.[1] In many cases, however, the explanation of the results is not straightforward theoretically. Moreover, there has, as yet, been no unequivocal demonstration of the necessary high gain-length product ($10<gL<20$) which could lead to a useful laser beam.

THEORETICAL MODELLING

Recent theoretical modelling has concentrated on a massive slab target geometry as there are practical difficulties with extending the length of fiber targets, on which our previous work[2] was based, beyond lengths of ~1cm. A one dimensional analysis of the slab case, in which the width of the line focus is equated to the radius of a cylindrical target[3], proved to be broadly in agreement with a more detailed two dimensional approach[4]. A peak time and space resolved gain on the $n=3\rightarrow2$ Balmer-α of ~9.5cm^{-1} was determined for a 70ps, 2ω pulse irradiating a 7μm C-fibre target at an optimised absorbed intensity of 1.6×10^{13} W/cm^2. This is projected to fall to ~4cm^{-1} in the case of slab targets irradiated by 100μm wide line focus at an optimised absorbed intensity of 6×10^{12} W/cm^2. However, since the coupling to the slab target is much higher, the efficiency of producing gain, (gL/P) where P is a fixed laser power, is anticipated to increase by a factor of two over the fiber case.

Use of a narrower focal width is expected to improve the recombination amplification process as it leads to more rapid cooling of the plasma through the two-dimensional nature of the resultant plasma expansion.

According to calculations, then, our capacity to produce high gain length products is maximised with a slab target both from the point of view of efficiency of production of gain and because extended length is possible with slabs.

EXPERIMENTAL OBJECTIVES

Observations on recombination XUV-lasers are intrinsically more difficult to interpret than those based on collisional excitation. The complicating factor is the masking of any gain by non-lasing emission on the same transition from other space and time regions in which amplification does not occur. Typically, the temporally and spatially integrated emission has a 70 times larger component from non-gain as opposed to gain regions. As a result, the apparent gain deduced from axial to transverse ratios, or from length variation, can be substantially different from the peak gain in space and time for moderate values of the peak gain length product, as shown in figure 1. This shows how the (measured) apparent gain differs from the peak gain of 4cm^{-1} as a function of measurement conditions and length.

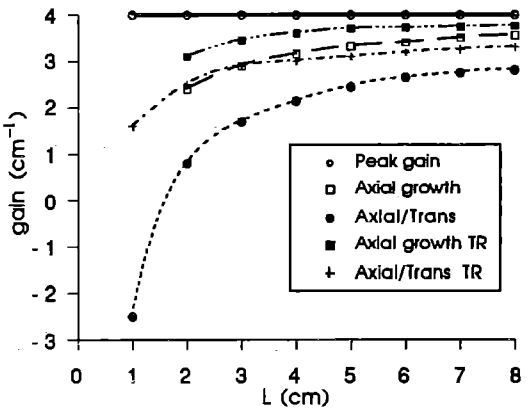

FIGURE 1 Apparent gain (where peak gain is 4cm^{-1}) as a function of plasma length as measured by simple axial growth and axial/transverse ratio methods. TR denotes a time resolved, space integrated measurement.

It can be seen from the figure that isolating the gain zone emission from the bulk plasma emission in space and/or time (thus preventing the amplified spontaneous emission being swamped by the bulk spontaneous emission) greatly reduces the difference between the apparent and peak gains. Note that this is not a serious problem in collisional laser systems since the plasma fluorescence on the lasing lines (which are not resonance transitions) is usually negligible.

However, it is the peak values which determine the capability to create a useful laser beam and it is these values which must be determined from experimental measurement. In this experiment we have used temporal and spatial resolution, although not simultaneously, in combination with long length plasmas (up to 4cm + 4cm in double target configuration[5]) in order to maximise the signals of interest.

EXPERIMENTAL DETAILS

The chamber in TAE was configured to allow six beams of VULCAN to be used in the off-axis line focus geometry[6]. In a 70ps pulse at 0.53μm, each beam was capable of providing uniform irradiation of up to 15mm x 25μm areas at incident intensities of $\leq 6.0 \times 10^{13}$ W/cm^2. Groups of three beams, incident from opposing sides, could be placed end to end, allowing slab targets of up to 40mm to be uniformly irradiated, either singly or in double target geometry. Optically polished slabs of glass, coated with ~0.5μm of CH and fabricated with a 25μm wire along their length, provided the standard target geometry with a limited number of ~20μm diameter C-fibers, suspended electrostatically[7], also studied. The 25μm wires were used to accurately align the targets and incident laser beams: the pointing of the target and focussing of the beams were adjusted with the aid of the wire and a split field alignment system. The target was then displaced vertically by 50→100μm so as to avoid irradiating the wire. The alignment of the target pointing relative to the spectrometer axis was ±1mrad and the co-incidence of the target and focal line, better than 5μm.

Two grazing incidence spectrometers, incorporating aperiodic (1200 l/mm average) flat-field gratings and double reflection filters[8], viewed the plasma axially and transversely (55° to the axis). These instruments were operated in both time integrated and time resolved modes. In the time integrated case, a vertical 190μm slit (parallel to target surface), placed ~50mm from the end of the plasma, provided spatial resolution with a magnification of x10 to the image plane. Information was obtained for a range of spatial slit positions up to ~550μm (ie ~8mrad to target centre) from the axis in the horizontal plane (normal to the target). Spectra were recorded on Kodak 101-01 film over a ~25mrad field of view centered at up to ~15mrad off-axis. The Kentech XUV streak camera used to provide temporal resolution (~50ps) was operated with the timing slit either parallel or orthogonal to the grating dispersion direction. In the first case, temporal information on the plasma emission in a particular direction (up to ~15mrad off-axis in the horizontal plane) is obtained over a spectral field of ~100Å. In the second case, the streak camera timing slit is rotated through 90° to provide temporal information on the plasma emission in a small spectral range (~2Å) over a ~25mrad angular field of view in the direction normal to the target surface. In the case of a high gL system, the lasing transition should prevail over any background continuum or non-lasing emission and we might expect to record a well defined beam as a function of angle (ie pointing) and time. By centering the timing slit on the 182Å Balmer-α transition, it was possible to study the emission for any evidence of an XUV laser "beam".

The timing of the XUV streak records relative to the laser pulse was estimated from the continuum emission. The results presented below are normalised in time such that the peak of the continuum is defined as time t=0. All temporally resolved spectra were recorded via image intensifiers onto individually calibrated ILFORD HP5 film strips which allowed the reduced data to be expressed in relative intensity units. In the case of this experiment, there was no need to normalise for filtering as the dynamic range of the instrument was sufficient to operate with no filtering for all lengths studied.

Plasma uniformity along the length of the plasma was monitored by two single slit cameras, filtered to detect 1keV and 2keV radiation. Both instruments employed a phosphor screen and image intensifier with final recording on HP5 film. A simple pinhole camera, detecting 300eV radiation on KODAK INDUSTREX C-type X-ray film, gave a measure of the focal width over a limited length (~5mm) of the plasma.

RESULTS AND ANALYSIS

Highly uniform plasmas were produced in lengths of up to (40mm + 40mm) and widths of ~30μm (fwhm at 300eV). From an initial analysis of the 1keV and 2keV image data, we have estimated that the incident laser intensity along the length of the plasma varied by no more than 30%.

High quality data were taken for two ranges of incident intensity at $1.8\pm0.4 \times 10^{13}$ W/cm^2 and $4.5\pm1.2 \times 10^{13}$ W/cm^2. For each intensity range, time-integrated/space-resolved and time-resolved/space-integrated data was recorded in the axial direction. (Data taken on the transverse spectrometer was either time-integrated or time-resolved but always volume integrated). The intensity levels used are significantly higher than the optimised modelling would suggest: they were chosen from experimental observations on the ratio of the CVI/CV resonance lines. The incident laser intensity was increased until the ratio of the lines was ~1:1, which corresponds to the lower intensity range. Data was also taken for an incident intensity of approximately twice that level.

The data taken on the angular variation of the 182Å line shows no "beam" effect: no discernible profile emerged above the bulk spontaneous emission signal over a temporal field of view of up to 2ns after the peak of the incident laser pulse.

The irradiation of the electrostatically suspended 20μm C-fibers produced some promising results. In this preliminary attempt, we successfully irradiated ~10mm at either end of a ~30mm long fiber; we infer that the deviation of the central portion of the fiber was of the order of 30→50μm. It is hoped that further

refinement of this technique will improve this performance.

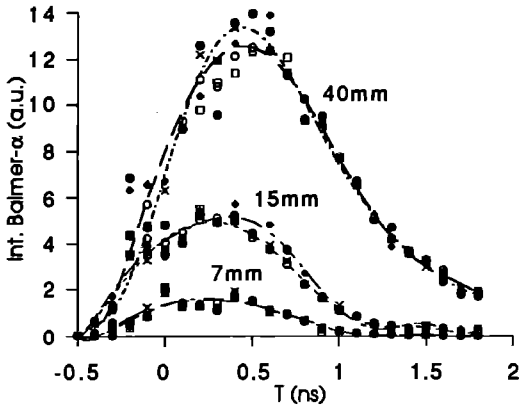

FIGURE 2 Spectrally integrated, line intensities of Balmer-α transitions as a function of time for 7, 15 and 40mm plasma lengths irradiated at 4.5±1.2 x 10^{13} W/cm^2. The dashed lines show two of the five polynomial fits at each length which were averaged for the purposes of gain determination.

Initial analysis has concentrated on an axial growth measurement from time resolved data on 7, 15 and 40mm plasma lengths and was carried out in the following way. For each of the three lengths, the spectrally integrated relative intensities of the Balmer-α and the n=4→2 Balmer-β (135Å) lines were determined in ~50ps intervals from 2-D densitometry of the streaked data, examples of which are shown in figure 2. Polynomial least squares fits, which were found to smoothly describe the temporal history of the Balmer-α and Balmer-β lines, were fitted to the data.

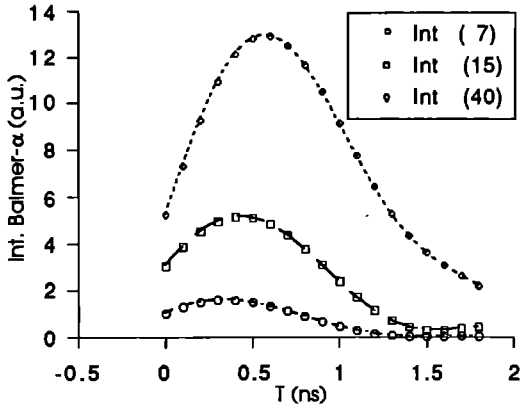

FIGURE 3 Average of five polynomial fits to data shown in figure 2 for plasma lengths of 7, 15 and 40mm irradiated at 4.5±1.2 x 10^{13} W/cm^2. The "data" points represent sample points in subsequent gain determination.

This process was repeated five times to ensure reproducibility of data interpretation (including definition of t=0 and limits of spectral integration). The small amount of scatter shown in figure 2 is an indication that the process is accurately reproducible. The final function used in the subsequent gain coefficient determination was an average of these five fitted temporal curves.

Reduced streak data and polynomial fits from 7, 15 and 40mm plasma lengths, irradiated at 4.5±1.2 x 10^{13} W/cm^2, are shown in figures 3 and 4 for the Balmer-α and Balmer -β transitions respectively.

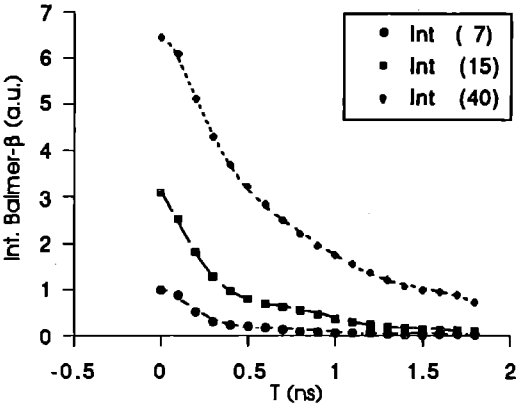

FIGURE 4 Average of five polynomial fits to five sets of spectrally integrated, line intensities of Balmer-β transitions as a function of time for 7, 15 and 40mm plasma lengths irradiated at 4.5±1.2 x 10^{13} W/cm^2. The "data" points represent sample points in subsequent gain determination.

Gain coefficients were determined, for both transitions, by fitting the polynomial intensity values of the three lengths, at a particular time, to the equation:

$$I(t) = \frac{E(t)}{g(t)}\left[e^{g(t)L} - 1\right]$$

where the recorded intensity at time t, I(t), is expressed in terms of the emissivity, E(t), gain coefficient, g(t), and plasma length, L.

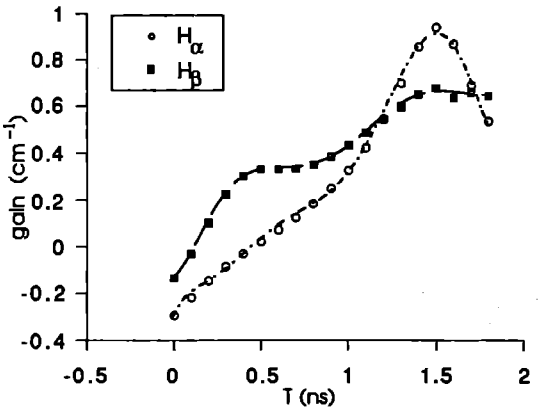

FIGURE 5 Gain as a function of time on the Balmer-α (H_α) and Balmer-β (H_β) transitions for an irradiance of 4.5±1.2 x 10^{13} W/cm^2.

Thus the variation of gain as a function of time was obtained for both the Balmer-α and Balmer-β lines and is presented in figure 5, with the fitted values of emissivity shown in figure 6. Data from the lower irradiance set is in the process of being

analysed in the same way: preliminary indications are of zero amplification on both lines.

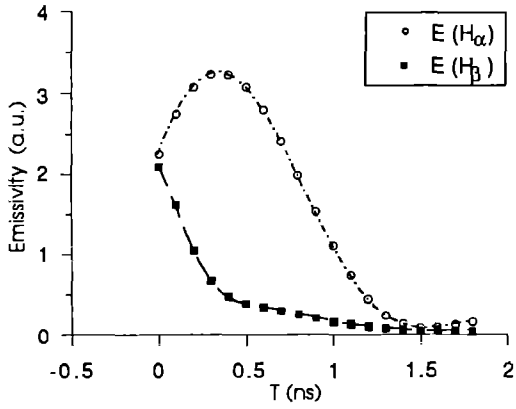

FIGURE 6 Fitted value of emissivity, E, for Balmer-α (H_α) and Balmer-β (H_β) lines as function of time for high energy shots.

CONCLUSION

The most obvious observation from the data is that the highest values of peak gL which were predicted by the modelling were not produced in this experiment. The highest value of gL for a 4cm plasma length was computed to be 16 assuming perfect uniformity and a trapping factor of $\varepsilon = 0.2$. If a classical model of trapping ($\varepsilon = 1.0$) is more appropriate, the computed value falls to 9.6. If non-uniformity of irradiation along the line focus reduces gain by a factor of about 2, as suggested by the analysis on page 47 ibid, gL would be about 5.

The relationship between the observed non-linearity of the intensity with length and the peak gL is complicated by the strong emission from non gain regions of the plasma as discussed earlier. Ideally, the curve of growth seen experimentally would be matched to that computed to deduce a peak gain value. The preliminary analysis here uses instead an apparent gain obtained from the non-linearity of the growth of intensity for lengths of 7, 15 and 40mm by forced fitting of the inappropriate ideal curve of growth for ASE in a homogeneous gain medium. The apparent gL deduced in this way for H_α has values $gL < 3.8$ at all times. It exceeds 2 (the level at which the non-linearity exceeds a factor of two and may be measured with some confidence) only at late times $t > 1$ns. The measured signals for the 7mm and 15mm plasma lengths are then at a small fraction of their peak and errors due to low level may be significant. Analysis of the errors of measurement has not yet been carried out and will be included in further work. Some evidence of such errors is seen in the apparent gain on H_β which is not expected to show gain theoretically and which shows apparent gain just exceeding 2 for times $t > 1$ns when signal levels for H_β are even more markedly reduced than for H_α.

The apparent gL is theoretically less than the peak gL and the difference increases for reducing apparent gL. With the analysis shown in fig 1, the apparent gL can be converted to its peak value. The apparent gL rises to 3.8 and the inferred peak value to 5.6. The appropriate enhancement factor for peak gain would be somewhat larger assuming $\varepsilon=1$, non-uniform irradiation and some lateral spreading of the plasma formation outside the optical line focus - all of which enhance the magnitude of the emission from the non gain region of the plasma relative to the amplified emission from the peak gain region.

Arguments can be advance therefore to show an upper limit of peak gL similar to the value of 5 estimated by the more pessimistic modelling. The effect of errors in measurement may however be significant and remain to be properly assessed.

Even if the peak gain is at the upper limit level, it is still much less than can be produced for similar intensity on slab targets with the GeXXIII laser discussed on page 3 ibid. This leads to the conclusion that whatever the subtleties of interpretation of the CVI slab target laser, its gain is not competitive with GeXXIII for producing XUV laser action at circa 20nm.

REFERENCES

[1] eg M H Key J Mod Opt **35** 575 (1988)

[2] eg A Carillon, M J Edwards, M Grande, M JdeC Henshaw, P Jaegle, G Jamelot, M H Key, G P Kiehn, A Klisnick, C L S Lewis, D O'Neill, G J Pert, S A Ramsden, C Regan, S J Rose, R Smith, and O Willi J Phys B **23** 147 (1990)

[3] N Tragin , M H Key, S J Rose J Mod Opt **37** 1 (1990)

[4] G J Pert and S J Rose App Phys B 51 (1990)

[5] D Neely, C L S Lewis, J Uhomoibhi, D M O'Neill, S A Ramsden, M H Key, B Shiwai, N Tragin and G J Tallents Ann Rep to LFC, pp 3-7 RAL-90-026 (1990)

[6] I N Ross, O Willi, G P Kiehn, R Corbett, C L S Lewis, L D Shorrock, M H Key, C J Hooker Appl Opt **26** 1584 (1987)

[7] C L S Lewis, J Uhomoibhi and J Jacoby ibid

[8] C L S Lewis, D Neely and A R Damerell Ann Rep to LFC, pp 73-76 RAL-90-026 (1990)

INVESTIGATIONS INTO THE EFFECT OF INCOHERENT OPTICAL SMOOTHING TECHNIQUES ON DRIVE UNIFORMITY

M. Desselberger, T. Afshar-rad, S. Viana, F. Khattak, P. Salamitou and O. Willi

Imperial College of Science and Technology, London SW7 2AZ.

Introduction and Background

It has been estimated (1) that in order to achieve the high degree of uniformity required for successful ICF implosions, a drive uniformity of better than 1% must be attained. This seems an especially daunting task in the light of the fact (excuse the pun) that focal spots generated from typical glass laser output beams exhibit intensity nonuniformities of 50% or more and reflects the importance currently being attached at RAL and elsewhere to optical smoothing techniques. A number of these have now been implemented, including Random Phase Plates (RPP), Induced Spatial Incoherence (ISI) and Smoothing by Spectral Dispersion (SSD). In the past decade, there has been much theoretical work on thermal and other instabilities which could be seeded by laser nonuniformities (for a review of some of these, see 2). Although some of the smoothing techniques are generating encouragingly uniform focal spot profiles, the question of how hydrodynamically stable the resulting drive is and how filamentation and backscattering thresholds might be affected remains very much open. Uniform focal spot profiles, as measured by time-integrated diagnostics, do not necessarily imply uniform drive symmetry due to the time-dependent nature of the smoothing process and of plasma dynamics. Recent theoretical efforts (3,4) have sought to address various aspects of this question. Very little pertinent experimental data on this crucial issue exists.

In a series of experiments performed recently at RAL (November, 1990 and January, 1991), we have experimentally examined the effect of the RPP and ISI smoothing techniques on drive uniformity. This was done using a novel technique, recently developed by our group at RAL, which provides highly spatially and temporally resolved information at densities close to the ablation surface and is thus ideally suited to such investigations.

Experimental Investigations

For a description of the technique and the experimental arrangement employed, see RAL Annual Report (1990), p. 30 or (5). Essentially, a spherical multilayered mirror is used to provide quasi-monochromatic images with high spatial resolution. A backlighter is used to generate an XUV probe beam (effectively monochromatic, due to the mirror) which probes the main plasma at densities very close to the ablation surface.

In the November experiment, the investigations centered on the comparison of ordinary coherent irradiation to RPP-type irradiation and examined possible scalelength dependences of the nonuniformities observed in the supercritical plasma blow-off. The detector used employed state-of-the-art microchannel plate gated imaging technology and demonstrated the effectiveness of this class of detectors in obtaining high quality, highly temporally resolved (150ps) 2-D images. Fig. 1 shows one such image, providing the first direct experimental evidence of density nonuniformities present near the ablation surface. The significance of this is discussed in the 1990 Annual Report article. Despite the high spatial resolution achieved with this system (demonstrated resolution: 0.8μm), the limiting factor was found to be the resolution afforded by the microchannel plate detector (50μm, even with end-spoiling).

To achieve even higher spatial resolution, a slightly different approach was taken in the January experiment. Although the experimental arrangement remained the same, the detector employed was Kodak VUV-101-01,7 film in the image plane with time resolution achieved by using a short pulse (≈100ps) backlighter. The film resolution is at least five

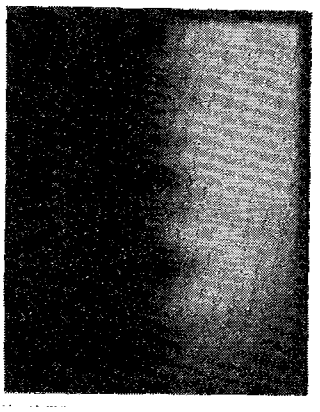

Figure 1:

Gold wire irradiated at $3x10^{13}$ Wcm^{-2}. Nonuniformities are clearly visible. This frame was taken 2.3ns after the peak of the drive pulse. (Laser incident from the right, no optical smoothing)

times better than that of the microchannel plate detector. The drawback, of course, is that the light arriving in the image plane cannot be gated as before, with the danger that strong self-emission from the target at the beginning of the pulse could expose the film completely. Upon testing this new method, however, it was found that with an appropriately small pinhole in the image plane of the backlighter target, the level of self-emission from the main target could easily be reduced to an acceptable level. With this prerequisite satisfied, the images obtained on film not only have higher spatial resolution but also provide records of both the self-emission from the target in the early stages of the irradiation and of the backlit blow-off plasma at later times (when the level of plasma self-emission is too low to expose the film). Thus the plasma is recorded at early times (< 50ps) by self-emission and the same plasma is recorded at later times by delayed short-pulse backlighting (in our case, the backlighter was timed to arrive at between 1-2ns after the peak of the main pulse). This enables correlations between structure in the early plasma and in ensuing blow-off to be established.

A further difference in the January experiment was that the main target was irradiated from both sides, allowing two types of irradiation to be compared on the same shot. Fig. 2 shows one such image, where tight-focussed and defocussed ISI irradiation are being compared and show dramatic differences. The structure in the blow-off (backlit plasma) can unequivocally be traced back to structure in the early plasma (self-emission).

Returning to the question of how smoothed laser beams affect drive symmetry, it must be re-emphasized that even ISI- or SSD- smoothed laser beams contain the ≥50% intensity nonuniformities found in ordinary coherent beams on timescales short compared to the coherence time. It can be stated, from the results of these investigations, that structure in the blow-off plasma persists despite the use of these techniques, and is the result of nonuniformities in the plasma generated early in time by hot/cold spots in the intensity profile. At early times the plasma is cold and has very fast hydrodynamic response timescales (comparable to the laser coherence time, in our case this was 2ps). Also, the capacity for thermal smoothing of intensity nonuniformities is very limited at this stage due to the close proximity of the critical and ablation surfaces. The plasma responds to these differences in the mass ablation rate at different points and the nonuniformities thus generated persist in the blow-off. Exactly why they persist in the blow-off is a different issue - the nonunifomities seeded at early times may be subject to any of the large number of proposed instability mechanisms which apply in the supercritical density region. What can be said is that since at early times virtually no smoothing can take place, this effect is expected to be, at least to some extent, independent of target material. The target materials used in these investigations were Gold and Copper. The Copper targets appeared to exhibit less nonuniform structure, but this could be due to opacity and self-emission level differences, to which the technique is very sensitive.

Figure 2: VUV 101 film image clearly showing small scale nonuniformities. Conditions are the same as in Fig. 1, except that ISI smoothing is being used. The early time self emission, aswell as the late time backlit plasma are captured on the same shot.

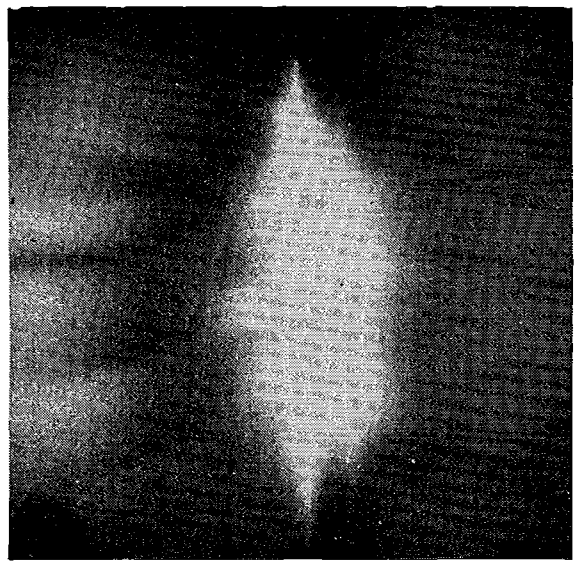

In order to establish conclusively that the short-scale ($\approx 10\mu m$) nonuniformities observed are indeed due to diffraction-limited laser intensity nonuniformities ($\approx 10\mu m$ in our case, since f/10 lenses were used) - even if these only exist at high levels at the beginning of the pulse before any smoothing has taken place - a focal spot devoid of such short scale structure must be generated. To do this, an f/40 lens was used with the beam apertured to one half of its original width, giving a diffraction-limited scale for interference structure of $80\mu m$. The beam energy was adjusted accordingly to give the same irradiance in the focal plane. As expected, no structure was observed in the self-emission or in the backlit blow-off (100ps backlighter arriving 2ns after the peak of the drive pulse) at scalelengths below the diffraction-limited value ($80\mu m$).

Since f/40 lenses pose alignment stability problems (and other practical problems) in ICF implosion-type arrangements, another approach was investigated. A plasma was preformed using burn-through foils to indirectly drive (with x-rays) the target before interacting with the optical drive. The theory in this case is that despite the nonuniformity of the optical drive on the burnthrough foil, the radiation field generated is almost perfectly isotropic and will produce a uniform plasma. When the optical irradiation interacts with this preformed plasma, it is no longer interacting with a cold solid but with a plasma (hydrodynamic timescale $\approx$100ps, and in which the ablation and critical density surfaces are seperated by some tens of microns) which will not be able to respond and will smooth out the short timescale (2ps), large amplitude ($\approx$50%) intensity variations in the laser irradiation.

The x-ray drive did indeed produce a uniform plasma, as was evident from the lack of structure in the self-emission. Further, no structure was visible in the self-emission produced by the interaction of the optical beam with the preformed plasma, nor in the blow-off framed over 100ps by the short-pulse backlighter. In the investigations involving indirect drive, only Copper targets were used. This result immediately suggests that a possible scenario for the uniform implosion of ICF targets is to use a double-pulse-type system where the first pulse drives a burn-through preformation stage, and the second pulse interacts directly with the preformed plasma. A double-pulse is within the capability of glass laser systems, where amplifiers do not run at gain saturation levels.

Summary and Conclusions

The ability of the RPP and ISI smoothing techniques to produce uniform drive has been investigated using a novel technique providing highly temporally and spatially resolved images at densities close to the ablation surface. It was found that despite the uniform time-averaged intensity profiles generated with these smoothing techniques, the large amplitude nonuniformities existing at early times seed nonuniformities at the ablation surface which, at later times, persist in the blow-off plasma. The nonuniformities in the superdense blow-off plasma could be directly correlated to these early-time structures. The use of indirect drive to preform a plasma with which the optical beam then interacts appears to be an effective way of combating these problems.

References

1. S.E. Bodner, J. Fusion Energy 1, 221 (1981).
2. M.G. Haines, Phys. Rev. Lett. 47, 917 (1981) and the references therein.
3. I.R.G. Williams, G.J. Rickard and A.R. Bell,'Investigations of Pressure Nonuniformity in Laser-Irradiated Targets using Incoherent Optical Smoothing,' Laser and Particle Beams 9, No2 (1991), in print.
4. D.F. DuBois, B. Bezzerides and H.A. Rose, 'Collective Instabilities of Many Overlapping Laser Beams with Finite Bandwidth,' Los Alamos Nat. Lab. (1991) preprint.
5. M. Desselberger, T. Afshar-rad, S. Viana, F. Khattak and O. Willi, 'Time-Resolved Imaging at 130 Angstroms with Submicron Spatial Resolution,' Applied Optics (June 1991 issue), in print.

MEASUREMENT AND ANALYSIS OF RADIATION TRANSPORT IN RADIATIVELY HEATED FOILS

J. Edwards, M. Dunne, L. Gizzi, O. Willi
Blackett Laboratory, Imperial College of Science, Technology and Medicine, London SW7 2BZ, U.K.

S.J. Rose
Rutherford Appleton Laboratory, Chilton, Didcot, Oxon. OX11 0QX U.K.

C.A. Back, C. Chenais-Popovics
Ecole Polytechnique, Laboratoire PMI, Palaiseau 91128, Cedex, France

1. Introduction

The importance of radiation transport both as a mechanism for the transfer of energy under certain laser and target conditions and for spectral analysis is well known and has been discussed in a number of articles (see for example 1-11). Here we present experimental measurements of radiation transport in thin plastic targets in which radiation transport is predicted to dominate the energy transfer. Planar foil targets were heated directly by soft X-rays emitted through the rear of a second laser heated high Z layer deposited on a thin plastic substrate. First, the soft X-ray emission from the rear of the high Z foil was investigated as a function of target design. Then a suitable target was used as a source of soft X-rays for heating a sample foil. The soft X-rays transmitted through the samples were measured using time resolved XUV spectroscopy in the 10-70A spectral wavelength region. The experimental conditions have been simulated with a 1D radiation hydrodynamics code and atomic physics data has been calclulated with a multi-configuration Dirac-Fock code for spectral analysis.

2. Experimental Arrangement

Six frequency doubled RPP smoothed beams of the VULCAN glass laser at the Rutherford Appleton Laboratory were used in a cluster configuration to irradiate a thin high Z layer (0.1μm Au or 0.2μm Bi) which was supported on a thin plastic substrate typically 1μm thick (hereafter the source foil). The laser pulse length was typically 600ps and the focal spot typically 500μm. The soft X-rays emitted through the rear of the target were then used to heat a second, plastic foil (hereafter the sample) which was orientated parallel to the source target and was separated from it by approximately 230μm. The soft X-rays transmitted through the second foil were analysed using a time-resolving XUV spectrometer with spectral and temporal resolutions of approximately 0.2A and 100ps respectively. Absolute time-resolved and time-integrated measurements of broad band spectral fluxes from the rear of the targets were also made using filtered vacuum photodiodes.

3. Modelling

3.1 Radiation Hydrodynamics

The experimental conditions are simulated using a multi-group radiation transport model coupled to the 1D Lagrangian hydrodynamics code MEDUSA.[12] The radiation transport model uses group-averaged Planck mean opacities calculated from a screened-hydrogenic average-atom (AA) calculation which is performed in-line with the hydrodynamics and assumes L.T.E.. This assumption was found to be a good approximation during most of the simulations when a time-dependent AA model based on XSN[13] was used to calculate level occupation probabilities. The behaviour of the source target is not calculated. Instead, the experimentally measured spectrum emitted from the rear of the source foil is used in the calculation to heat the sample.

3.2 Spectral Analysis

For spectral identification and analysis a multi-configuration-Dirac-Fock code is used to calculate atomic physics data (energy levels and oscillator strengths).[14] Configuration abundances for particular plasma conditions are then calculated by solving Saha's equation (i.e. assuming L.T.E.). b-b cross-sections are then calculated according to

$$\sigma(\nu) = (\pi e^2/mc)\ f\ \phi(\nu)$$

where f is the oscillator strength for the transition and ϕ is the line shape function. A radiative transfer algorithm is currently being developed for the prediction of absorption spectra.

4. Experimental Results

4.1 Photodiode Measurements

Measurements were made on bismuth layers 2000A thick deposited on 1 μm plastic substrates for laser irradiances between 1 and 5 10^{14} Wcm^{-2}

with a time-resolving XUV photodiode. The diode was positioned at an angle of 50° to the target normal. It was found that the soft X-ray pulse emitted to the rear of the target closely followed the laser pulse. In addition, a preliminary analysis suggests a conversion efficiency in the backward direction of approximately 7.5 $\pm$2% with no obvious dependence on the laser irradiance in the experimental range. This figure was obtained assuming a radiation field isotropic in the half plane at the rear of the target. The $\pm$2% is to account for the scatter in the data. This conversion efficiency corresponds to effective radiation temperatures in the range of 100-130 eV at the rear of the target. These values are in reasonable agreement with time integrated diode measurements taken at the same time and with other diode measurements taken under similar laser conditions without the use of RPP smoothing where a value of around 12% was found.[15,16] It should be noted that the 7.5% figure is determined as a fraction of the total laser energy delivered by the laser and does not take into account any losses due to diffraction from the phase plates.

It was found that the high Z layer thickness had a significant effect on the soft X-ray conversion efficiency. Measurements were made on targets with three different thicknesses of gold deposited on 1μm CH substrates. While the conversion efficiencies for 1000A thick gold layers were similar to those for bismuth with the same ρr at 7.5%, the value for thinner 500A targets increased to around 12% while that for thicker 2000A targets decreased to less than 4%. This is believed to be due to incomplete burnthrough of the Au layer as ρr is increased.

The target design used for the source foil was 2000A bismuth on 1μm CH. Although this did not produce the best conversion efficiency to soft X-rays, mass ablation rate measurements strongly suggest that the targets would not burn through during the laser pulse. This is supported by the increase in the conversion efficiency with thinner high Z layers. This should ensure that the sample foil was heated only by soft X-rays. Laser light transmission was not measured in these experiments and should be investigated for future work so that source target design can be optimised.

4.2 XUV Spectra

Figure 1 shows time-resolved XUV spectra observed for several different thicknesses of CH sample foil. The most noticeable features in the spectra are the sharp edge feature at around 45A, clear absorption structure below 45A particularly for the thinner foils and shifts of the edge feature towards shorter wavelength (higher energy) with time (by about 5-10eV) also for the thinner foils. For the 6μm sample, there appears to be no noticeable shifting of the edge feature with time. However, comparison with a reference spectrum filtered with a cold 2μm thick CH filter shows that the feature for the 6μm target is shifted by about 5-10eV to the red side of the cold edge position. The cold edge position corresponds very closely to that observed for the edge feature in the reference spectrum except at early times and is expected to be due largely to the instrumental filters which protect the mirrors and grating. The optical depth of the sample foils can be calculated as a function of time from the ratio of the observed spectrum to the reference spectrum. This process is currently underway. Here, initial estimates of the jump ratio (defined as the ratio of the intensity on the low energy side of the edge to that on the high energy side) at the edge feature are given so that effects due to the samples can be assessed.

For the source foil, the jump ratio is approximately 7 at early times and has reduced to 4-5 by the peak of the pulse. The values found when a sample foil is used are generally larger. A value of around 10 is found for a 1μm target for most of the time. This value decreases towards approximately 5 well after the peak of the pulse. In contrast, for a 3μm foil, the ratio is measured to be around 20 at early times, decreasing to 10-15 at later time. Because of the low signal for the 6μm case, a lower limit for the jump ratio of greater than 15-20 only could be measured. Therefore, it is clear that the presence of the sample foil has a direct effect on the jump ratio near the edge feature.

5. Discussion

The heating of a sample can be described as follows. The soft X-rays from the source are initially incident on the cold target material and are absorbed close to the surface over a distance of approximately a photon mean free path and a temperature gradient develops. As the foil becomes heated, preferentially at the front, it ionizes and becomes less opaque to the incident radiation which then propagates further into the target where it is absorbed in the cooler more opaque regions. The photon mean free path is a strong function of plasma conditions and photon energy so that the spectrum of the heating radiation is also important. In addition, we have found that in these circumstances the absorption of radiation emitted in the foil contributes significantly to the foil heating. Figure 2 shows predicted temperature profiles near the peak of the radiation pulse for 1μm and 6μm CH targets for an X-ray conversion efficiency from the source foil typical of the values measured by the photodiodes and corresponding to a radiation temperature of 100eV at the sample. It

is clear that the observed spectrum will be representative of a range of plasma conditions which will depend at least partly on the foil thickness.

It has been shown previously that while the overall features of the observed spectra are reproduced fairly well by the simulations, the small blue shift of the edge feature of just a few eV is not predicted.[9] The possible explanations for this are discussed below.

It is possible that the foil heating is considerably overestimated either due to an exaggeration of the flux from the source foil or to the treatment of the radiation hydrodynamics and that the edge feature is due to a bound-free (b-f) absorption edge resulting from partially ionized carbon ions. Figure 3 shows the approximate positions of b-f edges for all carbon ions in their ground states taking into account continuum lowering using the Stewart-Pyatt approximation.[17] The ionization energies were calculated from the MCDF code. The horizontal bars result from the range of continuum lowering calculated for plasma densities typical of those predicted to exist in the foils near the peak of the pulse (0.1-0.01 g/cc). For b-f absorption to be important in the spectra in the region of the experimentally observed edge feature, a significant fraction of the plasma would have to exist as neutral atoms and/or singly ionized ions since the b-f absorption features of all other ions are expected to exist at wavelengths below about 40A. The fraction of the plasma ions in a neutral or singly ionized state, necessary to produce the observed jump ratios of around 2-4 (found after taking into account the reference spectrum) can be estimated as follows. Approximately 0.1μm of cold material at solid density is required to produce a jump ratio of 2. Therefore, the fraction, f, of a sample foil, of initial thickness rμm at solid density, required to exist as neutral atoms or singly ionized ions to produce this jump ratio is approximately $f \sim 0.1/r$. Figure 4 shows carbon ion fraction calculated as a function of temperature using the Saha equation for a density of 0.01g/cc, a typical value for a 1μm sample near the peak of the pulse . For a 1μm foil $f \sim 0.1$, which, according to figure 4, can only be achieved for temperatures below about 10eV. Indeed, for the predicted temperatures of around 50eV the only significant b-f absorption features are predicted to be due to He- and H-like ions which exist at wavelengths below 35A. Therefore, for photoionization to be a viable explanation of the observed spectral characteristics of the thinner foils, the plasma heating would have to be overestimated in the modelling to a gross extent and this explanation is then made to seem very unlikely.

This is not necessarily the case for the thicker 6μm foil particularly at early time when a significant portion of the foil remains unheated (< 10eV) and in which larger temperature gradients exist. The small, approximately constant, red shift of the edge would then presumably be due to continuum lowering. However, considering the range of plasma conditions predicted to exist during the interaction, it would be surprising if an approximately constant red-shift resulted. Therefore, although from figures 2, 3 and 4 it is clear that b-f absorption in the region of the experimentally observed edge feature will be important, it is not expected to account for the small, approximately constant, red-shift.

Hitherto, we have not considered the effect of bound-bound (b-b) transitions on the spectra. Because of the large b-b cross-sections, absorption features due to b-b transitions of even the less abundant ion species and configurations in the plasma will be important and strong transitions will be observed over a large range of plasma conditions. This will be particularly important for the thicker foils used in the experiment not only because of the larger temperature gradients expected to exist but also because of the large optical depth. Figure 5 shows gf values of some 1s->np transitions between 30 and 45A calculated using the MCDF code for carbon ions. A significant number of transitions exist in the region of the cold carbon K-edge. Figure 6 shows traces taken across wavelength at three different times from a spectrum obtained from a source target (0.1μm Au on 1μm CH) when no sample target was present. (This data was obtained using a higher magnification streak camera than that of figure 1). The approximate positions of some of the 1s-2p and 1s-3p transitions are marked demonstrating evidence of absorption features due to at least He- and H-like carbon ions in the plastic support, consistent with figures 2 and 4. Absorption from less highly ionized species will become more important when samples are used since these must attain lower temperatures than the plastic support of the source target. Although more detailed predictions of the effect of b-b transitions on the absorption spectra require a detailed radiative transfer calculation for the target conditions and gradients, it is clear from figures 5 and 6 that b-b absorption is important in the spectral region just above (in energy) the observed edge feature. In addition, because of the comparatively low temperatures and high densities ($T \lesssim 30$eV, $\rho \sim 0.1$g/cc) predicted to exist towards the rear of the 6μm targets, b-b absorption due to significant fractions of neutral atoms and/or singly ionized ions may contribute substantially to the approximately constant red-shift of the observed edge feature and to the small blue-shift of the edge

STREAK RECORDS OF XUV BISMUTH SPECTRA TRANSMITTED THROUGH PLASTIC FOILS OF DIFFERENT THICKNESSES

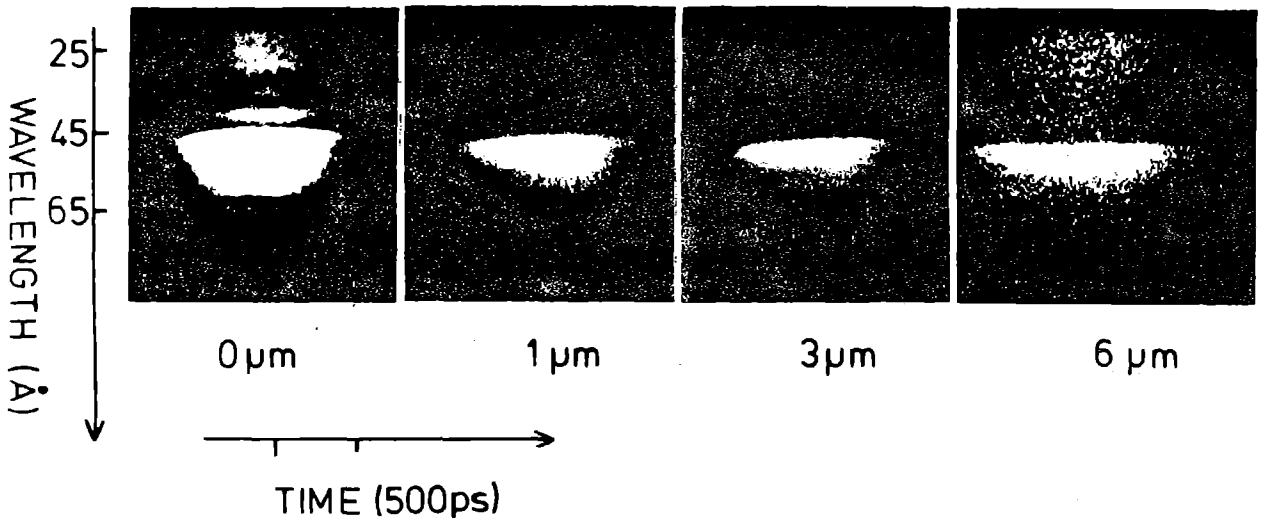

Figure 1. XUV streak data for radiatively heated CH foils.

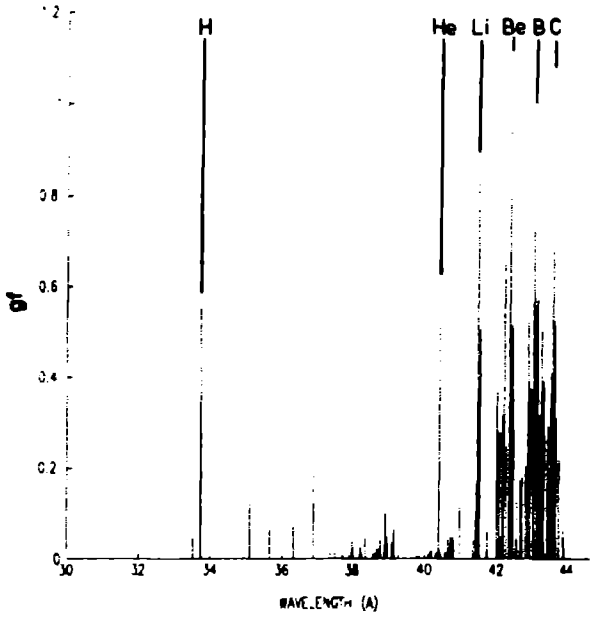

Figure 5. gf values vs wavelength for 1s-np transitions of carbon ions. 1s-2p transitions are marked by ion stage.

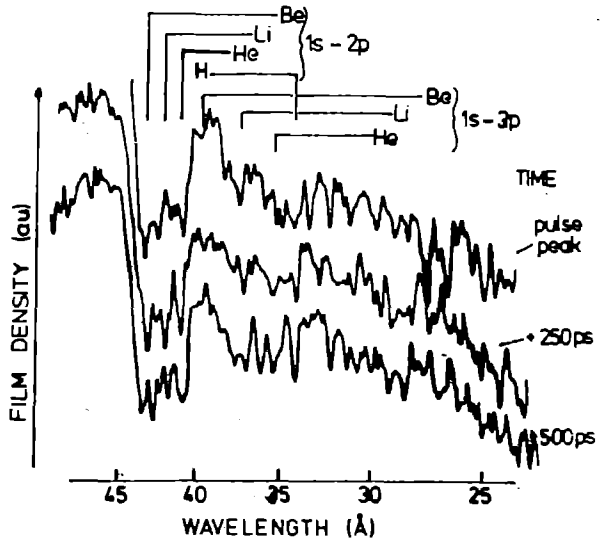

Figure 6. Traces taken across streak data from a source target.

observed for the thinner foils as they become heated and ionized. The calculated wavelengths of these transitions are shown in figure 5 and are very close to the wavelength of the cold carbon K-edge reported in the literature, 43.7A.

6. Conclusions

Radiation transport through radiatively heated plastic foils has been investigated using time-resolved XUV spectroscopy in the sub-KeV energy region. The experimental conditions were simulated with a multi-group radiation hydrodynamics code and global features of the observed spectra were reproduced fairly well by the modelling. However, the small blue-shift with time of the observed edge feature for thinner foils and the approximately constant red-shift of the feature for a 6μm sample were not predicted. It is expected that this is largely due to the omission of b-b transitions in the modelling. Future experiments must include direct measurements of target gradients and conditions so that our ability to model the energy transport in the samples and to predict spectra under these conditions can be better assessed.

References

1. D.G. Colombant et al., Phys. Fluids, **18**, 1687, (1975).
2. R.W. Lee, J.Q.S.R.T., **27**, 87, (1982).
3. R.W. Lee, J.Q.S.R.T., **27**, 243, (1982).
4. D. Duston et al., Phys. Rev. **A27**, 1441, (1983).
5. D. Duston et al., Phys. Rev. **A31**, 3220, (1985).
6. T. Mochizuki et al., Phys. Rev. **A36**, 3279, (1987).
7. J.M. Salter et al., J.Q.S.R.T., **39**, 139, (1988).
8. C. Chenais-Popovics et al., Phys. Rev. **A40**, 3194, (1989).
9. J. Edwards et al., Europhys. Lett., **11**, 631, (1990).
10. R. Sigel et al., P.R.L., **65**, 587, (1990).
11. J. Bruneau et al., P.R.L., **65**, 1435,(1990).
12. J.P. Christiansen et al., Comp. Phys. Commun., **7**, (1974).
13. W.A. Lokke and W.H. Grasberger, LLNL report, UCRL-52276, (1977).
14. I.P. Grant et al., Comp. Phys. Commun., **21**, 207, (1980). B.J. McKenzie et al., Comp. Phys. Commun., **21**, 233, (1980).
15. C.A. Back et al. these proceedings.
16. S.J Davidson Priv. comm.
17. J. Stewart and K. Pyatt, Astrophys. J., **144**, 1203, (1966).

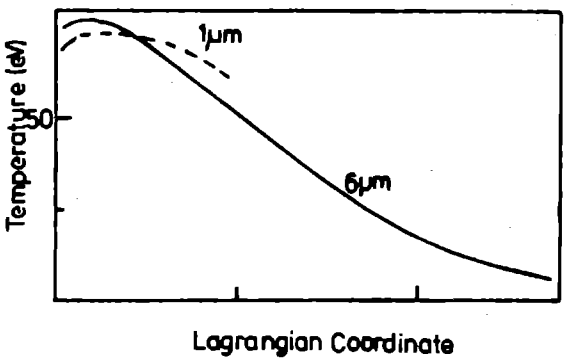

Figure 2. Predicted temperature profiles for 1μm and 6μm targets.

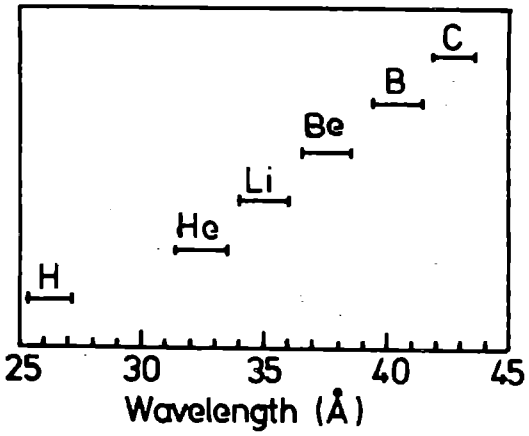

Figure 3. b-f edge wavelengths for carbon ions.

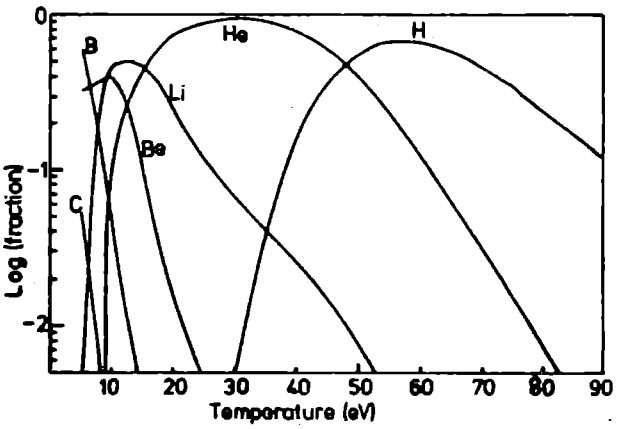

Figure 4. Carbon ion fractions vs temperature at 0.01 g/cc.

Sub-keV X-ray point projection absorption measurements

S.J.Davidson, D.Neely, C.L.S.Lewis and D.O'Neill
Queens University Belfast

Introduction

Point projection K-shell spectroscopy using Bragg crystals has become a well established technique[1,2], which has found use in both high density plasmas heated by X-rays[3] and low density plasmas relevant to X-ray laser designs[4]. In particular the 1s-2p spectrum has been shown to be a very sensitive diagnostic of ionisation in aluminium plasmas.

K-shell spectroscopy of lower -Z elements than aluminium or L-shell measurements of similar -Z elements require the technique to be extended to softer photon energies. The feasibility of such measurements has now been demonstrated for the particular cases of K-shell carbon and L-shell aluminium.

Experimental layout

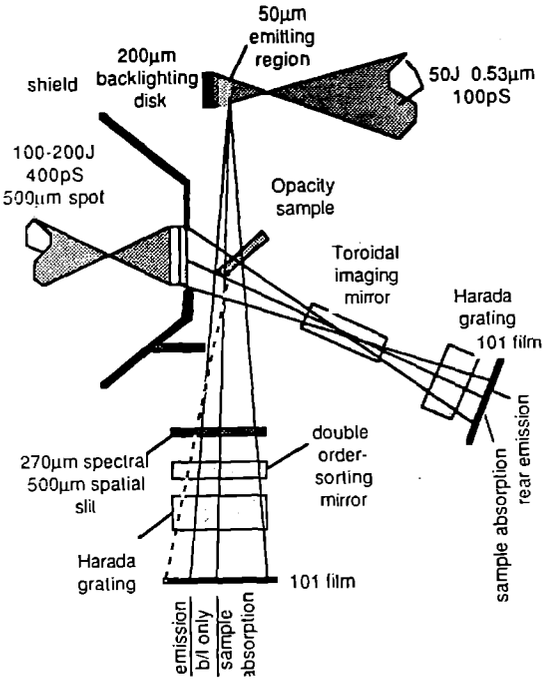

Fig 1. Experimental layout

The material of interest , in this case carbon or aluminium , was heated by soft X-rays emerging from the back of a 500Å gold foil irradiated by a VULCAN laser beam providing 100-250J of 0.53µm laser energy in 400 pS. X-rays emerging from the rear of the foil pass through a 0.5 µm parylene 'N' foil used as a physical support for the gold. Time resolved total flux measurements made using a calibrated X-ray photodiode indicated that the equivalent flux typically corresponded to a blackbody temperature of 100-120eV.

Spatial emission from the rear of the heating foil, was measured using a toroidal imaging mirror[5] coupled to a Harada[6] 2400 l/mm flatfield grating using calibrated[7] Kodak 101 film . The time integrated heating spectrum (fig. 2) contains 1s-np absorption from the parylene support foil. The degree of ionisation is similar to that of a uniform sample at 30eV and 0.02g/cc. This is not inconsistent with hydro simulations which suggest that the plastic temperature is spatially and temporally dependent reaching a peak temperature of 50eV.

Time integrated absorption by the less ionised heated sample seen in the lower part of the spectrum provides 1s-2p absorption lines at softer energies than the more ionised carbon at the rear of the heating foil.

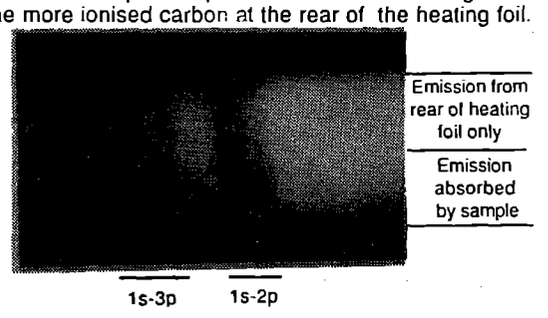

Fig.2 Toroidal spatially resolved spectrum of a heating foil half covered by a less ionised heated carbon sample

K-shell carbon absorption

Spatially resolved point projection absorption measurements of the heated sample used a short duration backlighter generated by focussing a 50J , 100pS, 0.53µm VULCAN laser beam onto a 200µm disk. The emitting region extended 50µm in the direction of the disk normal and extended 200µm vertically. The FWHM of the emission was measured to be 150pS.

This source positioned 32mm behind the sample projected a shadow of the sample onto the slit of a second 2400l/mm flatfield grating (figure 3.) The 1s-np absorption from a 3000Å parylene 'N' foil at 45° to the line of sight clearly shows the ionisation gradient as the distance from the heating foil increases.

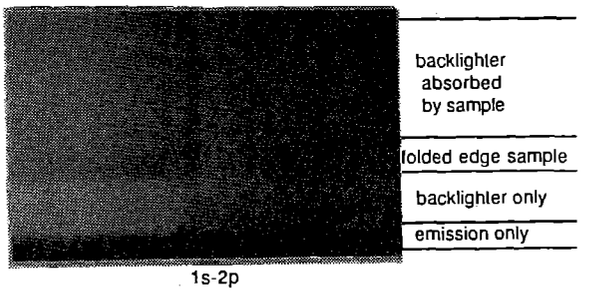

Fig 3. Typical point projection image of a carbon foil

Transmission of a typical carbon foil at distances of 180, 320 and 450µm from the heating foil are shown in figure 4.

Hydro calculations suggest that the the hottest region of the sample gets to 25eV with a density of 0.004g/cc. A calculation corresponding to two regions at 10 and 30 eV and 0.001g/cc shows that the qualitative features agree (Fig.5). The spectrum has marked similarities to previously reported aluminium K-shell measurments[8], in that the lack of strength in the 1s-2p lines is probably due to unresolved saturated absorption. It is interesting to note that the 1s-3p lines again sit on top of what appears to be a continuum lowered edge, but which may in reality, like the aluminium case, be many unresolved low probability transitions.

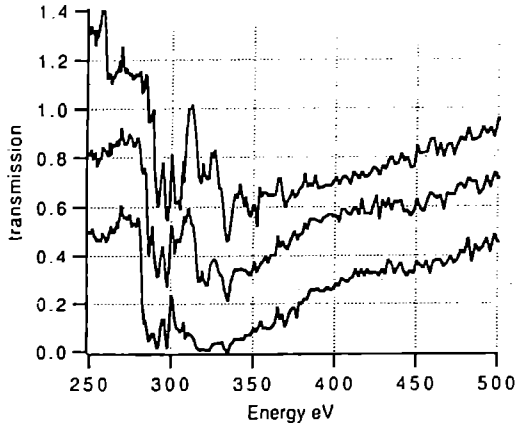

Fig 4 Transmission at various distances from heating foil (note top two graphs are shifted up for clarity by a transmission of 0.4 and 0.2 respectively)

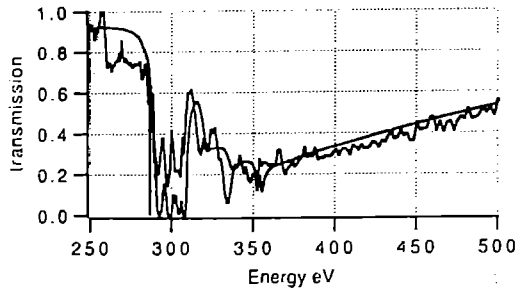

Fig 5 Comparison of hottest region of sample with calculated opacity

In terms of quantitative agreement there is some evidence that the carbon is less ionised than simple hydro calculations would suggest. More detailed modelling of both the burnthrough foil and the sample conditions are being carried out and will be reported at a later date.

Previous time resolved carbon edge measurements using much thicker carbon foils[9] found that the edge did not move as expected. These results suggest that the apparent edge was the saturated onset of the 1s-2p absorption lines. This would also explain the measured shift moving either side of the cold edge.

L-shell aluminium absorption

Measurements in the 70 eV photon region require the use of a 1200l/mm grating with a double reflection filter[5] to reduce the effect of higher order contributions.

The current experimental geometry was optimised to spatially image several millimetres of sample foil so that ionisation gradients due to the geometric coupling factor could be measured. The disadvantage of this approach is that the emitting area of sample is a factor of 30 greater than that of the backlighting source.

As the sample temperature increases, self emission eventually becomes comparable with the backlighter emission, providing an upper limit to the temperature at which absorption measurements can be made. Typical backlighter brightness and current target sizes appear to limit absorption measurements to sample temperatures of 10-15eV before sample self emission dominates. Typical measurements (Fig. 6) show that for the most ionised measurement (top graph) the edge has shifted to 80eV and distinct 2p-nl transitions are apparent.

Effects of ionisation gradients along a single foil are shown in figure 7. Also plotted is a calculation for aluminium at 10eV and 0.02g/cc. This comparison is only intended to indicate the degree of ionisation implied by the absorption spectrum. Uncertainties in the absolute value of the aluminium transmission could be as large as +/- 50% due to second order corrections and subtraction of the large self emission signal

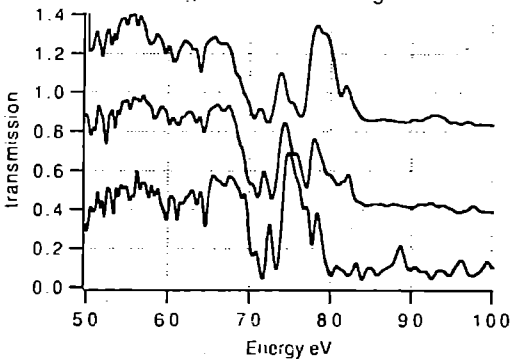

Fig 6Aluminium absorption spectrum (Note top two graphs shifted up by 0.4 and 0.8 respectively for clarity)

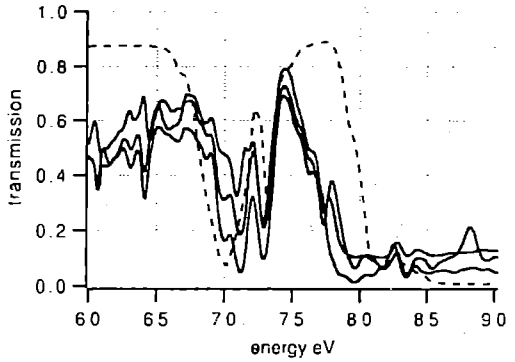

Fig 7. Comparison of theory and calculation for L-shell aluminium

Measured emission lines correspond to 2p3d and 2p-3s transitions ion-stages IV,V and VI of aluminium. Detailed comparison of the of the emission and absorption spectra with calculations requires temperature gradients to be properly modelled. Unlike the carbon case where the 1s-2p features stand alone allowing more ionised features to be seen in the presence of less ionised features, the aluminium edge for less ionised material will obscure higher energy edges of more ionised material

Conclusions

Feasibility of sub-keV absorption spectroscopy has been demonstrated. Ionisation gradients due to the heating geometry show that sub keV K and L spectra show promise in terms of being a diagnostic of plasma conditions. Higher temperature measurements and the use of tamped samples will become more feasible if the size of the sample is reduced to decrease self emission.

Detailed hydro simulations of the current geometry and calculations of NLTE effects in order to obtain more quantitative comparisons are in progress and will be reported at a later date.

References

[1] C.L.S.Lewis and J.McGlinchey,Opt. Comm. ,53, 179 (1985)
[2]S.Davidson C.C.Smith, J.M.Foster, K.A.Warburton, S.Rose, Appl. Phys. Letts. 52, 10 (1988)
[3]J.Abdallah Jnr.,R.E.Clark J.Appl. Phys. 69, 23, 1991
[4] D.O.Neill,C.L.S.Lewis,D.Neely et al. Phys Rev. A 40 330,1989
[5]IC.L.S.Lewis,D.Neely and A.R.Damerell "Reflection filtered optics..." 1990 RAL Annual Report
[6]N.Nakamo,H.kuroda,T.Kita,T.Harada,Appl.Opl.,23,2386 (1984)
[7]D.Neely ,Private Communication
[8]S.J.Davidson, c.L.Lewis, D.O'Neill "K-shell absorption spectra of aluminium" Proceedings of 19th ECLIM, Madrid 1988
[9]J.Edwards,1990 Conference on dense plasma physics, Sarasota ,Florida

DENSITY MEASUREMENTS OF A CAPILLARY PRODUCED PLASMA

W.J. Blyth, N.C. Woolsey, J.S. Wark
Clarendon Lab, Oxford

N. Edison, P. Young, R.W. Lee
LLNL, Livermore, California 94550

A. Zigler
Soreq Nuclear Research Centre, Yavne, 70600, Israel

Introduction

In assigning temperatures and densities to laser produced plasmas the main tool is X-ray spectroscopy. Experimental spectra are compared to spectra which are produced by computer simulation codes such as RATION[1] and a best fit procedure is used. These codes are purely theoretical and have no experimental verification mainly because of the difficulty in producing a single temperature uniform density plasma to compare with the codes.

Zigler and co-workers have developed a capillary discharge device which is capable of producing plasmas of densities 10^{19} -10^{22} cm^{-3}, 12 x 0.5 mm in size and ambient temperatures of around 1 eV.[2] It works by discharging a kilovolt charge from a capacitor through an insulating material. This discharge is violent enough to ablate material from the walls of the insulator creating a low temperature plasma which expands out through the slit producing a slab of plasma of the dimensions of the slit (see fig 1).

This device was studied at LLNL in August 1990 to test the density uniformity and scalelengths that could be acheived. Density measurements were made using interferometry and two-dimensional interferograms were produced which give information on the spatial density distribution.

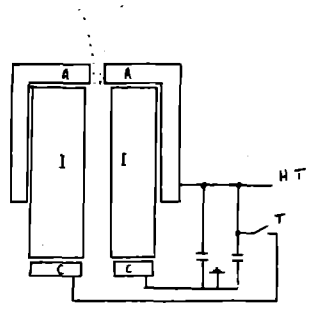

Fig.1 The Capillary Device (side view)
T: Trigger C: Cathode
I: Insulator (teflon) A: Anode

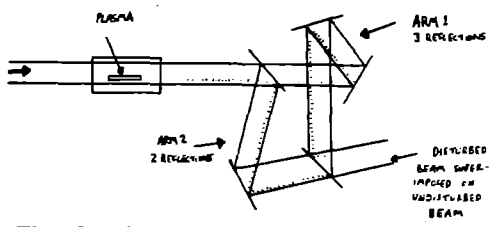

Fig. 2 The Interferometer

The capillary device is shown from above with the part of the beam incident on the plasma subsequently shaded.

Density Measurements

The density of the plasma was measured using the interferometer arrangement shown in fig 2. One arm of the interferometer reflects the beam twice leaving it spatially unchanged. The other arm reflects the beam three times inverting it spatially so that when the two parts of the beam come back together at the second beamsplitter, the part of the beam that passes through the plasma interferes with the undisturbed part of the beam creating a fringe pattern (as in fig 3) which is determined by the plasma electron density N_e. The refractive index of a plasma is given by

$n = (1 - \omega_p/\omega)^{1/2}$ $\omega_p = N_e e^2 / \varepsilon m$ = plasma frequency

ω=frequency of probe light

Thus the refractive index depends on the electron density and the frequency of the probe light. A plasma has a refractive index of less than one giving positive fringe shifts on the interferogram while an unionized gas has a refractive index greater than one giving negative fringe shifts. Since the plasma studied here is at a temperature of 1 eV, it is not fully ionized and so it gives both positive and negative fringe shifts, the negative fringe shifts being more predominant near the edges of the plasma where it is cooler and hence less ionized. This makes interpretation of a single interferogram ambiguous. This problem was overcome by probing the plasma with two different frequencies simultaneously (1.05μm and 0.53 μm). The two frequencies were viewed separately by splitting them using a monochromatic mirror. The difference in the positive fringe shifts between the two frequencies then gives a unique density measurement for the plasma.

Fig. 3 Interferogram

Fringe shifts are measured relative to the undisturbed pattern at the edge of the picture.

Results

Interferograms for the plasmas such as fig3 were obtained. Electron densities were derived from these by counting the number of fringes by which the pattern has been shifted at a certain point relative to the undisturbed part of the pattern at the edge of the picture. For each fringe by which the pattern is shifted the part of the beam which passed through the plasma has been phase shifted by one wavelength. This gives a measure of refractive index and hence of the electron density at that point. The results for the interferogram in fig 3 are shown in fig 4.

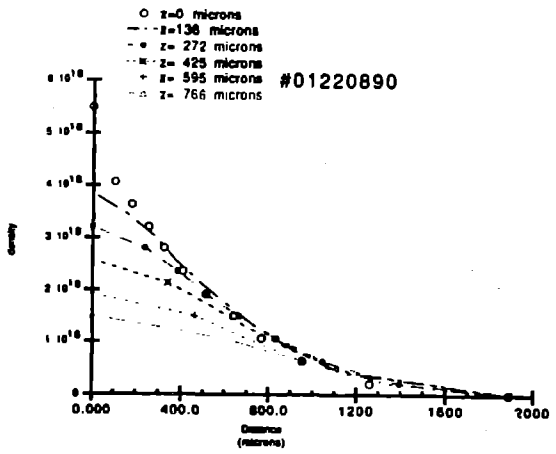

Fig. 4 Electron density as a function of distance from the centre of the plasma for various heights above the slit.(Calculated from the interferogram in fig. 3)

The results show that the capillary device is capable of producing plasmas which are very uniform over this large scalelength. The densities measured as shown in fig 4 are the electron densities for a carbon/fluorine plasma which at a temperature of 1 eV is only about 10% singly ionized. Thus the total number of electrons is two orders of magnitude higher than this, but most of them are still bound to the ions. Upon laser heating we expect to ionize the fluorine to H-like and He-like species thus yeilding a much larger electron density. One must also take into account that the temperature is falling off towards the edges of the slab of plasma so that the ionization level is not as great at the edges. This suggests that the ion uniformity is better than is suggested by fig 4.

Conclusion and Future Work

We have shown that the capillary device is capable of producing uniform plasmas which are suitable for testing theoretical predictions of x-ray emmission spectra of hot plasmas. The cool plasmas produced by the capillary can be heated with a line focus arrangement to produce a hot uniform plasma and the x-ray emmission can be recorded. This is the subject of an experiment using VULCAN in TA East in July 1991. Large uniform plasmas are also useful for modelling reactor size laser fusion targets. This device can be used for studying instabilities such as Brillouin scattering in a long scalelength plasma. The potential of this device as a test-bed for these studies will become more apparent after the laser heating experiment in July when we will establish the uniformity of the heated plasmas.

References

1. R.W. Lee, B.L. Whitten and R.E. Strout II, JQSRT 32 , 91 (1985).

2. A. Zigler et al., Phys. Rev. A, 35. 4446 (1987).

PROGRESS IN THERMONUCLEAR PARTICLE STUDIES AND RELATED EXPERIMENTS

A P Fews*, M J Lamb+, C Regan+, M Savage+

***University of Bristol,**
+Queens University, Belfast.

1. RAYLEIGH TAYLOR INSTABILITY

1.1 EXPERIMENTAL

The Rayleigh Taylor instability has been studied by the technique of α-particle backlighting in which α-particles shadow a planar foil in which instability has been induced. Since the α-particle technique implicitly measures the path lengths through the foil, the experiment directly measures the induced mass modulation and a direct measurement of R-T growth can be made.

We have recently used this technique to study accelerated foils driven by laser beams smoothed by random phase plates (RPP) and induced spatial incoherence (ISI).

The foils were driven using the 150mm diameter beam, with energies at 2ω routinely in the range 200 to 250J over 2ns. The energy available on the ISI drive was typically in the range 100 to 150J.

The technique is illustrated in Figure 1. An implosion of a DT filled microballoon is used as a source of thermonuclear α-particles. These particles are used to illuminate the accelerated foil in which fluid instabilities have been generated, shown here to the right of the DT shell. The implosions were made from glass walled microballoons of diameter ~600μm and wall thickness ~1μm and were driven using the 12 VULCAN beams. For most of the shots the implosions were driven by RPP smoothed beams. RPP driven implosions are typically characterised by small implosion cores, ~20 - 50 μm, and a significantly narrower spectral width than the previous (NUHART) mode. Yields of up to 10^9 have been achieved from phase plate driven implosions.

The system is entirely colinear, and thus the foil shadow image is recorded in front of the drive beam, and the particles probe the plasma at normal incidence. The α-particles are recorded in CR-39 plastic detector which allows the position and energy of the particles to be recorded to high precision. In addition an α-particle camera was placed behind the

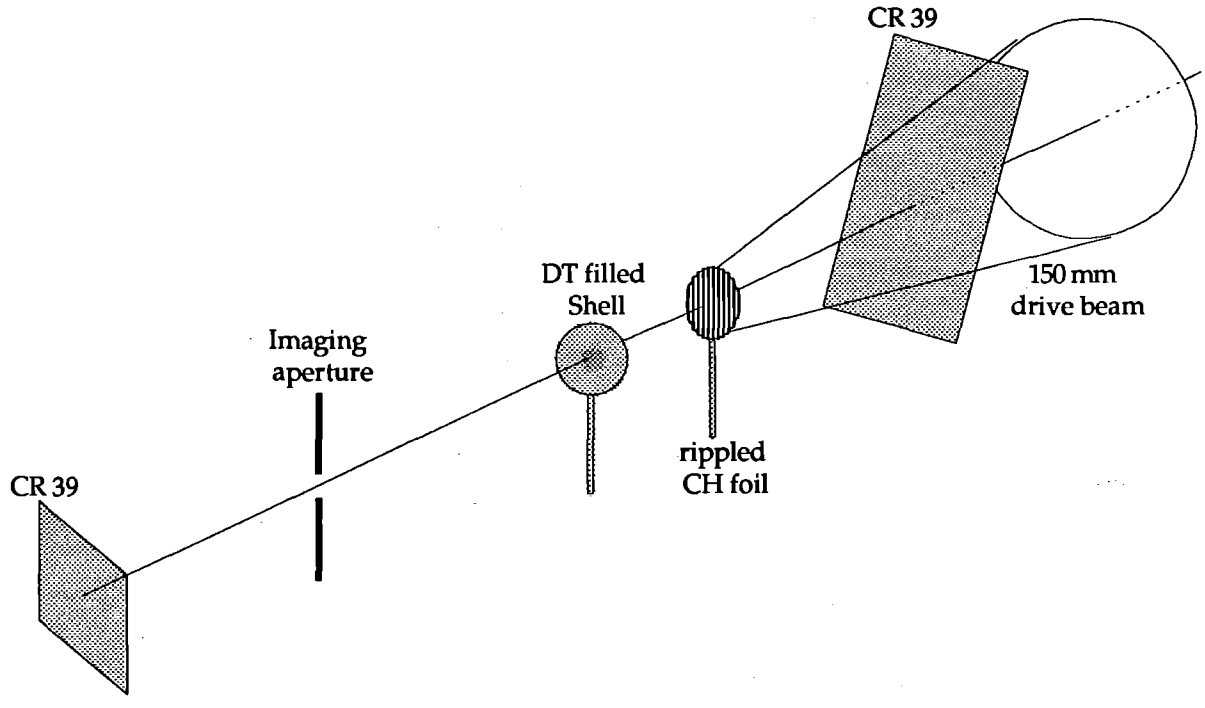

Figure 1. The basic experimental configuration. Particles from the implosion shadow the foil and are detected in the CR-39, placed over the backlighting lens, ensuring the detection axis is co-linear with the drive axis. A subsidiary imaging system, shown here to the left of the implosion recorded the spatial and spectral characteristics of the α-source on the line directed at the foil. The diagram is not drawn to scale.

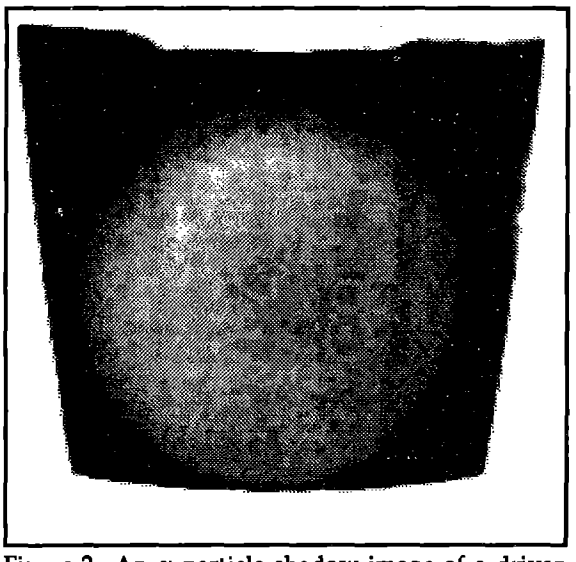

Figure 2. An α-particle shadow image of a driven foil. Lighter areas represent thicker regions of the foil. The foil was circular, of diameter ~550 μm.

implosion, shown to the left of the shell in the diagram. This recorded the spatial image of the α-source and its spectral shape, on the same axis as the foil diagnostics on the other side of the implosion. Since the α-particle range is greater than the ρ.r of the shell, and the reacting ions emit the α-particles isotropically, this image will be an identical mirror image to that on the other side of the target. This will be used in the foil reconstruction described in section 3 below.

The unique feature of the α-particle technique is the ability to measure the induced mass modulation directly, which does not require a spatial image of the foil. However, the core sizes from RPP driven implosions enable a spatial image to be generated. An example of this is shown in Fig 2 which shows an image of a driven foil, of diameter 550 μm, made by ~2.10^6 α-particles. The foil was driven by an ISI smoothed beam. Lighter regions represent thicker regions of the foil. The foil was of initial thickness 8μm with 1μm seed cuts on a 10μm period. The image has a spatial resolution of ~20μm, although we hope to improve this, as described later. The foil was probed at a time of 0.75ns into a drive pulse of irradiance $2.5.10^{13}$W.cm^{-2}. The image is significantly better than that observed previously, both in terms of the quality of the α-particle illumination and the uniformity of the foil after being driven. The smoothness of the image demonstrates the absence of large scale features in the foil image, which are caused by large scale artefacts in the focal spot of the drive beam.

Some illustrative results are shown in Fig 3. All the shots were driven by RPP smoothed drive, and the first shot shown was driven by an ISI smoothed beam. Fig 3(a) shows the distribution of particle ranges through the foil in shot 2/4/6/90., which was shown above in Fig 2. The particle range spectrum recorded directly from the implosion is shown in Fig 3(b). The maximum entropy deconvolution procedure (Fews et al, 1991) was then used to generate the foil thickness (ie mass modulation) spectrum from these graphs. The spectrum produced is shown in Fig 3(c). Note that this is reversed in position from Fig 3(a), because low thickness corresponds to high range. The data has been scaled to correspond to the CH composition of the foil. A feature can still be clearly seen at 8μm corresponding to the initial foil thickness, but substantial induced modulation is also present. Note that because of the ρ.r of the implosion, the foil thickness distribution is cut at 12μm- approximately 10% of the distribution lies beyond this point. Fig 3(d) shows the thickness spectrum recorded from show 2/25/5/90 which was probed at a time 1.2ns into a drive of irradiance $5.2.10^{13}$W.cm^{-2}. The foil had 10μm wide seed cuts of depth 1μm. It can be seen that the foil has nearly broken up, with the most prominent feature at thickness <4μm. In this case the spectrum is cut at a thickness ~14μm. Fig 3(e) shows the thickness spectrum recorded from shot 3/29/5/90. This was probed at 0.75ns into a drive of irradiance $5.9.10^{13}$W.cm^{-2} and had seed cuts of depth 1μm and spacing 20μm. The thickness spectrum is cut at a range ~12.5μm. The spectrum has been broadened around the initial 8μm thickness , and a separate peak at low thickness has been generated. Approximately 20% of the distribution has been lost at thicknesses grater than 12.5μm. This shot was also simulated using the POLLUX code, and the results from this are given below. Finally Fig 3(f) shows the thickness spectrum from a foil probed at the same time and driven with the same energy as Fig 3(e) but with no seed modulations. It can be seen that little modulation has been induced. This indicates that in this experiment, the modulations have been induced solely by the seedings in the foil, and not by any artefacts in the drive beam. This confirms our indication from the final shot of our previous experiment that foil modulations, which are seen on flat foils driven by unsmoothed laser beams, are absent when adequate beams smoothing is used. Therefore the beam quality present on the 150mm beam with RPP and ISI smoothing is now sufficient to enable RT growth rates to be measured.

1.2 THEORETICAL

The two dimensional plasma code POLLUX has been used to simulate the behaviour of 8μm thick CH targets with 1μm deep by 20μm wide grooves cut on one surface. In these simulations a 2ns pulse was incident on the grooved surface with irradiance in the range 2-6x10^{13}W.cm^{-2},corresponding to the experimental conditions. A mesh consisting of 98 x48 cells measuring 98x98μm was used, with the 2D density array being plotted out at the probe times determined from the experiment. The deformation

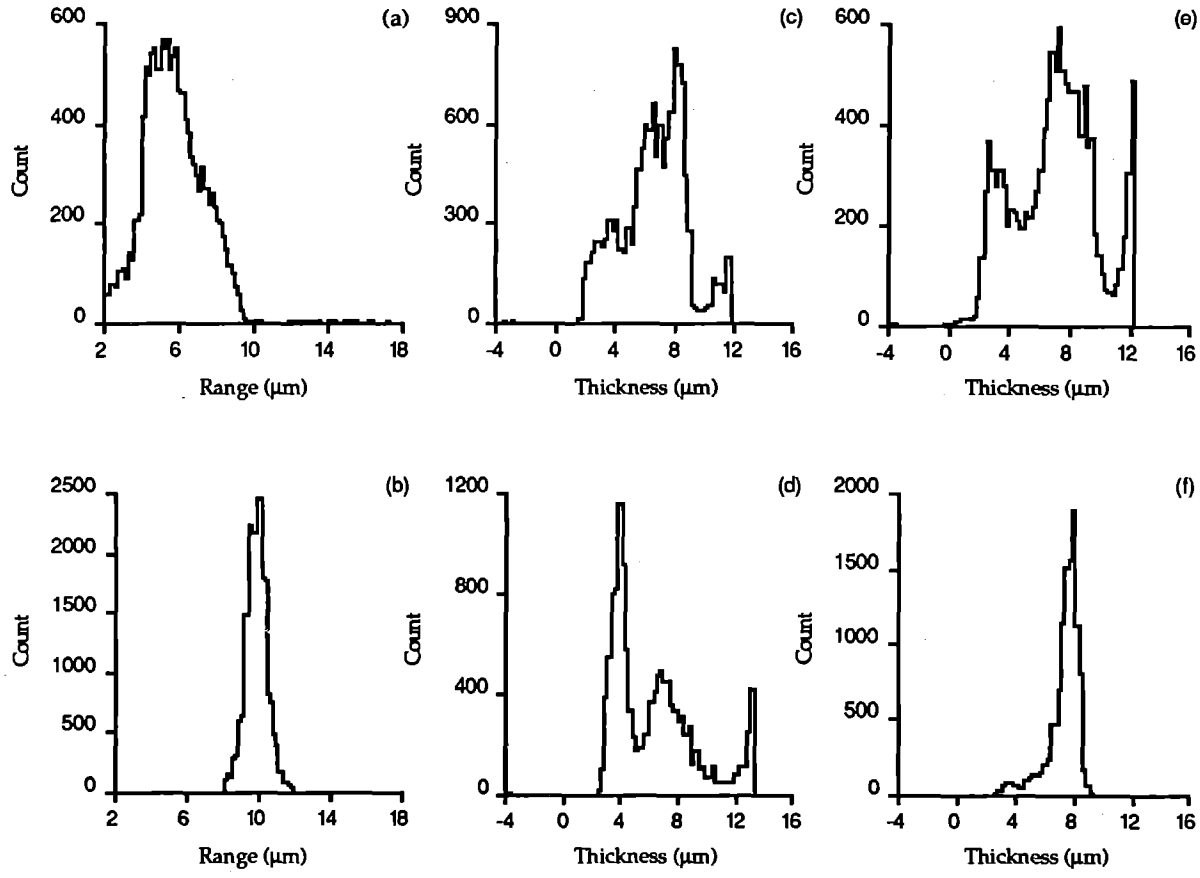

Figure 3. (a) and (b) shows the α-particle range spectrum measured, respectively through the foil and from the implosion. (c) shows the deconvolution of (a) from (b) showing the actual foil thickness spectrum with source broadening removed, probed at 0.75ns into an ISI drive pulse of irradiance $2.5.10^{13}$W.cm^{-2} (d) and (e) shows a thickness spectrum probed at 1.2ns and 0.75ns into the drive pulse. of RPP smoothed beams of irradiance ~$5.5.10^{13}$W.cm^{-2}. (f) shows a flat (unseeded) foil probed at 0.75ns into the drive. See text for other details.

of the target and its eventual breakup can be clearly seen from the printouts. Experimentally, the foil thicknesses are determined from the energy loss of the 3.5MeV DT α-particles., measured in the CR-39 detector. The code simulates this by means of an additional subroutine in POLLUX which estimates the α-particle energy loss at various times. Stopping powers for CH plastic have been calculated by Dr. S J Rose (RAL) for densities in the range 10^{-3} to 10 g.cm^{-2} temperatures $2..6.10^{-5}$ to 10 KeV and α-particle energies from 10^{-3} to 3.5 MeV. The particle energy loss within each cell is determined from the stopping power which is calculated by interpolation assuming a linear dependence of log(stopping power) on density, temperature and particle energy. This interpolation is adequate for the α-energies>0.05 MeV, those which are experimentally determinable.

Fig 4 (a) shows the contour plot of density as a function of position at the start of a POLLUX run. Position is indicated by the cell number within the mesh. Density is marked on the contour lines in units of g.cm^{-2}. A simulation was made of shot #3 29/5/90, corresponding to the experimental measurement shown in Fig 3(e). The irradiance was $5.9.10^{13}$ W.cm^{-2}. Fig 4(b) shows the corresponding POLLUX simulation. It can be seen that it both cases the foil has reached an advanced stage of instability, but the foil has not quite been burned through. Further analysis of this data is currently in progress.

Fig 5 shows a simulation of the energy of the α-particles leaving the plasma, plotted against position and time for an irradiance of $2.5.10^{13}$ W.cm^{-2}. Initially the energy out is a step function of position due to the seed grooves cut in the target surface. As the target is heated the energy out varies in line with the target deformation. These results should allow a direct comparison to be made with the measured data.

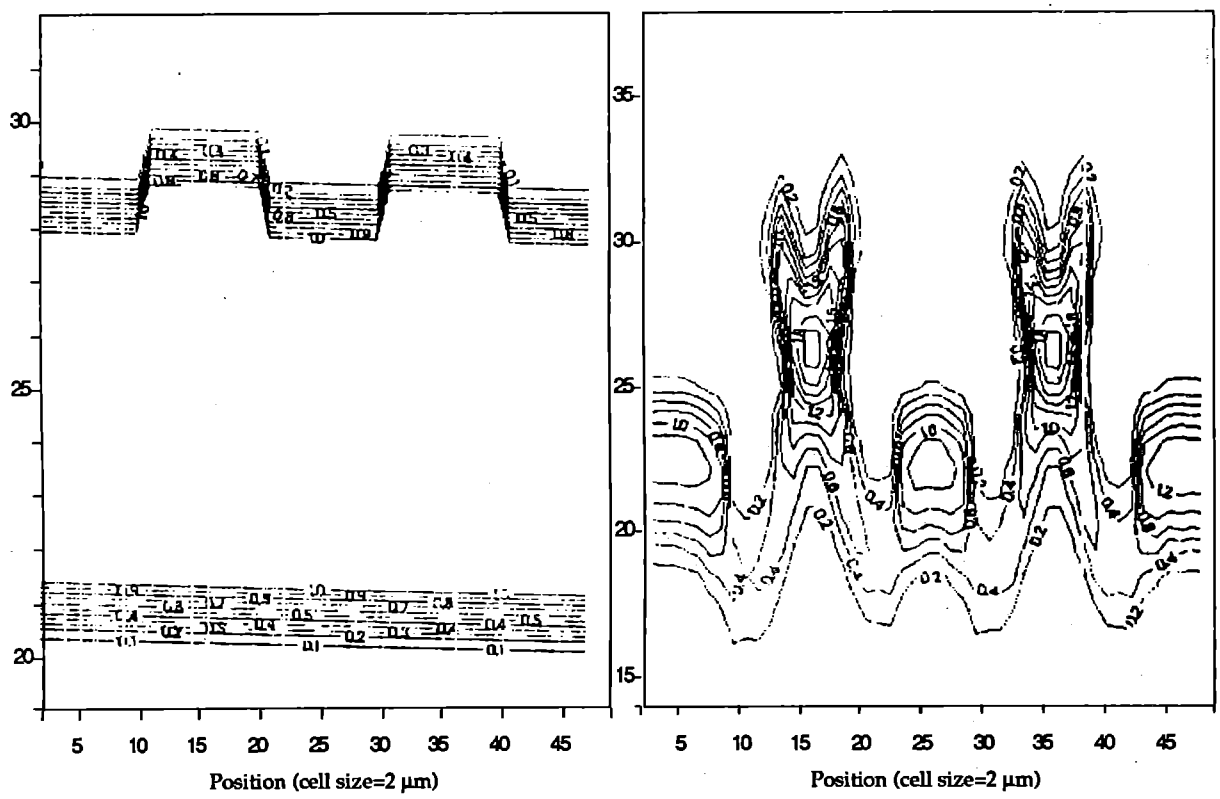

Fig 4. 4(a) shows the contour plots of foil density as a function of position used as input to the POLLUX code. Position is indicated by the cell number within the mesh. Density is marked on the contour lines in $g.cm^{-2}$. 4(b) shows the resulting profile at a time of 0.75ns, and corresponding to the conditions of the measured foil thickness distribution of shot 3/29/5/90, shown in Fig 3(e). The y axis shows the cell position through the foil (1 cell= 1 micron).

2. IMPLOSION TARGETS

We have continued our characterisation of DT filled shells supplied as part of our collaboration with the Lebedev Physical Institute, Moscow.

In particular we investigated the use of clusters in the microballoons glass to check for observable effects on the implosion. Two cluster sources were tested, 100 Angstrom Ag clusters, and 400 Angstrom Co clusters. The Ag clusters appeared to produce a modest improvement in particle yield, although the result is not statistically significant at present. The Co clusters had a detrimental effect, reducing the observed yield by more than a factor of 10.

Particle yields of up to 10^9 have been obtained from RPP driven implosions, which are only a factor of 3 lower than the peak NUHART yield of 3.10^9. This performance is dependent on having sufficient laser energy so that the implosion core is generated by the drive no later than the end of the drive pulse. We are continuing to investigate the under performance of very thin walled shells- this is likely to be caused by the total ablation of the shell wall during the laser pulse. In these cases no core is formed.

3. PARTICLE IMAGING

Significant improvements are being made to the maximum entropy deconvolution techniques. The technique has been successfully applied to spectral (ie one dimensional) deconvolution, of α-particle spectra to separate particle range loss in a foil from spectral broadening in the source implosion; and to penumbral imaging of the α-particle emission.

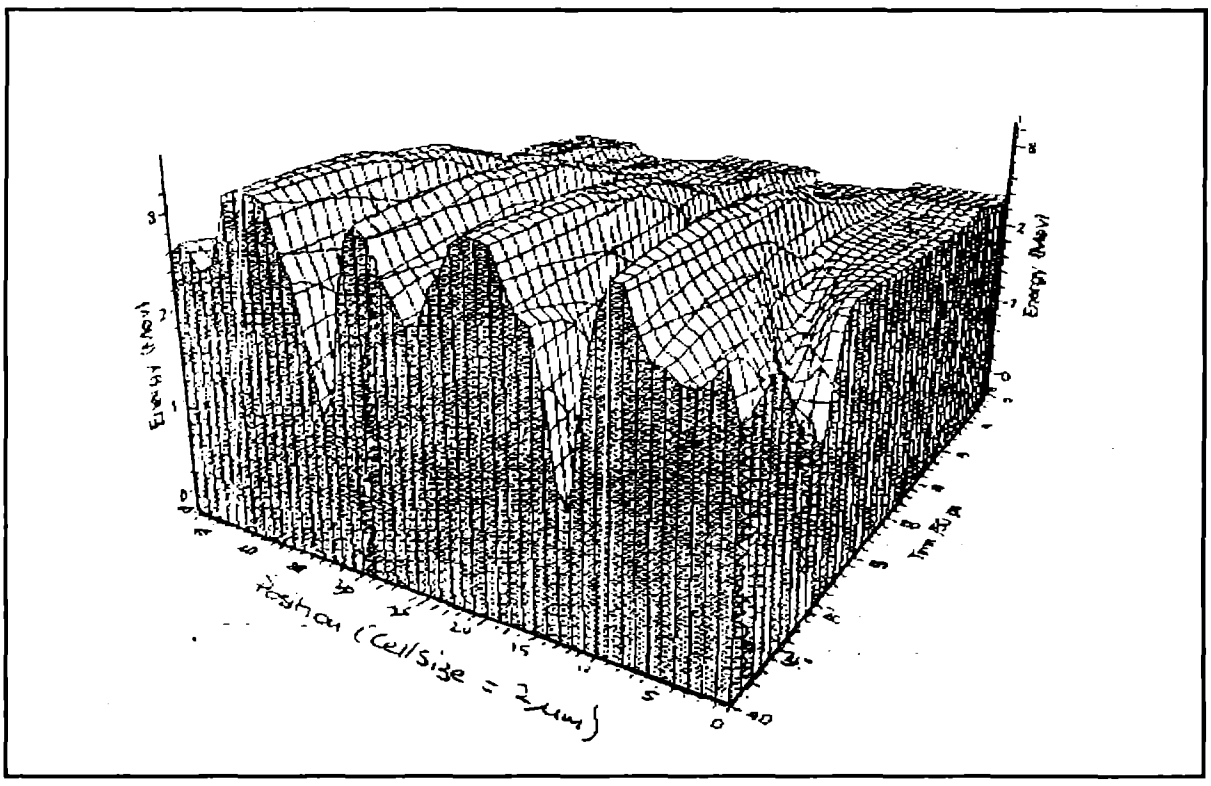

Fig 5. The calculated α-particle energies through the foils a function of time and position. At time zero, the initial step function modulation can be seen at the back of the simulation. The progressive deformation of the foil can be clearly seen.

The technique is now being extended to an exact statistical treatment of the counting errors to permit α-particle core sizes to be obtained from images containing as few as 150 particles.

This successful approach is being extended, both from 2D and 3D. In 2 dimensions, coded aperture masks will be fully integrated into the maximum entropy approach. This will enable the advantages of coded mask imaging to be combined with the maximum entropy technique, giving an increase of a factor of ten in the particle count in the images. In this way the resolution is not necessarily limited to the mask cell size, since the mesh pattern of the masks is treated as a multiple penumbral aperture.

Three dimensional imaging is also being developed in two aspects: 3D reconstruction of the α-emission from the implosion from a set of 3 or 4 2D penumbral images. This is a fully integrated 3D solution and not a combination of a set of decoded 2D images, which will permit a full visualisation of the core shape. This shape is possibly determined by direct effects due, for example, to beam imbalance.

Secondly, 3D foil imaging is being developed, in which the foil is represented with 2 spatial dimensions by 1 range (energy) dimension. This will analyse the experimental geometry shown in Fig 1 and will use the spectral and spatial α-image of the source core from the co-linear α-particle camera together with the range spectra recorded through the foil to sharpen the α-image of the foil. In this manner the entire system is considered together.

4. REFERENCES

A P Fews , M J Lamb and M Savage " Thermonuclear Particle Imaging" Central Laser Facility Annual Report, 1990. A full version of this paper is currently in preparation.

MEASUREMENTS OF ION CORRELATION IN A HIGH DENSITY PLASMA USING AN ELLIPTICAL SPECTROMETER

D A Goodman[1], A Ridgeley[2], A MacPhee[2] and T A Hall[1]

[1]University of Essex
[2]Rutherford Appleton Laboratory

INTRODUCTION

Previous Annual Reports, and previously references papers [1], have described how ion correlation effects in a dense, shocked compressed plasma may be determined through measurement of the Extended X-ray Absorption Fine Structure, or EXAFS phenomena. However, the experimental geometry of these experiments placed certain constraints upon the quality of the EXAFS structure that could be measured. The elliptical spectrometer has been developed to avoid some of these problems, and to function as a very flexible pump and probe spectrometer which is particularly suited to EXAFS measurement

(1) THE ELLIPTICAL SPECTROMETER

The spectrometer, which is described in section 7 of this report, is based around an elliptically curved crystal,and is represented schematically, in fig 1, below.

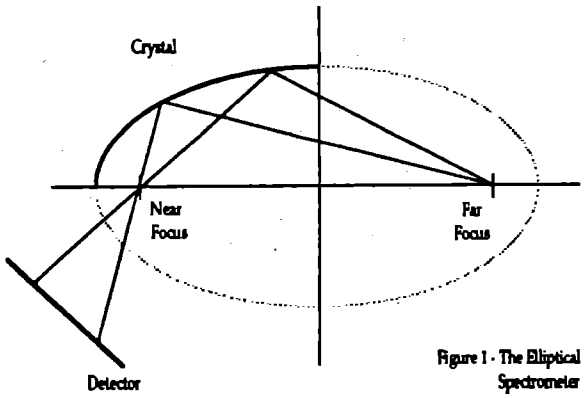

Figure 1 - The Elliptical Spectrometer

A short pulse of x-rays, generated at one of the elliptical foci (the Far Focus in figure 1), is incident upon the crystal. Those x-rays which conform to the Bragg condition are reflected so as to converge at the other ellipse foci, before diverging onto a suitably placed detector. In this manner line spectra may be measured or, if a suitable continuum source of x-rays is employed, a thin metal foil may be placed at the convergent focus and an absorption spectrum obtained.

The elliptical spectrometer has many advantages over the conventional planar crystal mini-spectrometers which were previously used for EXAFS measurement[2]. The relative merits of the two spectrometers are discussed below.

The dispersed x-rays recorded by the plane crystal spectrometer have passed through different regions of the target; and in the process have probed different plasma conditions which result from non-uniformities in the drive beam and variations in the target thickness. The elliptical and cylindrical nature of the curved crystal, however, ensures a line focus at the convergent focus. Thus in any arbitrary horizontal plane the dispersed spectrum is derived from a single point on the compressed foil, i.e. from a plasma with almost uniform density and temperature.

The line focus from the elliptically curved crystal, is larger than the absorbing target (figure 2). This allows the simultaneous recording of EXAFS from both compressed and uncompressed regions of the target, and the recording of the uninhibited continuum directly from the source. Analysis of these adjacent data regions ensures that any structure, which may be present in the backlighting continuum, may be removed from the EXAFS data, and that any shift in the EXAFS structure, and in particular of the K-edge position, of the shocked and unshocked regions may be accurately measured.

In contrast to the plane crystal arrangement the dispersing element is placed before the EXAFS sample. The foil is, therefore, only penetrated by the required diagnosing wavelengths, and is not exposed to direct polychromatic radiation from the backlighting source, which causes unwanted heating in the sample and a deterioration in the EXAFS structure. This arrangement does have the disadvantage, however, that the dispersing element is not able to act as a narrow bandpass filter and thus shield the detector from the radiation which is emitted from the compressed sample.

The backlighting radiation within the elliptical spectrometer is much more spatially compact than within the plane crystal spectrometer, which enables more effective shielding of the detector from undispersed backlighting radiation .

The diagnosing radiation from the elliptical crystal is incident upon the foil at a shallower angle than is seen in the linear arrangement, thereby increasing the pathlength of the radiation within the target. Thus the transmitted flux may be optimised, to suit the detector, by use of a thinner foil, which has a correspondingly smaller longitudinal variation in density during compression.

The modular nature of the elliptical spectrometer ensures that the x-ray detector may be easily changed, thus a traditional film detector maybe replaced with a solid state device. The feasibility of a PDA device for K-edge studies, and its superior signal to noise performance has already been evaluated in an experiment[3] performed at the Rutherford Laboratory in Feb '88.

Figure 2 - Line Focus probing of Foil Target

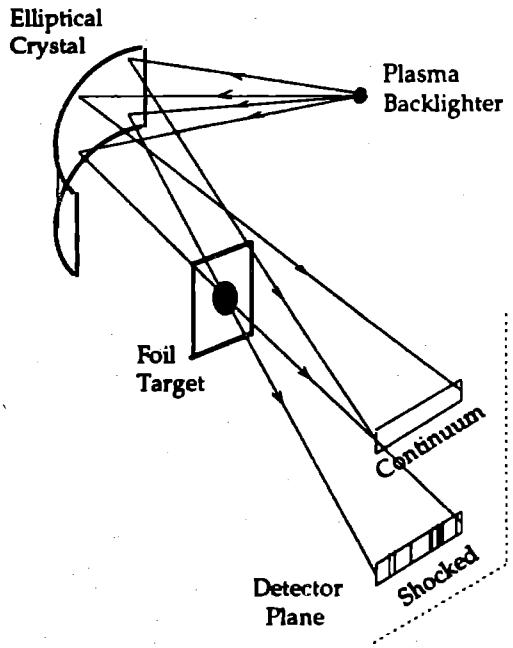

(3) EXPERIMENTAL PRACTICE

The EXAFS targets take the form of a 3 mm square planar sandwich, comprising a 1.8 μm aluminium foil coated on both sides with 4 μm of E-parylene. The aluminium is of a sufficient thickness to allow a reasonably uniform compression throughout, whilst the E-parylene coating performs several functions. Firstly, the main target self emission is minimised, reducing any preheat of the aluminium core. Secondly the parylene ensures that the shock is well formed before reaching the aluminium layer, and thirdly that there is no coronal aluminium plasma to distort a shocked EXAFS absorption structure. Each planar target is pierced with a 500 mm hole, which is used to align of the VULCAN beams onto the target.

The backlighting targets comprise a 100 mm diameter copper lollipop, coated firstly with 10 mm parylene and ultimately with 0.5 mm uranium. Uranium has been well established as a suitable backlighting source for aluminium EXAFS measurements[1,4]

The experiment required that Laser radiation be focussed at the two foci of the elliptical spectrometer, necessitating changes to the chamber flanges and the 'space frame' gantry of Target Area East. Five of the six cluster beams in TAE were used to produce the backlighting radiation, each delivered approximately 15 J in 100 ps within a 100 μm diameter focal area. The sample was shocked by the action of the laser energy at the second focus. A single beam from the VULCAN system was split in two,and focussed upon opposite sides of the planar EXAFS target. The two beams delivered a total of 7 J green energy , during a pulse of 1 ns duration, upon a focal area of 500 μm. The time delay between the arrival of the laser energy at the backlighter and foil target was varied, to provide time resolved studies of the material throughout the duration of the laser shock. The Beam geometry is shown schematically in figure 3.

Random Phase Plates were placed in the beam paths, close to the target chamber, in order to present a smoother beam profile to both the backlighting and foil targets.

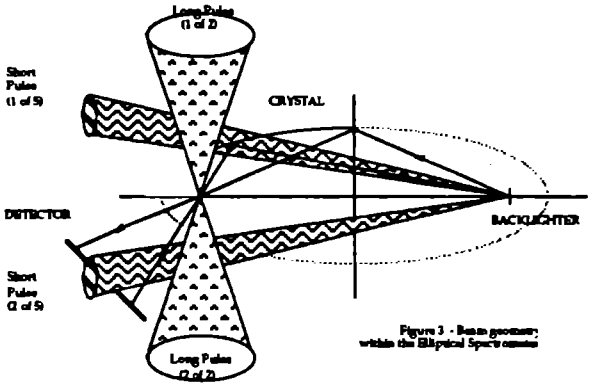

Figure 3 - Beam geometry within the Elliptical Spectrometer

(4) RESULTS

Compressed and uncompressed aluminium EXAFS have been successfully measured with the elliptical spectrometer using both x-ray film and a two dimensional CCD detector. The EXAFS data is of a much higher quality than any previously measured with a laser plasma backlighter, and it is expected that far more accurate estimations of the ion coupling parameter and the plasma temperature may be obtained.

Data analysis is currently underway ay the University of Essex. Some preliminary results from the small fraction of data which has been examined so far is presented in figures 4-5 below. The data is derived from a single shot, in which the backlighting pulse is centered about the longer, laser driven shock.

Figure 4a shows the measured values of the aluminium absorption coefficient as a function of energy from unshocked aluminium which has been normalised to the background absorption level. The first three EXAFS modulations may be clearly seen. Fig 4b shows the absorption structure from the shocked component of the target. Two modulations can be seen, with severely decreased amplitudes and extended periods. The normalised EXAFS curves are analysed through the Fourier transform codes at the Daresbury laboratory in a manner described in the work of Djaoui et.al.[5] Figure 5 shows the first shell fit, of the Fourier transform, of the normalised, unshocked, data. The Fourier transform peaks at r = 2.86 angstroms, which is the accepted interatomic spacing of uncompressed aluminium. Similar analysis of the shocked data component shows a pronounced shift in position of the Fourier peak,which is indicative of a high compression within the foil sample. Unfortunately, it is not possible to quantify this shift at such an early stage in the data analysis

The strength of the compressive shock applied during the experiment, was limited by emission from the foil target. It was found that, for irradiances in excess of $5x10^{11}$ w/cm^2, emission from the plastic coating of the aluminium sandwich targets began to fog the x-ray detector, resulting in a deterioration in the signal to noise ratio of the EXAFS structure.

Figure 4 - Shocked and Unshocked EXAFS

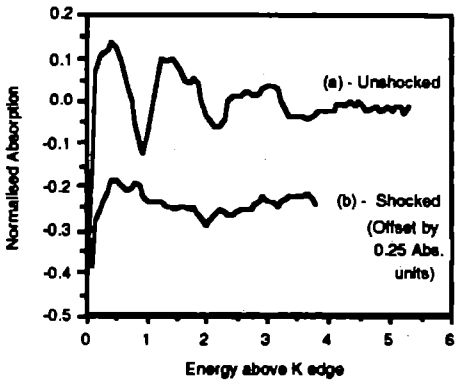

Figure 5 - Fourier Transform of EXAFS

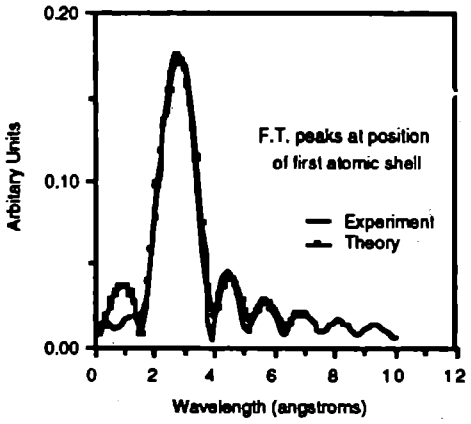

REFERENCES

1 T.A.Hall et.al. *Phys Rev Lett* 60 2034 (1988)

2 B.A.Shiwai et.al *Improvements to measurements of ion correlation* To be published

3 D.A.Goodman et.al. *J .Xray Sci .Tech.* 1 162 (1989)

4 *Annual Report to the laeser facility* Rutherford Appleton Laboratory RAL-88-042 (1988) A3-1

5 A.Djaoui et.al *Las.Part.Beams* 8 N° 1-2 319 (1990)

INVESTIGATION OF NEUTRAL PARTICLE EMISSION FROM PLANE LAYERED TARGETS UNDER VARIED IRRADIATION CONDITIONS.

T A Hall[1], R Evans[1], Z Ahmad[1]

Y A Zakhrenkov[2]

[1]University of Essex.

[2]Lebedev Insitute of Physics, Moscow.

Plane multi-layered targets were subjected to a variety of laser irradiation conditions in order to investigate the spatial structure and velocity profile of the subsequent neutral particle emissions.

Introduction

In previous experiments [1] neutral particles have been detected from laser imploded microshell targets. The main sources of these neutral particles were identified : firstly ion recombination of the coronal plasma results in a spectrum of relatively fast neutral atoms. In micro-balloon implosion experiments the ions in the dense imploded core rapidly recombine and result in a neutral particle spectrum where the velocity distribution has a strong peak near to the implosion velocity (approx 10^7 cms^{-1}). In targets that are non-uniformly irradiated, parts of the shell are not directly heated by the laser and result in a larger number of neutrals over a wider range of velocities. A final source of neutral particles comes from scattered laser light and/or X-ray emission from the target which heats surrounding objects such as the target support stalk. Using a combination of time of flight and pinhole imaging techniques it is possible to distinguish between some of these different sources [2].

As the previous experimental results were analysed it was clear that there was still some possible confusion, particularly between coronal recombined neutrals and these associated with non-uniform irradiation. A series of experiments have been carried out in planar geometry with various types of targets to attempt to identify and quantify the different sources. The experimental set-up can be seen in Figure 1. At the same time it was felt that neutral particles may explain some of the discrepancies in ablation pressure measurements made in the early 80's [3].

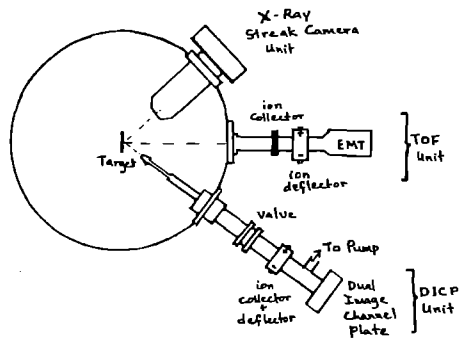

Figure 1 - Experimental set-up

Most of the targets used were 0.1μm, 0.2μm or 0.6μm of AL coating on glass slides (approx 1mm thick) and similar SiO coatings on thick Aluminium. In order to observe the effects of edge phenomena lollipop targets were used, these were 100μm diameter Al on SiO (Al=2μm, SiO=0.1μm).

The laser energy used was between 1 and 60J on the target at a wavelength of 0.53μm. Two main pulse durations were used, 1ns and 3.5ns.

The size of the laser spot on the target was varied using Random Phase Plates (RPP). Spot sizes of 60μm (no RPP present), 125μm, 250μm and 500μm were used.

The signals from the ion collectors and the neutral particle electron multipliers were displayed on an oscilloscope and the neutral particle images were observed on photographic film placed in light tight contact with the fibre optic screen of the MCP.

Results and discussion

So far, only a very rudimentary analysis of the data has been carried out. The X-ray streak records have been processed and mass ablation rates for the various configurations have been calculated. These results are shown in Figure 2 for 500μm diameter focal spot. The neutral particle data is still under analysis since absolute calibration of the detector is not yet complete. However, preliminary data for 500μm spot diameter and long and short laser pulses are shown in Figures 3 and 4 respectively. For both of these cases the mass ablation rate measured due to neutrals changes very rapidly with irradiation, but in the case of the long pulse data the ablation rate decreases with irradiation whereas for the short pulse data the ablation rate of the neutrals increases with irradiation.

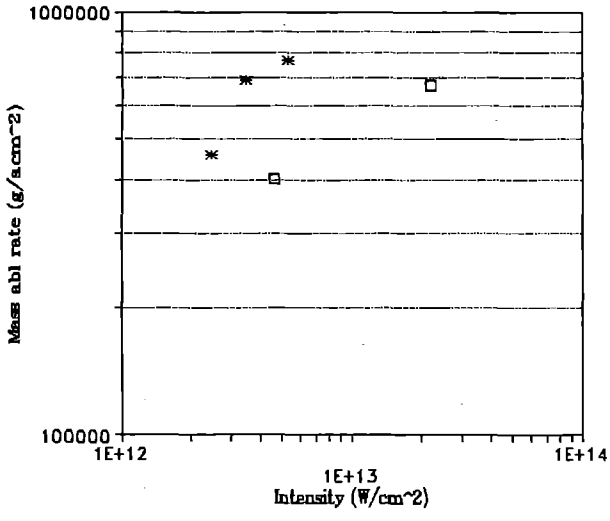

Figure 2 - Mass ablation rate calculated using X-ray data.
□-Short pulse ✱-Long pulse

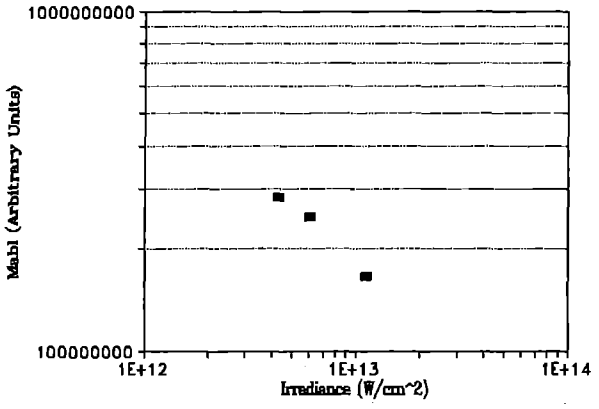

Figure 3 - Mabl from neutral data with long pulses

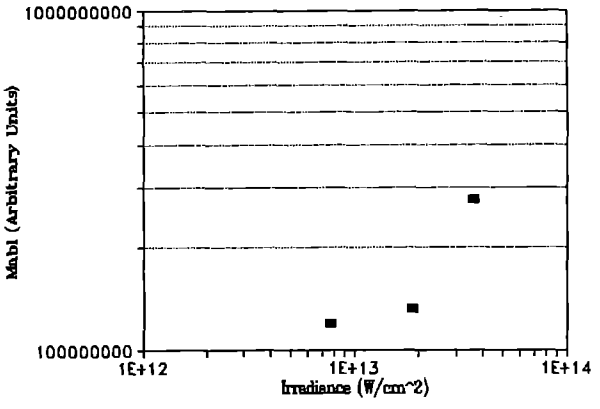

Figure 4 - Mabl from neutral data with short pulses

References.

1. T A Hall et al, RAL Annual Report 1990.
2. A A Erokhin, Y A Zakharenkov et al, JETP Lett. 1990, 51.No 11 p553-556.
3. P Cunningham, C L S Lewis et al, Annual Report to the Laser Facility Committee 1981, p4.10-4.46.

DEVELOPMENT IN X-RAY CONTACT MICROSCOPY TECHNIQUES IN TA4.

R.A.Cotton[1], A.J.Jackson[2], A.Ridgeley[2], A.D.Stead[1] and T.W.Ford[1].

[1] Royal Holloway and Bedford New College.
[2] Rutherford Appleton Laboratory.

INTRODUCTION.

The technique of soft X-ray contact microscopy (SXCM), imaging hydrated organic specimens at sub-optical resolutions, has great potential for becoming a valuable imaging technique throughout the life-science community. Progress in the past has been somewhat limited by a lack of suitable X-ray sources which have been sufficiently well characterised and a lack of comprehensive studies on the factors which limit the resolution and quality of images.

The crucial factor determining whether an X-ray source is suitable for SXCM of hydrated, living specimens is whether a sufficiently high X-ray flux in the so called "water window" region of the X-ray spectrum (0.28-0.53keV) can be administered in a sufficiently short time, so as to avoid blurring due to subject movement (both radiation induced and natural movement) and radiation damage.

The most promising X-ray source is that of a high temperature plasma and in particular plasmas generated by focusing a high powered laser onto a solid target. SXCM using laser generated plasma sources was first performed at RAL[1] in 1986 using the large Nd:Glass laser "VULCAN", delivering up to 100J of infra-red radiation on target.

It became clear that for SXCM to progress rapidly, a smaller, more readily available system, which was reliable, easy to use, with a well characterized X-ray source was needed. Work started in TA4 to set-up such a system to attempt to bring SXCM to the stage were it may become a routine biological imaging tool.

MATERIALS AND METHODS.

The vacuum target chamber used in the present experiments has been described elsewhere[2]. The X-ray detectors used were 125 PIN 100N X-ray diodes (Alrad Instruments Ltd) with an entrance window thickness of 0.25μm. A 100nm thick Si_3N_4 window coated with a 500nm layer of vanadium was used as a filter to isolate the water window region of the spectrum. However, such a filter begins to transmit radiation on the high energy side of the water window. This hard X-ray component of the total signal can be measured using a beryllium filter. This can then be subtracted from the signal measured with the vanadium filter, leaving only the water window component. The maximum laser energy available is approximately 10J operating at the lasers fundamental wavelength of 1.06μm. The pulse duration is approximately 2ns, with a repetition rate of one shot every two minutes. The beam can be focused a spot size of order 100μm with the 15cm focal length lens used in these experiments. Three X-ray diodes (XRD) and several vanadium filters were cross-calibrated to enable the relative X-ray flux to be accurately maintained, independent of the diode or filter used. It was found that the detection system initially picked up substantial electrical noise generated by the laser system resulting in large fluctuations in the measured signals from the X-ray diodes. By constructing two nominally identical channels the sources of noise pick up were isolated, enabling the noise to be reduced to below a 5% level.

A data acquisition system was set up with a computer program to give a print-out of the plasma parameters after each laser shot. This system takes into account parameters including target-specimen distance, emission spectra for each target material, detector sensitivity, and filter transmission. On each laser shot the computer is fed with a value for the laser energy on target and the signals from two XRD's, one with a vanadium filter and the other with the beryllium filter. The data output is in the form of a hard copy stating the laser energy, the water window and hard X-ray conversion efficiencies and their relative components of the total X-ray emission, in addition to the most relevant quantity for SXCM, namely the X-ray fluence in the water window incident on the specimen. This is a major improvement in making the system more "user friendly".

RESULTS AND DISCUSSION.

The target materials used were gold, tungsten and molybdenum which are known to have X-ray emission lines which lie wholly or partly within the water window[3]. It was found that the maximum X-ray yield was achieved when the target material was positioned approximately at focus, although the position was not critical to within a few hundred microns around focus (see figure 1). This is well within the positioning capabilities of the present alignment system.

It was found that a substantial fraction of the laser energy was being lost in various optical components. These losses were reduced by replacing the entrance window to the chamber so that approximately 55% of the laser energy was incident on target, giving just over 5J maximum.

Table 1 shows the conversion efficiencies from laser radiation (on target) to "soft" ($0.28<h\nu<0.53$keV) and "hard" (>0.53keV) X-rays for the three target materials.

Figure 2 shows the X-ray fluence (both water window and hard components) incident on the specimen for 15 consecutive laser shots using tungsten target material. The shot-to shot reproducibility of the present system is substantially better than in previous experiments using large laser systems[1].

During the experiments it was noted that a second laser shot at the same portion of the target material resulted in a slight increase in the soft X-ray flux and a fairly large increase in the hard X-ray flux. This is due to a partial confinement of the plasma due to the formation a crater in the solid target by the first laser shot. Further laser shots usually resulted in the wire breaking. Figure 3 shows

this data for 6 pairs of lasers shots for tungsten target material.

CONCLUSIONS

TA4 has been set up for the routine imaging of biological specimens using the technique of soft X-ray contact microscopy. The laser generated plasma X-ray source has been characterised and optimised for X-ray emission in the water window. All aspects of the technique have been improved making the technique widely accessible to all areas of the life science community. Very encouraging images of hydrated specimens, including various mosses, bacteria and brain tissue with Alzheimers disease, have been taken[4].

ACKNOWLEDGEMENTS

This work is supported by an SERC Grant GR/F 81514. We are grateful to Pete Anastasi and Dean Morris of Kings College London for the manufacture and subsequent coating of the Si_3N_4 windows. To the RAL support staff on "Vulcan" and, in particular to Dave Pepler for writing the data acquisition program for TA4.

REFERENCES.

1. R.W.Eason et al, Optica Acta 33(4), 501 (1986).
2. A.Damerall et al, RAL annual report RAL-88-042, 140 (1988).
3. K.Eidmann & T.Kishimoto, Appl.Phys.Lett. 49(7), 377 (1986).
4. A.D.Stead et al. This volume

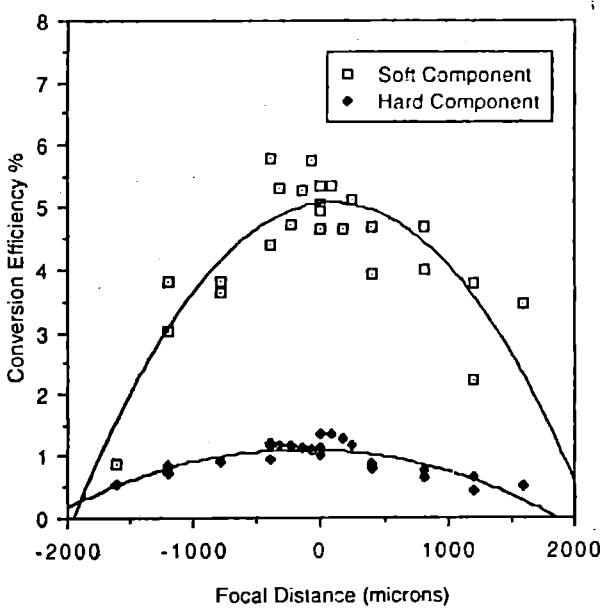

Figure 1: Conversion efficiencies for the hard and soft X-ray components for tungsten target material as a function of target position relative to focus.

Target Material	Water window Conversion efficiency %	Hard X-ray Conversion efficiency %
Gold	6.7	2.3
Tungsten	5.4	1.1
Molybdenum	4.6	1.7

Table 1: Conversion efficiencies from laser radiation to water window and hard X-rays for gold, tungsten, and molybdenum target material.

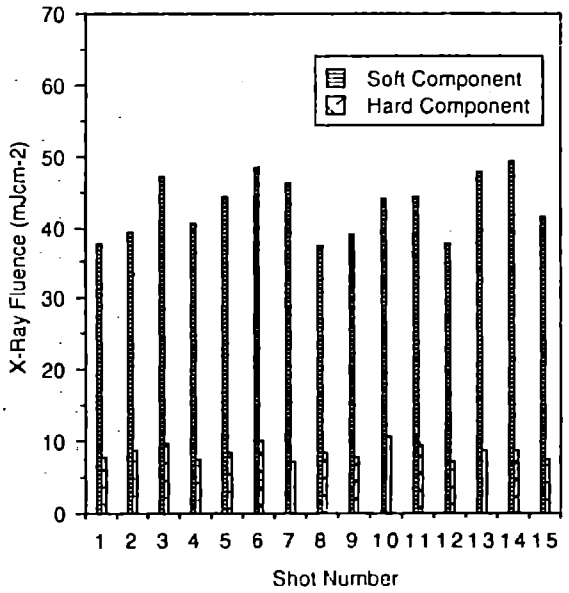

Figure 2: The hard and soft X-ray fluence incident on the specimen, at a target-specimen distance of 1cm, for 15 consecutive laser shots, showing the shot-to shot variation.

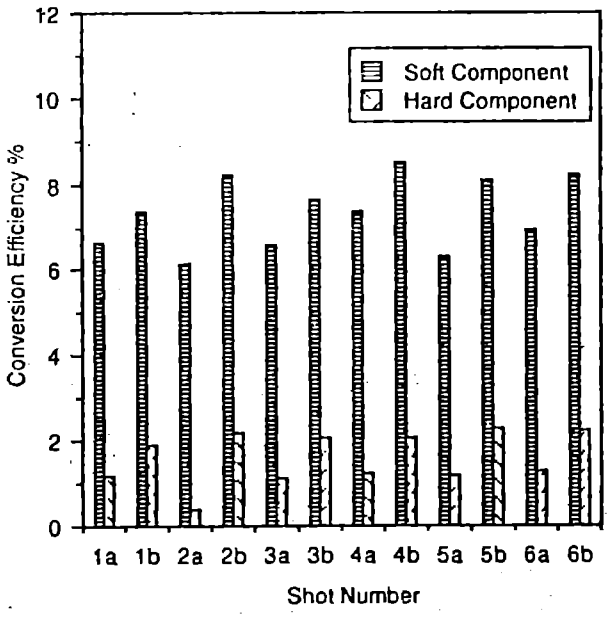

Figure 3: Conversion efficiencies for the hard and soft X-ray components for tungsten target material for a series of double shots on the same portion of the wire.

IMAGING BIOLOGICAL SPECIMENS WITH SOFT X-RAYS FROM LASER-PRODUCED PLASMAS IN TA4

A.D.Stead[1], R.A.Cotton[1], A.J.Jackson[2], A.Ridgeley[2] and T.W.Ford[1]

[1]Royal Holloway and Bedford New College
[2]Rutherford Appleton Laboratory

INTRODUCTION

The imaging of hydrated biological specimens with soft X-rays remains an important goal for the reasons reviewed elsewhere[1,2]. Successful imaging of hydrated biological material has been accomplished using high laser energies from VULCAN[3] and whilst good resolution of dried biological specimens has been obtained with lower laser energies in TA4[4] the images of hydrated biological specimens have not been as good[5].

Recent improvements in the operation of TA4 have now enabled routine imaging of biological specimens. The provision of diagnostics[6] permits more accurate development of the exposed resist and comparison of image quality with different X-ray fluences using either plain Si_3N_4 windows or windows coated with either aluminium or vanadium to act as UV filters.

It has been claimed that measurements of resolution using contact microscopy are fraught with difficulties since, as the resist is developed, features on the surface will diminish in size leading to an apparent "improved" resolution[7]. We have avoided this problem in the past by only measuring resolution from images of structures exhibiting a repeating structure - such features are common in diatoms but rare in other biological specimens[4]. In recent experiments we have used gold particles of known size to test the resolving power of the technique.

MATERIALS AND METHODS

The configuration of the imaging system of TA4 and operation of the diagnostics are described elsewhere[6] and the basic imaging method is that used previously[3]. Fresh, hydrated samples of plant hairs and moss protonema were imaged behind 90 - 120nm thick Si_3N_4 windows onto resists consisting of 1μm polymethylmethacrylate (PMMA) on silica wafers. For some exposures, the windows were coated (by evaporation) with defined thicknesses of aluminium or vanadium. Soft and hard X-ray fluence were recorded for each exposure. Resists were developed in mixtures of methyl iso-butyl ketone (MIBK) in isopropyl alcohol (IPA) with depth monitored by incident interference light microscopy (Leitz Dialux). When internal cellular detail was visible by light microscopy, development was stopped and the resist sputter coated (Polaron E1000) with Au:Pd and examined in a Cambridge S100 scanning electron microscope (SEM).

For resolution measurements, 50nm gold particles (Biocell) were air-dried onto the resist surface and then imaged through an uncoated window as described above. For comparison, the gold particles were also imaged directly by SEM.

RESULTS AND DISCUSSION

Claims for the resolving power of soft X-ray microscopy have often been very impressive. However, measurements derived from determining the linear dimensions of an image are inherently inaccurate[7]. Using regularly repeating structures, such as those in diatom frustules, we have measured a lower resolution limit of 60nm[4], though this was obtained with a dry specimen in which silica was the X-ray absorbing material. In most biological specimens it is carbon-containing material which is to be imaged and this will be held in an aqueous environment. In this sense, the use of gold particles is still far removed from the biological situation. However, it has permitted accurate assessment of the ability to resolve small single objects which will be critical if soft X-ray contact microscopy (SXCM) is to be used to map the distribution of highly labile cell components using gold-labelled antibodies. The size of gold particles imaged by SXCM compares well with the stated size of 50nm and with the appearance of such particles viewed by conventional SEM (figure 1).

Previous successful imaging of hydrated biological specimens at RAL has required the use of high laser energies; the images of Digitalis floral hairs required approximately 100J (IR) on target. These images showed cells containing numerous cytoplasmic strands running the length of the cells. Light microscopy studies of these cells show such strands traversing the central cytoplasm but treatment of the tissue for transmission electron microscopy (TEM) appears to destroy these structures[3]. Subsequent images of foliar epidermal hairs of tomato taken in TA4 with approximately 2J (IR) on target showed only minimal amounts of internal detail suggesting too low

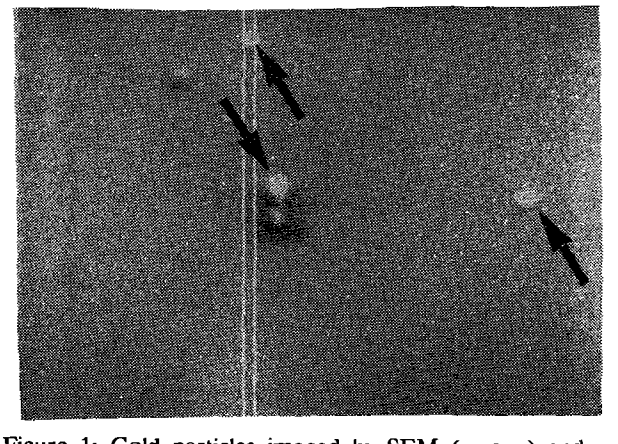

Figure 1: Gold particles imaged by SEM (arrows) and SXCM

Figure 2: Scanning electron micrographs of resist images of foliar hairs of tomato (a) 60mJ.cm^{-2} soft X-ray fluence; (b) 40mJ.cm^{-2} soft X-ray fluence, and protonema of the moss Brachythecium (c), (d) 41mJ.cm^{-2} soft X-ray fluence.

an X-ray fluence and/or insufficient development[5]. The enhanced X-ray fluence now possible in TA4, coupled with quantification of fluence received by the specimen (which enables the required resist development to be accurately predicted) has resulted in improved images of tomato hairs, after exposure to 60mJ.cm^{-2} and 8 minutes development in 50% MIBK in IPA. These show remarkable similarity to the earlier images of Digitalis hairs (figure 2a), in particular, the presence of numerous longitudinal transcellular strands, sometimes associated with cytoplasmic organelles. Images produced using the same system, but a lower soft X-ray fluence (40mJ.cm^{-2}), show a closer resemblance to those reported previously for TA4[5] with much less cellular detail visible (figure 2b) though an extension of the 5 minute development time may have disclosed greater detail. Nonetheless, some cytoplasmic strands can be observed. This suggests that the minimum soft X-ray fluence at the resist surface which can currently be used to image hydrated biological specimens, such as these epidermal hairs, is 50-60mJ.cm^{-2}.

Images have also been obtained of protonema of the moss Brachythecium using a similar soft X-ray fluence of 41mJ.cm^{-2} and a development time of 4 minutes (figures 2c;2d). The cell wall is clearly delimited in one image (figure 2c) as are some cytoplasmic organelles. The general appearance of the cell interior, whilst bearing some similarity to that of the epidermal hairs, suggests a more irregular granular composition rather than numerous transcellular strands.

ACKNOWLEDGEMENTS

This work was supported by SERC Grant GR/F 81514. We are grateful to Pete Anastasi and Dean Morris of Kings College, London for the manufacture and subsequent coating of the Si_3N_4 windows. The assistance of the staff of the E.M. Unit at RHBNC is also gratefully acknowledged.

REFERENCES

1. T.W.Ford et al. Elect. Microscop. Revs. *In Press*
2. A.D.Stead et al. *X-Ray Microscopy III In Press*
3. A.D.Stead & T.W.Ford Ann. Bot. 64 713 (1989)
4. T.W.Ford et al. J. X-ray. Sci. Technol. 1 207 (1989)
5. T.W.Ford et al. *Inst. Phys. Confr. Ser.* 98 527 (1990)
6. R.A.Cotton *this volume*
7. P.C.Cheng et al. Nucl. Instr. Meth. Phys. Res. A246 668 (1986)

MEASUREMENTS OF COMPRESSIVE AND TENSILE STRAIN DURING SHOCK BREAKOUT BY THE USE OF SUB-NANOSECOND X-RAY DIFFRACTION.

N. C. Woolsey, J. S. Wark, W. J. Blyth
Clarendon Laboratory, Oxford University, Parks Road, Oxford, OX1 3PU

INTRODUCTION

The study of strain evolution in shocked compressed materials is of great theoretical and practical importance. The present experimental aim is to extend the work previously reported[1-4] on shock breakout to a variety of shock compression strengths, durations and crystal thickness, and to look at the dependence of shock evolution on these three factors.

The major problem in the experimental determination of many questions outstanding in this area has been achieving the require time resolution, conventional techniques rely on the piezo-electric response of stress gauges or time resolving electrical output from pick-ups moving through uniform magnetic fields[5]. These are restricted to surface measurements and operating temporal limit at best of 1 nsec. As reported previously,[1] and else where[2,3,4] we have been able to overcome these limitations by the use of intense X-ray emission from laser generated plasmas.

EXPERIMENT

The targets used were (111) orientated single crystal silicon. Three different thicknesses were used (45 μm, 76 μm, 125 μm) with the target faces parallel to within 30 seconds of arc and

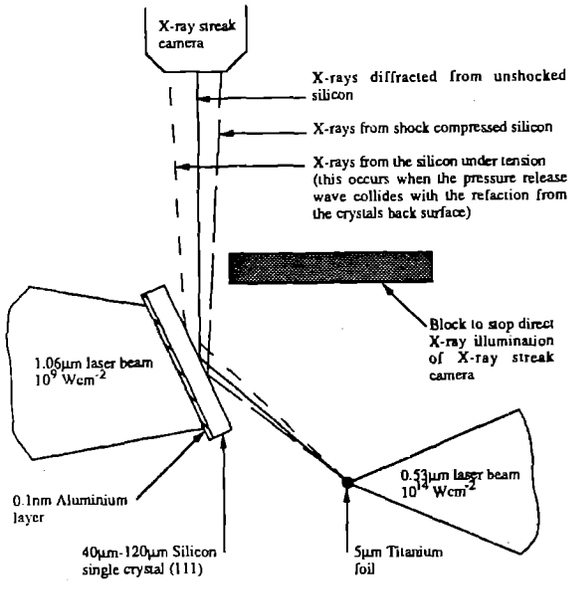

Figure 1. Schematic of the shock breakout experimental arrangement. The shift in diffraction off the crystal surface is shown clearly demonstrating the need for large focal spots (diameters >10mm) with good beam uniformity.

aligned to the (111) lattice planes better than 1/4°. One surface of the silicon was coated, with a 1000 Å layer of aluminium. (Previous investigations have concentrated on targets which have a plastic tamping layer over the aluminium, confining the aluminium plasma increasing the shock strength and duration.[1-4]. In this experiment we wished to study short duration rapid rise time shocks so a plastic tamping layer was not used.). A second

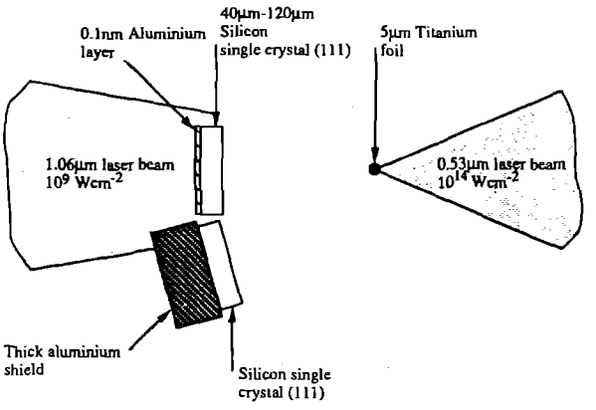

Figure 2. Diagram shows the alignment of two silicon (111) single crystals, one of which is shock compressed, the other shielded by an aluminium plate is not shocked. The latter crystal is rotated by an angle of ~15° to ensure the diffracted beam enters the slit of the X-ray steak camera. The two crystals are tilted to slightly different angles so the images are spacially seperated on the slit. (The X-ray streak camera is directly above the drawing , the slit centred on the shocked crystal.)

single crystal of silicon (111) (see Figure 2), was used as a spectrometer and recorded the helium-like emission from the plasma on an X-ray streak camera.

The plasma X-ray source was created by focussing a frequency doubled (0.53 μm) beam to a tight point (~60 μm diameter) on a 5 μm titanium foil. At irradiances of the order 10^{14} Wcm^{-2} the plasma is a prolific emitter of helium-like line radiation. This line radiation is Bragg diffracted from the crystal surface and then recorded on an X-ray streak camera. Diffraction images from both crystals were recorded simultaneously on the same X-ray streak camera with a time resolution of 40 psec, their angle to the X-ray source being slightly different so the images were spatially separated on the cameras' photocathode. The arrangement of the two targets is shown in Figure 2 (only the shocked target is shown in Figure 1 in the interest of clarity). The shocked target is aligned directly and normal to the X-ray source, the X-ray streak camera slit is above the diagram and in the plane of the titanium X-ray source and the centre of the shock crystal.. The secondary target is displace to one side and protected from the shock driving laser beam by an aluminium plate, it was necessary to rotate this crystal, as shown, by 15° in order to get the diffracted beam onto the X-ray streak camera slit.

The shock wave was generated by a second laser beam, focussed to a large focal spot, between 15 and 30 mm in diameter (Figure 1. outlines the need for such large focal spots). The ablation of the aluminium coating on the targets' surface launches a shock in to the silicon crystal. The shock strength was varied by adjusting the beam irradiance between 10^9 Wcm^{-2} and 10^{11} Wcm^{-2}. A shock duration study was carried using pulse lengths of 170 psec 600 psec and 1500 psec, with the temporal profile of the

shock driving beam being monitored on an optical streak camera, the images were recorder using an Oxford Framestore Applications image grabbing system.

RESULTS

Typical data recorded on the X-ray streak camera is shown in Figure 3. Two diffraction images are shown, the lower from the secondary unshocked crystal the upper from the shocked 76 μm thick crystal. The crystal was shocked with a 800 psec pulse at an irradiance of $5x10^{11}$ Wcm^{-2}, the reflected energy was measured to be less than 3%. The triple line structure is characteristic of Helium like emission, they are the resonance line (2.612 Å), intercombination line (2.625 Å) and unresolved dielectronic satellites of lithium like titanium (~2.635 Å). The values for compression and tension are also shown in the Figure, the tension is measured from the resonance line and compression from the dielectronic satellites. Time moves left to right, with zero time defined as the time the material is first observed to go into tension. The curve in the two spectra is a result of image intensifier distortion which can be removed.

In interpreting the data it should be recalled that the X-rays are not restricted to the surface but probe through a depth of crystal. The 1/e absorption depth in silicon for 2.61 Å radiation is 15.4 μm, at an angle of 24.5° (the Bragg angle) this gives a probe depth normal to the surface of 6.4 μm, since the radiation must also leave the crystal 6.4 μm represents the $(1/e)^2$ absorption depth. The shock velocity along the <111> direction in silicon was estimated as 9.8 μm/nsec, thus the whole shock wave thickness could be recorded at breakout for the 130 psec and 600 psec laser pulses.

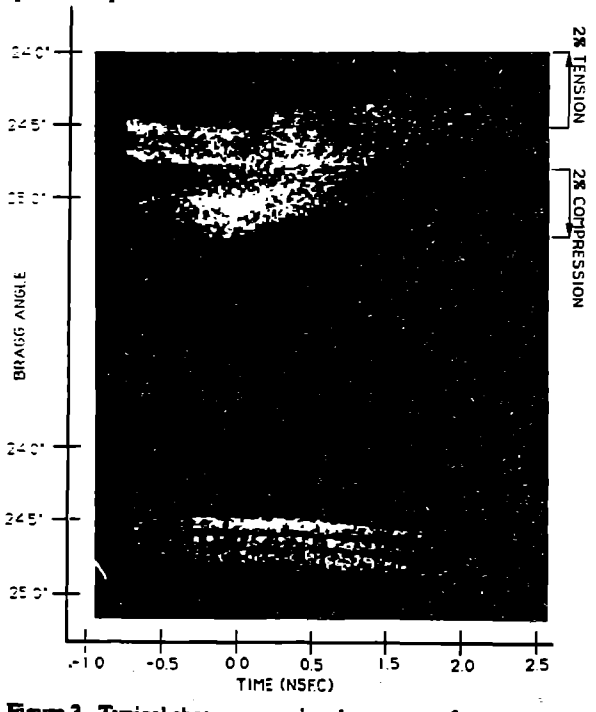

Figure 3. Typical shot compression data see text for commentary.

In diffraction from such highly strained crystals the probe depth is governed by photoelectric absorption, a kinematic process rather than extinction, a dynamical process. The intensity of the diffracted signal is also a function of the strain gradient. Figure 4 shows densitometer tracings through the shocked spectrum given in Figure 3. At time -400 psec the crystal is seen to be in compression, the shifted signal is still weak since the shock wave has still to hit the rear surface of the crystal the majority of the

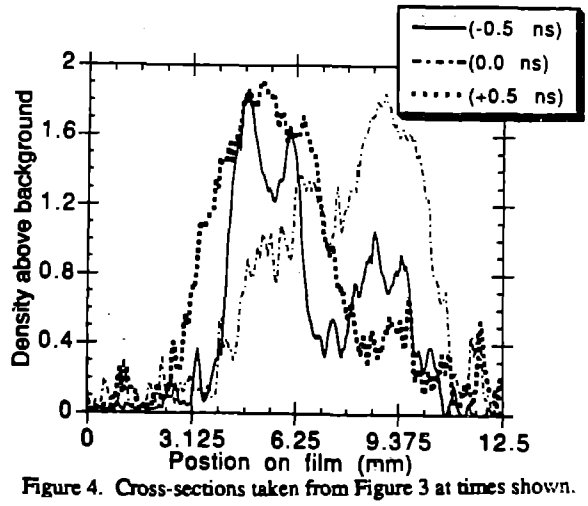

Figure 4. Cross-sections taken from Figure 3 at times shown.

probed material is undisturbed. At 0.0 nsec the signal from the compressed material increases with an almost complete disappearence of the undisturbed signal (~26.5° in Figure 3 and film position ~5 mm in Figure 4). This corresponds to the shock wave reaching the rear surface of the target, all the probed material is in a state of compression. At this point a pressure release wave forms (since the crystal face is a free surface), this wave travels back in to the crystal and collides with the release of the shock. The lattice is now seen to expand and (Figure 3 t=0.0 to ~2 nsec and Figure 4 t=+0.5 nsec). The collision of the two rarefactions can cause the lattice to break resulting in spallation.

Importantly the helium-like line emission from the plasma has been recorded for each shot (Figure 3). This will enable us to deconvolved the spectral structure from the shock data and allow shock information to extracted directly from film. Previously we have modelled the shock compression and convolved these numerical results with typical helium-like spectra. This simulation has then been compared with the cross sections extracted from film[1-4].

CONCLUSION

Shock breakout has been studied for three crystal thicknesses. We have taken data at three different pulse lengths and for at least two shock strengths. The helium-like emission from the plasma has been recorded with the shock data, this is of considerable importance since it will allow accurate shock profiles to be extracted from the data for the first time. The temporal profile of the shock driving laser pulse has also been recorded this should enable us to model the shock shape at the front surface of the silicon and will provide a direct comparison to the profile extracted from the breakout data.

REFERENCES

1. J. S. Wark, G. Keihn, R. R. Whitlock, D. Rily and N. C. Woolsey, Annual Report to the Laser Facility Committee Rutherford Appleton Report (1990).
2. J. S. Wark, R. R. Whitlock, A. Hauer, J. E. Swain, and P. J. Solone, Phys. Rev B Rap. Comm. 35, 9391 (1987).
3. J. S. Wark, R. R. Whitlock, A. Hauer, J. E. Swain, and P. J. Solone, Phys. Rev B 40, 5705 (1989).
4. J. S. Wark, G. Keihn, R. R. Whitlock, D. Riley and N. C. Woolsey, J. Appl. Phys. 68, 4532 (1990).
5. L. V. Al'tshuler, M. N. Pavlovskii and V. P. Drakin, Soviet Physics JETP 52, 260 (1967)

SUB-NANOSECOND X-RAY POWDER DIFFRACTION

N. C. Woolsey, J. S. Wark, W. J. Blyth

Clarendon Laboratory, Oxford University, Parks Road, Oxford, OX1 3PU.

INTRODUCTION

Over the past few years we have concentrated on the study of shock compressed single crystals. There have been a number of achievements, the first direct measurement of tensile strain during shock-breakout and unit cell measurements of lithium fluoride during hydrostatic compression. The intensities from single crystals is sufficiently high to allow single-shot diffraction measurements to be made, with powders the diffraction signal is expected to be 2 orders of magnitude lower. Last year we reported the first sub-nanosecond X-ray diffraction measurements made from a powder with a Seemann-Bohlin camera[1,2].

The extension of sub-nanosecond X-ray diffraction techniques to powders is important for many reasons. Firstly the majority of materials which have been studied by other workers with more conventional techniques and those materials of engineering interest are either polycrystalline or ceramics. Secondly, a long standing aim has been the investigation of shock induced phase changes. Time resolved X-ray diffraction provides a means of recording such structural changes at the lattice level[3] which should compliment and extend the conventional macroscopic measurements already made. X-ray diffraction, with plasmas as the source, has the further advantage of having a time resolution better than almost all other measurements.

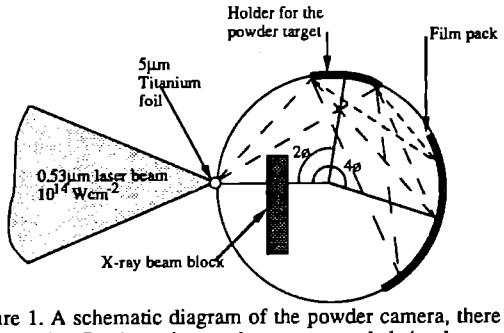

Figure 1. A schematic diagram of the powder camera, there are three (hkl) reflections shown, these are recorded simultaneously during one shot. The Bragg angle ø is shown for the centre reflection.

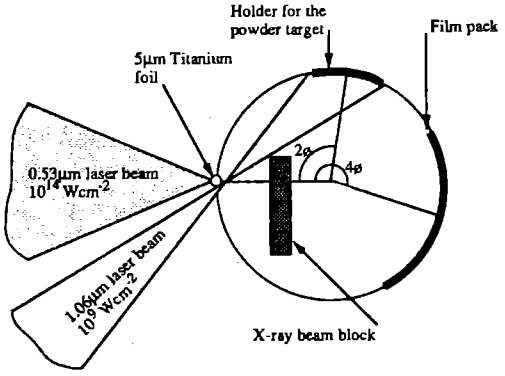

Figure 2. The powder camera,showing the laser beam configuration. As TAWest chamber only allows a spherical arrangement of beams, the X-ray source (titanium foil, generated with the 150mm backlighting beam) fixed at the centre, with the shock driving beam (108mm beam) focused but slightly displaced from centre, illuminating the powder target after the focus.

SEEMANN-BOHLIN CAMERA

The diffraction signal from a powder is inherently several orders of magnitude lower than a single crystal. This is due to the random orientation of the crystallites, to gain a diffraction single it is necessary to integrate over many crystallites. This can be achieved using a focussing camera, we reported the use Seemann-Bohlin camera and demonstrated its the feasibility for recording single shot diffraction images from powders last year[1,2]. The Seemann-Bohlin camera is shown in Figure 1. The original camera had a large focussing circle of radius 7.5 cm, a half size camera (focussing circle radius 3.75 cm) was built for the current experiment. This has the advantage of doubling the diffracted intensity (1/r dependence) of course this is offset by increasing the fogging by a factor of 4.

EXPERIMENT

In the previous experiment diffraction signals were recorded, however the recorded density on film was too low to extend shocked the powders. To overcome the intensity problem we designed a smaller Seemann-Bohlin camera and used the 150 mm backlighting beam in TAWest of the VULCAN laser facility. This beam can deliver up to 500 J in 1.06μm, it was frequency doubled with conversion efficiency of 40% to 0.53 μm and focussed on to a 5 μm titanium foil. At irradiances of 10^{14} Wcm^{-2} the plasma created is a prolific source of helium-like line radiation, this radiation is Bragg diffracted from the targets. A silicon (111) spectrometer measured the time integrated X-ray emission from the titanium source. The diffracted images were recorded on Kodak DEF II film.

A standard 108 mm beam (at 1.06 μm) was used to shock compress the powder and metal foil targets. TAWest has a fixed constructed designed for spherical geometry experiments. This restricted the laser beam arrangement to that shown schematically in Figure 2.

TARGETS

Two types of targets were used, compressed powder pellets and metal foils. The powders used were lithium fluoride (LiF), potassium chloride (KCl), potassium bromide (KBr) and caesium iodide (CsI). In order to ensure the diffraction from the powders was kinematic and the number particles over the target was maximised the powders were ground. Typical particle sizes were 20-30 μm for KCl and KBr and <5 μm for LiF and CsI.

Aluminium and zinc foils were also studied, they were checked by Laue X-ray diffraction to look for preferred orientation of the crystallites making up the foil and to ensure the grain size would be small enough, no strong preferred orientations were found and grain size was estimated to be <100 μm.

Target sizes were 2.0 cm by 3.2 cm with the compressed powders approximately 1 mm thick and an internal radius of 3.75 cm, the foils were 50 μm thick. Each of the targets were coated, on the inside face with 1000 Å of aluminium and then 20 μm of plastic, this design was adopted as it has been found to increase shock strenght and duration in single crystals[4].

RESULTS

Diffraction signals were recorded from all types of targets used. It was found up on shocking the targets the X-ray intensity at film was too low to record any shift, and in most cases the diffraction signal was lost altogether when the targets were shocked. What is notable, however, is the number of lattice planes which can be recorded in one shot. Figure 3 shows a densitometry trace across film where 6 (h,k,l) reflections can be seen. Shot 17191290 was taken from an unshocked KBr target the lines seen are the (311), (222), (400), (331), (420) from KBr. The additional line at ~66° is the (220) reflection from the aluminium powder camera.

One of the major problems encountered in this work has been fogging of the film, this is thought to be due to hot electron production from the titanium foil. In order to produce high levels titanium helium-α (2.612 Å) emission, a high irradience was used on target this inevitably produces hot electrons and fogging. Much of the fogging has been reduced by surrounding the titanium with a mylar tube, stopping the electrons. It is not possible to position this tube 'out-of-sight' of the film pack with the consequence of fogging the film as seen on the left of Figure 3.

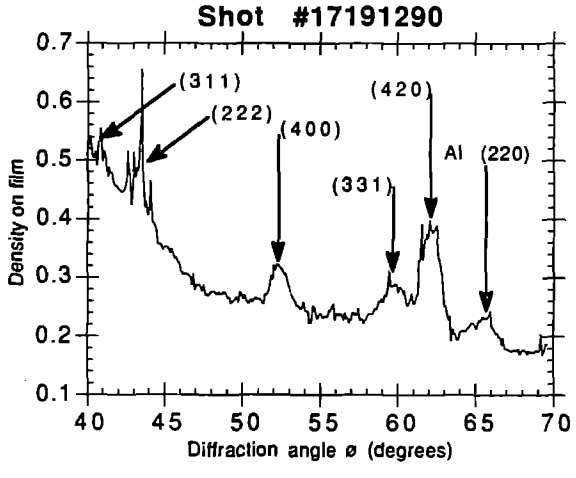

Figure 3. Densitometer trace showing 5 (hkl)'s from potassium bromide, and Al (220) reflection from the aluminium powder camera.

CONCLUSION

Enough data has been collected to allow a complete characterisation of the Seemann-Bohlin camera.

We have been able to record diffraction images from many lattice planes on single shots from both compressed powder targets and metal foils. The intensities are just below what we believe to be necessary to record shifts of the diffraction lines during shock compression. With an increase in intensity it should be possible to observe the compression of the lattice on many planes simultaneously allowing crude unit cell measurements to be made and enable us to make phase transition measurements in materials such as KCl and KBr[5-7].

FURTHER WORK

The intensity of the diffracted signal from the powder targets was found to be too low to see any shift in the lines when shocked. We are performing some line tracing simulations of the Seemann-Bohlin camera and propose to include X-ray absorption of the targets in the calculations. Early results suggest a spherically focussing target design, with both radius of curvature at 3.75 cm, will give the increase X-ray flux to record a shocked image. Although this will only allow a perfect focus at Bragg angle of 45° (i.e 180° on the camera), we expect an order of magnitude improvement on film for most angles.

REFERENCES

1. JS Wark, NC Woolsey and D Riley *Annual Report to the Laser Facility Committee* Rutherford Appleton Laboratory (1990)
2. NC Woolsey, JS Wark, D Riley *J. Appl. Cryst.* Fast Comm., **23** 441 (1990)
3. Q Johnson and AC Mitchell *Phys. Rev. Lett.* **29** 1369 (1972)
4. JS Wark, RR Whitlock, AA Hauer, JE Swain and PJ Solone *Phys. Rev.* B**35** 9391 (1987)
5. LV Al'tshuler, MN Pavlovskii and VP Drakin *Soviet Physics JETP* **52** 260 (1967)
6. LV Al'tshuler et al. *Soviet Physics-Solid State* **9** 2417 (1968)
7. DB Hayes *J. Appl. Phys.***45** 1208 (1974)

THREE DIMENSIONAL SIMULATIONS OF THE IMPLOSION OF INERTIAL CONFINEMENT FUSION TARGETS

R. P. J. Town and A. R. Bell

Imperial College, London

An important issue facing Inertial Confinement Fusion (I.C.F.) is implosion symmetry. A typical I.C.F. target can be characterised as passing through three phases: acceleration, coasting and deceleration (1). We have written a 3 dimensional (3D) spherical hydrodynamics code called PLATO to model the growth of asymmetries during the coasting and deceleration phase. We are exploiting the symmetry imposed on the target by the Rutherford Appleton Laboratory's 12 beam Vulcan laser system to reduce the computational grid.

In a typical I.C.F. implosion a shock wave is launched into the stationary fuel. The shock wave is reflected at the origin and travels outward colliding with the incoming shell. To a good approximation we found that the radius of the inner surface ($R1$) obeys $R1 = R1_{mc} + 0.5g(t - t_{mc})^2$ where $R1_{mc}$ is the inner surface radius at the time t_{mc} of maximum compression (1). When the central hot spot region satisfies the conditions for fusion, it ignites and a burn wave propagates outwards. The deceleration phase ends at this time with the remainder of the shell rapidly expanding. In the absence of α particle heating the shell continues to obey equation (1). It is during this deceleration phase that the inner surface of the shell is RT unstable.

The simulations to study the deceleration phase were modelled in one dimension during the coasting phase. The radial cells were uniform with a resolution of $0.5\mu m$. There were 10 grid points in each of the θ and ϕ direction giving 20 cells per wavelength. Additional simulations performed with 30 cells per wavelength showed no substantial difference. The initial conditions closely follow those of the 2D cylindrical simulations of Sakagami and Nishihara (3). A $60\mu m$ thick unperturbed shell of density $5.0g/cm^3$ at an initial radius of $130\mu m$ was intialised travelling inwards, coasting at a velocity of $1.5 \times 10^7 cm/s$ into a stationary fuel of density $0.5g/cm^3$. The region outside the shell had a density of $0.5g/cm^3$ and the same initial inward velocity. A uniform pressure of $2.0 \times 10^{13} dyne/cm^2$ was used in all regions. When the reflected shock wave was almost incident on the inner surface of the shell, at 0.626 nsecs, the one dimensional density profile ($\rho_{1D}(R)$) was converted to 3D and perturbed by imposing a variation of amplitude (δR) in the position of the inner surface ($R1$) over a width w. We assume that each laser beam generates the same angular pattern. The perturbation is thus the sum of the Legendre polynomials from all twelve beams. Modes one to five are not perturbed; the symmetry of the laser beams cancels these modes. The lowest order mode which can be imposed on a balanced 12 beam system is the sixth order Legendre polynomial summed over the laser beam poles. The density profile ($\rho(R, \theta, \phi)$) is thus given by equation (2):

$$\rho(R, \theta, \phi) = \rho_{1D}(R + \delta R \sum_{b=1}^{12} P_6(\cos(\xi_b))) \qquad (2)$$

where

$$\delta R = \begin{cases} \frac{\delta_0}{2}(\cos(\frac{2\pi(R-R1)}{w}) + 1), & \text{if } R - R1 < \frac{w}{2}, \\ 0.0, & \text{otherwise} \end{cases}$$

and $\cos(\xi_b) = \cos(\theta)\cos(\theta_b) + \sin(\theta)\sin(\theta_b)\cos(\phi - \phi_b)$.The angle ξ_b is the angular distance from the bth laser beam which is sited at the coordinates (θ_b, ϕ_b).

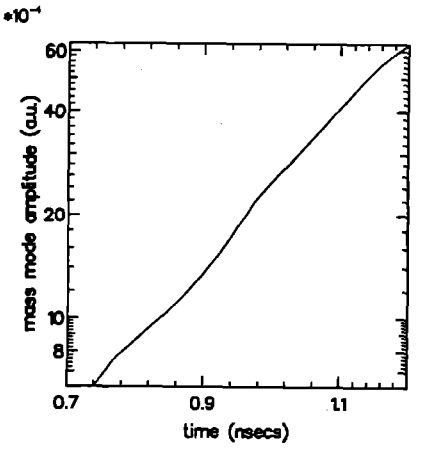

Figure 1: The time evolution of the mass mode amplitude.

The arrangement of the laser beams implies that the mass distribution ($\sigma(\theta, \phi)$) can be expressed as the sum of all Legendre polynomials summed over the laser beams:

$$\sigma(\theta, \phi) = \sum_{n=0}^{\infty} a_n \sum_{b=1}^{12} P_n(\cos(\xi_b)) \qquad (3)$$

where the coefficient a_n is the mass amplitude of the nth mode. In an analogous way to Fourier theory we can obtain the coefficient of the kth mode as follows. At selected times the mass distribution is obtained by integrating from the centre through the shell to the outer boundary the product of the density and radius squared. This is multiplied by the kth Lengendre polynomial and integrated over all angles. This gives us a measure of the RT growth, which we refer to as the mass mode amplitude. The evolution of the mass perturbation is a signature of the RT instability; in secular growth no such movement of mass would be noted. An alternative measure of the RT growth is to calculate the distance ($\Delta R1$) between the tip of the spike ($R1_{min}$) and the head of the bubble ($R1_{max}$).

Firstly we model the linear regime by placing a small amplitude ($\delta_0 = 0.005R1$), moderate width ($w = 0.5R1$) perturbation. In figure 1 the time evolution of the mode amplitude is plotted. The straight line indicates linear growth with a growth rate of $5.41 nsec^{-1}$. For the simulation parameters the classical growth rate is $6.15 nsec^{-1}$. A reduction of only 10% to approximately 90% classical is inferred. This small reduction is to be expected: unlike the acceleration phase there are no additional physical effects (such as ablation dynamics) to markedly reduce the classical behaviour. 2D simulations with the same initial conditions were also performed. The reduction from the classical growth rate in the 2D simulations was identical to the reduction observed in 3D. In the linear phase the 3D problem essentially decouples into two 2D problems: there is no interaction between the two 2D modes hence the growth is the same as in the 2D case.

To assess the non-linear behaviour the initial amplitude of the perturbation was increased ($\delta_0 = 0.1R1$) so that the linear regime saturated quickly. As previously reported (4) we observed a single well-defined bubble rising up surrounded by a series of interconnecting spikes falling to form ridges, termed the 'bubble-ridge' arrangement. When the perturbation was inverted thin spikes penetrated into the fuel which were surrounded by a valley of interconnecting bubbles. This we termed the 'spike-valley' arrangement.

In figure 2 we plot the evolution of $\Delta R1$ for both the normal and inverted arrangements. We see that there appears to be no difference in the evolution and growth of each arrangement. We achieved a best fit to an $\eta g t^2$ law with a value of $\eta = 0.23$. We have compared this with corresponding simulations in 2D spherical and cylindrical geometries. The 2D spherical case has a slightly larger η of 0.25. However, in cylindrical geometry $\eta = 0.18$. The mass mode amplitude evolves in quite a different way (figure 3). Now the 'bubble-ridge' arrangement has a higher growth rate than 'spike valley'. In both cases the mass mode amplitude evolves proportional to gt^2. Mass is redistributed more quickly in the 'bubble-ridge' arrangement resulting in the earlier disruption of the shell. This conclusion is supported by 2D simulations. 2D spherical simulations with the bubble centred on the pole of the coordinate system show growth comparable with the 3D 'bubble-ridge' arrangement. However 2D cylindrical simulations show lower growth.

The differences between 2D and 3D and between the two 2D geometries can be explained by considering the nature of the 'bubble' in the different geometries. In the 'bubble-ridge' arrangement we have a truly 3D bubble surrounded by a ridge of interconnecting spikes. Similarly in the 2D spherical case, where bubble is centred on the pole, the bubble is essentially 3D, surrounded by a ridge around the waist. In the 2D cylindrical case the bubble is in reality a valley running around the sphere. In the 3D case the bubble has a larger boundary to feed mass into the spike then the 2D cylindrical case. Let us assume that the growth can be expressed as the product of the length of the boundary between the bubble and spike and the velocity of mass flowing across the boundary normalised to the area of the bubble. In 3D the boundary $= 2\pi r$, where r is the radius of the bubble and the normalising area is πr^2 giving a ratio of boundary to $area^{1/2}$ equal to $2\sqrt{\pi}$. In 2D the boundary is $2a$, where a is the length of the bubble under consideration, with an area of a^2 giving a corresponding ratio of boundary

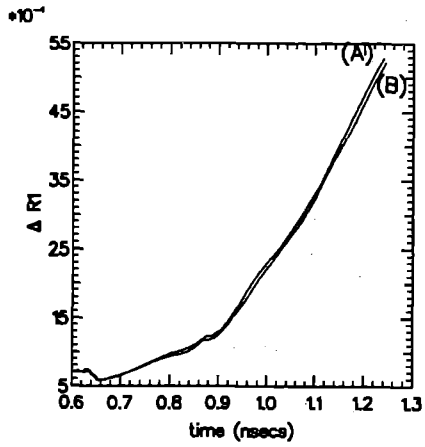

Figure 2: The time evolution of the diference ($\Delta R1$) between the head of the bubble and the tip of the spike for the 'bubble-ridge' (A) and 'spike-valley' (B) arrangements.

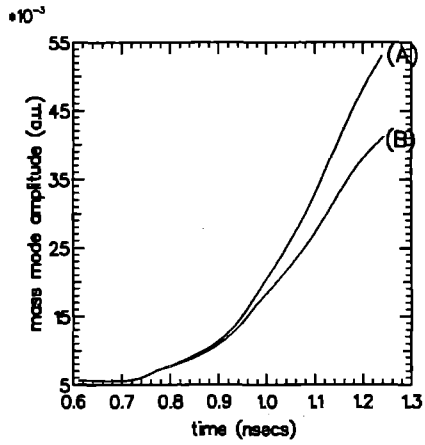

Figure 3: The time evolution of the sixth order mass mode amplitude for the 'bubble-ridge' (A) and the 'spike-valley' (B) simulations.

to $area^{1/2}$ equal to 2. The boundary around a bubble is $\sqrt{\pi}$ times larger in 3D than 2D allowing mass to pass from the bubble to the spike more easily in 3D, hence giving a faster growth.

Sakagami and Nishihara (5) find a much larger difference between 2D and 3D. They find 0.2 in 2D, but $\eta = 0.8$—1.1 in 3D. Sakagami and Nishihara characterise the growth in terms of a mode amplitude calculated by integrating the mass density in the radial direction away from the centre of the target. This can only be related to gt^2 (a distance) by scaling the amplitude by a dimensional quantity. There is considerable uncertainty in the required scaling factor which is further complicated by the change in density and size of the target as it compresses. We suspect that the explanation of their large η lies in the choice of scaling factor.

In conclusion we have reported 3D simulations of the deceleration phase of an I.C.F. target. We have obtained linear RT growth rates which are 90% of the classical value. These have been found to be identical to similar 2D cylindrical and spherical results. In the non-linear regime we have found a faster mode evolution in 3D simulations than in 2D cylindrical geometry. This has been attributed to the greater bubble-spike boundary in 3D. We have observed two possible geometries in which the RT instability can grow in 3D: the 'bubble-ridge' and 'spike-valley' arrangements. The mass mode evolution of the 'bubble-ridge' geometry is faster. Shell integrity is maintained for longer if the shell is driven more strongly immediately under the beams rather than at the intersections of the beams.

REFERENCES

1. D. L. Book and S. E. Bodner, Phys. Fluids 30, 367 (1987)
2. Lord Rayleigh, Theory of Sound (Dover, New York, 1945) 2nd Edition
   G. I. Taylor, Proc. Roy. Soc. London, Ser A 201, 192 (1950)
3. H. Sakagami and K. Nishihara, Phys. Fluids B 2, 2715 (1990)
4. R. P. J. Town and A. R. Bell *Annual Report to the Laser Facility Committee* Rutherford Appleton Laboratory Report RAL-90-026 Sect A4 (1990)
5. H. Sakagami and K. Nishihara, Phys. Rev. Lett. 65, 432 (1990)

COLLISIONLESS ABSORPTION OF SHORT PULSES

Paul Gibbon[1*], A.R. Bell[2]
[1]Max-Planck-Inst. f. biophys. Chemie, D-3400 Göttingen, Germany
[2]Blackett Laboratory, Imperial College London SW7 2BZ, England

One of the central issues in sub-picosecond interaction with matter is whether the laser energy can be coupled to the target with high efficiency. This factor will ultimately determine the viability of a number of prospective short-pulse X-ray laser schemes [1]; a very low efficiency will offer little advantage over the long-pulse, high-energy techniques. [2]

Analysis of recent experiments with sub-ps laser-plasma interaction has to date rested on collisional absorption models; laser energy is absorbed via inverse-Bremsstrahlung over a distance s $\simeq 2c/\omega_p$, which is short compared to a wavelength when $n_e/n_c \gg 1$. In the limit $\nu_{ei}/\omega_o \ll 1$, and $v_{osc}/c \ll 1$, the absorbed fraction is approximately $2\nu_{ei}/\omega_p$. A more detailed account of this model (including oblique p- and s-polarized light) can be found in Ref.[3].

While there is good agreement with experimental data at low intensities, it is not clear that theses results can be extrapolated to higher intensity; no experiments have yet been performed (with $1/4\mu m$ lasers) in the region $I_o = 10^{17} - 10^{19} W cm^{-2}$. Collisional absorption will decrease for two reasons: firstly as the quiver velocity exceeds the thermal velocity; secondly as the temperature increases via heating from the laser. A quantitative absorption calculation would require a fully self-consistent treatment of these effects, including non-local thermal transport.

There are other mechanisms which may contribute to the high-intensity absorption: resonance absorption can occur in density gradients $L/\lambda \geq 0.2$; vacuum heating [4] may yield absorption fractions over 50%; and skin effects[5] probably play a role too.

We have studied collisionless absorption in steep gradients using a 1.5D Particle-in-Cell code[6]. Since all three of

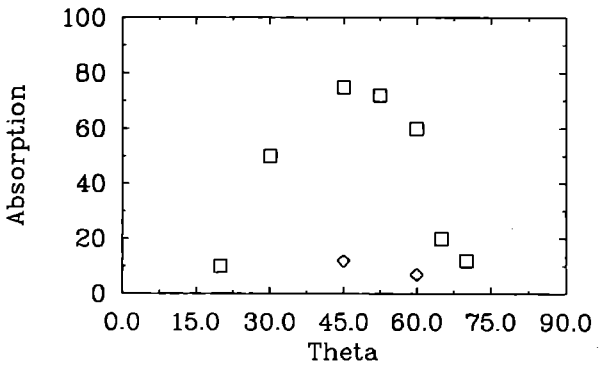

Figure 1: Absorption vs angle of incidence for $L/\lambda = 0.1$ (squares) and $L/\lambda = 0.01$ (diamonds)

the above-mentioned effects may occur in the 'steep-gradient' plasmas generated by sub-ps pulses, we have attempted to find out which effect dominates over a range of laser and plasma parameters. Some results are shown below.

Characteristic angular dependence of absorption is shown in Figure 1 for two density gradients. The curve for $L/\lambda = 0.1$ shows higher absorption than for classical resonance absorption, and appears to agree with collisional fluid theory.[3] The second curve for $L/\lambda = 0.01$ shows very low absorption over all angles, in contrast to the Fresnel solution for $L/\lambda \to 0$.

Intensity dependence for two cases is shown in Figure 2. Peak absorption ($\eta \sim 80\%$ is found at $I\lambda^2 = 10^{16}$ for $L/\lambda = 0.1$, and at $I\lambda^2 = 3 \times 10^{14}$ for $L/\lambda = 0.04$. The scaling of $(I\lambda^2)_{max}$ with L/λ is currently under investigation. Physically, one expects maximum absorption when the excursions of electrons in the evanescent electric field take them all the way out into the vacuum, where they experience the full laser field. The 'Brunel' effect will then dominate the heating with the skin layer of the solid. This should occur when $v_{osc/c} \sim k_o L$, but the true scaling is complicated by the build-up of space-charge in the vacuum region.

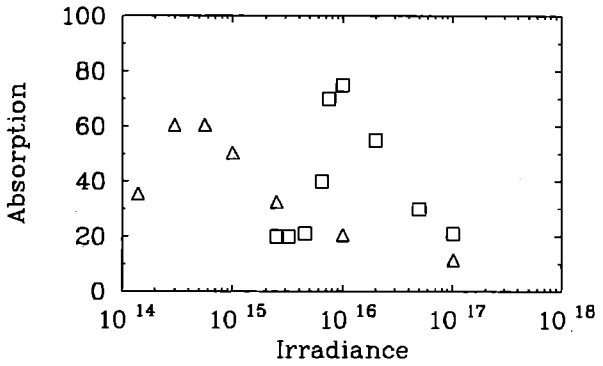

Figure 2: Absorption vs laser irradiance for $L/\lambda = 0.1$ (squares) and $L/\lambda = 0.04$ (triangles)

References

[1] M.M. Murnane, H.C. Kapteyn, M.D. Rosen, and R.W. Falcone, Science **251**, 531 (1991).

[2] M.H. Key, Nature **316**, 314 (1985).

[3] R. Fedosejevs, R. Ottman, R. Sigel, G. Kühnle, S. Szatmari, and F.P. Schäfer, Appl. Phys. B **50**, 79 (1990).

[4] F. Brunel, Phys. Rev. Lett. **87**, 52 (1987).

[5] W. Rozmus and V.T. Tikhonchuk, Phys. Rev. A **42**, 7401 (1990).

[6] P. Gibbon and A.R. Bell in *Annual Report to the LFC*, Report RAL-90- (1990).

STATIC HOMOGENEOUS FIELD IN DENSE HIGH-Z PLASMAS

S.Pfalzner[1], S.J.Rose[2]

[1]GSI, Darmstadt

[2]Rutherford Appleton Laboratory

INTRODUCTION

During the interaction of very high power laser radiation with matter, if the electric field due to the laser is comparable with, or greater than the electric field from the atomic nucleus, it is no longer possible to consider the effect of the laser as a perturbation to the atomic electronic structure [1,2]. In this work we are starting to investigate the effect of such high-power laser interaction with matter by considering the effect of a static electric field on the electronic structure of material. We use a non-perturbative technique which calculates the electronic structure within the Thomas-Fermi model self-consistently with an external electric field.

2 D - THOMAS-FERMI MODEL

The standard Thomas-Fermi (TF) model includes only electrostatic electron- electron interaction and the Pauli principle is the only quantum feature. The Thomas-Fermi equation describes the potential as a function of the distance from the nucleus

$$\Delta V = \frac{32\pi^2}{3(2\pi\hbar)^3}\left(2me(V(\vec{r}) - V_o)\right)$$

with $V(\vec{r}) = -e\int \frac{n_e(\vec{r})d\vec{r}}{|\vec{r}-\vec{r}'|} + V_{ex} + \frac{Ze}{r}$. Brewczyk and Gajda [3] showed that the time-dependent external field can be replaced by a static one if the ionization process is non-resonant and the laser frequncy less than $\sim 10^{15}$ s^{-1}. With $V_{ex} = -zE$ the TF equation in polar coordinates is then

$$\left(\frac{\partial^2}{\partial x^2} + \frac{1}{x}\frac{\partial}{\partial y}(1-y^2)\frac{\partial}{\partial y}\right)u = \frac{u^{3/2}}{x^{1/2}}.$$

where $r = \mu x$, $\mu = Z^{-1/3}(3\pi/4)^{2/3}\frac{\hbar^2}{2mc^2}$, $u = \frac{r}{Ze}(V - V_0)$ and $y = \cos(\theta)$.

In the case of a dense plasma the boundary conditions are

$$u(x \to 0) = 1 \qquad \frac{u}{x} - u' = -xyE|_{x=x_o}$$

where $x_o = \left(\frac{4\pi n_i}{3}\right)^{-1/3}$ is the boundary of the atom. Fig.1 shows a contour plot of the potential resulting from the numerical solution of these equations. The influence of the field is larger the smaller the density of the surrounding plasma. The result shows that the effect of the field is to grossly distort the electronic structure within the atom which suggests that estimates of the strong field ionization degree using the spherical symmetric solution of the TF equation may not be appropriate. Using a definition of the ionization degree of the standard Thomas-Fermi model, in which the average degree of ionization is simply the electron number density at the ion-sphere radius multiplied by the ion-sphere volume, we intend to calculate upper and lower bounds to the ionisation degree caused by the electric field. This method can be extended to the temperature-dependent case as well as to include exchange and correlation corrections of the Thomas-Fermi model.

REFERENCES

1. P.Agostini, F.Fabre, G.Mainfray, G.Petite,N.K.Rahman, Phys.Rev.Lett **42** 1127 (1979)

2. A.L'Huiller, L.A.Lompre, G.Mainfray, C.Magnus, Phys. Rev A **27**, 2503, (1983)

3. M.Brewczyk, M.Gajda, J.Phys.B **21**, L838 (1989)

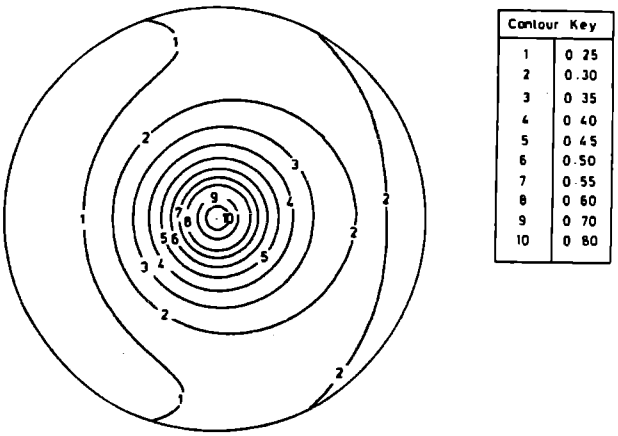

Figure 1: Contour plot of u for iron at $78gcm^{-3}$

IONIZATION CHARACTERISTICS IN HOT DENSE PLASMA

J. Edwards[1] and S. J. Rose[2]

[1] Blackett Laboratory, Imperial College of Science, Technology and Medicine, London SW7 2BZ, UK.
[2] Rutherford Appleton Laboratory, Chilton, Didcot, Oxon. OX11 0QX, UK.

Introduction.

The generation of hot, dense plasma by the irradiation of solid targets with ultra-short, picosecond and sub-picosecond laser pulses has recently been reported.[1-6] These plasmas are of great interest for basic atomic and plasma physics studies, X-ray laser research and for the generation of ultra-short X-ray sources. However, there is currently much uncertainty as to the plasma conditions that may be achieved. This is because laser absorption mechanisms at the surface of a solid target are uncertain for such short pulse durations and the resulting plasma will be highly transient. Detailed measurements of the plasma conditions are not yet possible because of the limited temporal resolution (~1ps) of current spectroscopic instruments. Plasma ionization times are central to the problem of creating hot, dense plasmas with ultra-short laser pulses and here we present zero-dimensional, time-dependent, average-atom calculations of ionization characteristics of hot, dense plasmas of different atomic number, temperature and density.

Model.

A time-dependent, screened-hydrogenic, average-atom model, (NIMP - non-LTE Ionized Material Package), has been used to calculate the ionization characteristics in aluminium (Z=13), iron (Z=26) and tin (Z=50) plasmas at a density of 1 gcm^{-3} for electron temperatures of 0.1, 0.5 and 1 keV. The model is similar to the ionization model contained in the X-ray laser package used successfully to model experiments[7] and is based on the XSN model of Lokke and Grasberger.[8] The physical processes included in the calculation of the (de)population of an atomic level are: collisional (de)excitation; collisional ionization and three body recombination; photoexcitation, stimulated emission, and spontaneous decay; photoionization and radiative stimulated and spontaneous recombination. Multi-photon processes and pressure ionization are ignored. Suprathermal components of the electron velocity distribution, recently observed in short pulse experiments[9], have not been considered, although this will alter the ionization balance somewhat.[10]

The prescriptions for calculating the energy levels and collisional rates are given in ref. 8, whilst the radiative rates are calculated using a more accurate description of the radiation field. The energy spectrum is described by 501 points equally spaced up to a maximum value chosen so as to accurately describe the radiation field. When the radiation field is zero, the only non-zero contribution to the radiative rates is from the spontaneous decay and radiative recombination. When a radiation field is included in the calculations, it is taken to be Planckian at the material temperature. These two extremes probably bracket the total energy density of the radiation field that is associated with the plasma although selective pumping effects which may occur due to non-Planckian components will not be assessed.

The number, N, of principal quantum levels considered to be bound for the calculations was estimated by solution of the Dirac equation in a Thomas-Fermi potential for the appropriate plasma conditions.[11] For the cases considered, N was found to vary between approximately 3 (Z=13, T_e=100eV) and 6 (Z=50, T_e=1keV) and N=6 was chosen for the rate calculations reported here. Using N=6 for aluminium at 1 gcm^{-3} and 0.5 keV resulted in a slightly more rapid ionization than for N=3 because the number of levels available for excitation and thus the number of routes for ionization are increased. The steady-state Z^* was enhanced when N=3 (by 5%) because the overall density of states of the ion is less than for N=6.

The set of N first-order, non-linear, coupled differential equations describing the temporal behaviour of the system[8] is solved using a fully implicit iterative technique. Iterations are performed until convergence on the free electron density is achieved according to the condition $[Z^*(new)-Z^*(old)]/Z^*(old)<10^{-6}$. The plasma is initially taken to be in a state for which the average degree of ionization, Z^*, is unity with the remainder of the Z-1 electrons per ion distributed amongst the bound levels according to the Auf-bau principal. This initial condition is somewhat arbitrary. To assess any effect on the solutions of the initial condition, a simulation was performed with $Z^*_{initial}$=3 for Z=13 and T_e=0.5 keV. The solutions for the two values of $Z^*_{initial}$ converged very rapidly and were almost indistinguishable by 10 fs. This occurs because the time scale for excitation and ionization from the less tightly bound, outer levels is considerably smaller than that from the K and L shells. Therefore, the choice of initial conditions does not appear to be critical under these circumstances. The time step, Δt, was held constant throughout all of the calculations at 10^{-16}s and was chosen such that $\Delta t \ll 1/(\text{maximum rate})$. The method of solution was found to be accurate in that a time step of 10^{-17}s reproduced the results of all calculations almost exactly, except at very early times (<10 fs).

Results.

Figures 1(a), (b) and (c) show Z^* as a function of time for Z=13, Z=26 and Z=50 respectively. As can be seen, for these conditions, Z^* is dominated by collisions and the presence of a radiation field has only a small effect, increasing the value of Z^* by no more than about 10% at any time. As expected, the effect is largest for T_r=T_e=1keV when the radiation field is most intense. At 100 eV, no noticeable differences in the ionization are observed. It is evident that in the case of aluminium and iron, the steady-state solutions are approached at earlier times when the radiation field is included at the higher temperatures.

The effect of the ambient radiation field is to photopump electrons from states with low principal quantum number to those which are less tightly bound and into the continuum. The degree to which this affects the ionization characteristics of the plasma depends on the properties of the ions and the radiation field as well as the plasma conditions. In general, the radiative rates become more important in determining the level occupation probabilities as the principal quantum number is decreased. The largest effect is therefore expected for lower principal quantum numbers. This is demonstrated in figure 2 where the occupation probabilities of the first four levels of iron are shown as a function of time for T_r=T_e=0.5keV. The largest difference is seen for n=2, T_r being insufficient to significantly affect n=1. In contrast, the solutions for n=3 and n=4 are very similar in both cases indicating the dominance of the electron collisional processes for these levels. In each case, as here, beginning with the outer shell, the shells are stripped sequentially.

Simulations were also performed for an aluminium plasma at 0.5keV with no ambient radiation field and plasma densities of 0.5, 0.05 and 0.005 gcm^{-3}. These values were chosen because at 0.05 gcm^{-3} the electron density varies between 1.1 10^{21} (Z^*=1) and 1.5 10^{22} cm^{-3} (Z^*=13) which is in the region of the critical value for most modern, high power, short pulse lasers. Figure 3 shows Z^* calculated as a function of time for each of the densities. The calculation at 1 gcm^{-3} is shown for reference. It can be seen that the ionization rate is proportional to the plasma density. For example, the time to reach Z^*=6 is approximately 7, 70 and 700 fs for densities of 0.5, 0.05 and 0.005 gcm^{-3} respectively. This density dependence is to be expected since the excitation and ionization rates used in the model are proportional to the electron density. It is noted that dielectronic recombination is not included in the calculation which will increase the ionization time slightly for the lower density calculations.

Discussion.

The above results suggest that the formation of highly ionized plasmas by the irradiation of solid targets with ultra-short laser pulses (≥100fs) will not be inhibited by the finite ionization times of the plasma constituents provided the laser energy can be absorbed at or transported to sufficiently high densities (≥ 1 gcm^{-3}) on these time scales. In contrast, we note that for aluminium at electron densities around critical (0.05 gcm^{-3}), high degrees of ionization are achieved on time scales ≥ 100fs indicating that the plasma ionization may be limited by the finite ionization times. These predictions, however, have been made assuming an equilibrium (Maxwellian) distribution for the particle velocities. To assess the validity of this assumption we define for the free electrons an average inelastic collision time τ_i, and a characteristic thermalisation time, τ_t. Departures from a Maxwellian velocity distribution will be small on average provided $\tau_i \gg \tau_t$. τ_t can be estimated from an expression given by Spitzer[12] and in this case reduces to

$$\tau_t \sim 5\times10^{-15}\, T_e[\mathrm{keV}]^{3/2}\, A / \rho(\mathrm{g/cc})Z^* \ \mathrm{sec}$$

As the ionization progresses, the values of τ_t decrease as the electron density increases. During the period of ionization, the average inelastic collision time might be approximated by $Z^*/(dZ^*/dt)$ which is the average time for an electron to cause a single ionization of an ion. From figures 1(a)-(c) it may be seen that $Z^*/(dZ^*/dt)$ decreases with increasing temperature but increases as the ionization progresses and the less tightly bound outer shells become ionized. Therefore, the ratio $\Gamma=\tau_i/\tau_t$ is expected to be largest for low temperatures and late times. For ρ=1gcm^{-3} and 0.1keV, at early times, Γ varies between ~0.1 and ~1.0 (depending on the material). The ratio rises rapidly reaching approximately 10 between 5 and 20fs. In contrast, at 1keV, Γ begins at approximately 10^{-2}, again rising rapidly and reaching unity between 5 and 25fs. Thus, some departures from equilibrium seem inevitable, particularly at earlier times and at the higher temperatures. At later times, the condition for a Maxwellian velocity distribution appear to be satisfied. We emphasise that these estimates indicate only very roughly whether non-Maxwellian electron velocity distributions will develop both because of the average nature of the ionization and thermalisation times and because inelastic processes other than ionization have not been included. Finally, we note that at high irradiances (≥10^{17} Wcm^{-2}), multi-photon processes, which will also contribute to non-equilibrium components in the electron velocity distribution may become important[13].

Summary.

In summary a, 0D, time-dependent, average-atom model has been used to estimate the ionization characteristics in aluminium, iron and tin plasmas at 1 gcm^{-3} with electron temperatures of 0.1, 0.5 and 1keV. It was found that highly ionized plasmas were formed in less than 100 fs suggesting that the finite plasma ionization times should not inhibit the formation of highly ionized material by the irradiation of solid targets with ultra-short (≥ 100 fs) laser pulses provided the laser energy can be absorbed at or transported to a sufficiently high density on this time scale. Calculations carried out at lower densities showed the ionization rate to be proportional to the plasma density.

REFERENCES

1. Landen O. L., Campbell E. M. and Perry M. D., Opt. Commun., 63, 253, 1987.
2. Kuhlke D., Herpers U. and von der Linde D., Appl. Phys. Lett., 50, 1785, 1987.
3. Nam C. H., Tighe W., Suckewer S., Seeley J. F., Feldman U. and Woltz L. A., Phys. Rev. Lett., 59, 2427, 1987.
4. Cobble J. A., Kyrala G. A., Hauer A. A., Taylor A. J., Gomez C. C., Delamater N. D. and Schappert G. T., Phys. Rev. A, 39, 454, 1989.
5. Murnane M. M., Kapteyn H. C. and Falcone R. W., Phys. Rev. Lett., 62, 155, 1989.
6. Willi O., Kiehn G., Edwards J., Barrow V., Smith R. A., Wark J. and Turcu E., Europhys. Lett., 10, 141, 1989.
7. Pert G. J. and Rose S. J., accepted in Appl. Phys..
8. Lokke W. A. and Grasberger W. H., Lawrence Livermore National Laboratory Report, UCRL-52276, 1977.
9. Willi O., Afshar-rad T., Barrow V., Edwards J. and Smith R., STS Press, McLean, Virginia VA 1990, in press.
10. Apruzese J. P., Burkhalter P. G., Rogerson J. E., Davis J., Seely J. F., Brown C. M., Newman D. A., Clark R. W., Knauer J. P. and Bradley. D. K., Phys. Rev. A, 39, 5697, 1989.
11. The Thomas-Fermi calculation is for a plasma in LTE but is considered to give a realistic estimate of the number of bound states for the rate equations.
12. Spitzer L., Physics of Fully Ionized Gases, Interscience, London, 1956.
13. Burnett K., priv. comm..

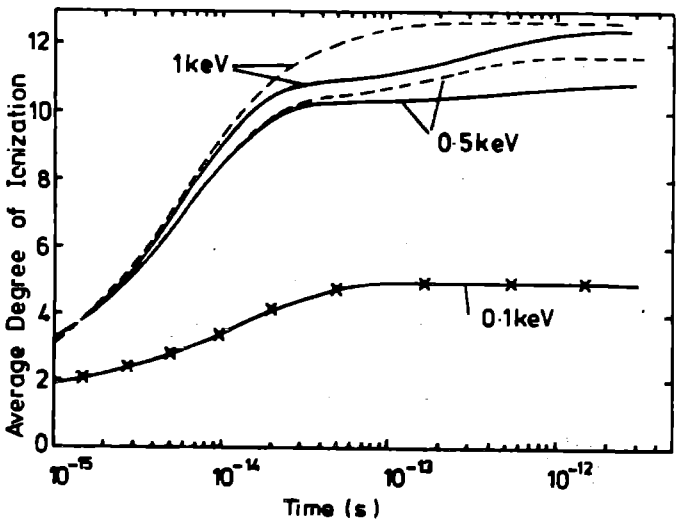

Figure 1(a). Average degree of ionization calculated as a function of time for aluminium plasmas at 1gcm^{-3} and with electron temperatures of 0.1, 0.5 and 1keV. (———) no ambient radiation field, (– – – –) including an ambient Planckian radiation field at the material temperature, (×) no noticeable differences between solutions with and without the radiation field.

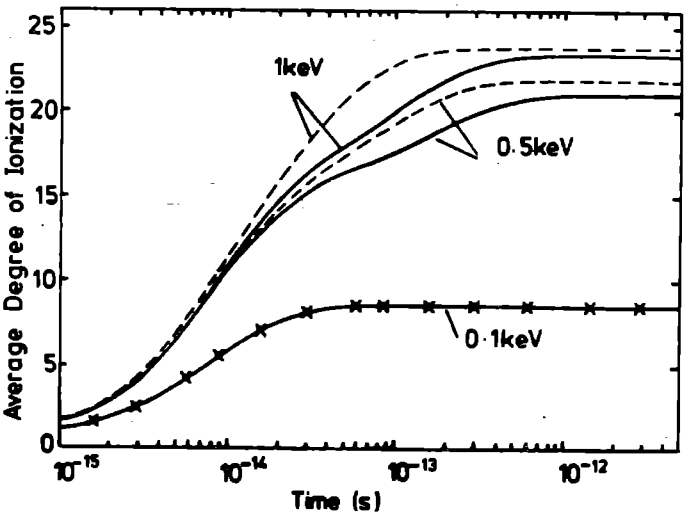

Figure 1(b). As figure 1(a) but for iron plasmas.

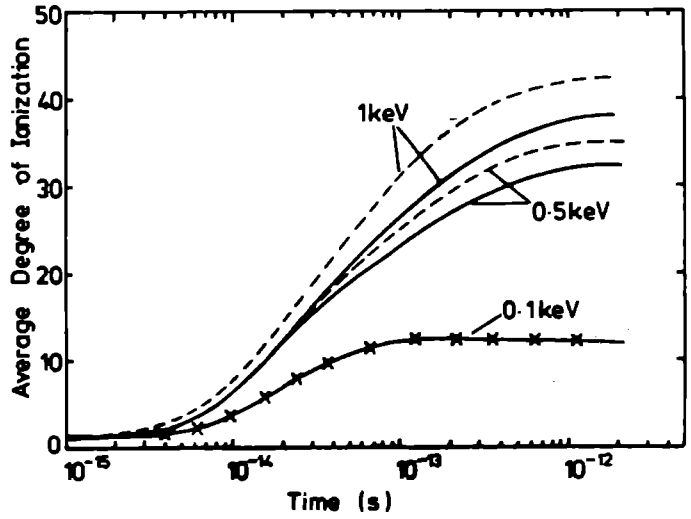

Figure 1(c). As figure 1(a) but for tin plasmas.

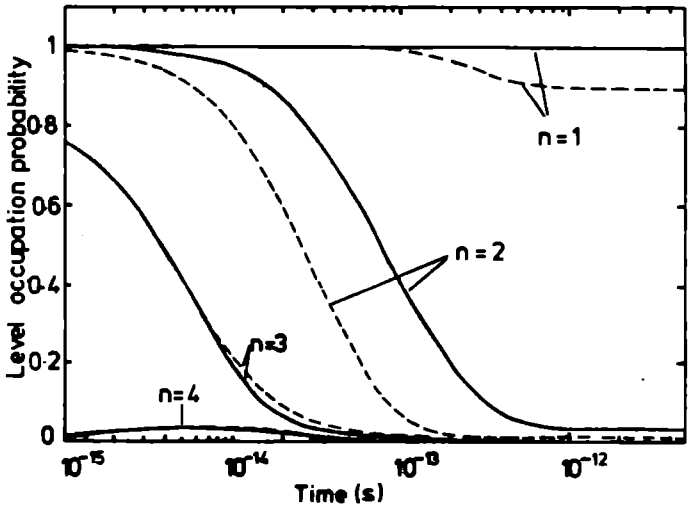

Figure 2. Average occupation probabilities of the first four levels of iron calculated as a function of time for a plasma density of 1gcm^{-3} and an electron temperature of 0.5keV. (———) no ambient radiation field, (– – – –) including an ambient Planckian radiation field at the material temperature.

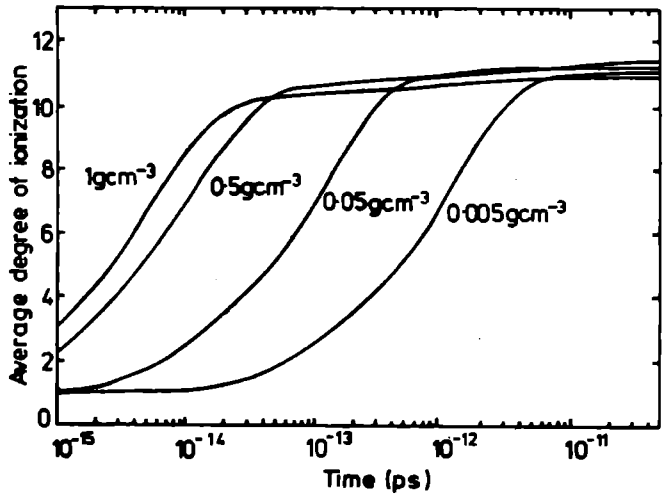

Figure 3. Average degree of ionization calculated as a function of time for aluminium plasmas with an electron temperature of 0.5keV and densities of 1, 0.5, 0.05 and 0.005 gcm^{-3}.

MODELLING STUDY OF RECOMBINATION LASERS

M H Key+, N Tragin*, S J Rose
Rutherford Appleton Laboratory
+Also at Department of Physics, University of Oxford
*CEC grant

1. Introduction

Recombination based XUV lasers continue to be potentially important through requiring less powerful pump lasers than collisionally excited types[1] , but to date they have not operated at sufficient gain to produce saturated laser action and there remains some confusion about the power needed to excite them. In particular some reports quote small gain length products produced with unusually low pump power[2] [3] [4]. Work with fibre targets has an extensive theoretical basis[5] [6] and has given encouraging experimental results for C VI[7] and F IX[8] for fibre lengths restricted to about 1 cm and gl values to about 4. Experimental difficulty has prevented the use of longer fibre targets and our interest has therefore recently been focused on slab targets. It has been shown in our earlier work[7] that a reasonable approximation for modelling the production of gain on slab targets can be obtained with a 1D hydro/energy transport/atomic physics code by considering cylindrically symmetrical irradiation of a target with cylinder diameter equal to the width of a line focus on a flat slab. We continue the use of this approach here in a more extensive modelling study taking advantage of the speed of 1D modelling to permit a range of calculations which would require an impractical amount of computer time if calculated in 2D.

A helpful representation of the production of gain by recombination to hydrogenic ions is given in figure 1 which is discussed more fully elsewhere[8]. Adiabatic cooling is the basis of the main approach used with recombination lasers. Figure 1 shows that the C VI laser (with initial plasma conditions for heating by a 1 μm laser of typically n_e - 10^{21} cm^{-3}, kT_e - 180 eV) requires a major reduction in density as well as cooling to produce gain. A numerically computed cooling characteristic for a 7 μm fibre target irradiated by ~ 70 ps pulse is shown and exhibits a less than adiabatic cooling rate due to 3 body recombination heating. The contours indicate the maximum possible gain for system with 100% bare nuclei. Slow cooling leads to loss of bare nuclei by recombination thus to delayed termination of trapping therefore to less gain. Rapid cooling and early termination of trapping is the key to producing high gain.

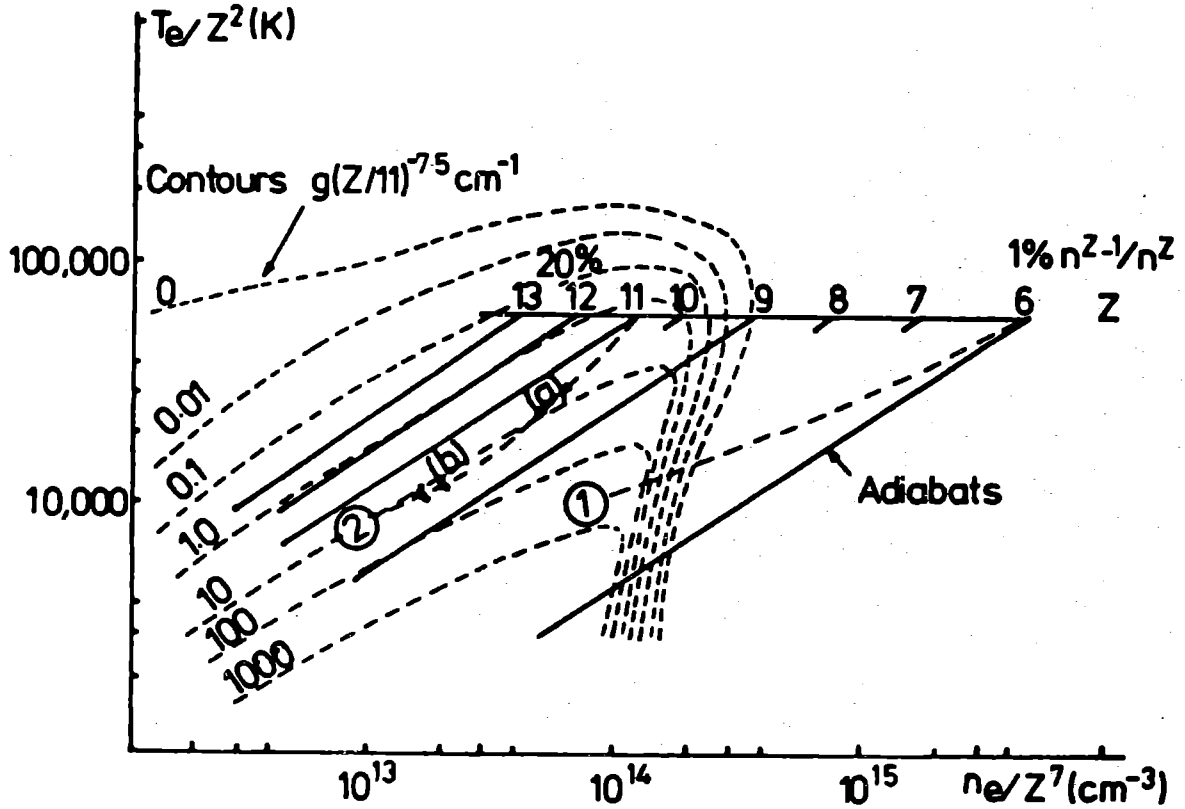

Fig 1 Contours of maximum gain for recombination lasers as explained in the text.

2. C VI

These effects have been modelled for C VI using a multiplier on the Sobolev opacity of 0.2 determined empirically to give a fit to experimental data[7].

Figures 2 and 3 show how line focus width and pulse length affect the time and space resolved peak gain g, the efficiency of producing gain gl/p and the optimum intensity on target I, where in each case the intensity on the target has been varied to find the maximum possible gain. Of interest in figures 2 and 3 is that gain and efficiency both improve with reduced width of line focus. Shorter pulses give higher gain but there is an optimum pulse length for efficiency.

The fall off in line integrated gain due to variation of intensity along the line focus has been modelled in a simplified way by considering the average gain $(g_1 + g_2)/2$ on each space/ time path through two plasmas of equal length but different intensity I_1 and I_2 on the target. The maximum gain (time and space resolved) for any ray through the two plasmas is computed and optimised by varying the average intensity $(I_1 + I_2)/2$. The results shown, in figure 4, for increasing ratio I_1/I_2, suggest that 4:1 variation in intensity can be compensated by a two fold increase in average intensity on target with only a two fold loss of gain. Non uniform irradiation, therefore seems an unlikely explanation for significantly reduced gain in long plasmas. Sensitivity of computed gain to the multiplier on the trapping factor is not very severe for C VI as illustrated by figure 5.

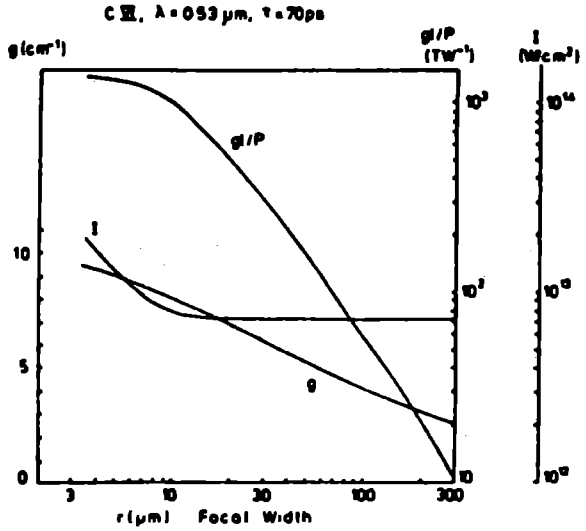

Fig 2 Effect of varying line focus width, C VI

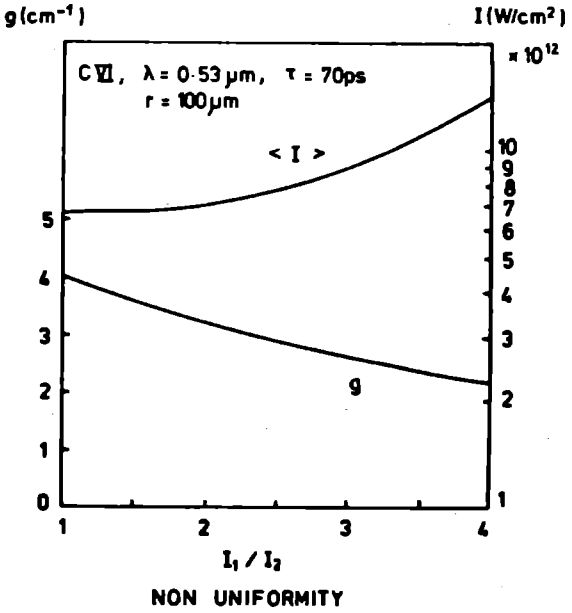

Fig 4 Effect of intensity variation along the line focus, C VI

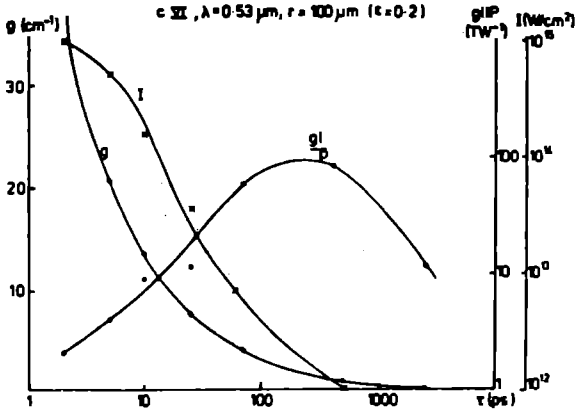

Fig 3 Effect of varying laser pulse duration, C VI

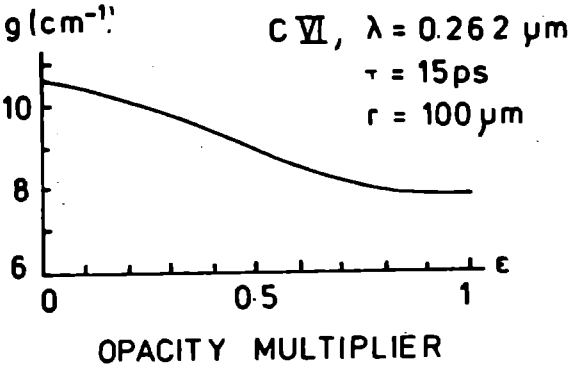

Fig 5 Effect of varying the opacity multiplier ε, C VI

3. Na XI and Mg XII

Isoelectronic extrapolation to Na XI brings a different situation also illustrated in figure 1 in which the initial conditions are higher temperature kT_e - 670 eV, and higher initial density n_e - 2 x 10^{21} cm^{-3} resulting from the more intense irradiation of the target. The plasma parameters are already within the potential gain region and require only cooling (to reduce collisional population of n = 2 from n = 1) and cessation of trapping for production of gain. Cooling for a numerically modelled 7 μm fibre target is seen to be more rapid than adiabatic due to conduction to the cold target being more effective at higher temperature.

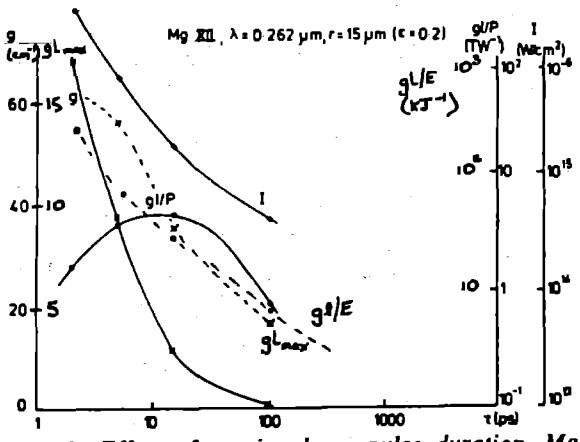

Fig 6 Effect of varying laser pulse duration, Mg XII

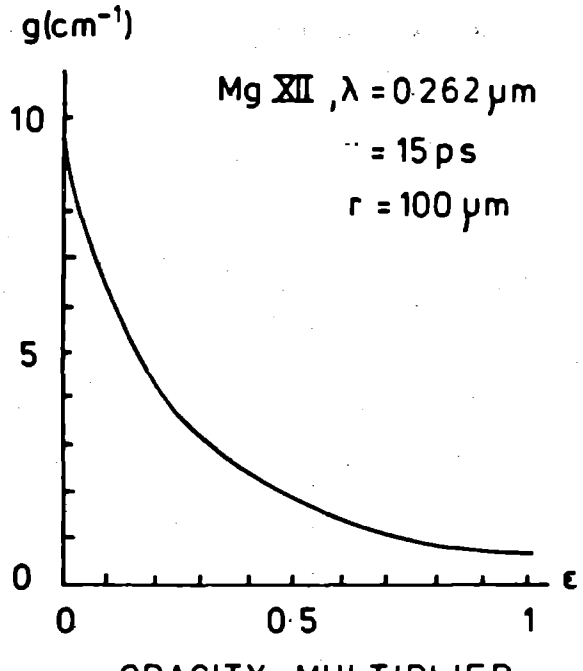

Fig 8 Effect of varying the opacity multiplier ε, Mg XII

Here again shorter pulses give higher gain by raising the initial density of the plasma as hydrodynamic response is reduced(10) (11). The pulse length variation of g and gl/p is shown in figure 6 for Mg XII and has an efficiency peak at shorter pulse length than C VI. Sensitivity to line focus width shown in figure 7 is similar to that for C VI. Also shown is the maximum gain length gl due to refraction and this is seen to increase for shorter pulses as does the energy efficiency of producing gain gl/E. Sensitivity to trapping is greater for larger plasmas (long pulse large line width) and acute for Mg XII, as shown in figure 8. The effect of non uniform irradiation on gain is similar to that for C VI, (figure 9).

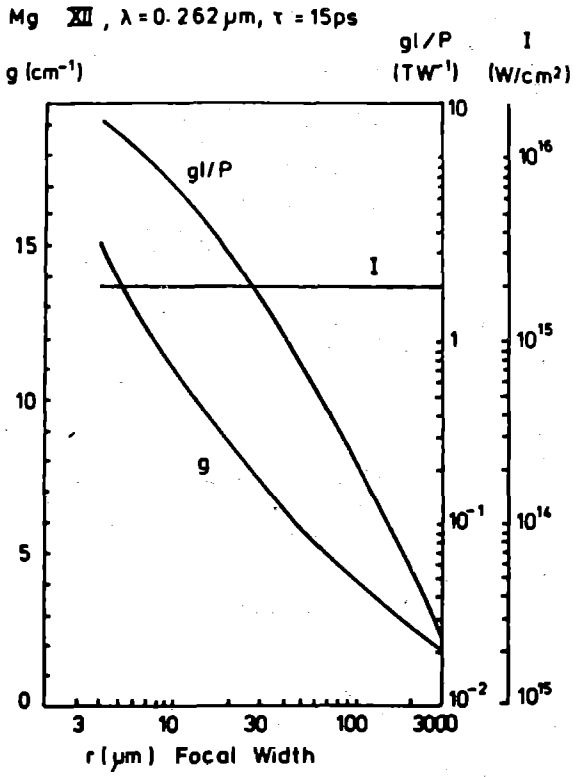

Fig 7 Effect of varying line focus width, Mg XII

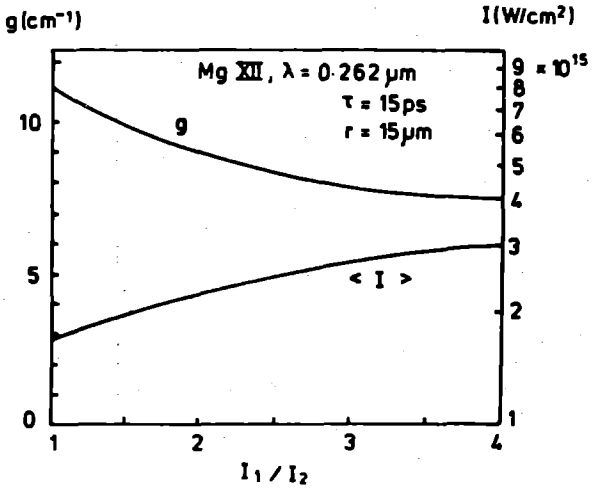

Fig 9 Effect of intensity variation along the line focus, Mg XII

4. Space and time averaging and apparent gain

The apparent gain, deduced from axial/transverse intensity ratio or non linear increase of axial intensity with length, varies strongly with the length of plasma if measurements are space time integrated (or time resolved but space integrated or vice versa). This is because the recombination gain occurs late in time and in a limited region of the plasma. We have previously analysed the problem for C VI[12] and attention is drawn to it here as a possible source of error in measurements on systems with relatively small values of the peak (time and space resolved) gl. Figure 10 shows how a 'secure' observation of gain with axial/transverse intensity ratio > 2 or ratio of intensity for L and L/2 > 4 requires quite significant peak gl values > 5 for a typical case of a C VI laser.

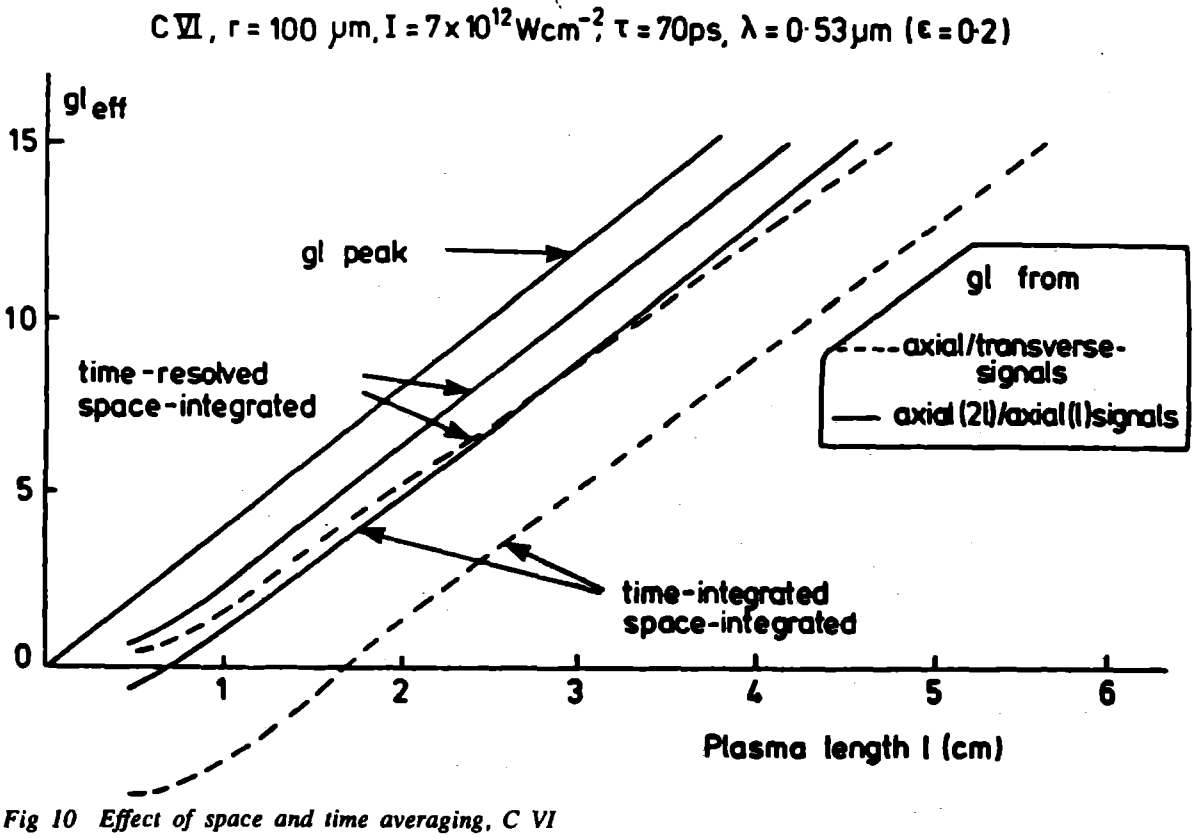

Fig 10 Effect of space and time averaging, C VI

5. References

1. M H Key, J Mod Opt 35 575 (1988).
2. P Jaegle et al ibid
3. T Hara et al ibid
4. D Kim et al ibid.
5. G J Pert, J Phys B 12 2067 (1979).
6. G J Pert, S J Rose, Appl Phys B 50, 307 (1980)
7. C VI C Chenais-Popovics et al, Phys Rev Letts 59 2161 (1987).
8. F IX M Grande et al, Opt Comm 74 309 (1990)
9. N Tragin, M H Key, S J Rose, J Mod Opt 37 435 (1990).
10. M H Key, Annual Report of the Central Laser Facility, Rutherford Appleton Laboratory Report RAL-89-045, 119 (1989).
11. M H Key et al, Annual Report of the Central Laser Facility, Rutherford Appleton Laboratory Report RAL-89-045, 25 (1989).
12. Y Kato et al, Appl Phys B 50 247 (1990).
13. H Azuma et al, Opt Lett 15 1011 (1990).
14. N Tragin, M H Key, S J Rose, Annual Report to the Central Laser Facility, Rutherford Appleton Laboratory Report RAL-89-026, 46 (1990).

ROLE OF DOUBLY EXCITED STATES IN RECOMBINATION X-RAY LASERS

M.T.M Lightbody and Geoff J Pert

Department of Physics
University of York

1 Introduction

Theoretical modeling of recombination x-ray laser experiments requires the calculation of various ion state populations, including those of the laser upper, lower and ground levels. This in turn requires the solution of a large set of coupled linear equations. In the steady state and when the system is in thermal equilibrium this is relatively straightforward, as the rate coefficients can be worked out from the local thermodynamic properties. The presence of radiative transitions introduces potentially long range coupling into the problem via the photons that result from these transitions. This means that the rate coefficients can only be determined when the radiation transport problem is solved. Fortunately, the rapid expansion of the plasma allows use of the escape probability, or trapping factor, approximation, Sobelev (1957), Pert (1976). In this approximation the radiative transition rates are multiplied by a trapping factor f : $0 < f < 1$ which is related to the probability that an emitted photon can escape the system. However, introduction of trapping into gain simulations leads to a discrepancy between theory and experiment, Pert and Rose (1990). It has subsequently been found that multiplying f by an empirical factor η restores agreement between experiment and theory. However, there is as yet little theoretical basis for the use of such a factor. In this report some reasons for the observed reduction of trapping are proposed. These are based on the role that doubly excited He-like ions can play in the various relevent physical processes.

There are two major effects considered here. Firstly we consider the production of satellite lines to the basic hydrogenic line, particularly the trapped Lyman alpha line. Secondly we calculate autoionisation rates for ions in the state (2,m). What we are looking for are mechanisms that can reduce the trapping of the lower laser to ground transition because it is trapping on this line that will repopulate the lower laser level and eventually destroy the population inversion. We consider several possibilities in the next section.

2 Doubly excited He-like states

The argument against consideration of doubly excited He-like states is that such levels are energetically unstable because they lie a long way above the ionisation energy of the ground state and would thus be difficult to produce. However, in the case under consideration here, the various ion stages are populated though recombination. Therefore, significant populations of such doubly excited states can be expected. The Helium-like ions that are of interest here are those that are in an (n,m) configuration, with n = 2 or 3 and m in the range $n < m < \infty$. Significant populations of these states can modify the various transition rates and frequencies involved in the laser process. For example, the presence of an outer spectator electron (n,m) in an ion that is undergoing a Lyman-alpha transition (n going from 2 to 1 in a Hydrogenic ion) will lead to a shift in frequency away from the Hydrogenic value. This gives rise to a series of satellite lines to the L_α line. The optical depth for these photons will be very much smaller than for those emitted within the Lymann line, leading to an overall reduction in trapping on the line. The magnitude of this effect will depend upon the frequency shift, the satellite line intensity and the population of these doubly excited (2,n) states. The code MCDF was used to determine the frequency and strength of the satellite lines. The populations of doubly excited states were calculated using a specifically written program, COLRAD.

A second possibility is that the (2,m) states will rapidly auto-ionise. This is of importance because they provide a radiationless decay channel for the lower-laser-to-ground transition. If this auto-ionisation rate is a significant fraction of the radiative rate then we can expect a reduction of the trapping on this line. Furthermore this reduction can be calculated and therefore gives the theory more predictive power. The magnitude of the effect will depend on the Auto-ionisation rate from level (2,m) to (1,∞), as well as on the population of the state (2,m). The auto-ionisation rate was calculated from a formula given by Ansari (1970), based on the Burgess approximation, Burgess (1964). Again, the population of doubly excited levels was calculated using the code COLRAD.

A further possibility is that the presence of a spectator in a helium-like ion will shift the original He-like ground to first excited state sufficiently to allow the He-like ion to absorb L_α photons. This would be important because it would reduce the number of L_α photons available to repopulate the lower laser level.

3 Results

All the rates and frequencies that were calculated were those relevent to Fluorine systems. In table (1) we give the energy shift of the basic L_α transition ($2P- > 1S$) due to the presence of a spectator electron ($2Pm, S- > 1S, mS$).

Transition	E cm-1 $\times 10^3$	$\Delta E \times 10^{-3}$
2p --> 1s	6673.685	0.00
2p3s --> 1s3s	6647.351	3.70
2p4s --> 1s4s	6663.000	1.30
2p5s --> 1s5s	6668.591	0.52
2p6s --> 1s6s	6672.369	0.04

Figure 1: Energies of L_α Satellites

The energies were calculated using MCDF. These energy shifts should be compared with the expected L_α linewidth $\Delta\nu/\nu_0$ of approximately 10^{-4}. It can be seen that the spectator electron has to be fairly deep lying (m = 3,4,5) in order that the satellite line lies outside the original linewidth. The rate for this process relative to the L_α rate will depend on the population of the (2,m) level to the hydrogenic (2,∞) level. Table (2) gives some example values for these ratios. As can be seen the values are fairly small, indicating that this process will not make much contribution to the decay of the L_α line.

Density = 1.0d+21 T=70 eV

n	m	Ratio from Saha	Ratio from COLRAD
H-like			
0	2	1.0000E+00	1.0000E+00
He-like			
2	2	6.4830E-02	2.7942E-04
2	3	2.1049E-02	6.4295E-03
2	4	1.9932E-02	1.5336E-02
2	5	2.3357E-02	2.1432E-02
2	6	2.8824E-02	2.7729E-02
2	7	3.5771E-02	3.4980E-02
2	8	4.4010E-02	4.3315E-02
2	9	5.3467E-02	5.2770E-02
2	10	6.4099E-02	6.3331E-02

Figure 2: Populations of (2,m) levels relative to the Hydrogenic (2,∞)

The contribution to the decay through auto-ionisation will depend on the product of the autoionisation rate from (2,m) to (1,∞), $A_{2m,2\infty}$ with the above population ratio, Ansari (1970). This must be summed over all m in order to obtain the total contribution to the decay through this channel. Table (3) gives some values for this total decay rate. The results indicate that the radiationless decay of doubly excited states formed through recombination is a significant fraction of the radiative decay rate of the L_α line. This suggests that autoionisation of such states can lead to a reduction of the trapping on the L_α line. This is because the autoionisation decay is radiationless and thus leads to a reduction in the number of L_α photons in the system. Below we summarise some of the rates involving doubly excited states and compare them with the L_α radiative rate.

rho=5.0d+20 t=70 z=9		rho=1.0d+21 t=70 z=9	
2	1.1679E+10	2	1.8283E+10
3	1.6370E+10	3	5.5400E+10
4	1.3279E+10	4	3.1357E+10
5	6.7146E+09	5	1.4360E+10
6	3.6056E+09	6	7.4665E+09
7	2.1316E+09	7	4.3578E+09
8	1.3614E+09	8	2.7677E+09
9	9.2276E+08	9	1.8712E+09
10	6.5459E+08	10	1.3260E+09

rho=5.0d+21 t=70 z=9		rho=1.0d+22 t=70 z=9	
2	3.3342E+11	2	1.4002E+12
3	5.9669E+11	3	1.3871E+12
4	1.8818E+11	4	3.8838E+11
5	7.6587E+10	5	1.5464E+11
6	3.8496E+10	6	7.7302E+10
7	2.2193E+10	7	4.4483E+10
8	1.4024E+10	8	2.8091E+10
9	9.4600E+09	9	1.8943E+10
10	6.6981E+09	10	1.3411E+10

Figure 3: Autoionisation rates compared with the L_α rate

4 Rates for radiative processes in Fluorine

In this section we list some of the rates for radiative processes in Fluorine.

- Radiative rate for the L_α line:

$$A_{L_\alpha} = 2.8 \times 10^{12}.q(2,\infty)s^{-1} \quad (1)$$

- 1) Recombination into level (2,m) followed by autoionisation into level (2,∞).

$$R^A_{2,1} = A(2,m:1,\infty).q(2,m) \quad (2)$$

Summing the population ratio over all m gives a numerical value for this rate:

$$R^A_{2,1} = 3.68 \times 10^{11}.q(2,\infty)s^{-1} \quad (3)$$

So the autoionisation rate relative to the radiative rate is approximately:

$$\frac{R^A_{L_\alpha}}{A_{L_\alpha}} = 1.07 \times 10^{-1} \quad (4)$$

- Satellite ratio. We sum over the satellite rates, determined from the oscillator strength package in MCDF to obtain a rate relative to the basic L_α rate of:

$$\frac{AL_\alpha + m}{A_{L_\alpha}} = 4.5 \times 10^{-3} \quad (5)$$

5 Conclusions

The most important process involving doubly excited He-like ions is the autoionisation of states (2,m) to (1,∞). This will provide a radiationless decay channel for the lower laser to ground state transition in a recombination x-ray laser. As a consequence there will be fewer L_α photons available to repopulate the lower laser level, helping to maintain the population inversion and sustain the gain. This will have a similar qualitative effect on the gain as a reduction in trapping. Efforts are currently underway to put the ideas presented above on a more quantitative basis.

6 References

- Ansari SM, Elwert G , (1970), Z.NATURF, Vol.25a, pp1781-97
- Burgess A, (1964), ASTROPHYS J., Vol.139, pp776-80
- Pert GJ, (1976), J. PHYS. B, Vol.9, pp3301
- Pert GJ and Rose SJ, (1990), APPL PHYS B, Vol.50, pp307
- Sobelev VV, (1957), SOV. ASTRON. AJ, Vol.1, pp665

Coupling of atomic processes to the energy balance in a rapidly changing plasma

A Djaoui, SJ Rose

Rutherford Appleton Laboratory

INTRODUCTION

The hydrodynamics and thermodynamics of laser produced plasmas are usually modelled by solving the Navier-Stokes equation for the motion and the energy balance equations for the electron and ion temperatures. In partially ionized plasmas the collisional and radiative atomic processes of ionization and recombination, excitation and de-excitation of bound electrons must be included as they can involve a large fraction of the internal energy. This energy coupling is complicated and has only been included in an approximate way in the past. Key [1], for example, showed that ionization energy resulted in a lower radiation-driven breakdown wave velocity. Early numerical schemes calculated the ionization equilibrium under steady state conditions and used the resulting equation of state for non-steady state situations. For rapidly heated or cooled plasmas the steady-state approximation is not valid. Adequate algorithms, were developed to tackle the problem [2,3]. These solved a collisional-radiative (CR) model for the ionization, simultaneously with the electron energy equation, but only the ground states were taken into account. Transitions between the excited states were omitted since they required long computing times. For large rates, when the system is near equilibrium, the inclusion of ionization energy into the electron energy balance equation can lead to oscillations in the temperature. Pert [2] imposed an energy limit on the heat exchange by ionization in order to supress the oscillations. Gauthier *et al* [3] developed a scheme where the coupled finite difference equations governing the ionization dynamics and the electron energy balance are treated implicitly and no limit was required. All the reported calculations, however, are for relatively low Z materials and with transitions between excited levels neglected.

An alternative approach is to use the average atom (AA) model, which requires the solution of the rate equations for one average ion only. It is then possible to account for all excited levels without too much increase in computing time. Excitation/de-excitation energies are much larger than ionization/recombination energies , they can therefore dominate the energy exchanges. As a result of this, we found it necessary to impose an energy limit which is, in many respects, similar to that used in reference [2]. The coupling of the AA excitation/ionization model to our 1D lagrangian code MEDUSA is described in the next section.

ATOMIC PROCESSES

The free electron energy balance equation, including excitation/ionization energies (and their reverse processes) can be written as;

$$\frac{3}{2}kZ^*\frac{dT_e}{dt} + \frac{3}{2}kT_e\frac{dZ^*}{dt} = S(T_e) + Q(T_e) \quad (1)$$

where Z^* is the average ionization state of the plasma, T_e the electron temperature. The two terms on the LHS represent the change in internal energy as a result of changes in temperature and number of free electrons respectively. $S(T_e)$ includes sources and sinks of energy resulting from absorption of laser light, thermal conduction, electron-ion energy exchange, bremsstrahlung as well as the $-pdV$ term. $Q(T_e)$ includes terms from other atomic processes. In the AA model [4], the level population P_n of principal quantum level n having energy E_n is given by;

$$\frac{dP_n}{dt} = A_n(T_e)(1. - \frac{P_n}{2n^2}) - B_n(T_e)P_n \quad (2)$$

$A_n(T_e)$ is the total rate of all the transitions into level n and $B_n(T_e)$ the total rate of the transitions out of level n.

Table 1: Atomic processes involving bound electrons and their effect on the free electron energy balance. The contributions to $Q(T_e)dt$ and dZ^* in eq. 1 are shown in the two last columns respectively.

EFFECT OF COLLISIONAL AND RADIATIVE PROCESSES ON FREE ELECTRON ENERGY BALANCE				
Atomic Process	Initial State	Final State	Change in Free electron energy	Change in Free electrons
Collisional Excitation	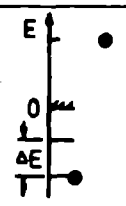		$-\Delta E$	0
Collisional De-excitation	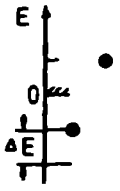	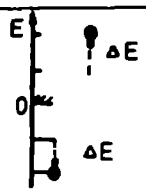	$+\Delta E$	0
Collisional Ionization	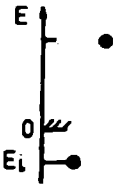	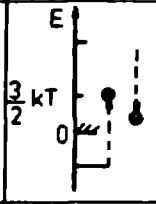	$-\lvert E_i \rvert$	$+1$
3 Body Recombination	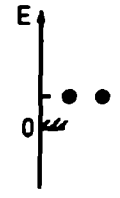	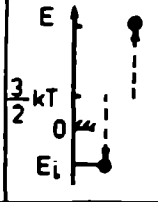	$+\lvert E_i \rvert$	-1
Radiative Recombination	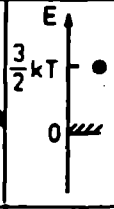	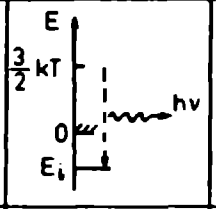	$-\frac{3}{2}$kT	-1
Bound-Bound Radiation		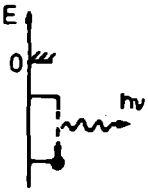	0	0
Free-Free Radiation	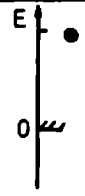	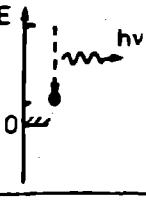	$-h\nu$	0

dZ^*/dt and $Q(T_e)$ can be written as;

$$\frac{\mathbf{dZ^*}}{\mathbf{dt}} = \sum_n P_n R^c_{nc} - Z^* \sum_n R^c_{cn}(1. - \frac{P_n}{2n^2}) - Z^* \sum_n R^r_{cn}(1. - \frac{P_n}{2n^2}) \quad (3)$$

$$\mathbf{Q(T_e)} = -\sum_n \sum_m P_m R^c_{mn}(1. - \frac{P_n}{2n^2})(E_n - E_m) + \sum_n P_n R^c_{nc} E_n - Z^* \sum_n R^c_{cn}(1. - \frac{P_n}{2n^2})E_n - Z^* \sum_n R^r_{cn}(1. - \frac{P_n}{2n^2})\frac{3}{2}kT_e \quad (4)$$

where the different terms on the RHS represent collisional excitation/de-excitation (rate R^c_{mn}, for transition from level m to n), collisional ionization (rate R^c_{nc}), three body recombination (rate R^c_{cn}), radiative recombination (rate R^r_{cn}).

Table 1 depicts the collisional and radiative processes and their contribution to Z^* and $Q(T_e)$. It is seen that only collisional processes and bremstrahlung have a direct effect on the electron temperature. Radiative recombination does not change the electron temperature; this is because the corresponding terms in eq. 1 cancel. These processes only affect the energy balance through the induced changes in level populations and the resulting changes in collisional rates. This is also true of line radiation.

EXCITATION/IONIZATION ENERGY LIMIT

The finite difference form of the energy equation is written as;

$$(\frac{3}{2}kZ^*)^{n-\frac{1}{2}}(T_e^n - T_e^{n-1}) = \left[S^{n-\frac{1}{2}}(T_e) + R^{n-\frac{1}{2}}(T_e)\right]\Delta t^{n-\frac{1}{2}} \quad (5)$$

Where $R(T_e) = Q(T_e) - \frac{3}{2}kT_e dZ^*/dt$. Superscript $n-1$ refers to the quantities before time step $\Delta t^{n-\frac{1}{2}}$, n to the quantities after the timestep and $n-\frac{1}{2}$ to the average of the quantities before and after the timestep. Eq. 5 is iterated until the difference $|T^{n,i} - T^{n,i-1}|$ between the temperatures as given by iteration i and $i-1$, is below a prescribed small value. We found that convergence is improved if the average between the temperatures from the two latest iterations is used in the rates in eq. 2 instead of the value from the last iteration. Convergence is usually achieved in about 3 iterations.

At large excitation and/or ionization rates, the energy sink in eq. 1 or eq. 5 can be significant compared to the internal energy of the system, when iterating, this leads to a cooling of the system. The temperature is then low enough for the system to recombine in the following iteration. Recombination contributes a positive source term which again results in a high temperature. This cycle is repeated and results in oscillations in the temperature. We therefore set a limit on the ionization energy which is equal to the total energy input into the system from all sources. For a given timestep $\Delta t^{n-\frac{1}{2}}$, this is simply $S^n(T_e^n)\Delta t^{n-\frac{1}{2}}$. In a typical run on a high-Z material, this limit amounts to up to 30 per cent of the total internal energy. In this way oscillations from one iteration to the other are eliminated.

CONCLUSION

We have developed an algorithm for the solution of the coupled equations governing the free electron energy balance equation and the non-lte rates equation for the populations of bound levels. The coupling is treated fully and both ionization/recombination and transitions between excited states are taken into account. To stablize the scheme with the use of hydrodynamic time steps an energy limit is imposed on ionization and collisional excitation. This is now working in a new version of the 1D lagrangian code, named MED102.

REFERENCES

[1] M.H. Key, J. Phys. B. (Atom. Molec. Phys.) Ser. 2., Vol **2** 544-550, 1969.

[2] G.J. Pert, Journal of Computational Physics, **27**, 241-255, 1978.

[3] J. C. Gauthier, J. P. Geindre, N. Grandjouan and J. Virmont, J. Phys. D: Appl. Phys., **16**, 321-331, 1983.

[4] W. A. Lokke and W. H. Grasberger, "XSNQ-U: A non-lte emission and asorption coefficient subroutine", UCRL- 52276, Lawrence Livermore National Laboratory, Livermore CA 94550 1977.

THERMAL INSTABILITIES IN LASER-PRODUCED PLASMAS

Bill Crum and Geoff J Pert

Department of Physics
University of York

INTRODUCTION

As part of continuing work to examine the role of Benard-like unstable growth in laser-plasma systems [1] simulations have been conducted on simplified systems which at first sight might appear to bear little relation to experiment. It was hoped that insight into what must be a complex phenomenon would be gained from studying such systems. All cases featured a cylindrically symmetric target with energy representing laser-heating deposited in the two rows of cells closest to the axis ie at the centre of the target. The work was carried out using a version of the two-dimensional code POLLUX developed by Pert (and others) over many years. Our version WILBUR features a two-dimensional orthogonal quasi-lagrangian mesh [2]. The plasma is treated as a two-temperature fluid with equilibration between the ions and the electrons. The hydrodynamic techniques used were common to all the cases studied and it was the method of energy transport that was varied to simulate different conduction regimes. The spatial resolution of the mesh was fixed along the axis but changed along a radius. The rezoner insured that targets of differing radii could be studied without shocks being smeared out too much. All the simulations to be described were performed using a mesh of 86 (z) by 80 (r) cells. The target configuration is summarised in figure 1.

CASES COVERED

The target was initially at rest with a Gaussian radial density profile. A density perturbation of $\pm 10\%$ nominal was applied to the target in the axial direction extending 10% of the initial target radius into the target.

The initial density profile had its' peak at a density of the order of critical. This combination of profile and peak with the target heated in the centre was intended to simulate the situation at late times in laser-irradiated targets. In the absence of the perturbation and externally input energy the flow would then be self-similar and one dimensional in the radial direction. For each type of energy transport studied, a series of simulations were performed varying the ratio of the scale-lengths in the two directions (λ/R). This length-ratio was a dimensionless product common to all the systems studied which gave a measure of how the perturbation wavelength (λ) and the Gaussian half-width ($\propto R$) together affected the growth of instability.

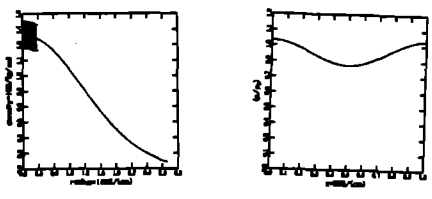

Figure 1: Initial Target Configuration

The simplest case to begin with was that of no conductivity where the supplied energy could only heat the target in the vicinity of the region of deposition. This was a purely hydrodynamic problem and was expected to be the most unstable configuration as no thermal smoothing could act to damp out the applied perturbation. From here we went to the other extreme of an infinitely thermally conducting system. In this case the energy density at any one time was kept constant across the target although the total energy in the system did increase with time. Next a more marginal case was covered where the actual transportation of energy remained instantaneous but the amount deposited was weighted by the density at that point. This crudely represented an inverse-Bremsstrahlung type of absorption, the very type expected to be prevalent in a laser-produced plasma once the peak-density drops below critical. Finally an examination of a one-temperature system with constant thermal diffusivity was carried out. It is intended to show how the value of the diffusivity could be adjusted to show a transition between the two extremes described above.

RESULTS

Unstable growth was apparent and an exponential phase could be identified in most cases. Values for the growth constant were obtained by assuming a relationship of the form $d = ae^{\omega t}$ (with d a measure of growth in the system) over this region to obtain a value for ω.

The variation of ω with (λ/R) for the zero-conduction case is summarised in figure 2. As might be expected, the growth-constant ω increases with $1/R$ which is proportional to the inverse Gaussian half-width. As expected the largest values for ω were obtained under this regime.

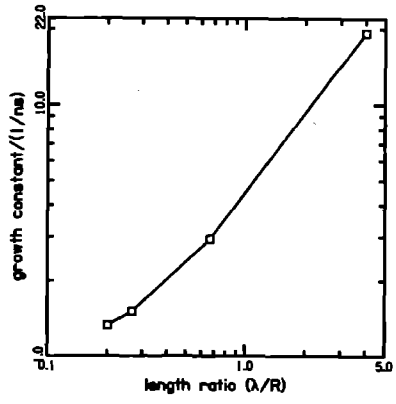

Figure 2: Variation In Growth Constant With (λ/R) in the Zero-Conduction Case

The second extreme was that of infinite conduction. Unlike the first case no growth could be detected and the perturbation damped quickly until it was virtually undetectable. At any time during the expansion, the one dimensional density profile was that of an isothermal self-similar expansion into vacuum, the actual value of the temperature a function of how much energy had by that stage been injected into the system. Figure 3 shows radial density profiles

at $t = 00ps$ and $t = 600ps$. The error bars indicate the maximum deviation of the density from the average taken along a row at that radius. The existence of the perturbation is clear at $t = 00ps$ but is undetectable at the later time. Such radical damping was to be expected in the infinitely conducting regime. Damping rates could not be determined with any degree of confidence for such cases.

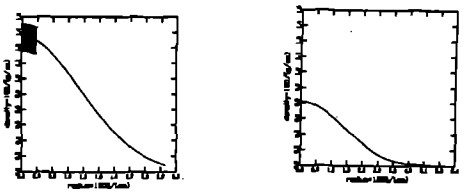

Figure 3: Radial Density Profile At t=00ps and t=600ps in the Infinitely Conducting Case

More detail about the instability was gauged from the density-weighted deposition case. The onset of growth was delayed with respect to some of the other cases. This was thought to be because for all but the thinnest targets looked at, the transverse density perturbation was localised on a relatively flat region of the radial density profile. As growth is expected to arise in regions of large density gradient the perturbation would exist in a region of relatively uniform temperature. Typically the single wavelength perturbation damped out after generating higher frequency ripples in the axial density distributions. With increasing time the rippled region spread through the radial distribution.

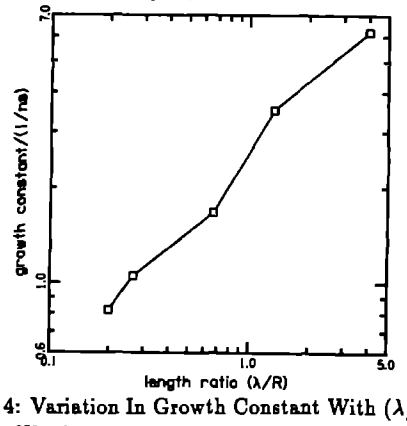

Figure 4: Variation In Growth Constant With (λ/R) in the Density-Weighted- Case

The constant-conduction cases were carried out using a modified version of the code in which the ions carried both momentum and thermal energy. The nominal value of the thermal diffusivity used was obtained by setting a dimensionless parameter describing the system to unity and then solving for the diffusivity, the other variables (density, power and radius) all being known. For diffusivities between one hundredth and one hundred times this nominal value a characteristic s-shaped growth curve was obtained (figure 5).

The form of the curve is readily explained. The method of assessing growth calculates the average deviation in the density distribution from a one-dimensional expansion over the whole computational mesh. Hence at $t = 00ps$ the original perturbation to the density dominates but diminishes in time (as thermal conduction acts quickly to reduce density gradients). Then the growth phase picks up as can clearly be seen in the central region of the graph but at about $t = 600ps$ saturates and indeed at later times the average deviation from the one-dimensional case falls rapidly. Although a growth phase is seen it is very small compared with the adiabatic case.

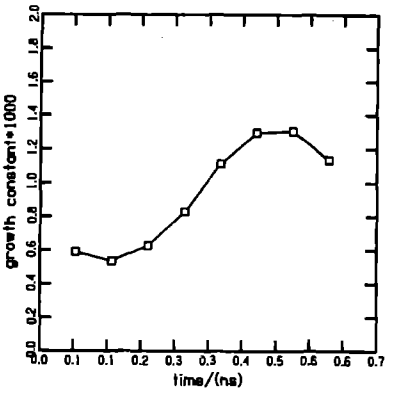

Figure 5: Growth Against Time For Constant χ

CONCLUSIONS

Work is progressing to try and draw together the results from the above case-studies into a more coherent form and in particular to examine the transition from conduction-dominated to hydro-dominated regimes in the constant diffusivity set. The large differences in growth between the adiabatic and conducting cases are thought to arise as a result of the vastly different hydrodynamics of the two systems. We are also attempting an analytic analysis of the pure-hydrodynamic (zero-conduction) case but do not expect it to bear all that much resemblance to the simulated case due to the existence of a shock driven outwards in the simulations. It is hoped that the resemblance will be sufficient to show that the pure hydrodynamic case is inherently unstable which is what our simulations suggest. The next step is to simulate a full experimental situation.

REFERENCES

[1] Basset D, Willi O, Pert G J, Evans R G *Central Laser Facility Annual Report* RAL-87-041 p.57, 1979

[2] Pert G J *Journal of Computational Physics* **43** No. 1 1983

STIMULATED RAMAN SCATTERING: COLLISIONAL DAMPING AND THE LONG-WAVELENGTH SPECTRAL GAP

H.C. Barr, T.J.M. Boyd and A.P. Mackwood

University of Essex

INTRODUCTION

Stimulated Raman scattering (SRS) is a parametric instability in which an incident (laser) electromagnetic light wave with an intensity above the threshold decays into a scattered light wave (slw) and an electron plasma wave (epw)[1]. Conservation of energy and momentum require that $\omega_0 = \omega_s + \omega$, $\underline{k}_0 = \underline{k}_s + \underline{k}$ where $(\omega_0, \underline{k}_0)$, $(\omega_s, \underline{k}_s)$, $(\omega, \underline{k})$ are the frequency and wave number of the incident photon, the scattered photon and the plasma wave respectively. The instability is of importance to successful laser fusion schemes mainly on account of the capacity of the epw to accelerate electrons to high energies. These can penetrate and preheat target cores, adversely affecting compression efficiencies. The spectrum of the emission, emitted into wavelengths between λ_0 and $2\lambda_0$ (λ_0 is the laser photon wavelength), is dependent upon the laser wavelength used, the laser intensity I_0, the damping mechanisms present - Landau and collisional, and convective losses. The latter in turn depend on the shape of the density profile. The nature of the instability, whether absolute or convective, depends also on the density profile although the distinction between these two types is less distinct than sometimes believed. Here, we examine the influence of collisional (and Landau) damping on SRS from an overdense monotonic density ramp. It has been recognised[2] that SRS is absolutely unstable at any of the possible scattered wavelengths when there is feedback between, in this case, the backward and forward scattering resonances, each individually acting as a 'Rosenbluth' convective amplifier (CA).

The inclusion of Landau and collisional damping alters the picture in the following ways. In the first place, no growth or amplification of any kind occurs unless

$$\gamma_0 > (\gamma_1\gamma_2)^{1/2} \qquad (1)$$

where γ_1, γ_2 are the slw and epw damping rates. In underdense homogeneous plasma ($n < n_c/4$), WKB theory predicts absolute growth (i.e. at the location of the source) above a threshold given by

$$2\gamma_0 > (\upsilon_1/\upsilon_2)^{1/2}\gamma_2 + (\upsilon_2/\upsilon_1)^{1/2}\gamma_1 \qquad (2)$$

This is a necessary condition in an inhomogeneous plasma. In heavily Landau-damped regimes, usually taken to mean $k\lambda_D \geq 0.3$, we expect SRS to be suppressed. This occurs for scattering at lower densities and leads to attenuation of the emission spectrum at short wavelengths referred to as the Landau cut-off. This cut-off is sometimes used as a temperature diagnostic. As we shall see below, the Landau cut-off is **not** implied by eqn. (4), namely it is still present in the absence of slw damping. Inverse bremsstrahlung of the slw is effective at higher densities and particularly so for scattering near the $n_c/4$ density surface, this being the reflection density for the slw of frequency $\omega_s \approx \omega_0/2$. If collisional damping is sufficiently strong, as occurs in higher Z targets (Z is the effective ion charge), at lower temperatures, or with short wavelength laser irradiation, then eqn. (1) may imply a long wavelength cut-off for reasons other than the disappearance of the quarter critical density surface.[4] Even if conditions (1) or (2) are satisfied emission may not be observed if the slw is absorbed as it propagates out of the plasma. However this does not indicate that SRS is not occurring. It may still be significant and capable of the damaging electron acceleration referred to above. In the discussion to follow we have removed such absorption from the convective gain factors calculated. The behaviour exhibits considerable detail with the degree of sensitivity of resonances to parameter changes forming one important aspect in the interpretation of results.

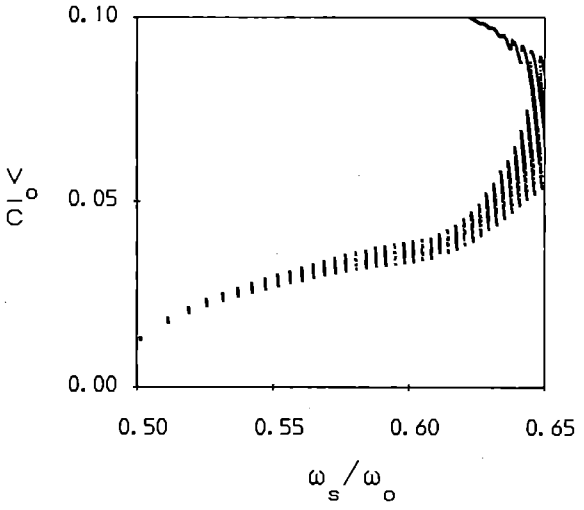

Figure 1 The convective gain contour showing a gain of exp(2π) in scattered wave intensity for an overdense weakly collisional (Z = 10) plasma. The contours are very narrow loops at the centre of which sit the absolute instability threshold eigenstates (not shown). Gain in excess of exp(2π) lie within the loops or above the open contour visible at high frequency. Other regions experience effectively no gain.

The description adopted assumes an electron plasma inhomogeneous in one direction only (the x direction, say) with a prescribed ambient electron density $n_0(x)$. For the purposes of this paper we assume a linear density ramp and use throughout a scalelength of $167\lambda_0$ from vacuum to the laser critical density. A temperature of 1.7KeV is also used throughout. Only backwards and forwards scattering parallel to the density gradient are considered here. Landau and collisional damping are included phenomenologically in the coupled wave equations for the slw and epw. The equations are solved numerically in the frequency domain allowing rigorous boundary conditions to be applied with control over the frequency. The code has been described in past Annual Reports.[5]

The model implicitly includes all backwards and forwards scattering resonances as well as wave reflections. It should be noted that reflections occur at all locations at which the plasma is inhomogeneous and not solely at the geometrical reflection points. This acts as a **distributed** feedback mechanism which permits absolute instability to occur by a relatively local feedback between back and forward scattering resonances although at raised thresholds. Lowest absolute thresholds occur when feedback is maximum (when forward scattered light is totally reflected and damping is minimum). Low feedback recovers the Rosenbluth CA.

RESULTS

Figures 1 and 2 show absolute and convective instability thresholds for plasmas having Z = 10 and Z = 79 for λ_o = 0.35 μm as typical examples of low and high collisionality cases. The contours indicate an intensity amplification of exp(2π), the value conventionally accepted as the "convective threshold". In Figure 1 the regions of the v_o - ω_s plane giving amplifications of exp(2π) or greater are extremely limited, confined to areas within very narrow loops centred on the absolute instability eigenfrequencies. The loops are barely resolvable on the scale of this figure. The regions outside these loops correspond to frequency-intensity values which result in effectively no amplification. This indicates the extreme sensitivity of these resonances to the values of the scattered light frequency and the laser intensity. The sensitivity decreases somewhat towards higher frequencies and, indeed, the contours open up as the Landau cut-off is approached at $\omega_s \approx 0.65\,\omega_o$. At frequencies below the Landau cut-off feedback is high and collisionality low. Absolute and convective thresholds are therefore effectively identical, still lowest for scattering from the $n_c/4$ region although not strongly so.

Figure 2, the strongly collisional case, portrays a contrasting picture in its convective behaviour. Absolute instability thresholds are qualitatively similar to the low Z case, except that collisions have raised all thresholds. What is quite different is the extent of the threshold frequency plane which gives rise to amplifications greater than exp(2π). The figure shows that **any** frequency and intensity above the contour exceeds the convective threshold. Only the first eigenfrequency at $\omega_s = 0.5\omega_o$ is enclosed within an exp(2π) contour loop in the way that all the low Z eigenfrequencies were. Other eigenfrequencies are such that all intermediate frequencies (i.e. away from the eigenfrequencies) experience large amplification. In practice, there will be no distinction between growth convectively saturated at high amplification and the continuing temporal growth of absolute instability. Some other nonlinear agency may restrict both before they are distinguishable. The convective threshold for frequencies below the Landau cut-off is seen to be almost independent of frequency. All frequencies down to $\omega_o/2$ should achieve observable amplifications. It is possible then that the eigenfrequencies detuned by some agency would still achieve significant amplification.

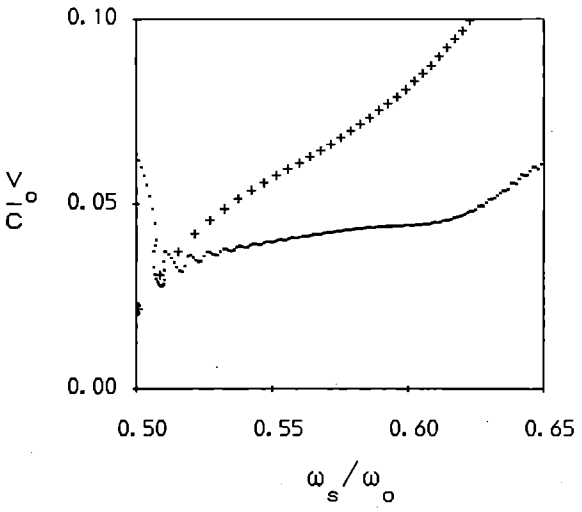

Figure 2 The absolute instability threshold eigenstates (crosses) and the contour showing a gain of exp(2π) in scattered wave intensity versus scattered frequency for an overdense strongly collisional (Z = 79) plasma. All intensities above the open contour experience gains in excess of exp(2π).

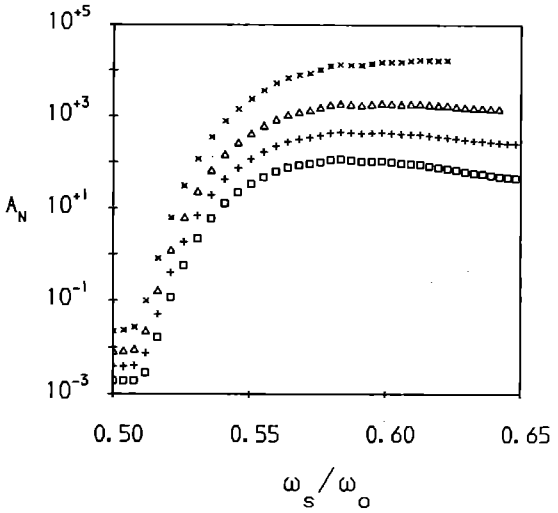

Figure 3 The normalized amplifications at frequencies ±0.1% removed from the eigenfrequencies when v_o = 0.1c and for Z = 10( ), 30(+),50(Δ),79(x).

This is in contrast to the low Z highly sensitive case in which detuning would effectively switch off the instability. Therefore in this highly collisional case no long wavelength cut-off or gap should be apparent.

How then might a long wavelength cut-off or gap arise in the low Z case given that the lowest threshold is still that for scattering from the $n_c/4$ surface into frequencies at $\omega_o/2$? What the data suggests is that it is just those low frequency eigenstates which are most sensitive (as seen in Figure 3 and Figure 6) to frequency detuning and to changes in laser intensity. Therefore the presence of noise , even thermal density fluctuations, may be sufficient to detune such resonances. In both low and high Z plasmas it is the intermediate frequencies which are the least sensitive and give the widest bands of large amplification. In the high Z case detuning may shift the eigenfrequency away from a given value yet that frequency may still experience large convective gain whereas in the low Z case the 'off resonant' frequencies give virtually no amplification whatever.

The sensitivity to changes in frequency is indicated in another way in Figure 3 which plots normalized amplifications for frequencies removed from the absolute instability eigenfrequencies by ± 0.1% for a variety of target materials (Z = 10, 30, 50, 79). In other words, these are frequencies detuned by 0.1%. It is clear from this, firstly, that it is the intermediate frequencies that are least susceptible to detuning and secondly that low Z eigenstates are more sensitive than the high Z states.

REFERENCES

1. C.S. Liu, M.N. Rosenbluth and R.B. White, Phys.Fluids, 17, 1211 (1974)
2. P. Koch and E.A. Williams, Phys.Fluids 27, 2346 (1984)
3. E.A. Williams and T.W. Johnston, Phys.Fluids B1, 188 (1989)
4. R.P. Drake, E.A. Williams, P.E. Young, Kent Estabrook, W.L. Kruer,
   D.S. Montgomery, H.A. Baldis and T.W. Johnston, Phys.Fluids B1, 2217 (1989)
5. H.C. Barr, T.J.M. Boyd and A.P. Mackwood, Phys.Fluids B1, 1157 (1989)

Annual Report to the Laser Facility Committee, Rutherford Appleton Laboratory Report RAL-90- (1990).

UPGRADE OF THE TOODLES PROPAGATION CODE

C I Glasgow, I N Ross
Rutherford Appleton Laboratory

Introduction

The TOODLES propagation code was set up to model the propagation characteristics of the Nd:glass laser. It was a paraxial ray tracing code which could take into account radially and temporally varying quantities and the laser system could contain a selection of rod or disc amplifiers, lenses, apertures, attenuators and soft apertures. A square or Gaussian radial or temporal distribution was assumed for the input beam which derived from a point source on axis.

We report on progress in upgrading TOODLES to enable it to include asymmetric distributions in the x-y plane (non-radially symmetric) and to include finite source size. In addition to the extension to large source size the new TOODLES, which should perhaps be renamed THREEDLES!, will include asymmetric amplifier gain distributions, the possibility of modelling asymmetric Raman amplifiers and the inclusion of off-axis and tilted components. The additional removal of the paraxial approximation will enable the code to assess component aberrations.

Principles

In a source plane, the input beam is constructed having an arbitrary brightness distribution and consisting of a number of rays each having an input energy, which varies with time, an x-y coordinate in the transverse plane and a $\theta - \phi$ coordinate in the angular plane. These rays are propagated through the components of the system by exact ray tracing and in any plane a ray will have a new x-y and new $\theta - \phi$ coordinate, and a new energy determined by gain or loss in the earlier components of the system. Beam profiles in space, angle or time can be constructed in any required plane from the ray coordinates and energies.

Each component subroutine must now be modified to allow propagation of this beam through that component.

The rod amplifier is separated into a number of axial planes to enable the code to take account of axial gain variations and to properly model gain saturation. It is thought that effects such as rapid repumping and amplified spontaneous emission can also be included later. The rod amplifier subroutine is now operating satisfactorily and figure 1 shows examples of input and output fluence distributions under conditions of uniform pumping and heavy saturation.

A lens subroutine has also been developed for exact ray tracing through spherical or flat surfaces. Figure 2 demonstrates severe field aberrations when imaging an off axis point (20° off-axis) using an F/10 lens.

Work continues to enable the inclusion of soft apertures and disc amplifiers and to extend the amplifiers to include repumping and ASE and enable us to model off-axis pumping of Raman amplifiers.

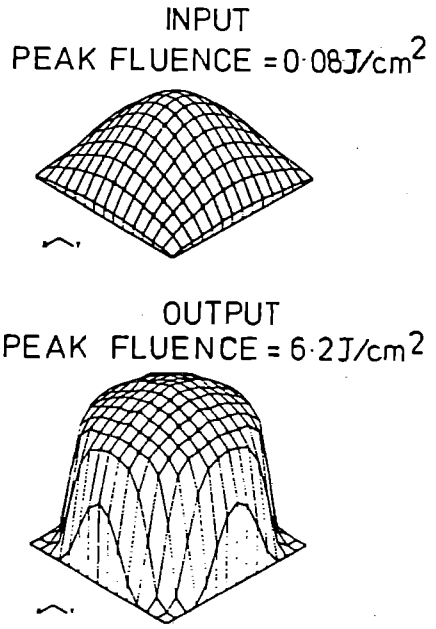

Figure 1

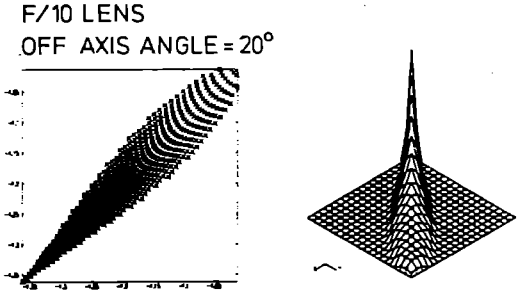

Figure 2

INTRODUCTION AND OPERATIONAL STATISTICS

C B Edwards and C N Danson
Rutherford Appleton Laboratory

The current reporting period marks the first full year of Vulcan operations following the Phase I upgrade. Fifteen full-scale experiments were conducted, in addition to an intensive programme in TA 4.

Shot statistics for the period are summarised in Table I. All target areas have been operational, with 1799 full disc shots being delivered during experiments, with a shot failure rate of less than 3%.

TA 4 operations have been extremely productive during the past year, with a total of 1064 shots delivered in support of an expanding programme including contact x-ray microscopy, multi-layer X-UV mirror testing, high resolution crystal specroscopy, and absolute x-ray wavelength measurement. TA 4 uses the Vulcan oscillators and rod amplifiers in the interval between disc firings, and is designed to be as unobtrusive as possible to the experimental programmes in the main target areas. This policy has been very successful, and TA 4 is in almost constant use.

A highlight of the development programme during the past year has been the further refinement of Random Phase Plates for beam smoothing and shaping. The technology has been extended to operation in the ultra-violet for use with the Sprite Raman shifted KrF facility, and to the generation of a wide range of spatial profiles including line focus generation.

In July, operations were suspended for one week during the RAL Open Days. The Vulcan laser and associated target areas were extremely popular with visitors, and the opportunity was taken to publicise the High Power Laser Programme to a wide audience.

Staff shortages have been a particularly serious problem for the operations group during the year due a combination of further staff losses, and the imposition of a recruitment ban. The Operations Group continues to rely heavily on the assistance and co-operation of the user community, particularly in the provision of operator cover in Target Areas during periods of late running. Their contribution to the success of the operations and experimental programme at the Facility is gratefully acknowledged.

Total number of shots	5986
Total number of disc shots to target areas	1799
Total number of disc shots to TA West	198
Total number of disc shots to TA East	851
Total number of disc shots to TA 2	750
Total number of target shots to TA 4	1064

Experimental period	TA West	TA East	TA 2
		Experiment (Nº of disc shots)	
18 March - 14 April		K-edge shifts (95)	Sub-kev opacity (117)
15 April - 9 June	Implosions (86)	X-ray conversion (165)	
10 June - 8 July		X-ray laser (87)	Thomson scattering (91)
8 July - 14 July	OPEN DAYS		
15 July - 2 Sept		EXAFS (107)	Plasma jets (103)
3 Sept - 28 Oct		X-ray laser (123)	
29 Oct - 21 Dec	X-ray diffraction (112)	Radiation transport (174)	Neutral particle det. (117)
2 Jan - 17 Feb		Plasma jets (100)	Line focus dev. (183)
18 Feb - 24 Mar			Shock breakout (197)

Table 1: Vulcan shot statistics for the year to March 1991

RAL-91-025

DEVELOPMENT OF RANDOM PHASE PLATE SMOOTHING TECHNOLOGY

CN Danson, R Bann[1], D Pepler, I Ross, J Exley[2], D Hardie[3] and S Sails[3]
Rutherford Appleton Laboratory
[1] Now at Spectron Lasers, Rugby
[2] South Bank Polytechnic
[3] Newcastle upon Tyne Polytechnic

INTRODUCTION

Focal spot smoothing techniques have been developed primarily to improve the quality of data from laser plasma interaction experiments on high power laser systems. The method employed by Kato et al (1984) was the use of Random Phase Plates (RPPs). These consist of a random array of transmitting areas which induce a phase shift of either 0 or π . This is placed prior to the final focussing lens which produces a far field distribution containing a multi-beam, high spatial frequency, interference pattern.

The central maxima of the diffraction

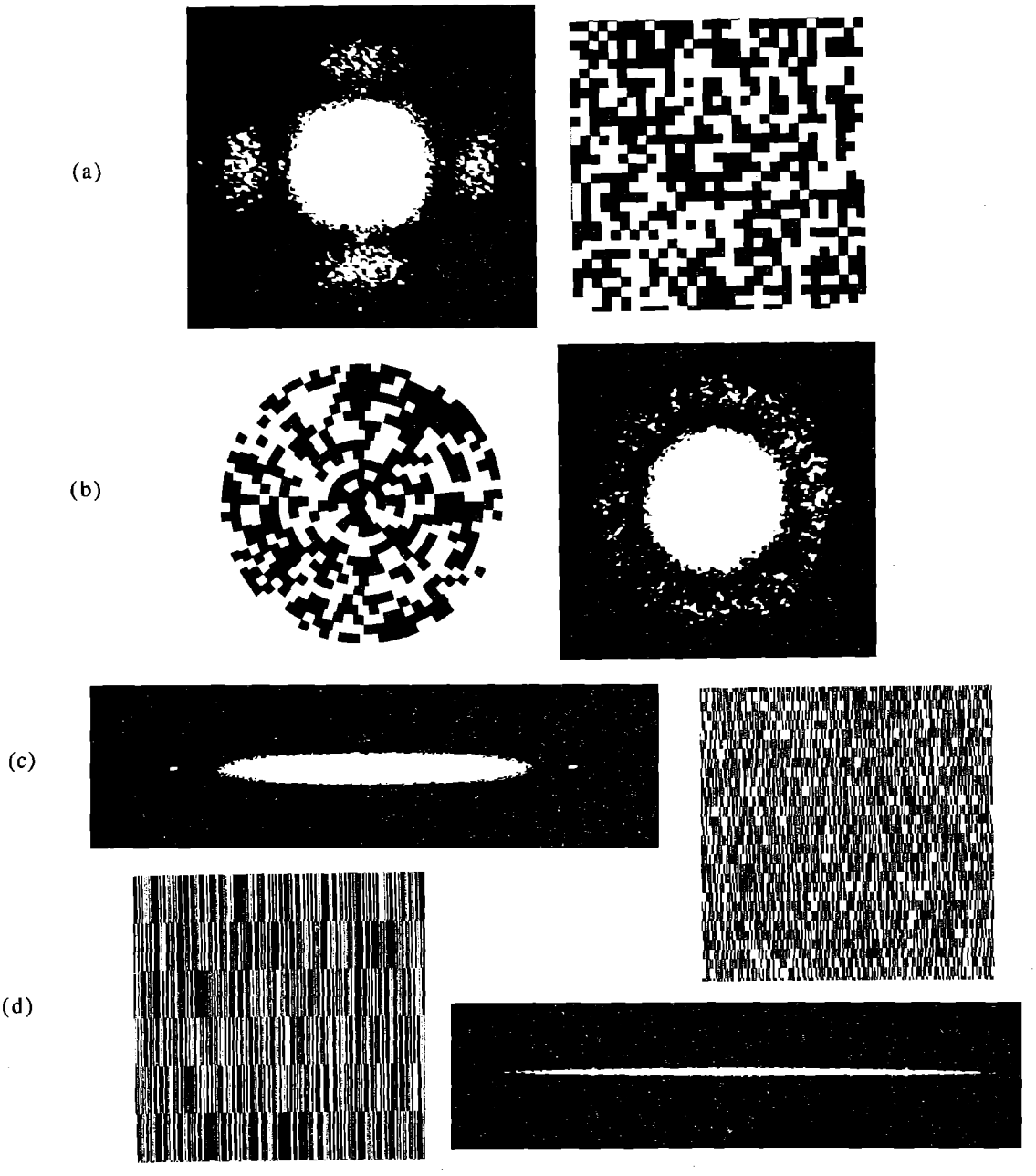

Figure 1. Examples of the masks that have been used to manufacture Random Phase Plates and their associated far-field images.
(a) Standard square profile, relative magnification of far-field image = 4.8, (b) Circular mask design, rel. mag. = 4.8, (c) asymmetric mask design (rectangular elements), rel. mag. = 1.3, (d) line focus mask design, rel. mag. = 1.0

pattern contains about 80% of the incident energy, and it's dimensions (FWHM) are given by $f\lambda/d$ (where f is the focal length of the lens, λ is the laser wavelength and d is the element size of the RPP).

PRODUCTION OF RPPs

RPPs are manufactured at RAL using a photolithographic process. This process may be broadly divided into three stages:

(i) Computer generation of a suitable matrix for the required plate. This pattern is normally produced on acetate from a 'Linotronic' high resolution printer, using software written in-house. The best 'Linotronic' printer available at present has a resolution of 3386 dpi. This allows a minimum element size of 7.5 microns.

(ii) The production of a master mask by duplicating the acetate pattern onto a chrome coated quartz plate. This is done using optical photolithography.

(iii) The production of the RRPs by transfering the mask pattern onto a uv sensitive coating which has been spun onto a suitable substrate. The thickness of the coating can be carefully controlled to produce a π phase shift at the wavelength being used. Operational wavelengths have included 1053, 527 and 268 nm.

The advantage of this production technique for focal spot smoothing is the high speed and low cost of manufacture, the ability to produce RPP's for different wavelengths and the range of focal spots that can be generated. The photolithographical coatings have been shown to have high laser induced damage thresholds (> 5 J cm^{-2} in 1 ns pulse @ 527 nm) making them suitable in the manufacture of RPPs.

RANGE OF RPPs AVAILABLE

A variety of focal spot profiles can be produced using RPPs by suitable design of the mask. Figure 1 shows four examples of mask design with their associated focal profiles.

These focal profiles were produced using a cw Argon ion laser operating at 527 nm. The laser was expanded and collimated at a beam diameter of 100 mm. This was then passed through the RPP under test before being focussed by a 4 m focal length lens. The images were recorded on HP5 film.

All the masks shown in Figure 1 can have a range of element sizes. This was detailed in last years report which showed that the square masks, shown in Figure 1(a), can be produced with element sizes from 10 mm down to 50 microns, allowing a large array of focal spot sizes to be generated. The mask in Figure 1(b) is of our own design producing a circularly symmetric far-field distribution. One of the advantages of this design is that the energy density in the wings of the focal spot is significantly less than with the square mask design.

The mask in Figure 1(c) has different element sizes in the x and y directions producing an asymmetric focal profile. If very much different sizes are used in the x and y directions a line focus can be produced. This is shown in Figure 1(d).

HIGH ASPECT RATIO LINE FOCII

To generate a line focus with an aspect ratio of 100:1 a suitable mask was first produced. This consisted of an array of elements 100 microns in one direction and 10 mm in the other. Part of the element array used on this mask is shown in Figure 2.

This mask was then used to produce RPP's. The test plates were made for green operation, other plates were then produced to operate at 268 nm (KrF pumped Raman) and at 1.053 microns (Nd:YLF). Far field images were obtained using the off-line far-field monitor.

The far field image shown in Figure 3 demonstrates the effectiveness of the RPP. It shows that the aspect ratio used on the mask is accurately transfered to the far-field of the RPP. Low intensity spots are generated at the end of the line. These are part of a grid diffraction pattern from imperfect edge definition on the RPP. This effect will be minimised as the manufacturing techniques are refined.

To generate a range of line focii a number of different mask designs have been used with aspect ratios of 10:1, 50:1, 100:1, 200:1 and 500:1. This does not mean we are limited to these dimensions and it is possible to generate masks to suit individual experiments.

Application Of These RPPs In The UV

The 100:1 aspect ratio mask was used to produce a RPP suitable for 268 nm operation. This was then used in an experiment by Tallents et al (1991) on the Sprite Raman shifted KrF facility at RAL to assess the feasibility of using this method of generating line focii for x-ray laser experiments. A pinhole camera was used to monitor the line focus plasma. The resolution of

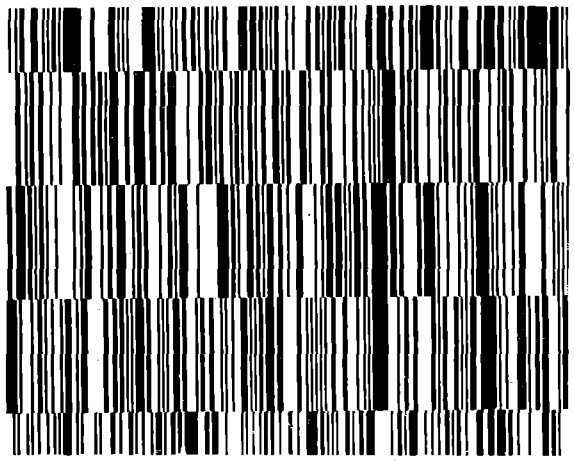

Figure 2. Magnified image of part of the mask used to generate the 100:1 aspect ratio line focus.

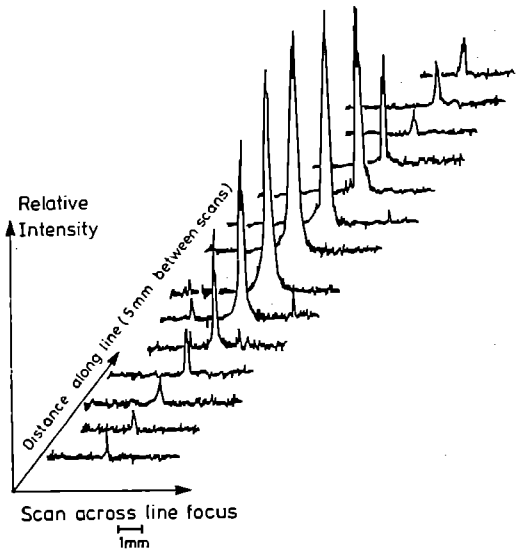

Figure 3. Far-field intensity distribution of the 100:1 aspect ratio line focus.

the camera was approximately 12 microns and was set to observe x-ray emission at 1.5 keV. The focal spot generated was approximately 660 μm in length and 16 μm in width showing very little lateral energy transport at irradiences necessary for Na and F recombination x-ray lasers.

In summary RPPs have been used in conjunction with standard aspheric focussing lenses to produce high aspect ratio line focii. Preliminary experiments have shown that these could be used for x-ray laser experiments. Further development is taking place to generate line focii with longer lengths and increased uniformity.

Infrared Line Focii

Experiments have been conducted to demonstrate the feasability of using high aspect ratio line focii in the infrared. The RPPs were used in conjunction with 1m focal length aspheric lenses. The standard line focii RPPs produce substructure which would make the plates unsuitable for x-ray laser experiments. This is mainly due to the speckle size, which for this experimental configuration was 16 times larger than for the Sprite UV experiments.

There are several possibilities of improving the distribution within the line focii and these are being persued at present.

FAST FOURIER TRANSFORM ANALYSIS OF RPPs

RPPs are relatively simply to manufacture and use for the purpose of producing smooth focal spots although it is not very easy to make a RPP to generate a specific focal spot distribution. This is because the RPP is a binary phase plate, only having two independent phases. A RPP capable of forming a general focal spot would have to have etched into its surface an analogue phase, continuous between 0 and π .

However, it is possible using the Fast Fourier Transform (FFT), to analyse what any given binary phase plate and laser beam profile would produce at focus, and thereby predict which mask design would be well worth constructing.

After a simple translation, the RPP pattern of 0 and π phases and the incident beam amplitude form the input to the FFT computation. The FFT, literally being a complex mathematical expression requires the real and imaginary components of the amplitude, A (x) and phase Ø (x) to be separated as shown below.

$$Z(x) = A(x)\,[\,\mathrm{Cos}(\emptyset(x)) + i\,\mathrm{Sin}(\emptyset(x))\,]$$

A PASCAL program was written to implement the FFT. The FFT routines were tested by simulating a single aperture. This was achieved by setting the phase array to zero for all x, and the amplitude array to one for only a small part of x. The result of the FFT was an approximation to the Sinc^2 function, with greater accuracy achieved by using longer arrays. However the number of elements in the data arrays was restricted to 1024, due to the memory constraints placed by the use of Turbo Pascal 4. Although this does give sufficient resolution for initial studies, it will be necessary to use lengths of the order of 20000 to analyse some designs with very small structures.

Basically, the phase and amplitude arrays simulate a physical phase plate of a unit dimension, and increasing the number of array elements, increases the number of frequencies analysed by the FFT. The number of phased cells within that array can be much less than the number of elements, and determines the size and intensity of the focal spot distribution. A large number of (narrow) cells within the array, will produce a wide focal spot, whereas a smaller number of (wide) cells will produce a narrow focal spot.

Thus if one chooses to have an array length of 640, (coincides with the number of pixels in a VGA graphics display), and 32 cells within that array length, each cell will be 20 array elements wide, and the focal spot will be 2 X 32 elements wide. More generally the focal spot width will be twice the number of cells being used.

The intensity of the focal spot distribution, although having interference peaks and troughs superimposed on a Sinc^2 function, is also dependent on the number of cells, and is given by -

$$\mathrm{Intensity}(x) = \mathrm{Sinc}^2(x) \,/\, \mathrm{Number\ of\ cells}$$

In order to understand more fully the nature of the focal spot produced by the RPP, a series of tests were made to see how sensitive the focal spot distribution is to errors in the RPP.

The areas of the 0 and π phase structures are each nominaly set to 50% of the whole. This is

known to produce a minimum in the focus, on axis, and is far more desirable than having a high intensity spike. With 50% of the beam in each phase, on axis they cancel exactly. Thus any deviation from the norm will start to bring the central spike up, and eventually if all the RPP is at 0 or π phase, then all that is produced is the normal $Sinc^2$ focus, with an intensity of one. The percentage error limit is set where the central spike becomes more intense than any other part of the focus, and this occurs at about 50% ± 5%.

Another possible error is in the absolute value of the phase. The nominal error in phase is obviously zero, and as above, any deviation from the norm will increase the intensity of the central spike, again leading to the $Sinc^2$ focus. In practice the phase error will be non-zero with π ± 5 % being more likely. Test made with a 50% phase ratio and using $I(x) \times \pi$, where $0.0 \leq I(x) \leq 1.0$, showed that, π ± 10% is acceptable.

Tests were also made on the sensitivity to input beam amplitude, and it has been found that there is a high degree of tolerence in this area. Even with an input amplitude of random data between 0 and 1, the basic shape of the focal spot distribution remained, but with 10% - 15% of the energy transfered out into the wings.

Finally the internal structure of the phase plate mask was examined. The focal spot depends on the number of elements, the number of cells, and the phase of those cells. Even keeping the phase ratio at 50%, the phase error zero, and the amplitude one throughout different mask designs produce markedly diverse focii.

The FFT analysis of one standard mask is shown in figure 4(a). This shows the calculated far-field intensity distribution from a one dimensional RPP mask.

The distribution agrees very well with that obtained in practice (high frequency modulation of a $Sinc^2$ function), and further demonstrates the accuracy of the FFT routines. This being the case the distribution shown in figure 4(b), is very encouraging. It is the FFT of a new mask pattern that when constructed should produce the top-hat profile shown. Both figures are to the same scale and contain 92% and 85% respectively in their central maxima, but it is immediately apparent that the intensity modulation in the far-field is much reduced with the new mask design. An approximation of each mask design runs along the bottom of each graph. A mask to this new design is expected to be made and tested in the very near future.

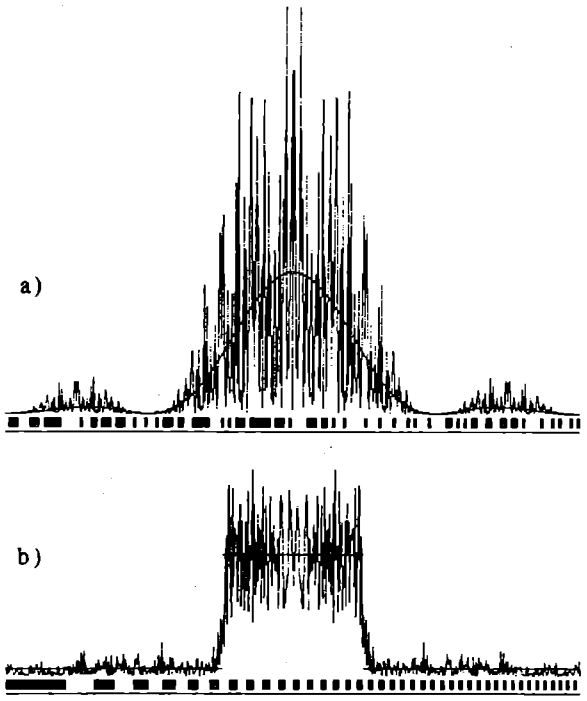

Figure 4. FFT calculated intensity distributions
a) standard square cell RPP
b) variable cell RPP.

CONCLUSION

We have used RPP technology to produce smoothing for a selection of focal profiles. It has proved to be a flexible smoothing approach with the ability to produce a large range of focal spot sizes, in a cost effective manner.

All the RPPs discussed have been used in a variety of experiments from investigation of plasma instabilities to implosion studies. The quality of data from these experiments has been greatly increased.

We are now in a position to accurately model the performance of any RPP prior to manufacture and can therefore investigate more complex element shapes and arrays to produce greater uniformity in more ideal shaped profiles.

REFERENCES

Kato Y et al 1984 Phys Rev Lett, Vol 53, Nº 11, pp1057-64.

Tallents G J, Jacoby J, Key M H, Kodama R, Norreys P, Baldis H, Dunn J and Brown D. Proc SPIE (1991) to be published.

Development of a Novel Fibre Target Mount for High gl Recombination X-Ray Lasers

C L S Lewis, J Uhomoibhi
Queen's University Belfast

J Jacoby
Rutherford Appleton Laboratory

Fibre targets are well suited for recombination X-ray lasers [1]. Due to their small diameter (several μm), fibres provide excellent, two dimensional cooling. By coating carbon fibres with different materials, they offer a wide range of target elements.

Fibres have been successfully used in different experiments producing a high gain coefficient [2,3,4]. However, it has not been possible to achieve a high value for the product of gain times active laser medium length (gl) for free-ended fibre targets. This is mainly because long length fibres could not be confined within the line width of VULCAN focus (30 μm). The problem may be more severe when fibres are used in the 12 μm wide SPRITE line focus.

Several methods have been tested to mount a fibre. Short length fibres (≤1cm) do not require additional support since their bending under gravity is negligible compared to the fibre diameter. Long length fibres (several c m) on the other hand, do require support. Although both ends of the fibre can be supported to achieve straightness, this would not be appropriate for x-ray laser experiments, where one end of the fibre should be visible to observe the laser activity along the axis of the fibre target. Thus, electrostatic fibre mounts have been developed as an alternative tool to align fibres.

A first device [5] was developed, where a carbon fibre had one end clamped at earth potential, while the other end was attracted by a cylindrical electrode at high negtive potential. This electrode was provided with a central hole to allow a direct view to the free end of the fibre. Negative electrodes were found to allow higher voltages than their positive counterparts. For positive electrodes, discharges were observed from the needle-like end of the fibre.

Tests of the first device showed that the fibre was easily held in place between the electrodes. But the fibre straightness was found to be influenced by surrounding earth plane structures in the mount and as a result the fibre was not as straight as required. The local curvature of the fibre was found to be influenced also by other materials when brought close to the fibre. This necessitated the development of a fibre mount with a symmetric electrostatic shielding (Fig. 1)

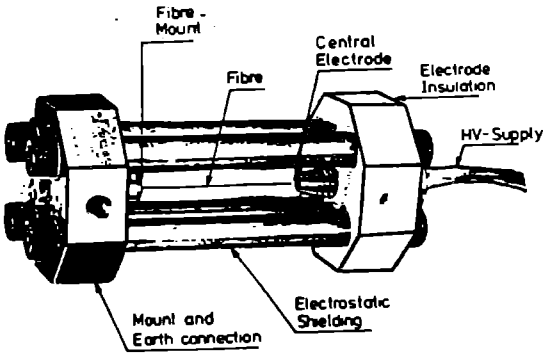

Fig. 1 Electrostatic fibre mount with a symmetric electrostatic shielding. One end of the fibre is connected to earth potential. The other end is attracted by a high negative potential. A hollow electrode allows a direct end-on view at the fibre

The mount consists of four bars of brass material (60±0.5mm long x 6±0.5mm diameter) in four-field symmetry parallel to the fibre. The distance between the outer surfaces of the fibre and the bars was of the

order of about 25±0.5mm. The fibre was glued to a 100 μm diameter Molybdenum wire, centrally positioned in the mount. An enclosed cylinder is ideal but not useful since the shielding structure must also allow alignment and laser pump beams access to the fibre.

From preliminary measurements made with this mount, where a 30±0.5mm length of fibre was employed, a straightness was achieved for up to 20 mm, considering the free end of the fibre as the point of origin. The clamped end of the fibre was found to show an initial deviation of about 40±5 μm, which probably must have been due to the off-centre method used in mounting the fibre in its holder. This was estimated at 50±5 μm. To overcome this problem of initial deviation at the base of support, it is planned to mount future fibres in the centre of capillary tubes which for the fibres, can also act as a guide.

In conclusion, the required straightness of fibres has been achieved for up to 20mm length, to within an accuracy of ± 5 μm. This paves the way for future high gl recombination x-ray laser experiments using fibres.

We would like to acknowledge the assistance of the following people: C.Brown, A. Damerell, K. Miles, W. Lord, W.Lester and the staff of the CLF.

References

[1] R.C. Elton: X-Ray Lasers, Academic Press, New York, p.39,156ff (1990)

[2] D. Jacoby, G.J. Pert, S.A. Ramsden, L.D. Shorock, G.J. Tallents: Optics Comm. 3 7, 193 (1981); J. Phys. B 15, 3557 (1982)

[3] C. Chennais-Popovics et al.: Phys. Rev. Letters 59, 2161 (1987)

[4] C.L.S. Lewis: Plas. Phys. & Contr. Fusion 30, 35 (1988)

[5] J. Uhomoibhi, C.L.S. Lewis: (Private Communications)

CHARACTERISATION AND EVALUATION OF PLANE MULTILAYERED MIRRORS

D S Urch and E Martins

Chemistry Department
Queen Mary and Westfield College
Mile End Road LONDON E1 4NS

INTRODUCTION

Plane multilayered mirrors resemble natural crystals in the way in which they reflect X-rays. The great advantage of such mirrors is that they can be fabricated to any desired 2d spacing in the tens or hundreds of Angstroms range. Multilayers differ from natural crystals in that refraction effects are much more in evidence, especially at very long (>100Å) wavelengths. The Bragg equation, $n\lambda = 2d \sin\theta$, can be modified to take account of this refraction, thus

$$n\lambda = 2d_{\infty}(1 - \delta_{\lambda} \sin^{-2}\theta) \qquad (1)$$

where n = the order of reflection
λ = the wavelength of radiation
θ = the angle of reflection
d_{∞} = the effective interlayer spacing for normal incidence (ie no refraction)
δ_{λ} = the refraction constant at wavelength λ.

Thus if θ is measured for different orders of reflection it will be possible to determine both $2d_{\infty}$ and δ_{λ}. This report will outline how a conventional X-ray emission on spectrometer may be adapted to characterise plane multilayer mirrors by the measurement of the limiting (no refraction) 2d value, $2d_{\infty}$, and the refraction constant δ_{λ} at appropriate wavelengths. A qualitative evaluation of reflectivity, by comparison with crystals such as octadecyl hydrogen maleate (2d = 63,5 Å) or rubidium acid phthalate (2d = 26,12 Å) is also possible.

EXPERIMENTAL PROCEDURE

The equipment used is a Philips PW1410 X-ray fluorescence spectrometer in which the characteristic X-rays from a sample are reflected, after collimation, from a plane crystal and detected in a thin window gas-flow proportional counter (1μ mylar window, 90% argon + 10% methane at 1 bar); subsequent amplification and counting of the output planes is by Harwell 2000 series electronics; ratemeter output is presented as a function of angle on a standard x,t chart recorder. As the emphasis in this work is on soft X-rays the conventional scandium anode sealed X-ray tube, effective for the stimulation of characteristic X-rays up to about 10 Å, was often replaced with an open window gas-discharge tube (Compagnie Générale de Radiologie - Elent - 10) for long wavelength work (up to 200 Å). The range of samples to be used in the characterisation of a specific multilayer would depend upon its 2d value; a list of suitable samples and their characteristic wavelengths is given in table 1.

The plane multilayer to be investigated is mounted on an aluminium sledge and replaces one of usual spectrometer crystals. The dimensions of the sledge limit the size of the multilayer that can be studied at present to 80 x 30 x 5 mm. As a five position sledge holder is fitted within the spectrometer up to five multilayers could, in principle, be studied more or less at the same time. In practice it is much more convenient to retain two or three well characterised crystals (or multilayers) so that experimental conditions can be confirmed for each sample and so that the performance of the 'unknown' multilayer can be compared with that of an established device.

Table 1

Sample	Radiation	Wavelength
boron oxide, or silica	O Kα	23.55
silicon nitride	N Kα	31.57
graphite	C Kα	44.79
boron oxide	B Kα	67.88
niobium	Nb M ζ	72.23
beryllium sulphate	S $L_{2,3}$ M	76.8
beryllium sulphate	S $L_{2,3}$ M	79.7
zirconium	Zr M ζ	81.75
yttrium oxide	Y M ζ	93.59
lithium phosphate	P $L_{2,3}$ M	98.15
lithium phosphate	P $L_{2,3}$ M	103.3
beryllium sulphate	Be Kα	113.5
silicon	Si $L_{2,3}$ M	136.2
silica	Si $L_{2,3}$ M	139.6

RESULTS

The results that will be presented and discussed here were obtained with a commercial (OVONYX) plane multilayer with a nominal 2d spacing of 200 Å. But the method is quite general and has been applied to a range of plane multilayers supplied by A. Ridgely of the Rutherford Appleton Laboratory.

As the multilayer had a large 2d spacing all the experiments were carrried out using the C.G.R. Elent-10 open window source for excitation. The samples used are listed in table 1. In the case of O Kα, N Kα, C Kα, and B Kα most possible high orders were also measured; 1 through 7 for O, 1 through 5 for N, 1 through 4 for C and 1 and 2 for B. The angles at which reflections were observed are recorded in table 2, together with 'effective 2d' values. These data can then be plotted graphically using a modified form of equation (1);

$$(n\lambda/\sin\theta) = 2d_{\infty} - 2d_{\infty}\cdot\delta_{\lambda}\cdot(\sin^{2}\theta)^{-1}, \qquad (2)$$

by plotting $(n\lambda/\sin\theta)$, ie 'effective 2d' versus $(\sin^{2}\theta)^{-1}$. This is done in the figure. The straight lines show that the behaviour of the plane multilayer can be described by equation (2). The fact that all the lines converge to a single point enables $2d_{\infty}$ to be read off the graph directly (210, 4 Å in this case). From the slope of each line the corresponding value of δ_{λ} can be calculated: these results are listed in table 3. For long wavelength lines where multiple orders were not observed the values of δ_{λ} can be calculated directly from equation (1), since $2d_{\infty}$ has been found. Values of δ_{λ} calculated in this way are also included in table 3.

CONCLUSIONS

A conventional X-ray emission spectrometer can be used to characterise plane multilayer mirrors. The refraction constant can be measured at a range of different wavelengths.

ACKNOWLEDGEMENTS

The authors gratefully acknoledge the help and support of A. Ridgely (RAL), for his interest in this method of multilayer evaluation and for supplying multilayers to test.

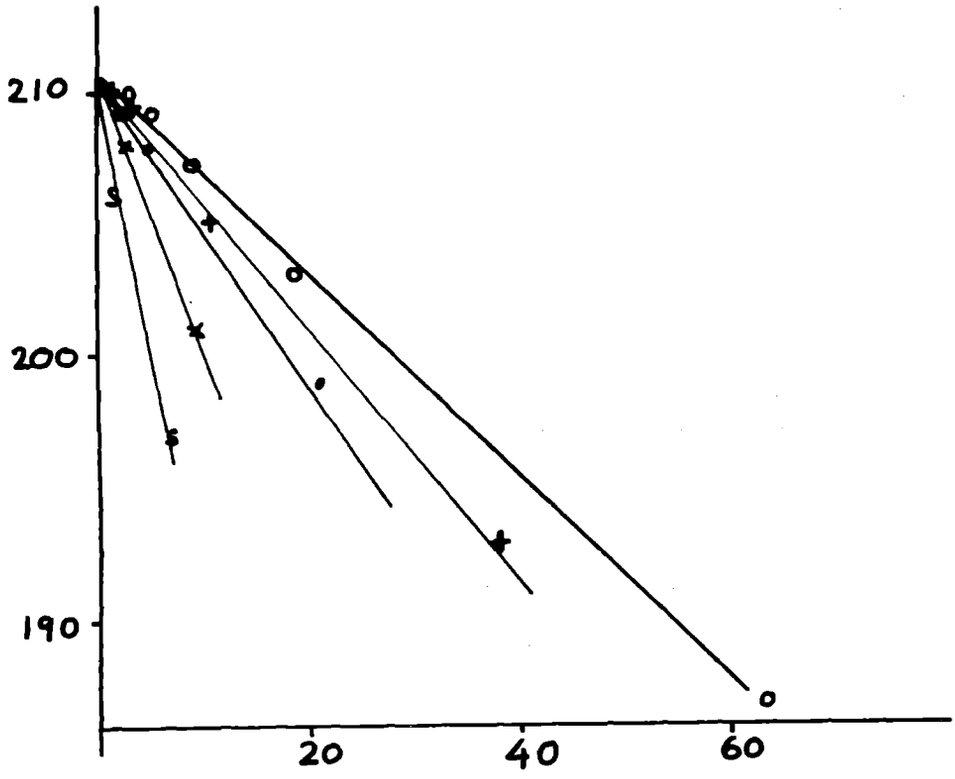

Figure ($n\lambda/\sin\theta$) vertical axis versus $(\sin^2\theta)^{-1}$, horizontal axis. Data points for the various orders of different X-ray wavelengths are distinguished thus:

open circles , O Kα (23.55 Å) + , N Kα (31.57 Å) X, B Kα (67.88 Å)

solid dots , C Kα (44.79 Å) S , S $L_{2,3}$M (76.8 Å)

Table 2

X-ray line	Order	Observed angle (2θ)	"effective 2d"
O Kα	I	14.5	187
N Kα	I	18.8	193
C Kα	I	26.0	199
O Kα	II	26.8	203
N Kα	II	35.8	205
B Kα	I	39.4	201
O Kα	III	39.9	207
Nb M ζ	I	43.0	197
S $L_{2,3}$ M	I	45.9	197
S $L_{2,3}$ M	I	48.0	196
Zr M ζ	I	49.7	195
C Kα	II	50.9	208
Y M ζ	I	58.0	193
O Kα	IV	53.7	209
Be Kα	I	76	184
O Kα	V	68.4	210
N Kα	IV	74.3	209
C Kα	IV	80.0	209
B Kα	II	81.4	208
Si $L_{2,3}$ M	I	91.1	191
O Kα	VI	84.9	209
N Kα	V	97.5	210
O Kα	VII	103.7	210
C Kα	IV	117.4	210

Table 3

Diffraction constants ($\delta\lambda \times 10^3$)

Wavelength	
23.55	1.8
31.57	2.3
44.79	3.0
67.88	5.1
72.22	8.6
76.8	9.7
79.7	11
81.75	13
93.59	19
98.15	21
103.3	22
104.3	21
116.1	30
136.2	47

An Elliptically Curved Crystal Spectrometer for EXAFS

D Goodman and T A Hall
University of Essex

A Ridgeley, A R Damerell, S Hancock and D Rodkiss
Rutherford Appleton Laboratory

1. Introduction

The proposal to use an elliptically curved crystal spectrometer is for EXAFS studies was published in the 1989 Annual Report[1]. Since then an elliptical spectrometer has been built and used successfully to record aluminium EXAFS spectra during an experiment in TAE during August 1990. The EXAFS experiment is described in Section A3 of this Annual Report. The anticipated advantages of the elliptical configuration are listed in that work.

Most of the advantages anticipated from this instrument were in fact realised, including the convenient use of a CCD detector in place of X-ray film.

Using the properties of an ellipse, the following expressions for the Bragg angle θ can also be derived.

$$\sin 2\theta = \frac{2\epsilon(1-\epsilon\cos\phi)\sin\phi}{1-2\epsilon\cos\phi+\epsilon^2} \quad (ii)$$

Using the Coddington equation

$$\frac{1}{u}+\frac{1}{v}=\frac{2}{R\sin\theta}$$

the following expression for R is obtained

$$R=\frac{u(2a-v)}{a\sin\theta} \quad (iii)$$

Equation (i), (ii) and (iii) can now be used together with the Bragg relationship

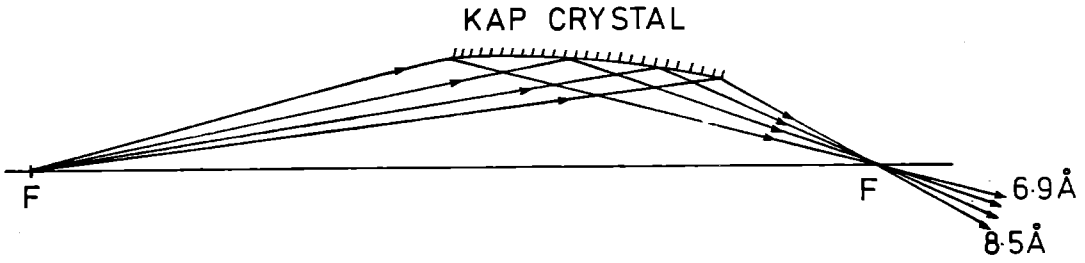

Fig.1 Optical arrangement for KAP elliptically curved crystal.

2. Instrument Design

The basic design parameters are derived from the equation of the ellipse in polar coordinates

$$v=\frac{l}{1-\epsilon\cos\phi}=\frac{a(1-\epsilon^2)}{1-\epsilon\cos\phi} \quad (i)$$

Where v is the object distance
Where l is the semi-latus rectum section of the ellipse
Where e is the eccentricity of the ellipse
Where ϕ is the polar angle
Where a is the semi-major axis of the ellipse.

$$n\lambda = 2d\sin\theta$$

to choose a spectrometer design appropriate to the task in hand. For aluminium EXAFS work the wavelength range 7-8Å must be covered.

The crystal finally chosen for the EXAFS elliptical spectrometer was KAP. TlAP, as used in previous EXAFS experiments with a flat crystal was not a practability because of difficulties with cleaving and bending TlAP crystals. NH_4AP which has a high 2nd order reflectivity[2] was also tried, but this crystal exhibited over-mosaicing on being bent, giving rise to spurious structure.

The final design parameters chosen for a KAP crystal were an eccentricity of 0.966 and focal separation of 106.8 mm The optical arrangement is shown in Fig 1.

The crystal is a cleaved section from a block of KAP crystal 50 mm long and 10 mm wide. Crystals 200-300μm thick can be obtained by simple cleaving methods using a razor blade. The elliptical shape is achieved by constraining the crystal against an elliptical former by means of two end clips. The elliptical former has the same length and width as the crystal, and was made using a computer numerically controlled (CNC) machine.

The crystal mount is itself mounted on a brass plate with an X-Y micrometer adjustment for focusing (fig 2). Also mounted on the plate are two target mounts adjustable, on in X and Y, the other in X and Y rotated through 25° . The detector is also mounted on the plate, but adjustable only in the direction of the emerging beam.

mounting in the TA4 chamber and the third in the TAE chamber for the EXAFS experiment.

This makes it possible to focus the crystal on the first base-plate away from and in advance of the main experiment, then to verify it produces an X-ray spectrum in TA4, prior to executing the main experiment in TAE. During the trial run in TA4, targets were aligned remote from the target chamber by means of a system of viewing microscopes arranged around the first base-plate. This alignment procedure was more complicated to set up than the flat crystal arrangement, but target alignment was quicker after the initial set up.

3. Instrument Performance

Using the end clip method of bending the crystal it was possible to achieve a uniform elliptical shape over almost the whole crystal length. A few mms at each end of the crystal did not conform to elliptical curvature and this was manifest by a 'curl-round' at the ends of the spectrum. The 'curl-round' is caused by more than one wavelength being incident on

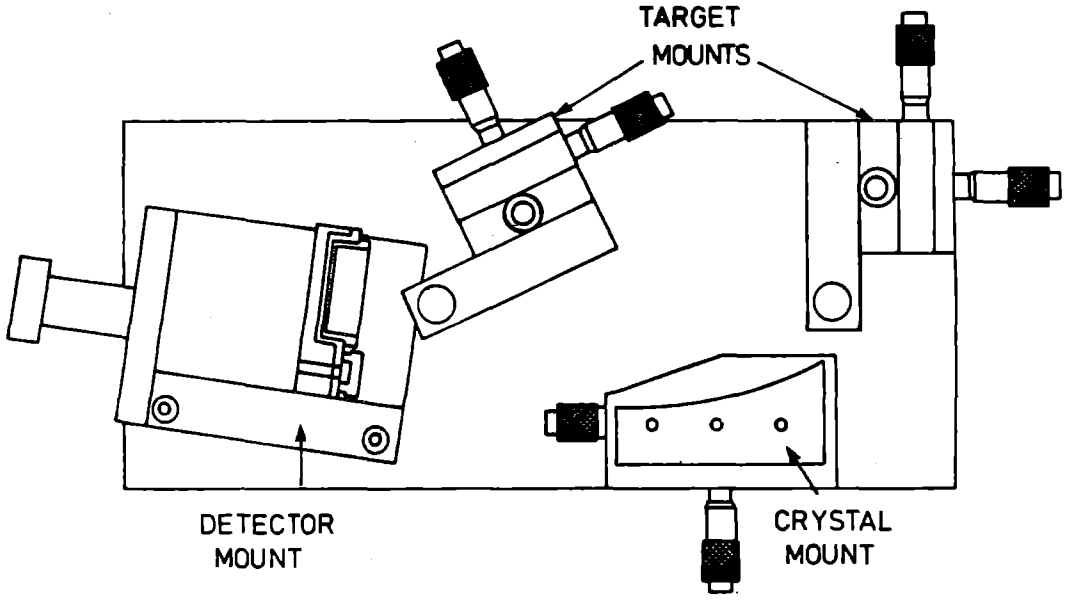

Fig.2 Configuration of mounting plate for focusing and alignment.

The mounting plate is itself mounted in a similar non-adjustable base plate by means of a kinematic mount. The base plate is triplicated, one plate for focussing, one for

the film at one point. The two ends of the crystal were masked off in use to avoid this 'curl-round'.

The crystal was protected from target debris by means of two 8μm polypropylene windows one at each end of the crystal. A 25 μm beryllium filter was placed in front of the detector to eliminate stray light and softer X-ray emission from the foil target.

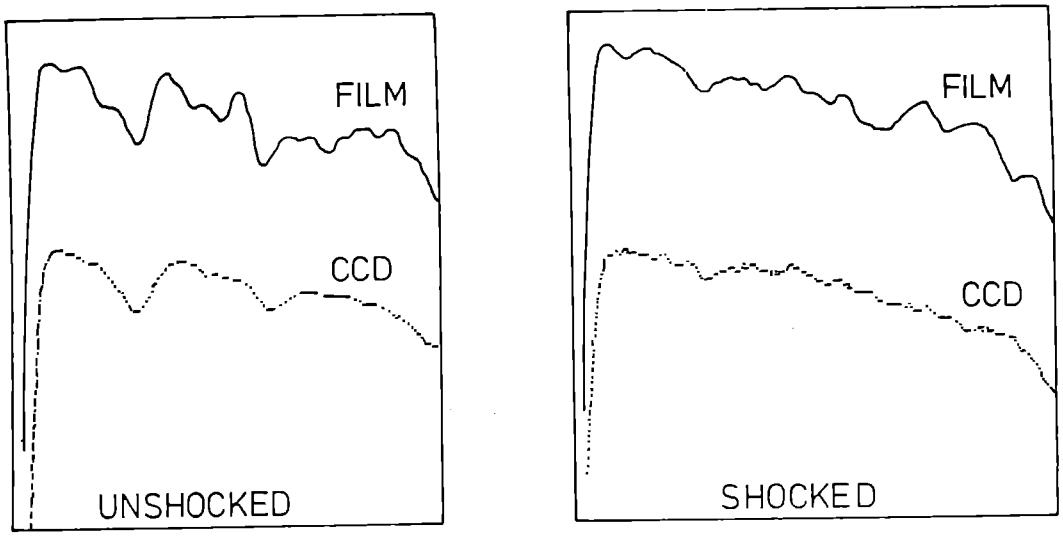

Fig3 Comparison of shocked and unschocked EXAFS spectra using X-ray film and CCD.

During the preliminary trials in TA4 a copper line spectrum and a uranium continuum spectrum were obtained, verifying the spectrometer was functioning. During the Aug 1990 experiment in TAE aluminium EXAFS spectra were obtained. Because of the line focus characteristics of the instrument shocked and unshocked spectra are obtained on the same shot. When a successful EXAFS run had been obtained using DEF X-ray film the film pack was replaced with a miniature COHU CCD camera in which the glass window had been removed from the CCD chip to make it sensitive to X-rays. This camera produced EXAFS spectra which were at least as good as those obtained using DEF film, and with the advantage of being easier to process. Fig 3 shows shocked and unshocked EXAFS spectra obtained by the two methods at similar times for the shocking pulse.

It was found that the amount of compression achievable with the elliptical arrangement was limited by undispersed hard X-ray emission from the foil target. An irradiance of more than 5 x 10^{11} W/cm^2 at this target produced an unacceptable amount of background in the detector.

4. Conclusions

It has been shown that the elliptical crystal geometry for EXAFS studies works. It has the advantage that shocked and unshocked EXAFS are recorded on the same shot. The compactness of the spectrum allows a CCD system to be readily employed.

The system is more difficult to set up initially than the flat crystal arrangements, but easier to operate when set up. Compresssion is limited by stray hard X-ray background at irradiances greater than 5 x 10^{11} W/cm^2 on the foil target.

References

1. T Hall, D Goodman and A Ridgeley, Annual Report to the Laser Facility Committee (1989) RAL-89-045, p 169.

2. P M Barrus, R L Blake, H Felthauser, E E Fenimore and A J Burek, Am Inst Phys 75, p 115 (1981).

The EXAFS Elliptical Spectrometer as a High resolution Instrument

A Ridgeley, RAL

1. Introduction

Crystal spectrometers used for analysis of laser-produced plasmas are usually limited in spectral resolution by the source size. This is because the unfocussed nature of the (generally) plane crystal geometry requires the source-detector distance to be kept small to maintain sufficient photon flux. High spectral resolution can be obtained by having the source a long way from the crystal[1], but at the expense of sensitivity.

Using the focussing properties of concavely curved crystal geometries it is possible to obtain high spectral resolution combined with high sensitivity. The classical geometry is the Johann configuration. This has been used for laser-produced plasmas at RAL by Dunn et al[2] using cylindrically curved crystals and by Basov et al[3] using spherically curved crystals.

The Johann configuration is ideally suited for an extended source (eg Tokamak) and suffers from the disadvantage when used with a laser-produced plasma source that the wavelength coverage is small even if the source is brought close to the crystal.

Poquérusse[4] has devised an ingenious spectrograph which uses a trapezoidal crystal elastically bent to form a non-uniformly curved shape. This can produce high resolution spectra over a wide wavelength range.

It is demonstrated that the elliptical spectrometer developed for EXAFS work can produce high resolution spectra over an intermediate wavelength range.

2. The Principle

Figure 1 shows the geometry of the elliptical crystal spectrometer developed for EXAFS. At each point along the length of a curved crystal there is a local radius of curvature R, and for any ray hitting the crystal at a Bragg angle θ the Johann focussing condition will apply at a distance $R\sin\theta$ on either side of the normal.

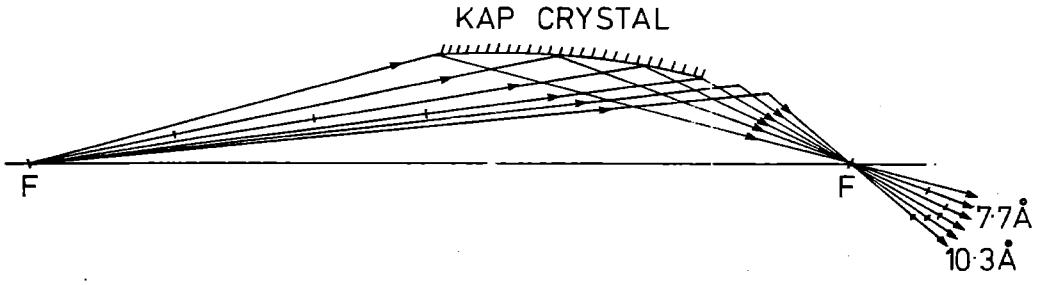

Fig.1. Elliptical spectrometer configuration showing Johann cross-over points.

Fig 1 shows how $R\sin\theta$ varies with θ for the outgoing rays. It is seen from the diagram there is a region where a compact detector would be expected to record an appreciable spectral range at a resolution determined by the crystal rocking curve width rather than the source size.

3. Theory

The simple idea expressed in section 2 must be analysed in greater depth, which is done from consideration of fig 2. For a given wavelength range defined by the crystal rocking curve width $\delta\theta$, rays from the source S_1S_2 satisfy the Bragg condition over the arc P_1P_2 of the crystal. C_1P_1 and C_2P_2 are the normals to the crystal at P_1 and P_2, C_1 and C_2 being the local centres of curvature. The simple treatment in Section 2 contains the implicit assumption that the curvature does not change significantly between P_1 and P_2 so that C_1 and C_2 can be assumed to be coincident. The rays will then appear to

emanate from a point source at 0, which may be between the real source and the crystal.

If C_1 and C_2 are coincident in Fig 2 it follows that

$$\delta\theta + \delta\phi - \delta\psi = 0,\ \delta\theta = \frac{\delta s}{R},\ \delta\phi = \frac{\delta a \sin\theta}{x} = \frac{\delta s}{x-u}$$

Where x = OP

Hence can be derived

$$\delta a = \frac{\delta s/x - \delta\theta}{\frac{\sin\theta}{u} - \frac{1}{R}} = \frac{\frac{\delta s}{x}}{\frac{\sin\theta}{u} - \frac{1}{R}} - \frac{\delta\theta}{\frac{\sin\theta}{u} - \frac{1}{R}} \qquad (i)$$

(a) (b)

The terms (a) and (b) in equation (i) represent the values of δa pertaining to $\delta\theta = 0$ and $\delta s = 0$ respectively and OP=Rsinθ.

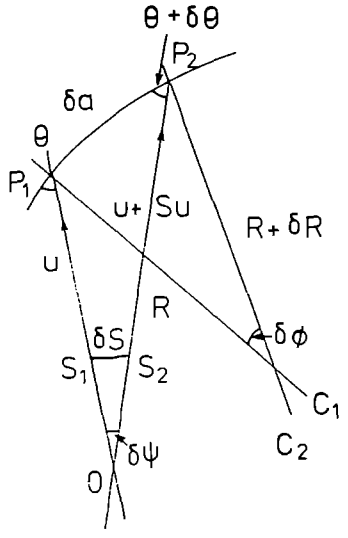

Fig.2 Ray geometry for curved crystal.

Since $\delta\theta$ is not known empirically the theory can be tested by deriving a gain factor G_λ defined as the ratio of δa for a curved crystal to δa for a flat crystal. It is assumed that $\delta\theta$ is not affected by bending the crystal.

For a flat crystal 1/R = 0 so we obtain

$$G_\lambda = \frac{R\sin\theta}{R\sin\theta - u} \qquad (ii)$$

Fig 3 shows a graph of G_λ against wavelength calculated for the KAP elliptically curved

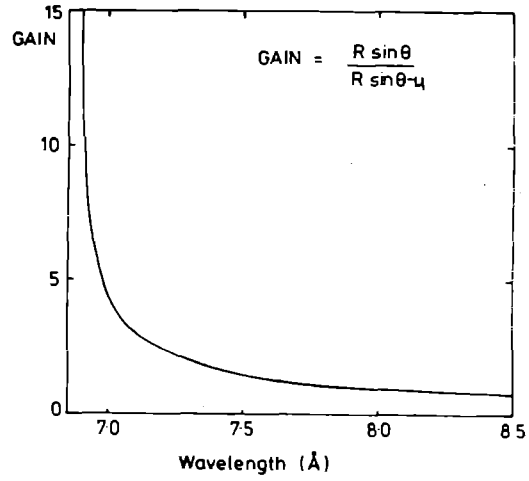

Fig.3 Variation of gain factor with wavelength for KAP elliptical crystal.

crystal spectrometer built for EXAFS use. It is seen that G_λ has values close to unity except close to the minimum wavelength of 6.89Å, where the value rises asymptopically to infinity. This would appear to indicate that the assumption is justified except close to the minimum wavelength,where it is expected not to, since all other wavelength pass through the Johann cross-over points for this wavelength.

References

(1) B C Fawcett, A Ridgeley, T P Hughes, Mon Not R Astr Soc (1979) 188, 365-370.

(2) J Dunn, R Barnsley, K D Evans, N J Peacock, Annual Report to the Laser Facility Committee (1988), RAL-88-042 P 146.

(3) N G Basov, Yu Mikhailov, A V Rode, G V Shlizkov, Annual Report to the Laser Facility Committee (1988) RAL-88-042 P 149.

(4) A Poquérusse, Optics Comm 58, 108-112 (1986).

KrF LASER DEVELOPMENT & EXPERIMENTS

M H Key*, M J Shaw
Rutherford Appleton Laboratory
*Also at the University of Oxford

Introduction

There has been further significant evolution of the objectives of the KrF laser development programme during the year. The report of the Scientific and Technical Working Group on the European Laser Facility was considered in the early part of the year by SERC's Committees but the recognition in the later months of the year that there were serious short-falls in SERC's finances for the next year and beyond led to a major cost-cutting exercise in the course of which it was decided by SERC Council to suspend SERC's involvement in ELF for the time being.

Until this decision in November 1990 the emphasis of the KrF laser development work was on the assessment of the KrF option for ELF. The year's work was the second of the two year programme which had been sanctioned by the Science Board with this objective.

Subsequent to the ELF decision effort was redirected towards consideration of a smaller scale new laser, Supersprite, which could be funded by SERC alone and which would have sufficiently advanced performance to make it a future replacement for the glass laser facility, Vulcan. At the end of the year, Science Board formally recognised the new situation and agreed to a further year's study and experimental investigation with a view to defining the Supersprite project at a level of detail such that decisions could be made in the autumn of 1991 on whether to proceed with it.

Technically and scientifically the year has been very successful. The Sprite facility has been used for a series of significant R&D studies.

The Raman chain has demonstrated exceptionally high brightness in 12 ps pulses. The brightness of 2 x 10^{19} cm^{-2} $sterad^{-1}$, so far demonstrated, exceeds by 25 times the typical performance of a glass laser generating UV third harmonic. At the other extreme, amplification of incoherent broadband radiation in the Sprite system has shown the capability of the KrF laser to produce extremely uniform irradiation at low brightness. The performance of the generator has been significantly improved through reliable transform-limited pulse production in a feedback stabilised synchronously pumped dye laser. The energy of the transform-limited pulse has been increased through the use of a titanium sapphire amplifier prior to third harmonic conversion.

Detailed measurements on the amplification characteristics of the large aperture Sprite module have been made and compared with theoretical models at a level of accuracy which gives good confidence in our predictive capability for KrF pulse performance in large systems.

Two full scale target shooting runs by user groups have been carried out using the high brightness 12 ps pulses and these have produced interesting new science. In the second of these, reflective focusing optics and a calcium fluoride optical train giving minimum 2 photon absorption losses was deployed to improve on target power. Focal spot size as small as 6 μm has been demonstrated for powers up to 0.5 TW.

Theoretical work on KrF modelling and Raman chain modelling has progressed significantly and particularly in the latter area. Current interest centres on the future possibility of further reduction of the Raman pulse duration using the "walk through" mode of operation of the waveguide amplifiers. Other theoretical work has studied future possibilities for experiments with the KrF beams.

The operational statistics for the year have been impressive, notably the delivery of almost 300 shots in the most recent target shooting run in the space of four weeks.

There has been valuable supporting R&D activity from University groups in the area of small angle scattering and generator development as well as in theoretical modelling.

The newly reactivated Supersprite design study is at an early stage but has made some headway. Consultation with facility users particularly over detailed options for target irradiation is an important aspect of the work. Practical development of components for the large aperture Supersprite amplifier module is well advanced. In particular, the new Marx generator has been operated at over 2 MV and the new design of laser triggered switch for the high voltage PFLs has been validated in operational tests at over 2 MV. Our modelling capability for pulsed power systems has also advanced as reported in this section. The next steps in pulse power development will couple the PFL to a diode rather than the present resistive load and study diode electron beam characteristics.

12 ps OPERATION OF THE SPRITE KrF PUMPED RAMAN LASER AT EXCEPTIONALLY HIGH BRIGHTNESS

E C Harvey, C J Hooker, +J R Houliston, +M H Key, A K Kidd,
J M D Lister, I N Ross and M J Shaw
Rutherford Appleton Laboratory
+Also at University of Oxford

Introduction

There is much current interest and a vigorous rate of development in the generation of beams of higher brightness from pulsed lasers. Table 1 summarises the achievements in the three main lines of development. The amplification of chirped pulses in solid state lasers and their subsequent compression has produced the highest powers to date but still has unsolved technical problems connected with pulse contrast ratio and, in the most recent work with the highest power[1] with the preservation of high quality wavefront in the compressed beam.

The second approach uses KrF lasers to generate directly pulses of circa 100 fsec duration[2]. The only pulse contrast problem here is that of amplified spontaneous emission which is in principle controllable and the highest brightness so far demonstrated has been with this approach[3].

The third line is that of the KrF pumped Raman laser which is being pursued particularly in the programme of the Central Laser Facility. In earlier work the Raman laser has been demonstrated with 40 ps pulses[4] and the present paper reports a reduction of pulse length to 12 ps and an increase of brightness to about 2×10^{19} W cm^{-2} sterad^{-1} in pulses of 12 ps duration. The power in the experiment was 0.5 TW and the energy was up to 5.8 J. The contrast ratio was $> 10^{10}$:1.

System	Brightness W cm^{-2} sterad^{-1}	Power TW	Pulse length psec	Contrast ratio	Source Reference
CPA in solid state lasers	2×10^{19}	20	1	10^4:1	(1)
VSP generation in KrF lasers	6×10^{19}	10	0.1	10^6:1	(3)
KrF laser pumped Raman laser	2×10^{19}	0.5	10-100	10^{10}:1	This paper

Table 1

The experimental system was that described previously[4] with certain modifications. In particular the angles of the pump beams in the beam combining Raman amplifier stages was reduced to 2.5° in order to reduce the transit time difference for the pump and Stokes beams to less than the duration of the pulse for 12 psec pulses. In addition an improved pulse generator, giving transform limited pulses, was developed as described by Hooker et al ibid. The main KrF amplifier stage (the 27 cm diameter Sprite amplifier) was improved in performance by the provision of an angled output window which had the effect of reducing de-pumping by parasitic oscillations which had previously limited the small signal gain of the system. A detailed study of the performance of the amplifier with the angled window has shown the gain to be at the ASE determined level and this improvement by a factor of about 5 in double transit ssg has contributed to an increase in the saturated output for amplified short pulses. The performance of the Sprite amplifier is discussed in detail by Harvey et al ibid. Finally, reduction of two photon losses for short pulses by installation of calcium-fluoride lenses in the recollimation at the output of the beam transport system from the second pass of the Sprite amplifier, together with a calcium-fluoride windows on the final Raman amplifier RA3, has given further improvement in the peak power. The beam transport to the target chamber has also been improved with a calcium-fluoride window in the target chamber and a reflecting off-axis paraboloid beam focusing system as described by Ross ibid.

The laser operating in the 12 ps mode has been used for two extensive target irradiation experiments in August/September 1990 and February/March 1991 and, in addition, characterisation measurements have been made on the output Stokes beam and on the performance of the Raman amplifier chain.

The Experiment

Pulse Generation

Pulses at 748 nm (the one third sub harmonic of the KrF laser) were generated in a sync pumped mode-locked oscillator with external feedback which produced transform-limited

pulses[5]. Amplification in a YAG pumped dye amplifier system, operating at 8 Hz, and third harmonic conversion, produced 12 ps pulses at the 248 nm KrF wavelength. A KrF discharge amplifier (EMG 103) amplified these pulses. After 1 pass a fraction of the energy was used to generate a Raman Stokes pulse by focusing in a 2.7 metre long methane gas cell at 4 bar pressure. The first Stokes beam was separated with a prism and amplified in a forward Raman amplifier consisting of a 3 metre long methane gas cell at 3 bar pressure in which the 268 nm Stokes pulse co propagated with a 248 nm pump pulse. The pump pulse for the first Raman amplifier and a separate KrF beam for subsequent amplification in the KrF laser chain were both derived from a second saturated amplifying pass through the KrF preamplifier. The performance of the Raman generator and the Raman amplifier have been discussed elsewhere[6]. The generator system produced 5 mJ in 12 ps in a near diffraction limited beam of 10 mm aperture at the KrF wavelength and 500 μJ in a beam of similar characteristics at the Raman Stokes wavelength[4].

KrF Laser

The KrF beam was amplified in two stages consisting of the 8 cm aperture preamplifier Goblin and the 27 cm output amplifier (Sprite) which are both e-beam pumped. These are operated in double-pass amplification and their small signal gain length products, without laser input and in equilibrium with their internally generated ASE, are respectively 7 and 8. Angular multiplexing with 8 beams was used to send pulses at 4 ns intervals through the amplifiers which were pumped for 100 ns and 60 ns respectively. The average energy reaching the Raman amplifiers was 1.2 J per pump beam after Fresnel and two photon losses in the output optics.

The Raman Amplifier System

The Raman amplifier chain following the Raman generator and preamplifier had three further stages illustrated in Fig 1. A Stokes beam of 1 cm diameter was amplified in a 2 metre long methane gas cell operating at 3 bar (RA1) pumped by a single co-propagating KrF laser pulse at about 0.2° to the axis of the Stokes beam. The next stage (RA2) was a 2.5 x 2.5 cm x 1 metre long reflective waveguide amplifier operating at 2 bar methane pressure and pumped by 8 beamlets at 1° to the axis. The beamlets were produced by a segmented mirror reflecting one of the KrF beams extracted from Sprite. The final stage (RA3) was an 8 cm x 8 cm x 1 m reflecting waveguide amplifier operating at 1 bar with pump beams at 2.5° to the axis. RA3 was pumped by seven of the main output beams, RA2 by a single main output beam subdivided by the segmented mirror and RA1 by an 8% fraction of one of the main beams. The chain also incorporated a multi-pass optical delay line in vacuum and two beam expanding spatial filters located between RA1 and RA2, and RA2 and RA3.

Fig.1 Raman Amplifier Chain

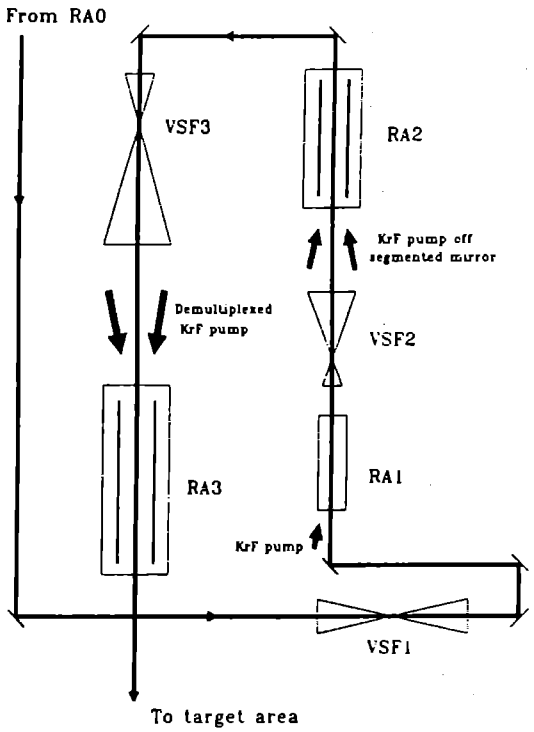

Results and Discussion

KrF Amplification

The performance of the KrF amplifiers was modelled using a Frantz Nodvik treatment of their saturable gain and loss. Their internally generated ASE and interstage ASE were modelled in a 1D approximation which has been shown to agree quite closely with more exact 3D modelling (Harvey et al ibid). General agreement was found between model and laboratory results. The EMG preamplifier was saturated on the second pass and gave an output energy density of about 3 E_{sat}. Amplification in Goblin was essentially unsaturated with an output energy density of 0.1 E_{sat}. The output from Sprite was saturated at 2 E_{sat}. The final output energy was reduced by 2 photon and Fresnel losses in the window of the amplifier and the lens used to recollimate each beam after optical multiplexing. ASE depumping of Sprite and Goblin significantly reduced the small signal gain in this mode of operation where the interpulse interval is large relative to the lifetime of the KrF excimer.

Raman Amplification

Fig 2 shows the experimental performance of the final beam combining Raman amplifier. Output energy up to 5.8 J was recorded for shots with the highest pump energy. The average pump energy for the data shown was 9 ± 3 J.

Fig 2 Final Raman Amplifier Performance

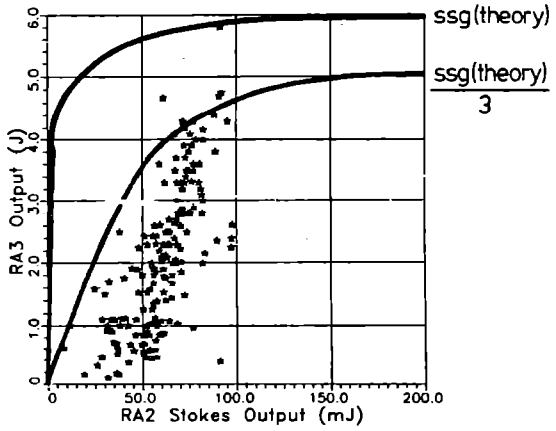

Efficiency of conversion was up to 65% after allowance for Fresnel and two photon losses. Raman amplification at 12 ps in methane is strongly transient since the transverse relaxation time T_2 = 30 ps. Saturated amplification in the transient limit can only be described by numerical modelling. Fig 2 also shows gain saturation of the final amplifier calculated using such a numerical model which describes parallel propagation of plane waves at the pump and Stokes frequency and assumes transform limited 12 psec pulses. The curves assume a constant value of pump energy over the whole range of input Stokes energies. It is interesting to note that the experimental results for low Stokes energy input into RA3 show levels of gain which correspond to the theoretically modelled gain only if it is assumed that the effective value of the small signal gain parameter $\gamma I_p l$ is reduced by a factor of about 3 relative to the experimental value. Measurements under more ideal conditions show a much smaller discrepancy[6].

The experimental situation differs from that in the modelling in several ways. The pulses in the experiment are close to transform limited at the generator but there is some deterioration of the quality of both the pump pulse and the Stokes pulse due to nonlinear interactions as they propagate through the KrF and Raman amplifier chains[7]. Measurements indicate that the Stokes pulse at RA3 is under 2 x transform limited and the pump pulse is about 2 x transform limited in bandwidth. Raman gain is well known to be reduced for non transform limited pulses.

The difference of axial velocity in the waveguide for the pump and Stokes waves gives a relative timing shift which, if it becomes comparable with the coherence time, will truncate the growth of the gain exponent at a level close to that at which this condition is reached. We estimate this effect would occur in RA3 if the propagation length exceeded 100 cm, which it does not.

The pump radiation is delivered in 7 beams at 2.5° to the guide axis with each beam separated from the others in angle. This effect is not included in the modelling and it leads to a relative transverse shift of the interacting parts of the Stoke and pump wavefronts making the amplification dependent on the transverse coherence.

Numerical modelling of these processes is currently being investigated. An interesting corollary is the possibility of amplifying a Stokes pulse which is shorter in duration than the pump pulse and using the temporal walk-through of the Stokes relative to the pump to couple all of the pump energy into a shorter pulse (K Hill et al ibid).

Beam divergence

The divergence of the pump beams was 30 times diffraction limited[8]. The far field pattern of the Stokes output from RA3 was measured both with a CCD camera at the focal plane of a 17 m focal length lens combination and also by measuring the energy fraction transmitted through a pinhole in the focal plane. The pinhole measurements indicated 90% of the energy within 30 μrad. The CCD camera showed a far field pattern with fwhm of 20 μrad (Fig 3). This corresponds to ~ 3 x diffraction limited beam quality.

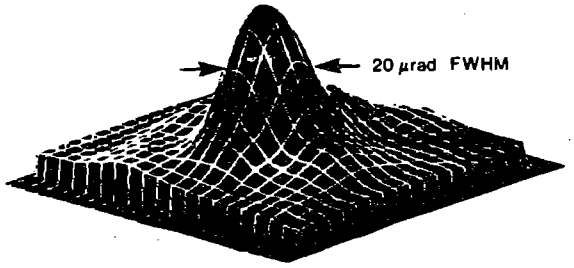

Fig 3 Stokes RA3 Output Far Field Pattern

There is clearly a major improvement in the divergence of the Stokes beam relative to pump beams and it seems probable that the Stokes beams could be made diffraction limited with further attention to the quality of the optical components in the Raman amplifier chain.

Brightness

The brightness of the Stokes beam was up to 2 x 10^{19} W cm^{-2} $sterad^{-1}$. This could be increased by a further factor of 9 x if diffraction limited operation were to be obtained. The pulse contrast ratio was previously shown to exceed 10^{10}:1. This level is expected also for 12 psec operation.

By increasing the aperture of the Stokes beam and maintaining diffraction limited quality, further increase in the brightness is theoretically possible. This would require increased pump energy to the Raman amplifier to match increased aperture. Increased pump energy is obtainable by increasing the number of optically multiplexed pump beams using a greater fraction of the pumped time of the output module and decreasing the interpulse interval. Alternatively, with the same interpulse interval a larger aperture amplifier such as the 60 cm Supersprite module currently under development would increase the pump power.

Conclusion

We have demonstrated operation of a KrF pumped Raman laser at brightness levels comparable with the best obtained by alternative methods which are applicable only to pulses of shorter duration. The Raman approach has the potential for considerable improvement and offers exciting prospects for future high performance laser facilities required for applications such as X-ray lasers and laser fusion.

References

1. C Sauteret et al, Optics Letters, Vol 16, No 4, 238, Feb 15 1991.

2. S Szatmari and F P Schäfer, Optics Communications, Vol 68, no 3, 196, 1 October 1988.

3. A J Taylor et al, Optics Letters, Vol 15, No 1, 39, 1 January 1990.

4. Ross et al, Opt Comm. Vol 78, 263 (1990).

5. C J Hooker et al, Optics Communications, Vol 80, No 5, 6, 375, 15 January 1991.

6. C J Hooker, J M D Lister and P A Rodgers, Accepted Optics Communications for publication.

7. I N Ross, W T Toner, C J Hooker, J R M Barr, I Coffey, J Mod Opt, Vol 37, 555 (1990).

8. J M D Lister et al, Accepted Optics Communications for publication.

A Feedback Stabilised Oscillator for SPRITE

C J Hooker, J M D Lister and I N Ross

Rutherford Appleton Laboratory

The requirement for a generator of short transform-limited pulses at the front end of Sprite resulted in the construction last year of a DFDL oscillator[1]. The output pulses had a FWHM of approximately 10ps, and were sufficiently close to the transform limit to allow the Raman amplifier chain to operate at pump-to-Stokes conversion efficiencies of up to 50%, compared to the 7% achieved previously[2]. The DFDL, however, was complicated to set up and align. In the summer of 1990 a simple technique was reported[3] for stabilising a synchronously mode-locked laser to give transform-limited pulses, and this technique was investigated using the Sprite oscillator.

The stabilisation is achieved by feeding back a small fraction (typically as little as 10^{-6} to 10^{-9}) of the laser output just ahead of the pulse circulating in the main cavity. The feedback may come either from an external cavity or from an arrangement such as that shown in Figure 1, which was used for our investigations of the technique[4].

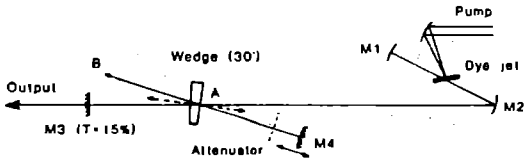

Figure 1. Experimental arrangement for feedback stabilisation of a dye laser.

In any synchronously mode-locked laser, there is a background of low-intensity radiation in the cavity, arising from fluorescence of the dye. The main pulse advances through this background as a consequence of gain saturation on its leading edge, and the phase and amplitude variations of the background are transferred to the pulse. This has been shown[5] to result in a rapid variation in pulse shape and spectral content. When the coherent feedback is present at a level where it dominates the stochastic background, the effect of the background fluctuations is greatly reduced, resulting in pulses which are essentially transform-limited.

These effects of feedback can be seen in Figure 2, which shows time-averaged autocorrelation traces and spectra of the sync-pumped laser output at 746nm (a) without feedback and (b) with feedback present. The disappearance of the coherence spike on the autocorrelation trace indicates that the high-frequency noise arising from the stochastic nature of the background radiation has been suppressed. At the same time, the spectrum of the output has been narrowed by a factor of 7.

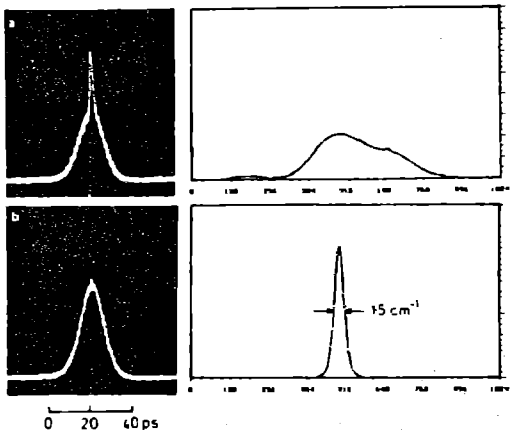

Figure 2. Effects of feedback stabilisation on autocorrelation trace and spectrum: (above) with no feedback and (below) with feedback present.

The experimental arrangement shown in Figure 1 was designed to investigate how the timing of the feedback affected the way the laser stabilisation occurred. M4, the feedback mirror, was adjustable over a range of 25 mm by a micrometer screw. A precise timing reference was obtained by observing fringes in the beam at B when the optical paths AM3 and AM4 were made equal. This point was reproducible to an accuracy of 50 microns, since the laser was not stabilised when the feedback was coincident with the main pulse, and its coherence time was of the order of a few hundred

femtoseconds. The level of feedback was varied by inserting attenuators before M4 as shown, the optical thickness of the filters used being taken into account when calculating the timing of the feedback pulse. At each level of feedback, M4 was scanned through the available range, and spectra and autocorrelation traces recorded at a number of positions.

Analysis of the autocorrelation traces with feedback present showed an excellent fit to a $sech^2$ pulse shape, and the spectrum of the output also fitted the calculated shape. Accordingly, actual pulse widths were determined from the autocorrelation traces assuming a $sech^2$ pulse shape.The time-bandwidth product of the pulses was evaluated, and is plotted as a function of feedback timing in Figure 3 for four different levels of feedback. The lines in the figure are purely to indicate the trends in the data, and are not theoretical curves or fits to the results.

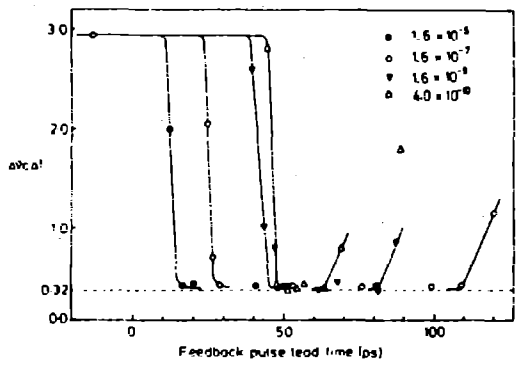

Figure 3. Time-bandwidth product as a function of feedback lead time for 10ps pulses, with different levels of feedback.

The plot has a number of interesting features. As the feedback is made earlier with respect to the main pulse, the time-bandwidth product decreases very suddenly to a value close to 0.32, which is the theoretically expected value for a $sech^2$ pulse shape. This is the point at which the narrowing of the spectrum and the collapse of the coherence spike on the autocorrelation trace occur. As the feedback is made earlier still, the pulse length increases slightly, and the spectrum becomes narrower, although the product remains constant, since at this point the pulses are transform-limited. The change in pulse length is at most 10%. Further advance of the feedback results first in the pulse shortening again, and subsequently in the loss of stabilisation, although the return to larger values of time-bandwidth product is more gradual.

As can be seen from Figure 3, the size of the region over which the pulses are transform limited depends on the level of feedback, and there is a minimum level of feedback below which stabilisation cannot be achieved at all. That minimum was of order 10^{-9} in our experiments, in which the output pulses typically had energies of 1 to 2 nJ. Thus the laser could be stabilised by an amount of feedback corresponding to a few tens of photons.

The stabilised dye laser has now been adopted as the standard short-pulse oscillator of the Sprite system. However, the feedback is now provided by an external cavity in order to avoid the loss due to the wedge, and an etalon has been introduced to obtain more sensitive wavelength tuning. The system has proved easy to set up and maintain, and operates reliably for long periods.

REFERENCES

1. M Steyer, I N Ross and J M D Lister; Annual Report to the LFC, RAL-90-026, B2.1, 90 (1990)

2. E C Harvey, C J Hooker and J M D Lister, Annual Report to the LFC, RAL-90-026, B1.4, 86 (1990)

3. P Beaud, J Q Bi, W Hodel and H P Weber, Optics Communications **80**, 31 (1990)

4. C J Hooker, J M D Lister and I N Ross, Optics Communications **80**, 375 (1991)

5. J M Catherall and G H C New, IEEE J Quantum Electronics **QE-22**, 1593 (1986)

Sprite ISI Tests

J M D Lister, M J Shaw, C J Hooker and E C Harvey

Rutherford Appleton Laboratory

1. Introduction

The requirement for high target irradiation uniformity, particularly for direct drive laser fusion, has created interest in a technique, pioneered by the Naval Research Laboratory, known as echelon-free induced spatial incoherence (ISI).[1] The concept requires the image of a smooth spatial profile, generated at the front end of the laser system, to be relayed through the amplifier chain and onto the target.

Optical imperfections in high power laser systems make it difficult to achieve uniform target illumination using coherent beams. Random spatial intensity variations are produced in the output by phase aberrations introduced by the many optical elements in the system. In conventional ISI, echelons are used at the output of the laser system to divide the beams into many beamlets, each with a different time delay.[2] If the delay increments are greater than the coherence time ($t_c = {}^1/_{\Delta\nu}$, where $\Delta\nu$ is the bandwidth), these beamlets are incoherent and will focus independently to the same diffraction profile at the target, and to a width determined by the beamlet size. The superposition of these beamlets will produce a smooth spatial profile when averaged over a time much greater than t_c. For a high power, multiple beam laser, this approach requires the use of an optically coated echelon for each beam line, operating at a high fluence level.

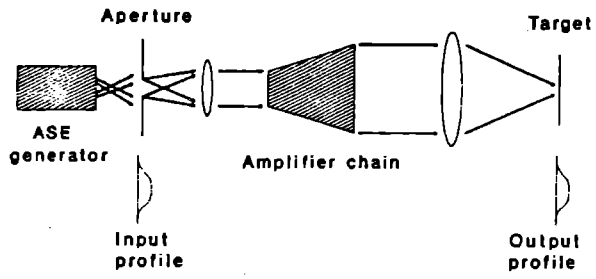

Figure 1: Schematic diagram for a broadband high power laser system using echelon-free ISI.

The alternative scheme described here (Fig 1) does not rely on the use of echelons. A broadband incoherent source uniformly illuminates an aperture at the front end of the laser system. The beam consists of many independent coherence zones. The speckle interference between the focal plane patterns produced by these zones fluctuates at intervals of the coherence time. KrF laser systems have been shown to have a bandwidth capability of $\Delta\nu \equiv 200\ cm^{-1}$, giving a coherence time of $t_c \equiv 150$ fs.[3] Such a system can therefore produce a smooth intensity profile on a time scale much shorter than the response time of a fusion target.

The choice of field angle for a given system is constrained by both upper and lower limits. The upper limit is determined by the maximum field angle permitted by the laser system, or by the minimum intensity required at the target. The lower limit is given by the minimum beam divergence required to produce sufficient smoothing of the beam profile at the target.

2. Experimental

The experiments were performed using the existing Sprite KrF amplifier chain. A Lambda-Physik EMG 103 KrF discharge laser was used as a broad band, partially coherent source. A high reflectivity plane mirror was used at the back of the laser cell to produce double pass amplified spontaneous emission (ASE) at the output. The KrF wavelength is 249 nm and the bandwidth was measured to be 62 cm^{-1} FWHM. The beam divergence was estimated to be 3 mrad, or 120 times the diffraction limit (120 x DL), and the pulse duration 20 ns. The central part of the output uniformly illuminates an aperture of diameter 8 mm. The image of this aperture is relayed by a series of lenses to the temporal encoding optics of the multiplexer. An iris placed at the far field of one of the imaging lenses provides a limiting aperture to control the field angle of the system. For simplicity, only four of the eight beam lines of the multiplexer are used. The beam expanding optics of the 8 cm e-beam amplifier Goblin relay the image as far as the final amplifier Sprite. Both modules are operated as double pass amplifiers. Provided that the spreading of the coherence zones due to diffraction is small compared to the apertures from the final amplifiers onwards, further image relaying beyond this point is not essential.[1] The four 8 cm diameter output beams are demultiplexed and then reflected from a closely spaced plane mirror array onto a large diameter concave mirror of focal length 8.5 m. An NO_2 cell provides variable attenuation allowing the beams to be focussed directly onto the UV sensitive CCD chip. The four beams focus to a single point where the camera and framestore system record and analyse the beam profiles.

Figure 2 shows 3D intensity plots of the four beams overlaid at the output image plane. 2(a) shows the profile produced by a coherent beam of bandwidth 2 cm^{-1} and divergence 100 mrad at the output (32 x DL). 2(b) and (c) show the profiles of the image relayed, partially coherent beams, and demonstrate the

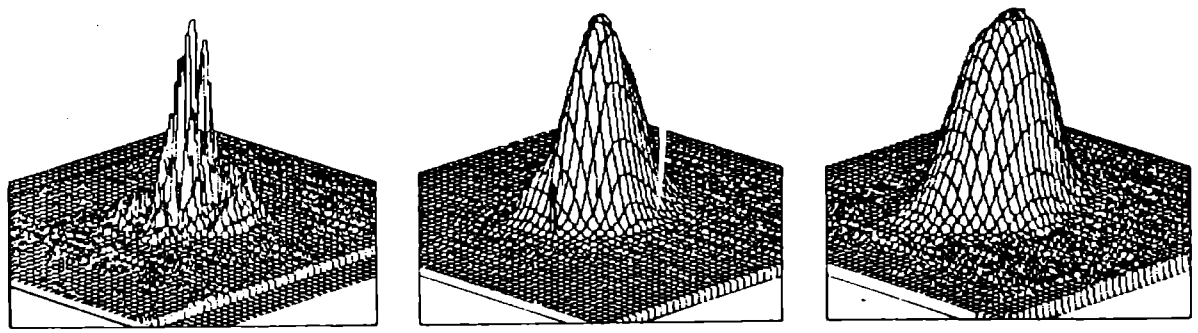

Figure 2: Intensity profiles of four multiplexed, overlaid beams. (a) narrow band coherent beams, (b) broad band incoherent beams (60 x DL), and (c) broad band incoherent beams (100 x DL).

effect of increasing the field angle of the system from 200 mrad (60 x DL) to about 330 mrad (100 x DL).

There is clearly a dramatic improvement in the profile uniformity at the target plane for the incoherent beams, and increasing the field angle produces a smoother profile at the expense of reducing the brightness. The profiles are not perfect reproductions of the input aperture because the image is not relayed through the final amplifier. To do this would require separate relaying lenses in each beam line, since the beam paths in the multiplexer and demultiplexer sections have different lengths.

In order to investigate the effect of amplification on the uniformity of the output profiles, further image relaying lenses were introduced into a single beam line. With the new set-up, an image of the input aperture was relayed through both Goblin and Sprite to a plane close to the focal plane of the output mirror. A single 20 ns pulse was amplified to an energy of 150 mJ in Goblin and to 30 J in Sprite. To ensure a smooth profile on target after amplification, it is important not to image the front-end aperture into either of the amplifiers. This would cause any non-uniformities in the e-beam pumping (and hence in the gain) to be imprinted onto the beam profile at the target. In the Sprite amplifier the pumping non-uniformity has been measured to be ±15% with a scalelength of about 10 cm. If the output is not strongly saturated (as was the case in this experiment) then the output beam uniformity will be considerably worse than the pumping uniformity, due to the exponential gain factor.

Figure 3 shows the profiles of the images recorded at the final image plane of the input aperture. In this case the camera was placed at the final image plane of the input aperture, rather than at the best focus of the output mirror. The area of these images is therefore greater than those shown in figure 2 for the four beam experiment. Amplification of the pulse in both the amplifiers introduced some distortion of the output profile on high energy shots, possibly due to non-uniform pumping of the final amplifier (Fig 3(c)). There was no discernible deterioration of the uniformity when the pulses were amplified using only the 8 cm amplifier (Fig 3(b)).

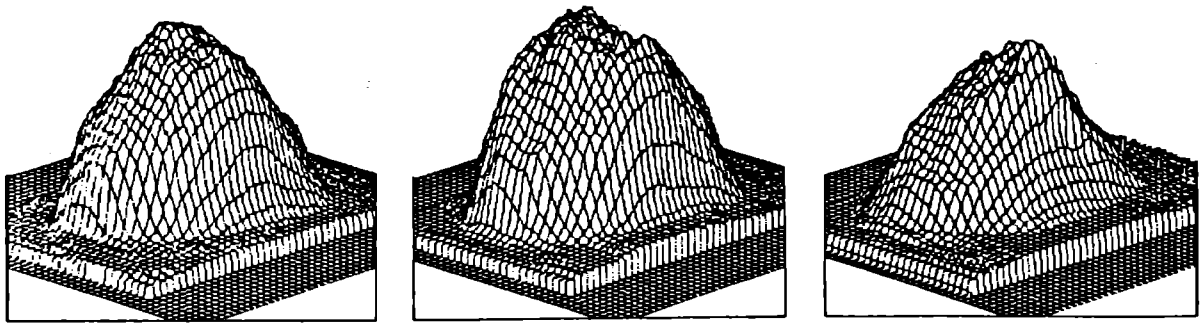

Figure 3: Single beam intensity profiles at the final image plane of the input aperture, (a) with no amplification (b) amplified in Goblin, and (c) amplified in both Goblin and Sprite.

References

1. R.H.Lehmberg and J.Goldhar, "Use of incoherence to produce smooth and controllable irradiation profiles with KrF fusion lasers," *Fusion Technology*, **2**, (1987) 532.

2. R.H.Lehmberg and S.P.Obenschain, "Use of induced spatial incoherence for uniform illumination of laser fusion targets," *Optics communications*, **46**, (1983) 27.

3. N.A.Kurnit and S.J.Thomas, "Advanced front-end development," *Inertial Confinement Fusion at Los Alamos*, **1**, (1989) VII E.

GAIN AND SATURATION MEASUREMENTS IN THE SPRITE AMPLIFIER

E C Harvey, C J Hooker, M H Key, A K Kidd, J M D Lister, M J Shaw
and W Leland[1]

Rutherford Appleton Laboratory
[1]Los Alamos National Laboratory, USA

INTRODUCTION

The combination of high gain and large aperture (27cm, with a pumped length of 100cm) which characterise the Sprite amplifier leads to high fluxes of amplified spontaneous emission (ASE) in the laser medium. The effect of ASE is to depump the laser amplifier, resulting in lower gain than would be generated by the applied pump rate in the absence of ASE.

EXPERIMENTAL DETAILS

The measurements described here were made using the full SPRITE laser system with two KrF preamplifiers, shown schematically in Fig.1. The pulses were of duration 6 ps and 40 ps, and were generated by a sync-pumped dye oscillator operating at 746 nm employing a linear external feedback cavity which results in transform-limited pulses[1]. The pulses were frequency tripled to 248 nm, spatially filtered to the diffraction limit and amplified to an energy of a few mJ in an EMG103 discharge excited amplifier. The pulses were carried on beams which were angularly multiplexed through first the Goblin and second the Sprite electron beam pumped amplifiers.

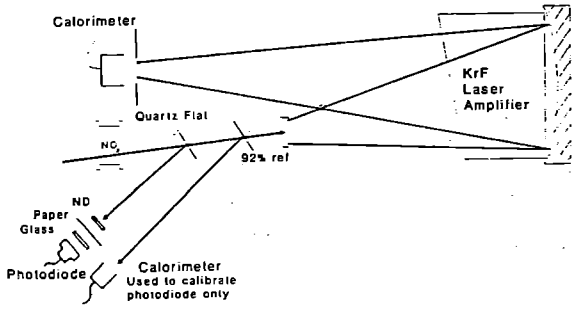

Fig.1. Experimental set-up for the measurement of the amplifier input/output characteristic.

Gain saturation in Sprite was measured by adjusting the attenuation of the preamplified beam with a combination of a cell filled to a variable pressure of NO_2 and calibrated normal incidence beam splitting mirrors.

The gas mix used in Sprite in these experiments was 2 / 38 /100 / 680 Torr of F_2 / He / Kr / Ar. The static absorption of the laser mix, mainly due to fluorine absorption, was measured to be 0.11 % cm^{-1} for this mix. The specific pump power into the amplifier was measured by recording the pressure jump in the laser cell due to the pumping electron beam.

The small signal absorption coefficient associated with the excited laser mix was measured at 268 nm. A 12 ps pulse of 268 nm light in a beam with a diameter of 20 mm and energy 20 μJ was double passed through the Sprite amplifier. A quartz wedge was used to split some of the light from the inward beam onto a vacuum photodiode fitted with a 268 nm interference filter. The collimated probe beam was reflected by a normal incidence, high reflectance, planar mirror back through the amplifier and onto the same photodiode as the initial split. The long path length separated the two pulses in time by about 100 ns and enabled a simple calculation of the absorption of the beam during the pumping of the KrF gas mix by measuring the two pulse heights on a single oscilloscope trace.

The uniformity of gain and ASE in the laser cell was investigated by imaging light from the amplifier with a CCD camera and gated framestore. The camera was placed 13 m from the front window, 0.5° from the laser axis. The majority of the visible radiation emitted is the result of Kr_2F^* emission[2], and since its precursor is KrF^*, it can be taken as indicative of the pump energy deposition. Fig. 2a shows a 3-D plot of the visible emission. The four gain peaks are adjacent to the four electron beams. The periphery between the beams is significantly underpumped compared to the rest of the aperture, however the variation from the average is within ± 15 % over the extracted aperture.

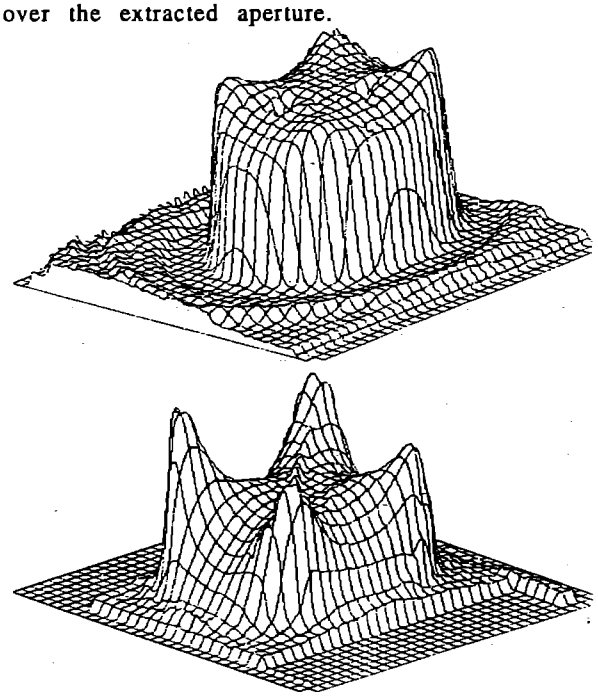

Fig.2. 3-D profile of the on-axis image of (a) visible fluorescence and (b) the on-axis image of ASE at 248 nm emitted by the Sprite laser amplifier. Electron beam voltage = 450 kV.

The 248 nm amplified spontaneous emission image is shown in Fig.2b. The ASE image is related to the fluorescence image by the double pass gain in the system. The peak-to-average in the ASE image is approximately 4.5 : 1. The same ratio is deduced from the 15% gain variation if 2gL=10 implying a gain coefficient of 5% cm^{-1}.

RESULTS

Fig. 3 shows the results of the gain measurements. The bulk of the data was taken at a Marx generator charging voltage of 65 kV which gave a deposition rate of 0.58 MW cm^{-3} into the gas. To investigate the effects of pulse length on saturation, two full gain characteristics were obtained for pulses of 6 and 40 ps duration. The gain in the small signal region is the same (within experimental error) for both pulse durations. In the saturated region however, the longer pulse data points lie above the shorter by about 10-15%. This observation is consistent with the higher effective saturation energy for the long pulse due to gain repumping of the B state from the C state. The measurement of Szatmári and Schäfer[3] of a 25% gain recovery with a time constant of 57 ps would imply a 14% larger effective saturation energy for the 40 ps pulse compared to the 6 ps pulse.

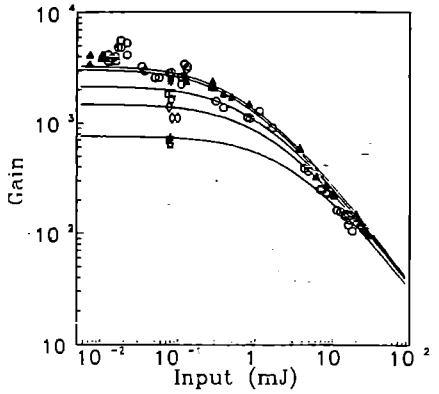

Fig. 3. Gain saturation curve for the Sprite laser amplifier at various pump rates. Full triangles are for a pulse duration of 40 ps. All other points are for a pulse duration of 6 ps.

Other data points shown in Fig. 3 are for a pulse duration of 6 ps and a fixed input energy of approximately 100 μJ and varying pump rate (obtained by varying the Marx generator charging voltage). These data points were taken at a pulse duration of 6 ps. To obtain the small signal gain coefficient for the various pump rates, the data were analysed using a simple rate equation model with a non-saturable loss term included[4]. The pulse fluence obeys the equation:

$$\frac{dE}{dz} = g_{ss} E_{sat}(1 - e^{E/E_s}) - \alpha E \qquad (1)$$

where E_{sat} is the saturation fluence, g_{ss} the small signal gain coefficient and α the non saturable loss coefficient both in the presence of ASE depumping.

The pump rate dependent small signal loss coefficients measured at 268nm were added to the static loss coefficient measured at 248nm to yield a total loss coefficient. The resulting values were taken as representative of the non saturable loss coefficients at 248nm.

With the value of α at the different pump rates so obtained, Eqn. 1 is fitted to the extended data points in Fig. 4 to yield values for small signal gain coefficient and saturation fluence. The 40 ps data is best fitted with a saturation fluence of 2.0 ± 0.2 mJ cm^{-2} and the 6 ps data with 1.8 ± 0.2 mJ cm^{-2}. These values are in reasonable agreement with previous measurements of saturation fluence (see, for example, Ref.5). Finally, the 6 ps saturation fluence is used together with the gain obtained at 100 μJ input and various pump rates to give the small signal gain coefficient, g_{ss} as a function of specific pump power.

The results are given in Table I and plotted in Fig. 4. The gain coefficient and the loss coefficient both increase with pump rate but α increases more rapidly leading to a fall in the gain-to-loss ratio g_{ss}/α with increasing pump rate.

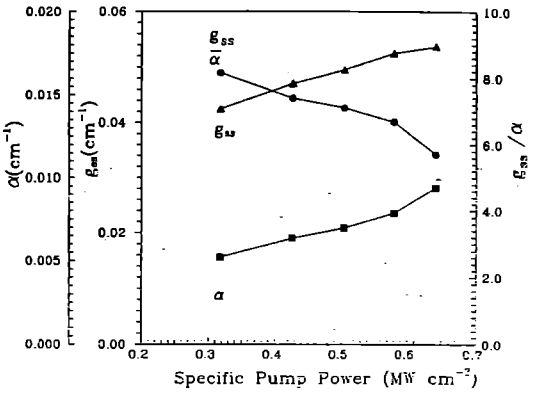

Fig. 4. Measured small signal gain and loss coefficients and gain-to-loss ratio as a function of specific pump power.

The small signal gain coefficient in the absence of ASE depumping, g_0 is a function of pump rate and gas composition and is estimated by $g_0 = \epsilon W/I_{sat}$ where ϵ is the fluorescence (or formation) efficiency and I_{sat} the saturation intensity which can be estimated from a knowledge of the quenched lifetime of the laser level[6]. A simple numerical expression, consistent with observations, is used for I_{sat}[7]. Values so obtained are given in Table I. It can be seen that g_0 is substantially greater than the measured g_{ss} and the difference increases as the pump rate increases.

The absorption coefficient is also affected by ASE since part of it is saturable. If we assume that the saturable part has the same saturation intensity as the gain coefficient then the absorption coefficient may be written as:

$$\alpha = \frac{\alpha_s}{(1 + I_{ASE}/I_{sat})} + \alpha_{ns} \qquad (2)$$

where α_s is the saturable part of the coefficient and α_{ns} is the non saturable part. The latter is taken to be made up of two parts: $\alpha_{ns} = \alpha_d + \alpha(F_2)$ where α_d is the dynamic (pump rate dependent) part and $\alpha(F_2)$ is the part due to fluorine absorption. Using this constraint and the fact that the saturable absorption saturates in the same way as gain, then the total absorption coefficient may be usefully approximated by the following expression:

$$\alpha = \frac{g_{ss}}{35} + \frac{g_0}{15} + \alpha(F_2) \qquad (3)$$

The small-signal absorption coefficient, α_0 derived from this expression (with $g_{ss} = g_0$) is given in Table I as is the CW saturation parameter $(g_0 - \alpha_0)/\alpha_{ns}$. As the pump rate increases, this parameter increases slightly in marked contrast to the decrease in the measured value of g_{ss}/α. Thus the CW performance would be enhanced by high pumping rates whilst the single pulse performance gets worse.

THEORY

Two codes are used here to model the experimental data. The first is a three-dimensional steady-state code developed at Los Alamos[8]. Briefly, an iterative algorithm is used which considers ASE photon transport throughout the active medium either by direct paths or by diffuse reflection from the side walls. For two-pass energy extraction, specular reflection in the end mirror is also included. The code does not include stimulated emission caused by ASE photons. Side wall reflection is included by specifying the fraction of all incident photons returned to the medium. The angular distribution of returned photons is assumed to follow a Lambertian cosine law.

The second code is a time-dependent one-dimensional model developed at RAL, described in detail elsewhere[9]. The code is designed to handle the case where one or more short pulses are present in the laser amplifier in addition to ASE. A source term for ASE is $Ad\Omega = (\tau_u/\tau_{sp})(\Delta\nu_a/\Delta\nu_s)(d\Omega/4\pi)$, which is that fraction of the inversion density which spontaneously emits photons into the right bandwidth and solid angle to be amplified by the rest of the system. The ratio of the upper level to the radiative lifetime, τ_u/τ_{sp}, is estimated from a simple kinetics code[7] and is given in Table I for the experimental conditions used above.

RESULTS OF SIMULATIONS

The 3-D code takes the wall reflectivity of Sprite to be 0.2 in agreement with near normal incidence measurements on the actual etched titanium foil used in the Sprite amplifier[10]. The 1-D code takes no account of wall reflections. The finite mirror reflectivity and other intra-amplifier losses are taken account of in both codes.

Fig. 5 shows results from the codes used to predict the effect of ASE depumping on the residual net small-signal gain, $(g_{ss}-\alpha)$, as a function of pumped small-signal gain, g_o, for the Sprite amplifier. Also shown in Fig. 5 are the experimentally determined values of $(g_{ss}-\alpha)$ versus g_o obtained from the pressure jump measurements.

Table I. Measured and Predicted Gain and Loss Coefficients

F_2 : He : Kr : Ar

2 : 38 : 100 : 680 Torr

W (MW/cm^3)	g_0 (%/cm) calc.	I_{sat} (MW/cm^2) calc.	τ_u/τ_{sp} calc.	g_{ss} (%/cm) expt.	α (%/cm) expt.	α_0 (%/cm) calc.	$\frac{(g_0 - \alpha_0)}{\alpha_{ns}}$ (%/cm) calc.
0.32	4.95	1.24	0.37	4.25	0.521	0.58	9.9
0.43	6.08	1.36	0.34	4.70	0.636	0.69	10.5
0.50	6.70	1.43	0.32	4.95	0.697	0.75	10.6
0.58	7.34	1.52	0.30	5.25	0.785	0.81	10.9
0.64	7.77	1.58	0.29	5.37	0.941	0.85	11.0

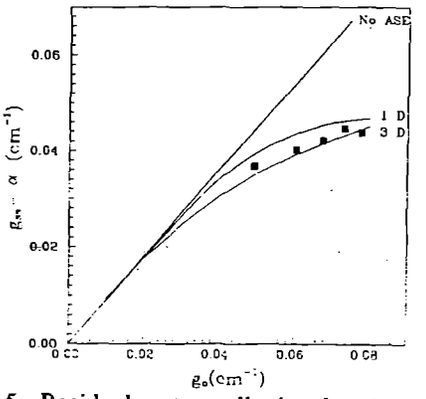

Fig. 5. Residual net small signal gain coefficient, $g_{ss} - \alpha$ as a function of the pumped small signal gain coefficient, g_0. The straight line gives the no ASE case and the two curves give the results of the 1-D and 3-D codes. Experimental points are shown as solid squares.

This figure demonstrates good agreement between experiment and the results of the three-dimensional simulation - the error in estimating (g_{ss}-α) is within 3% at all values of pumped small-signal gain, g_0. The one-dimensional ASE code underestimates the effect of ASE depumping on amplifier gain, but agrees to within 5% with the measured values. The small discrepancy may be explained by the fact that the code takes no account of wall-directed ASE nor of reflections from the walls. Excellent agreement between experiment and code can be obtained by arbitarily increasing the value of $Ad\Omega$ which increases the amount of ASE in the amplifier.

REFERENCES

[1] C. J. Hooker, J. M. D. Lister and I. N. Ross, Optics Comm., **80**, 375 (1991).

[2] H. H. Nakano, R. M. Hill, D. C. Lorents, D. L. Huestis and M. V. McCusker "New electronic-transition laser systems Part I: Electron pumped systems" Stanford Research Institute Technical Report SRI Nº MP 76-99, (1976) unpublished.

[3] S. Szatmári and F. P. Schäfer, J. Opt. Soc. Am. B, **4**, 1943 (1987).

[4] P. W. Milonni, R. B. Gibson and A. J. Taylor, J. Opt. Soc. Am. B, **5**, 1360 (1988).

[5] A. Endoh, M. Watanabe and S. Watanabe, Optics Lett., **12**, 906 (1987).

[6] M. J. Shaw, Appl. Phys. B, **30**, 5 (1983).

[7] E. C. Harvey and M.J.Shaw, Laser and Part. Beams, to be published (1991).

[8] W. T. Leland, in "Inertial Confinement Fusion at Los Alamos", Report No. LA-UR-89-2675 Vol II, (1989), unpublished.

[9] C. J. Hooker, I. N. Ross and M. J. Shaw, "Modelling multiple pulse amplification in KrF lasers", Rutherford Appleton Laboratory Report No. RAL-87-041, 226 (1987).

[10] R Gohri and E. C. Harvey, Annual Report to Laser Facility Committee (1991) unpublished.

Multiple-Pulse Extraction of Sprite

C J Hooker, E C Harvey*, A K Kidd, J M D Lister and M J Shaw

Rutherford Appleton Laboratory
*Exitech Ltd.

As a preliminary to operating the final Raman amplifier of the Sprite system, RA3, with multiplexed extraction beams, a series of experiments was performed to investigate the efficiency of multiple-pulse extraction of Goblin and Sprite. The Raman multiplexing scheme requires a train of four pulses to be propagated along each of the eight beam lines through the KrF amplifier chain, giving 32 pulses in total. The pulse trains will then be demultiplexed to give four groups of pump pulses, each of which will amplify one Stokes pulse.

The pulse train was generated in the oscillator prior to the first KrF amplifier, using the optical arrangement shown in Figure 1. This has the advantage of producing four equal pulses containing 40% of the input energy, but there is a "tail" to the pulse train of up to five more pulses, which proved to be a problem. By careful timing of the discharge amplifier the trailing pulses could be partly suppressed, but they were still present at a substantial level. After its formation, the pulse train followed the normal path through the EMG 103 and the two electron-beam amplifiers.

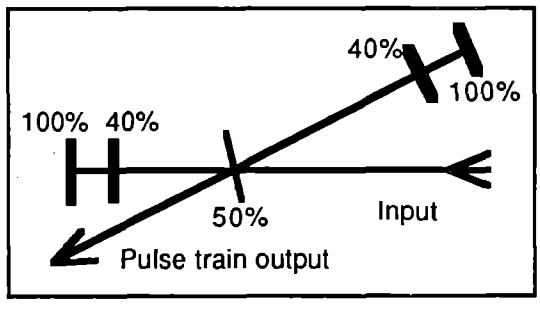

Figure 1. Schematic of the pulse train generator.

The beam sent to the Raman generator is split off at a point after the EMG 103, so in consequence a train of Stokes pulses was generated where a single pulse was required. The train of pump pulses to RA0 was therefore advanced by 3ns so that the leading Stokes pulse was amplified by the last of the four principal KrF pulses. The later Stokes pulses were still amplified by the trailing pulses in the KrF train, and to overcome this the time intervals between the KrF pulses were adjusted by a few tens of picoseconds so that only the leading Stokes pulse was correctly timed in RA0. The result, as required, was a single amplified Stokes pulse.

The one further change made to the system was to decrease the multiplexing interval through Sprite and Goblin from 5ns to 4ns. The effect of this was to position the first pulse of the train on one beam about 200ps before the unwanted fifth pulse of the preceeding pulse train. In Sprite, which was fairly heavily saturated, the trailing pulses were suppressed since they saw reduced gain. The shortening of the total pulse train through Sprite also reduced the likelihood of the first or last pulses being lost due to trigger jitter.

During the run, outputs of up to 34 Joules were obtained, measured as energy available to pump the Raman amplifiers. This compares with 10 to 10.5 Joules normally obtained with single pulses. Although a factor of four increase might have been expected, in practice the decrease of the multiplexing interval led to the total extraction time from Sprite being reduced from 42 to 35ns (overall length of the pulse sequence plus the round-trip time through the Sprite cell), a factor of 0.83. A more realistic value for the expected energy with multiple pulses is thus 42 x 0.83 = 35 Joules, which is almost exactly what was observed. The slight loss of available energy is offset by the increased reproducibility of output in the presence of jitter in Sprite timing.

TITANIUM SAPPHIRE (TiS) AMPLIFIERS

M Amit+, J M D Lister, I N Ross
Rutherford Appleton Laboratory
+On Sabbatical from Laser Department, Nuclear Research, Negev, Beer-Sheva, Israel

The high saturation fluence high efficiency, high damage threshold, low ASE level and low nonlinear refractive index of TiS make it an efficient amplifier for short pulses of wavelength between 700 and 900 nm. It is attractive to use such an amplifier to generate higher energy at 746 nm in the SPRITE oscillator and hence boost the high contrast 249 nm pulse injected into the KrF amplifier chain where it is important to minimise the small signal gain of the chain.

The proposed scheme for including a TiS amplifier in the SPRITE front end is shown in figure 1. The TiS rod is end-pumped at 532 nm from a double Q-switched Nd:YAG laser. Single pass gain measurements were carried out giving the measured gain curve shown in figure 2. As can be seen these measurements are in agreement with calculation based on published properties of TiS. Using this performance data together with nonlinear index data and efficiency data for third harmonic generation and assuming an input from the dye amplifiers of 200 μJ and a 532 nm pump energy of 300 mJ, the expected performance of the scheme in figure 1 is shown in figure 3. The three regions of the graph correspond to long pulse (gain limited), intermediate pulse (THG efficiency limited) and short pulse (power and THG efficiency limited. Thus we can expect at say 10 ps, a 249 nm energy of about 5 mJ which is over two orders of magnitude higher than is obtainable with the dye amplifiers alone and can eliminate the need for one or even both passes of the first excimer amplifier.

The limit to the performance of a TiS amplifier for long pulses, and used as above with little saturation, is the gain. The rod gain α exp (pump fluence) and is limited by the need to stay well below the damage threshold. The gain has been taken to be limited to about 10 in single pass and damage threshold was reached at a gain of about 40.

The short pulse limit of the TiS determined by self-focusing depends upon the gain and gives, in this example, a maximum intensity of about 100 GW/cm^2. At the third harmonic the efficiency of conversion is reduced for short pulses due to dispersion and nonlinear effects in the harmonic crystals.

For future developments the TiS system is scaleable to higher energy using larger aperture crystals and higher pump energies. With current technology we can predict 249 nm pulses with power as high as 50 GW and energies as high as 0.5 J at 10 ps.

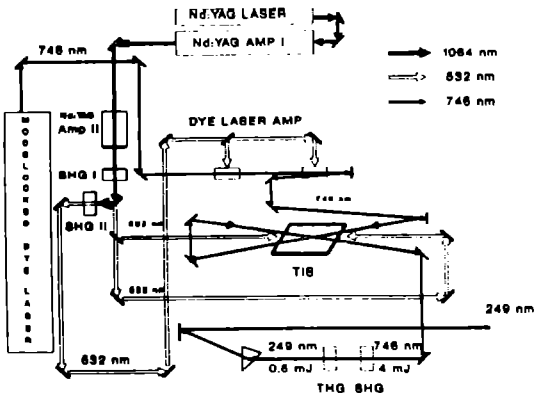

Fig 1 SPRITE front end

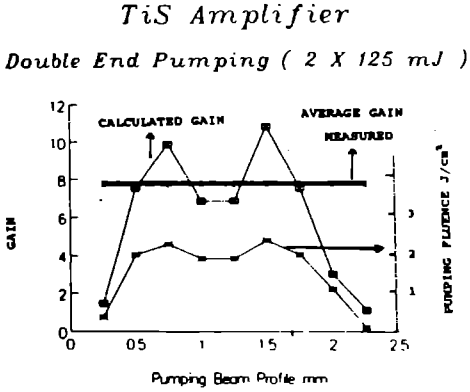

Fig 2 746 nm single pass calculation and measurement gain.

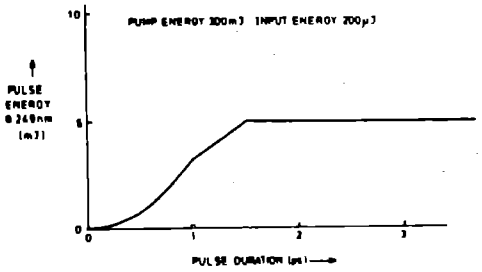

Fig 3 Predicted performance of Titanium Sapphire short pulse amplifier.

SUPERSPRITE SYSTEM DESIGN

B W H Edwards, P Hatton, C J Hooker, M H Key, A K Kidd,
I N Ross and M J Shaw

Rutherford Appleton Laboratory

INTRODUCTION

SERC has decided for the time being, for financial reasons, to suspend its involvement in the ELF initiative and to focus attention instead on the design of a KrF laser system capable of considerably enhancing the high power laser performance at the CLF. The recommendations made in the 1988 Challis Report in favour of KrF development still apply, particularly since reliable operation at ultra high brightness has now been demonstrated from the Sprite system. Consequently, the current design study has the objective of producing a fully costed, site specific design for a new KrF laser system. Some of the initial considerations in this study are outlined here. It is expected that the work will be complete by the Autumn of '91.

OVERALL DESIGN PHILOSOPHY

The possible funding scenario is such that cost minimisation will be very important. To this end, the design should use of existing components, in particular the Supersprite amplifier module being developed in R7 should be the final KrF amplifier. Also, the use of existing buildings will be necessary to house the new laser to avoid major building costs.

The cost implications of the laser architecture are an initial consideration. For the ELF design, a hybrid architecture, employing direct illumination using broad-band echelon-free ISI beams as well as Raman combined beams was proposed [1]. The scheme required a large number of beams (50-100) and was well suited to a laser of 100 kJ class with pulse durations of a few ns required for spherical compression at this energy. It is not however consistent with ~ kJ energy and a relatively modest number of beams. Thus it is proposed that the new design be based on Raman beam combining alone. The sort of performance which might be expected given the choice of final KrF amplifier is as follows:

Supersprite system specifications

Wavelength	268 nm
Energy on target (1ns)	> 1 kJ
Power on target (10 ps)	> 50 TW
Beam brightness	> 10^{19} W cm^{-2} sterad^{-1}
Laser bandwidth	transform limited
Target chambers	12 beam compression
	8/16 beam high power

The energy is comparable to the existing green "on target" energy from Vulcan but is significantly larger than that which could be achieved at 0.25 μm. The power and brightness specifications, however exceed that available from Vulcan by more than an order of magnitude.

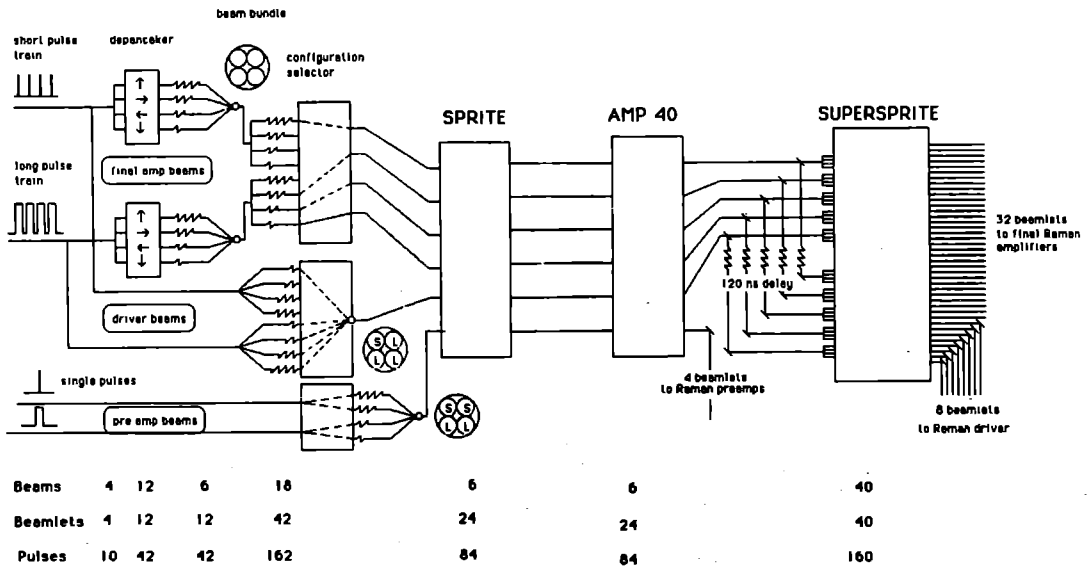

Fig. 1 Possible KrF staging for the Supersprite laser system.

SYSTEM ARCHITECTURE

The laser architecture being considered is based on the Sprite KrF-pumped Raman laser system. Figure 1 shows a KrF chain at present under study. Amplifier staging considerations [2] have shown that it should be possible to use just three e-beam pumped KrF amplifiers. These would be the Supersprite module, the existing Sprite module with an increased run time and a new module called here AMP 40 based on the successful Ashura module from ETL [3]. The specifications of these amplifiers are as follows:

KrF module parameters.

	SPRITE	AMP 40	SUPERSPRITE
Aperture	270 mm	400 mm	600 mm
Runtime	130 ns	130 ns	240 ns
Energy*	50 J	500 J	4000 J
Pulses	84	84	160

* Maximum output energy at the module, 1.5 ns pulse.

The beam bundling arrangement at the front of the KrF amplifiers allows the selection of a number of different configurations of long or short pulses. Each beamlet carries a 4-pulse train with a pulse spacing of 1.5 ns. The beamlets are bundled 4 at a time into 6 "beams" which are image relayed through the first two amplifiers. The beamlets are arranged to overlap in space and fill the amplifiers when they pass through them. Before the final amplifier the beams are separated to give a total of 40 beamlets, 32 of which are used to pump the final Raman amplifier and the remaining 8 to pump the driver amplifier.

The Raman amplifier chain is shown in Figure 2. It consists of two similar chains of Raman amplifiers, for long pulses and short pulses. The final four amplifiers are common to the system. The driver and final amplifiers are 4-fold-multiplexed giving a maximum of 16 beams to target. With this system the following arrangements of beams to target would be available.

Long (L) and short (S) pulses available to target.

TA1	TA2
16 L	-
12 L, 4 S	-
12 L	4 S
8 L	8 S
4 L	12 S
-	16 S

The long pulses would be in the range 300 ps - 1.5 ns. The short pulses in the range of 5 ps - 300 ps. Twelve beam compression with high power backlighting beams is thus catered for. Where shown, simultaneous operation of the supposed two target areas would be possible with the energy or power rating being proportional to the number of beams to that target area.

SITING

A number of possible sites for the Supersprite system have been considered. The present Vulcan and Sprite areas are too small and would make the changeover period considerably longer than a new site. Two new "greenfield" sites have been looked at viz. R40 and R12. R40 has adequate area for the laser but would require additional buildings to accommodate offices/support labs since it is far from the main office areas. R12, on the other hand, looks well suited for the new laser system. It is not too far from present areas, has adequate space and support labs/offices and has the potential to be further developed in the future if need be.

REFERENCES

(1) Report of the Scientific and Technical working group on the European High Performance Laser Facility. Feb. 1990 (unpublished).

(2) A Kidd and M H Key "Supersprite KrF amplifier staging", this report.

(3) Y Owadano et al Laser and Particle beams 7, 383, (1989).

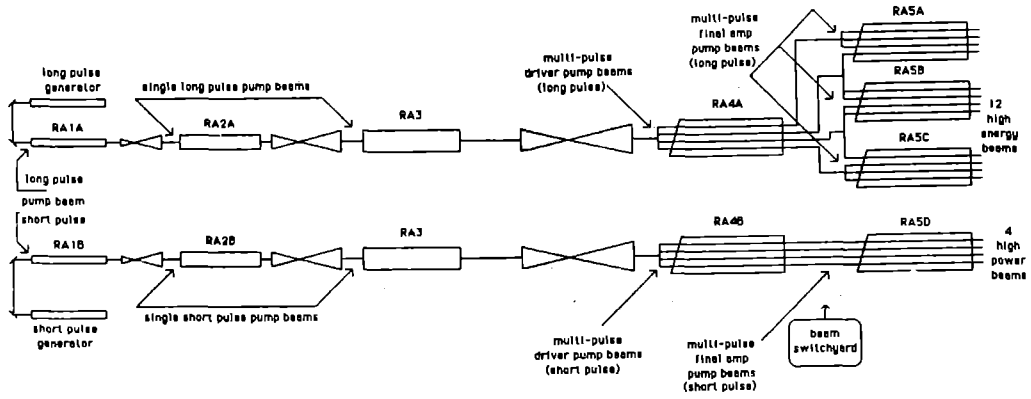

Fig. 2 Possible Raman amplifier staging for the Supersprite laser system.

Supersprite Gain Staging Analysis

A. K. Kidd and M. H. Key

Rutherford Appleton Laboratory

INTRODUCTION

Design studies for Supersprite have been made using a KrF extraction code [1,2]. The variation of amplifier efficiency, gain and output intensity with pulse length and spacing has been investigated.

CW AND SHORT PULSE EXTRACTION EFFICIENCY

A train of pulses is input to the extraction code. The extraction efficiency, η, is defined as

$$\eta = \frac{E_{out} - E_{in}}{\left(\frac{t}{\tau}\right) g_o L} \qquad (1)$$

where t is the pulse spacing. Figure 1 shows the extraction efficiency vs. output fluence for the Sprite amplifier for a pulse spacing of 1.5 nsec ($\equiv 0.75\tau_{upper}$). The three curves correspond to pulse lengths of 20 psec ($\equiv 0.01\tau_{upper}$), 0.75 nsec ($\equiv 0.50\tau_{upper}$) and 1.5 nsec ($\equiv 1.0\tau_{upper}$; ie the CW limit). Each point on the curves corresponds to a successive doubling of input energy per pulse, commencing at $0.001E_{sat}$.

Figure 1 is indicative of the behaviour of extraction efficiency vs. pulse length vs. pulse separation and implies that a drop in η_{opt} of only 5% from the CW limit is experienced by short (20 psec) pulses at this pulse spacing. For 0.75 nsec pulses (Figure 1), the difference is only 2%. In both cases, this corresponds to an input energy per pulse of $0.25E_{sat}$.

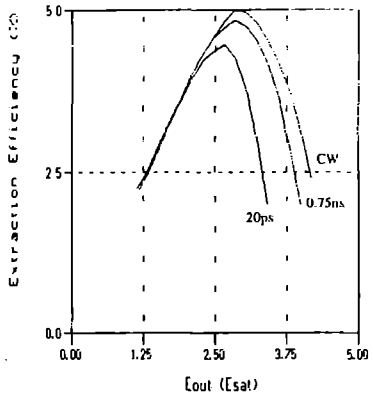

Figure 1: Extraction efficiency as a function of input intensity for the cases of:
a. pulse length 20 psec,
b. pulse length 0.75 nsec
and c. CW limit
for a pulse separation of $\Delta t_p = 0.75\tau$ (1.5 nsec).

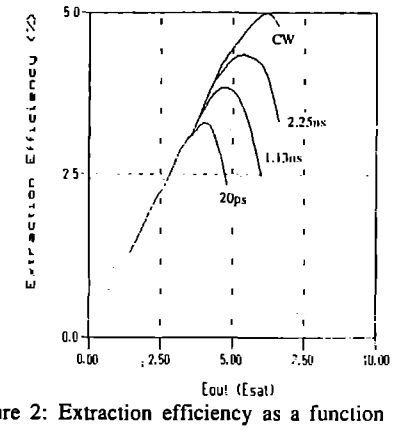

Figure 2: Extraction efficiency as a function of input intensity for the cases of:
a. pulse length 20 psec,
b. pulse length 1.13 nsec
c. pulse length 2.25 nsec
and d. CW limit
for a pulse separation of $\Delta t_p = 1.50\tau$ (3.0 nsec).

Figure 1 also suggests that for short pulse amplification, the drop in extraction efficiency from the CW limit for a pulse interval of $0.75\tau_{upper}$ is small enough to allow a greater spacing. Figure 2 shows the corresponding extraction efficiency vs. output fluence for the Sprite amplifier for a pulse spacing of 3.0 nsec ($\equiv 1.50\tau_{upper}$). The four curves correspond to pulse lengths of 20 psec ($\equiv 0.01\tau_{upper}$), 0.75 nsec ($\equiv 0.38\tau_{upper}$), 1.5 nsec ($\equiv 0.75\tau_{upper}$) and 3.0 nsec ($\equiv 1.5\tau_{upper}$; CW). Again, η_{opt} is 50%, but now the 20 psec pulse suffers a drop to 33%.

The optimum CW efficiency is given analytically by [3]:

$$\eta_{opt} = 1 - 2\left[\frac{\alpha}{g_o}\right]^{0.5} + \left[\frac{\alpha}{g_o}\right] \qquad (2)$$

where $\left[\frac{g_o}{\alpha}\right]$ is the amplifier gain-to-loss ratio. For Sprite, this is measured [1] to be 9.1. Hence, the optimum CW extraction efficiency, η_{opt}, should be 44.7%. From Figure 1, η_{opt} is calculated numerically to be 50%. The reason for this discrepancy is believed to be the fact that the gain oscillates when the amplifier turns on. This problem can be avoided by considering an increased number of input pulses and ensuring that the pulse train length exceeds a few round-trip cavity times ($\tau_{cavity} \approx 1.65$nsec).

SUPERSPRITE GAIN STAGING

A chain of three e-beam pumped KrF* amplifiers is being considered for Supersprite [4]. These are:

	Amplifier	Description
(1)	**Sprite**	The present 27cm amplifier.
(2)	**Amp2**	Based on the Ashura output amplifier module at ETL, with a slightly larger aperture (35 cm in this example).
(3)	**SuperSprite**	The final amplifier has a 60 cm aperture.

The saturation intensity in each amplifier is calculated for a specific gas mix [5]. The typical gas mix in Sprite is 40/100/^800 (F_2(5% in He)/Kr/^Ar), resulting in a value of I_{sat} of 1.53 $MWcm^{-2}$ and an upper state lifetime of 2.0 nsec. For the Ashura amplifier at ETL, the gas mix is 90/165/1100, implying a value of I_{sat} of 2.34 $MWcm^{-2}$ [6] whilst it is proposed to run Supersprite with a krypton-rich mix (nominal gas mix 100/180/^1200) at 2.7 $MWcm^{-2}$. For both of these amplifiers, the upper state lifetime τ_{upper} is 1.0 nsec.

The performance of the chain of amplifiers has been analysed for a 1 nsec pulse spacing for four pulse lengths:

(1) 10 psec,
(2) 100 psec,
(3) 300 psec
and (4) 1 nsec (≡ CW).

Account is taken of fluorine absorption losses in the unpumped regions of each amplifier, optical losses both within the amplifiers and due to the interstage coupling losses and non-linear (two photon absorption) losses.

Figures 3a and 3b show the CW and short pulse saturation behaviour of the Sprite amplifier and the Amp2 and Supersprite amplifiers, respectively. These design curves relate pulsed and CW gain and output intensity and ASE gain as a function of input intensity. Again, ten or twenty pulses of equal magnitude are input to the code, and the simulation repeated with increasing pulse energy. The pulse length is 10 psec and the pulse interval is 1 nsec, corresponding to $0.5\tau_{upper}$ for Sprite and $1.0\tau_{upper}$ for Amp2 and Supersprite. Figure 3a reveals that both the gain and output intensity are indistinguishable for CW and pulsed operation of Sprite. However, for the remaining two amplifiers, the output intensity of the short pulse deviates from the CW limit in the large signal gain region (Figure 3b). Also shown in Figure 3 is the gain experienced by the ASE immediately prior to the passage of the saturating pulse.

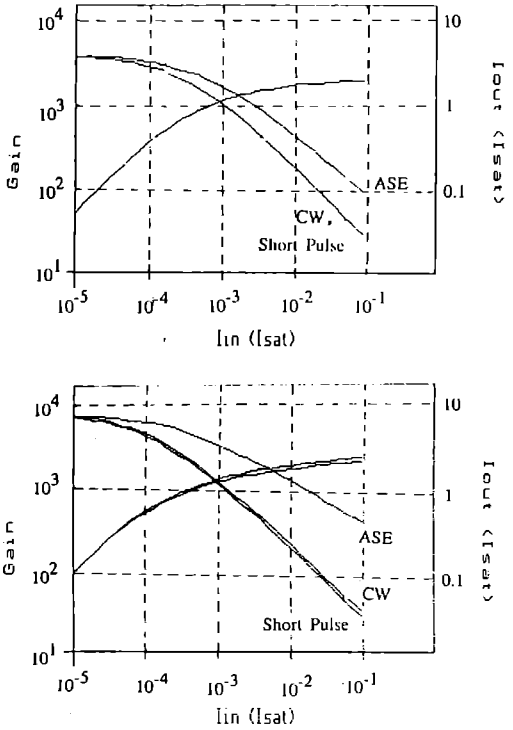

Figure 3. CW and short pulse saturation in:
(a) the Sprite amplifier
and (b) the Amp2 and Supersprite amplifiers
for a 1 nsec pulse spacing. Also shown is the ASE gain.

An example of a staging calculation is as follows. The driver is either the EMG103 or the KrF system may be directly driven by a Ti:Sapphire source, The input to the chain consists of four pulses in one beam. The total energy in the four pulses is 10mJ and the pulse spacing is 1 nanosecond. This beam is 12-way multiplexed prior to amplification in Sprite (48 pulses in 12 beams). A further 2-way multiplex is applied before both Amp2 (96 pulses in 24 beams) and Supersprite (192 pulses in 48 beams).

The aperture of Sprite is 27cm whilst the specified aperture of Supersprite is 60cm. The aperture of the intermediate Amp2 driver is taken to be 35cm. The ratio of these apertures, ie 1/1.3/2.2, is used to scale all relevant parameters in the Supersprite system. For example, the thickness of the Supersprite beam pipe output lens is 2.2 times that of Sprite, while its area is increased by a factor of $(2.2)^2$. All amplifier windows are assumed to be fused silica (TPA coefficient, β = 0.07) and all beam pipe lenses are calcium fluoride (β = 0.008). In addition to this scaling factor, the increased gas pressure and hence fluorine concentration is taken into account in the determination of the degree of absorption due to fluorine in the unpumped regions of Ashura and Supersprite. Table 1 summarises the parameters associated with each amplifier in the system.

Table 1. Parameters associated with Sprite, Amp2 and Supersprite as used in the gain staging analysis

Amplifier →	Sprite	Amp2	Supersprite
Aperture diameter, ϕ (cm)	27	35	60
Amplifier length, L (cm)	100	130	220
Scaling factor	1.0	1.3	2.2
O/P window area (cm^2)	575	960	2825
O/P window thickness (cm)	2.0	2.6	4.4
Beam pipe I/P lens thickness (cm)	0.20	0.26	0.44
Beam pipe I/P lens diameter (cm)	2.0	2.60	4.44
Beam pipe I/P lens area (cm^2)	3.1	5.31	15.5
Beam pipe O/P lens thickness (cm)	0.22	0.75	1.1
Beam pipe O/P lens diameter (cm)	3.0	10.0	15.0
Beam pipe O/P lens area (cm^2)	7.1	78.5	177
Duration of e^--beam pumping (ns)	60	120	240
Upper state lifetime, τ_{upper} (ns)	1.95	1.0	1.0
Saturation intensity, I_{sat} ($MWcm^{-2}$)	1.53	2.34	2.70
Fill factor	0.8	0.8	0.8
Saturation energy, E_{sat} (J) (80% fill)	1.15	1.92	5.65
n ($=\Delta t_p/\tau$)	0.5	1.0	1.0
Length of unpumped F_2 (front end) (cm)	57	74	127
Transmission of F_2 (front end)[(a)] (%)	93.9	83.1	70.5
Length of unpumped F_2 (back end) (cm)	25	32	56
Transmission of F_2 (back end)[(a)] (%)	97.3	92.3	85.7
No. of pulses	48	96	192
No. of beams	12	24	48

Notes: (a) Static fluorine absorption coefficient, α, is measured to be 0.111%cm^{-1} [1].

Table 2 lists the pulse energies and optical/fluorine losses at each stage in the chain.

The total energies produced at the output of the respective beam pipe lenses are 14.5, 290 and 1484 joules. Two-photon absorption (TPA) losses are a maximum of 9.2% in the output window (fused silica) of the Supersprite module.

A similar analysis is performed for amplified spontaneous emission by preceding the saturating pulse with an infinitesimal pulse which experiences the ASE-depumped gain of the amplifier. Account is taken of passive losses only (Fresnel reflections at optical surfaces, $\mathcal{R}$ = 5%) and F_2 absorption. The overall system gain $\left[\sum \exp((g-\alpha)L)\right]$ for ASE is 17.9.

For the case of 100 psec pulses, this is still in the short pulse regime ($T_p/\Delta t_p$=0.1) and the design curves for the 10 psec case can be applied. Two-photon losses are reduced by an order of magnitude such that the maximum non-linear loss in any optic is about 1%. The output energies from each stage are 14.7, 318 and 1873 joules. The system output is approximately 25% higher than that of the 10 psec case. The system output energy shows a 40% increase over the 10 psec case at 2093J.

Table 2. Energies and optical losses at various points in the KrF chain for 10 psec pulses

Amplifier →	Sprite	Amp2	Supersprite
Input beam transport passive losses (%)	24.8	14.5	14.5
E_{in} per pulse at beam pipe I/P lens (J)	1.58×10^{-4}	0.129	1.29
TPA loss in beam pipe I/P lens (%)	<0.01	0.6	2.3
(including passive losses (%))	9.75	10.3	12.0
E_{in} per pulse incident on cell (J)	1.43×10^{-4}	0.116	1.14
TPA loss in amplifier I/P window (%)	<0.01	0.2	1.0
(including passive losses (%))	9.75	10.0	10.7
Energy per pulse within cell (J)	1.29×10^{-4}	0.104	1.02
F_2 absorption loss on 1st transit (%)	6.1	16.9	29.5
E_{in} per pulse to 1st transit (J)	1.21×10^{-4}	0.0864	0.718
E_{in} (total) to 1st transit (J)	5.81×10^{-3}	8.29	138
E_{in} per pulse to 1st transit (E_{sat})	1.05×10^{-4}	0.0450	0.127
I_{in} to 1st transit (I_{sat})	2.10×10^{-4}	0.0450	0.127
	(n=0.5)	(n=1.0)	(n=1.0)
F_2 absn/optics loss after 1st transit (%)	27	32	39
Pulse gain	3500	60	23
ASE gain	4400	180	74
I_{out} from 2nd transit (I_{sat})	0.735	2.70	2.92
E_{out} per pulse from 2nd transit (E_{sat})	0.368	2.70	2.92
E_{out} per pulse from 2nd transit (J)	0.423	5.18	16.50
E_{out} (total) from 2nd transit (J)	20.3	498	3170
F_2 absorption loss after 2nd transit (%)	6.1	16.9	29.5
E_{out} per pulse after F_2 absorption (J)	0.397	4.30	11.6
TPA loss in amplifier O/P window (%)	0.8	6.1	9.2
(including passive losses (%))	10.5	15.9	18.9
E_{out} per pulse from cell (J)	0.355	3.62	9.41
TPA loss in beam pipe O/P lens (%)	0.7	2.2	3.6
(including passive losses and turning mirror (%))	14.9	16.5	17.9
Energy per pulse from beam pipe + turning mirror (J)	0.302	3.02	7.73
Energy (total) from beam pipe + turning mirror (J)	14.5	290	1484

In this example, the predominant sources of energy loss are due to fluorine in the larger aperture amplifiers (30% on the output transit of Supersprite alone). The output energy of the system is summarised in Table 3 for the three pulse lengths. In improved designs, fluorine absorption will be reduced by operating with lower fluorine concentration. Optimisation of the multiplexing will lead to variation of the pulse interval and beam multiplexing details.

Table 3. Output energy of the KrF chain

t_p (psec)	Output Energy (kJ)
10	1.5
100	1.9
300	2.1

REFERENCES

1. E. C. Harvey, C. J. Hooker, M. H. Key, A. K. Kidd, J. M. D. Lister, M. J. Shaw and W. T. Leland, "Picosecond gain and saturation measurements in an ASE-depumped KrF laser amplifier", submitted to J. Appl. Phys. (1991).

2. A. K. Kidd, M. H. Key and C. J. Hooker, "A simulation code for the study of multiple pulse amplification in KrF lasers", RAL internal report (1990).

3. M. H. Key, M. J. Shaw, I. N. Ross, P. A. Rodgers and M. C. Gower, "Analysis of high power KrF laser systems", RAL-89-133 (1989).

4. A. K. Kidd and M. H. Key, "Supersprite gain staging analysis", RAL internal report No. SSA/3/91/AK (1991).

5. E. C. Harvey and M. J. Shaw, "A simple kinetic model for electron-beam-pumped KrF lasers", Lasers and Part. Beams, to be published (1991).

6. Y. Owadano, I. Okuda, Y. Matsumoto, M. Tanimoto, T. Tomie, K. Koyama and M. Yano, "Development of a high-power KrF laser syatem, Ashura", Laser and Part. Beams, 7 (3), pp.383-392 (1989).

SUPERSPRITE MARX GENERATOR DEVELOPMENT

G J Hirst, M J Shaw and B W H Edwards

Rutherford Appleton Laboratory

INTRODUCTION

Installation of the Supersprite Marx system was described in last year's Annual Report[1] since when the number of shots on the Marx has increased from just 6 to more than 260. These have covered a wide range of operating voltages and have involved both pulse-forming line (PFL) and resistive loads. Preliminary tests of the output switch have taken place (detailed in another section of this Report) and the Marx and Transfer Tank have been tested to their maximum design voltages. The Trigger Marx has also been characterised. A prototype e-beam diode has been designed and is now out to manufacture.

LOW VOLTAGE OPERATION

The main reason for operating the Marx at low voltage (i.e. at charging voltages below ±50 kV) was to test the single output switch. Triggering the Marx at charging voltages as low as ±18 kV proved to be possible, although even with just one atmosphere of air in the spark gaps this was very difficult. At this voltage the output switch did not self-break so the charge on the erected Marx rang into the PFL and back again, the energy being dissipated in the Marx and PFL resistances. Measurements of the ringing waveform allowed estimates of these resistances and of the Marx inductance to be made, using the computer circuit model which is also described elsewhere in this Report.

The circuit used for the Marx, the Transfer Tank and the PFL is shown in figure 1. The Marx capacitance and charging voltage, the Transfer Tank inductance and the PFL impedance and resistance have all either been measured independently or estimated from first principles. The remaining component values have been deduced by fitting the predicted Marx output voltage, shown in figure 2, to the measured trace. On the scale of figure 2 the fitted and measured waveforms are indistinguishable except for a discrepancy in the first 400 ns, which is described below.

The Marx inductance controls the frequency of the damped oscillations in figure 2 and the Marx parallel resistance produces the slow exponential decay which underlies them. These two variables are easy to fit. The decay of the oscillations themselves is due mainly to the Marx series resistance labelled R in figure 1. It is not possible to reproduce the measured waveform using a single value for R and figure 2 has been generated by setting R equal to 12 Ω for the first 400 ns and to 1.4 Ω thereafter. While

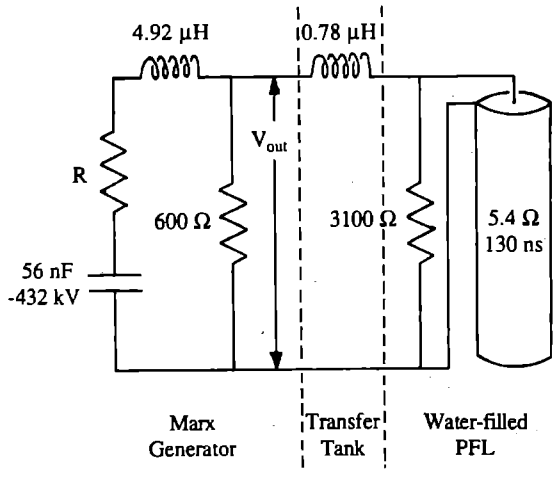

Figure 1: Circuit used to model the Marx system

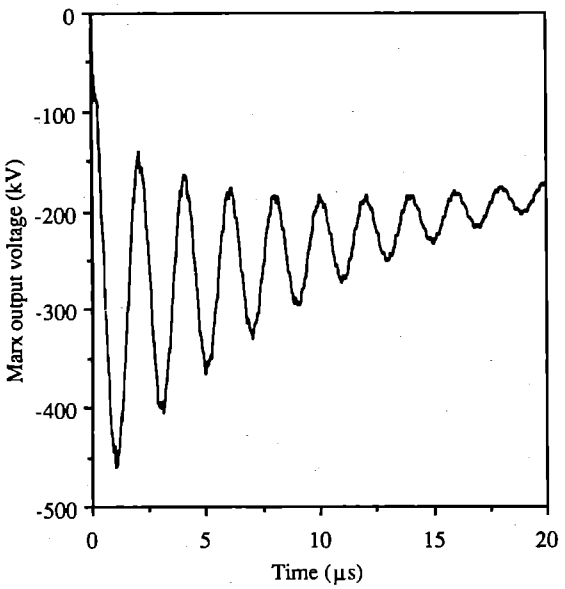

Figure 2: Marx output predicted using the circuit of figure 1

this is obviously unphysical it does produce the correct heights for the oscillation peaks. In reality the first 400 ns reflects the conditions set up during the Marx erection, with large, rapid oscillations caused by stray Marx capacitances discharging into the Transfer Tank inductance. This situation is too complex to model with a simple LCR circuit.

HIGH VOLTAGE OPERATION

High voltage Marx tests have been carried out with liquid-filled 25 cm diameter resistive loads, mounted either in the Marx tank or, latterly, in the Transfer Tank. The first resistor was 30 cm long, made from uPVC piping and filled with $CuSO_4$ solution to give a 50 Ω resistance. It shattered on its first 1.55 MV shot after four shots at 1.33 MV. The cause was a longitudinal crack in the resistor's wall resulting from internal pressure-jumps on earlier shots. It seems that uPVC is too brittle to withstand these.

The second resistor was made from high density polythene piping, as used for underground gas mains. A 30 cm length of this was fitted with stainless steel electrodes and was filled with dishwasher powder solution[2], again to a resistance of 50 Ω. The resistor was mounted vertically at the top of the Transfer Tank, allowing a small air gap in the hollow anode to absorb the expansion of the electrolyte. Unfortunately this anode shape increased the electric field within the resistor and there was an internal track on an attempted 1.77 MV shot. This failure was less destructive than that of the first resistor, resulting in a snapped tie-rod, some deformation of a spun aluminium field shaper and a small leakage of electrolyte into the Transfer Tank.

The latest load is very similar to the second design except that it is 55 cm long and that the anode cavity is covered with a wire mesh to reduce the field. Its resistance has also been reduced to 20 Ω. It has withstood tens of 1.7 MV shots at significantly higher energies than its predecessors and will in future be used with a self-closing oil gap as part of the Marx protection circuitry.

The Marx itself has been d.c. charged to its maximum voltage of ±100 kV and has been fired 8 times at that voltage. The peak output was limited by the load resistance to 1.7 MV, equal to the proposed operating voltage, but the output pulse duration was

longer than under normal conditions so the stress applied to the Marx was greater. Assuming a $t^{1/3}$ stress dependence[3] these tests represent about 20% more stress than would occur normally. It is proposed to extend the testing to stresses of 35% above normal.

As well as testing for pulsed breakdown within the Marx we have also tried to establish a reliable operating pressure for the Marx switches (Physics International T508A spark gaps). This should be as low as possible, for low jitter triggering, but not so low that the switches frequently self-break. The manufacturers of the switches suggest that the self-break voltage for the full gap is related to the SF_6 pressure by the formula

$$V_{sb}(kV) = 77 + 6.33\, p_{gap}(psia)$$

with the suggestion that the gaps should be operated at 75% of self-break. Over the last 78 shots the Supersprite Marx has self-broken three times at voltages below 75% of this V_{sb} (twice at 74% and once at 67%). While this rate is higher than might have been expected it was not felt necessary to operate the Marx at a lower fraction of V_{sb}. (These results were obtained with Marx voltages between ±80 kV and ±100 kV and charging times which varied between 120 s and 180 s.)

TRIGGERING TESTS

The Supersprite Marx switches are triggered via mid-plane electrodes coupled to their trigger sources by 2 kΩ resistors. For the bottom six switches the common trigger source is the 5-stage Trigger Marx generator. Each of the top six switches is fired from the mid-plane electrode of its neighbour in the bottom six. A fairly low timing jitter of the main Marx is necessary if the PFLs are to be correctly charged when their output switches are fired.

A good measure of the trigger performance is the delay between the application of the trigger pulse and the firing of the last Marx switch. This delay, and its jitter, become smaller as the trigger voltage is increased and as the Marx switches are operated nearer to self-break. Both of these parameters were varied to establish the optimum operating point for the trigger system.

The Trigger Marx output pulse, measured at the point where the six resistors from the bottom gaps are connected together, rises to peak volts in about 80 ns and then decays exponentially with a time constant of about 10 µs. Its peak voltage can be varied from 150 kV to 460 kV. The effects of such a variation are shown in figure 3 which plots the Marx delay against the peak trigger voltage for a positive trigger polarity. (The Marx delay is defined, somewhat arbitrarily, as the time between the trigger

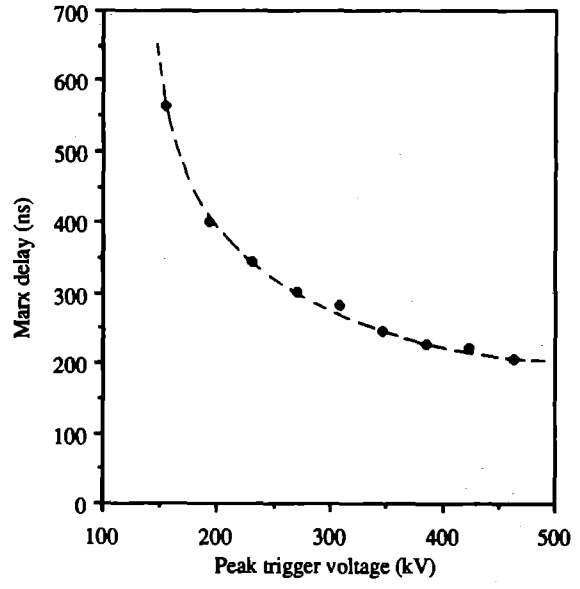

Figure 3: Marx delay as a function of the peak trigger voltage for positive trigger polarity

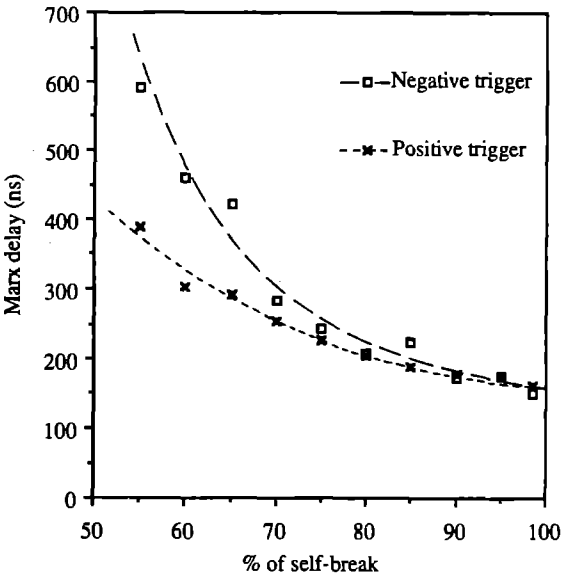

Figure 4: Marx delay as a function of the percentage of Marx self-break, taken with ± 90 kV Marx charging

voltage reaching 40% of its peak value and the Marx output voltage reaching 35% of its peak value.) These measurements were taken with a Marx charging voltage of ±90 kV and a Marx spark gap pressure of 26 psia of SF_6. The Marx delay continues to decrease with increasing trigger voltage all the way to the maximum value of 460 kV. However the improvement above 350 kV is small and is probably not worth the extra strain imposed on the trigger system components.

Varying the Marx self-break voltage, by varying the spark gap pressure, produces the results shown in figure 4, where the self-break voltage is that given by the formula above. The peak trigger voltage for these shots was ±385 kV. It was clear that a positive trigger polarity produced a lower Marx delay for a given percentage of self-break, perhaps because with positive triggering a larger voltage was developed across the lower half of each gap as the Marx erected negatively. The only drawback of this polarity might have been a voltage reversal for the Trigger Marx capacitors during the main Marx erection. Fortunately the isolation between the two Marxes was sufficient to prevent this. Positive trigger polarity has therefore recently been adopted as standard.

The jitter on the Marx delay was measured for 385 kV triggering at 75% of self-break. It was 3.0 ns for positive polarity (1σ, 8 shots) and 9.9 ns for negative polarity (1σ, 11 shots). The reduction in delay is slight above 75% of self-break whereas the incidence of actual self-breaks starts to become unacceptable. Operation at this point is therefore expected to be the norm.

ACKNOWLEDGEMENTS

It is a pleasure to acknowledge the many and varied contributions from the CLF Engineering Support staff, in particular D Baker, P Gottfeldt, H Medhurst and D Wood.

REFERENCES

1. G J Hirst, M J Shaw, E M Madraszek and J E Boon, *Annual Report to the Laser Facility Committee*, Rutherford Appleton Laboratory Report RAL-90-026 Section B3.1 (1990)

2. G J Hirst, *Annual Report to the Laser Facility Committee*, Rutherford Appleton Laboratory Report RAL-90-026 Section B3.3 (1990)

3. J C Martin, *Nanosecond Pulse Techniques*, AWRE Aldermaston Report SSWA/JCM/704/49 (1970)

LASER TRIGGERED SWITCHES FOR SUPERSPRITE

G J Hirst, R Bailly-Salins*, S Hancock and M J Shaw

Rutherford Appleton Laboratory
*On leave from CEA, 21120 Is-sur-Tille, France

INTRODUCTION

The design for the Supersprite output switches was given in last year's Report[1]. Since then a prototype has been manufactured, installed and tested at low voltage. High voltage testing of a second-generation switch is about to start (April 1991).

Each switch is a two-electrode spark-gap in a coaxial housing filled with SF_6 gas. The gas pressure controls the self-break voltage of the switch and at 4 bara the Supersprite switches should self-break at 2.1 MV. They will normally be triggered at 1.7 MV, using the focussed beam from a KrF discharge laser to produce gas breakdown in part of the 70 mm interelectrode gap.

The switch inductance must be kept low so that the load voltage can rise sufficiently rapidly. The inductance is calculated to be 260 nH if the switch has a single arc-channel and 190 nH if three-channel operation can be achieved.

EXPERIMENTAL APPARATUS

The prototype switch was identical to that in reference 1 except for its internal optics. It had been proposed to use a single 45° prism with its input face faceted to split the trigger laser beam into three beamlets. These would then be internally reflected and pass through the single curved output face to three separate foci. Unfortunately proof-of-principle experiments confirmed that astigmatism would keep the peak intensity below the breakdown threshold. A modified set of optics was therefore designed using a simpler prism, a mirror and three discrete lenses.

The switch was connected to a single 5.5 Ω water-filled pulse-forming line (PFL) which was in turn pulse-charged from the Supersprite Marx generator[2]. Beyond the switch was a 1.4 m long, 21 Ω oil-filled line, terminated by a resistive dummy-load.

The single-pulse energy of the trigger laser (Lambda Physik EMG 150) was 0.55 J in 25 ns, with a 200 μrad beam-divergence. About 25% of this was focussed into the spark gap.

Monitors included voltage probes on the Marx output, the switch and the load and a film camera used to record the number of arcs in the spark gap.

RESULTS AND DISCUSSION

The prototype switch was limited to operation at 1 bara, at which pressure its self-break voltage was found to be 600-800 kV, depending on the PFL charge-time. These low values, combined with the mismatch between the Marx capacity and that of the single PFL, required operation of the Marx at very low charge voltages when the switch was being laser triggered. The low Marx voltage led to a very high timing jitter, making synchronisation between the switch voltage and the trigger laser very difficult. This in turn had a strong effect on the load voltage waveform and prevented an accurate determination of the switch inductance as a function of the number of arc-channels.

Three-channel operation of the switch, shown in figure 1, was achieved on 2 out of 42 attempts, with a very faint third channel visible on 2 others. Two-channel operation was achieved 15 times. Figure 1 shows clearly that the three arcs were not all equally bright, suggesting an unequal current distribution. This was usually the case. It can also be seen that the arcs were kinked. The central third of each arc followed the path of its trigger laser beamlet, although the length of the laser-produced plasma in the absence of any applied voltage was only 2-3 mm. Each arc broke away from its laser beam at the ends and followed the electric field lines back to the electrodes.

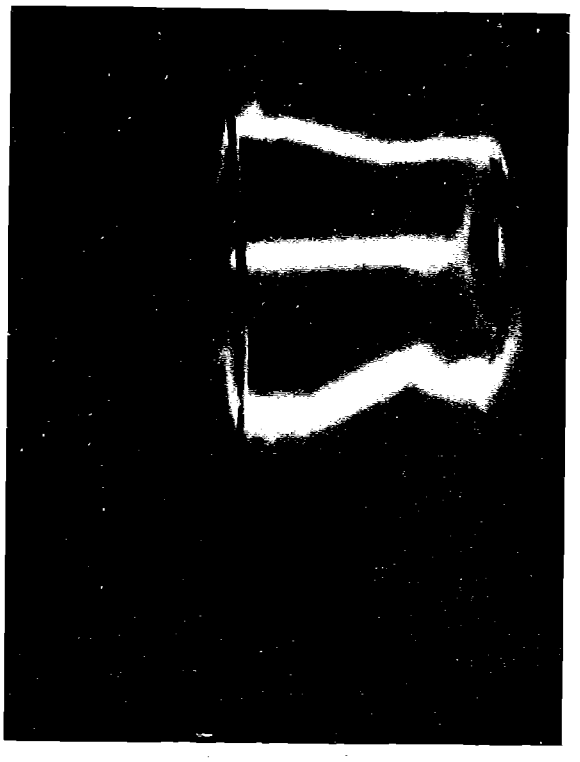

Figure 1: Photograph of three-channel operation of the switch.

The factors controlling the number of arc-channels were easier to eliminate than to determine. The trigger laser timing did not seem to be important provided, of course, that it preceded self-breakdown. On one occasion the Marx triggered very late, resulting in breakdown of the gap at least 500 ns and probably 1 μs after the trigger laser. Two arcs, following two of the laser beamlets, still resulted. The balance of energy between the trigger laser beamlets did not seem to be too critical either. At least once a single arc followed the path of the weakest beamlet.

In all likelihood the number of arcs depends statistically on the rate at which the gap voltage falls, the number being high if the rate is low. The rate will be high if the load impedance is high so more arcs might be expected in the next set of tests where the line impedance after the switch has been reduced to 12 Ω. The increased gas pressure in the next tests will also increase the resistive-phase time of the gap[3] which should in turn increase the number of channels.

REFERENCES

1. E M Madraszek and R Bailly-Salins, *Annual Report to the Laser Facility Committee*, Rutherford Appleton Laboratory Report RAL-90-026 Section B3.3 (1990)

2. G J Hirst, M J Shaw, E M Madraszek and J E Boon, *Annual Report to the Laser Facility Committee*, Rutherford Appleton Laboratory Report RAL-90-026 Section B3.1 (1990)

3. J.C.Martin, *Duration of the Resistive Phase and Inductance of Spark Channels*, Atomic Weapons Research Establishment Report SSWA/JCM/1065/25, Aldermaston (1965)

PULSED POWER MODELLING OF THE SUPERSPRITE SYSTEM

R Bailly-Salins, G J Hirst

Based on an NRL report (Ref1), a versatile transmission line code has been written in Pascal for a microcomputer. As far as we are concerned, this code gives voltage, current, power and energy in an electrical network but it can be adapted to solve thermal, optical and mechanical problems.

A capacitor C and an inductor L are represented by arbitrarily short line elements (transit time T) whose respective impedances Z=T/C and Z=L/T are low and high. A simple RLC circuit and its equivalent transmission line model are shown as:

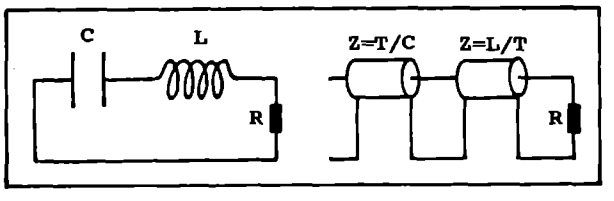

At each end of a transmission line there are voltage waves propagating in 2 directions: the wave VOUT that is incident on the end from within the element and the wave VIN that leaves the end by traveling into the element.

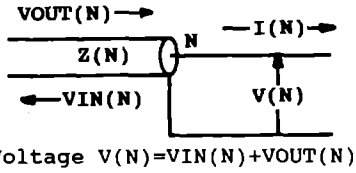

Voltage V(N)=VIN(N)+VOUT(N)

Current I(N)= [VOUT(N)-VIN(N)]/Z(N)

Power $P(N)=([VOUT(N)]^2-[VIN(N)]^2)/Z(N)$

To predict the behaviour of a circuit against time, the code keeps track of the instantaneous values of the 2 traveling voltage waves at the ends of each line element rather than following particular waves around the circuit. Such a method allows us to consider separately the transit of a wave from N to N1 and the impedance mismatching between N1 and N2.

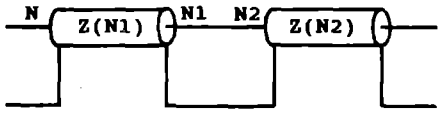

VOUT(N1,t)=VIN[N,t-T(N1)]

VIN(N1,t)=VOUT(N2,t)(2Z(N1)/[Z(N1)+Z(N2)])
+VOUT(N1,t)([Z(N2)-Z(N1)]/[Z(N2)+Z(N1)])

If we deal with a parallel or a series tee, the expressions of VIN are given by

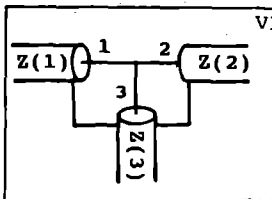

VIN(1)=VOUT(1)[2/Z(1)D-1]
+VOUT(2)[2/Z(2)D]
+VOUT(3)[2/Z(3)D]

D=1/Z(1)+1/Z(2)+1/Z(3)

VIN(2) and VIN(3) are obtained by circular permutation of (1),(2),(3)

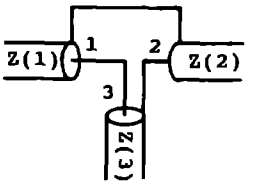

VIN(1)=VOUT(1)[1-2Z(1)/D]
+VOUT(2)[2Z(1)/D]
+VOUT(3)[2Z(1)/D]

VIN(2)=VOUT(1)[2Z(2)/D]
+VOUT(2)[1-2Z(2)/D]
-VOUT(3)[2Z(2)/D]

VIN(3)=VOUT(1)[2Z(3)/D]
-VOUT(2)[2Z(3)/D]
+VOUT(3)[1-2Z(3)/D]

D=Z(1)+Z(2)+Z(3)

If a shunt or a series resistor R comes between 2 line elements, the above relations are still valid, taking Z(3)=R and VOUT(3)=VIN(3)=0.

The electrical modelling of SUPERSPRITE (the 60cm amplifier or AMP60) is shown in the next figure where the equivalent transmission lines are given for a computation time step T=1ns. We can see the Marx generator with its capacitor bank (56nF, initial charge -1900kV), inductance (5000nH), series resistance (1.5ohm) and parallel resistance (500ohm).

The energy stored in the Marx is discharged into 3 coaxial water lines (125ns, 5.5ohm) via the so-called transfer tank. If the laser triggered switches are kept off, we get a damped oscillation whose caracteristic time is approximately $2\pi\sqrt{LC}$=2800ns where L and C are the inductance and the capacitance of the Marx and pulse forming line circuit.

Normally, the switches are fired at 1220ns and a fraction V[Volt] of the voltage is applied to the diode connected by means of a coaxial 11ohm oil line fork. The diode impedance Z is modelled by two resistors whose values are given by the Child-Langmuir law, modified by Friedlander for relativistic electron beams (Ref2).

If V<=-531000:
$Z=-V/(S/d^2)2700(\sqrt{1-V/511000}-0.85)^2$

If -531000<V<0: $Z=429000/(S/d^2)\sqrt{-V}$

If V>=0: Z=100000ohm.

S is the cathode area and d is the cathode anode distance.

Motion of the conducting plasma, generated from the cathode surface (and possibly from the anode surface) will result in a dynamic reduction of d. The effect is shown below for a linear variation at speed v=0.004cm/ns.

Assuming v=0, the voltage, the power and the energy for each diode are plotted in the figures. The rise time of the electric voltage pulse is good with dV/dt=30kV/ns but it can be improved to dV/dt=180kV/ns by using a -900kV self-breaking sparkgap (prepulse suppressor).

All these results are very usefull before starting the first experimental tests of SUPERSPRITE. Fault conditions have also been simulated, but we should not need the results.

Ref1 - D D Hinshelwood. BERTHA, a versatile transmission line and circuit code. NRL Memorandum Report 5185. 1983.

Ref2 - L G Schlitt and L P Bradley. The physics of relativistic electron beams in rectangular and cylindrical geometries. UCRL 77203, LLNL, 1975.

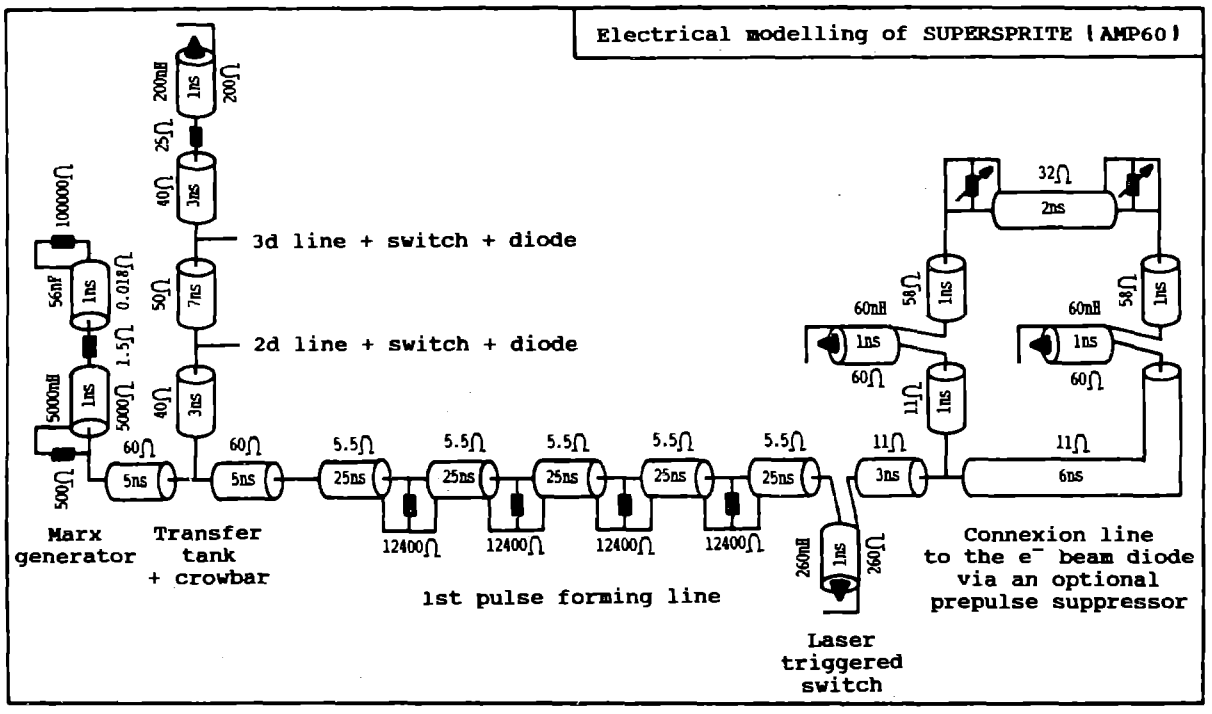

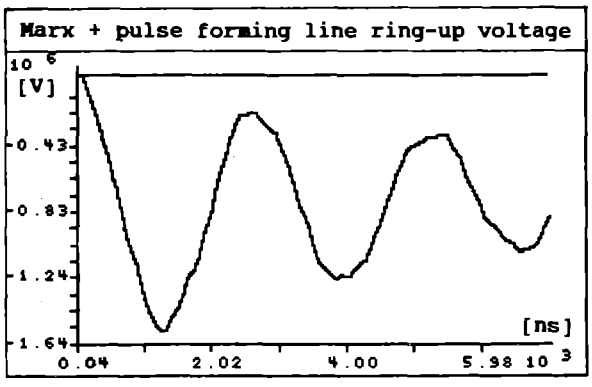

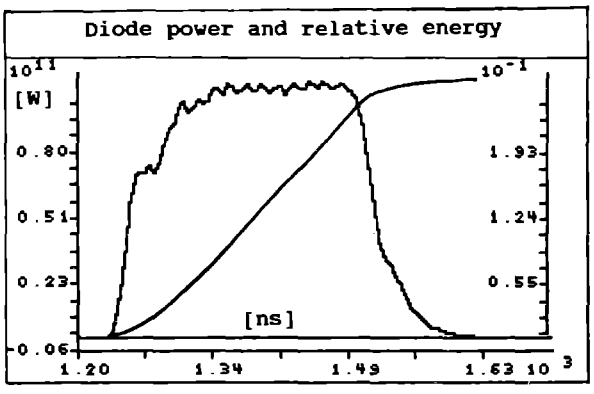

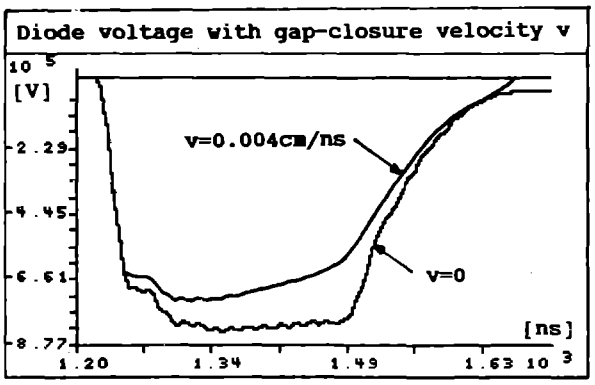

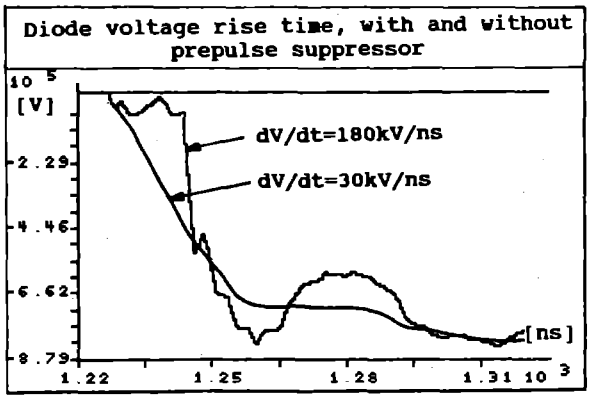

STUDIES OF PLASMAS PRODUCED BY 12 PS KrF LASER PULSES

V. Barrow, J. Edwards, L. A. Gizzi, F. Y. Khattak, D. Riley, S. M. Viana and O. Willi

The Blackett Laboratory, Imperial College,

London

INTRODUCTION

The considerable interest in the interaction of short high power laser pulses with matter and its application is now well established throughout the laser-plasma community. High density, high temperature plasmas are produced which are highly transient without significantly being affected by hydrodynamic motion. Consequently processes such as dense plasma effects, ionization dynamics, thermal electron transport, laser plasma interaction, radiative cooling, can be investigated in a novel regime.

We have recently studied (1-4) some of these processes by irradiating solid and thin layered target with the 12 ps KrF laser system of the CLF.

EXPERIMENTAL ARRANGEMENT

The 12 ps - 268 nm SPRITE laser pulse was focussed onto layered and solid targets using an off-axis diffraction limited paraboloid. Energy losses due to two photon absorption in the transmitting focussing optics were then limited. With the low laser beam divergence and the use of CaF_2 windows, incident laser intensities of up to $3*10^{17}$ Wcm^{-2} obtained in a focal spot 10 μm in diameter. A range of almost three orders of magnitude in intensity could be explored by varying both focal spot size and laser energy.

The characterization of plasma conditions was carried out by means of time resolved X-ray and X-UV spectroscopy with very high temporal resolution. Also, preliminary measurements including visible spectroscopy and calorimetry were performed on the backscattered laser light in order to study the process in the novel short pulse regime.

RESULTS AND DISCUSSION

The electron density and temperature and their temporal evolution was inferred from Stark profiles and line ratios of different ionization stages observed by X-Ray and X-UV time resolved spectra. Electron densities above 10^{23} cm^{-3} were inferred by the Stark broadening of H-like Aluminium lines when solid Al target were irradiated at 10^{17} Wcm^{-2} (see Fig.1). Initial electron temperatures of 1.2 keV were obtained by

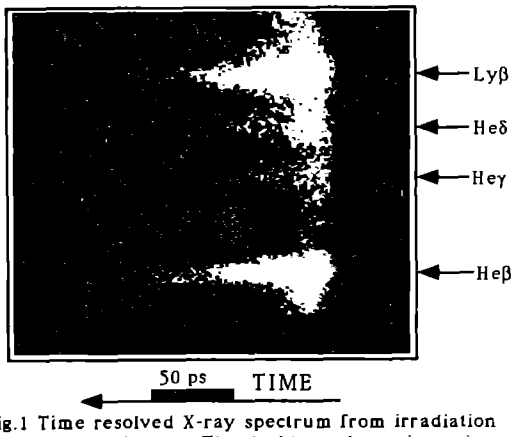

Fig.1 Time resolved X-ray spectrum from irradiation of a solid Al target. The incident laser intensity was 3.0E16 Wcm-2.

comparison of experimental line ratios with those predicted by a time dependent Average Atom model coupled to the hydro-code MEDUSA. Indeed, substantially different results were produced when a similar analysis was performed using a steady

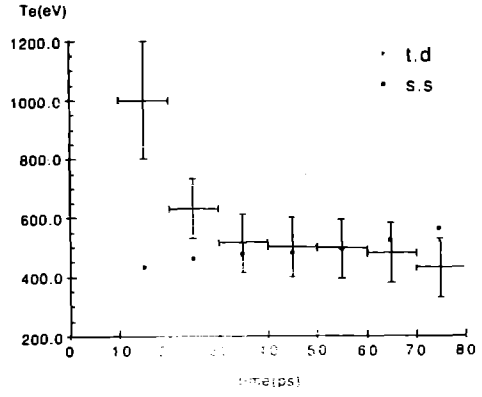

Fig.2 Temporal evolution of electron temperature obtained by a time dependent (t.d.) and a steady state (s. s.) analysis.

state model (RATION) to predict line ratios from plasma conditions (see Fig.2).

The Random Phase Plate technique was employed for the production of high aspect ratio cylindrical aluminium plasmas. The simple introduction of RPP with rectangular elements before the main focussing optics resulted in a fairly uniform line focus (see Fig.3). Time resolved XUV spectroscopy showed that conditions suitable for the study of the H-like recombination X-ray laser were produced.

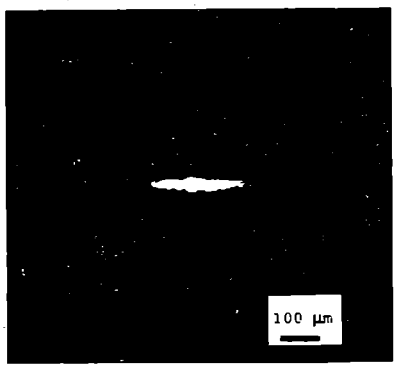

Fig.3 X-ray pin-hole camera image of plasma produced by irradiation of solid Al target with line focus generated by the Random Phase Plate Array. The average laser intensity was 2.0E14 Wcm-2.

A better understanding of basic plasma parameters can be achieved if X-ray and X-UV emission can be resolved during the laser pulse. The use of a new ultra-fast X-ray camera with a 1 ps temporal resolution coupled to an X-UV flat-field spectrometer resulted in the first time resolved X-UV spectra within the laser pulselength. Fig.4 shows a typical spectrum of the X-UV radiation produced when a multi-layer target (CH-Al-Mylar) was irradiated at an incident laser irradiance of 10^{16} Wcm^{-2}. The propagation of the heat front can be monitored as line emission from the different layers of the target and their relative delays are detected. A comparison with the predictions of numerical simulation (MEDUSA) can give information on the parameters involved in the modelling including, for example, the flux limiter. Although a detailed absorption measurement is not yet available, valuable information concerning the coupling of laser radiation with plasma can be

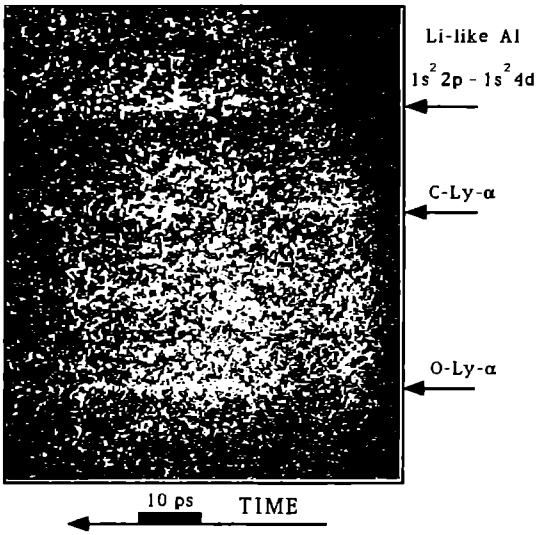

Fig.4 Time resolved X-UV spectrum from irradiation of a layered target (0.1μm CH-0.2μm Al-Mylar). The laser intensity incident on the CH layer was 3.0E16 Wcm-2

gained by the analysis of the backscattered laser light from solid targets. Reflectivities between 5 and 30% of the incident laser light were measured when the irradiance ranged from $2*10^{14}$ to $8*10^{16}$ Wcm^{-2} giving an indication of a poor laser-plasma coupling in the high intensity regime.

REFERENCES

1. "Observations of high density plasmas produced with picosecond high power KrF irradiation", 18th Annual Anomalous Absorption Conference, Quebec (1988).

2. "Observations of high density plasmas produced with a picosecond high power KrF laser", 4th Topical Meeting on Short Wavelength Coherent Radiation: Generation and Applications, North Falmouth (1988).

3. "Observation of high density plasmas with a picosecond high power KrF laser", Topical Meeting on High Energy Density Physics with subpicosecond Lasers, Utah (1989).

4. "Interaction of high power subpicosecond laser pulses with matter", 12th International Conference on Lasers & Applications, New Orleans (1989).

5. I. Ross, SPRITE progress meeting, Rutherford Appleton Laboratory, 23. Jan. 1991.

Experiments with 'SPRITE' 12 ps Facility

*G J Tallents, +M H Key, +P Norreys, +J Jacoby, +R Kodama, +N Tragin,
•H Baldis, •J Dunn, °D Brown

*Department of Physics, University of Essex, Wivenhoe Park, Colchester Park, Essex CO4 3SQ, UK
+Rutherford Appleton Laboratory, Chilton, Didcot, Oxon OX11 0QX, UK
•National Research Council, Ottawa, Canada K1N 9B4
°Royal Holloway and Bedford New College, University of London, Egham, Surrey TW20 0EX, UK

Recent numerical simulation studies have shown that the gain obtained in recombination X-ray laser experiments increases with decreasing wavelength and decreasing pulse length of the heating laser pulse[1] and increases when the line width is narrowed[2]. It is therefore of great interest to study the lateral and axial thermal energy transport for SPRITE (wavelength = 0.268 μm) short pulse, narrow line focus irradiation, and to determine whether lateral energy transport reduces the heating of the plasma. In addition, we have recently reported energy transport measurements for 20 psec, 0.5 μm and 0.35 μm laser irradiation of planar targets with a focal spot of 50 μm[3][4], as well as 40 psec, 0.268 μm irradiation of similar targets with a focal spot of 8 μm(4). For comparison, we present results here for 12 psec, 0.268 μm laser irradiation in a 8 μm focal spot.

The KrF pumped Raman laser SPRITE[5] delivered up to 3 J in a 12 psec pulse. The measured contrast ratio was better than 10^{10}:1 which means that there was no pre-pulse to distort the results. A novel method of using a random phase plate to generate the line focus was developed by CLF staff and employed in this experiment[6]. A random phase plate splits the laser beam into a large number of individual beamlets and introduces a phase difference of 0 or π between them. Each beamlet is focused to a focal spot of diameter D given by $D = f\lambda/d$, where f is the focal length of the lens, λ is the wavelength of the incident radiation, and d is the element size of the random phase mask. If the element size is rectangular and of high aspect ratio, a line focus is produced.

An aspheric doublet lens of 25 cm focal length was used to focus the 8.0 cm diameter beam. The elements of the random phase plate had aspect ratios of 100:1 and 50:1 (the larger element size was 1 cm). This provided line foci of 10 x 660 microns and 10 x 330 μm FWHM respectively at the focal plane of the aspheric lens. An 8 μm spot focus was obtained with the lens alone.

With the Sprite KrF pumped Raman laser delivering up to 3 J in a pulse length of 12 psec, it was found that there was a 40% transmission through the focusing optics due to two photon absorption in the fused silica elements. This meant that the incident irradiance for the line focus studies was 5×10^{14} or 3×10^{15} W cm^{-2} for the two lengths of line focus.

The energy transport was recorded using layered disc targets. A 0.25 μm thick layer of NaF was buried below a plastic layer of variable thickness. The heat penetration into the target was studied by recording the emission spectrum of both Na and F on flat Beryl (2d = 15.95Å) and KAP (2d = 26.663Å) crystal spectrometers. The spatial profile of the focused laser energy along the line can be described by a sinh2 function. The diameters of the disc targets were chosen to fall within the FWHM of the line focus, so they were either 550 or 270 μm.

A pinhole camera was employed to measure the spatial distribution of the X-ray emission. The pinhole diameter was 10 μm in diameter, the magnification was 5.3, so the spatial resolution was 12 μm. The X-ray image was filtered by 5 μm thick mylar and 0.5 μm thick Aluminium. Both spectra and pinhole images were recorded on DEF film and the calibration of Henke et al[7] was used to convert the film densities to intensities incident on the film. In the results reported here, the profile of the X-ray image was assumed to be gaussian and the spatial resolution of the camera was removed by a simple deconvolution. Figure 1 shows the width of the X-ray image as a function of the overlay thickness of the plastic ablator. It can be seen that the average width of the line focus with no overlay is 16 ± 3 μm, which means that there is very little lateral energy transport (the optical line focus width was 10 μm). The axial heat penetration is ~0.2μm.

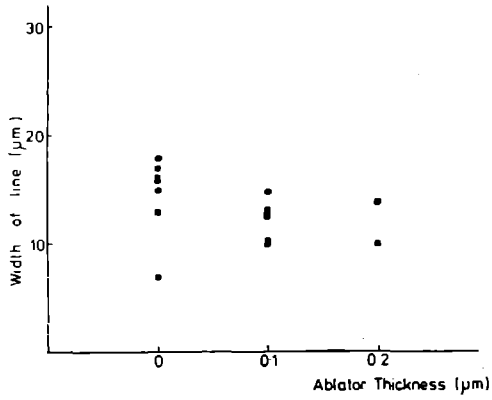

Fig 1 Width of X-ray image as a function of plastic overlay thickness for line focus irradiation.

When the random phase plate was removed and the laser energy focused into a spot of diameter 8 μm, the incident irradiance onto target was $1\text{-}2 \times 10^{17}$ Wcm^{-2}. Figure 2 shows the X-ray image size as a function of the CH overlay thickness. The X-ray image with no overlay is about 36 μm wide and gradually reduces as the ablator thickness increases. There is clearly lateral energy transport from the optical focus width of 10 μm. A more detailed discussion of the importance of lateral transport in these experiments has been presented[8].

We are grateful to the Sprite laser operations team of the SERC Central Laser Facility for provision of the Raman beam and to C N Danson for the RPA plates.

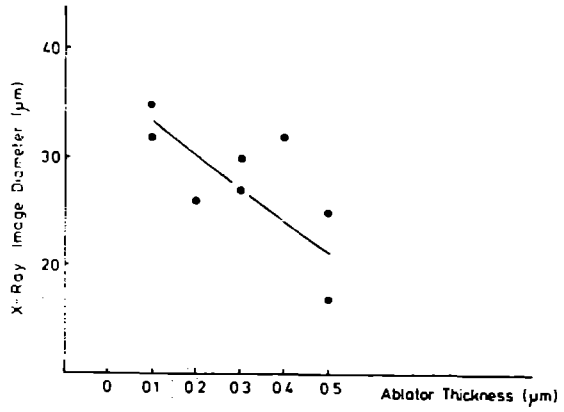

Figure 2. Width of X-ray image as a function of the plastic overlay thickness for spot focus irradiation.

REFERENCES

(1) N Tragin, M H Key, S J Rose, J Modern Optics 37 (4) 435 1990.

(2) N Tragin, M H Key, S J Rose, X-ray Lasers, 1991 IOP Publishers, Bristol (Ed G J Tallents) pp 163-7.

(3) G J Tallents, M H Key, P Norreys, D Brown, J Dunn, H Baldis, Phys Rev 40A 2857 1989.

(4) G J Tallents, M H Key, P Norreys, N Tragin, J Dunn, H Baldis, D Brown, SPIE Conf Proc 1229 p138 1989.

(5) See various articles in this Annual Report.

(6) C Danson, X-ray Lasers 1991, IOP Publishers, Bristol, UK, (Ed G J Tallents) pp 81-4..

(7) B L Henke, Y Y Uejio, G F Stone, C H Dittmore, F G Fujiwara, J Opt Soc Am B3 1540 1986.

(8) G J Tallents, M H Key, P Norreys, J Jacoby, R Kodama, N Tragin, H Baldis, J Dunn and D Brown, SPIE Conf Proc 1413, 1991.

REFLECTIVE FOCUSING OPTICS FOR SPRITE

I N Ross
Rutherford Appleton Laboratory

Introduction

At current performance levels for SPRITE (4J in 10 ps) the output beam intensity is about 7 GW/cm^2 leading to a two photon absorption of 50% in 2 cm of fused silica or 5% in 2 cm of CaF_2. In the absence of availability of CaF_2 focusing lenses it is necessary to use reflective focusing optics and it has been decided to use an off-axis paraboloid (OAP). Suitable designs have been considered to generate both point and line focus in the existing target chamber and to set up an effective alignment system.

Point Focus

Figure 1 shows the point focus design. The vacuum window is CaF_2 and a subsidiary mirror inside the chamber is necessary to enable use of existing ports. The off-axis paraboloid chosen is F/3 with ϕ110 mm aperture and an off axis angle of 15°. Its surface accuracy is $\lambda/4$ in the visible and it is coated for 100% reflection at both 249 and 268 nm. The back surface is normal to the paraboloid axis (input beam direction) and an inspection polish on this surface provides a useful reference for alignment of the OAP.

Alignment

Alignment targets A and B, see figure 1, provide reference marks fixed to the target chamber. The OAP back surface is aligned normal to a He Ne beam which has been referenced onto these marks. This procedure establishes the correct tilt for the OAP to provide an aberration-free focus at the centre of the target chamber. A second He Ne expanded and aligned to the KrF beam is referenced onto the first He Ne and hence can be used for alignment and focusing onto target. Observation of the point focus image quality using a microscope objective demonstrated close to diffraction limited performance and enabled an estimation that the alignment tolerance of the OAP is about 1 mrad.

Line Focus

A scheme similar to figure 1 can be used for a line focus and this is shown in figure 2. This design uses the OAP in series with a tilted spherical mirror and by minor adjustments to the geometry and input beam diameter the line focus length can be varied from 4 to 10 mm.

An alternative generator of fine foci was also considered. The addition of a random phase plate in figure 1 will result in a line focus. However, this line focus is subject to transverse aberrations for long line foci. A direct measurement of linewidth as a function of off-axis distance was made, figure 3, from which we conclude that linewidths can be kept below 15 µm using SPRITE for line foci lengths up to about 3 mm.

Conclusions

Point and line focus schemes have been designed and implemented on SPRITE. Experiments already conducted using the point focus arrangement have demonstrated focal spot sizes limited only by the beam divergence and it has not proved difficult to carry out the alignment and focusing of the OAP.

The ability to use low power lasers of arbitrary wavelength for alignment and focusing is a definite advantage of these reflective optics schemes.

Figure 1

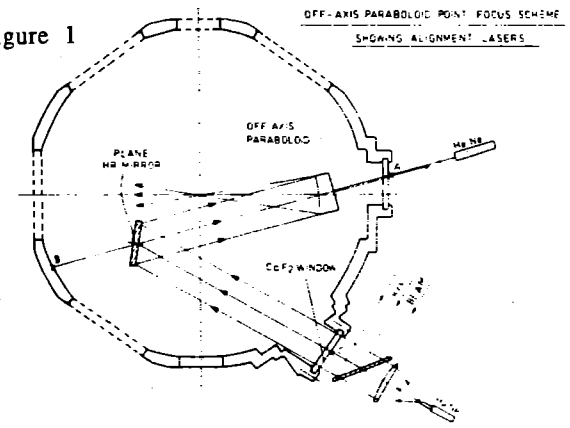

Figure 2

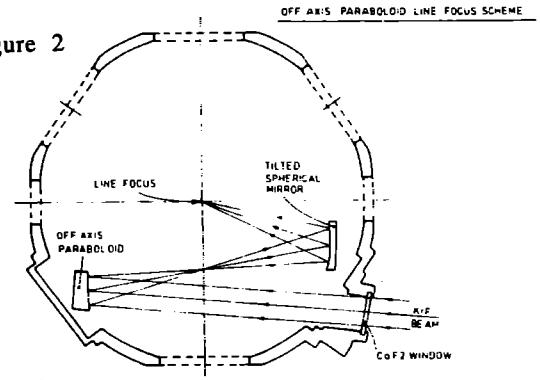

Figure 3

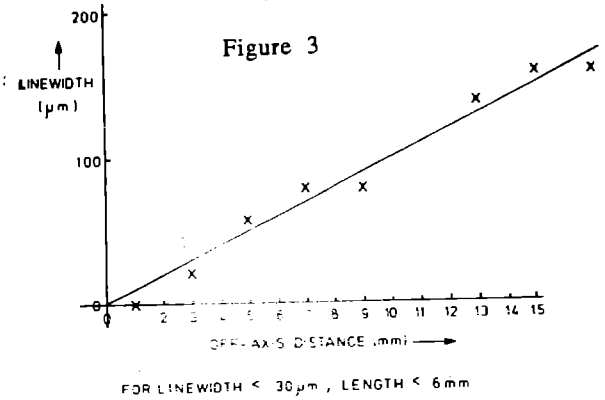

FOR LINEWIDTH < 30µm , LENGTH < 6mm

KrF System Modelling

A. K. Kidd and M. H. Key

Rutherford Appleton Laboratory

INTRODUCTION

Over the past year, the KrF modelling effort has been aimed at improvement of understanding of the performance of the present SPRITE laser system and analyses of gain staging designs for SUPERSPRITE. A KrF extraction code [1] is used as a test-bed for multiple-pulse, double-pass amplification in single amplifiers. A system code [2] incorporates optical losses in the SPRITE laser system and may be used to study multi-pass amplification in KrF amplifier chains.

DEVELOPMENT OF KrF EXTRACTION CODE

A one-dimensional KrF extraction code developed at RAL [1] has been modified and extended in the following way:

1. The inclusion of passive and non-linear optical losses at the windows and back mirror of the amplifier together with absorption losses in the unpumped regions of the amplifier.

2. Computed small-signal gain within the amplifier is found to exhibit Statz de Mars type oscillations as the ASE depletion of gain reaches equilibrium. Such oscillations are not seen in the ASE output from Sprite, which has a slower turn-on of gain than the model. A delay time prior to the arrival of the pulse to be amplified of approximately 2-3 times the round-trip cavity time has therefore been used in modelling the amplification of pulses in Sprite.

3. A coefficient associated with the ASE source intensity is:

$$A d\Omega = \left[\frac{\Delta\upsilon_A}{\Delta\upsilon_s}\right]\left[\frac{\tau_u}{\tau_s}\right]\left[\frac{d\Omega}{4\pi}\right] \qquad (1)$$

where the first term is the effect of line narrowing (approximately 0.35 for the stage gains of interest here) and the last term is the fraction of spontaneously emitted photons which propagate within the solid angle to be amplified. The second term is the ratio of the collisional-radiative lifetime of the KrF^* upper state lifetime to the spontaneous lifetime of 6.7 nsec [3]. The upper state lifetime is a function of gas mix and total pressure and is below 1 nsec for krypton-rich mixtures. The saturation intensity, I_{sat}, of the module varies inversely with τ_u according to [4]:

$$I_{sat}(Wcm^{-2}) = \frac{h\upsilon}{\sigma\tau_u} + 2.5\times10^{-7}p_{Ar}^2 + 2.2\times10^{-6}p_{Kr}(p_{Ar}+p_{Kr}) + 7.7\times10^{-2}p_{F_2} + 2.1W\,\frac{p_{Ar}+1.08p_{Kr}}{p_{Ar}+p_{Kr}}\,\frac{1}{p_{F2}} \qquad (2)$$

where W is the e^--beam pumping density ($MWcm^{-3}$) and gas pressures are expressed in torr. The stimulated emission cross-section of KrF^*, $\sigma = 2.6\times10^{-16}$ cm^2 [3]. I_{sat} is calculated to be 1.5 $MWcm^{-2}$ for the Sprite amplifier operated under present conditions of 2/100/700 torr of F_2/Kr/Ar.

4. Following depletion by a saturating pulse, the gain repumps exponentially to its steady-state value. However, this repumping is characterised by a fast (approximately 50 psec) time constant (due to B-C state mixing) which recovers 25% of the depleted B-state population, and a slower (> 1 nsec) component associated with the collisionally determined upper state lifetime, τ_u [5]. The code now takes account of this in a manner which gives the correct gain recovery between pulses by increasing the saturation fluence by 25% to 2.7 $mJcm^{-2}$.

EXAMPLES OF MODELLING PULSES

Figure 1 shows the effects of ASE depumping on the amplifier small-signal gain. Also shown in Figure 1 are experimentally determined values of ASE-depumped gain, $(g_{ss}-\alpha)$ vs. the pumped small-signal gain, g_o. The RAL code slightly underestimates the effect of ASE depumping on amplifier gain because no account is taken of wall reflections. A curve-fit is obtained by increasing the assumed solid angles of ASE emission by a factor of 1.3. A more realistic treatment of wall-reflected ASE is presently being incorporated into the code based on recent measurements [6].

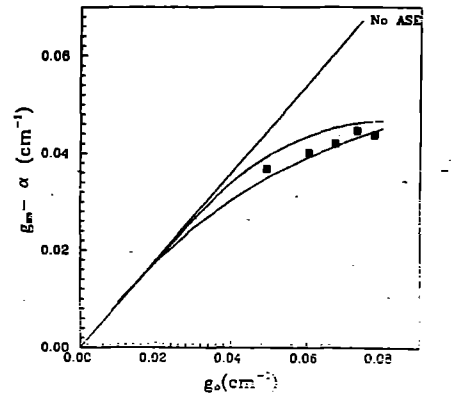

Figure 1: Effect of ASE depumping on residual net SSG, $(g_{ss}-\alpha)$ as a function of pumped SSG, g_o for the Sprite amplifier including experimental results:

Upper trace: No ASE depumping
Middle trace: Code predictions
Lower trace: Code predictions with increased solid angle.

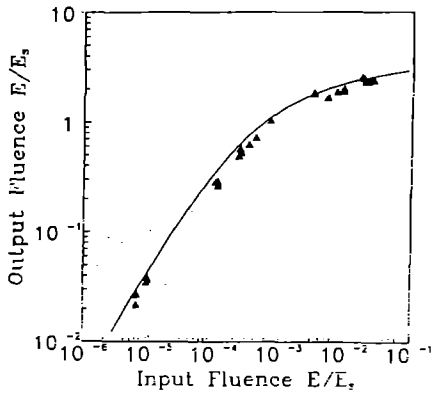

Figure 2: Comparison of code predictions for the input vs. output energy characteristic of 6 ps pulses in the Sprite amplifier with experimental values.

The KrF extraction code has been used to simulate single-pulse amplification in the Sprite amplifier and the results are shown in Fig.2. The predicted results are compared with recent experimental data for conditions of pumped small-signal gain g_o of 7.3%cm^{-1} and a gain-to-loss ratio g_o/α of 9.1, appropriate to a pump rate of 0.58 MWcm^{-3} [1].

The computer model gives results within a few percent of experimental data. The small overestimate in the model is attributable to the overestimate of small-signal gain discussed above.

A system model [2] has been developed which considers gain depletion due to propagation of ASE and pulses through a chain of amplifiers. Picosecond pulse energies are monitored through the system and account is taken of the effect of ASE depumping of the gain due to coupling between amplifier stages. The code has been used to model multiple pulse amplification in the SPRITE laser system. Fig.3 shows good agreement between the output vs. input energy per beam (four pulses) obtained from the code using an increased solid angle of emission with experimental data [7,Section B1] for 32-pulse amplification,

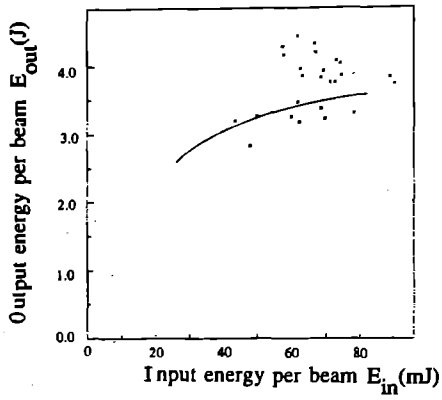

Figure 3: Comparison of code predictions for the input vs. output energy per beam for 32-pulse amplification in the SPRITE laser system with experimental values: t_p = 6 psec, Δt_p = 1 nsec.

The maximum output fluence of the Sprite amplifier is $3.4E_{sat}$ (single-pulse), $2.7E_{sat}$ (8-pulse) and $2.1E_{sat}$ (32-pulse). Table 1 summarises the performance of the preamplifier, Goblin and Sprite in a typical single-pulse amplification experiment. The dominant loss mechanism which limits the system output is two-photon absorption (TPA) which is concentrated in the 8cm diameter lenses in the Sprite beam pipe. These have now been replaced by calcium fluoride which has a lower TPA coefficient.

Table 1. Single pulse amplification in the SPRITE laser system

Amplifier	Output Fluence	
EMG103	$3xE_{sat}$	Saturated on 2nd pass
Goblin	$0.1xE_{sat}$	Unsaturated
Sprite	$2xE_{sat}$	Saturated

Based on the good agreement with experiment of these modelling tests, the code is being used to assess the performance of various staging options for the Supersprite facility as discussed in Section B2.

FUTURE DEVELOPMENTS

Work is underway to incorporate the extraction code described above into a larger code. This model includes electron-beam energy deposition which calculates the pumping rate profile within the amplifier [8]. The information is input to a detailed KrF* kinetics code [9] which calculates the temporal variation of the pumped small-signal gain, g_o (Figure 4), absorption and saturation intensity for arbitrary gas mixtures and pump pulse waveforms. Finally, these calculated quantities are linked to the optical extraction model for multiple-pass amplification. The three subprograms are integrated into one model and run sequentially. Eventually, a fourth submodel may be incorporated to calculate electron temperature for use in the estimation of temperature-dependent kinetic rates.

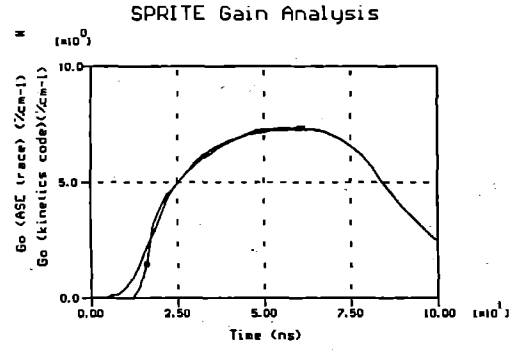

Figure 4. Comparison of KrF* kinetics code prediction of small-signal gain, g_o with value deduced from ASE observations as a function of time.

REFERENCES

1. E. C. Harvey, C. J. Hooker, M. H. Key, A. K. Kidd, J. M. D. Lister, M. J. Shaw and W. T. Leland, "Picosecond gain and saturation measurements in an ASE-depumped KrF laser amplifier", submitted to J. Appl. Phys. (1991).

2. A. K. Kidd, M. H. Key and C. J. Hooker, "A simulation code for the study of multiple pulse amplification in KrF lasers", RAL internal report (1990).

3. P. J. Hay and T. H. Dunning, "The electronic states of KrF", J. Chem. Phys., 66 (3), pp.1306-1316 (1977).

4. M. H. Key, M. J. Shaw, I. N. Ross, P. A. Rodgers and M. C. Gower, "Analysis of high power KrF laser systems", RAL-89-133 (1989).

5. S. Szàtmari and F. P. Schäfer, "Comparitive study of the gain dynamics of XeCl and KrF with subpicosecond resolution", J. Opt. Soc. Am. B., 4 (12), p.1943 (1987).

6. R. K. Gohri and E. C. Harvey, "Foil reflectivity measurements", Annual Report contribution (1991).

7. E. C. Harvey, C. J. Hooker, A. K. Kidd and J. M. D. Lister, "Performance of the Sprite amplifier used in a Raman beam multiplexing configuration", RAL internal report (1990).

8. J. Sangha and A. K. Kidd, "Electron-Beam Energy Deposition Simulations", RAL internal report (1991).

9. A. K. Kidd, "A kinetics code for the study of aperture scaling of KrF lasers", RAL internal report (1990).

RAMAN LASER MODELLING

K. E. Hill*, G. H. C. New* and P. A. Rodgers+

*Imperial College, London.

+Rutherford Appleton Laboratory (present address: IOP Publishing, Bristol).

Introduction

The radiation and material excitation fields for transient Raman amplification with collinear beams, when expressed in the slowly varying envelope approximation, satisfy the equations

$$[d/dz+(1/v_p)d/dt]A_p = -qA_s\cos\phi$$
$$[d/dz+(1/v_s)d/dt]A_s = \omega_p/\omega_s\ qA_p\cos\phi$$
$$[1/T_2+d/dt]q = C_{12}A_sA_p\cos\phi$$

$$[d/dz+(1/v_p)d/dt]\phi_p = -qA_s/A_p\sin\phi$$
$$[d/dz+(1/v_s)d/dt]\phi_s = -\omega_p/\omega_s\ qA_p/A_s\sin\phi$$
$$[1/T_2+d/dt]\phi_q = -C_{12}\ A_sA_p/q\ \sin\phi$$

where $\phi = \phi_q + \phi_s - \phi_p$.

$E_p = A_p\exp(-i\phi_p)$ and $E_s = A_s\exp(-i\phi_s)$ are the pump and Stokes complex field envelopes at frequencies ω_p and ω_s. These two fields are coupled through a material excitation, or phonon, $Q = q\exp(-i\phi_q)$ (frequency $\omega_p - \omega_s$). The timescale of the interaction is set by T_2 (27ps in methane) and this together with C_{12} determines the strength of the interaction. The 1-D stimulated Raman scattering (SRS) code, previously reported [1], can be used to solve these equations for noisy non-transform limited pulses. The code has now been modified to include the effects of angularly separated beams.

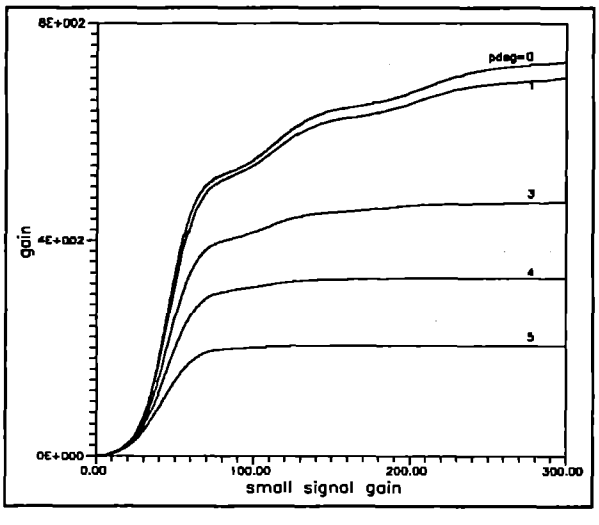

Figure 1: Gain vs small signal gain for 10ps transform limited Gaussian pulses with initial delay 2ps. T2=27ps,wp/ws=1.08, Ip/Is=10000 at input. Pump angle (pdeg) in degrees is shown.

Dispersion

Raman amplifiers pumped by angularly separated pump beams with off-axis angles give rise to an effective dispersion in the amplifier since the pump and Stokes velocities along the axis, v_p and v_s, are different. The effect of dispersion in the amplifier is the introduction of a relative dephasing of the pump and Stokes waves in a distance [2]

$$l_d = c/(\Delta\omega(1-\cos\theta))$$

where θ is the pump angle to the guide axis and $\Delta\omega$ is the linewidth of the pump. The simplest way of modelling the interaction of two beams which cross at some non-zero angle is to introduce dispersion into the existing 1-D code by setting $v_p > v_s$. This is an approximation since it does not rigorously take into account other 2-D effects due to the angular separation of the beams such as the coupling of temporal and spatial incoherence, although it will give a better understanding of effects resulting from pulse walkthrough.

Figure 1 shows the energy gain vs small signal gain for 10ps transform limited Gaussian pulses with increasing dispersion. As the angle between the beams is increased the gain is reduced. This illustrates the effect of pulse walkthrough because as the angle is increased the effective interaction distance becomes the dephasing distance when this is less than the amplifier length (1m). Once the pulses have walked through each other the interaction and amplification essentially stop.

Noise And The Influence Of Phase Pulling

Phase pulling of a Stokes wave in transient SRS occurs when the temporal phase variations within the Stokes pulse are not correlated with those in the pump pulse and when the initial Stokes pulse is weak compared to the pump. Under these conditions the temporal phase variations of the Stokes pulse change until they match those of the pump pulse [3] ($\phi = 0$ in the equations above). In this condition, the phonon wave (which depends upon the correlation of the pump and Stokes pulses) can grow and the gain is enhanced. Before phase-locking is established the gain along the amplifier will (on average) be

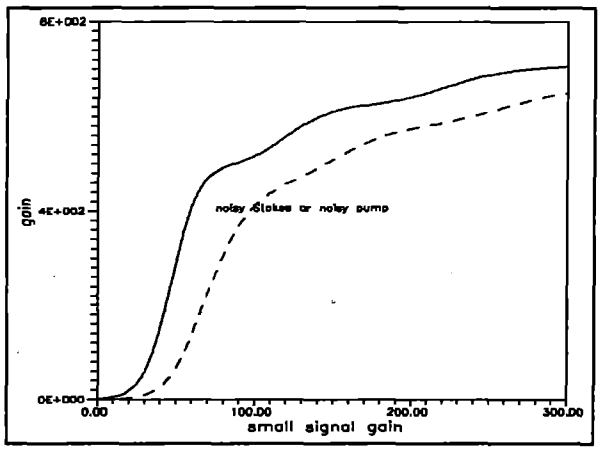

Figure 2: pdeg=0. Gain vs small signal gain for the case of transform limited pulses (solid) and noisy Stokes or noisy pump pulses (dashed) with tc=1ps. Parameters as in figure 1.

less for noisy pulses than for transform limited pulses of the same average energy. This is because the timescale of the Raman process has effectively been reduced from T_2 to the timescale of the noise fluctuations in the pulse and the strength of the interaction is correspondingly less.

In figure 2 gain vs small-signal-gain curves are plotted for the case of no dispersion. The parameters are the same as in figure 1 but here the dashed curves (2 superimposed) represent the gain expected in the presence of phase noise on either the pump or the Stokes pulse. The noisy pulses are generated in the code by the method described in [1] which produces pulses with amplitude and phase random fluctuations on the timescale t_c = 1ps (this means that the 10ps pulses are approximately ten times transform limited) and then by renormalising the pulses so that the amplitude profiles are smooth and only the phase is noisy. The dashed curves represent the average of a large number of random shots (the shot to shot variations are large) but the resultant curves are superimposed. This means that it does not matter whether the phase noise is on the pump or the

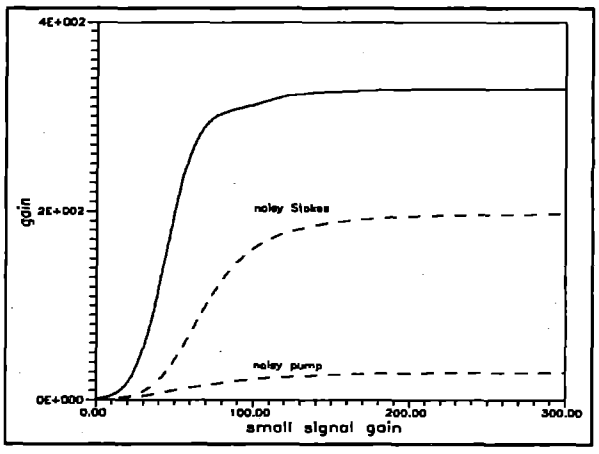

Figure 3: As in figure 2, but here pdeg=4

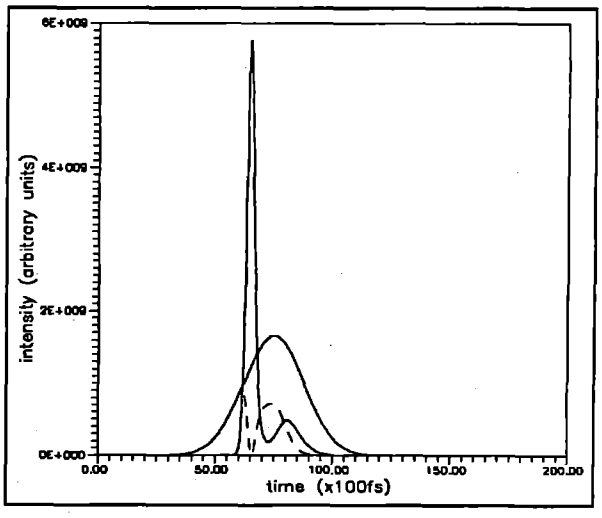

Figure 4: The initial 30ps Gaussian pump pulse and the output pump (dashed) and Stokes pulses for a small signal gain of 100. Input is a 3ps Stokes with energy of pump 3000 times energy of Stokes.

Stokes pulse since the effect of phase-locking is the same.

In figure 3 dispersion has been introduced into the problem by assuming an angle of 4 degrees between the two beams. In this case it matters which pulse the noise is on. The effect of non-collinear propagation is to reduce the gain. This is due both to the reduced interaction length because of the pulse walkthrough and also to the reduction in the degree of phase-locking which is established. Figure 3 suggests that in the presence of dispersion phase-locking is less efficient when the noisy phase is on the pump than when it is on the Stokes.

Chirped Pulse Amplification

If the initial pump pulse is much broader than the initial Stokes pulse, the dispersion can be advantageous. For, by timing the pulses so that the seeded Stokes pulse can be amplified as it passes through the pump pulse can lead to high energy conversion efficiencies from a long pump pulse into a short, intense Stokes pulse (figure4). The code is currently being used to investigate chirped pulse amplification in the context of experimental work at RAL.

References

[1]: P. A. Rodgers, *Annual Report to the Laser Facility Committee* Rutherford Appleton Laboratory Report RAL-90-026, p83, (1990).

[2]: J. R. M. Barr, N. J. Everall, C. J. Hooker, J. P. Partanen and M. J. Shaw, Proc. of SPIE **874**, (1988).

[3]: M. D. Duncan, R. Mahon, L. L. Tankersley, G. Hilfer and J. Reintjes, J. Opt. Soc. Am **B7**, 202, (1990).

CHIRPED PULSE AMPLIFICATION FOR KrF

J R Houliston[1], M H Key[1] and I N Ross

Rutherford Appleton Laboratory
[1]Also at University of Oxford

The application of CPA to KrF laser systems allowing high energy extraction in sub-picosecond pulses has been analysed and a theoretical characterisation of a diffraction grating based Treacy[1] stretcher/compressor system has been carried out.

Saturated amplification of sub-picosecond pulses (to several mJ/cm^2) can lead to peak intensities which exceed the threshold for self-focusing and two-photon absorption (TPA) in amplifier gas cell windows (eg at 0.5 mJ/cm^2 in a 100 fs pulse TPA depletes 30% of pulse energy in the 2 cm thick SiO_2 Sprite KrF amplifier output window and the B-integral nonlinear phase change is approximately $\pi/4$)[2].

It is proposed to avoid these deleterious nonlinear effects by stretching sub-picosecond pulses to over 5 ps prior to amplification. After saturated amplification (to ≈ 6 mJ/cm^2) the pulses are recompressed to their initial duration. Implementation of this technique on the 27 cm diameter Sprite amplifier using 100 fs pulses and allowing for 40% energy loss in the compression stage would produce 20 TW output power which if diffraction limited would have a brightness of 7.10^{21} W/cm^2/sterad.

The stretcher consists of a pair of identical antiparallel diffraction gratings placed symmetrically outside but within a focal length of two identical lenses in a unit magnification telescope arrangement (figure 1). The compressor consists of a pair of parallel identical diffraction gratings.

Fig 1 Pulse Stretching-Compression Setup Using Diffraction Gratings

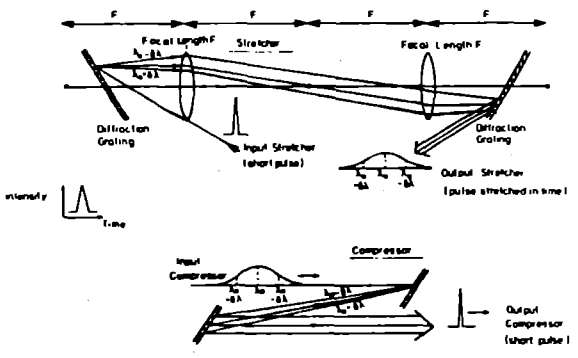

Geometrical analysis of optical path length in the system gives a theoretical characterisation of stretching and recompression performance. Equation 1 gives temporal stretching, $\Delta\tau$, in terms of the perpendicular distance between a stretcher grating and the outer focal point of its neighbouring lens ($l_{stretch}$), the grating diffraction order (m), the grating line density (a), the pulse wavelength (λ), the pulse bandwidth ($\Delta\lambda$) and the angle of diffraction (θ_d).

$$\Delta\tau = \frac{1}{c} \times \frac{2 l_{stretch} \times m^2 \times a^2 \times \lambda \times \Delta\lambda}{\cos^3\theta_d} \qquad (1)$$

Figure 2 shows logarithmic plots of stretching in ps of a 165 fs bandwidth limited 248.5 nm pulse per unit beam path length in the compressor as a function of angle of incidence for different density gratings. The gratings are used in the first order with incident and diffracted beams on opposite sides of the grating normal. Stretching of 10 ps/m can be obtained by using 2000 l/mm gratings with angle of diffraction approaching 80° or by using very high density holographic gratings (over 4000 l/mm) in near Littrow configuration.

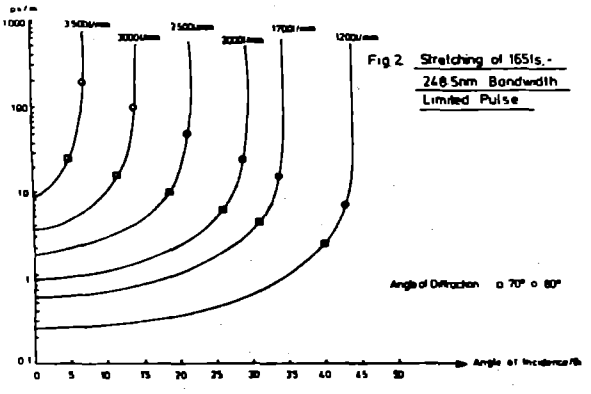

The conditions for perfect recompression of a stretched pulse to its initial duration have been established. Stretcher and compressor gratings must have equal line density, the angle of incidence of the input beam on the first grating of both systems must be identical and the perpendicular distance between the compressor gratings must equal twice the perpendicular distance between a stretcher grating and the outer focal point of its neighbouring lens. Imperfect matching of the stretcher and compressor results in a low pulse contrast ratio which at high intensities leads to pre-pulse plasma formation on target.

Beam diffraction destroys the wavelength-time relationship of a stretched pulse and under perfect recompression conditions recompression is only possible to within the fidelity factor, F, of the initial pulse duration (in equation 2, N is the number of lines illuminated on the grating by the incident beam).

$$F = \left(1 + \frac{\lambda}{N \times \Delta\lambda}\right)^2 \qquad (2)$$

The ability to control final pulse temporal profile by spectral filtering of the chirped pulse at the Fourier plane of the stretcher has been analysed. Section C 3.3 in this report presents novel auto-aligning grating geometries and reports on an extended experimental programme that is being carried out to verify the theory and to gain experimental confidence in the scheme in view of implementing CPA on existing KrF laser systems.

REFERENCES

1. E B Treacy — IEEE J. Quant. Electr. QE-5 (1969) 454.
2. M H Key et al. — Analysis of High Power KrF Laser Systems, RAL Report 89-133, December 1989.

REFLECTIVITY OF STEEP-GRADIENT PLASMAS IN INTENSE FEMTOSECOND LASER PULSES

S. C. Rae and K. Burnett

Clarendon Laboratory, Department of Physics, University of Oxford, Parks Road, Oxford OX1 3PU

One use for the Sprite KrF laser, which as yet has not been fully exploited, is its use as an amplifier for intense femtosecond laser pulses. Plasmas formed by focusing such intense laser pulses onto solid targets are of great interest, and are fundamentally different from long-pulse plasmas produced in, for example, inertial confinement fusion experiments. Apart from possible applications as pulsed x-ray sources and x-ray lasers, femtosecond-pulse plasmas also provide an opportunity to study hot, solid-density material, and to investigate a range of nonlinear, high-field effects.

In a femtosecond-pulse plasma, hydrodynamic expansion is limited, and the density gradient scale length is typically less than a laser wavelength. The lack of a large underdense region means that parametric laser-plasma coupling processes (such as stimulated Raman and Brillouin scattering) are greatly reduced. Absorption of laser light occurs mainly through electron-ion collisions (inverse bremsstrahlung) or resonance absorption. The intense electric field drives various nonlinear processes, such as modifications to the electron-ion collision rate and field-induced ionization.

The critical parameter for high-field effects in collisional absorption is the ratio of the oscillation velocity of a free electron in the field, $v_{osc} = eE_0/m\omega_0$, to the thermal velocity, $v_{th} = (T_e/m)^{1/2}$. At intensities such that $v_{osc} \gtrsim v_{th}$, collisional absorption is reduced below its low-field value. This nonlinear process has been studied extensively in the past, but its effect on the reflectivity of a given plasma is not immediately obvious, since it depends strongly on the penetration depth.

We have solved the wave equation for laser light incident on a steep-gradient plasma, with the inclusion of a nonlinear electron-ion collision rate, and incorporating spatial dispersion and wavebreaking effects. Under certain conditions the reflectivity shows a strong intensity-dependence.

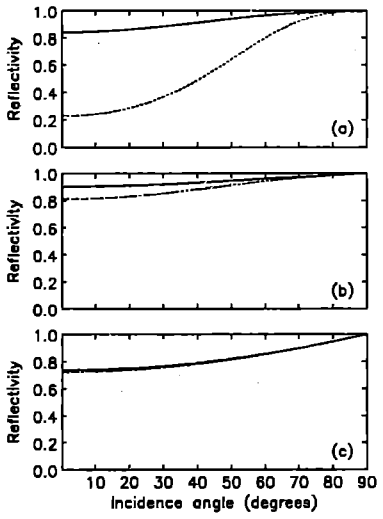

Figure 1: Angular dependence of reflectivity for s-polarised light and scale lengths (a) $L/\lambda_0 = 1.0$, (b) $L/\lambda_0 = 0.1$, and (c) $L/\lambda_0 = 0.01$. Curves shown for 10^{14} W/cm^2 (broken line) and 10^{17} W/cm^2 (solid line).

Figure 2: As in Fig. 1, but for p-polarised light.

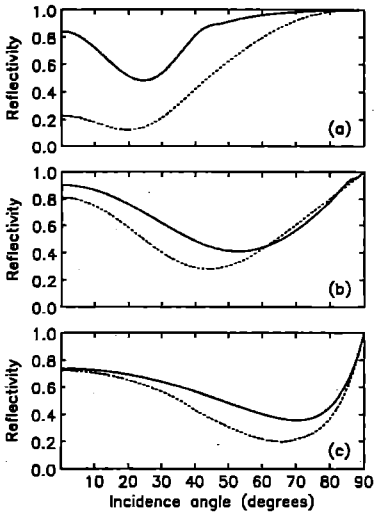

We have calculated the reflectivity of a fixed, exponential-profile plasma, assuming only collisional and resonance absorption, by numerically solving the wave equation using a matrix method. We use a dielectric function,

$$\epsilon = 1 - \frac{n_e/n_{cr}}{1 + i\nu/\omega_0} . \qquad (1)$$

The collision rate ν is calculated from a Spitzer-type expression,

$$\nu = \frac{4\sqrt{2\pi}}{3} \frac{Zn_e e^4 \ln\Lambda}{m^{1/2}T_e^{3/2}} , \qquad (2)$$

with a reduction factor due to the oscillatory motion of the electrons,

$$F = \left(1 + \langle v_{osc}^2 \rangle / 3v_{th}^2\right)^{-3/2} . \qquad (3)$$

In the case of p-polarised light, the resonantly-driven plasma wave is limited in amplitude by the onset of wavebreaking.

In order to show the effect of the nonlinearity, we show in Fig. 1 and Fig. 2 the calculated reflectivity as a function of the angle of incidence for two different intensities. At 10^{14} W/cm^2 the nonlinearity has little effect on the calculated reflectivity, but at higher intensities the reflectivity is greater than that predicted by a simple linear model. The discrepancy is small for a step-like plasma (with scale length $L \sim 0.01\,\lambda_0$), but increases for longer scale lengths ($L \sim \lambda_0$). With p-polarized light, the angular dependence becomes sharper at higher intensities, and there is a narrow resonance region in the plasma around the critical density where the local electric field can reach many times the incident field. This suggests that even with femtosecond pulses and steep plasma gradients, wavebreaking can lead to the production of very hot electrons. The full investigation of these phenomena would require a time-dependent dynamical treatment.

KrF PUMPED RAMAN LASERS AS X-RAY LASER DRIVERS

M H Key+, E Harvey, G J Hirst, C J Hooker, J Jacoby*, R Kodama**,
J Lister, P Norreys, P Rodgers, S J Rose, I N Ross, M J Shaw,
G Tallents@, N Tragin*,

SERC Rutherford Appleton Laboratory
+Also at Department of Physics, University of Oxford
*CEC visiting research associate
**On leave from Osaka University
@University of Essex

1. Introduction

Recent progress in developing KrF laser pumped Raman lasers has shown their potential as X-ray laser drivers. The combination of short wavelength (268 nm) with low beam divergence and high beam intensity gives the possibility of very high focused intensity in very narrow line foci. An 8 cm x 8 cm beam combining Raman amplifier in the Sprite system has generated 0.4 TW, 12 ps pulses with 20 μrad beam divergence. A 10 μm wide line focus has been produced and plasmas from a NaF target have been studied at irradiances up to 3 x 10^{14} W cm^{-2}. Numerical simulations suggest that the Sprite system should be able to produce high recombination gain in F IX at 8.1 nm and that larger scale KrF pumped Raman lasers which are being considered for future UK and European facilities would be ideal drivers for Mg XII at 4.5 nm.

2. Raman Laser as an X-ray Laser Driver

The potential for using the 0.4 TW Raman beam as a recombination laser driver has been assessed from simulations of the type discussed in Section B4 for slab targets.

Sprite Raman Beam as a Recombination Laser Driver 0.4 TW 15 μm focus				
C VI	5 x 10^{13}	21	130	6.0
F IX	3.3x10^{14}	24	21	0.9
Mg XII	1.7x10^{15}	11	2	0.2
	I_{opt} Wcm^{-2}	g_{peak} cm^{-1}	gl	l cm

Table 1

Table 1 shows results computed for C VI, F IX and Mg XII which indicate that F IX is particularly attractive as a test case to be driven by the present Raman beam. The projected gl value for this system is high but is computed assuming a 0.2 multiplier on the Sobolev opacity(5). A more conservative assessment (ε = 1) would reduce this gain by a factor of 2-3 . In addition the average gain should be reduced by a factor of about 2 to take account of inhomogeneities in the irradiation along the line focus(5). Due assessment would also be needed of the effect of spatial integration on a temporally resolved measurement which suggests(5) that minimum gl values for secure observation of gain should exceed 5. All these conditions are seen to be met for the Raman beam with F IX. Optimisation of target irradiation for 12 psec pulses at λ = 268 nm is shown in Figure 1.

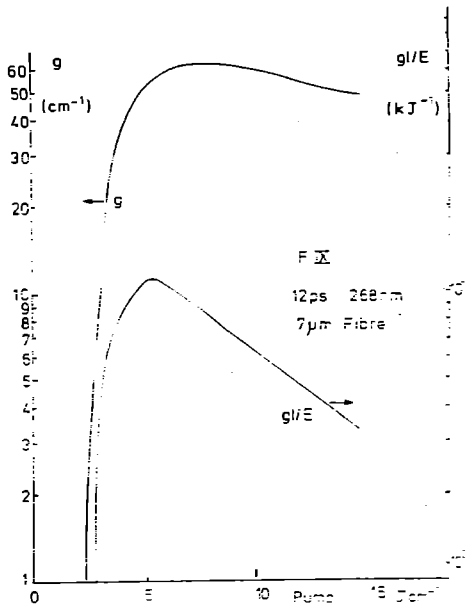

Fig 1 Ordinate gain g and energy efficiency producing gain gl/E assuming opacity at 0.2 of classical for F IX recombination. Abscissa - absorbed energy per unit length on a 7 μm diameter fibre.

Fibre targets of 7 μm diameter have been considered here in anticipation of one sided irradiation of LiF coated C fibres. The calculation gives the total energy per cm of fibre. The modelling is indicative of the required energy density on the target surface which is found to be almost independent of pulse length and target radius for small changes in other parameters. The total energy required can be assessed from Figure 1 with due regard to the fraction of the surface of an ideal cylinder which is irradiated.

The case of Mg XII shown in Table 1 is of particular interest for the future. The optimised driving intensity of 1.7 x 10^{15} W cm^{-2} can be produced only over a 2 mm length with the existing Raman beam. The Raman beam is however scalable in power. Firstly, multiple beam extraction from the Raman amplifier by angular multiplexing is possible and 4-beam operation has recently been demonstrated(6). Secondly, the beam aperture is scalable with appropriate scaling of the aperture of the pumping KrF laser. Designs for a Supersprite facility have Raman beam power up to 100 TW.

Brightness of the beam is an essential consideration for driving of recombination lasers. It is readily shown that for an intensity I_b and divergence $d\theta$ in the Raman beam the required diameter D of the Raman amplifier is given by $D = (I_l/I_b)ld\theta$ where I_l is the intensity in the laser target and l its length, so that where higher intensity I_l is required to drive the X-ray laser target of length l, higher power and beam size is required in the Raman beam. The width of the line focus is typically by 2.5 $Dd\theta$ for a system with f/2.5 focusing. If this width becomes larger than the lateral transport determined plasma spread which, as shown earlier, was 20 μm for irradiation by 12 ps pulse at 5 x 10^{14} W cm^{-2} (and increases for irradiation at higher intensity), then there are diminishing returns in increasing the power of the pump laser and better results would be obtained by increasing its brightness.

This consideration means that the Raman laser as a driver has important advantages over a glass laser. Typically the brightness of a short wavelength glass laser beam is 7 x 10^{17} W cm^{-2} $sterad^{-1}$ compared to the already demonstrated brightness of the Sprite Raman beam is 2 x 10^{19} W cm^{-2} $sterad^{-1}$ and there seems no reason why the brightness of the Raman beam should not be increased closer to the diffraction limit in view of the fact that its quality is limited only by the quality of the injected low power Stokes beam which converts pump power from beams of arbitrary quality into high quality Stokes output.

It may be concluded therefore that the KrF pumped Raman laser has important potential as a driver for recombination X-ray lasers in the future.

3. References

1. I N Ross et al, Opt Comm 78 263 (1990)
2. P Simon et al, Opt Lett 12 1207 (1989).
3. G J Tallents et al, Proc SPIE 138, 1229 (1990).
4. M H Key in Handbook of Plasma Phys 3, S Witkowski, P M Rubenchick Eds. Publ Elsevier North Holland (in press).
5. M H Key, N Tragin, S J Rose, ibid.
6. C J Hooker et al, Proc Int Conf on Lasers 90, Publ. Soc Opt Quant Electr.
7. Report and Reference Papers of the Scientific and Technical Working Group for the European Laser Facility, ELF, Feb 1990.

SCALING OF STAGNATION-FREE IMPLOSIONS TO A MULTI-KILOJOULE KrF LASER

P.A.Norreys, M.H.Key,
Central Laser Facility, Rutherford Appleton Laboratory,
Chilton, Didcot, Oxon., OX11 0QX, UK.

1. Introduction

The investigation of the ablatively driven, stagnation free implosion mode in direct drive inertial confinement fusion research has led to record yields of 1×10^{13} neutrons at the Institute of Laser Engineering, Osaka University[1] (13 kJ, 0.53 μm) and 2×10^{13} neutrons at the Lawrence Livermore National Laboratory[2](20 kJ, 0.35 μm). Investigations of this scheme have also been reported from the Laboratory of Laser Energetics, University of Rochester[3] and from the SERC Central Laser Facility at the Rutherford Appleton Laboratory[4]. All these studies have used glass lasers of rather high brightness but less good uniformity of focused intensity. We are interested in the implosion performance that might be obtained with a KrF laser operating with very smooth but less bright beams produced with echelon-free ISI.

In low aspect ratio, ablatively driven implosions, neutron production is ideally concentrated in two phases - the initial shock wave reflection the centre and from the final adiabatic phase of the implosion. High densities can be obtained during the adiabatic (or stagnation) phase if the driving laser pulse is shaped to reduce shock wave preheating of the thermonuclear fuel. The Rayleigh-Taylor instability with a high mode number may occur during the latter phase causing fuel-shell mixing that both lowers the plasma temperature and disrupts the symmetry of the implosion, reducing the compressed density.

To avoid this, neutron production can be concentrated in the initial shock reflection from the centre and the adiabatic (or stagnation) phase eliminated. Strictly speaking, this can only occur when the static pressure of the fuel is greater than the dynamical pressure of the pusher. This is the stagnation-free implosion mode.

In this mode, a thin walled shell (or pusher) is a driven by intense laser radiation. Most of the shell is ablated during the implosion and, as the shell is accelerated over a large distance, it acquires a high implosion velocity. By matching the leading edge of the Gaussian laser pulse to the maximum acceleration of the shell, the shock waves generated at different times by the accelerating shell collapse simultaneously at the centre, creating thermonuclear fusion in a stagnation-free implosion.

The SERC is investigating the potential of a multi-kilojoule UV KrF gas laser 'SUPERSPRITE'[5] to replace of the present 1 kJ 0.53 μm glass laser facility VULCAN. It is therefore interesting to investigate the scaling of the fusion yield in the stagnation-free implosion mode with laser wavelength and intensity.

2. Dynamics of Stagnation-Free Implosions.

The one dimensional Lagrangian hydrodynamic code MEDUSA[6][7] was used to investigate the dynamics of stagnation-free implosions. The MEDUSA code includes a calculation of the radiation transport by the multi-group method and ionisation by an average ion model. The heat flow is described by the classical flux-limited Spitzer-Harm electron thermal conductivity.

To check the accuracy of the MEDUSA code, simulations were performed using the experimental conditions of the high neutron yield experiments at ILE, Osaka University[1]. 13 kJ of laser energy (λ = 0.53 μm) was incident on a glass microballoon of radius 613.5 μm (shell thickness 1.31 μm) in a 1.0 nsec Gaussian pulse. The absorbed laser energy was 75% of the incident energy. The observed yield was 9.8×10^{12} neutrons.

Figure 1 shows the radius-time diagram for this implosion. The laser pulse peaked at t = 1.20 nsec. The heat flux limit has to be chosen to

match the measured implosion time. This is important because the neutron yield is critically dependent on the temperature of the plasma and this is a strong function of the implosion velocity (ie T_i a V^2). In these simulations the best match was given by a flux limit of f=0.03.

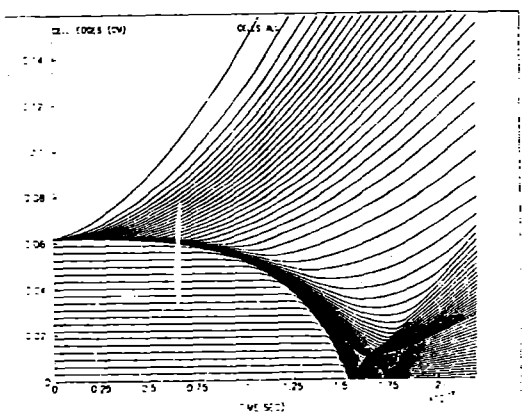

Figure 1. The implosion trajectory of the simulation for all zones and with a heat flux limit of f=0.03.

Figure 2. shows the trajectory of the 20 zones in the fuel in more detail. At the beginning of the stagnation phase, the integrated neutron yield was 7.9×10^{12} at t=1.63 nsec and rose to 1.7×10^{13} when the shock reconverged at the centre at t=1.74 nsec. The explosive growth of the Rayleigh-Taylor instability at stagnation quenches the burn of the fuel very rapidly. This observation is also in agreement with the simulation results of Osaka University.

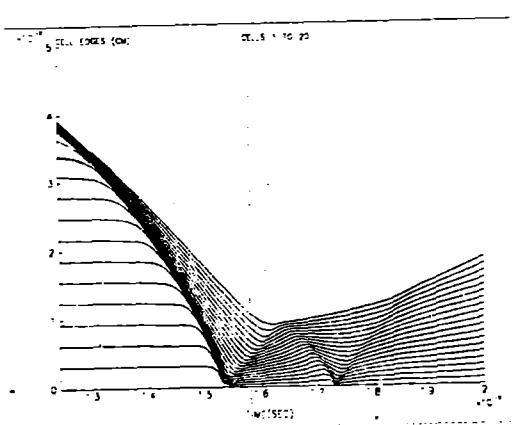

Figure 2. The implosion trajectory of the fuel.

Figure 3 shows the experimentally determined neutron yield as a function of aspect ratio from ILE, Osaka University[1]. The integrated neutron yield from the MEDUSA simulations are also plotted. It can be seen that the simulated yields are at least a factor of two greater than the observed neutron yield and are in reasonable agreement with the simulated results from the ILESTA-BG hydrodynamic code.

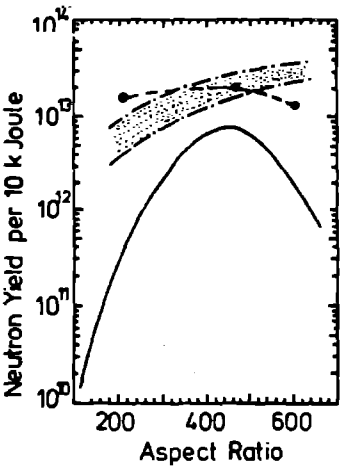

Figure 3. Neutron yields from high aspect ratio target implosions from ILE, Osaka University (solid line); simulated yields from the MEDUSA code (dotted line); simulated yields from the ILESTA-BG code (shaded area).

This good agreement between experiment and numerical modelling means that the reasonable confidence can be given to numerical scaling stagnation-free implosions.

3. Example of Scaling to 3.5 kJ KrF Laser

It has recently been demonstrated on the KrF laser SPRITE that echelon-free Induced Spatial Incoherence can be introduced into the laser chain which allows a highly uniform beam profile on target to be achieved[8][9]. However, this method of ISI production means that the beam divergence is relatively large (~ 200 μrad) and consequently the brightness of the laser beam on target is smaller than for a glass laser.

In the following simulations, there were two different irradiances on target, 2.5×10^{13} Wcm^{-2} and 1.0×10^{14} Wcm^{-2} (corresponding to two different beam divergences of the echelon-free ISI system). The incident laser energy was 2.5 kJ (allowing for the losses in the focussing optics) in a 1.0 nsec Gaussian pulse. It was

assumed that tangential focussing would be employed so that the absorbed laser energy was estimated to be 90%. The radii of the glass microballoon was 750 μm and 446 μm for the lower and higher irradiances respectively. The DT gas pressure was set at 6.0 atmospheres for both simulation runs.

The flux limit for these simulations was set a f=0.1, because the temperature of the plasma is smaller for UV laser irradiation and the temperature gradients in the plasma are not as steep.

Figure (4) shows the neutron yields at the beginning of the stagnation phase for these two different irradiances. These have been plotted because the experimental yields discussed in section 2 were equal to, or greater than, the simulated yields at this point in time.

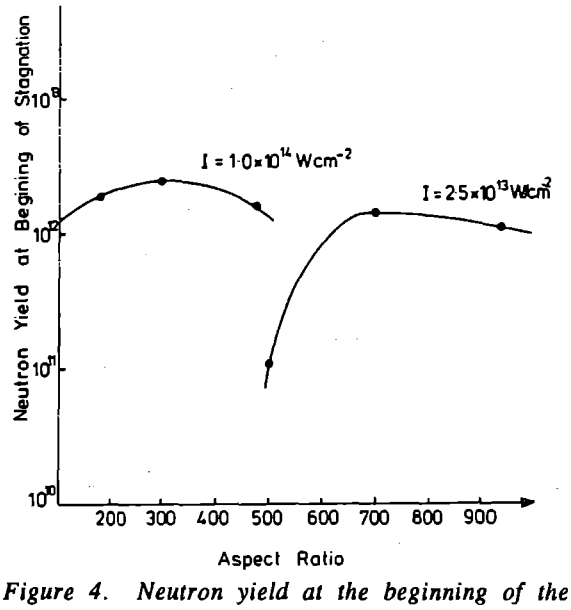

Figure 4. Neutron yield at the beginning of the stagnation phase for targets of diameters 750 and 446 μm and irradiances $2.5x10^{13}$ Wcm^{-2} and $1.0x10^{14}Wcm^{-2}$ respectively.

It can be seen for the lower irradiance case, there is an order of magnitude increase in neutron yield at an aspect ratio of ~ 600. This is due to shell burn-through when the laser is directly heating the fuel material. It is unlikely that this yield can be achieved in practice because of the poor modelling of electron thermal conduction in the code. It is equally unlikely that such large targets with very high aspect ratios can be easily fabricated. It is likely that for lower irradiances, a maximum yield of 10^{11} will possible.

For the higher irradiance case, the peak neutron yield is $2.5x10^{12}$. This occurs at an aspect ratio of 300 and no shell burn-through was noted in these simulations. Of course, the absorption of laser energy will need to be measured carefully and detailed comparison with experiment will be required.

8. References

(1) H.Takabe, M.Yamanaka, K.Mima, C.Yamanaka, H.Azechi, N.Miyanaga, M.Nakatsuka, T.Jitsuno, T.Norimatsu, M.Takagi, H.Nishimura, M.Nakai, T.Yabe, T.Sasaki, K.Yoshida, K.Nishihara, Y.Kato, Y.Izawa, T.Yamanaka, S.Nakai, Phys. Fluids 31(10), 2885 (1988)

(2) E.M.Campbell, J.T.Hunt, E.S.Bliss, D.R.Speck, R.P.Drake, Rev. Sci. Instrum. 57, 2101 (1986)

(3) M.C.Richardson, P.W.McKenty, R.L.Keck, F.J.Marshall, D.M.Roback, C.P.Verdon, R.L.McCrory, J.M.Soures, S.M.Lane, Phys. Rev. Lett. 56, 2048 (1986).

(4) M.H.Key, M.Yamanaka, A.J.Cole, M.Grande, P.Rumsby, M J Lamb, S Saadat, E Robertson, A P Fews, P A Norreys, C.Yamanaka, H.Takabe, T.Norimatsu, Y.Kato, S.Nakai, Optics Commun. 21, 184 (1989).

(5) M.H.Key, M.J.Shaw, I.N.Ross, P.A.Rodgers, M.Gower, 'Analysis of high power KrF laser systems' Rutherford Appleton Laboratory report RAL-89-133 (1989)

(6) J.P.Christiansen, D.E.T.F.Ashby, K.V.Roberts Computer Phys. Commun. 7, 271 (1974).

(7) P.A.Rodgers, A.M.Rogoyski, S.J.Rose, 'MED101: a laser plasma simulation code - user guide', Rutherford Appleton Laboratory report RAL-89-127 (1989)

(8) J.M.Lister et al Optics Commun. (in press)

(9) R.Lemhburg, J.Goldhar Fusion Technology 11, 532 (1987)

SPRITE SHOT STATISTICS

M J Shaw

Rutherford Appleton Laboratory

INTRODUCTION

The total number of shots fired on the Sprite system during the year ending March '91 was 2049, of these, 754 were target shots. In this year, shot number 10,000 of the Sprite system was celebrated. The shots fired per month are shown in Fig.1.

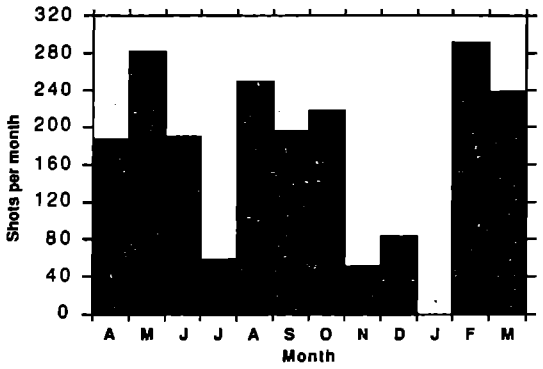

Fig. 1 Sprite shot record, 1990/91

TARGET SHOOTING

Three periods of target shooting have taken place. In May/June 260 shots were delivered to target for the IC group using a single Raman beam at 268 nm. The oscillator used was a DFDL and the nominal pulse length was 15 ps. The average laser energy was 1.3 J.

In August/September 160 shots were delivered to target for the RAL/Essex group using the Raman beam. In this case the oscillator was changed to a cavity stabilised scheme and the pulse energy was increased to 3.0 J on average. Less than half this energy was available to target due to two-photon losses in the silica target chamber optics. The pulse length was reduced to 12ps. Measurements were made of spot focus and line focus sizes. Irradiances of 3×10^{17} W/cm^2 for the spot focus and 5×10^{14} W/cm^2 in a line of 8mm length were obtained.

Target shooting took place in February/March for the IC group. A total of 293 target shots were delivered in 4 weeks. The pulse duration was again 12 ps with the an average laser energy of 2. 8 J. Energy delivery to target was substantially improved (to T = 60%) by the use of CaF_2 target chamber windows and an off-axis parabolic focussing mirror. The far field monitor (see Fig. 2) gave an equivalent spot size of 6 μm FWHM which would indicate an intensity of 5×10^{17} W / cm^2 on target. A verification experiment shot 90 % of the laser energy through a 10 μm pinhole.

LASER CHARACTERISATION

During September and October extensive experiments were undertaken to characterise the Sprite amplifier in the single (ps) pulse regime. The gain and gain-to-loss ratio have been measured and found to be in agreement with code calculations. ASE was found to be of major importance in determining the gain.

During November a few simple experiments were undertaken to demonstrate the feasibility of using induced spatial incoherence (ISI) on Sprite. Considerable beam smoothing was obtained.

In December, the Sprite oscillator was reconfigured to produce 4 pulses of 10 ps duration on each beamline, a total of 32 pulses for the 8 lines. These pulses were amplified in Goblin and Sprite to give a total of 34 J available to pump the final Raman amplifier.

Results from these laser characterisation experiments are presented elsewhere in this report.

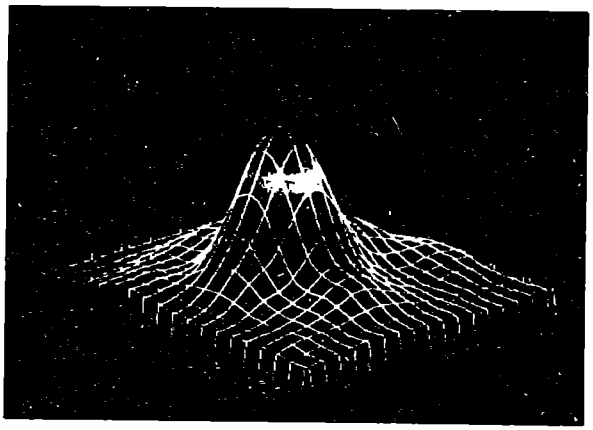

Fig. 2 Far-field beam profile of the Sprite Raman beam. The FWHM is 20 μRad corresponding to 6 μm on target.

Sprite System Engineering

A R Damerell and C J Hooker

Rutherford Appleton Laboratory

A number of changes have been made to the Sprite system in the past year. These include changes to the e-beam machines, the optical layout in the multiplexer room, a new control room and some more automated control and safety features.

Analysis of Sprite performance data led to the belief that ASE reflected back into the gain region from the output window was causing a serious reduction in the available output energy. In order to overcome this, a new angled window mount was designed, which holds the output window at an angle of 22.5 degrees to the axis of the Sprite cell. The mount is spaced away from the gain region by 40 cm, and the inside of the spacer is grooved to trap the reflected light and avoid feeding it back into the amplifier. This has been extremely successful, and Sprite's performance now approaches that expected from modelling.

The lifetime of Goblin's foils has been a problem during the year; typically a foil has survived for between 200 and 500 shots before failing. This is in contrast to Sprite's foils, which have lifetimes measured in thousands of shots. All the failures have occurred in the same manner, where a small dimple has been found in the foil in the middle of the hibachi apertures, with a pinhole puncture at its very centre. It may be that vibrations in the foil are weakening it, leading to failure. A new hibachi foil support has been designed, with elongated apertures instead of nearly square ones, which it is hoped will solve the problem by reducing the foil vibrations.

The location formerly occupied by the Sprite workshop in R2 has been taken over to make a new, enlarged, control room for Sprite. This has greatly increased the area available, and resulted in an improved working environment for the operations crew. The loading bay has been partitioned off, and the corridor beside the multiplexer room is now used as a display area, with windows to allow visitors to see into the multiplexer room itself.

The Raman multiplexing experiment, which is described more fully in section B1.5, required a certain amount of engineering, principally a new set of vacuum spatial filters and supports for the beam-splitting optics, the timing delay adjustments for the individual Stokes beams and the input lenses to RA3.

A computer-controlled interlock system has been designed for the laser and target areas in the Sprite complex, and is currently being installed. This will improve on the old system by providing more flexible but in many ways more rigorous safety checking to ensure that unauthorised people cannot operate hazardous devices or enter rooms where hazards exist. A display in the control room will show the operator the state of the system, and individual displays outside doors and inside areas will indicate what hazards are present and what precautions to take before entering. It is expected that similar systems will be implemented in other parts of the CLF in due course, and the program and hardware have been designed with with this in view.

Another aspect of Sprite shortly to come under computer control is the pressurising of the spark gaps in the pulsed-power machines. A system of solenoid valves and gas pressure sensors will be controlled from a PC, and the program will flush and fill the gaps to preset pressures. The only operator input required is the charging voltages of Goblin and Sprite.

Foil Reflectivity Measurements

R K Gohri and E C Harvey

Rutherford Appleton Laboratory

The importance of Amplified Spontaneous Emission (ASE) in depleting the gain in large electron-beam pumped KrF lasers used for short pulse amplification has been highlighted elsewhere in this report (B1.4). One of the parameters for which there is little data is the 248 nm reflectivity of the titanium foil which forms the laser cell - particularly after etching by the fluorine. The foil reflectivity is needed in codes which model the ASE within the laser cell.

Since it is difficult to measure diffuse reflections accurately, we chose to measure the fraction of the incident beam absorbed by the foil. A calibrated copper constantan thermocouple was spot welded to the back of a sample foil to monitor the change in temperature during irradiation by a laser beam.

Two foil samples were used, each of size 5 cm x 2 cm x 35 μm. One foil sample had been in service in Sprite for more than two years and the other was of unused titanium. The mass of each was accurately measured before the samples were made flat and mounted onto a holder, using nylon stand-off posts, attached to a rotating base .

A Lambda Physik LPX105, operating at 248 nm, delivered 70 mJ in a 20 ns pulse in a 1 x 2 cm beam at a repetition rate of 3 Hz. A quartz plate was used to split off 9% of the incident beam to monitor the laser energy during the experiment. The apparatus was shielded to eliminate the hazard of scattered laser radiation, and to exclude draughts from the region of the foil.

The rate of change of temperature in the foil is given by

$$\frac{dT}{dt} = \frac{W_A}{mc_p} - k(T - T_0) \qquad (1)$$

$$W_A = W_I(1 - R) \qquad (2)$$

where T = foil temperature (K)
T_0 = Ambient temperature (K)
C_p = Specific heat capacity ($JK^{-1}g^{-1}$)
W_A = Power absorbed (W)
W_I = Incident power (W)
R = fraction reflected
k = cooling constant (s^{-1})

The foil was first exposed to the laser beam and allowed to reach a steady state temperature T_m monitored by the thermocouple. The laser beam was then turned off and the cooling curve obtained. The cooling constant was determined from (1) in the absence of any heating, thus

$$k = \frac{1}{t} \ln \frac{(T_m - T_0)}{(T - T_0)} \qquad (3)$$

The foil reflectivity could then be calculated using equations (1) and (2).

The foil angles were selected in a random order to distribute any effects due to long exposures to the high intensity beam - particularly burn damage on the foil. Equivalent measurements for both positive and negative rotations about the normal were recorded.

It was found that the cooling constant varied across the foil surface, probably due to non-uniform heating of the foil, and therefore had to be calculated at each angle.

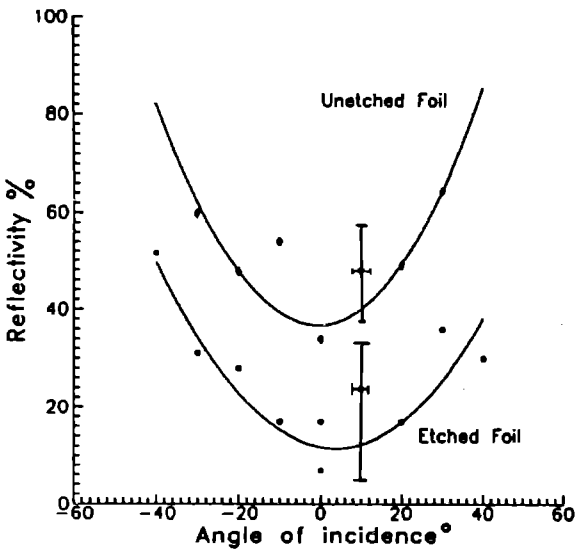

Figure 1. 249nm reflectivity vs. angle of incidence for etched and unetched titanium foils.

The asymmetry of the curves in Fig 1 is probably due to a slight shift in the position of the beam on the non-uniform surface of the foil, and to an asymmetric beam cross-section. Two readings were taken at normal incidence, one at the start of the experiment and the other at the end. The last result for the etched foil shows a 12% higher reflectivity, due to laser beam damage to the surface leading to increasing reflectivity as the experiment progressed. This accounts for the large vertical error bars in Fig 1. At normal incidence, the reflectivity was 12±10% for the etched foil and 34^{+10}_{-20}% for the unetched foil.

OPTICAL SCATTER MEASUREMENTS FROM LASER OPTICS

David T Sheerin and David C Emmony

Loughborough University of Technology

INTRODUCTION

It is very important to know the scatter characteristics around the specular direction of UV optics in any multiplexed system. Light scattered by optical components leads to noise, especially when amplified by a gain medium leading to a reduction in final peak power. This can be a particular problem if many multiplexed beams are being used as the interbeam angle can be of the order of a few mR[1]. To offset any "crosstalk" problems it is desirable to ascertain the near angle scattering characteristics of an optic and how they will change as a function of time. This latter requirement is especially important for optical surfaces exposed to fluorine environments as a gradual degradation of the surface can seriously affect the optical performance of the system. Described here is the design and construction of a scatterometer that is similar in many ways to the types of instruments that are currently being used at various laboratories to measure optical scatter[2-4].

EXPERIMENTAL ARRANGEMENT

The basis for the experiment was a 10 mW HeNe laser (633 nm) and an array of photodiodes. A block diagram representing the major constituents of the apparatus is shown below. The signal obtained from one of the photodiodes was first amplified, converted to an eight-bit code by an analogue-to-digital converter and then sent to the computer for subsequent analysis. Because the scattered light intensity could differ by 3 or 4 orders of magnitude over the angular range of detection, it was decided that data reduction of the form of a log ratio was to be employed. This was to allow the data to be compressed into, at most, 8 bits. When measuring scattered light as a function of component quality, the instrument's own scatter and beam profile limit the minimum angle at which scattered light from the test object can be detected. It is therefore of interest to minimise the instrumental 'signature' when taking low angle scatter data. This was achieved by having an aperture placed directly behind the sampling region so that the photodiode could not "see" light further back up the optical system. The sample under test was mounted in the output window aperture of an Oxford Lasers excimer laser model KX2 which will be used for fluorine and laser discharge aging of the components. Beam fluctuations from the laser itself were removed by the first spatial filter which converted beam wander to variations in beam power which in turn were accounted for by the beam splitter. The second spatial filter removed scatter due to the cover slide used to sample the beam power.

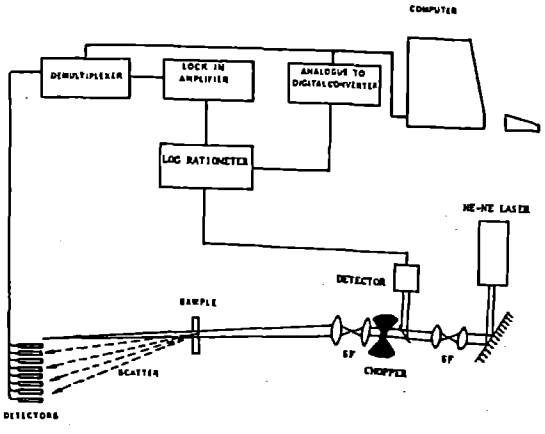

RESULTS

Scatter data are usually presented as the ratio of scattered light normalised to the incident light power and plotted as a function of angle from specular. Nicodemus said[5] that if this quantity is also normalised by the cosine of the angle between the surface normal and the direction of scatter then the resulting expression is the differential scattered radiance normalised by the incident irradiance. For optics in transmission, which is the case here, this expression has become known as the Bidirectional Transmissive Distribution Function. This function, BTDF, is defined as:

$$BTDF = \frac{P_i/P_s}{\Omega \cos(\theta_s)} \quad (1)$$

where P_s is the scattered power measured by the detector with an aperture that subtends a solid angle of Ω at the sample. The cos (θ_s) term gives the projection of the solid angle Ω onto the sample surface. The incident power on the sample is represented by P_i.

Shown below is a typical BTDF trace at near specular angles of a BaF_2 window on a silica substrate.

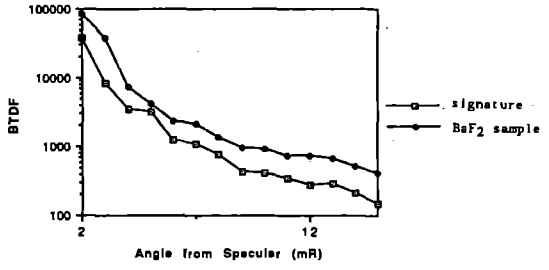

FURTHER WORK

The study to date has yielded results using a HeNe laser. However, in order to provide useful data for windows to be used for the Sprite project, a UV source operating near 248 nm must be used. It is therefore proposed that the Inova + ADP system (generating 257 nm radiation) be used to assess the scattering qualities at this wavelength so that a comparison between these two wavelengths can be made. If any correlation is evident then this relatively simple system may be used to infer a quality control on the suitability of the optic to UV irradiation merely from looking at its scatter function at visible wavelengths.

REFERENCES

1. Key M.H. et al. 1989 Analysis of High Power KrF Laser Systems - Report No. RAL-89-133.
2. Stover J.C. et al. Opt. Eng. 24, p. 404 (1985).
3. Cheever D.R. et al. Proc. SPIE 818, p. 13 (1987).
4. Stover J.C. et al. Opt. Eng. 23, p. 406 (1984).
5. Nicodemus F.E. et al. NBS Monograph 160, US Dept. of Commerce, Oct. 1977.

DEVELOPMENT OF A VARIABLE PULSE-WIDTH TRANSFORM-LIMITED DYE LASER

D. Xenakis and M.H.R. Hutchinson

Blackett Laboratory, Imperial College, London.

Introduction

This report describes the progress on the variable pulse duration transform-limited dye laser system being constructed at Imperial College. One use of such a laser would be as a seed to the Raman laser system at RAL. The aims of the present project are to develop a system with the following properties:

(i) Transform limited operation
(ii) Variable pulse-width between ~10-100 ps
(iii) Wavelength tunability in the region around 497 nm.

A schematic outline of the system being investigated is shown on figure 1. It uses an excimer-pumped tunable, long-pulse, narrow bandwidth dye laser as the seed laser. The output of this will be amplified by a travelling wave amplifier (TWA) which will be pumped by a short pulse pump laser.[1] The TWA acts as a high-gain optical gate, amplifying just a small time-slice of the seed pulse. By adjusting the mismatch of the sweep speed of pumping of the TWA to the group velocity of light in the amplifier cell a varying pulse-width of the output is expected. The minimum pulse duration should be less than or equal to the pump pulse whereas the maximum pulse duration attainable should be equal to the transit time of the light through the amplifier dye cell.

The picosecond Laser

To date, we have developed the short pulse pump laser for the TWA. This consists of a cascade of dye laser stages pumped by an XeCl excimer[2] which provides a pulse of ~30 picoseconds duration. Three distinct pulse-shortening stages have been employed, tested and evaluated (see figure 2):

(i) Quenched Dye Laser (QDL)
(ii) Short Cavity Laser(SCL)
(iii) Gated saturable Absorber(GSA)

The Quenched Dye laser

The QDL produces short pulses by combining two separate cavities of different lengths and 'quality factors' (Q) around a single dye cell. In this case the shorter cavity consists of the two opposite walls of a fused silica dye cell while the longer one is formed by placing an aluminium mirror a few millimeters away, which couples with one of the walls of the cell. The laser is pumped a few times above threshold by a small part of an excimer beam (≤2 mJ). The high pumping level induces fast relaxation oscillations in the short, low Q cavity. The longer resonator is aligned so that it saturates the gain just after the first oscillation occurs, resulting in a single pulse output along the direction defined by the short resonator. The output can then be isolated using an aperture.

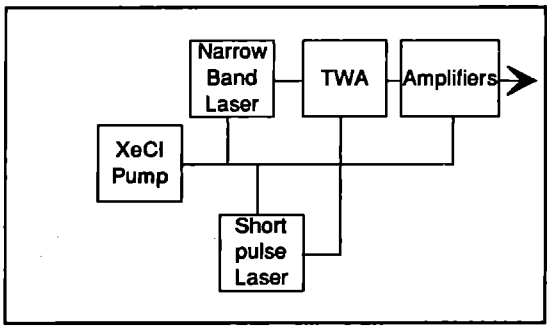

Figure 1: Outline of the Laser System

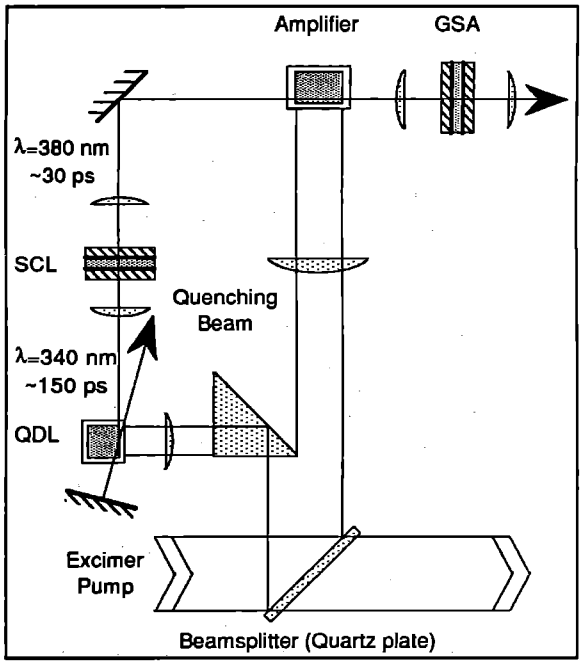

Figure 2: Outline of the ps Dye laser

The dye cell was a commercially available cell of 10 mm internal length and 12.5 mm outer. A solution of 5×10^{-3} M Paraterphenyl in cyclohexane was used and this produced pulses of 340 nm wavelength and approximately 100 ps risetime measured with a Hadland Imacon 500 streak camera.

The Short Cavity Laser

The SCL operates in a very similar fashion to the QDL in that the usable output consists of the relaxation oscillations of an overpumped dye laser. In this case however, there is no need to quench the gain as the output is automatically a single pulse. The resonator is pumped longitudinally from the output of the QDL. It is just 0.5 mm long and is formed by an input coupler with a dichroic coating which has ~70% transmission at the pumping wavelength of

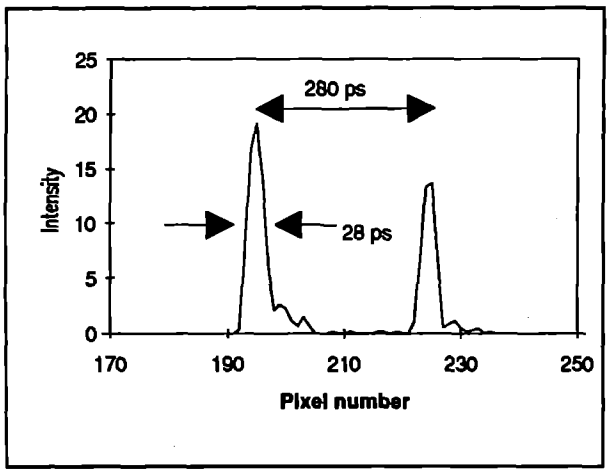

Figure 3: Streak camera output of the amplified SCL pulse. The second peak is generated by a beam splitter for temporal calibration purposes.

340 nm and ~95% reflectance at the lasing wavelength of 380 nm, and an output coupler with ~80% reflectance at 380 nm. Using a dye solution of 10^{-2} M butyl-BPD in Methanol and adjusting the pumping rate by fine-tuning the focusing lens, a single pulse can be reliably produced. After the SCL an excimer pumped dye amplifier stage brings the energy to the μJ level. The amplifier cell is 25 mm long and contains 2 $\times 10^{-4}$ M QUI in Dioxane. The synchronization of the amplifier to the output of the SCL is critical in maximizing the gain and minimizing the Amplified Spontaneous Emission (ASE). The SCL pulse should arrive very close to the peak, on the rising edge of the pump pulse. The output pulse-width was measured with a Hadland Imacon 500 streak camera and was found to be 28±5 ps (see Figure 3). The trailing edge of the pulse is due to ASE and is characteristic of these overpumped systems. This could be eliminated by improved alignment.

The Gated Saturable Absorber

The use of a GSA to further shorten and clean up the pulse has been investigated. The output from the dye amplifier was injected into the gated absorber stage (fig. 2). It consists of a dye (1×10^{-3} M BBOT in ethanol,) contained in a resonator of 1 mm length and arranged so that it produces laser action at *its* fluorescence peak. Saturation of the absorption by the dye shortens the risetime of the transmitted pulse, whereas the stimulated emission shortens its fall-time.[3] The main reason for using the GSA was to clean up the pulse coming from the SCL as it was anticipated that it would contain a long ASE tail. However, as mentioned above, the SCL output is sufficiently clean for use as the travelling wave amplifier pump and the pulse shortening observed was less than a factor of two. Hence the use of the GSA was not pursued since the added complexity of the system outweighed its limited benefits.

The remaining pump energy from the excimer laser (about 80% of the total) can now be used to amplify the narrow-bandwidth short-pulse output produced after the TWA to levels appropriate for frequency doubling to the ultraviolet for use in both KrF and Raman systems.

Assembly of the tunable, narrowband, long-pulse excimer-pumped seed laser is under way. Further work includes the construction and characterization of the travelling wave amplifier.

Acknowledgements

Discussions with Drs. M. Steyer and I.N. Ross on experimental details are gratefully acknowledged.

References

1. J. Hebling and J. Kuhl, *Opt. Commun.* **73**, 375 (1989).
2. S. Szatmari, *Opt. Quantum Electron.* **21**, 55 (1989).
3. Ch.G. Christov and I.V. Tomov, *Opt. Quantum Electron.* **18**, 137 (1986).

C: LASER SUPPORT FACILITY

W T TONER

INTRODUCTION

Elementary particle physics, physics based archaeology and astrophysically relevant chemistry appear for the first time in this section alongside more traditional topics in chemistry, biochemistry, cell biology and atomic physics illustrating the extraordinary breadth of the applications of lasers in scientific research and the continued growth of the Laser Support Facility user base. Novel results include the demonstration of the photo-oxidation of water by triplet Ubiquinone, the first experimentally determined rate constants for MeSiH, the induction of cell proliferation by exposure to light and the extension of the covariance mapping techniques to three dimensions in the study of multiphoton multiple ionisation of molecules.

Facility staff and user groups have put considerable efforts into improvements in techniques in the past year to ensure future scientific progress. This can be seen in the work on transition element halides and the opto-galvanic atlas of Neon; the picosecond pump and probe experiments, where sensitivity is now of the order of 10^{-4}; the laser flash photolysis apparatus, already in use for new science; the far red Raman spectra obtained with the Ti-Sapphire laser; the high quality picosecond TR^3 spectra now being obtained in the high repetition rate system at RAL; the operation of a high precision frequency locked laser system in an accelerator environment, and the high yields of point source soft X-rays.

The major facilities available at RAL and in the Loan Pool are listed in Table I and have not changed since last year although numerous improvements (discussed in Section C4) have been implemented.

TABLE I

LASER SUPPORT FACILITY EQUIPMENT

Picosecond Systems at RAL

2 cw modelocked pump lasers; sub-picosecond oscillator; 2 cavity dumped oscillators; injection-locked YAG pump and dye amplifier (10 Hz); copper vapour pump and dye amplifier (6 KHz). Pump-probe absorption system; single photon counting; streak camera. Wavelengths from the UV to the far infrared are available, with further amplification at the excimer wavelengths.

Nanosecond Systems at RAL

2 high repetition rate fluoride excimer lasers; laser-plasma X-ray source;
2 high repetition rate XeCl excimer lasers pumping dye lasers; BBO and Raman wavelength conversion. 5 watt ion laser. Raman spectrometer. Laser-flash-photolysis Flash photolysis system.

Loan Pool

4 YAG-pumped tunable dye lasers with frequency doubling and mixing; Excimer-pumped dye laser; fluoride excimer laser; 5 watt cw Ar ion laser with dye laser or Ti-sapphire laser; streak camera; gated integrators.

LASER EXCITATION SPECTROSCOPY OF JET COOLED MOLECULES FORMED FROM INVOLATILE SOLIDS

J.M.Brown[1], I.R.Beattie[2], S.H.Ashworth[1], N.M.Lakin[1]
[1]OxfordUniversity
[2]SouthamptonUniversity

One of the problems with the high resolution gas phase spectroscopy of involatile solids is that, at the high temperatures required to generate sufficient vapour pressure the spectra obtained are broad and structureless and therefore yield little information. In our experiment, the molecules are produced in a heated nozzle and seeded into an inert gas stream which undergoes a free expansion into a rapidly pumped vacuum chamber. The isoenthalpic expansion converts rotational, and to a lesser extent vibrational, energy into translational energy (the molecules are rotationally cooled to about 10K). Laser excitation spectroscopy is performed by collecting the fluorescence induced in the jet by irradiating it with the beam from a narrow band tunable dye laser [1]. The excimer pumped dye laser at the LSF was used in this way to record the spectra of several species.

During two four week allocation periods we were able to make several major improvements to our apparatus.

We tested a new design of collection optics and were able to show that suitable irising can reduce the apparent fluorescence lifetime of excited molecules from 1.2μs to 0.4μs. This means that we are viewing a smaller area of the jet and, when not laser limited, achieve better resolution.

Modifications to the nozzle source made last year [2, 3] resulted in much colder spectra than had previously been obtained but this was accompanied by a marked decrease in the sensitivity of detection. A compromise was developed which restored sensitivity but results in marginally warmer spectra than reported last year. Signal to noise was shown to increase when residual blackbody radiation from the hot nozzle is masked out in the collection optics and also when a Brewster's angle exit window for the laser beam is installed.

Superior quality spectra for InOH and $FeCl_2$ were recorded and observations on $NiCl_2$ extended. All spectra were calibrated by simultaneaously recording the optogalvanic spectrum of the Ne discharge in an Fe hollow cathode lamp. Survey work was also done on MnF_2.

We were able to extend the observations of the cold spectrum of $NiCl_2$ in the 460 nm region [1] to both higher and lower frequency. The vibrational cooling was confirmed by recording bands originating from a ground state in which one quantum of the symmetric stretching mode is excited. In the current expansion conditions these signals are some ten times less intense than the $v' = 0 \leftarrow v'' = 0$ bands, reflecting the much lower population of $v'' = 1$ than $v''= 0$. We had hoped to see bands corresponding to the excitaion of two quanta of the antisymmetric stretching mode in the upper state. No such assignments were possible but there are still some unassigned signals which we wish to investigate further.

The analysis of the 460 nm system is going well but the stronger system at 360 nm is proving a more difficult nut to crack. To this end we attempted stimulated emission pumping (SEP) of the more intense bands in the 360 nm spectrum. This utilises two dye lasers to record what is effectively a dispersed fluorescence spectrum. Unfortunately we were singularly unsuccessful and so instead used an optical multichannel analysiser (OMA) belonging to the RAL to detect the fluorescence dispersed by a monochromator. Figure 1 shows some typical recordings. The linewidth is rather large so that accurate quantitative information is hard to obtain, however there a great deal of qualitative information is contained in the recordings.

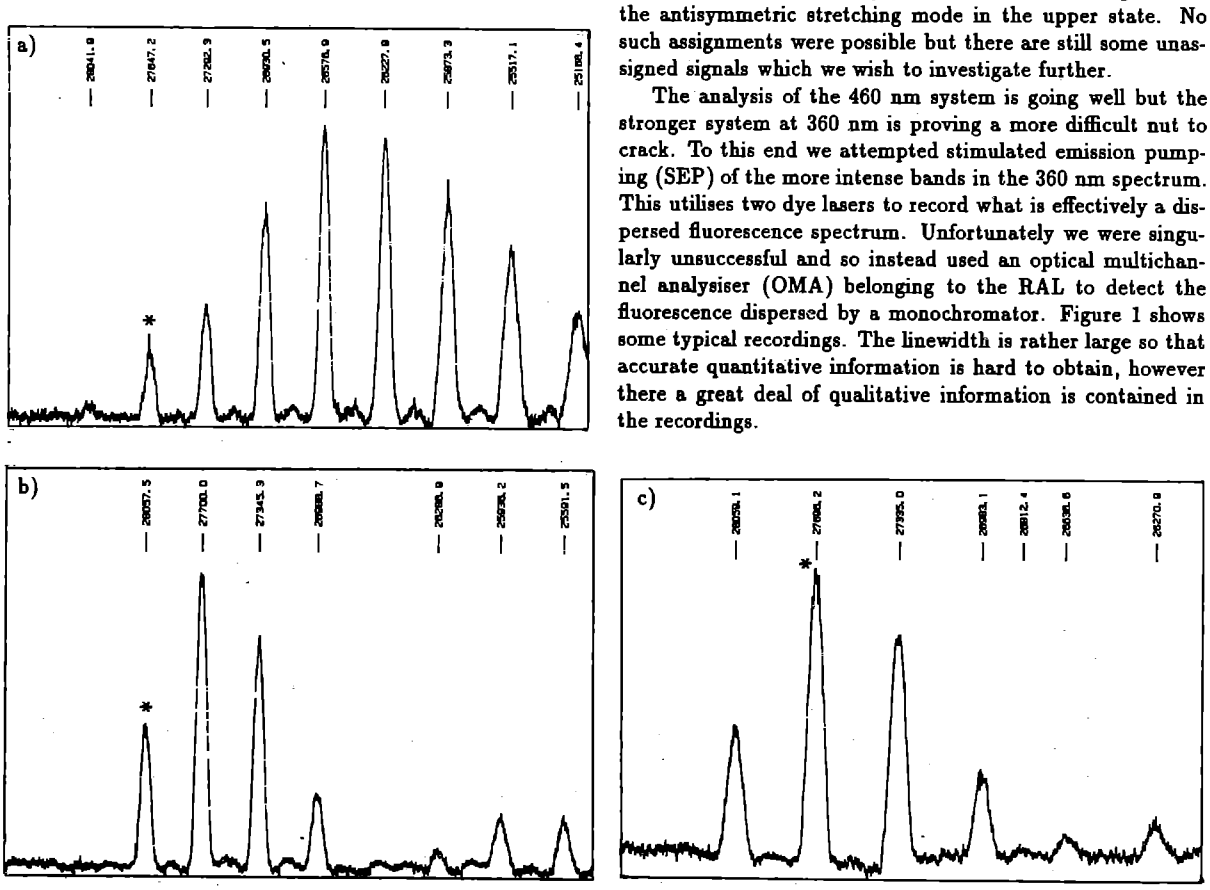

Figure 1: Dispersed fluorescence of bands in the 360 nm system of $NiCl_2$ recorded using the OMA. These are designated a) Band B2 b) Band C3 c) Band C2 in reference [4]. The excitation wavelength is denoted by *.

At the moment the bands in the 360nm spectrum have only been given arbitrary designations which group those of similar structure. These recordings confirm this grouping as similar bands in the total fluorescence spectrum have similar dispersed fluorescence (figures 1b and 1c). These scans also prove that at least two upper electronic states are involved in the transition since, for example, figure 1a shows a much longer weaker progression than seen in figures 1b or 1c.

We can also see immediately by the anti-Stokes lines in figures 1a and 1c that these originate from an excited vibrational level in the ground state. This allows unambiguous assignment of the vibrational transition which, in a couple of cases, contradicts those published [4]. These observations also show that the ground state of the 360 nm system is not as efficiently cooled as that of the 460 nm system.

This work also suggests that SEP might be more successful on the bands where a strong progression is seen in the dipersed fluorescence rather than those which have a greater absorption intensity.

Scans of some bands in the 360 nm spectrum were attempted using the intracavity etalon. This could partially resolve structure and reveal much about the nature of the bands. Unfortunately we were unable to scan the etalon in this region.

A new method for the production of InOH has been developed. A motor driven syringe was used to inject water at a constant rate into the heated region of the nozzle. The water vapour is entrained in argon flowing over a sample of molten indium at 870°C. This gave a higher signal level than the previous method of production [2] and observations were extended to cover the region 330-373 nm.

A large number of new signals were seen which fall into two classes: those where the rotational fine structure could be resolved without the use of the etalon and those where it could not be. The molecule responsible for the unresolved bands is unknown but the resolved bands are thought to be due to InOH. These resolved bands have classical rotational profiles involving P, R and, in some cases, Q branches. Figure 2a shows a band where all three branches are present. A progression of bands was observed with a separation of approximately 86cm^{-1}.

When the experiment was repeated with D_2O in the syringe instead of water a similar set of resolved and unresolved bands were seen. A portion of the spectrum showing several resolved bands is shown in figure 2b. The separation of rotational lines is smaller than that shown in figure 2a and was consistent with calculated values for InOD. The separation of bands in the vibrational progression is reduced by a factor of approximately $\sqrt{2}$ indicating that these bands may correspond to excitation of the upper state bending mode. These bands are each accompanied by a weaker satellite band to higher frequency (figure 2b). This may be due to excitation of rotational K sublevels in the upper electronic state. Further work including dispersed fluorescence is needed before we can be certain that the spectrum can be attributed to InOH.

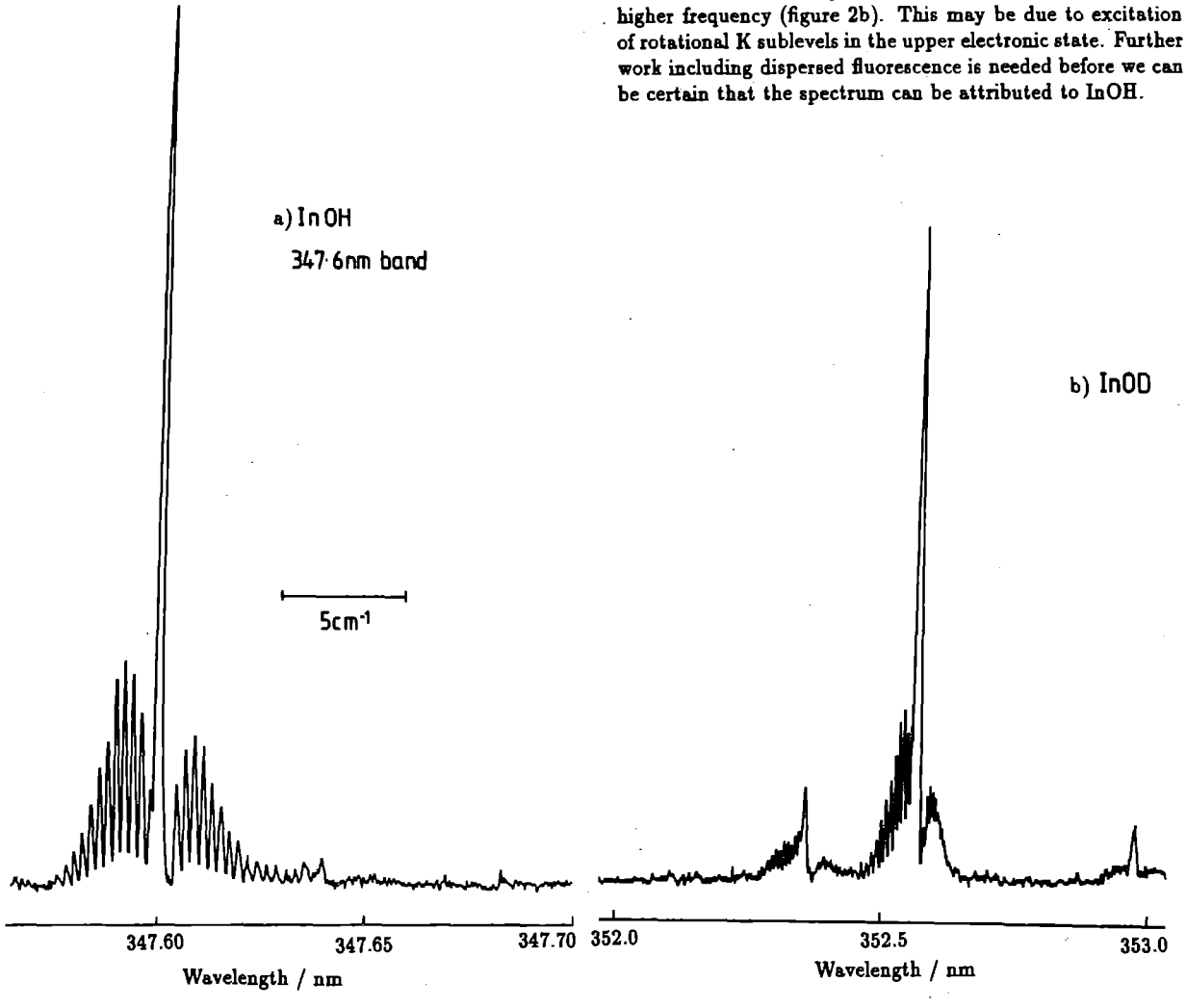

Figure 2: Part of the band systems attributed to a) InOH and b) InOD. Analagous bands from both spectra are shown.

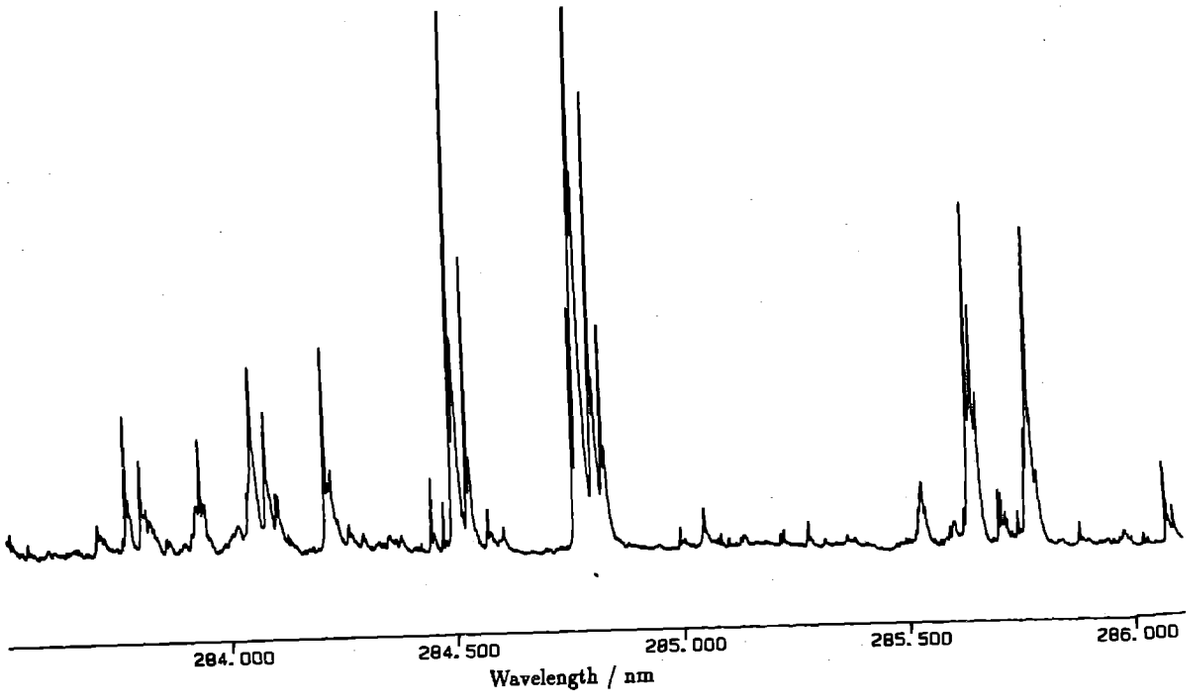

Figure 3: A portion of the spectrum of $FeCl_2$. None of the signals are as yet assigned but the structure of individual bands may be attributable to different isotopomers of $FeCl_2$.

The reaction between hot Fe and CCl_4 proved to be an inefficient and unreliable way to produce $FeCl_2$. In the past we have used solid samples of $FeCl_2$ and have been plagued by nozzle blocking. This now appears to have been circumvented by using specially prepared anhydrous $FeCl_2$ samples. By frequency doubling the laser radiation observations have been extended to cover the region 268-295 nm. The spectrum shown in figure 3 is of far higher quality and rotationally colder than obtained before. The regularity of the structure throughout the spectrum gives us reason to believe that it will a tractable analytical problem.

Two weak signals which might be due to MnF_2 were observed between 345-375 nm by heating the solid to 950°C. At this temperature the solid is very corrosive and attacks both the alumina crucible and nozzle. These chemical problems must be overcome before further work can be done on this compound.

References

[1] F.J. Grieman, S.H. Ashworth, J.M. Brown and I.R. Beattie *J. Chem. Phys.*, **92**, 6365 (1990).

[2] *Annual Report to the Laser Facility Committee* Rutherford Appleton Laboratory Report RAL-90-026, p.129.

[3] S.H. Ashworth, F.J. Grieman and J.M. Brown *Chem. Phys. Letters*, **175**, 660 (1990).

[4] L.R. Zink, F.J. Grieman, J.M. Brown, T.R. Gilson, and I.R. Beattie *J. Molec. Spectrosc.*, **146**, 225 (1991).

FLUORESCENCE SPECTROSCOPY OF JET-COOLED CF_3NO AND $CCLF_2NO$

Alex W. Simpson, Donna M. Wetzel and Josef Pfab
Department of Chemistry, Heriot-Watt University,
Riccarton, Edinburgh EH14 4AS

INTRODUCTION

We have previously studied the photodissociation dynamics of perhalogenated C-nitrosomethanes in the visible.[1,2,3] These compounds have structured electronic spectra due to an n,π*-transition centred on the NO chromophore, emit fluorescence in the red and near-IR region and undergo predissociation with formation of a trihalogen methyl radical and NO.[4] The jet-cooling technique permits substantial simplification of the electronic spectra and the excitation of single vibronic levels with a pulsed tunable dye laser in a convenient region of the visible. Our studies of the state-selective photolysis of three jet-cooled fluorine containing C-nitrosomethanes (CF_3NO, $CClF_2NO$ and CCl_2FNO) have shown that predissociation occurs on a time scale of a few hundred nanoseconds down into the sub-nanosecond range depending on the energy in excess of the C-N bond dissociation energy provided by the photon. The rotational state distributions of the NO fragment mirror statistical distributions indicating that energy is randomised prior to the dissociation event. The bi-exponential fluorescence decay behaviour of the parents and deviations from statistical internal state distributions of the NO photoproduct indicated that intersystem crossing and the lowest triplet state $\tilde{a}\,^3A''$ are involved in the photophysics and photodissociation of these molecules.

The objectives of the present work were to extend studies of the excitation spectra in order to provide more detailed information on the conformational properties of CF_3NO and $CClF_2NO$ in the ground electronic state.

EXPERIMENTAL

CF_3NO and $CClF_2NO$ were jet-cooled by pulsed expansion of 5-20% mixtures with Ar using total stagnation pressures near 500 Torr. The expansion was crossed by the output beam of the Datachrome dye laser which was pumped with the 532 nm second harmonic of the Nd:YAG laser. Fluorescence was collected by a BK7 aspheric condenser lens, and imaged through a Schott glass cut-off filter onto a red-sensitive photomultiplier for recording excitation spectra. The dispersed fluorescence spectra were recorded by imaging the luminescence onto

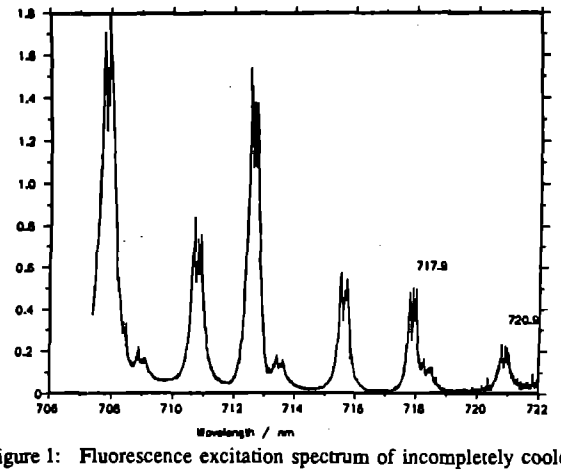

Figure 1: Fluorescence excitation spectrum of incompletely cooled CF_3NO near the O_0^0 origin (717.9 nm).

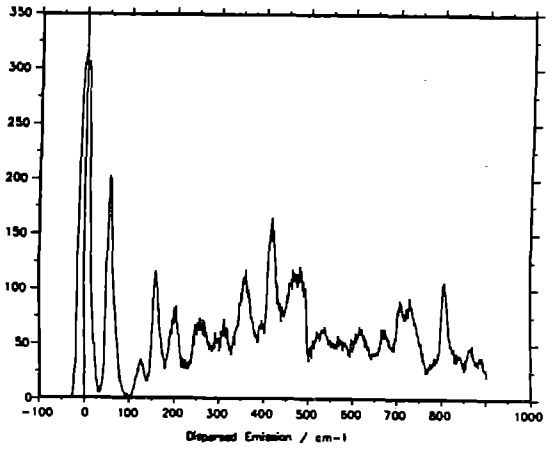

Figure 2: Dispersed emission spectrum of CF_3NO - transition excited: 12_0^{6e}.

the entrance slit of a small 20 cm grating monochromator. The PMT signals were terminated into 50 Ω, processed by a gated integrator/boxcar averager and recorded by computer after A to D conversion. The digital spectra were recorded with an IBM-XT microcomputer and further processed and plotted using the mainframe computer facilities.

RESULTS AND DISCUSSION

Fig. 1 shows a small part of the fluorescence excitation spectrum of CF_3NO recorded close to the nozzle orifice where cooling is incomplete. The O_0^0 electronic origin corresponds to the relatively weak feature near 717.9 nm and the strong bands near 713 and 708 nm are the first two members of a progression in the torsional mode (12_0^1 and 12_0^2). A second weaker progression 12_1^0, 12_1^1 and 12_1^2 starts with the band at 720.9 nm and continues with the bands near 716 and 712 nm. The very weak bands to the red of the origin (718 nm) and the strong 713 and 708 nm bands are easily assigned to the progression 12_2^1, 12_2^2 and 12_2^3. The intensity of the hot band progressions associated with 12_1^0 and 12_2^0 increases steeply with increasing temperature so that the region near the weak Franck-Condon forbidden origin becomes entirely dominated by hot bands.

The key feature explaining the unusual intensity distribution of the CF_3NO excitation spectrum arises from a change in the dihedral conformation of the molecule from eclipsed in the ground to staggered in the excited state.[2] Thus the O_0^0 origin becomes Franck-Condon forbidden and therefore very weak.

One of a range of dispersed fluorescence spectra we have recorded for jet-cooled CF_3NO is shown in Fig. 2. The example chosen records the emission spectrum obtained when the laser excites the 12_0^{6e} transition. The 12^{6e} level lies close to the top of the excited state torsional potential function where the a/e splitting of the levels becomes substantial. Note, that the 12_2^{6e} band is missing in the emission spectrum confirming that the 6e assignment of the upper level is correct since e-e transitions are symmetry forbidden for Δv = even bands.

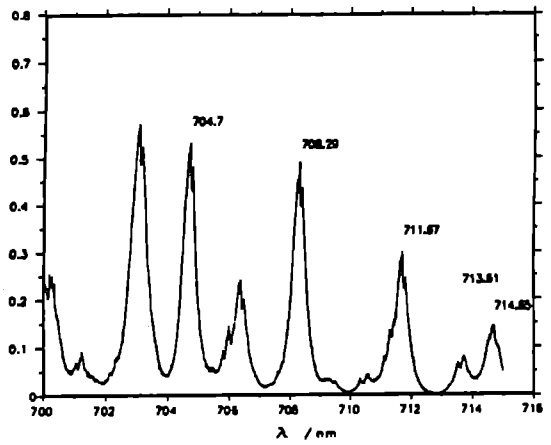

Figure 3: Fluorescence excitation spectrum of incompletely cooled $CClF_2NO$ near the O_0^0 origin.

A small portion of the fluorescence excitation spectrum of incompletely cooled $CClF_2NO$ is shown in Fig. 3. The excitation spectrum is again dominated by prominent progressions in the torsional mode 12 with the notably stronger O_0^0 origin, as compared to CF_3NO, appearing near 704.7 nm and the 12_1^1 sequence band at higher energy near 703 nm. The bands descending in intensity towards the near-IR from 708.3 nm (12_1^0), 711.7 nm (12_2^0) and 714.6 nm (12_3^0) form a progression in the ground state torsion and readily provide the positions of the first four ground state levels.

Dispersed emission spectra like the example shown in Fig. 4, which we recorded on excitation of the 12_0^1 feature confirm these assignments and provide additional information on the Franck-Condon factors of these transitions.

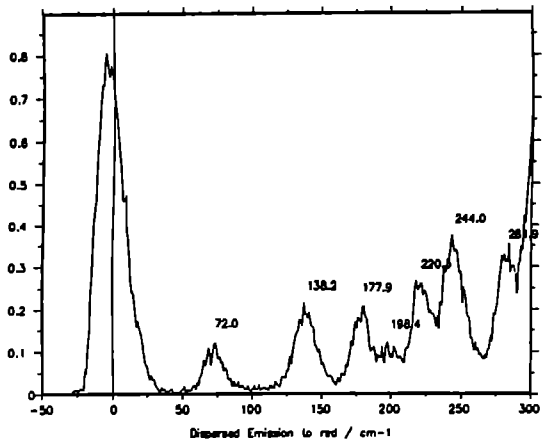

Figure 4: Dispersed emission spectrum of $CClF_2NO$ - transition excited: 12_0^1.

CONCLUSIONS

The $\tilde{A}\ ^1A'' \leftarrow \tilde{X}\ ^1A'$ electronic transitions in CF_3NO and $CClF_2NO$ arise from an n,π* promotion in the bent C-NO chromophore, that is accompanied by an eclipsed→staggered conformational change and an opening up of the CNO angle. This leads to prominent progressions in low frequency torsional and bending/rocking modes and a remarkable sensitivity of the spectrum to changes in temperature. The analysis of hot band progressions in the fluorescence excitation spectrum provides an efficient and experimentally straightforward method for deducing the torsional energy levels in the ground state, and this taken in conjunction with an analysis of the relative intensities will define the ground state potential functions for the torsion in these molecules in considerable detail. Additional information on vibronic symmetries and Franck-Condon factors is available from the dispersed fluorescence spectra.

We have now begun to analyse the data using a one-dimensional hindered internal rotor model and hope to have sufficient data to provide a reliable ground state potential function. For CF_3NO the earlier discrepancy between the microwave and optical ground state data of Levy *et al.* has been removed by the inclusion of a V_6'' term and by allowing the internal rotation constant F'' to vary with the torsional angle α.[4,5] Our present results confirm the revised electronic origin and excited state potential reported previously. In contrast, the new data on CF_3NO do confirm that the ground state torsional levels first deduced by Levy *et al.* are correct. We hope that the two sets of data can now be combined to provide better agreement between the observed and calculated emission specta.

For $CClF_2NO$ we now have a more reliable ground state geometry based on an electron diffraction study and on *ab initio* calculations, which will be used to obtain the dependence of F'' and, with suitable changes, of F' on the torsional angle. The interpretation of excitation and emission spectra of $CClF_2NO$ is complicated by the fact that two distinct rotamers must be present in the ground and excited state, but only one conformer has been clearly identified in each case so far.

Our results demonstrate that hot band excitation spectra and dispersed emission spectra can reveal new information on conformational properties that is difficult to obtain by microwave, IR and Raman spectroscopies. We conclude, however, that double-resonance techniques may ultimately be needed to obtain information on the Franck-Condon disfavoured regions of the ground and excited state potentials.

REFERENCES

1. J.A. Dyet, M.R.S. McCoustra and J. Pfab, J. Chem. Soc., Faraday Trans. 86, 2049 (1990).
2. J.A. Dyet, M.R.S. McCoustra and J. Pfab, J. Chem. Soc., Faraday Trans. 2, 84, 463 (1988).
3. M.R.S. McCoustra, J.A. Dyet and J. Pfab, Laser Chem. 9, 289 (1988).
4. D.W. Knight and A.P. Cox, Chem. Phys. Lett. 132, 103 (1986).
5. B.M. DeKoven, K.H. Fung, D.H. Levy, L.D. Hoffland and K.G. Spears, J. Chem. Phys. 74, 4755 (1981).

Fluorescence Spectroscopy of Styrene and 2-, 3-, and 4-Methylstyrene in a Supersonic Jet

J.Michael Hollas and Philip F.Taday

University of Reading

INTRODUCTION

Interest in the structure of styrene (STY), 2-methylstyrene (2MS), 3-methylstyrene (3MS) and 4-methylstyrene (4MS) centres on the possible torsional motions within the molecules. In STY

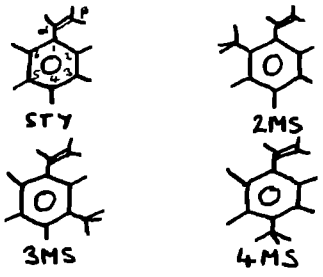

there is only the C(1)-C(α) torsional motion of the vinyl group relative to the ring while, in 2MS, 3MS and 4MS, there is also the torsional motion of the methyl group relative to the ring.

The vinyl torsional potential function for STY has been shown to be[1]

$$V(\phi)/cm^{-1} = \frac{1}{2}[1070(1 - \cos 2\phi) - 275(1 - \cos 4\phi) \qquad (1)$$

where ϕ is the torsional angle. The vibrational levels were obtained from observations in the gas phase absorption, single vibronic level fluorescence (SVLF), and Raman spectra. The large, negative value of V_4 = -275 cm^{-1} leads to a very flat-bottomed potential. The molecule is planar, but only just.

In 2MS, only one rotational isomer (rotamer) has been found and this is assumed to be the trans rotamer, which is the one shown, in which steric hindrance is minimised.

On the other hand, both the cis and trans rotamers of 3MS have been found in the mass-resolved excitation spectrum[2].

EXPERIMENTAL

As for the work reported previously[3] the Quantel Datachrom Nd:YAG pumped dye laser from the Central Laser Facility Loan Pool was used for much of the work but a Molectron nitrogen pumped dye laser was also used.

The dye laser radiation was frequency doubled into the near ultraviolet. For the fluorescence excitation (FE) spectra, autotracking was necessary. For the supersonic jet, helium carrier gas was used at a backing pressure of 1.4 atm. A nozzle diameter of 100 μm resulted in rotational and vibrational temperatures of about 10 K and 100 K respectively.

RESULTS

STYRENE. Figure 1 shows a single

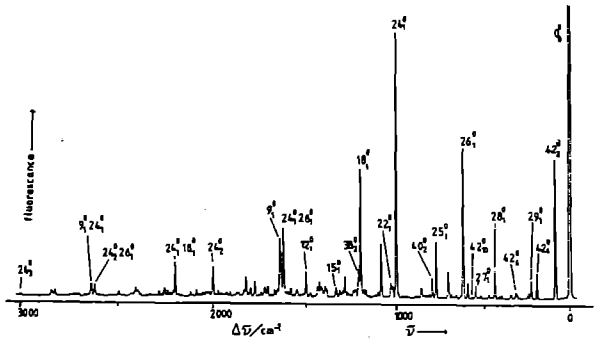

Figure 1: SVLF spectrum of styrene

vibronic level fluorescence (SVLF), or dispersed fluorescence, spectrum of STY with excitation in the pure electronic transition (0_0^0 band). There is a prominent progression in the C(1)-C(α) torsional vibration ν_{42} with the vibrational selection rule restricting the transitions to those with Δv_{42} even. The progression extends up to v_{42} = 10, further than was possible in the corresponding gas phase spectrum[1], and the positions of the bands confirm the potential in eq (1).

2-METHYLSTYRENE. Figure 2 shows a SVLF

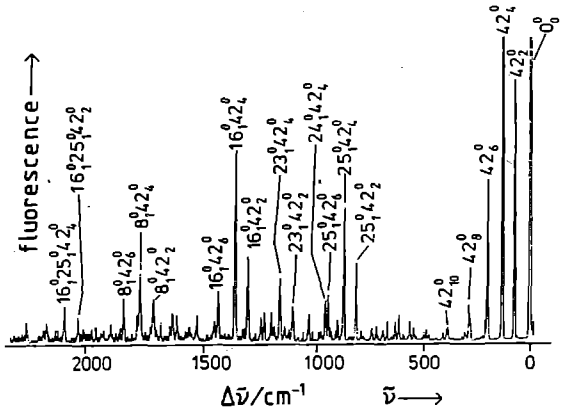

Figure 2: SVLF spectrum of 2-methylstyrene

spectrum of 2MS with excitation in the 0_0^0 band. One obvious difference from that of STY in Fig. 1 is the intensity distribution in the prominent progression in the C(1)-C(α) torsional vibration ν_{42}. The fact that the maximum intensity is in the 42_4^0 band indicates a geometry change from S_0 to S_1.

Fitting the observed levels to a torsional potential function analogous to that in eq (1) gives

$$V(\phi)/cm^{-1} = \frac{1}{2}[670(1 - \cos 2\phi) - 420(1 - \cos 4\phi) \quad (2)$$

Here, V_4 is so large and negative that the potential is not flat-bottomed , as in STY, but shows an energy barrier 151 cm^{-1} high. The molecule is non-planar with the vinyl group twisted about 33° out-of-plane in the equilibrium configuration.

No activity of methyl torsional motion is observed in the spectrum.

3-METHYLSTYRENE. The FE spectrum of 3MS shows two sets of bands, assigned to the cis and trans rotamers. SVLF spectra, with the laser tuned to bands of either rotamer, show progressions in both the C(1)-C(α) torsional vibration ν_{42} and the CH_3 torsional motion ν_τ. Examples of these SVLF spectra are shown in Fig.3

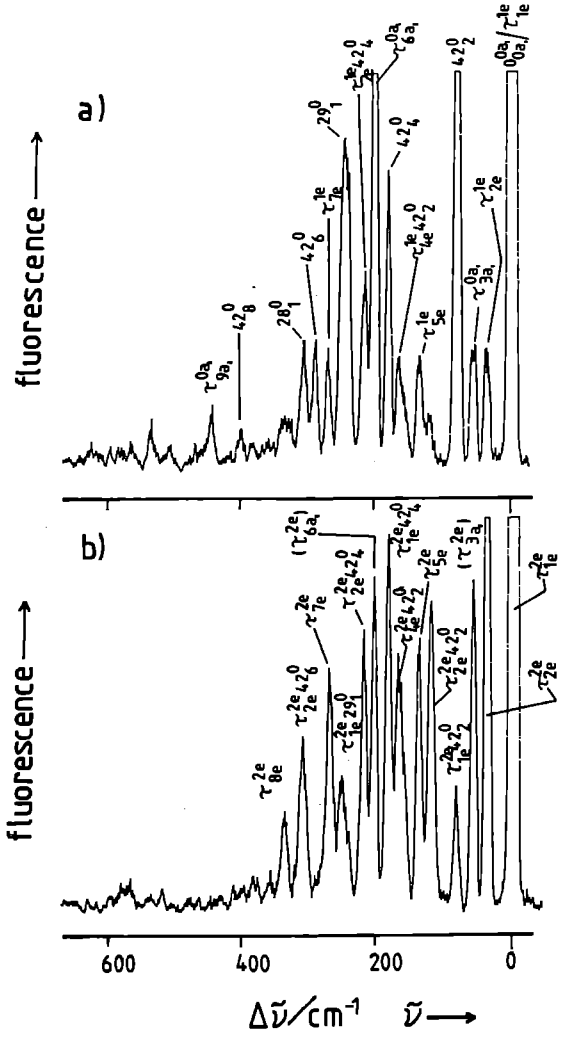

Figure 3: SVLF spectra of trans-3-methylstyrene with excitation in (a) the $0^{0a_1}_{0a_1}/\tau^{1e}_{1e}$ coincident bands and (b) the τ^{2e}_{1e} band

which shows spectra of the trans rotamer with excitation in the coincident $0^{0a_1}_{0a_1}/\tau^{1e}_{1e}$ and τ^{2e}_{1e} bands.

Many methyl torsional energy levels have been observed and fitted to the potential function

$$V(\phi)/cm^{-1} = \frac{1}{2}[45.0(1 - \cos 3\phi)] \quad (3)$$

for the cis rotamer and

$$V(\phi)/cm^{-1} = \frac{1}{2}[52(1 - \cos 3\phi) + 19(1 - \cos 6\phi) \quad (4)$$

for the trans rotamer. Both potential functions refer to the S_0 (ground) electronic state.

The barrier height of 45 cm^{-1} in cis-3MS and 52 cm^{-1} in trans-3MS is considerably higher than that of only 5 cm^{-1} in toluene. In the excited electronic state S_1 there is a large increase in the barrier height to 165 cm^{-1} in cis-3MS and 79 cm^{-1} in trans-3MS.

The C(1)-C(α) torsional potential function is similar to that for STY[1] except for a small energy difference of 8.9 cm^{-1} between the two rotamers, cis-3MS being the more stable.

4-METHYLSTYRENE. The corresponding work on 4MS has been published[4]. SVLF and FE spectra both show progressions in methyl torsional motion which result in a potential function

$$V(\phi)/cm^{-1} = \frac{1}{2}[(-17\ 1)(1 - \cos 6\phi)] \quad (5)$$

in S_0 and

$$V(\phi)/cm^{-1} = \frac{1}{2}[(-17\ 4)(1 - \cos 6\phi)] \quad (6)$$

in S_1. The low barrier height of 17 cm^{-1} in both electronic states is typical of a 4-substituted toluene.

The C(1)-C(α) torsional potential in S_0 was found to be

$$V(\phi)/cm^{-1} = \frac{1}{2}[(943\ 58)(1 - \cos 2\phi) - (208\ 31)(1 - \cos 4\phi) \quad (7)$$

As for STY, the vinyl group of 4MS is coplanar with the benzene ring but the large, negative V_4 results in a very flat-bottomed potential.

REFERENCES

1. J.M.Hollas, H.Musa, T.Ridley, P.H.Turner, K.H.Weisenberger and V.Fawcett, J.Mol.Spectrosc.,94, 437(1982).
2. V.H.Grassian, E.R.Bernstein, H.V.Secor, and J.I.Seeman, J.Phys.Chem., 93, 3470(1989).
3. A.C.P.Alves, K.H.Hassan, J.M.Hollas and P.F.Taday, Annual Report to the Laser Facility Committee, RAL-90-026, p131(1990).
4. J.M.Hollas and P.F.Taday, J.Chem.Soc. Faraday Trans., 86, 217(1990).

LASER-INDUCED FLUORESCENCE OF REACTIVE METALLOCENES $(\eta^5\text{-}C_5H_5)_2M$ (M = Re, W, Mo) AND $(\eta^5\text{-}C_5Me_5)_2Re$

Steven E. J. Bell, Jeremy N. Hill, Andrew McCamley and Robin N. Perutz

University of York, U.K.

INTRODUCTION

In the report on our preliminary investigations[1] of laser-induced fluorescence (LIF) at the LSF , we showed that four different open-shell metallocenes exhibited intense and well structured emission. We concentrated on the LIF of Cp_2M (Cp = η^5-C_5H_5, Cp* = η^5-C_5Me_5) in nitrogen matrices using a nanosecond pulsed dye laser system. This enabled us to (i) detect fluorescence from Cp_2W, something not possible with CW lasers (ii) to measure the excited state lifetimes of Cp_2Re and set limits on the lifetimes of the others, (iii) to record partial excitation spectra. This stage of the work has now been published.[2] From this initial work, it became clear that for more quantitative results, the laser energy had to be measured accurately *while recording spectra.* In addition, the dependence of fluorescent intensity on laser energy had to be examined to determine whether or not this emission was the result of a single photon process. Our further objectives were (i) to complete the excitation profiles of fluorescence for all four compounds in nitrogen matrices, (ii) to investigate the effect of dilution on spectra and fluorescence lifetimes, (iii) to investigate the effect of changing the matrix gas from nitrogen to argon. Most of these objectives have now been achieved , and the results are described below.

RESULTS

Dependence of LIF on laser energy. In order to measure the laser energy accurately a photomultiplier coupled to a boxcar was employed, providing measurement of the average energy to 5%. Satisfactory linear energy dependence was observed in all experiments when irradiating bands of low absorbance. For bands of high absorbance, the fluorescence intensity begins to saturate at higher energies (>1mJ). These experiments demonstrate conclusively that single photon processes are being observed and give us increased confidence in the excitation data recorded.

Cp_2Re: The excitation profile was completed showing the (0,0) band from absorption, emission and excitation to be coincident. As usual, there is a conspicuous progression in the symmetric ring-metal-ring stretching mode. In addition, a new peak is observed shifted 750 cm^{-1} from the origin, which is due to the symmetric ring breathing vibration ν'_3. This is not observed in the absorption spectrum. In this more dilute matrix, the main features are found to be the same as in the more concentrated matrix used previously. Notably, the fluorescence lifetime observed is the same as in the more concentrated matrix to within 2%.

Cp^*_2Re: The spectra of Cp^*_2Re are much sharper than those of Cp_2Re, but are complicated by the presence of two sets of bands, attributed to two different conformers, A and B. The effect on the emission spectrum of changing the excitation wavelength in a nitrogen matrix can be seen in fig 1. Complete excitation profiles have been plotted separately for all these bands. They clearly reveal that energy transfer occurs between the A and B conformers. Furthermore, the sum of the excitation spectra of the individual components forms the total excitation spectrum, which shows a striking resemblance to the absorption spectrum (fig 2). As anticipated from the absorption spectra, the

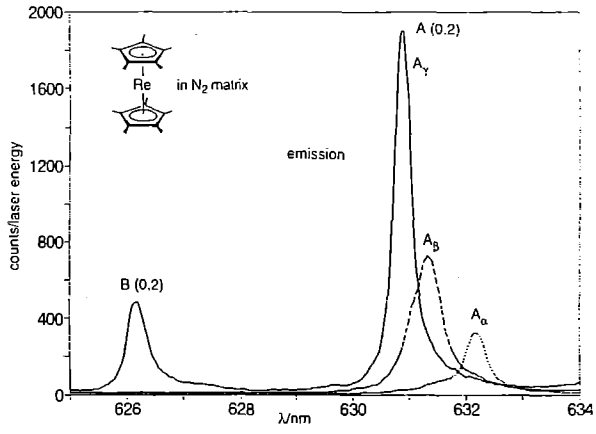

Figure 1. Expanded emission spectrum of Cp^*_2Re in N_2 matrix at 12 K, showing the (0,2) transition only. The transition has three components excited selectively according to the excitation wavelength. B(0,2) and A_γ for λex = 571.0 nm; A_β for λex = 575.2 nm and A_α for λex = 576.0 nm.

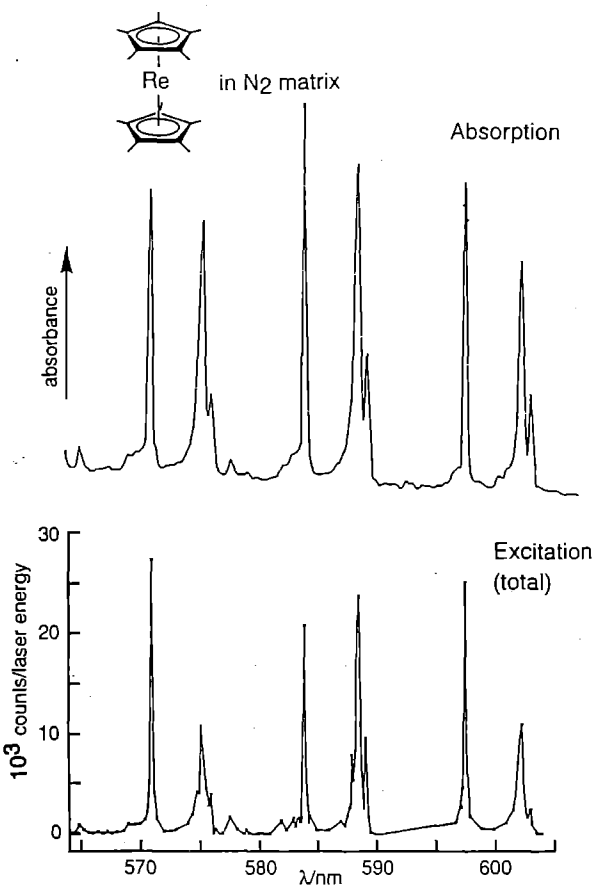

Figure 2. Top: Partial absorption spectrum for Cp^*_2Re in N_2 matrix at 12K. Bottom: Total excitation spectrum in same region for Cp^*_2Re resulting from the summation of excitation spectra for B(0,2), A_γ, A_β, and A_α shown in figure 1.

use of an argon matrix instead of nitrogen has a marked effect on the distribution between conformers. The distribution could be altered by annealing the matrix. It was a surprise to discover that there was an almost gaussian distribution of matrix sites in argon and that there was no energy transfer between conformers.

Cp_2Mo: The absorption spectrum in argon is appreciably broader than that of the other metallocenes so far mentioned (fig 3). The emission spectra, in contrast, can be considerably sharper. Using the A2 peak area (shaded), one can plot a site selective excitation profile. The result reveals much improved resolution compared to the absorption spectrum and allows the symmetric ring-metal-ring stretch, ν'_4 , to be more precisely determined. In addition the profile shows a peak shifted 720 cm^{-1} from the (0,0) band due to ν'_3 , that is not detectable in the absorption spectrum.

CONCLUSIONS

These results clearly demonstrate the improvement in spectral resolution possible using LIF enabling us to measure several previously unobserved totally symmetric vibrations. The improvements in measurement of the laser energy have made the excitation profiles more quantitative, and have allowed us to show that we are examining single photon phenomena. The effect of dilution has been investigated and has been shown to have no effect on lifetime of Cp_2Re. The change in matrix gas has shown some interesting features in the case of Cp^*_2Re. The excited state lifetimes still remain elusive and it is hoped to use single photon counting apparatus with a faster time resolution to determine these in the near future.

REFERENCES

1. S. E. J. Bell et al. *Annual Report to the Laser Facility Committee* Rutherford Appleton Laboratory Report RAL-90-026 143 (1990)
2. S. E. J. Bell et al. J. Phys. Chem. **94** 3876 (1990)

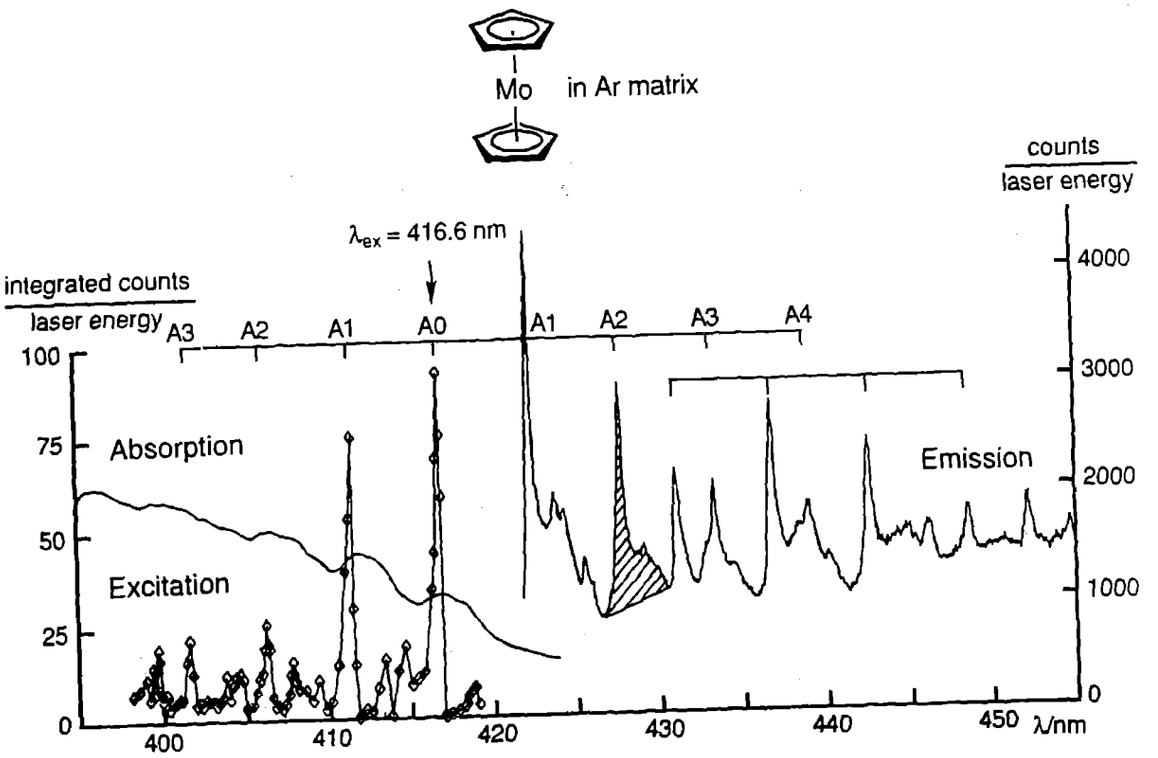

Figure 3. Right: Emission spectrum of Cp_2Mo in an Ar matrix at 12K; λex = 416.6 *nm*. Left upper: Absorption spectum of Cp_2Mo in Ar matrix. Left lower: Excitation spectrum from the A2 emission band area (shaded).

TIME RESOLVED SPECTROSCOPIC STUDIES OF PHTHALOCYANINE TRIPLET STATES

A. Beeby, A.J. MacRobert, A.W. Parker*, M.S.C. Simpson and D. Phillips

Department of Chemistry, Imperial College, London SW7 2AY
* Laser Support Facility, Rutherford Appleton Laboratory, Didcot, Oxon.

Introduction

Metallophthalocyanines have received a great deal of attention as photosensitisers for the photodynamic destruction of malignant cells, bacteria and viruses. Their action is believed to be mediated by the triplet state which may undergo two reaction pathways; Type I and Type II. In a Type I reaction the triplet state undergoes electron transfer with a biological substrate. The radical pair produced may go on to react with molecular oxygen, resulting in the oxidation of the substrate causing cell death. In the Type II mechanism the excited state of the sensitiser transfers energy to molecular oxygen to generate $^1\Delta_g$ O_2 ($^1O_2$). This chemically reactive species goes on to attack biological substrates and the ensuing reactions cause cell damage and death.

$$^3Pc^* + S \rightarrow Pc^{\cdot\pm} + S^{\cdot\mp}$$

Type I

$$S^{\cdot\mp} + O_2 \rightarrow \rightarrow \text{cell death}$$

$$^3Pc + O_2\,(^3\Sigma_g) \rightarrow Pc + O_2\,(^1\Delta_g)$$

Type II

$$O_2\,(^1\Delta_g) + S \rightarrow \rightarrow \text{cell death}$$

The sensitisers studied here are the water soluble sulphonated aluminum phthalocyanines, AlS_nPc, where n indicates the number of sulphonate groups on the macrocycle and has a value of 2, 3 or 4. These compounds exhibit a surprising range of biological activity *in vivo* despite their very similar photophysical properties *in vitro*. The aim of this study was to examine the triplet state photophysics of these compounds in the presence of biological substrates such as amino acids and proteins. The triplet states properties may be studied by laser flash photolysis.

Experimental

The Laser Support Facility ns laser flash photolysis apparatus was used for these measurements and is described fully elsewhere in this report. Briefly, the system utilises an excimer pumped dye laser as the pump and a continuous tungsten lamp as the probe. The probe beam is split and monitored by a time-gated optical multi channel analyser (OMA III) and a monochromator/photodiode/digitial storage oscilloscope combination. The phthalocyanines were pumped at 660-675nm with energies in the range 5-0.05mJ per pulse. Each transient was acquired as the average of 256 laser shots.
Samples were dissolved in water or phosphate buffered saline (pH 7.4) and concentrations were typically 2-5 x 10^{-6} M, giving an optical density of 0.4-1.0 at the pump wavelength. Where necessary degassing was achieved by Ar bubbling.

Results and Discussion

The transient spectra of AlS_2Pc in degassed water shown in Figure 1 were recorded using the OMA system. These time gated spectra clearly illustrate the depletion of the ground state as the ΔOD's at 360 and 670nm and the absorption by the triplet state at 480nm.

FIGURE 1 TRANSIENT SPECTRA OF AlS_2Pc IN H_2O

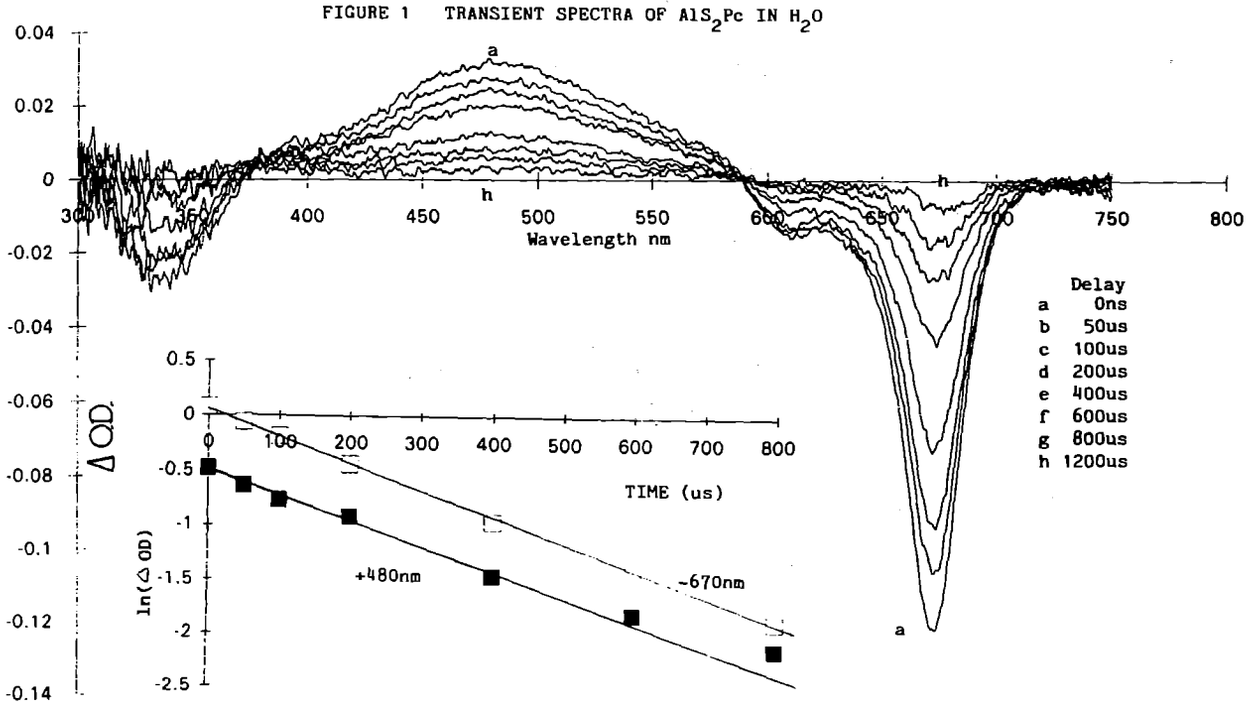

Knowing the depletion of the singlet state and its extinction coefficient it is possible to calculate the extinction coefficient of the triplet state, ε_T. Thus, from the data in Figure 1 we can calculate that for AlS_2Pc ,$\varepsilon_{T(480nm)} = 3.8 \pm 0.2 \times 10^4$ mol^{-1} cm^{-1} which corresponds well with literature values 3.6×10^4 mol^{-1} cm^{-1} for other phthalocyanines[1]. The OMA data may also be used to determine the rate constant of the excited states decay and the recovery of the singlet state as shown in the inset. Both values give a lifetime of $420 \pm 20\mu s$ for the excited state.

Under the conditions used the triplet state lifetime, (τ_t), of sulphonated aluminium phthalocyanines decays by a first order process in aqueous and organic solutions. A typical decay is illustrated in Figure 2. The lifetimes under various conditions are listed in Table 1. Importantly ,the observed lifetime is affected by the total concentration of phthalocyanine, from a concentration sudy of AlS_2Pc in PBS in the range 0 - 5μM we have determined the lifetime at infinite dilution to be 600μs and the bimolecular quenching rate constant $k = 1.7 \pm 0.1 \times 10^8$ dm^{-3} mol^{-1} s^{-1}. For all of the quenching studies presented here the concentration of the phthalocyanines was held contant at 2.5μM.

In aqueous solution the measured excited state triplet lifetime is dependent on the pH. Aluminium sulphonated phthalocyanines exist in aggregated forms below pH 5 with a concomitant reduction in the intensity of the transients optical density and a triplet lifetime to ca. 330±50 μs. Similarly, surfactants such as Triton X-100 facilitate disaggregration and the triplet lifetime of 2.5μM AlS_2Pc in this increases to 640±20 μs.

In the presence of 1mM N-acetyl tryptophanamide (NATA), tryptophan or cysteine no significant change in the triplet lifetime was observed. Thus we can show that the rate constants for bi-molecular quenching of the triplet state by these compounds are less than 10^5 $mol^{-1}dm^3s^{-1}$.

Human serum albumin (HSA) is an alpha helical globular protein and an important carrier in the bloodstream. AlS_nPcs bind to HSA as indicated by a bathochromic shift of 5nm in the absorption and fluorescence spectra. The fractional concentration of AlS_nPc bound to HSA increases significantly up to a molar ratio HSA:AlSPc of 75:2.5 μM and the excited triplet lifetime increases accordingly, as illustrated by Figure 3. At a molar ratio of 100:2.5 μM there is no significant increase in triplet lifetime although there is a difference in the maximum lifetime obtained for AlS_2Pc, AlS_3Pc, AlS_4Pc, 875±25 μs, 830±15 μs & 700±20 μs respectively. Sulphonated aluminium phthalocyanines aggregate even at very low concentrations despite electrostatic repulsions between the macrocycles. The addition of HSA facilitates disaggregation thereby increasing the triplet lifetime. Furthermore, a structural rigidity is inferred on binding to the protein which may inhibit the triplet states relaxation from T_1 to S_0.

Figure 2. Typical transient decay of AlS2Pc in water at 480nm, ex = 670nm, 0.3mJ per pulse

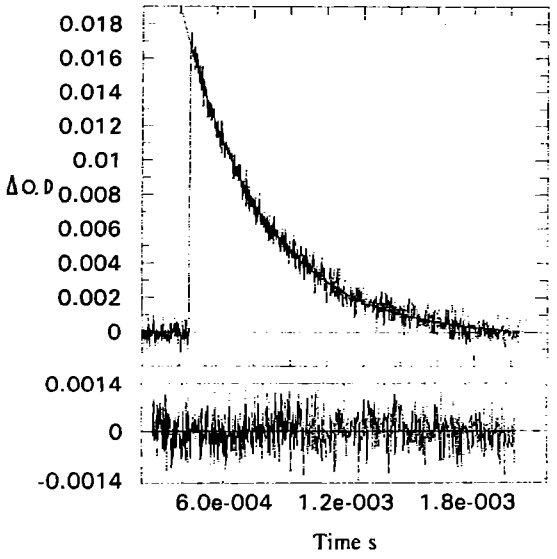

Table 1 Excited state triplet lifetimes, τ_T, of AlS_2Pc in various solvents and biological media

* All are in phosphate buffered saline solution ,pH=7.4, (pD=7.8)

Solvent	$\tau_T * 10^6$ s^{-1}	Media*		$\tau_T * 10^6$ s^{-1}
H_2O	420 ± 20	HSA	(100 μM)	875 ± 20
D_2O	990 ± 10	HSA-D_2O	(100 μM)	1580 ± 30
CH_3OH	690 ± 10	NATA	(3 mM)	420 ± 20
CH_3OD	700 ± 10	Tryptophan	(1 mM)	420 ± 20
CD_3OD	1420 ± 20	Cysteine	(100 μM)	420 ± 20
DMSO	1280 ± 30	LDL	(100 μM)	1000 ± 50
Triton X 100	630 ± 20	Lysozyme	(450 μM)	630 ± 30

Abbreviations:

DMSO	Dimethyl sulphoxide	NATA	N-Acetyl Tryptophanamide
LDL	Low Density Lipoprotein	HSA	Human Serum Albumin

Figure 3. Variation of triplet lifetime of AlS2Pc at 480nm with fractional concentration of HSA

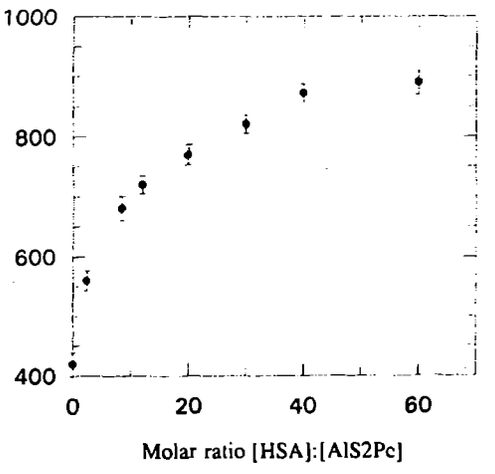

The triplet lifetime of AlS_2Pc bound to a low density lipoprotein (LDL) has been determined to be 1000±50 μs. LDL is a far larger molecule believed to be responsible for transport in the bloodstream and delivery of the sensitisers to the tumor site and consists of protein (22%) and lipid (78%). Importantly, in none of the transient spectra from the degassed protein solutions was there evidence for the formation of the phthalocyanine radical, suggesting that the Type I process is not occuring between the protein and its bound sensitiser.

The triplet states of AlS_2Pc, AlS_3Pc and AlS_4Pc in PBS and HSA (100μM) were quenched by oxygen in both H_2O and D_2O. The bimolecular rate constant constants were determined in each case by varying the concentration of dissolved oxygen and found to be $2.2\pm0.3\times10^9$ $dm^3mol^{-1}\ s^{-1}$ in PBS and $2.2\pm0.3\times10^8$ $dm^3mol^{-1}\ s^{-1}$ in the presence of HSA indicating that the protein matrix offers some protection to the macrocycle from the quencher. Further studies were carried out with hydroquinone which was used to probe the effect of binding of AlS_nPc (n = 2, 3, 4) to HSA in 50 μM solutions. By monitoring the quenching of the triplet state by its T_1-T_n absorption at 480nm as a function of the concentration of hydroquinone in PBS at pH 7.4 the bimolecular rate constants for AlS_2Pc, AlS_3Pc and AlS_4Pc were determined as $2.0\pm0.5\times10^8$ $dm^3\ mol^{-1}s^{-1}$, in agreement with previously measured values[2]. In HSA significant departure from a single exponential decay was observed, possibly due to binding of the quencher to the protein. In both cases the formation of the AlS_nPc radical anion could be observed in the flash photolysis experiment by its characteristic absorption at λ= 610nm using either the photodiode or the OMA system.

Inspection of the values in Table 1 shows that on replacing H_2O with D_2O there is a marked effect on the triplet lifetime of AlS_2Pc, in contrast with values previously reported in the literature[3]. Furthermore, in D_2O and at a pH below 4 the triplet lifetime is dramatically reduced to 400±10 μs, but at a pH above 8 is increased to 1200±50 μs.

A similar phenomenon was observed between methanol and deuterated methanol solutions of AlS_2Pc. The lifetime is increased from 650±10μs in CH_3OH to 1420±30μs in CD_3OD, but was relatively unchanged by CH_3OD. A similar effect was measured for AlS_3Pc and AlS_4Pc in D_2O,the observed triplet lifetimes being 1400±20μs and 750±40μs respectively. The marginal increase for AlS_4Pc can be attributed to aggregation since in the presence of human serum albumin (HSA) and D_2O the triplet lifetimes of AlS_2Pc, AlS_3Pc and AlS_4Pc are, within experimental error, identical, τ_T = 1600±40μs. This difference is believed to arise from -OH/D or -OCH/D_3 replacing the axially bound chloride ion which influences the rate of internal conversion and intersystem crossing. Further investgations of this observation are underway.

Conclusions

We have demonstrated that it is possible to study the triplet state of the phthalocyanine sensitisers using the Laser Support Facilty's laser flash photolysis apparatus. The triplet lifetime of the AlS_nPcs have been determined under a variety of conditions. In solution we have observed ground state quenching of the excited state and have determined a lifetime at infinite dilution of 600μs. On binding to proteins the lifetime of the excited state increases, suggesting that the bound sensitiser is offered some protection from quenching species in solution, which is supported by the O_2 and hydroquinone studies. The studies in deuterated solvents have shown that solvation of the phthalocyanines plays an important role in governing the kinetics of the S↔T processes.

Future work will include the determination of the quantum yields of triplet formation and the addition of a near-IR sensitive Ge photodiode, capable of detecting $^1O_2$ by it's 1270nm phosphorescence.

References

1 J. McVie, R.S. Sinclair and T.G. Truscott, J.Chem. Soc. Faraday 2, 1870 (1978)

2 I. McCubbin, University of London, PhD Thesis (1985)

3 J. Davila and A. Harriman, Photochem. Photochem, **51** 9-19 (1990)

REACTIONS OF DRUG AND ANTIOXIDANT FREE RADICALS STUDIED BY NANOSECOND LASER FLASH PHOTOLYSIS

Roger H Bisby[1] and Anthony W Parker[2]

[1]University of Salford
[2]Rutherford Appleton Laboratory

INTRODUCTION

Certain drugs and pollutants are metabolised in cells to free radical intermediates which impose oxidative stress and which may ultimately be responsible for toxicity. One electron oxidation of a drug, as may occur in the cell, may also be achieved by optical excitation and ionisation. Since free radical reactions are usually very rapid, having rate constants which may approach the diffusion-controlled limit, nanosecond laser flash photolysis is a valuable technique with which to generate and study the reactions of such species.

A typical animal cell contains a number of potential free radical scavengers, including ascorbate (vitamin C), urate, and non-protein thiols such as reduced glutathione. Cell membranes also contain α-tocopherol, which protects against lipid peroxidation. Together with antoxidative enzymes, these substances act in synergy to protect the cell against oxidative stress (1).

Amongst the drugs which have been proposed to exert toxicity by free radical mechanisms are three substituted aminophenols - acetaminophen (or paracetamol, an analgesic), amodiaquine (an antimalarial drug) and minocycline (an antibiotic). Laser flash photolysis has been employed in this exploratory investigation to follow specific steps in the pathway from drug-derived free radical generation to detoxification by antioxidant systems.

DRUG FREE RADICALS

The three drugs mentioned above all have absorption bands which may be excited by the 308nm emission of the Lumonics HE460 XeCl excimer. Transient radicals were detected by their absorption spectra. During the exploratory investigation transient absorptions were observed after flash photolysis of aqueous solutions of both acetaminophen and minocycline. The spectrum of the transient from flash photolysis of minocycline was found to be very similar to that of the one-electron oxidation product of minocycline measured using pulse radiolysis. The spectrum from flash photolysis of the acetaminophen solution was very weak, indicating that photolysis would be more effective at a shorter wavelength where the extinction coefficient is higher.

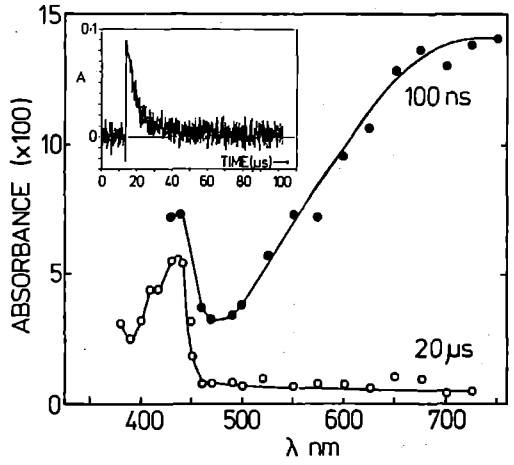

FIGURE 1 Transient spectra from flash photolysis of a deaerated solution containing SDS (40mM), α-tocopherol (0.8mM), and phosphate buffer (25mM) at pH 7.2, measured 100ns and 20μs after the flash. The inset shows the decay of the hydrated electron absorption at 725nm.

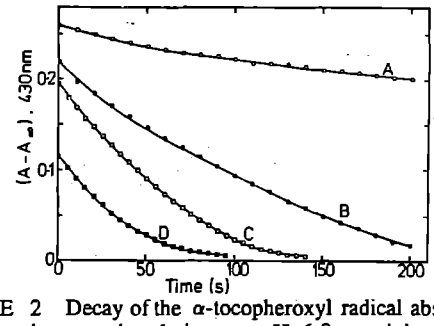

FIGURE 2 Decay of the α-tocopheroxyl radical absorption at 430nm in aerated solutions at pH 6.8 containing HTAC (40mm), α-tocopherol (1mM), EDTA (50μM), phosphate (25mM) and glutathione. Concentrations of glutathione were A-zero; B 303μM; C 588μM; D 857μM.

REACTIONS OF THE TOCOPHEROL RADICAL

The transient spectra observed during nanosecond laser flash photolysis of a deaerated solution of α-tocopherol in sodium dodecyl sulphate (SDS) micelles are shown in Figure 2. Immediately after the laser pulse, the spectrum of the hydrated electron is observed. This decays rapidly (lifetime ~10μs) and 20μs after the laser pulse only the characteristic spectrum (2) of the α-tocopheroxyl radical remains. The yield of the α-tocopheroxyl radical was found to be directly proportional to laser flash intensity, showing that the radical is formed in a monophotonic process.

The decay of the α-tocopheroxyl absorption was measured in solutions containing ascorbate (vitamin C). In the negatively charged SDS micelles the reaction, corresponding to reduction of the α-tocopheroxyl radical by the negatively charged ascorbate ion, was found to have a second order rate constant of $(3.8\pm0.2) \times 10^4$ M^{-1} s^{-1}. In positively charged hexadecyltrimethylammonium chloride (HTAC) micelles, the rate of the reaction increased to $(7.2\pm0.2)\times 10^7$ M^{-1} s^{-1}. This reaction is a model for the very important recycling of α-tocopherol in cellular membranes by the much larger aqueous pool of ascorbate. In homogenous solution the reaction has a rate constant of ~ 10^6 M^{-1} s^{-1} (3), and our results show the important influence of interfacial potential on the reaction rate.

The α-tocopheroxyl radical was found to be unexpectedly stable in aerated solutions of HTAC. This permitted its rate of reaction with another cellular reducing agent, reduced glutathione, to be measured for the first time. The results obtained, shown in Figure 2, indicate that the reduction of the α-tocopheroxyl radical by glutathione is relatively very slow, with a second order rate constant of ~25 M^{-1} s^{-1} estimated from the initial rate of the reaction.

CONCLUSIONS

Nanosecond laser flash photolysis has been shown to be useful in generating free radical species derived from drugs and antioxidants and for measuring the rates of their reactions. It has an advantage over other methods in that it can produce radicals, such as the α-tocopheroxyl radical, both in solution in the presence of high concentrations of other solutes and within structures such as micelles and membranes.

REFERENCES

1. H Sies (Ed.) "Oxidative Stress" Academic Press, London (1985)
2. RH Bisby et al. Free Rad Res Comms 4 251 (1986)
3. JE Packer et al. Nature 278 737 (1979)

LASER PHOTODISSOCIATION STUDIES USING AN ION TRAP MASS SPECTROMETER

C.S. Creaser, M.R.S. McCoustra and K.E. O'Neill.

School of Chemical Sciences
University of East Anglia
Norwich, NR4 7TJ.

INTRODUCTION

The three dimensional ion trap was first described by Paul and Steinwedel[1] in 1960. It consists of three hyperbolic electrodes which create a three dimensional quadrupole field, in which ions are trapped by the application of RF, or combined RF and DC, voltages to the ring electrode. The stability of an ion in the ion trap depends upon its mass to charge ratio and the magnitude of the applied voltages. The conditions may be adjusted to enable ions of a single mass to charge ratio to be stored. The ion trap mass spectrometer (ITMS) has been used to study photodissociation (PD) of trapped ion populations created in such a way.[2,3,4] In a conventional mass spectrometer ions are irradiated in a single pass through the laser beam, which may be aligned either coaxially with or perpendicular to the ion beam. Although the ions themselves may possess substantial photoabsorption cross sections, the high ion beam velocities may lead to small interaction times which yield low PD efficiencies. In the ion trap the possible irradiation period can be much longer than in a conventional spectrometer, leading to higher dissociation efficiencies.

The aims of this loan were to operate the ITMS using the interface previously described[4] whilst introducing samples on a gas chromatograph (GC), and also to demonstrate the use of a second fibre optic interface which allows sample introduction from a liquid reservoir, on the GC, or using a direct insertion probe. Photodissociation tandem mass spectrometry with gas chromatographic sample introduction had not previously been reported until this work.

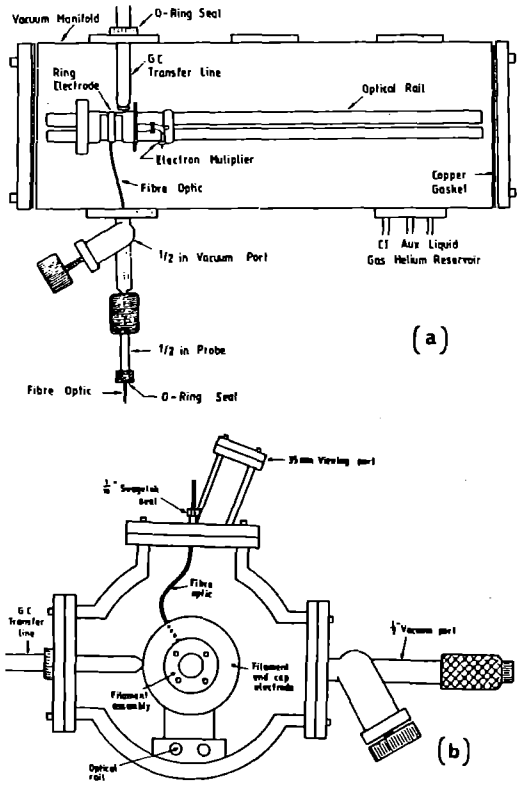

Figure 1: Fibre optic interfaces for photodissociation.

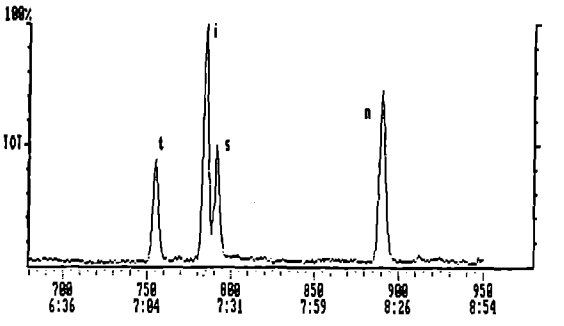

Figure 2: GC chromatogram for the PD products of a mixture of *n*, *i*, *s* and *t*-butyl benzene (573 nm).

EXPERIMENTAL

The ion trap mass spectrometer (Finnigan MAT) was modified by drilling a hole through the ring electrode into which one end of a 1mm silica fibre optic (Vuman Ltd.) was inserted. Two configurations were adopted for the introduction of the fibre into the vacuum housing: either through a modified probe with an o-ring seal, via the vacuum probe lock (Fig. 1(a)), or through a 1/16" Swagelok union in a modified flange located perpendicular to the GC transfer line and the probe lock (Fig. 1(b)). Light from a pulsed Nd:YAG laser or from a pulsed Nd:YAG pumped Rh6G dye laser (JK2000; SERC Laser Support Facility) was coupled into the silica fibre with a three axis delivery system (Vuman, model FD-1000-2). The beam intensity was attenuated to 2mJ (visible) or to less than 1mJ (UV) to accommodate the damage threshold of the silica fibre. Optical transmission of the fibre system was estimated to be in excess of 50% at all wavelengths longer than 250 nm. The opening and closing of the laser cavity shutter were controlled from the spectrometer data system at the appropriate time in the RF cycle.

A mixture of butyl benzenes were investigated using photons of 563nm and 573nm from the dye laser, which was pumped with the 532nm harmonic of the Nd:YAG laser operating at 10Hz. The mixture was separated on a directly interfaced 30m x 0.22mm id DB17 column (J&W Scientific) fitted in a Varian 3400 gas chromatograph. The oven temperature was maintained isothermally at 80°C, the injector at 250°C and the transfer line at 250°C. Split injections were carried out with a split flow of 20 cm^3/min. The butyl benzene ions were formed by electron ionisation and the precursor ions (m/z 134) isolated using a DC/RF isolation routine.[5] The precursor ions were subjected to five pulses of laser light per microscan. Background spectra were recorded under the same conditions as the PD spectra but without laser irradiation of the trapped ions. In a later series of experiments individual butyl benzene isomers were introduced on the GC and irradiated using the fourth harmonic of the Nd:YAG laser (266nm). The injections were carried out in splitless mode, and the GC programme was 50°C for 1 min, ramp to 100°C at 5°/min, hold 5 min. The injector temperature was 180°C and the transfer line was held at 200°C. The GC was fitted with a 50m x 0.22mm id RSL200-BP column (Alltech Ltd.) which was directly interfaced to the mass spectrometer.

RESULTS AND DISCUSSION

The GC chromatogram for the PD products of the isolated molecular ions (m/z 134) of the butyl benzene isomers after gas chromatographic separation and irradiation at 573nm is shown in Fig. 2. The background subtracted spectra of *n*- and *t*-butyl benzene are shown in Fig. 3. Background subtraction was used to remove residual collisionally activated dissociation (CAD) product ions formed as a result of the long residence time of the

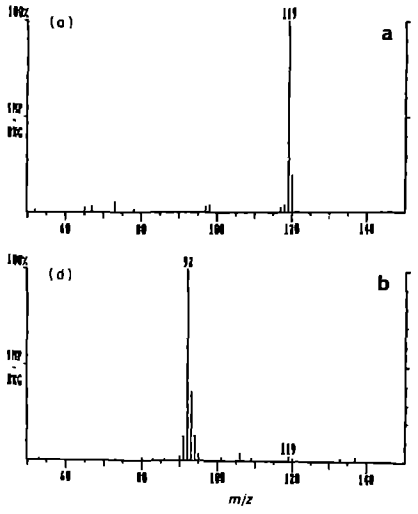

Figure 3: PD product ion mass spectra of (a) *t*- and (b) *n*-butyl benzene irradiated at 573 nm.

precursor ions in the trap during laser illumination. This is the first recorded example of GC-PD-MS, and the results were reported by this group at the 18th meeting of the British Mass Spectrometry Society.[6,7] Irradiation at this wavelength is suitable for photodissociation of the butyl benzenes and gives good efficiencies. However PD using UV excitation is more useful as a general tool applicable to a wide range of compounds. Figure 4 shows preliminary data obtained from *n*- and *t*-butyl benzene using GC introduction and subsequent irradiation at 266nm, demonstrating that PD can be carried out in the UV region using a fibre optic to couple the photons to the spectrometer.

The fragmentation efficiencies (FE) of the photodissociation process were determined as follows:

$$F.E. = \frac{\Sigma I_{product}}{\Sigma I_{product} + \Sigma I_{precursor}}$$

The PD efficiencies were found to be in the range 57%-89% at 573nm and in the range 87%-100% at 266nm. This is comparable to the efficiencies observed in bulk introduction experiments using the butyl benzene isomers irradiated at 532nm and to the corresponding efficiencies for CAD.

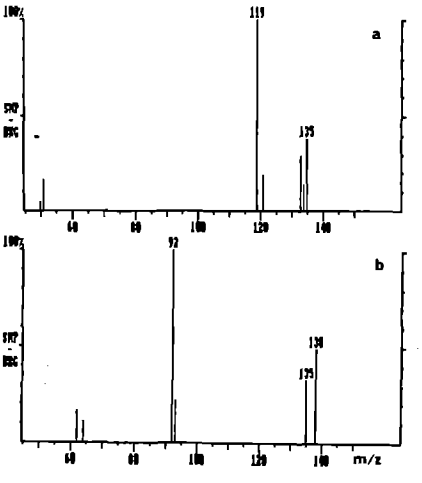

Figure 4: PD product ion mass spectra of (a) *t*- and (b) *n*-butyl benzene irradiated at 266 nm.

CONCLUSION

Photodissociation can be readily carried out in the ion-trap using a simple fibre optic interface for both directly introduced samples and, more importantly, for samples introduced by gas chromatography. The internal energy of the ion undergoing dissociation is determined by the photon energy and the collision energy in PD and CAD respectively. The tuning procedure for a CAD experiment is extensive as the frequency of the auxiliary RF voltage (tickle voltage) applied must be fine-tuned to the secular frequency of oscillation of the target ion, and can vary with the sample loading of the trap.[8] In a photodissociation experiment the laser wavelength determines the energy deposited in the trapped ion, consequently allowing greater control of the dissociation process than with induced CAD. The detection levels for the GC-PD-MS experiments are compatible with narrow-bore fused-silica capillary columns, thus allowing the method to be applied to the analysis of complex mixtures in which the analyte absorbs in the visible or UV region. Problems of optical damage to the silica fibre, which necessitated its return to Vuman for repair, however, prevented extension of these studies to compounds other than the butyl benzenes.

ACKNOWLEDGEMENTS

We acknowledge support from the SERC, the SERC Laser Support Facility and ICI Agrochemicals.

REFERENCES

1. W. Paul, H. Steinwedel; US Patent 2,939,952; (1960)
2. R.J. Hughes, R.E. March, A.B. Young; *Can. J. Chem.*; **61**; 824-833; (1983)
3. J.N. Louris, J.S. Brodbelt, R.G. Cooks; *Int. J. Mass Spectrom. Ion Proc.*; **75**; 345-352; (1987)
4. C.S. Creaser, M.R.S. McCoustra, D.S. Mitchell, K.E. O'Neill, *Annual Report to the Laser Facility Committee,* Rutherford Appleton Laboratory, p128, (1990)
5. C.S. Creaser, D.S. Mitchell, K.E. O'Neill, *Int. J. Mass Spectrom. Ion Proc.*; in press
6. C.S. Creaser, M.R.S. McCoustra, D.S. Mitchell, K.E. O'Neill, Proc. XVIII British Mass Spectrom. Conf., London, pp49, (1990)
7. C.S. Creaser, M.R.S. McCoustra, K.E. O'Neill, *Org. Mass Spectrom.*, **26**, 335-338 (1991)
8. J.F.J. Todd, A.D. Penman, D.A. Thornber, R.D. Smith, *Rapid Comm. Mass. Spectrom.*, **4**, 108, (1990)

REACTIONS OF GROUND STATE OXYGEN ATOMS

J.C. Whitehead and F. Winterbottom

Chemistry Department
Manchester University
Manchester M13 9PL, UK

INTRODUCTION

The reactions of ground-state oxygen atoms, $O(^3P)$, with organic hydrides are of considerable importance in our understanding of combustion processes. In general, these systems possess activation energy barriers to reaction that can only be overcome by supplying energy. A convenient way of providing this energy is in the form of kinetic energy by using translationally "hot" oxygen atoms. This can be achieved in two ways. Firstly, by using supersonic molecular beam sources a range of $O(^3P)$ + RH reactions have been studied[1-5] using laser-induced fluorescence (LIF) detection of the OH reaction product. Secondly, photolysis of NO_2 at an appropriate wavelength can yield "hot" oxygen atoms and forms the basis of the pulse/probe experiment for studying O + HX reactions.[6-8] Both the crossed molecular-beam and pulse/probe experimental arrangements ensure that the reaction products (OH) are detected under collision-free conditions giving nascent vibrational, rotational and fine structure state distributions. Here we report a pulse/probe study of the production of ground-state $OH(^2\Pi)$ from the reactions of $O(^3P)$ with cyclohexane and cyclooctane.

EXPERIMENTAL

A slowly flowing mixture of NO_2 and the appropriate hydride (total pressure $\sim$ 80 m Torr; NO_2:RH ratio is 5:1) was photolysed by a 351 nm XeF excimer laser pulse yielding $O(^3P)$ atoms from the NO_2. (The orangic molecules do not photolyse at 351 nm). After a short delay ($\sim$ 200 ns) the OH internal state distributions were probed by LIF using a tuneable UV laser system (Spectron YAG, Quanta Ray PDL and WEX) operating on the $A\ ^2\Sigma^+ \leftarrow X\ ^2\Pi$ system of OH. The fluorescence was observed by a photomultiplier (EMI 9659QB) after passing through a broad band filter consisting of a UG11 colour glass filter and 1 cm of 2M $NiSO_4$. The signal was fed to the 50 Ω input of a boxcar integrator (SRS SR 250/280). The OH vibrational, rotational, spin-orbit and lambda doublet populations were measured for each reaction using the (0,0) and (1,1) bands. A portion of the LIF spectrum for O + cyclohexane is shown in Figure 1.

RESULTS AND DISCUSSION

The rotational state distributions for both reactions show a very low degree of rotational excitation for the OH product (6 and 5% of the total available energy for O + $c\text{-}C_6H_{12}$ and $c\text{-}C_8H_{16}$, respectively). This result is taken to indicate that the reaction is a direct one involving abstraction of the hydrogen atom via a tightly collinear O-H-R transition state which dissociates with almost none of the reaction energy being disposed into product rotation. Similar behaviour has been found for other reactions of $O(^3P)$ with organic hydrides.[1-5]

The vibrational energy partitioning into v=0 and v=1 shows a marked difference between the two cyclic hydrocarbons. P(v=1)/P(v=0) = 0.14 for O + $c\text{-}C_6H_{12}$ and = 1.77 for O + $c\text{-}C_8H_{16}$. This increase in vibrational excitation follows the increasing reaction exoergicity for O + $c\text{-}C_8H_{16}$ compared with O + $c\text{-}C_6H_{12}$; a correlation which has been noted for other O + RH reactions.

The reactions show a specificity for populating the $^2\Pi_{3/2}$ spin-orbit state of OH in v=0 and v=1 in the case of O + $c\text{-}C_6H_{12}$ and for OH in v=1 in the case of O + $c\text{-}C_8H_{16}$. The specificity ranges between 1.6 and 2.0. Such a spin-orbit specificity

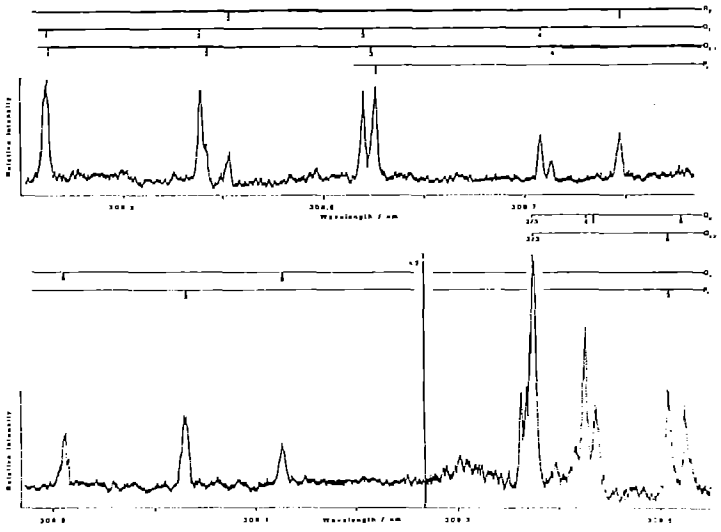

Figure 1 Portion of the $OH(A \leftarrow X)$ LIF spectrum resulting from the $O(^3P)$ + C_6H_{12} reaction showing the Q branch of the (0,0) band.

has only previously been observed for O + cyclohexane[1,3] and there has been no such specificity reported for any of the other O + RH reactions studied.[1-5] If the O + RH reaction is strictly adiabatic (treating R as a structureless particle) with no surface crossings, OH is expected to be produced with a spin-orbit distribution that reflects the initial $O(^3P_J)$ spin-orbit distribution. However, if there is complete spin-orbit mixing of the reaction potential energy surfaces with many surface crossings during the reactive collision, then the specificity of OH spin-orbit states will be destroyed. It has been suggested that the mixing can be a result of electron delocalisation in the organic radical fragment resulting from the reaction[1,3]. For these cyclic unsaturated reagents, the amount of possible electron delocalisation that can occur in the radical product is limited allowing for OH spin-orbit specificity to be observed in these reactions.

REFERENCES

1. P. Andersen and A.C. Luntz, J. Chem. Phys. 72 5842 (1980).

2. K. Kleinermanns and A.C. Luntz, J. Chem. Phys. 77, 3533, 3537 (1982).

3. N.J. Dutton, I.W. Fletcher and J.C. Whitehead, Mol. Phys. 52, 2620 (1984).

4. N.J. Dutton, I.W. Fletcher and J.C. Whitehead, J. Phys. Chem. 89, 569 (1985).

5. N.J. Barry, I.W. Fletcher and J.C. Whitehead, J. Phys. Chem. 90, 4911 (1986).

6. K.G. Kendrick, D.J. Rakestraw and R.N. Zare, Faraday Disc. Chem. Soc. 84, 39 (1987).

7. C.R. Park. G.D. White and J.R. Wiesenfeld, J. Phys. Chem. 92, 152 (1988).

8. J.C. Whitehead and F. Winterbottom, Chem. Phys. Lett. 177, 207 (1991).

Λ-DOUBLET ENERGY TRANSFER IN OH($X^2\Pi$)

M. N. R. Ashfold, I. D. Bennet, S. M. Holland,
R. J. Leaver and D. J. Winkett

University of Bristol

INTRODUCTION

A very important parameter in current models [1-4] for the OH interstellar maser is the rate of collision induced population transfer between Λ-doublet states. Experimental measurements of these quantities are nonexistant. Indeed, it is only very recently that it has proved possible to make reliable measurements of vibrational [5] and rotational [6] energy transfer rates within the ground electronic state of the OH radical.

Prior to the current laser loan we had already undertaken preliminary experiments [7] which demonstrated one method of preparing single v,J,Λ quantum states of OH(X) and thus appeared to open the way to (at least relative) rate measurements of collision induced Λ-doublet and rotational state population transfer in this radical. These proving experiments employed the H+NO reaction as the source of OH(X) radicals, and the excitation scheme shown as an inset to fig. 1 in order to achieve Λ-doublet specificity. The Raman shifted output of a Nd-YAG pumped dye laser (2nd Stokes in H_2) was used to excite the $\Delta v = +2$ overtone transition in OH(X). A Q (rather than P or R) branch line was chosen because only for these is the Λ-doublet splitting greater than the available dye laser bandwidth. The Q branch linestrengths in this $^2\Pi$-$^2\Pi$ vibrational band fall off rapidly with increasing J; hence our choice of a level with low J quantum number. The specificity of this preparation scheme was demonstrated by using a second Nd-YAG pumped dye laser (frequency doubled) to record the (1,2) band of the OH($A^2\Sigma^+$-$X^2\Pi$) laser induced fluorescence (LIF) excitation spectrum. With minimal time delay between the preparation and probe lasers these experiments yielded the expected simple pattern of just one P, Q and R branch line originating from the initially prepared v,J,Λ level (see fig. 1). With increasing time delay both Λ-doublet and rotational energy transfer within the v=2 level were observed to occur, with roughly comparable efficiency with the ill-defined mixture of collision partners (mainly Ar, but also H_2O, NO and NO_2) used in the preliminary study. The present laser loan was sought in order that we might reinvestigate these processes under conditions which approximate more closely to those prevailing in the interstellar medium (i.e. where non-polar species such as H atoms and H_2 molecules constitute the dominant collision partners). If these studies also show Λ-doublet population transfer in OH(X) to occur with such facility it may well prove necessary to revise some of the current models for the OH interstellar maser [4].

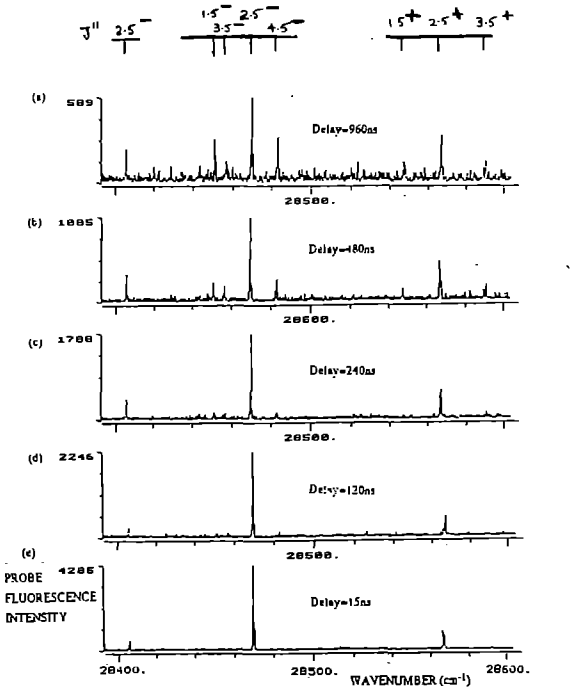

Fig. 1 LIF excitation spectra of the OH(A-X) 1,2 band as a function of time delay following selective population of the v''=2, J''=2.5, − parity Λ-doublet. Collision-induced rotational energy transfer into neighbouring levels with J''=1.5 and 3.5 is clearly evident.

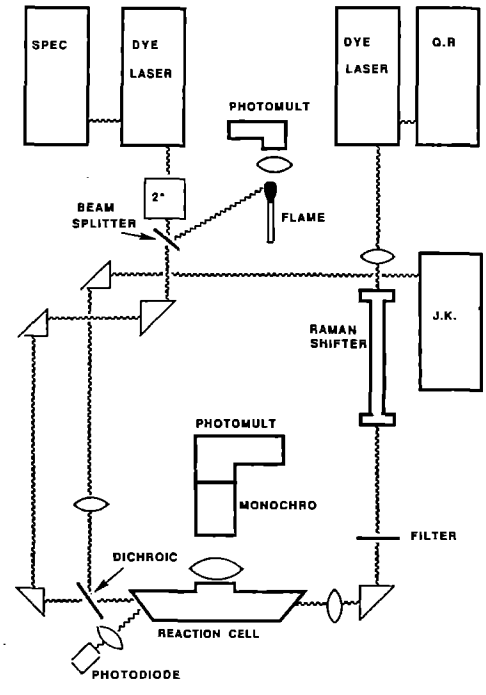

Fig. 2 Schematic of the experimental arrangement used in the present studies.

EXPERIMENTAL

A schematic of the three laser set-up employed in the present experiments is shown in fig. 2. The principal difference between these and the earlier experiments [7] is the OH(X) radical production scheme. The availability of the frequency quadrupled JK 2000 Nd-YAG laser from the Laser Loan Pool allows us to use 266nm photolysis of H_2O_2 as a clean, efficient source of OH(X) radicals with little internal excitation, but substantial translational excitation [8]. This we cool by carrying out the photolysis in the presence of excess buffer gas (e.g. H_2). Then, after a suitable time delay, the internally and translationally relaxed $OH(X)_{v=0}$ radicals will be excited to the selected v=2,J,Λ quantum state and subsequently probed via LIF on the A-X (1,2) transition as previously.

RESULTS

These experiments are still ongoing at the time for submission of this Report. To date we have:

(i) established operating conditions under which it is possible to consistently obtain >10mJ output at 266nm from the JK 2000 loan laser with acceptable temporal drift in the energy.

(ii) successfully demonstrated production of $OH(X)_{v=0}$ radicals in the 266nm photolysis of H_2O_2, and the fact that these can be translationally cooled through collisions with buffer gas - see fig.3.

We have not yet succeeded in detecting $OH(X)_{v=0}$ radicals following IR pumping to the selected Λ-doublet state. This work is on-going.

ACKNOWLEDGEMENTS

Financial support from SERC is gratefully acknowledged, as is the enthusiastic assistance given by Dr. Sue Tavender when installing the loan laser under uncomfortably cramped conditions and the subsequent, consistently excellent, support of Mr. K. N. Rosser.

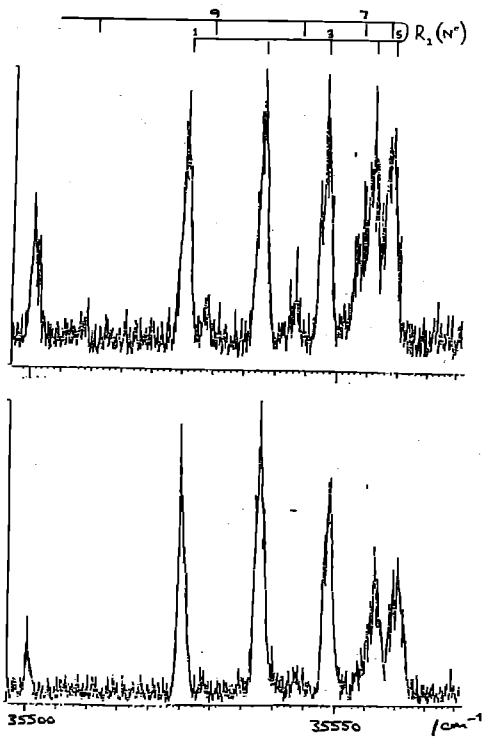

Fig. 3 LIF excitation spectra of part of the OH(A-X) 1,0 band: (a) 0.2Torr H_2O_2, 200ns pump-probe time delay, (b) 0.2Torr H_2O_2 plus 10Torr air, time delay as in (a). Analysis of the observed line intensities and widths shows that, under these conditions, the collision-free fragment mean recoil velocity (essentially a monoenergetic distribution with $\bar{v}$=3700ms^{-1} [8]) and rotational temperature (T_R~1530K [8]) have partially relaxed to (a) an (approximately) Boltzman distribution of similar mean volocity and T_R=625K and (b) a Boltzmann distribution with most probable velocity $\bar{v}$=2900ms^{-1} and T_R=450K.

REFERENCES

1. W. D. Gwinn, B. E. Turner, W. M. Goss and G. L. Blackman, Astrophys. J. 179, 789, (1973)
2. R. N. Dixon and D. Field, Proc. Roy. Soc. A368, 99, (1979)
3. P. Andresen and R. Schinke in *Molecular Photodissociation Dynamics* (eds. M. N. R. Ashfold and J. E. Baggott), Royal Society of Chemistry, London, (1987), Chap. 3
4. For a survey, see D. R. Flower, "Molecular collisions in the Interstellar Medium", Cambridge Univ. Press, 1990.
5. G. A. Raiche, J. B. Jeffries, K. J. Rensberger and D. R. Crosley, J. Chem. Phys. 92, 7258, (1990) and references therein
6. A. Schiffmann and D. J. Nesbitt, unpublished results
7. R. J. Leaver, B. Sc. Thesis, University of Bristol, 1990
8. K. H. Gericke, S. Klee, F. J. Comes and R. N. Dixon, J. Chem. Phys. 85, 4463, (1986)

TIME RESOLVED KINETIC STUDIES OF THE REACTIONS OF GAS-PHASE METHYLSILYLENE

R. Becerra[1], M.A. Blitz[2], H.M. Frey[2], B. Mason[2], R. Walsh[2] and I.M. Watts[2]

[1] C.S.I.C., Madrid,
[2] University of Reading

INTRODUCTION

Silylenes are ubiquitous intermediates in both thermal and photochemical decompositions of silanes and organosilanes. We have studied by means of laser flash photolysis/laser absorption the kinetics of reactions of $SiMe_2$[1-3], SiH_2,[4,5] and PhSiH[6]. In several of these studies the silylenes were detected for the first time in the gas-phase[1,6]. Moreover a number of these investigations were carried out using lasers supplied by the Laser Support Facility[2,6]. Accounts of these studies have appeared in previous annual reports[7]. Measured rate constants (at ca 298 K) are relatively high with many reactions occurring faster than 1 in 10^3 collisions. Mechanisms are of the acid/base type and appear to depend on a delicate balance between the electrophilic and nucleophilic character of the silylenes and substrate molecules.

Methylsilylene, MeSiH, has not previously been studied but would appear to be relatively straight forward to generate from a rational precursor molecule. Studies of the kinetics of its reactions will indicate whether or not it is intermediate in reactivity between SiH_2 and $SiMe_2$. It will also make possible a direct comparison between Me and Ph substitution in a silylene.

EXPERIMENTAL

The apparatus and equipment used for these studies was similar to that employed in earlier studies of $SiMe_2$ and is described in detail elsewhere[1-3]. Briefly, transients from the decomposition of 1,2-dimethyldisilane were generated by pulsed 193 nm photolysis (Oxford KX2 ArF exciplex laser). Transient absorptions were detected and monitored in the wavelength range 460-520 nm using the Spectra Physics 2025 Argon Ion Laser provided by the Laser Facility loan scheme. A multipass arrangement gave total path detection lengths of up to 4.8 m although usually ca 1.4 m was employed in our high temperature cell. Absorption signals were detected using a dual photodiode/differential amplifier combination and stored in a transient recorder interfaced to a BBC micro computer used as a signal averager. The precursor substance, 1,2-dimethyldisilane (DMDS), was kindly supplied by E. Hengge (University of Graz) and was ca 95% pure.

RESULTS

Preliminary experiments with ca 50 mTorr of DMDS diluted in Argon (6 Torr) at 295 K revealed absorption signals (extrapolated to zero time) in the wavelength range 460-520 nm as shown in figure 1. These signals decayed rapidly at rates independent of wavelength, total pressure and laser intensity. Because the absorption intensities appear to show no wavelength dependence in this range a comparison is made with the known spectra of $SiMe_2$ in both the gas phase and frozen matrix. Matrix isolation studies on other bulkier silylenes[8] suggest little effect of H-for-Me substitutions on the spectrum. Thus while the spectral evidence is not conclusive the absorption is in the right place. More compelling evidence comes from end-product studies of Si-H insertion reactions[9], using g.c. analysis.

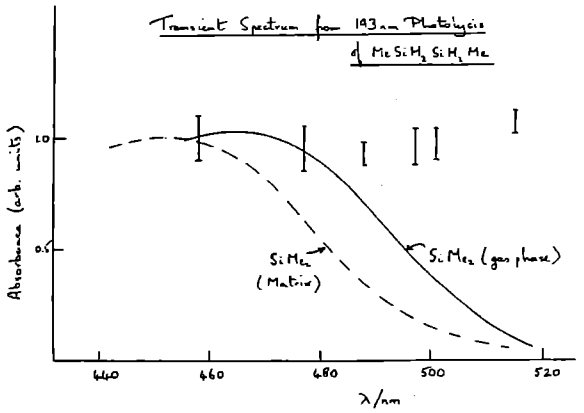

Figure 1 Absorbances (spectrum) attributed to MeSiH

Kinetic experiments were carried out with mixtures containing 20-100 mTorr of DMDS with partial pressures of substrate in the range 3-600 mTorr and total pressures 6 Torr (made up with Argon). Experiments were made difficult by erratic amounts of dust formation. This tended to vary from experiment to experiment. For data processing purposes only runs with little or no dust were used. Signal decays (averaged for 20-30 laser shots) were single exponential and second order rate constants were determined by measuring the pseudo-first order decay constants as a function of added substrate. Reasonable linear dependencies were found. The reactants investigated thus far are SiH_4 and Me_3SiH. Experiments were carried out in the temperature range 359-544 K, with at least four different temperatures for each reactant. The measured rate constants were fitted to the Arrhenius equation by least-means-squares analysis and the parameters obtained are shown in table 1. Error limits (not shown) are ± 0.5 (log A) and ca ± 4 kJ mol^{-1} (Ea). These rate data for MeSiH were more difficult to obtain than those for $SiMe_2$, as a result of a combination of relatively inefficient MeSiH production combined with high decay rates.

Table 1 Arrhenius Parameters for MeSiH insertion reactions

Substrate	log A[a]	E_a[b]
SiH_4	-11.41	-7.5
Me_3SiH	-12.81	-18.5

a. Units: cm^3 $molecule^{-1}$ s^{-1} b. Units: kJ mol^{-1}

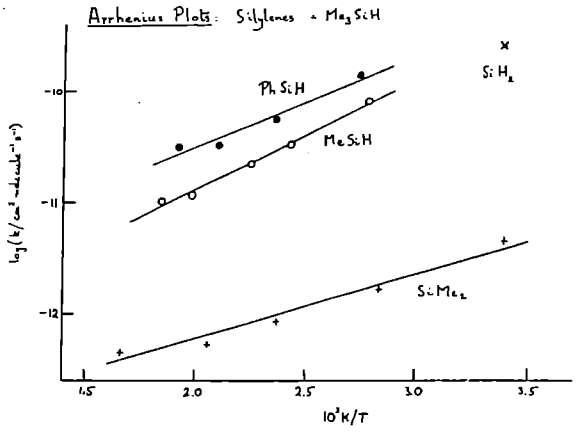

Figure 2 Arrhenius Plots for insertion reactions of silylenes (various) with Me_3SiH

DISCUSSION

The measurements reported here represent the first experimentally determined rate constants for MeSiH. Three features of the data emerge clearly from these results. (i) The reaction with Me_3SiH is faster than that with SiH_4 (on a per Si-H bond basis). This is consistent with similar observations for $SiMe_2$[1,3], SiH_2[5] and PhSiH[6]. (ii) Rate constants decrease with increasing temperature, i.e. activation energies are negative. This is also consistent with findings for $SiMe_2$[3], PhSiH[6] and SiH_2[10]. (iii) MeSiH is much more reactive than $SiMe_2$ over the same temperature range. Figure 2 shows a comparison of rate constants for all the silylenes studied in our laboratories in reaction with Me_3SiH. This indicates that Me and Ph substitution make relatively little difference to the reactivity of silylene. MeSiH and PhSiH are comparable with one another and also with SiH, (although at present only a room temperature value is available for this case[5]).

These results offer further support for the operation of a complex mechanism[3] in which the initial interaction produces an intermediate which may either redissociate or go on to react. This possibility is shown in the following equation:

$$MeSiH + Me_3SiH \leftrightarrows Complex \rightarrow MeSiH_2SiMe_3$$

The nature of the complex is not known but we favour a structure containing a weak Si.....Si bond formed by nucleophilic interaction of the silylene lone pair with the substrate Si atom[3]. The favoured structure and potential energy surface for this reaction are shown in figure 3. This kind of potential surface has been discussed previously and shown to lead to the typical negative activation energies observed in these reactions[3].

At present we have no certain explanation for the significant difference in reactivity of MeSiH and $SiMe_2$. We plan to carry out further kinetic studies of MeSiH to investigate its reactivity with other substrates. Reports of this work have been presented at two international meetings[11,12].

REFERENCES

1. J.E. Baggott, M.A. Blitz, H.M. Frey, P.D. Lightfoot and R. Walsh, Chem. Phys. Lett. **135** 39 (1987).
2. J.E. Baggott et al, J. Chem. Soc., Faraday Trans. 2 **84** 515 (1988).
3. J.E. Baggott et al, J. Am. Chem. Soc. **112** 8337 (1990).
4. J.E. Baggott et al, J. Phys. Chem. **92** 4025 (1988).
5. J.E. Baggott et al, J. Chem. Soc., Faraday Trans. **86** 27 (1990).
6. M.A. Blitz, H.M. Frey, F.D. Tabbutt and R. Walsh, J. Phys. Chem. **94** 3294 (1990).
7. SERC Central Laser Facility; Annual Report 1988, p 172; Annual Report 1989, p 240; Annual Report 1990, p 115.
8. M.J. Michalczyk et al, Silicon, Germanium, Tin and Lead Compounds **9** 75 (1986).
9. N. Al-Rubaiey and R. Walsh, unpublished results.
10. B. Mason, experiments in progress.
11. R. Becerra et al, 9th International Symposium on Organo-Silicon Chemistry, Edinburgh, July 1990.
12. R. Walsh, 11th International Symposium on Gas Kinetics, Assisi, Italy, Sept 1990.

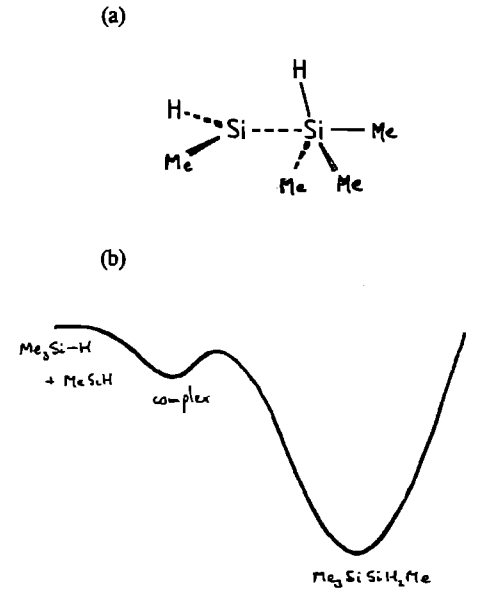

Figure 3 (a) Structure of MeSiH + Me_3SiH complex
(b) Potential energy surface (qualitative)

CO_2 LASER DESORPTION TIME-OF-FLIGHT MASS SPECTROMETRY OF POLYATOMIC MOLECULES: EFFECT OF SUBSTRATE THERMAL PROPERTIES ON DESORPTION EFFICIENCY.

M.J.Dale, A.C.Jones, G.A.Keenan and P.R.R.Langridge-Smith.

University of Edinburgh.

INTRODUCTION.

Pulsed CO_2 laser desorption is being used increasingly in mass spectrometry to vaporise involatile or thermally labile organic compounds as intact neutral molecules. However, the mechanism of the desorption process is not well understood. Zare and Levine[1] have proposed a mechanism whereby sufficiently rapid heating of a surface by incident laser radiation can result in the desorption of adsorbed molecules without dissociation of intramolecular bonds. It is argued that energy is efficiently transferred from the phonon modes of the heated surface to the low frequency physisorption bond, whereas a "bottleneck" occurs in the flow of energy from this bond to other chemical bonds in the adsorbed species due to the frequency mismatch between these bonds.

CO_2 laser desorption can also be used for the direct production of ionised molecules; these nascent ions are generally quasimolecular species resulting from cation attachment of Na^+ or K^+ to the sample molecule. The ionisation process has been accounted for[2] in terms of thermionic emission of alkali cations which attach to neutral molecules in the gas phase.

We report here the results of an investigation of the effect of substrate thermal properties on the desorption of polyatomic molecules from multilayer solid samples (100's of monolayers thick or more). A one dimensional heat diffusion model[3,4] was used to predict the transient temperature profile produced in the substrate by the incident laser radiation.

EXPERIMENTAL.

The laser desorption time-of-flight mass spectrometer system used in these experiments has been described in a previous report[5]. Sample desorption was carried out using a pulsed TEA CO_2 laser (Alltec 854MS) producing a maximum of 400mJ of 10.6μm radiation in a 100ns pulse. The sample (deposited as a solid from solution) was desorbed from the surface of a 5mm diameter rod of the substrate material. The desorbed species were entrained in a pulsed jet of helium and the entrained neutrals were photoionsed by the 266nm (4th harmonic) output of a JK2000 Nd:YAG laser. The photoions were mass analysed in a linear time-of-flight mass spectrometer. The intensity of photoionised desorbed neutrals and of nascent ions (ionic species produced in the desorption process) were monitored as a function of desorption laser energy density for three substrate materials, namely stainless steel, brass and fused silica. Desorption energy densities in the range 1-6J.cm^{-2} (power densities 10-60MW.cm^{-2}) were used. Experiments were carried out on two sample molecules: perylene (a polycyclic aromatic hydrocarbon, mass 252amu) and tryptophan (an aromatic amino acid, mass 204amu).

The CO_2 laser-induced temperature rise in the substrate was simulated by a numerical solution of the one dimensional heat transfer equation using a finite difference method[3,4]. In this model the substrate is divided into a series of elements along a line perpendicular to the surface. The transient temperature profile is calculated as a function of depth along this line.

RESULTS AND DISCUSSION

(a)Temperature simulations.

The differing thermal behaviour of the three substrate materials is illustrated in Figure 1, which shows the simulated temperature profiles induced by a 100ns CO_2 laser pulse with energy density 3J.cm^{-2}. The predicted maximum surface temperatures, shown by curves (a), are 1050K for stainless steel, 1600K for brass and 4750K for fused silica. Fused silica behaves differently from the metallic substrates in that its temperature decays more slowly with respect to both time and depth.

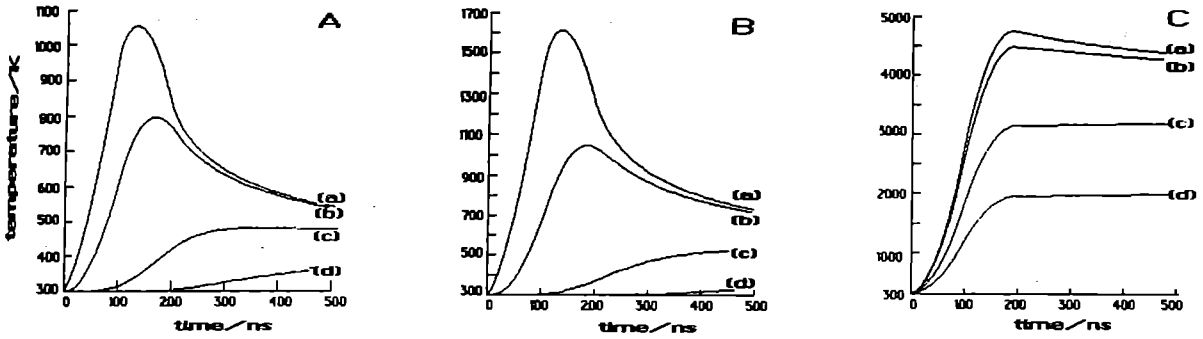

Figure 1. Simulated transient temperature profiles induced in stainless steel(A), brass(B) and fused silica(C) by 3J.cm^{-2} of laser radiation. Profiles are shown at (a)the substrate surface and at depths of (b)0.5μm, (c)2μm, (d)4μm below the surface.

(b)Experimental results.

The minimum CO_2 laser energy density required to produce gas phase neutral molecules was found to differ significantly among the three substrates, with the threshold for desorption increasing in the order fused silica < brass < stainless steel. For example, for perylene samples with an estimated average thickness of at least 0.1μm, the following thresholds were obtained: fused silica, <1J.cm^{-2}; brass, 1J.cm^{-2}; stainless steel, 2.5J.cm^{-2}. (These threshold values correspond to the CO_2 laser energy density required for production of sufficient neutral molecules to give rise to a detectable photoion signal). The predicted maximum surface temperatures for these laser intensities are 740K for brass and 930K for stainless steel. In the case of fused silica, the threshold appeared to lie considerably below 1J.cm^{-2}; the thermal model predicts that an energy density of 300-400mJ.cm^{-2} would be required to produce a surface temperature in the range 700-900K, i.e. comparable to that predicted for the other two substrates. In the case of tryptophan, the same trend was observed in desorption behaviour; however, for all three substrates the threshold energy lay below the minimum experimental value of 1J.cm^{-2}. The lower observed thresholds for this molecule may be due to higher volatility or a greater photoionisation cross section at 266nm, or to a combination of these factors.

The relative desorption efficiencies observed experimentally for the three substrates are in good qualitative agreement with the behaviour predicted on the basis of their thermal properties. This is consistent with a thermal model for the desorption process, involving rapid laser-induced heating of the substrate surface.

For both tryptophan and perylene, nascent ion production was observed at threshold energy densities (calculated maximum surface temperatures) of 3J.cm^{-2} (~1600K) for the brass substrate and 1J.cm^{-2} (~1800K) for fused silica. The threshold for nascent ion production from stainless steel was greater than the maximum energy density used, 6J.cm^{-2} (~1800K). Although the existing experimental arrangement did not allow mass analysis of the nascent ions, they were observed in the absence of sample and therefore originated from the substrate, not the sample. The calculated surface temperatures at which these ions appeared are in line with those previously reported by van der Peyl *et al*[2] for desorption of alkali ions. The latter work also indicated a lower activation energy for thermionic emission of Na^+ from quartz than from stainless steel.

REFERENCES

1.R.N.Zare and R.D.Levine, Chem.Phys.Lett. 136 593 (1987).

2.G.J.Q.van der Peyl, J.Haverkamp and P.G.Kistemaker, Intern.J.Mass Spectrom. 42 125 (1982).

3.J-M.Philippoz, R.Zenobi and R.N.Zare, Chem.Phys.Lett.158 12 (1989).

4.J.F.Ready,*Effects of High Power Laser Radiation* (Academic Press,NY 1952).

5.A.C.Jones, G.A.Keenan and P.R.R. Langridge-Smith, *Annual Report to the Laser Facility Committee 1990* RAL-90-026 127 (1990).

NON–THERMAL LASER INDUCED DESORPTION AND ENERGY TRANSFER FOR MOLECULES ADSORBED ON SURFACES.

S.D. Hooke[1], A.W. Parker[2], K.v. Puttkammer[1], A. Takami[1], C.J.S.M. Simpson[1]

[1]Physical Chemistry Laboratory, Oxford University
[2]Rutherford Appleton Laboratory

INTRODUCTION

We have investigated two different laser induced desorption processes. Both are non–thermal, or spectroscopic processes, in which the laser energy is absorbed by molecules on the surface rather than directly heating the surface as occurs with thermal desorption. In the first case we have investigated the non–dissociative desorption of methyl–pyrazine from quartz. In the second case the dissociative desorption of 3–cyclopentenone. For the first investigation we used a tunable frequency doubled excimer pumped dye laser and for the second a Questek ArF excimer laser.

UV LASER INDUCED DESORPTION OF METHYL–PYRAZINE FROM QUARTZ.

Laser induced desorption is complex. Several different processes are involved. Direct thermal heating of the surface is minimised by using dielectric materials which are as nearly as possible transparent to the laser radiation. Despite this some thermal heating may occur and very weakly adsorbed species such as Xe or Ar atoms may be desorbed even though they do not directly absorb the laser radiation. A good test as to whether the compound of interest is thermally desorbed is to compare its behaviour with that of a molecule which has a similar binding energy to the surface but does not absorb the laser radiation.

The desorption signal depends upon the laser wavelength, the molecular absorption coefficient at this wavelength, the laser fluence, the area of molecules illuminated, the thickness of the adsorbed layer, the number of shots employed and the surface temperature. By making systematic measurements we have been able to unravel the interelated effects.

Explosive desorption: This occurs for thick layers of molecules with large absorption coefficients at the wavelength used when high fluences are used. These factors are all interelated. A theoretical treatment of explosive desorption has been given by Lin [1]. In this research we avoided conditions which give rise to explosive desorption.

The effect of wavelength: We have found that when other conditions are kept constant desorption ceases abruptly beyond a certain wavelength. We now consider that this is probably due to the sharp decrease in absorption coefficient. At shorter wavelengths we have found that the yields reflect the absorption coefficients in the gas phase.

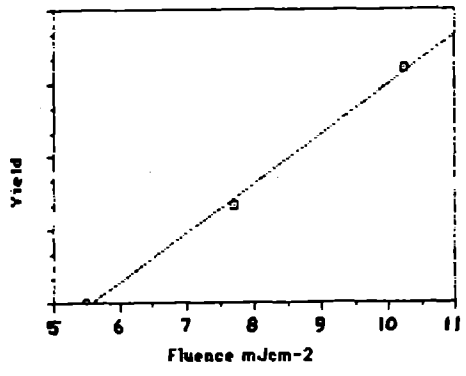

Fig. 1: The fluence cut–off at 5.5 mJ cm^{-2}.

below which no desorption can be detected.

The yields also depend linearly on the area of adsorbed molecules illuminated. Hence, in this region if a small diameter of the surface is illuminated a high fluence must be used in order for a large enough desorption signal to be generated. At one stage a one millimetre diameter beam was employed. This was a bad idea since the fluence necessary to see any signal lead to the likelihood of surface heating. In the present research we used a 5mm laser beam generated using an expansion telescope.

A fluence cut off: We have found that for a constant illuminated area there is a very sharp fluence cut off below which we can detect no desorption (see fig.1). This suggests that there must be at least two competing channels for the dissipation of the absorbed energy and that it is necessary to saturate one of them before desorption can take place.

The influence of laser shots: We have confirmed the finding that after a number of laser shots the signals become too small to measure. This is not because all of the adsorbed molecules have been desorbed. In fact a very small fraction will have been desorbed and if the fluence is increased this leads to reappearance of the signal. This effect has been observed frequently. It presumably reflects the fact that there are slightly different binding energies for different molecular sites

The translational temperatures of the desorbed molecules: The highest mass observed upon desorption corresponds to the undissociated molecule. The cracking pattern is found to be identical to that of the gas phase mass spectrum which indicates that the desorption process must be non–dissociative. The velocity distributions are close to a single Boltzmann fit with temperatures of about 1000K which are about intermediate between those for thermal desorption (at around 400K) and the very high temperatures found for explosive desorption.

The cross sections for this process are very small being about 10^{-18} cm^{-2}. The quantum yield is about 10^{-4} molecules per quantum absorbed so the process is very inefficient.

These results have been published in the Journal of Electron Spectroscopy and Related Phenomena [2].

DISSOCIATIVE DESORPTION: MOLECULAR DYNAMICS AT SURFACES.

Many studies have been carried out on the laser induced desorption of NO from surfaces since this molecule is readily detected by laser induced fluorescence and therefore its rotational and vibrational states monitored [3–5]. More recently Ertl and co–workers have investigated the dissociative desorption of NO from NO_2 following laser excitation [3] . However such studies have not been undertaken for carbonyl compounds.

GAS PHASE INVESTIGATIONS.

My first step in this project was to work in the gas phase at Cornell University with Professor Paul Houston. They have a tunable vacuum UV laser which they have used for a number of years to investigate the nascent vibrational and rotational state of CO formed from the dissociation of small carbonyl molecules in a molecular jet. I had been told that Polanyi's group had tried to desorb acetone from an LiF surface and only formed polymers which stayed adsorbed. I decided to work with 3–cyclopentenone which both thermally and photochemically dissociates to give butadiene and CO. Synchronous planar dissociation is expected to give CO which is highly vibrationally excited due to the CO bond length change and little rotational excitation due to the symmetry of the process. In fact we found that the photodissociation at 193nm leads to extremely highly rotationally excited CO with J up to 70 and with much less vibrational excitation – an amazing result.

The next step in this project has been to initiate photodissociation on a surface. This has proceeded very well. Working at the Rutherford Appleton Laboratory we have used a Questek ArF laser to dissociate and desorb monolayers of 3–cyclopentenone. The molecules do not polymerise on the surface. Mass spectra time of flight (TOF) measurements show that undissociated molecules are desorbed along with the butadiene and CO fragments. However the ratio of the butadiene product to the parent molecule is about three times higher than would be expected from the mass spectrum cracking ratios if a purely non–dissociative desorption process was to be involved. there must, therefore, be some dissociative desorption occurring at the same time. This has been confirmed by doing Temperature Programmed Desorption (TPD) spectra both after a series of laser shots and in the absence of any laser excitation. We observe a peak in the butadiene spectrum after laser shots which does not appear in the simple TPD spectrum of pure 3–cyclopentenone (see fig.2). This extra peak can only arise from butadiene which has been formed following the dissociative desorption and has then been trapped on the cold surface.

We have calculated that the number of CO molecules desorbed is sufficient for us to investigate their nascent rotational and vibrational states using vacuum UV laser induced fluorescence. Since this laser has been working successfully at Cornell and Professor Houston has provided both me and Dr. Toner with detailed instructions for its construction and operation it is now possible to build a copy of the laser and to use it in conjunction with my surface machine. The way is now open for a joint research project to embark upon this fascinating area of surface chemistry.

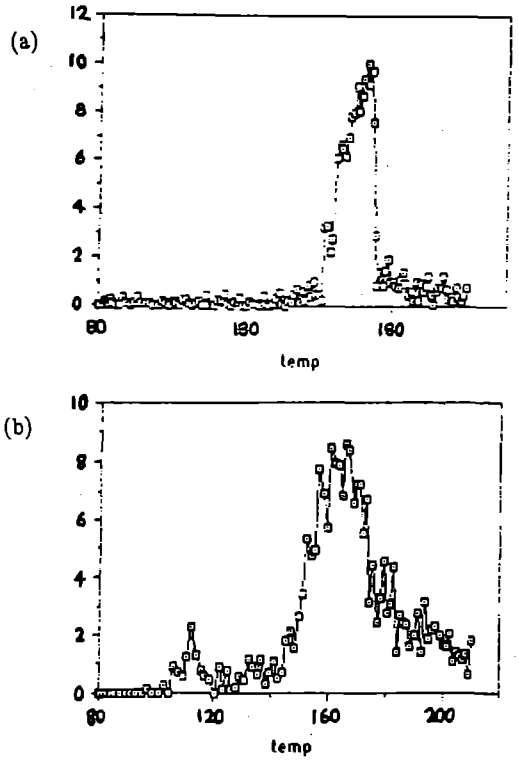

Fig. 2: Temperature programmed desorption of monolayers showing (a), butadiene formed from 3–cyclopentenone in the mass spectrometer for no laser pulses and (b), following 20 laser shots showing butadiene formed by photolysis on the surface.

[1] B. Fain and S. H. Lin
J. Chem. Phys. 91, 2726 (1989)
[2] S. J. Clemett, A. W. Parker. K. v. Puttkammer, A. Takami, and C. J. S. M. Simpson.
J. Elect. Spec. and Rel. Phenom.
54/55 (1990) 211–220
[3] E. Hasselbrink, S. Jakubith, S. Nettesheim, M. Wolf, A. Cassuto and G. Ertl.
J. Chem. Phys. 92 (1990) 3154
[4] F. Budde, A. V. Hamza, P. M. Ferm, G. Ertl, D. Weide, P. Andresen, and H. –J. Freund.
Phys. Rev. Lett. 60 (1988) 1518
[5] S. A. Buntin, L. J. Richter. R. R. Cavanagh, and D. S. King Phys. Rev. Lett. 61 (1988) 1321

TALKS

Dr. C. J. S. M. Simpson
International Conference on "Vibrations at Surfaces"
Shelter Island, N. Y. 1990

Dr. K. v. Puttkamer
University of Hannover, Germany, 1990
University of Bayreuth, Germany, 1991
University of Bochum, Germany, 1991
University of Munich, Germany, 1991

THESES

Gareth Edwards:
"Laser induced desorption from surfaces"
(Chemistry Part II, 1989)
Christopher Kingsley:
"Ultraviolet laser induced desorption"
(Chemistry Part II, 1989)
Simon Clemett:
"Non–thermal laser induced desorption and energy transfer on surfaces"
(Chemistry Part II, 1990)

FAR RED RESONANCE RAMAN STUDIES OF CLOSED AND EXTENDED CHAIN TETRAPYRROLES

M P Russell, J N Moore and R E Hester

Department of Chemistry, University of York

INTRODUCTION

Raman spectroscopy is a mature technique which is now used in a wide range of both analytical and research applications. However, the need remains for a more widely applicable range of Raman methods. To obtain high quality Raman and resonance Raman spectra for a variety of samples, the exciting laser radiation must be available over a wide region of the spectrum (near-IR to UV). In the past, conventional steady-state Raman experiments have been limited by the small number of discrete lasing lines available from the traditional Ar and Kr ion laser sources.

In this project, we have explored a new technique for Raman spectroscopy with significance for its application to both chemical and biochemical systems and which will allow (i) the off-resonance study of many fluorescent systems and (ii) widely tunable resonance Raman spectroscopy of those with far red electronic absorption bands. We have used the output of the novel Ti:Sapphire solid state laser to obtain a light source which will be capable of probing Raman and resonance Raman spectra using excitation wavelengths in the range of 660 - 1100 nm. This continuous tunability in the far red is likely to be a key feature for many future Raman studies.

Our immediate interest in developing this system is in order to study both the normal and the resonance Raman spectroscopy of open and closed chain tetrapyrroles. These molecules serve as essential model systems which will enable subsequent work to be undertaken on the role of these chromophores in the plant protein phytochrome [1], and in plant and bacterial photoreaction centres [2]. We have started to explore the applicability of this approach to these biochemical systems, and present preliminary results.

FAR RED RAMAN SPECTROSCOPY

The experimental arrangement for far red resonance Raman studies is shown in Figure 1. The Ar ion - pumped Ti:Sapphire laser system provided by the RAL loan operated to specification, being capable of producing > 500 mW output. A problem for Raman studies was the discovery that the Ti:Sapphire laser produces a significant though weak output over a range of wavelengths other than that of the principal lasing line. Although relatively weak, this could be strong in comparison to the Raman signal. An optical filtering arrangement to isolate the lasing line will be required for future work where weak signals are to be observed in this wavelength region.

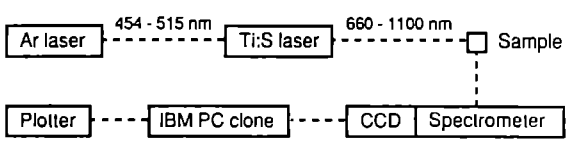

Figure 1: Experimental configuration

The detection system in York comprised a Spex double spectrometer and a Wright Instruments UV-enhanced CCD system. This is optimised for UV/visible performance. The spectrometer optics are most efficient at 500 nm (relative throughput of ca. 50 % at 1000 nm), and the CCD is most efficient at 700 nm, losing efficiency sharply in the far red. Nevertheless, we were able to obtain good quality Raman spectra over a limited region in the far red. An indication of the limitations in this region provided by our current apparatus is given by a comparison of a normal Raman spectrum obtained using a standard excitation line at 406 nm and using far red excitation at 828 nm (Fig 2). The response of the detection system increases by < x 2 across the spectrum for the visible spectrum (top curve), whereas it decreases by ca. x 1000 for the far red spectrum. Thus, the severe loss of sensitivity at wavelengths longer than 950 nm is clear. This limits the useful range of our detection to, for example, < 2000 cm^{-1} for 800 nm excitation, or < 600 cm^{-1} for 900 nm excitation.

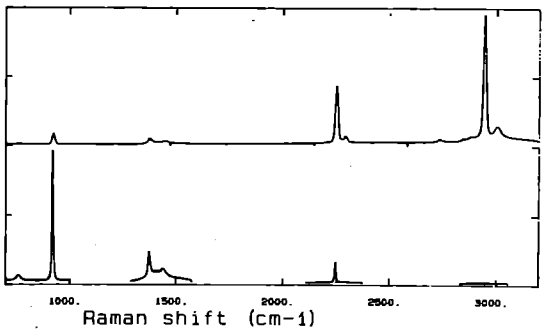

Figure 2: Normal Raman spectra of CH_3CN illustrating detection system sensitivity loss in the far red. Top: 406 nm excitation; bottom: 828 nm excitation using 200 mW power and 300 s data collection. Each spectrum scaled to most intense peak.

Preliminary studies were undertaken to establish that standard solvent spectra could be obtained in short acquisition times with good signal/noise (Fig 3).

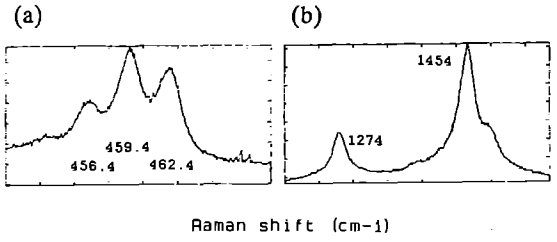

Figure 3: Far red Raman spectra of (a) CCl_4 (300s data collection) and (b) EtOH (60 s). Both excited at 778 nm.

TETRAPYRROLE AND RELATED SYSTEMS

β-carotene is a molecule which has been well characterised using both normal and resonance Raman studies [3]. It is a system which has relevance to our proposed studies of photosynthetic reaction centres [2]. It was chosen here as a well characterised sample which could be studied under non-resonance conditions. A far red normal Raman spectrum is shown below (Fig 4). Even at 10 mM concentration and low laser power at the sample, the solute bands are clearly observed with good S/N. For off-resonance conditions this is a good result.

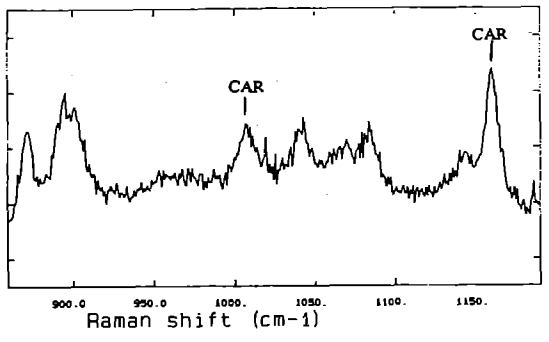

Figure 4: Normal Raman spectrum of β-carotene in hexane (10 mM). Excitation line 828 nm. 600 s data acquisition time using 30 mW laser power. The carotene bands are indicated on the spectrum.

We have obtained RR spectra of the open chain tetrapyrrole biliverdin in resonance with both short and long wavelength electronic absorption bands, using Kr and Ti:Sapphire lasers, respectively, as illustrated in Fig 5. The principal bands are in agreement with literature values for biliverdin dimethyl ester [1].

In order to study the closed chain tetrapyrroles present in bacterial reaction centres a cryostat was incorporated into our Raman apparatus. We have observed far red Raman spectra of bacterial reaction centres stabilised at 77 K (Fig 6).

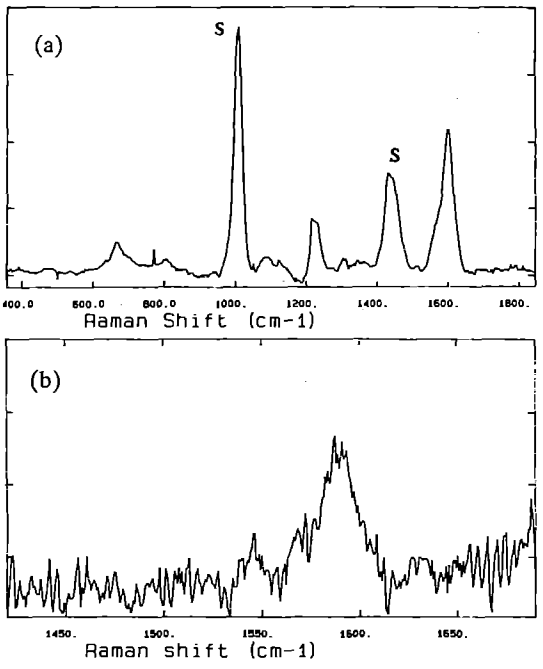

Figure 5: Resonance Raman spectra of biliverdin in methanol (1 mM). Solvent bands are indicated by S. Excitation line (a) 413.1 nm and (b) 773 nm.

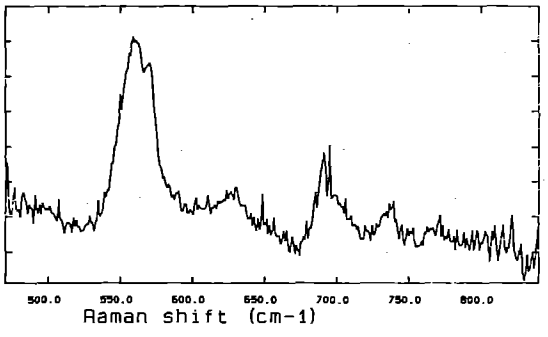

Figure 6: Far red resonance Raman spectrum of bacterial reaction centre at 77 K. Excitation line 808 nm. Laser power 50 mW. Acquisition time 1200s.

CONCLUSION

Our feasibility study of the use of a Ti:Sapphire laser system for obtaining far red Raman spectra has been successful. In addition, our preliminary results show that this is an excellent laser source for such studies of tetrapyrrole and related systems.

ACKNOWLEDGEMENTS

We thank Prof M Lutz and Dr A Mattioli for providing the bacterial reaction centre samples.

REFERENCES

1. R E Holt et al. J Am Chem Soc 111 9156 (1989)
2. B Robert et al. in *Time-resolved Spectroscopy*, Adv. Spectrosc. 18, eds. RJH Clark and RE Hester (Wiley, Chichester, 1989), Ch 7
3. S Saito et al. J Raman Spectrosc 14 299 (1983)

A RESONANCE RAMAN STUDY OF THE VIBRATIONAL INTERACTIONS BETWEEN SOLVENT AND SOLUTE MOLECULES (1) UROTROPINE IN LIQ.SO_2

J Tomkinson, A W Parker, A Prince

Rutherford Appleton Laboratory

Introduction

The structure and dynamics of solutions is of great interest [1]. Most work in this field has used H_20 as the solvent, because of its great solvating versatility. The bulk properties which provide this versatility in H_20 are, dielectric constant and dipole moment. At the molecular level waters particular solvent properties are due to its ability to act as a good donor (through the oxygen lone pairs) and also as an acceptor (through its hydrogen bonding capacity). However, this very versatility complicates our understanding of the solvation process at the molecular level. Thus solutes that appear to promote the 'structure' of H_20 are more soluble [2]. The study of the liquefied noble gases as solvents avoids these problems. Such solvents depend exclusively upon their dielectric properties and they do not form solvates.

One useful solvent intermediate between the versatile but complex H_20 and the simple but limited noble gas is liquid SO_2. This solvent acts predominantly as an acceptor through sulphur. It is a general solvent for arenes and used commercially for the separation of benzene in the preparation of kerosine [3]. The structure of pure liquid SO_2 was published recently [4].

Urotropine, or hexamethylene tetramine ($(CH_2)_6N_4$) is a vibrationaly well understood [5]. tetrahedral molecule. The white Urotropine dissolves readily in SO_2 producing a pale yellow solution. The only significant feature in the UV/visible spectrum of the solution occurs at 410 nm. This band originates from those SO_2 molecules that accept the Urotropine (nitrogen) lone pairs. When the liq. SO_2 is evaporated away a stable white solid Urotropine: SO_2 remains, [7]. The Raman spectrum of the solid has been studied by this technique, the SO_2 molecule was strongly bound to the Urotropine and was characterised by a band at 1108 cm^{-1}.

Experimental

The resonance Raman spectra of pure SO_2 (liq) and a saturated Urotropine: SO_2 (liq) solution were obtained (at boiling point ca 5°C and 410 nm). A specially designed optical cell was constructed. This allowed small volumes of the liquid to pass, via a silica capillary, through the incident beam. Condensation on the capillary was prevented by flowing dry N_2 gas over the beam area. Evacuation of the noxious SO_2 fumes proved more difficult than anticipated, and the majority of the experimental work was therefore postponed. Better fume extraction facilities are currently being incorporated into the apperatus to allow investigations to continue.

Results and Discussions

The results in the 1000 to 1200 cm^{-1} region are shown in fig. 1. There is only one band in the pure liquid in this range, the symmetric stretch ν_1 (1151cm^{-1}, gas phase). In our liquid spectrum this occurs at 1141 cm^{-1}. In the spectrum of the solution the $\nu_1(SO_2)$ band appears to lower frequency,1139 cm^{-1} and a new band appears at 1041 cm^{-1}.

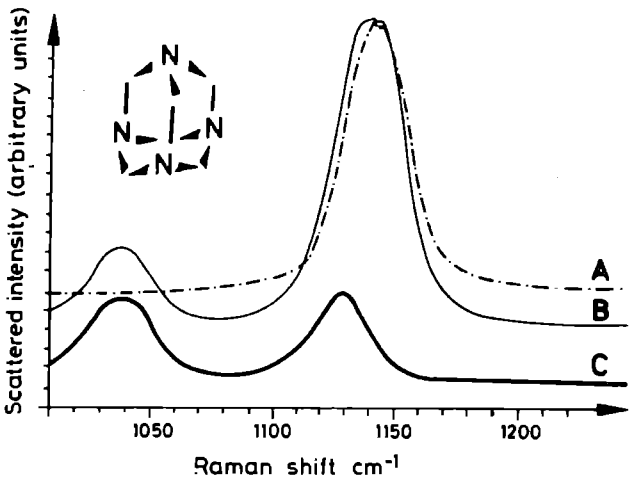

Fig 1

The resonance Raman spectrum of liq SO_2 (A), Urotropine in liq SO_2 (B), difference. Spectrum (C).

This new band probably arises from the ν_3 vibration of the Urotropine (A_1, observed at 1042 cm^{-1} in the pure solid). The reason for the apparent shift of $\nu_1(SO_2)$ is in the presence of a new type of SO_2 in the solution. These are the solvate molecules bound to the utotropine, and the extra electrons they have accepted weakens their S-O bonds. The difference spectrum (fig. 1C) shows that $\nu_1(SO_2$ bound to Urotropine in solution) occurs at 1129 cm^{-1}. The strongly bound SO_2 molecule observed in the solid solvate (Urotropine : SO_2) at 1108 cm^{-1} is absent. Therefore only one, weak, solute-solvent interaction is present in the solution.

Future Work

Further investigations in this system are expected when the fume evacuation apparatus is installed. A larger diameter silica transfer tube will allow a larger sample size, and less background distortion in the beam area. This modification of the apparatus will allow investigations to lower Raman shifts, ca 100cm^{-1}. In this spectral region the solvate-solute stretching and deformation modes are anticipated. We shall also apply Job's method to extract the solvate co-ordination number for Urotropine.

Beyond these immediate aims our programme includes inelastic neutron scattering techniques. These will allow us to extract eigenvector values for the vibrations of the Urotropine in its solvent cage. Ultimately the simultaneous use of pulsed resonance raman and pulsed neutron experiments are foreseeable if some what tentative.

References

1. Frank H. S and Wen W-Y. Faraday Discussions 24 (1957) 133
2. Waddington T.C. Inorg and Radio Chem, 1 (1965) 254
3. Alvarez, M et al. Mol Phys 66 (1989) 397
4. Jobic, M and Lauter, H J J Chem. Phys 88 (1988) 5450
5. Tomkinson, J. Unpublished Work
6. Santos, P. S., Lieder, R. J. Mol Struc 144 (1986) 39

Redox Reactions of Triplet Ubiquinone with Water Studied by TR3

A W Parker[1], R E Hester[2], D Phillips[3] and S Umapathy[2]

[1]Rutherford Appleton Laboratory
[2]University of York
[3] Imperial College

1. Introduction

This work reports our continued investigations on photochemically produced intermediates (electronically excited states and radicals formed via electron and proton transfer) of ubiquinone (UQ) using time resolved resonance Raman (TR^3) spectroscopy[1]. Quinones are well established as playing major roles in aerobic respiration and energy yielding photosynthesis. Their major importance comes from their ability to participate in electron transport pathways (eg mitochondrial and chloroplast) which fully utilise their reversible redox properties. Earlier studies concentrated on identifying the species formed from photolysis of UQ in various organic solvents. In ethanol triplet uqibuinone, ^3UQ, was found to react with the solvent via both electron and hydrogen atom transfer, giving the semiquinone radical anion ($UQ^{\cdot-}$) and neutral radical ($UQH\cdot$) respectively. Due to the high reactivity of ^3UQ with the solvent the triplet state lifetime was too short for observation and could only be detected in the more inert solvent cyclohexane.

Preliminary results revealed the formation of $UQ^{\cdot-}$ on photolysis (248 nm) of aqueous solutions of UQ (1×10^{-3} mol dm^{-3}). If electronically excited, UQ can directly oxidise water via electron transfer then it has a significantly different photochemistry from other quinones, eg, benzoquinone (BQ), duroquinone, and anthraquinones. Further work has been necessary to establish how this photo-oxidation process occurs.

2. Results and Discussion

Ubiquinone in Water (pH=6 and pH=2)

Improved TR^3 spectra from the photolysis of aqueous solutions of UQ (1×10^{-3} mol dm^{-3}) using 248 nm pump and 440 nm Raman probe laser wavelengths have been obtained, figure 1(a). Comparison of this spectrum with the one obtained from the photolysis of UQ in the presence of NO_2^- in ethanol[1], all of the Raman bands are assigned to $UQ^{\cdot-}$. There are several possible routes for formation of $UQ^{\cdot-}$ from excited singlet ubiquinone, ^1UQ, or triplet ubiquinone, ^3UQ viz;

(i) $^1UQ + H_2O \rightarrow UQ^{\cdot-} + H^+ + \cdot OH$ (from singlet)

(ii) $UQ + H_2O \xrightarrow{h\nu,\ 248\,nm} {}^1UQ + H_2O \xrightarrow{h\nu,\ 248\,nm} UQ^{\cdot-} + H^+ + \cdot OH$

(two 248nm photons)

(iii) $^1UQ + H_2O \xrightarrow{ISC} {}^3UQ + H_2O \rightarrow UQ^{\cdot-} + H^+ + \cdot OH$

(by intersystem crossing, ISC, to form triplet)

(iv) $^3UQ + H_2O \xrightarrow[248 \text{ or } 440\,nm]{h\nu} UQ^{\cdot-} + H^+ + \cdot OH$

(excitation of triplet by pump or probe laser)

(v) $^3UQ + H_2O \rightarrow {}^3(UQ\text{---}H_2O) \xrightarrow[440\,nm]{h\nu} UQ^{\cdot-} + H^+ + OH$

(photodecomposition of excited water complex).

In order to establish which mechanism is operative, the relative yield of $UQ^{\cdot-}$ (measured from the net integral of the 1617 cm^{-1} band) was found for different pump and probe laser powers. A linear dependence was observed for both lasers. This eliminates mechanisms (ii), (iv), and (v) and indicates that photo-oxidation of water occurs via the singlet or triplet state. By performing TR^3 experiments with pump/probe time delays of 0, 35, 100 and 250 ns the maximum $UQ^{\cdot-}$ concentration is established between 35 and 240 ns. The ^1UQ lifetime is of the order of 20 ps, (cf singlet BQ)[2], and if reaction occurs from the singlet state it is expected to be completed on this time scale. We therefore conclude that the photo-oxidation of water to take place via ^3UQ forming $UQ^{\cdot-}$.

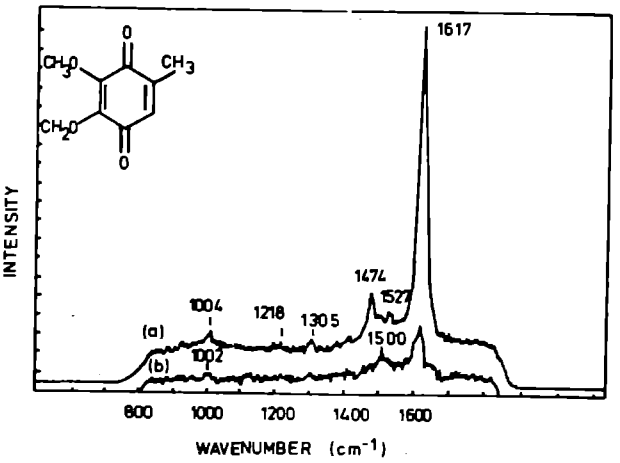

Figure 1(a) UQ (1.0×10^{-3} mol dm^{-3}) in H_2O, pH 6, pump 248 nm, probe 440 nm, time delay 80 ns. (b) as for (a) but pH 2, adjusted with HCl. Probe only spectra have been subtracted from both spectra.

This result is in contrast to the photochemistry of other quinones. In mixed H_2O:methanol (90:10) BQ has been found to undergo hydrogen atom abstraction, from the methanol C-H bond, forming BQH·, via the vibrationally relaxed triplet state(2). In pure neutral water ^{3}BQ also photo-oxidises water to give BQH· but via a two photon (266 nm) process. Absorption of the first photon by ground state BQ produces ^{1}B Q which within the duration of a 10 ns laser pulse intersystem crosses to create ^{3}BQ which absorbs a second photon from the same laser pulse;

$$BQ \xrightarrow[266nm]{h\nu} {}^1BQ \xrightarrow{ISC} {}^3BQ \xrightarrow[266\ nm]{h\nu} BQH\cdot + \cdot OH$$

This higher excited triplet state then rapidly photo-oxidises water[3] forming BQH·. There is also evidence to suggest that single photon absorption producing ^{3}BQ can lead to low yields of BQH· but the photo-oxidation takes place at a slower rate[4,5]. Triplet sulphonated anthraquinone, however, complexes with water molecules and under TR[3] conditions the complex absorbs a probe photon. This induces photo-ionisation yielding the quinone anion[6]. Electronically excited duroquinone shows no reaction with water[7] or ethanol[8].

Variation of the pump/probe time delay and analysing the net integral of the 1617 cm^{-1} band at each time delay gives the UQ$^{\cdot-}$ lifetime as 28.3 (+/- 1.0) μs.

The pK_a of UQ$^{\cdot-}$ is 5.40,[9] by lowering the pH of the solution to pH 2.0, using HCl, and photolysing all UQ$^{\cdot-}$ formed will be directly converted into the neutral ubisemiquinone, UQH·, ie

$$UQ^{\cdot-} + H+ \rightarrow UQH\cdot$$

The absorption spectrum of UQH· has a broad absorption centred at 440 nm[10]. Thus, for the probe wavelength used (440 nm) both UQ$^{\cdot-}$ and UQH· are in resonance. The Raman spectrum, figure 1(b), obtained under acidified conditions has three main bands. Two of these bands are at similar wavenumber values to those observed for UQ$^{\cdot-}$ ie 1002 and 1617 cm-1. To establish whether all the bands are due to UQH· the experiments have been repeated in D_2O.

Ubiquinone in Deuterated Water (pD=6 and pD=2)

TR[3] spectra for D_2O solutions of UQ at pD6, figure 2(a), show no differences with spectra obtained in H_2O at the same pH, figure 1(a). This supports our assignment of UQ$^{\cdot-}$ as no exchange of H atoms for D atoms has taken place. Using DCl to acidify D_2O, pD=2, solutions of UQ it is expected to convert all UQ$^{\cdot-}$ formed from the photolysis pulse into UQD·,

$$UQ^{\cdot-} + D^+ \rightarrow UQD\cdot$$

Comparison of the acidified H_2O, figure 1(b), and acidified D_2O, figure2(b), Raman spectra shows two differences. The 1617 cm^{-1} band has shifted to 1606 cm^{-1} and the 1002 cm^{-1} band has disappeared. The 1507 cm^{-1} band remains the same in both spectra. The most intense band in the Raman spectrum of UQ$^{\cdot-}$ is 1617 cm^{-1} and it is plausible that the band observed at this position in the acidified H_2O solution is due to UQ$^{\cdot-}$. But, as this band is not observed in the acidified D_2O experiment total conversion to UQD·/UQH· at the pH/pD and pump/probe time delays used must have occurred. With this reasoning we assign all the observed bands in the acidified solutions to UQD·/UQH·.

Raman Band Assignments

Having identified the species responsible for each Raman spectrum, we are now able to assign the Raman bands. The Raman spectra obtained for benzoquinone radical anion, BQ$^{\cdot-}$, and benzosemiquinone, BQH·, have been studied in detail[11,12]. The Raman spectra for BQH· and UQH· show similarities, using this analogy we make the band assignments given in the table, this uses the Wilson convention of reference 11. The two a_g normal modes of double bond character in the ground state, S_o, and the symmetric C=C ring bonds (ν_{8a}) and the two C=O stretches (ν_{7a}), are accidentally degenerate. Hence, these bands are unresolved and are found at 1607 cm^{-1}.

In the Raman spectrum of BQ$^{\cdot-}$ the most intense line appears at 1619 cm^{-1}, this is assigned to C=C (ν_{8a}) symmetric stretch and we assign our very strong 1617 cm^{-1} band to this. The bands at 1474 and 1527 cm^{-1} are due to C=O (7a) and C=C (ν_{8b}) and present difficulty in absolute assignment. In BQ$^{\cdot-}$ only the C=O stretch is observed[11,12]. In UQ$^{\cdot-}$ the C=C and remaining C=O bonds are affected by different amounts

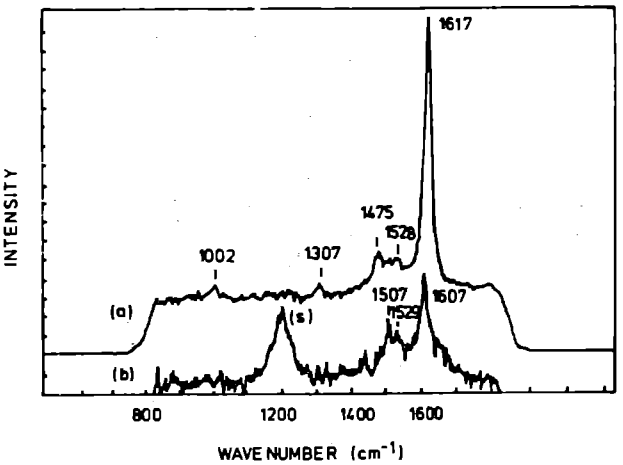

Figure 2(a) UQ (1.0 x 10^{-3} mol dm^{-3}) in D_2O, pD 6, pump 248 nm, probe 440 nm, time delay 80 ns, probe only spectrum subtracted. (b) as for (a) but pD2, adjusted with DCl, probe only not subtracted, S represents solvent band.

Raman Vibrational Assignments (cm^{-1}) for UQ^{-}, UQH· and UQD·

UQ (So)	$UQ/H_2O/H^+$		$UQ/D_2O/D^+$		Assignment/(mode)
	UQ^{-}	UQH·	UQ^{-}	UQD·	
1607					C=C (8a) C=C (7a)
	1617	1617	1617	1607	C=C str (8a)
	1527		1528	1529vw	C=C str (8b)
	1474	1506	1475	1507	C=0 str (7a)
	1305		1307		C-C str (14)
	1218				C-H bend/C-0-C str
	1004	1002	1002		C-C ring breath

and degeneracy observed in the ground state is lost. A theoretical study using Hartree-Fock methods has been made on BQ and BQ^{-} and the estimates for the Raman vibrational frequencies made[13]. Agreement with the experimentally observed values is generally good. They illustrate the trend that C=0 (ν_{7a}) is shifted below the C=C (ν_{8b}). From this we tentatively assign the 1474 cm^{-1} as C=0 (ν_{7a}) and 1527cm^{-1} as C=C (ν_{8b}). The three weak bands at 1305, 1218 and 1004 cm^{-1} show no resemblence with the Raman spectrum of BQ^{-} and this difference must be due to the two methoxy and methyl ring substituents of UQ, the table contains suggestions for these bands.

For the UQH· and UQD· the spectra show similarities to BQH· and the assignments given in the table are based on these[11]. However, in BQH· and BQD· the most intense band, C=C (ν_{8a}) stretch, is at the same frequency, 1613 cm^{-1}, in both Raman spectra. This is not the case in our experiments where the bands are 1617 and 1607 cm^{-1} for UQH· and UQD· respectively. It is unlikely that this is a solvation effect as there are no frequency shifts between UQ^{-} in D_2O and UQ^{-} in H_2O. The deuterium shift indicates a weak coupling of the COH/COD bond angle deformation vibration with the C=C (ν_{8a}) stretch in the vibrational mode observed at 1607 cm^{-1}.

3. Conclusions

It has been shown that the photochemistry of UQ in aqueous solution is different from other quinones. The overall process from 248 nm excitation of UQ is photo-oxidation of water by ^3UQ:

$$UQ \xrightarrow[248\ nm]{h\nu} {}^1UQ \rightarrow {}^3UQ + H_2O \rightarrow UQ^{-} + H^+ + \cdot OH$$

References

1. R E Hester, A W Parker, D Phillips and S Umapathy, Ann Rep Laser Div SERC (1989) 253.
2. R Rossetti and L E Brus, J Am Chem Soc (1986), 108, 4718.
3. S M Beck and L E Brus, J Am Chem Soc (1982), 104, 1103.
4. S M Beck and L E Brus, J Am Chem Soc, (1982), 104, 4789.
5. J C Ronfard-Harret and E Amouyal, J Chem Soc Faraday Trans 1, (1980), 76, 2432.
6. D Phillips, J N Moore and R E Hester, J Chem Soc Faraday Trans 2, (1986), 82, 2093.
7. E Amouyal and R Bensasson, J Chem Soc Faraday Trans 1, (1976), 72, 1274.
8. I McCubbin, D Phillips and R E Hester, J Chem Soc Faraday Trans 2, (1987), 83, 1519.
9. K B Patel, and R L Wilson, J Chem Soc Faraday Trans 1, (1973), 69, 814.
10. E J Land and A J Swallow, J Biol Chem (1970), 245, 1890.
11. G N R Tripathi and R H Schuler, J Phy Chem (1987), 91, 5881.
12. R E Hester and K P J Williams, J Chem Soc Faraday Trans 2, (1982), 78, 573.
13. D M Chipman and M F Prebenda, J Phys Chem (1986), 90, 5557.

TIME-RESOLVED RESONANCE RAMAN SPECTROSCOPY (TR^3) OF PORPHYRINS AND METALLO-PORPHYRINS

Steven E J Bell[1], Ala Al-Obaidi[2], Laurent Chinsky[3] and Ronald E Hester[2]

[1]The Queens University of Belfast [2]University of York
[3]Universite Pierre et Marie Curie

INTRODUCTION

Electronically-excited porphyrins and metallo-porphyrins have been used for purposes as diverse as solar-energy conversion and light-activated cancer treatments. Although an extensive body of literature exists on the Raman spectroscopy of ground-state porphyrins studies on the electronically-excited materials are at a very preliminary stage. We have initiated a wide-ranging and systematic research programme on the Raman spectroscopy of electronically excited porphyrins and metalloporphyrins both in homogeneous solution and in biologically relevant environments.

We have previously reported[1] the Raman spectrum of the triplet excited-state of Fe(TPP) (TPP= tetra-phenyl porphyrin) and discussed the differences between it and that of the very much longer-lived triplet Zn(TPP) complex. In this report we describe the extension of this work to related materials in which we have systematically altered both the structures of the porphyrin ligands and the nature of the central metal ion. In addition we show the results of studies of one of these materials, a water-soluble copper porphyrin, which is shown to interact with a synthetic DNA material following photoexcitation.

RESULTS AND DISCUSSION

Triplet-State Materials in Homogeneous solution.

A range of free-base and metallo-porphyrins were electronically excited by *c.a.*1mJ laser pulses at 414 nm, a wavelength which is near to their absorption maxima. Raman spectra were then probed, at a series of time delays, using 450 nm laser pulses. This probe wavelength was chosen because it lies close to the absorption maxima of the triplet excited-states of all the complexes investigated.

For both the free-base and zinc porphyrins excited-state lifetimes in air saturated solutions are of the order of 1-2 us. We have found that time-resolved Raman spectra clerly show both the initial formation of triplet-states and their subsequent decay to the ground state on this timescale. A representitive data set is shown in figure 1. Raman spectra of the triplet state of the free-base and zinc metallated complexes were similar in that both were dominated by vibrations of the meso phenyl (or substituted- phenyl) rings. These features are at 1236 and 1597 cm^{-1} in figure 1. In the case of the free-base materials a number of additional features were observed, this is to be expected since

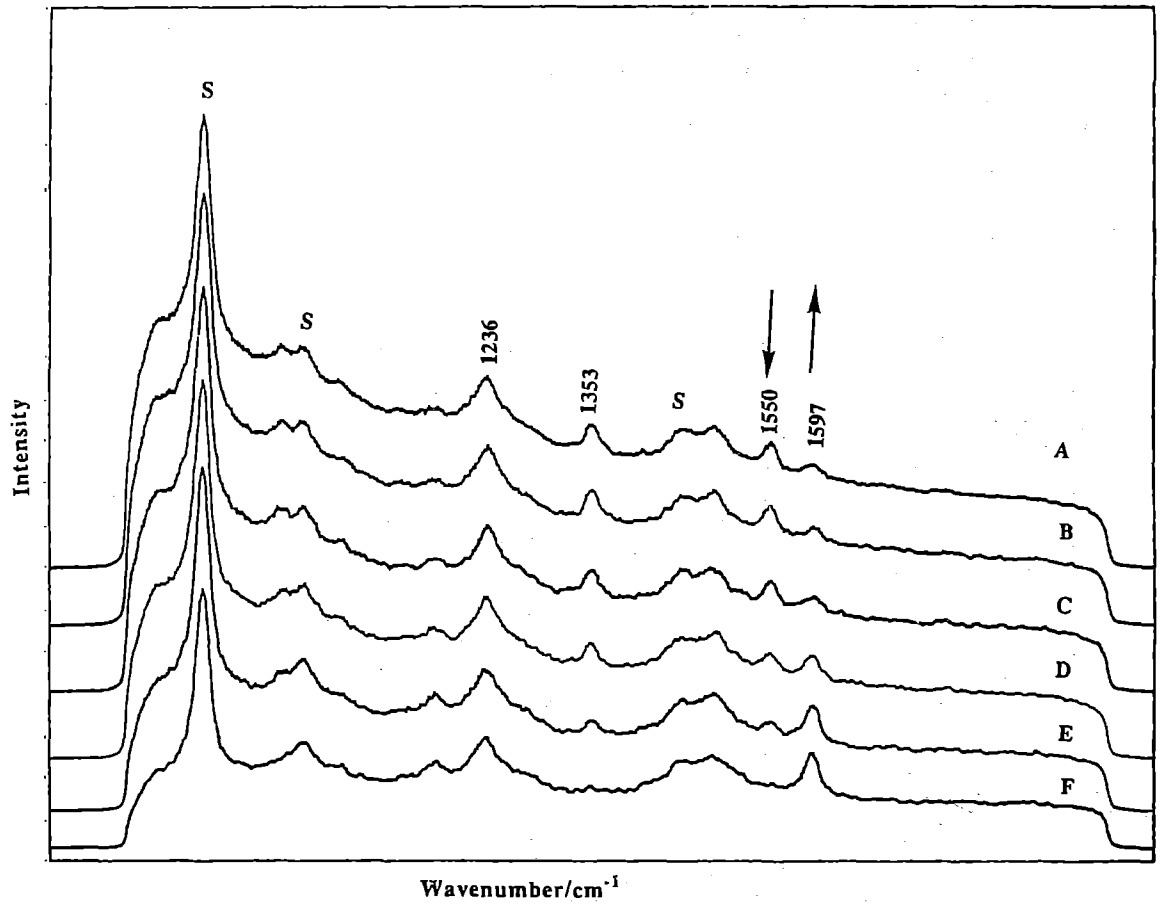

Figure 1: TR^3 Spectra of $Zn(PCO_2CH_3)$ in THF. (A) probe only, remaining spectra with pump-and-probe delays of (B) 2 us, (C) 1 us, (D) 500 ns, (E) 200 ns, (F) 50 ns. (PCO_2CH_3= methyl ester of TPPC). Solvent bands are marked S.

the symmetry of the free-base is lower that that of simple metallated complexes, such as Zn(TPP). In the latter case all four pyrrole rings are equivalent while in the free-base they are seperated into two non-equivalent pairs. Detailed vibrational mode assignments for the triplet free-base complexes are not yet available. However the task of making such assignments has been considerably simplified by our approach of using water-soluble complexes since this has essentially removed the problem of interfering solvent bands, which mask important spectral regions, and allowed us to obtain high quality data.

One anomalous result was observed for free-base TPPC (TPPC= tetra-4-carboxylatophenyl porphyrin). Irradiation of this porphyrin under identical conditions to those which, with other complexes, gave essentially complete conversion of ground- to excited-state, gave Raman spectra which showed a significant proportion of ground-state was present in the sample during the probe pulse. However, stepwise reduction in the energy of the probe pulse gave spectra with a larger proportion excited- to ground-state features. This implies that in this material the photoloysing pump pulse completely converts the ground-state porphyrin to the triplet state but that the interrogating probe pulse does not simply Raman scatter from the excited-state. Instead it populates a higher-lying triplet state which rapidly relaxes to the ground- state. This secondary photolysis/ relaxation process must occur on the timescale of 10 ns since it is complete within the duration of the probe laser pulse. Two-laser flash photolysis studies under high laser fluence conditions, similar to those used in Raman experiments, are currently in progress.

Porphyrin-DNA Interactions

The binding of porphyrins to DNA has been studied by a variety of spectroscopic methods and it is known that Cu(II) porphyrins are selectively intercalated at G-C sites. In addition it has been reported that excitation of the water soluble metalloporphyrin Cu(TMPyP) (TMPyP= tetra-4-N-methypyridyl porphyrin) in the presence of DNA with laser pulses of ns duration gives spectra which, in addition to ground-state features at 1574 and 1370 cm^{-1}, have new bands at 1558 and 1353 cm^{-1}.[2] Moreover these bands only appear in the presence of DNA or the synthetic nucleic acid Poly(dA-dT), and not in the presence of Poly(dG-dC). On the basis of laser fluence calculations a lifetime of 20 ps was determined for the new transient species which was assigned as an exciplex formed between the porphyrin and A-T base pairs.

By photolysing aqueous solutions of the Cu(TMPyP):Poly(dA-dT) complex with 545 nm laser pulses and synchronously probing the solution using excitation wavelengths within the Soret transition of the porphyrin we have obtained resonance Raman excitation profiles of both the ground-state and transient species. In essence the experiments involved creation of an unknown, but constant, population of the transient within the duration of the photolysis pulse. Raman spectra of this population were generated by the synchronous probe pulse whose wavelength was changed to appropriate values covering a broad spectral range. Intensities of the ground-state and transient Raman bands were then measured with respect to an ethanol internal standard. Global fitting of this data gave plots of absolute intensity of Raman bands against probe wavelength i.e. resonance Raman excitation profiles (RREPs).

The RREPs of the ground-state features at 1574 and 1370 cm^{-1} were near-identical and both closely followed the absorption spectrum of the ground-state complex in this region as shown in figure 2. The close correspondence between RREPs and absorption spectra give us confidence that the experimental technique is free from systematic errors such as secondary photolysis by the probe laser pulses. The RREPs of

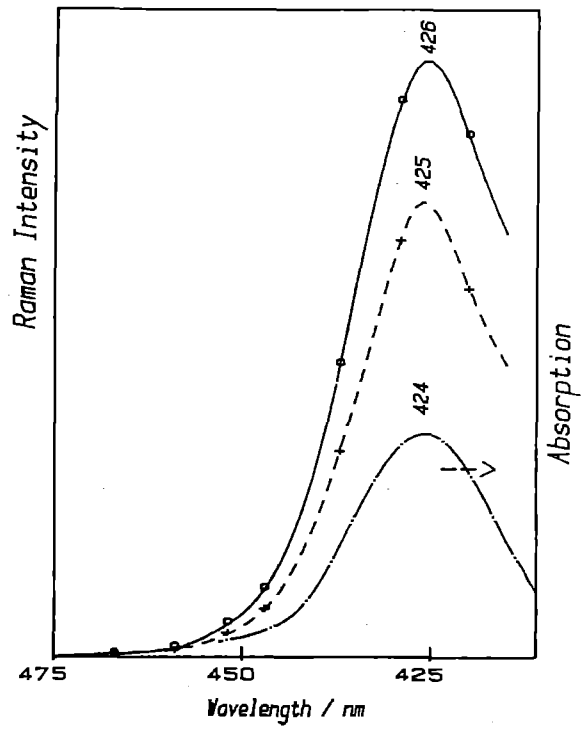

Figure 2: Resonance Raman excitation profiles of the Cu(TMPyP):Poly(dA-dt) complex. Top: 1370 cm^{-1} band. Centre: 1574 cm^{-1} band. Bottom: absorption spectrum of the complex.

the transient features at 1558 and 1353 cm^{-1} were again found to be similar to each other but in this case they peak at 430 nm, which is 4 nm to the red of the ground-state RREPs and absorption spectra. Detailed discussion of the origin of this red-shift in the Soret absorption band of the transient exciplex species is inappropriate in this report but a full account has been submitted for publication.[3]

REFERENCES

1. JA Austin, SEJ Bell and R E Hester and *Annual Report to the Laser Facility Committee* Rutherford Appleton Laboratory Report RAL-90-026 153 (1990).
2. P-Y Turpin, L Chinsky, A Laige, M Tsuboi, JR Kincaid and K Nakamoto *Photochem. Photobiol* **51** 519 (1990).
3. L Chinsky, P-Y Turpin, A Al-Obaidi, SEJ Bell and RE Hester *J Phys Chem in press 1991*.

ACKNOWLEDGEMENTS

We are glad to acknowledege the technical assistance of the staff of the LSF, in particular Dr A.W. Parker, in carrying out the TR^3 experiments in homogenous solution.

The Experiment that reaches parts other Experiments don't: Second Harmonic Generation at the Liquid-Liquid Interface.

Jeremy G. Frey and Andy J. Bell

Department of Chemistry, University of Southampton

Ted J. Vandernoot

Department of Chemistry, QMW

The properties of the interface between two liquids, for example oil and water, are important in both industrial and biological processes. One of the most costly parts of an industrial manufacture of pure chemicals is the separation of the required product from the other components of the mixtures that usually result from the manufacturing process. In an effort to understand the and improve the liquid extraction procedures we are investigating the properties of the liquid interface by the technique of Surface Second Harmonic Generation[1]. In the Second Harmonic (or SHG) technique relatively intense pulsed laser radiation impinges on the sample and while most of the light is simply reflected or transmitted a very small fraction undergoes a non-linear process and is converted to light of twice the original frequency. The analysis of the properties of this second harmonic wave enables the arrangement of molecules at an interface to be investigated.

The Second Harmonic Generation technique shows a high degree of selectivity towards an interface (liquid/air[2] or liquid/liquid[3] for example) and this despite the fact that a liquid/liquid interface in buried under at least a bulk layer of liquid. The selectivity arises because the technique is sensitive to molecules which do not have a centre-of-symmetry. In the bulk liquids there is on average a centre-of-symmetry, but at the interface, the molecules will know 'up from down' and give a significant SHG signal. The preliminary experiments conducted so far have been on the orientation of the molecule para-nitrophenol adsorbed at the water/air and water/heptane (a model for water/oil systems). We have been able to obtain information on the ordering of the adsorbed para-nitrophenol at the surface or interface.

The visible radiation from the RAL amplified picosecond laser system was incident on the upper liquid surface at $\theta = 30°$ to the surface normal. The second harmonic radiation was detected with either s or p polarisation and the polarisation angle of the incident radiation altered by a half-wave plate. A UV blocking filter ensured that no second harmonic radiation generated in the lenses or half-wave plate reached the surface under study. A set of UG5 filters and a monochrometer ensured the second harmonic signal could be discriminated from any reflected visible radiation. The SHG signal was normalised to account for changes in the laser intensity by passing a small portion of the laser power though a KDP crystal. A check was made on the fused silica glass surfaces needed to contain the samples and this showed no significant second harmonic generation at these interfaces.

The intensity of the second harmonic wave generated at the interface was studied as a function of the polarisation angle (α) of the incident visible radiation for the SHG radiation polarised parallel or perpendicular to the plane of incidence (figure 1). In the case of the liquid-liquid system the influence of the upper liquid layer on the angle of incidence ($\theta = 21.1°$ at the heptane/water boundary) and polarisation angle must be considered. The analysis of the SHG effect is done separately for the components of the electric field of the fundamental radiation parallel (i.e. in) the plane of incidence and perpendicular to the plane of incidence gives the following dependence of the SHG signal on the polarisation angle (α).

$$I_s = (a\cos^2\alpha + b\sin^2\alpha)^2 \qquad (1)$$

$$I_p = (c\cos\alpha\sin\alpha)^2 \qquad (2)$$

The relationship of the three coefficients a, b and c to the three distinct and measurable (in an axially symmetric environment) components of the second order susceptibility tensor is given in equation (3). We have assumed that a, b and c are real so that the relative signs of a and b are determined, however this still leaves the ambiguity of the sign of c. This causes a particular problem for the results on para-nitrophenol at 600nm since the molecule has an absorption at about 320nm, so it is not possible to assume, as it is far from resonance, that the zxx and xzx components of the tensor are equal. The ambiguity is resolved by requiring a consistent interpretation of the data across all the experiments which results in the tensor components (normalised to the zzz component).

$$\begin{aligned} c &= \chi_{xzx}\sin\theta \\ b &= \chi_{zxx}\sin\theta \\ a &= \chi_{zzz}\sin^3\theta + (\chi_{zxx} - \chi_{xzx})\sin\theta\cos^2\theta \end{aligned} \qquad (3)$$

Table 1
Derived components of the laboratory susceptability and molecular hyperpolarisability tensors

Susceptibility	PNP - Water/Air	PNP - Heptane/Water
zzz	1.0	1.0
zxx	-0.059	0.17
xzx	0.17	0.135
β_{zzz}/β_{zxx}	-2.8	-3.9

If the dominant components of the molecular hyperpolarisability are assumed to be β_{zzz} and β_{zxx}[4] then the final row of the table is obtained[5]. The large difference in the ratio for the water/air and water/heptane systems may arise from the different environments shifting the absorption band and thus the degree of resonance (in the absence of resonant enhancement β_{zzz} would be very small). If the susceptibility components are interpreted in terms of a freely rotating but tilted para-nitrophenol molecule then the tilt angle from the surface normal would be 28° for the air and 26° for the heptane interface. It is not reasonable to expect that the molecules are this highly ordered and the experiment is only sensitive to the ratio of the order parameters[5] B_{20}/B_{10}. For the air/water interface this ratio is 0.46 and for the heptane/water interface, 0.53. Futher analysis is needed to compare the results obtained here with the orientation of phenol measured by SHG at the water/air interface[2,6]

In the first phase of the experiments we were also able to look at a number of other compounds. Prompted by the special features of the SHG technique (see title) we investigated the liquid/air interface formed by Heineken; it gave rise to a surprisingly large signal and we are looking into what could be the cause.

References

1. Y.R. Shen, Nature (London), **337**, 519, (1989).

2. J.M. Hicks, K. Kemnitz, K.B. Eisenthal and T.F. Heinz, J. Phys. Chem., **90**, 560, (1986).

3. S.G. Grubb, M.W. Kim, Th. Rasing, and Y.R. Shen, Langmuir, **4**, 452, (1988).

4. S.J. Lalama and A.F. Garito, Phys. Rev. A, **30**, 1179, (1979).

5. B. Dick, Chem. Phys., **96**, 199, (1985).

6. K. Kemnitz, K. Bhattacharya, J.M. Hicks, G.R. Pinto, K.B. Eisenthal and T.F. Heinz, Chem. Phys. Lett., **131**, 285, (1986)..

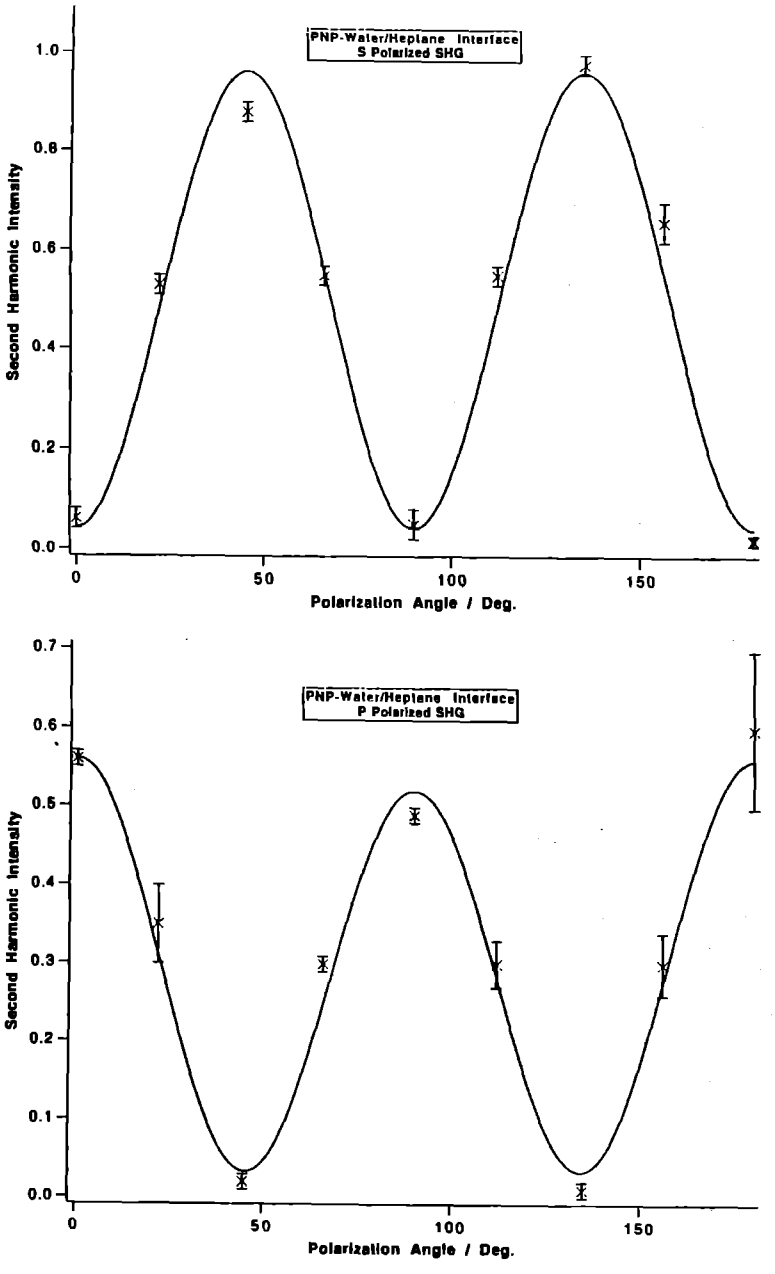

Figure 1

The s- and p-polarised surface second harmonic intensity obtained as a function of the polarisation of the incident 600nm radiation. The RAL picosecond laser system produced pulses of under 1 psec duration, about 200 J at 10Hz repetition rate. The SHG signal was normalised to a reference beam derived by doubling the visible radiation with a KDP crystal.

Picosecond Pump-Probe Laser Flash Photolysis Studies Of Azomethine Dyes And Photochromic Materials

F. Wilkinson[a], D.R. Worrall[a], M. Naftaly[a], J. Hobley[a], D.J. McGarvey[a] and A. Goodwin[a]
A.J. Langley[b] and W. Shaikh[b]

[a]University of Technology, Loughborough, Leicestershire LE11 3TU
[b]Rutherford-Appleton Laboratory, Chilton, Oxfordshire

Azomethine Dyes

Pyrazolotriazole azomethine dyes are important compounds in photographic imaging, being the dyes of choice as the magenta component in colour photographic paper, and as such there is interest in understanding their photophysical properties with a view to improving their light stability. Using nanosecond laser flash photolysis, we observe only photoisomerisation of these compounds about the azomethine linkage, the photoisomer decaying back to the stable ground state conformer thermally on timescales varying from microseconds to milliseconds, depending upon the substituent in the 6 position on the pyrazolotriazole moeity (figure 1).

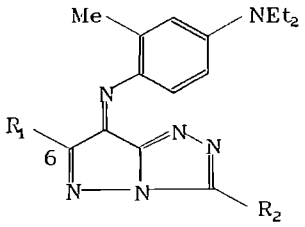

Figure 1: General structure of pyrazolotriazole azomethine dyes

Production of the photoisomer is prompt within the time resolution of the nanosecond apparatus, indicating that the excited states of the compounds are very short lived. In the last report[1], we presented the first ever observation of the excited states of these compounds using picosecond pump-probe laser flash photolysis. Subsequent to this initial work, we have been able to improve the resolution of our experiments to gain accurate kinetic data concerning these compounds. Following picosecond pulse excitation, the compounds rapidly relax within approximately 50ps in methanol solution to give a long lived species assigned as the isomer observed on nanosecond timescales, there being at least two intermediate states involved. The transient observed on picosecond timescales can thus be fitted using an equation of the following form:

$$f(t) = C_1 e^{(-t/\tau_1)} + C_2 e^{(-t/\tau_2)} + C_3$$

where C_1, C_2 and C_3 are dependent upon the extinction coefficients of the states involved as a function of wavelength, and τ_1 and τ_2 are independent of wavelength. However, there is a dependence of these relaxation times on solvent properties, as evidenced by the differing rates of decay in methanol and di-n-butylphthalate solutions shown in figure 2. Here, in methanol, τ_1 and τ_2 are 2ps and 5ps, while in di-n-butylphthalate solution these are 3ps and 8ps, respectively. Full details of this work have already been published[2].

Investigations involving these compounds in glycerol/methanol mixtures demonstrate a lengthening of the lifetimes as the fraction of glycerol increases, as would be expected as the relaxation appears to involve large amplitude motion about the azomethine bond. Changing the nature of the solvent from polar to non-polar appears to have little effect on the lifetimes of the excited states, suggesting little solvent interaction with the states involved.

Other preliminary work on these compounds has been conducted investigating the effects of molecular modification on the relaxation rates. Initial results indicate that modification of the pattern of nitrogen atoms in the pyrazolotriazole moeity has little effect on the excited state lifetimes.

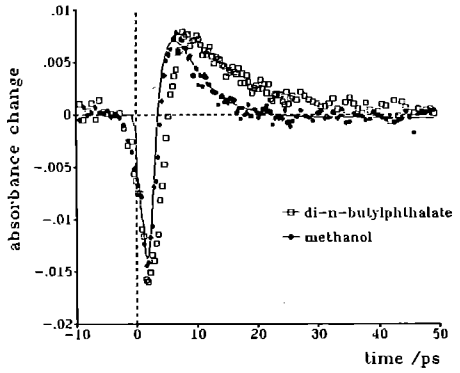

Figure 2: Decay of excited states of pyrazolotriazole azomethine dye at 640nm probe in methanol and di-n-butylphthalate

An interesting observation made during this allocation has been the presence of a coherent coupling artefact between the pump and probe beams. This is considered somewhat unusual since the probe in these experiments is derived by continuum generation, so obviously in this process the modulation of the stimulating pulse is preserved through to the continuum pulse. The synchronously pumped dye laser was being operated at this time without feedback in order to generate good continuum, and hence the bandwidth thereof was sufficient for there to be common wavelengths between the pump and probe, allowing coherent coupling to occur. This artefact is illustrated in figure 3.

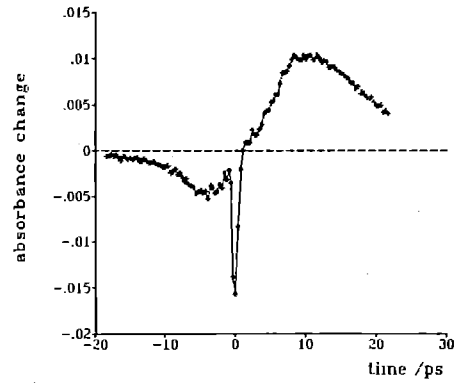

Figure 3: Coherent coupling artefact between pump and probe beams, observed on a kinetic trace from a pyrazolotriazole azomethine dye.

Fitting of a kinetic trace obtained with MeDOTC under similar conditions with an integrated gaussian function reveals that the coupling artefact is, as would be expected, located at t_{zero}, and hence its presence provides a convenient means of determining the pulse coincidence position.

PHOTOCHROMICS

Photochromism is a reversible transition of a chemical system between two states possessing appreciably different absorption spectra, such transformation being induced by photonic excitation. The present studies were concerned with the photoisomerisation of spiro-oxazines, the general structure of which is shown in Figure 4. The large change in absorption spectra of these compounds arises as follows. In the "closed" spiro form of the molecule the two halves are arranged in mutually perpendicular planes, giving rise to absorption in the near UV (300-400 nm). The photoinduced reaction cleaves the central C-O bond, allowing parts of the molecule to rotate to near-planar configurations. These "open" merocyanine forms absorb in the visible region around 590 nm.

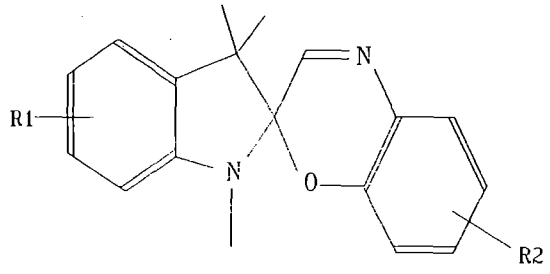

Figure 4: General structure of spiro-oxazines.

Studies by other workers using indolino-spiropyrans showed[3] that colouration risetime for these compounds is in the region of 1-2 ps. In contrast, our previous experiments at RAL (reported last year[1]) indicated that in spiro-oxazines colouration proceeds in two stages with widely differing risetimes: the fast step, probably associated with creation of an excited non-merocyanine state, has the risetime of about 1 ps; while the slow step, posibly due to rotation of isomers around the central bond, takes place on nanosecond timescales. The coloured form has a lifetime of many seconds.

In the present experiments we wished to study the reaction as a function of probe wavelength. Three photochromic compounds having different substituents were used. The measurements were carried out on $3x10^{-5}$M solutions in toluene. A flow cell was used to remove the coloured material from the probe path between shots. The pump was at 300 nm; while the probe was at 600, 580 and 550 nm.

RESULTS AND DISCUSSION

Figure 5 plots the growth in absorption following pump in one of the photochromics studied. Figure 5d shows an expanded view of the fast portion of the rise curve at 600 nm. Part of the rise takes place within the duration of the pump pulse. Following that, the rest of the rise occupies nearly 1.5 ns. It is seen that the proportion of the entire absorption increase being achieved within the pulse width is strongly dependent on probe wavelength. This was true for all three compounds tested.

The results obtained demonstrate clearly that photocolouration proceeds in at least two stages. The slow part of the colouration growth may be attributted to the fact that various merocyanine isomers require a relatively long time to rotate to their final position. The fast portion of the growth curve points to an instantaneous creation of an absorbing intermediate. The wavelength dependence indicates that this may be an excited non-merocyanine isomer.

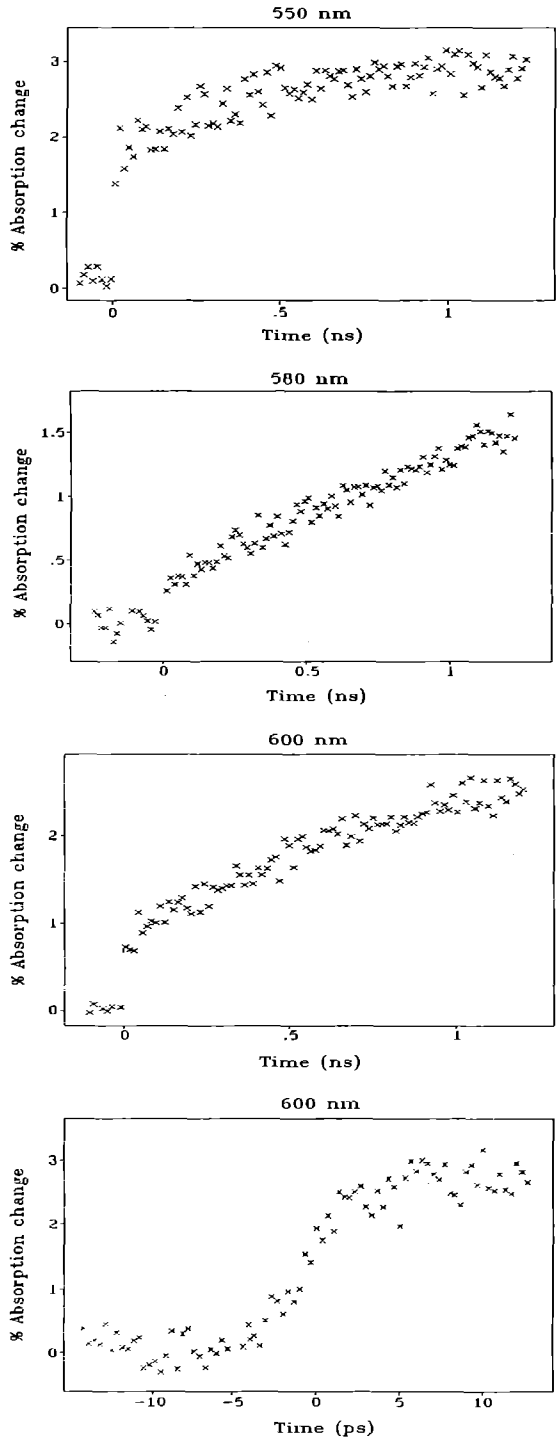

Figure 5: Change in absorption in a spiro-oxazine following excitation at 300 nm: probing at a) 550 nm; b) 580 nm; c) 600 nm; d) fast step at 600 nm.

References:

1. F. Wilkinson, D. Worrall, M. Naftaly, RAL Annual Report, 125 (1990)
2. F. Wilkinson, D. Worrall, R. Chittock, Chem. Phys. Lett., 174(5), 416 (1990)
3. N.P. Ernsting, B. Dick, and Th. Arthen-Engeland, Pure & Appl. Chem., 62(8), 1483 (1990)

THE KINETICS AND MECHANISM OF SOFT X-RAY INDUCED DNA DAMAGE IN MAMMALIAN CELLS

Rosalind A Meldrum,Jane Edgerton,Wendy Meaking,Edmund Turcu*, Christopher Reason*,Tony Damarell* and Christopher W Wharton.

School of Biochemistry,University of Birmingham,P O Box 363, Birmingham B15 2TT.

and

* Laser Division,Rutherford Laboratory,Chilton,Didcot,OXON.

INTRODUCTION

Mammalian cells are impermeable to negatively charged molecules. It is thus not possible to measure the rate of DNA synthesis by adding the immediate precusors of DNA [i.e. the nucleoside triphosphates] since they bear several negative charges in the form of phosphate anions and thus cannot enter the cells. An alternative approach,and one which we have used so far in our studies of the repair of X-ray damage,is to add the nucleoside itself,usually in the form of thymidine, that will readily enter the cell and subsequently be phosphorylated in situ to the triphosphate prior to incorporation into DNA [2,4]. While this approach is valid for measurements of DNA synnthesis that cover a considerable time period it is not applicable when it is desired to measure DNA synthesis over a short time period. The reason for this is that the phosphorylation process is not instantaneous and can introduce a lag into measurements of the initial rate of DNA synthesis after damage. In our related work on the repair of UV-induced damage in mammalian DNA [see accompanying report and previous Laser Facility Annual Reports [3]] we have been able to circumvent this problem by developing an electrical method for the permeabilisation of cells so that they will take up charged molecules. In the work on repair of UV damage the use of the electrical permeabilisation method necessitated a change from using surface grown cells to the use of cells which grow in suspension since the electrical method,which requires the exposure of the cells to a pulse of ca. 50-100 V/mm,has only been applied to suspension cells. In the study of the repair of soft X-ray damage it is essential to use cells grown on ≈ 2 μm polyester film since the X-rays [av. 1.1 keV] penetrate only some 5-10 μm into the cellular layer (or aqueous medium) and would thus not reach suspension cells. In this report we describe efforts we have made to achieve effective electrical permeabilisation of cells grown on such film.

ELECTRICAL PERMEABILISATION OF SURFACE GROWN CELLS.

In last year's report we described successful permeabilisation of cells grown on a plastic surface by using an electrical discharge between a set 25 μm wires spaced 1 mm apart across the plate [1]. Subsequent to this the Target Facility prepared a framework which carried such wires and allowed them to be placed on the surface of 2 μm film on which cells had been grown. This was spectacularly unsuccessful in that no permeabilisation occurred although the electrical discharge was accompanied by incandescence and sparks!

In order to prevent this electrical heating and damage a new former was constructed which used 100 μm wires strung 2 mm apart. Initially this was again unsuccessful. It was reasoned that the discharge was not confined to the layer of cells. This was achieved by applying gentle pressure from below so as to deform the plastic film so that it was in firm contact with the cellular layer and by reducing the volume of liquid to a minimum which just covered the wires. This had the effect of forcing the discharge current to follow a path close to the cells and thus expose them to the maximum field gradient.This scheme now worked well in tests which measured the uptake of the dye Trypan Blue which is excluded from cells which are not permeabilised.
This method was then used in some experiments in which cells were damaged with X-rays. At a dose of 50 rads and at 50 V/mm some repair induced incorporation of ^{3}H-thymidine triphosphate into DNA was seen but it is necessary to repeat these experiments since the cells were not in best condition at that time.

THE EFFECT OF DNA POLYMERASE INHIBITORS ON THE REPAIR OF SOFT X-RAY DAMAGE

In order that it will prove possible to be able to interpret the results of kinetic studies of DNA repair it is necessary to attempt to establish which enzymes are involved at the various stages of the process. We have used a series of DNA polymerase inhibitors in order to attempt to elucidate the involvement of α and β/δ in this form of repair. These experiments which were not time resolved used nonpermeabilised cells and involved measurement of thymidine uptake.

Fig. 1 shows the results of an experiment in which aphidicolin,which is a powerful inhibitor of α [but not β] polymerase,was included with the cells both prior to and after irradiation of the cells. A clear repair response,seen as enhanced

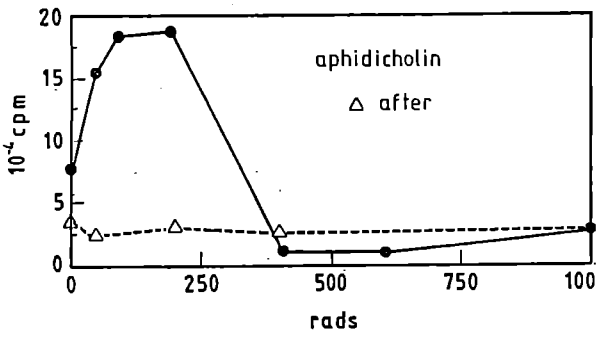

Fig. 1. The effect of aphidicolin on DNA repair synthesis induced by soft X-ray irradiation of V-79 cells grown on a 2 μm polyester film. DNA synthesis was measured over a two hour period after irradiation by determination of ^{3}H-thymidine uptake into DNA. Aphidicolin was present at 10 μM and ca. 10^{6} cells were used in each experiment. Solid line incubation with aphidicolin for 15 min prior to irradiationand then removed; dotted line also present after irradiation.

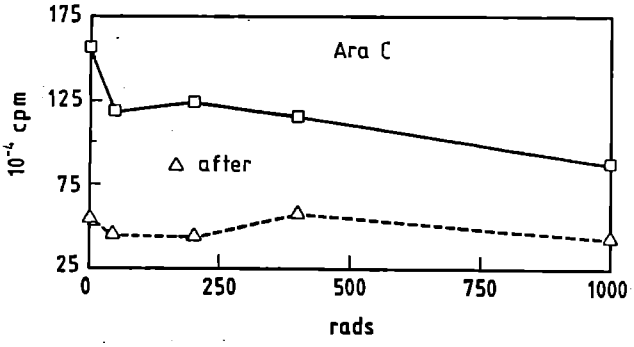

Fig. 2. The effect of arabinosyl- cytosine on soft X-ray induced repair DNA synthesis. Concentrations and conditions as in Fig. 1.

incorporation of ^{3}H-thymidine at low doses of X-rays,occurs when the inhibitor was included only prior to irradiation. When included also after irradiation this repair response was entirely eliminated. Aphidicolin is a tight binding inhibitor of polymerase α so it is surprising that it works as an inhibitor only when included after irradiation. This result shows that polymerase α,which is the main replication polymerase,is involved in the repair of soft X-ray induced damage. This,in turn, implies that altough only one residue is damaged 100 or more nucleotides are removed from the damaged DNA during the repair process since polymerase α can only work in single stranded gaps of 100 or more nucleotides.

The polymerase α inhibitor arabinosyl-cytosine (ara C) shows a somewhat different effect as compared with aphidicolin (see Fig. 2). When present either before or after irradiation it leads to a response to X-rays which is largely dose-independent. However when present after irradiation the level of DNA synthesis [replication?] is much reduced compared with exposure to this agent prior to irradiation.

The effect of dideoxythymidine (ddT),which is an inhibitor of polymerases β and δ,is more complex. When present prior to irradiation it appears to inhibit a repair response at low doses of X-rays but at higher doses which normally have a serious deleterious effect on cells some incrased DNA synthesis is seen.
When present after irradiation a small repair response is seen at low doses but no increase occurs at higher doses. It is notable that ddT is a very powerful inhibitor which allows very little DNA synthesis of any kind. Why this should be so when it is clear that α is involved and requires a gap of >100 nucleotides is unclear since it would be expected that α could function independently of β,which fills small gaps supposedly at the end of the repair process.

The experiments described above show that both polymerases α and α/δ are involved in repair of soft X-ray damage. This situation is similar to but less complicated than UV-induced repair. The conclusion is that the gap created during repair must be >100 nucleotides long;the gap is filled by α to ≈10 nucleotides after which the gap is closed by β/δ and sealed by ligase.

AUTOMATION OF EXPERIMENTS

Much of the background work we have been doing in relation to this project has been concerned with allowing automation of repair experiments. Repair of X-ray induced damage is rapid compared with overall repair of UV damage and the events which occur (and which we wish to study) immediately following damage are likely to be in the 0.1s or less time domain. It is therefore essential to be able to construct an automatic appartus similar to that used in our UV experiments.

REFERENCES

1) Rols & Tessie (1989) Eur. J. Biochem. 179,109.

2) Meldrum et al.,(1990) Laser Facility Annual Report,164-165.

3) Meldrum et al.,(1990) Laser Facility Anual Report,161-163.

4) Meldrum R A,Turcu I C E & Wharton C W (1990) Biochem. Soc. Trans. 18,1018-1019.

Kinetics and Mechanisms of DNA Repair in Mammalian Cells.

R.A.Meldrum, C.W.Wharton, W.Meaking, J.Edgerton and C.Reason.
Dept.of Biochemistry, University of Birmingham and Laser Division, Rutherford Appleton Lab., Chilton ,Didcot ,Oxon.

DNA repair fidelity and nucleotide imbalance

Experiments over the past year have focused on the fidelity of repair of DNA in the very early stages after damage.

The approach taken to assess the nature of the initial rapid burst of incorporation of labelled nucleotide or break trapping agent, previously described in annual reports, has been to examine the effect of the addition of different combinations of nucleotides on the distinctive features in the profiles of the time courses on DNA repair.

Considerable work has been done on the effect of an imbalance of nucleotides on the fidelity of DNA replication synthesis (Phear & Meuth,1989, Wong et al, 1990), but usually on isolated DNA of known sequences. We do not know the sequences of the DNA in the complete mammalian cells, and therefore cannot say when the correct nucleotide is being incorporated. However, the effect of nucleotide addition on the time courses of incorporation of labelled nucleotides during repair synthesis may be considered with reference to some of the observations made in the work on replication synthesis. Inhibition, acceleration or amplification of a burst of incorporation of labelled nucleotide by an imbalance of one or more nucleotides will imply nucleotide discrimination.

Fig 1. shows that an excess of TTP suppresses the incorporation of ^{32}P-ddATP over the whole time course of repair studied. An indiscriminate incorporation of TTP, which is not influenced by the sequence of the DNA, has been noted to take place during replication synthesis (Wong et al,1990). Our results suggest that this may be the case in repair synthesis, although caution should be exercised in interpreting this result , since ddATP is not a natural base. The experiment should therefore be repeated with ^{32}P-labelled ATP and excess TTP.

In fig.2A it can be seen that an excess of dCTP, dGTP and TTP attenuates the burst of incorporation of ^{32}P-dATP which then proceeds to a steady state without the fall seen in experiments with no added unlabelled nucleotides. The effect on the incorporation of ^{32}P-ddATP is very similar (fig 2B).

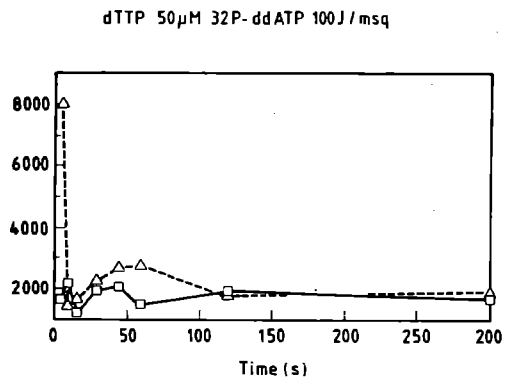

Fig.1 Effect of excess TTP on fidelity of repair synthesis.

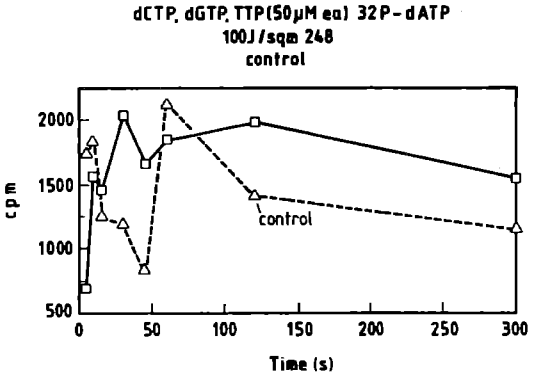

Fig 2A.

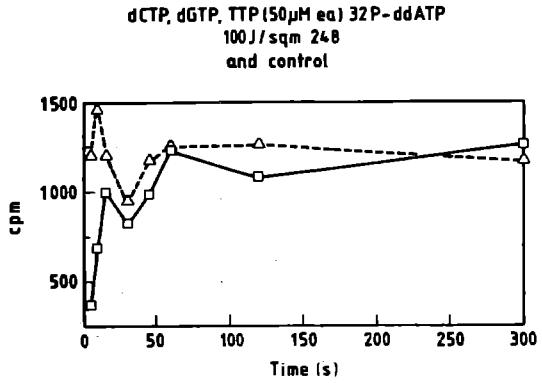

Fig2B.

Fig. 3 shows that dGTP and dCTP do not inhibit or attenuate the transient peak , commonly seen when radiolabelled nucleotide is added alone and which is formed by a burst of incorporation followed by loss of labelled material from the DNA.

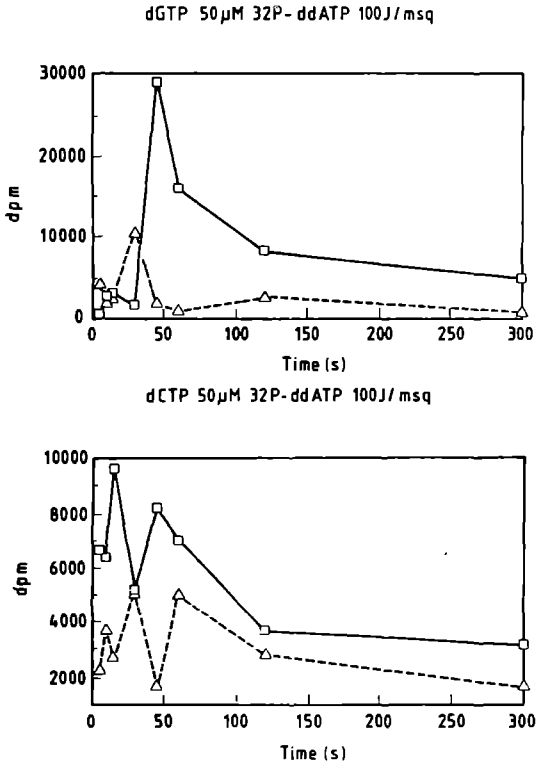

Fig3.

What do the above results say about fidelity of DNA repair synthesis at this early point after damage? An excess of three nucleotides over the radiolabelled ddATP or dATP may accelerate polymerisation of the DNA strand but overrides a proofreading enzyme which detects misincorporations and excises these, leading to the fall normally seen when excess nucleotides are absent. TTP appears to be a preferred nucleotide for incorporation when in excess. The nucleotides dCTP and dGTP do not seem to affect significantly the incorporation of ddATP.

In other experiments using radiolabelled TTP, dATP attenuates the burst of TTP incorporation and prevents a loss of that incorporation. In replication synthesis dATP was observed to increase the rate of misincorporation of nucleotides (Wong et al, 1990) so in repair synthesis excess dATP may also override a proofreading mechanism. There therefore, appear to be a number of parallels and similarities in the effects of imbalances of nucleotides on the fidelity of DNA replication synthesis and the effects of nucleotide imbalance on the time course profiles of DNA repair in the first few seconds after damage. At this very early point in repair synthesis, it would appear that polymerisation of DNA is carried out by the same enzyme as that active in replication synthesis. Since the polymerase in question appears to be closely associated with a proofreading enzyme, because of the very rapid onset of excision of misincorporated nucleotide, it is very likely δ-polymerase.

It will be noted from the above figs. that the incorporation of radiolabelled nucleotide into DNA in control cells is often initially higher than that of irradiated cells. The cells used are grown in suspension and do not reach a quiescent state , therefore a considerable amount of nucleotide may be initially incorporated at active replication forks. In irradiated cells these may have been stalled very rapidly by the damage, thus accounting for the lower initial uptake in these cells.

Nature of DNA damage which induces the initial burst of repair

We have also attempted to establish the true nature of DNA damage at this point where an early burst of repair polymerisation takes place, that is, whether the repair is due to the induction of direct single strand breaks or excision repair of UV induced dimers. Schulte-Frohlinde et al,1990 have measured the quantum yield of single strand DNA breaks produced by laser irradiation in DNA in solution. From this data we estimate that as many as 600 direct single strand DNA breaks could be induced in one cell by the dose of UV laser irradiation we have used. Attempts were made to estimate single strand breaks present immediately after irradiation. Cells were rapidly lysed and placed in alkaline medium. Alkaline conditions cause double stranded DNA to unwind and when breaks are present in the DNA this will occur at a higher rate. Ethidium bromide is added which interchelates in the remaining double stranded DNA. In this form it fluoresces if exited at 520nm. and loss of fluorescence will be proportional to breaks induced in the DNA. In experiments so far increased alkaline unwinding in DNA from irradiated cells was seen when compared to control cells, but it has as yet been impossible to calculate the number of breaks induced from

results because of variations in the technique which are promoted by the fact that we have to use different types of equipment when working at RAL(ie. sonicators,fluorimeter etc) from those in our home lab. where the technique has been standardised.

Electropermeabilisation of cells

Further work on electropermeabilisation has been carried out. Optimum permeabilisation of cells (ca. 80%) has previously been shown to occur when a voltage of between 300 and 400 volts is applied. Viability of the cells, as measured by cloning assays, was about 70% at voltages up to 360, but fell rapidly to 20% at 400 volts. A voltage of 360 is used in all experiments.Some resealing of cells is seen after electro-permeabilisation. About 30% of cells reseal in the first five minutes after permeabilisation but up to 30% remain open for over 30 minutes.

Effect of 351/340nm UV laser irradiation on DNA replication synthesis in mammalian cells

It has been described in previous annual reports how 340/351nm UV laser irradiation enhances DNA replication synthesis. In experiments which first showed this , one question still remained, that is , whether the enhanced incorporation of ^{3}H-TdR into DNA was due to more DNA being synthesised or that the cell's nucleotide pool was depleted by this irradiation, thereby increasing the specific activity of the radiolabelled nucleoside.
To test this, cells were prelabelled with ^{14}C-thymidine and post labelled (after irradiation) with ^{3}H-thymidine.The DNA was separated from the cells by TCA precipitation, and the supernatant which contained the nucleotides from the cell pool analysed by HPLC (high pressure liquid chromatography). The ratios of ^{14}C to ^{3}H were measured in the different thymidine nucleotide and nucleoside fractions. These showed no changes that indicated that a depletion of the cell's nucleotide pool had taken place, and thus confirmed that 340/351nm induced cells to make more DNA.

References .

Phear G. and Meuth M. (1989)
Molecular and Cellular Biology 9,4 p1810-1815
Wong I.,Patel S.S. and Johnson,K.A. (1990)
Biochemistry 30, 526-537

Publications

R.A.Meldrum & C.W.Wharton,
Stimulation of DNA synthesis by 340/351nm UV laser irradiation.
Biochem. Soc. Trans. 19,1193 (1991)R.A.Meldrum & C.W.Wharton, The kinetics of DNA repair following UV damage to mammalian cells. Biochem. Soc. Trans. 18, 1018 (1990)

LIGHT INDUCED STRESS RESPONSE IN MAMMALIAN CELLS

Gerald E. Adams and Ian J. Stratford

MRC Radiobiology Unit, Chilton, Didcot OX11 OSA, U.K.

INTRODUCTION

The origin of this project arose from observations made by Drs Wharton and Meldrum (University of Birmingham) during experiments on an established programme at the Central Laser Facility (CLF). In particular, they showed that a non-toxic dose of light at 351 nm given to mammalian cells resulted in a transient increase in DNA replication. We proposed that this phenomenon cuold be related to ongoing work in our Laboratory concerning the response of mammalian cells subjected to various biological or physical stresses, which include nutrient deprivation, mild hyperthermia and exposure to temporary hypoxia. Hypoxic "shock", while non-toxic in itself, is known to induce high levels of resistance to some anti-cancer drugs can also increase the metastatic potential of tumour cells.

The laser experiments were designed to investigate the extent of any homology between light-induced stress and stress response induced by other agents. Experiments have included investigation of (1) cellular response to the anti-cancer drug adriamycin (2) changes to the metastatic potential of murine tumour cells; (3) changes to the proliferation kinetics of cells in culture.

METHODS

Irradiations were carried out with the Questec XeF laser using light doses ranging from 2-200 kJ/m^2 at 351 nm. Cells in 3cm plastic Petri dishes were irradiated in phosphate buffered saline at the CLF, then transported to the MRC RBU for subsequent analysis. Routinely, the PBS was removed from the cells, replaced with growth medium and cells incubated at 37°C. At various times thereafter cells were prepared for treatment.

Response to adriamycin was measured following a 1 hour exposure of Chinese hamster V79 cells to the drug at 37°C. Drug was then removed and cell survival assayed by conventional colony forming techniques.

Proliferation was measured by plating V79 cells in growth medium into 24 well dishes as soon as practicable after irradiation. Dishes were incubated for 3 days before estimation of all numbers using a colorimetric MTT assay.

Metastasis experiments were carried out with murine KHT tumour cells. A solid tumour was excised from a tumour-bearing mouse and a single cell suspension prepared. Cells were irradiated as indicated above, then known cell numbers injected via the tail vein into recipient mice. Three weeks later mice were sacrificed and tumour colonies on the lungs (metastases) counted.

RESULTS

Figure 1 shows the change in optical density relative to control for cells given varying radiation doses and then allowed to proliferate for 3 days. At doses ranging from 2-20 kJ/m^2 there was no effect on proliferation compared with untreated cell cultures. However, following irradiation with 50 and 120 kJ/^{2} at 351 nm there was a substantial increase in cell number. This indicates that during the 3 days of incubation there was an increase in the rate of proliferation. These results were obtained for cells harvested from plateau phase cultures. No effect of light was observed on exponentially-growing cells. These observations are consistent with the findings of Wharton and Meldrum who showed a 40% increase in the DNA synthesis of plateau phase V79 cells in the 17 hours following irradiation; this was not observed in exponentially growing cells.

Recently, Hasan *et al.* at the MRC RBU have found a potential biochemical marker for hypoxic stress. Under ambient conditions the cellular ratio of xanthine oxidase/xanthine dehydrogenase (XO/XD) is fairly constant at 25%. With induction of hypoxia this ratio increases to about 80% and the kinetics of this change follow that for hypoxia-induced resistance to adriamycin light also induces these changes. The ratio of XO/XD was measured 4 and 24 hours following irradiation with 50 kJ/m^2. For both times the ratio was increased to greater than 50%. This is consistent with the increase in proliferation seen over this time period.

Light doses between 2 and 200 kJ/m^2 at 351 nm are not cytotoxic to cells, nevertheless V79 cells when treated with adriamycin become resistant compared to unirradiated controls. However, this result has proved difficult to reproduce. Experiments are in progress to investigate the possible complicating role of cell contact in this phenomenon.

Pulses of 351 nm light increase the effectiveness of KHT cells in forming metastatic lung colonies in mice. Injection of 2 x 10^4 tumour cells into mice normally gives rise to about 30 lung colonies. Pre-irradiation of the cells with 2 kJ/m^2 significantly increase the colony number. Doses of light ≥20 kJ/m^2 show little or no effect on colony number relative to controls.

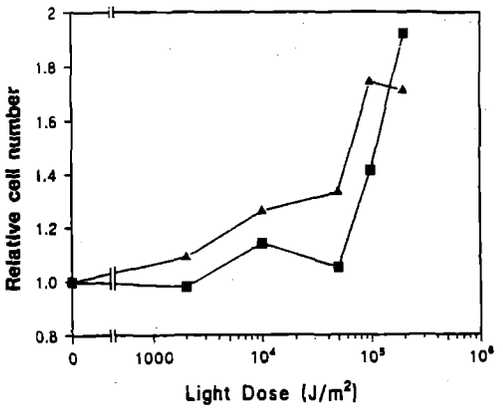

Figure 1. Effect of light dose on growth of V79 cells

DISCUSSION

Light of 351 nm clearly induces a cellular stress response. Effects include induction of temporary proliferation, changes in protein expression and enhancement of metastatic potential. There is some homology with the effects of hypoxic stress in that xanthine oxidase ratios also change and metastatic potential is increased. However, with the cell lines so far studied hypoxia does not appear to induce temporary proliferation.

Future work will include study of factors involved in cell signalling including up-regulation of protein kinases, changes in cellular membrane properties and the role of cell-to-cell contact.

Transient Absorbance Measurements in PSI

E H Evans[1], C Potter[1], R Sparrow[1],
M C W Evans[2], R Chittock[3], A J Langley[3],
W Shaikh[3] and W T Toner[3]

[1]Lancashire Polytechnic
[2]University College London
[3]Rutherford Appleton Laboratory

INTRODUCTION

In previous reports[1,2] we have described transients measured in Photosystem 1 (PSI) preparations from the cyanobacterium Chloroglea fritschii. The 700-715 nm region is dominated by a saturating bleach which is well described by

$$\frac{-\Delta A}{A_{680}}(1-exp-\frac{t}{\tau_R})\,x\,.....$$
$$.....[a(\lambda)\,exp-\frac{t}{\tau_F}+b(\lambda)(1-exp-\frac{t}{\tau_F})](1-exp-\frac{P}{P_0}) \qquad (1)$$

Where the risetime, τ_R, is less than 600 fsec; the recovery time t_F, is 30 ± 5 psec; the pump station fluence, P_0, is 10^{16} photons/cm^2 and the pump fluence P is in units of photons/cm^2.

The bleach strength functions a(λ), b(λ) both peak in the 705-710 nm region. The long-lived (lifetime >> 3 nsec) component b(λ) is readily suppressed in oxidising conditions but a(λ) decreases by less than a factor 2 on oxidation. The ratio of b/a at 706 nm is shown in Fig 1 for all samples measured in experimental sessions spanning a three year period. The mean value in oxidising conditions is consistent with zero and the mean in reducing conditions is 0.26. The values of the a(λ) parameter for the same set of data show a wide variation (a factor of 8) in which no clear systematic dependence on physical parameters could be found. There is however a clear difference between results from different experimental sessions.

The 670 to 700 nm region is much more complex and is subject to variations which mirror the variations in strength of the 705-710 nm bleach. All risetimes are prompt within the resolution of our measurements. There are three groups of time constants for bleach recovery: fast (3-12 psec), intermediate (20-30 psec) and long (>120 psec). The fast components dominate the appearance of the transients for pump fluences ~0.5 to 1 mJcm^{-2}; the long lived components are invariably small in magnitude (.05 to .25% of A_{680}). When the 700/715 nm bleach was large the pump intensity dependence at early times was well described by

$$\frac{-\Delta A}{A_{680}} = c\frac{P}{P_0}+d(1-exp-\frac{P}{P_0}) \qquad (2)$$

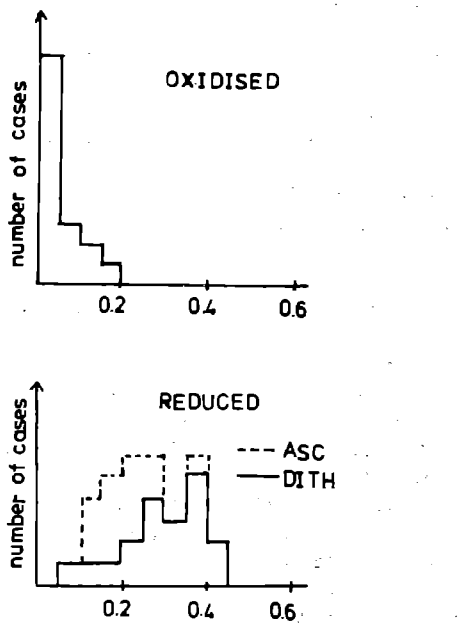

Fig.1. Histogram of ratios b(λ)/a(λ) at l = 706 nm for all samples in oxidised and reduced conditions.

with d=-c and P_0 having the same value as for the 700-715 nm data. In sessions when the 700-715 nm bleach was small, d was positive and "global" fits to time and pump intensity dependences in which each bleach recovery component could have independent values of c and d. show that the components having a fast recovery have d<0, the intermediate (20-30 psec) recovery has d>0 and the interpretation of the small long-lived components is ambiguous due to the presence of a small pump related background. The presence of a saturating (d>0) component in this region of intermediate lifetime when the saturating bleach at 706 nm is weak suggests that there is some, interchangeability between the components.

The transient absorbance data are complemented by fluorescence measurements of the same PSI preparations[3] The overall quantum yield is low (~1%) which is a measure of sample integrity[4] and the observed fluorescence shows a large component having a lifetime estimated at 30 psec and a double-peaked spectrum with λ_{max} = 690 and 710 nm. As the samples go from oxidised to neutral and to strongly reduced the ratio of the 710 nm to the 690 nm component increases by a factor of approximately two.

DISCUSSION

We have identified the long-lived 700-715 nm component as P700 and the precursor with a 30±5psec lifetime as a "funnel"[1]. The tight bunching of the ratio of these two components despite the wide variation of their magnitudes we take to be indicative of a very close and robust coupling between the species responsible. The 710 nm component of the fluorescence having a 30 psec lifetime is identified with the funnel species at 706 nm.

The identity of components in the 670-710 nm region is less clear. Fast recovering transients have been identified with light harvesting chlorophyll[1], but slower components show some variability, linked to the variations seen at 706 nm in different samples.

It seems probable that PSI can exist in two states; Type A, in which F_{706} funnels energy efficiently to a readily re-reducible P_{700}; Type B, in which the species responsible for F_{706} exists in a different state or binding conformation which shifts its ground state absorbance (and fluorescence) to 690 nm, thereby decoupling it from P700. The difference between Type A and Type B is small enough to respond to redox variations, seen also in our fluorescence data (4). It seems likely that the difference is related to re-reduction rate of P700, and may therefore reflect a change in protein conformation affecting this process.

References

1. E H Evans et al, Annual Report to Central Laser Facility p 66, 1990.

2. E H Evans, R Sparrow, R G Brown, R Chittock and W Toner, EBEC Reports, 5, 174 (1988).

3. R Sparrow, E H Evans, R G Brown and D J Shaw, Photochem. Photobiol, 5, 445 (1990).

4. R Nechushtai, S D Nourizadeh and J P Thronber, Biochim, Biophys Acta, 848, 193-200 (1986).

RESONANCE RAMAN SPECTROSCOPY OF 4-THIOTHYMIDINE AND OLIGONUCLEOTIDES CONTAINING THIS BASE

Bernard A. Connolly[1], Timothy R. Waters[1],
Christopher Wharton[2] and Anthony W. Parker[3]

[1]Department of Biochemistry, University of Southampton
[2]Department of Biochemistry, University of Birmingham
[3]Laser Support Facility, Rutherford Appleton Laboratory

INTRODUCTION

The modified base 4-thiothymidine is derived from its parent thymidine. Both of these bases are illustrated in figure 1. As can be seen the difference is that the oxygen atom at position four in thymidine is replaced by sulphur in 4-thiothymidine. This small substitution causes large changes in the chemical and physical properties of 4-thiothymidine as compared to thymidine. First thymidine absorbs light maximally at 265 nm. With thiothymidine this is shifted to 340 nm, well away from the absorbtion maxima of biological materials (260 nm for nucleic acids and 280 nm for proteins). Second thiothymidine contains the highly polarisable C=S chromophore and is therefore a much stronger Raman scatterer than thymidine. Due to the light absorbance at 340 nm it is possible to perform resonance Raman experiments using excitation at this wavelength. Finally 4-thiothymidine is much more chemically reactive than thymidine. The sulphur atom is a good nucleophile reacting with reagents such as methyl iodide. Alternatively incoming nucleophiles can attack at carbon 4 with sulphide displacement. 4-thiothymidine is also photo-reactive forming highly reactive free radicals on illumination at 340 nm.

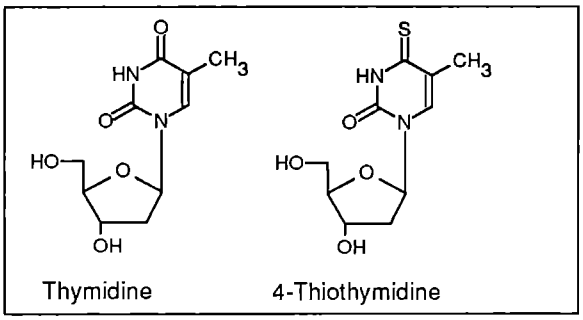

Figure 1

We recently developed methods for incorporating 4-thiothymidine into synthetic oligodeoxynucleotides. The method used the sulphenylmethyl (-SCH_3) group to protect the active thiol during synthesis. Although products were produced this protocol was far from satisfactory. Several side products were formed and the yields of purified desired product were low. The oligonucleotides synthesised were GACGA[^{4S}T]ATCGTC and GACGATA[^{4S}T]CGTC. These contain 4-thiothymidine residues within the recognition site for the Eco RV restriction endonuclease and modification methylase (GATATC). The properties of 4-thiothymidine, seen with the free base, were also found in these substituted oligodeoxynucleotides. Thus they had a U.V. absorbance maximum at 340 nm (as well as at 260 nm due to the four normal nucleotides). Additionally a circular dichroism transition at 340 nm was observed due to the presence of 4-thiothymidine. The oligonucleotides also showed the chemical and photo-reactivity expected for 4-thiothymidine. In particular irradiation at 340 nm led to the disappearance of the absorbtion at 340 nm and the destruction of the 4-thiothymidine base. Performing this irradiation in the presence of the Eco RV endonuclease or methylase led to photocrosslinking of the oligodeoxynucleotide to the proteins. We have recently improved the synthetic procedures to incorporate 4-thiothymidine into oligonucleotides. These use the p-nitrophenyl group (rather than the sulphenylmethyl) to protect the sulphur during synthesis. Far higher yields of products are obtained in greater purity.

RESULTS AND DISCUSSION

Initial resonance Raman experiments were performed using 4-thiothymidine and a Lumonics Excimer/FL3002 Dye laser set to 340 nm. Although some Raman bands could be observed this system was far from satisfactory. The main problem was the high power which led to both a large background fluorescence and extensive photodecomposition of the sample. Much better spectra were obtained using an Innova 90 Argon ion laser at 351 nm. Using this laser at relatively low power gave a relatively low fluorescence spectrum in relation to the Raman peaks. Pumping the sample continuously through the laser beam together with low power greatly reduced photodecomposition. Sample spectra are illustrated in figure 2 (2a before fluorescence background subtraction, 2b after fluorescence background subtraction) and represent a considerable improvement on those published in the 1990 Annual Report. The band at 706 cm^{-1} is assigned to the C=S stretching mode. The other bands have yet to be assigned. Although the set up described here gives good spectra for 4-thiothymidine it is not really suitable for oligodeoxynucleotides that contain this base. The main reason is the constant pumping of the sample through the laser beam. This requires a relatively large volume and so reasonably large quantities of material. Although the amounts required are accessible for 4-thiothymidine they are not for oligomers containing this base. However we have also used a rotating cell system which enables much smaller quantities of materials to be circulated through the laser beam. This set up has been optimised to give spectra of equivalent quality to those shown in figure 2. The amounts of material required are small enough so that these experiments are possible with oligodeoxynucleotides containing ^{4S}T, particularly when

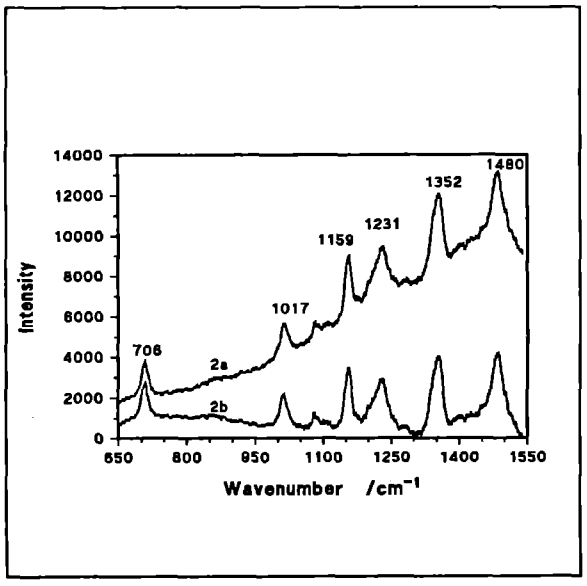

Figure 2

these are combined with the synthetic improvements mentioned above. It is now hoped to measure the spectra of these oligomers and also their spectra when bound to the Eco RV enzymes. From this we should be able to draw conclusions about both the free oligodeoxynucleotide structure and its structure when bound to the two proteins.

High Resolution Spectroscopy of the Muonium 1S-2S Transitions

P E G Baird[b], J R M Barr[c], C Bressler[a], P Curley[d], R Dixon[c], G H Eaton[f], A I Ferguson[d], H J Geerds[a], V W Hughes[e], K Jungmann[a], J Kenntner[a], M Lea[b], F E Maas[a], M Persaud[d], G zu Putlitz[a], P G H Sandars[b], W Schwarz[a], W T Toner[f], M Towrie[f], G Woodman[b], I L Zhang[a], Z Zhang[a]

[a]University of Heidelberg
[b]University of Oxford
[c]University of Southampton
[d]University of Strathclyde
[e]University of Yale
[f]Rutherford Appleton Laboratory

Muonium (μ^+e^-) is the bound state of a positive muon (μ^+) and an electron (e^-). This light hydrogen-like system is one of the most fundamental atoms in nature. It is ideal for testing bound state Quantum Electrodynamics (QED) and the behaviour of the muon as a pointlike heavy leptonic particle. Since muonium consists of two structureless leptions only, its energy levels can be calculated up to very high precision exclusively by QED. The system is also well-suited for the experimental determination of precise values for fundamental constants[1].

In this experiment we have observed with >98% confidence level a signal for the $1^2S_{1/2}(F=1)$ - $2^2S_{1/2}(F=1)$ two-photon transition using Doppler-free laser spectroscopy. Muonium atoms are produced with 60(3)% efficiency by electron capture after stopping 3000 positive muons of 20 MeV/c momentum from one double pulse of the ISIS muon channel close to the surface of a SiO_2 powder target. Between 50 and 100 of these atoms diffuse to the surface and leave the target into the surrounding vacuum with a Maxwell-Boltzmann distribution at thermal velocities of v = 7.43(2)mm/μs. About 1 cm above the target the atoms interact with two counter-propagating intense laser beams of $4mm^2$ cross section at 244 nm wavelength. A single laser beam is reflected back and forth 3 times between two 10cm separated mirrors before a third mirror reflects it back into itself.

The laser system consists of a Krypton ion laser pumped cw single mode single dye laser at 488nm wavelength and a pulsed excimer laser pumped dye laser amplifier. The pulsed blue light is frequency doubled in a β-BBO crystal. The system delivers up to 8 mJ UV energy in 17 ns long pulses at 25 Hz repetition rate (see fig 1). A fraction of the cw laser light at 488nm is frequency downshifted between 766 and 868 MHz by double passing an acousto-optic modulator. For the purpose of frequency calibration the cw laser is locked to the d_4 reference line in the spectrum of molecular $^{130}Te_2$ using saturation spectroscopy with the frequency downshifted cw laser beam. The frequency of the d_4 line is currently known with an accuracy of 1 ppb [2]. Locking times of several hours were achieved regularly. In the framework of this experiment a frequency locked laser system with 10^{-9} accuracy has been operated for the first time at an accelerator site.

The 1S-2S transition is detected by the photoionisation of the 2S state with a third photon in the same laser field. The muon released in this process is electrostatically accelerated to 1 keV and guided through a 1.66 m long energy and momentum selective path to a microchannel plate (MCP) particle detector of 40(20)% efficiency. The apparatus has been tested and optimised with the help of Doppler-free two-photon transitions in atomic hydrogen (H) [3]. The hydrogen atoms have been produced by photodetachment from organic molecules on the mirror surfaces close to the SiO_2 target. Protons have been detected on the MCP instead of muons as a signal for the hydrogen 1S-2S transition. Spectroscopy of atomic hydrogen in the very same apparatus under comparable conditions is essential for eliminating systematic effects.

The laser is fired 1.5 μs after the arrival of the muons from every second ISIS pulse. In the laser off phase we have the opportunity for a sensitive base line determination. We find 0.94(48) background counts per 10^5 pulses in good agreement with 0.49(49) counts with the laser being tuned by 2.6 GHz below resonance. A Lorentzian can be fitted to the dependence of the MCP count rate on the laser frequency (see Fig 2). The line centre is 843(15) MHz above the d_4 $^{130}Te_2$ reference line. The linewidth (FWHM) of 49(33) MHz is mainly due to the pulse laser bandwidth at 488 nm which has been determined independently by interferometric methods and from atomic hydrogen signals to be 40(7) MHz. The signal has been obtained with 19 h of data taking.

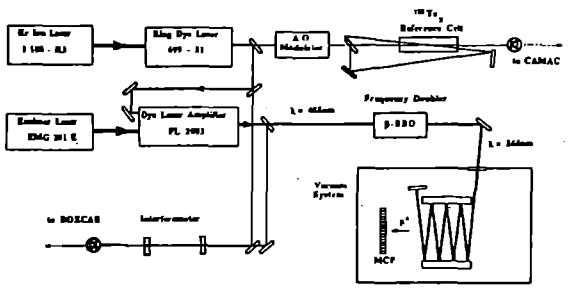

Figure 1: Lasers and optical system in the muonium 1S-2S experiment.

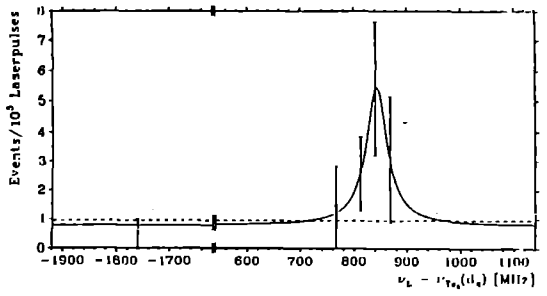

Figure 2: Doppler-free muonium 1S-2S signal. The dashed line indicates the background count level in the laser-off phase.

The signal is subject to various systematic effects. There is a shift of less than ±22 MHz due to the linear Doppler effect caused by the finite crossing angle of the beams of ≤0.4 mrad and the asymmetric atomic velocity distribution. The second order Doppler shift for muonium is 0.6 MHz. Static electric fields in the interaction region can be kept below E=5 V/cm. The corresponding dc-Stark shift $\Delta\nu_{dc\text{-}Stark} = 4.7\,E^2$ KHz cm^2/V^2 amounts to 0.12 MHz. The shift due to the dynamic Stark effect is $\Delta\nu_{ac\text{-}Stark}$=3.34 I HZ cm^2/Watt, where I is the laser intensity. It has been calculated numerically using a measured temporal and spatial beam profile. We find $\Delta\nu_{ac\text{-}Stark}$ = 32(10) MHz for muonium in a laser beam of 4 mJ pulse energy. The frequency shift in the pulsed dye amplifier has been measured using an interferometer and independently by comparison with hydrogen spectra to be 20(10) MHz at 488 nm. The corrected muonium 1S-2S transition frequency of 24455528023(58)(47) MHz is in agreement with QED calculations which yield 2455527959(2) MHz [4]. Our measurement represents a test of the 1S Lamb shift at the 1% level.

This work is supported by the BMFT (Germany), the SERC (United Kingdom) and the NSF (United States). We are grateful to he helpful people working at ISIS under the leadership of David Gray for various kinds of support.

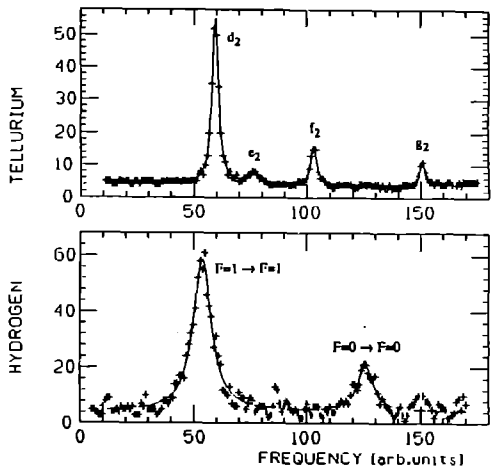

Figure 3: Doppler-free hydrogen 1S-2S two-photon signals together with a Doppler-free saturation spectrum of $^{130}Te_2$ as a frequency reference.

References

[1] V W Hughes and G zu Putlitz, in "Quantum Electrodynamics", ed T Kinoshita, World Scientific (1990).

[2] D H McIntyre and T W Hansch, Phys Rev A36, 4115, (1987).

[3] J R M Barr et al, Phys Rev Lett 56, 580 (1986).

[4] J R Sapirstein and D R Yennie, in "Quantum Electrodynamics", ed T Kinoshita, World Scientific (1990).

MULTIPHOTON MULTIPLE IONISATION OF N_2O PROBED BY THREE-DIMENSIONAL COVARIANCE MAPPING

L. J. Frasinski, P.A. Hatherly and K. Codling

J.J.Thomson Physical Laboratory, Whiteknights, P.O. Box 220, Reading RG6 2AF, Berks., U.K.

ABSTRACT

One can attempt to understand the complex dynamics of multiphoton multiple ionisation of triatomic molecules using conventional time-of-flight mass spectrometry, but only by applying three-dimensional covariance mapping can processes involving the simultaneous production of three charged fragments be unequivocally assigned to a specific parent molecular ion.

When homonuclear diatomic molecules such as N_2 are multiply-ionised using an intense subpicosecond laser, any attempt at analysis of the resulting fragmentation pattern using time-of-flight (TOF) mass spectrometry is seriously compromised by an inability to differentiate the asymmetric processes involving neutral fragments for example $[N_2^{2+}] \rightarrow N + N^{2+}$, from the symmetric ones, namely $[N_2^{4+}] \rightarrow N^{2+} + N^{2+}$. Equally, it is difficult to analyse TOF spectra of heteronuclear molecules such as CO if identical fragment atomic ions from different parent molecular ions have similar energies. These problems have been alleviated recently by the introduction of two-dimensional covariance mapping, which allows unequivocal correlation of fragment ion pairs with parent molecular ions[1,2] and thereby a more complete description of the dynamics of laser-molecule interactions.

In the case of the multiphoton multiple ionisation of triatomic molecules the situation is much more complex. One can produce similar two-dimensional covariance maps but these only serve to indicate correlations between pairs of fragment ions, whereas at the higher laser intensities it is quite probable that three correlated fragment ions will be produced. Although one might infer from a combination of one-dimensional TOF spectra and two-dimensional covariance maps that three ions have been created simultaneously, the only sure way of confirming a triple-ion process is by using three-dimensional covariance mapping. The present letter intends to show that such confirmation has been possible in the case of N_2O.

In the experiments described here, a laser of wavelength 600 nm, pulse length 0.6 ps, repetition rate 10 Hz and focused intensity somewhat in excess of 10^{15} W/cm^2, is used to multiply-ionise an assembly of N_2O molecules. A field across the interaction region accelerates the ions towards a short drift tube and thence to a pair of microchannel plate detectors[3]. The ion signal is fed directly to a digital oscilloscope and fig. 1 is typical of the TOF spectra obtained. In this case the E-field of the linearly-polarised laser beam lies along the axis of the drift tube. In the field ionisation model[4] a diatomic molecule is more easily ionised when its molecular axis lies along the laser E-field. A similar behaviour is expected for linear triatomic molecules such as N_2O. Since there is little time for molecular rotation, the ions will also be ejected preferentially along the drift tube axis, either towards ("forward" ions) or away from ("backward" ions) the microchannel plates.

The forward ions have TOFs that vary linearly with momentum component along the drift tube axis. The kinetic energy scales beneath the spectrum refer to these ions and were obtained by computer simulation of the well-characterised drift tube. The backward ions, of identical energy range, reverse their trajectories in the applied field and arrive almost simultaneously at the microchannel plates, regardless of their initial kinetic energies. These produce the sharp peaks in the TOF spectrum and their appearance allows immediate identification of the various fragment ions present in the focal region of the laser.

By observing the movement of the forward ion peaks as a function of the voltage, one can attempt to analyse the spectrum. However, with broad or weak features, it has proved impossible to make unambiguous determination of the kinetic energy and charge state of the various ions. For example, the broad feature at about 2.5 μs is due to overlapping N^{2+} and O^{2+} ions but it was difficult to quantitatively apportion the peak to these two species. Each ion has an energy peak at about 20 eV. At this point the covariance mapping technique was applied in order to allow correlation of pairs of charged particles. To achieve this, a new drift tube was constructed[5], a factor of two shorter than that used to produce fig. 1. This ensured 100% collection efficiency of forward *and* backward ions but at the expense of energy resolution. It also had the important feature that the ion TOF was a linear function of momentum component along the drift tube axis for both forward and backward ions.

The principle of covariance mapping has been described elsewhere[1] but a brief reminder is presented here. Suppose that for a given laser pulse, the following two-body fragmentation process occurs: $N_2O + nh\nu \rightarrow [N_2O^{2+}] \rightarrow N_b^+ + NO_f^+$, where subscripts f and b refer to forward and backward ions. If the N_b^+ fragment is detected at TOF t_1, there is an enhanced probability of detecting an NO_f^+ fragment at TOF t_2. This probability is considerably less than 100% because of poor detector efficiency. When one calculates, over many laser pulses, the covariance between the TOF points at which the fragments are detected, one obtains a positive value. This is given by the expression $C(t_1,t_2) = \langle X(t_1)X(t_2)\rangle - \langle X(t_1)\rangle\langle X(t_2)\rangle$, where X is the amplitude of the digitised signal. (In general $C = \langle XY\rangle - \langle X\rangle\langle Y\rangle$, where X and Y denote two different signals, but here $X = Y$ because only one detector is involved.) Because one does not know in advance which points on the TOF spectrum are correlated, one calculates the covariance for each pair (t_1,t_2) of TOF points (channels in the digital oscilloscope) and presents it in the form of a two-dimensional map such as fig. 2(a).

The linear relationship between TOF and momentum component along the drift tube axis suggests that the covariance map should be seen as a momentum correlation diagram. In the above two-body fragmentation, momentum conservation dictates that the correlated structure be in the form of a line. The two islands in the top right-hand corner of fig. 2(a) reflect the forward-backward and backward-forward fragments correlations. In order to allow the reader to recognise these correlations, a time-averaged, one-dimensional TOF spectrum is shown on the ordinate and abscissa. One sees that the upper of the two features involves N_f^+ and NO_b^+ ions whereas the

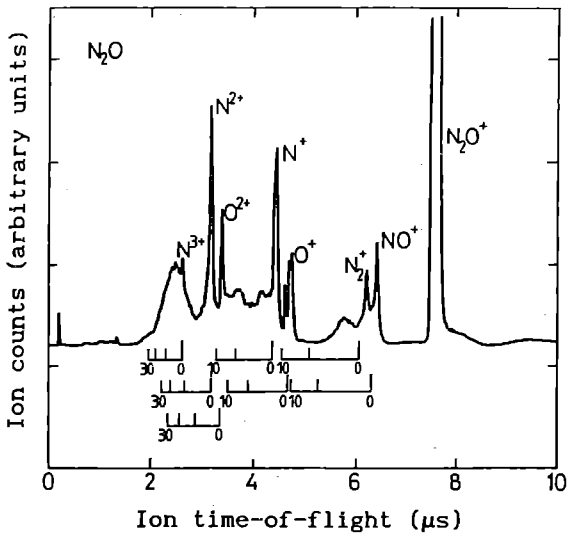

Figure 1: TOF spectrum of N_2O. The sharp peaks are associated with "backward" fragment ions. The connection between a particular group of "forward" ions and its energy scale is made by noting that each backward peak lies just to the right of the 0 eV position.

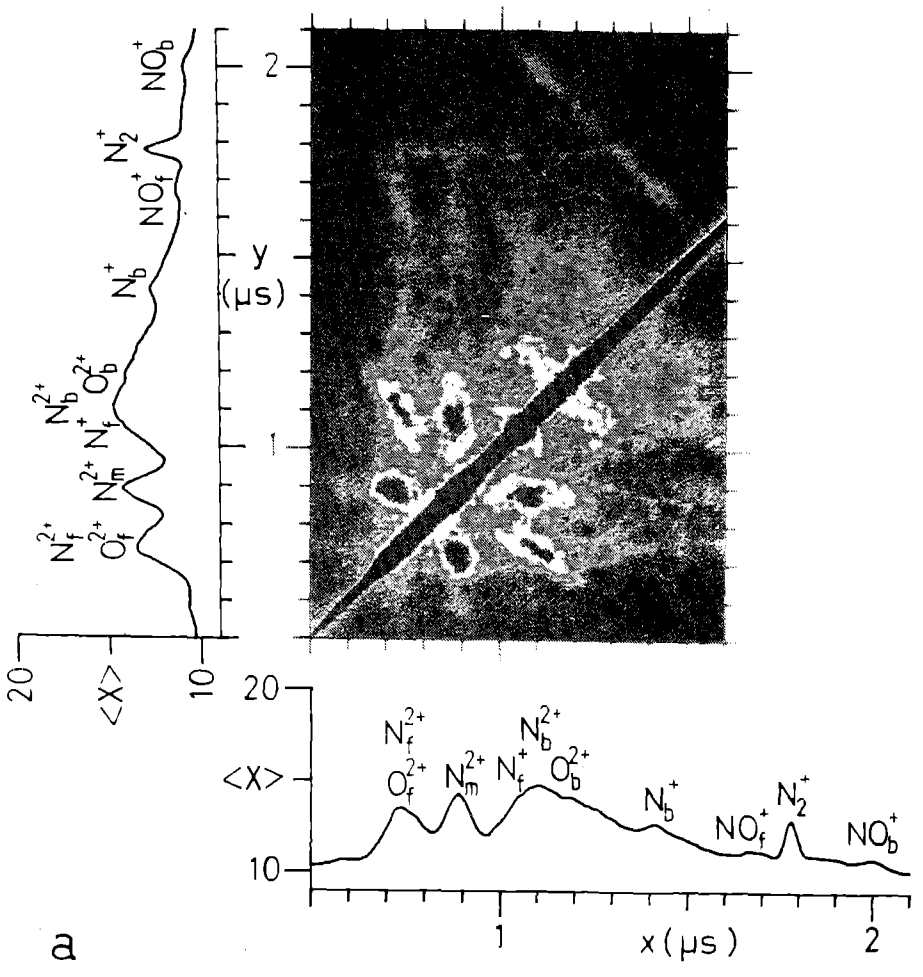

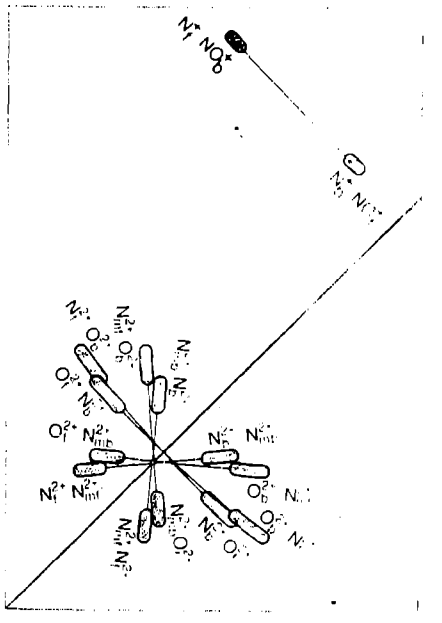

Fragment	mv	E (eV)
NO^+	1	1.5-2.0
N^+	1	3.2-4.3
N^{2+}	1	12-24
N_m^{2+}	0.1	0.1-0.2
O^{2+}	1.1	13-26

b

Figure 2:

(a) Two-dimensional map of N_2O. The conventional time-averaged TOF spectrum is placed along the x and y axes.

(b) Simulation of the two-dimensional map, see text for labelling. The table beneath gives the energy range of the ions.

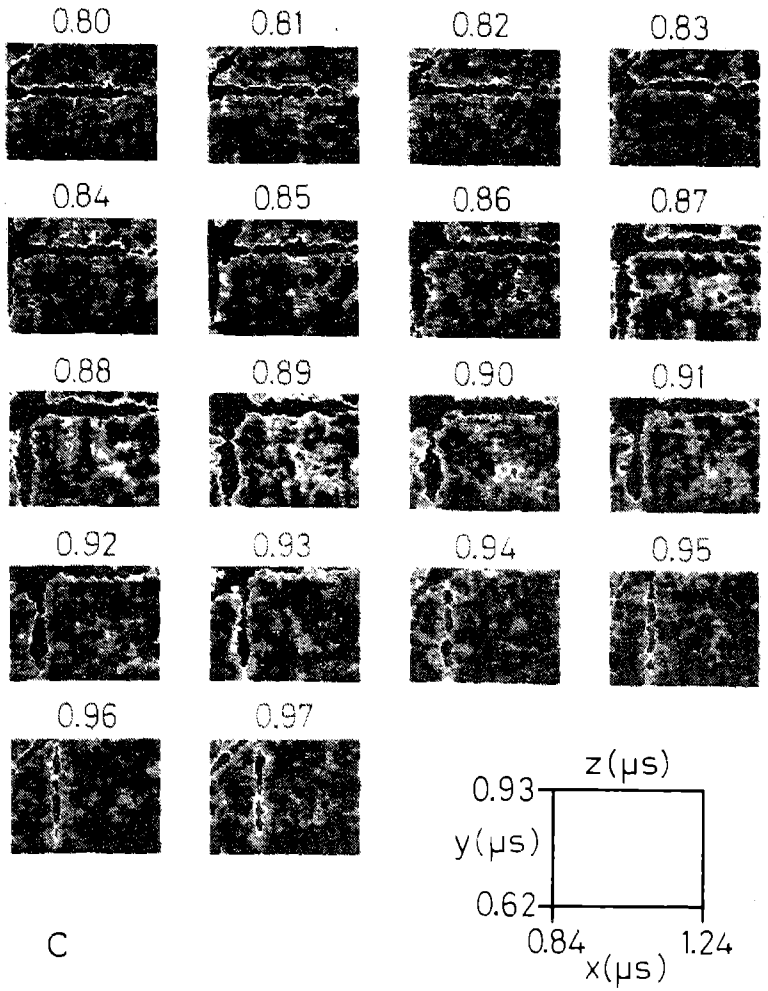

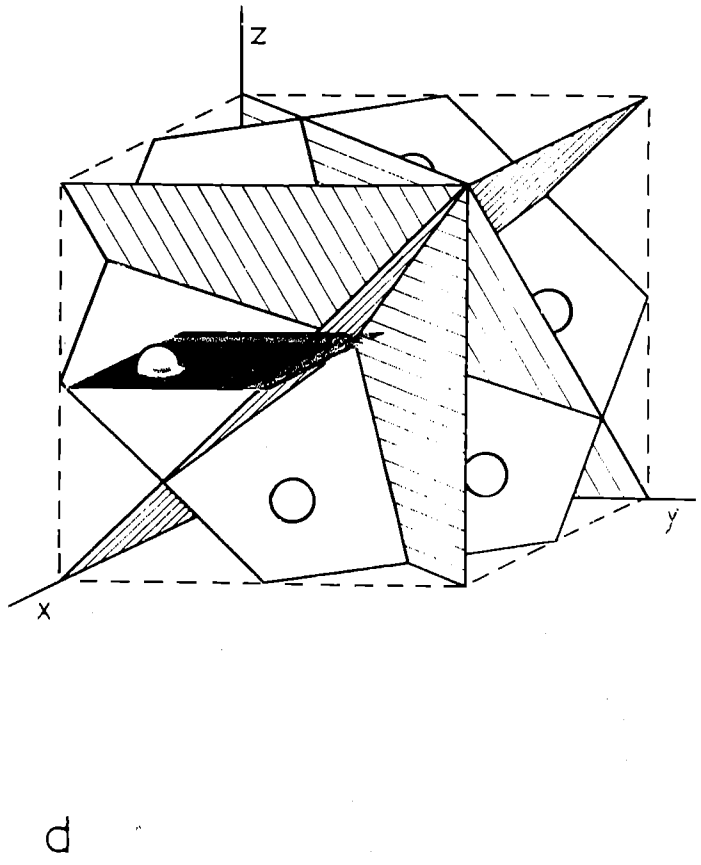

Figure 2:

(c) Slices of the three-dimensional map. One such slice is shown schematically in figure 2(d). The rectangle at the bottom right indicates the range of x and y; the values of z are given above each slice.

(d) A schematic three-dimensional map. The origin is at $x = y = z = 0.6$ μs and the cube extends to 1.2 μs. The strong red lines on the slice show intersections with the hatched autocorrelation planes.

lower involves N_b^+ and NO_f^+ ions (the order denotes ions on the x and y axes respectively). The tilt of the blue line, in this case 45°, gives the ion charge ratio and the intensity variation along the line gives the momentum distribution and hence the energy spread. Although the features are rather weak, one finds that the NO^+ ions have an energy range of 1.5 to 2.0 eV and, through momentum conservation, the N^+ ions must have an energy range of 3.2 to 4.3 eV. The computer simulation in fig. 2(b), alongside, gives the relevant correlations, the "length" of each island relating roughly to the momentum spread.

The above channel is clearly a minor one when compared to that responsible for the six main features in fig. 2(a). The strong red line at 45° is the autocorrelation line and is of no real interest here except that one obtains reflection symmetry in this line. Because of their location on the map (i.e. on the TOF spectrum), the features must be associated with doubly-charged ions. However, as pointed out in the introduction, any analysis using two-dimensional covariance mapping is bound to be ambiguous because one cannot differentiate the situation where pairs of ions are produced independently:

$$N_2O + nh\nu \rightarrow [N_2O^{4+}] \rightarrow N^{2+} + N_m^{2+} + O$$
$$\text{or} \quad " \quad \rightarrow N \quad + N_m^{2+} + O^{2+}$$
$$\text{or} \quad " \quad \rightarrow N^{2+} + N_m \quad + O^{2+},$$

from the situation where three ions are produced simultaneously:

$$N_2O + nh\nu \rightarrow [N_2O^{6+}] \rightarrow N^{2+} + N_m^{2+} + O^{2+}.$$

The subscript m denotes the middle N atom of N_2O ($N \equiv N_m = O$).

In order to remove this ambiguity, a three-dimensional covariance map is required. In this case one is looking for correlations between three points (t_1,t_2,t_3) in the TOF spectrum. The following expression is a natural extension to the two-dimensional case discussed earlier: $C(t_1,t_2,t_3) = \langle X(t_1)X(t_2)X(t_3)\rangle - \langle X(t_1)X(t_2)\rangle\langle X(t_3)\rangle - \langle X(t_1)X(t_3)\rangle\langle X(t_2)\rangle - \langle X(t_2)X(t_3)\rangle\langle X(t_1)\rangle + 2\langle X(t_1)\rangle\langle X(t_2)\rangle\langle X(t_3)\rangle$. This expression must be evaluated at all possible times t_1, t_2 and t_3 in the TOF spectrum in order to produce the three-dimensional map depicted schematically in fig. 2(d). There is one autocorrelation line, where $t_1 = t_2 = t_3$, and three autocorrelation planes, where $t_1 = t_2$, $t_2 = t_3$ and $t_1 = t_3$; these are shown hatched in the figure. Moreover, the map has three mirror symmetries with respect to these autocorrelation planes, giving sextuple repetition of any feature (circles in fig. 2(d)).

Apart from the auto-correlation planes themselves and any statistical noise, *only true triple fragment correlations* will give real counts on the map. The six 3-D correlation features corresponding to a single triple fragmentation channel, lie in a plane (the hexagon shown in fig. 2(d)) defined by momentum conservation. Since the momentum component along the drift tube axis is linearly related to the TOF (t), these 3-D features will occur at the following (x,y,z) co-ordinates (t_1,t_2,t_3), (t_2,t_3,t_1), (t_3,t_1,t_2), (t_2,t_1,t_3), (t_1,t_3,t_2) and (t_3,t_2,t_1). If one looks down on the cube from above, one sees the six features in the two-dimensional map, fig. 2(a).

In order to locate a specific 3-D feature one takes slices of the three-dimensional covariance map. One is guided to the approximate location of one of these features by the two-dimensional map. One such slice is shown schematically in fig. 2(d). (The red lines indicate where the autocorrelation planes cut through the slice.) If real, the feature should appear and disappear as one takes slices at increasing values of z. Examination of a number of such slices (18 are shown in fig. 2(c)) confirms that the feature is most obvious at $z \approx 0.89$ μs. Note that the feature lies at co-ordinates $x \approx 1.09$ μs and $y \approx 0.73$ μs, consistent with fig. 2(a). Inevitably there is a price to pay for adding a third dimension to the map. The signal-to-noise deteriorates, reflecting the fact that the covariance signal involves a triple product of detector efficiency (20–30%), rather than a double product.

Having confirmed that the main structures in fig. 2(a) are indeed due to a single triple-fragmentation process, a "best fit" is made to the data, see fig. 2(b). One notes that, rather than the six features discussed so far, there are twelve in all. This occurs because of the "forward-backward" and "backward-forward" momentum symmetry discussed earlier. In this instance the features group into six rather poorly resolved pairs because of the low momentum of the middle (N_m^{2+}) ion. For example, the sharp feature at about 45° situated below the autocorrelation line consists of two features: (N_b^{2+}, O_f^{2+}) and (O_b^{2+}, N_f^{2+}), where the order denotes fragment ions on the (x,y) axes. The table beneath the figure gives the most consistent picture of the fragmentation, showing the momentum of each ion along the drift tube axis and the associated energy range.

Clearly, momentum must be conserved along the axis, and one finds the momentum of the N_m^{2+} ion to be one tenth of that of the N^{2+} ion, with the N_m^{2+} ion moving slowly in the same direction as the N^{2+} ion. This is what might have been expected and is what is also seen in single photon ionisation at 470 eV.[6] The mean energies of the ions are as follows: $N^{2+} \approx 18$ eV; $N_m^{2+} \approx 0.15$ eV; $O^{2+} \approx 20$ eV. By rotating the E-vector of the laser through 90°, one can measure the momentum component of the various fragment ions in a direction perpendicular to the E-vector.[6] The resulting covariance maps indicate that these components are small, consistent with the field ionisation model.

The fit of the "Coulomb explosion" momenta, fig. 2(b), to the experimental map, fig. 2(a), is not perfect. One might be tempted to improve the fit by assuming three independent two-fragment-ion processes. In each of these processes the third neutral particle could be allowed to take away any momentum along the drift tube axis that one cares to assign to it. However, the 3-D map reveals that triple-ion fragmentation is the major channel. Any remaining disagreement between figs. 2(a) and 2(b) must therefore be attributed to poor statistics. There are few signs of $N^+ + N^+$, $N^+ + O^+$ or $N^+ + N^{2+}$ channels above the noise. The feature lying close to the autocorrelation line at about 1.2 μs is associated with $C^+ + C^+$ correlations from hydrocarbon impurities.

The total kinetic energy release (about 38 eV) seems to suggest that, as the three atoms move apart and as the laser field increases towards its peak value, there comes a point when the "molecule" is suddenly six-times ionised. If one assumes a simple model of mutual Coulomb repulsion, the atoms must be at least three times their normal internuclear separation at the time of multiple ionisation. It is puzzling that correlations involving single ions are so weak. For example, one might have expected to observe substantial features associated with the process $[N_2O^{3+}] \rightarrow N^+ + N_m^+ + O^+$; this would occur in regions around the focal spot. One is led to speculate that, as the laser E-field increases, six electrons are successively or collectively promoted to dynamic states of a new kind, stabilised by a combination of the oscillating E-field and the three potential wells. As the laser field increases to a point where stability can no longer be sustained, all six electrons are ejected simultaneously and three double-ions are produced. Clearly this interesting phenomenon deserves further investigation.

In conclusion, we have indicated how three-dimensional covariance mapping allows analysis of complex one-dimensional TOF spectra, involving three correlated charged fragments. Although the technique has been applied here to the multiphoton regime, there is no reason, in principle, why it cannot be used in single photon multiple ionisation. Indeed, covariance mapping should be seen as a general technique, applicable in many diverse situations where correlations are suspected.

We are pleased to acknowledge the Science and Engineering Research Council (UK) for their financial support. We are indebted to Drs. W.T. Toner and I.N. Ross of Rutherford Appleton Laboratory for providing the focused laser.

REFERENCES

1. L.J. Frasinski, K. Codling and P.A. Hatherly, Science **240** 1029 (1989)
2. L.J. Frasinski, K. Codling and P.A. Hatherly, Phys. Lett. **142** 499 (1989)
3. K. Codling, L.J. Frasinski and P.A. Hatherly, J.Phys. B **20** L525 (1987)
4. K. Codling, L.J. Frasinski and P.A. Hatherly, J. Phys. B **22** L321 (1989)
5. P.A. Hatherly, L.J. Frasinski, K. Codling, A.J. Langley and W. Shaikh, J.Phys. B **23** L291 (1990)
6. D.M. Hanson, C.I. Ma, K. Lee, D. Lupiano-Smith and D.Y. Kim, J.Chem.Phys. **93** 9200 (1990)

NONLINEAR OPTICS OF PS PULSES IN THE ULTRAVIOLET

I N Ross, W Shaikh, J Houliston
Rutherford Appleton Laboratory

Introduction

The first experiment of this programme was used to study the fundamental properties and potential of two main constituents in the programme; chirped pulse amplification (CPA) and the use of saturable absorbers (SA) in autocorrelators. In the absence of a KrF amplifier these basic aspects of the programme were undertaken at a convenient visible wavelength (600 mm) where experimentation was relatively easy and pulse energies up to 200 μJ were available at 10 Hz.

The principle of chirped pulse amplification (CPA) is to time stretch a short pulse before amplification and recompress it after amplification thus minimising nonlinear power dependent pulse distortion effects in the amplifier. The aims of these CPA tests were to establish confidence in the theory of grating pulse stretchers and compressors and to look at different possible designs to enable an optimum design to be achieved for subsequent experiments at 249 nm.

Most pulse width measurement techniques such as second harmonic autocorrelators require fairly high peak intensities, sensitive detectors and can be difficult to set up. With this in mind, a new autocorrelation technique using a saturable absorber was investigated. The proposed scheme relies on the absorber saturation working close to the 'ideal' in which the excited state has a long lifetime and does not exhibit absorption at the pump wavelength. We aimed to find a suitable material and demonstrate that we could measure pulse durations with comparable accuracy to a standard second harmonic (SH) autocorrelator and that it has the added potential for measuring pulse shapes.

Chirped Pulse Amplification

Two of the grating schemes investigated are shown in figure 1. These two are complementary schemes since 1a is used for pulse stretching and 1b is used for recompressing. These schemes have advantages over commonly used schemes in requiring only a single grating, being self-aligning and being half the length for a given stretch factor.

Section B4.3 presents the theory of these devices, from which we can derive the following relations

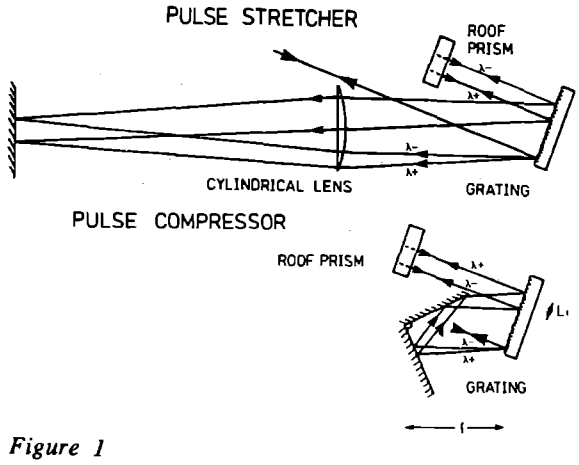

Figure 1

$$Stretch factor\ (S) = \frac{2l(\sin\alpha + \sin\beta)^2}{ct_o \cos^2\beta}\frac{\Delta\lambda}{\lambda} \qquad (1)$$

$$\frac{Recompressed\ pulse\ duration}{original\ pulse\ duration}\ (F) = 1 + \frac{p}{m}\left(\frac{L_1}{L_0} - 1\right)$$

@ p x diffraction limit; m x transform limit

In order that the temporal properties could be tested using a streak camera an initial pulse duration of 3 ps was chosen with a stretch factor of at least 10. The laser was operated with either transform limited (narrow spectrum) or non transform limited (broad spectrum) pulses. Other variables included beam size, geometry and length of grating arrangement and laser pulse duration. Typical streak profiles are shown in figure 2 demonstrating input, stretched and recompressed pulses. In this case the measured stretch factor (S) of 12 corresponds to the calculated value of 9.

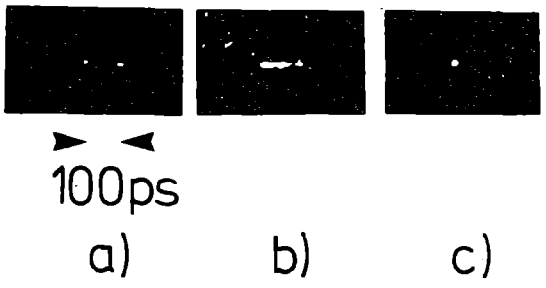

Figure 2 Streak camera records
a) input pulse with timing fiducial
b) stretched pulse
c) recompressed pulse

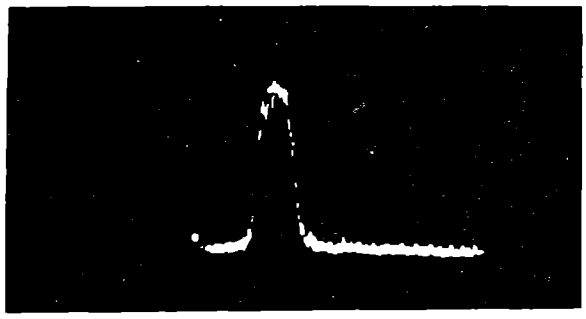

Figure 3 Square temporal pulse using spectral filtering

Since the stretched pulse has a linear chirp it is possible to control the temporal shape of this pulse by spectral filtering. This can be conveniently carried out in the Fourier plane of the pulse stretcher, see figure 1a. As an example a slit aperture in this plane leads to a 'square' pulse in time as demonstrated by the streak record shown in figure 3.

Discussion

The simple stretch and compress grating schemes used proved effective and operated according to expectation. The viability of exerting control over the pulse profile via spectral filtering was demonstrated. The effects of beam diffraction in limiting the fidelity of the recompressed pulse were analysed and can be a serious limitation for transform limited pulses. In this case and for diffraction limited pulses equation (1) reduces to

$$F = \frac{L_1}{L_0} \qquad (2)$$

and for good fidelity (F = 1), the grating and beam size must be large compared to the dispersion.

Saturable Absorber Autocorrelator

The saturable absorber is assumed to be operating in the transient regime where its relaxation time (τ_R) » pulse duration (τ_p). Thus

$$\textit{Transmission } T(p) = \frac{1}{1+(\frac{1}{T_0}-1)e^{-p}}$$

where T_0 = *small signal transmission*; $p = F/F_s$

F = *input pulse fluence*; F_s = *saturation fluence* $= \frac{h\nu}{\sigma}$

If the pump pulse is heavily saturating the risetime of transmission is short compared to the pulse risetime and it is this feature which enables the autocorrelator to give better pulse

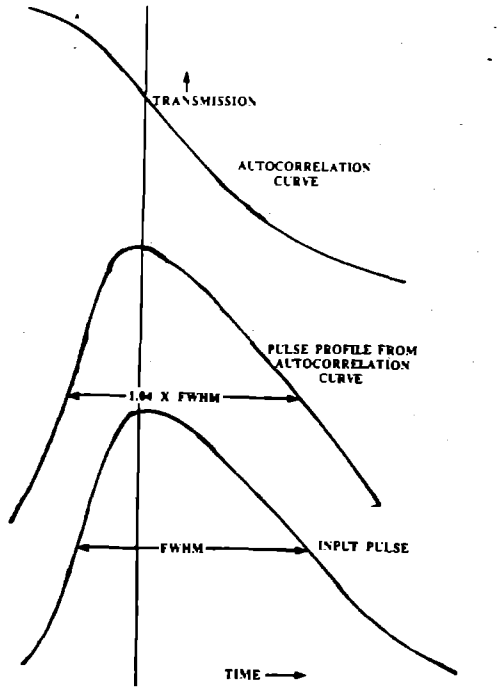

Calculated performance of saturable absorber autocorrelator for an asymmetric pulse

Figure 4

shape information than a conventional autocorrelator.

Figure 4 shows the calculated SA autocorrelator response for an asymmetric pulse. Also shown are the differential of this curve together with the original pulse shape showing that direct pulse shape information can be obtained simply with this technique. The transmission risetime of the SA was calculated to be 0.26 x pulse risetime leading to an expected overestimate but only by a factor ≈ 1.033. We see that the computed curve has a FWHM of 1.04 x that of the input pulse.

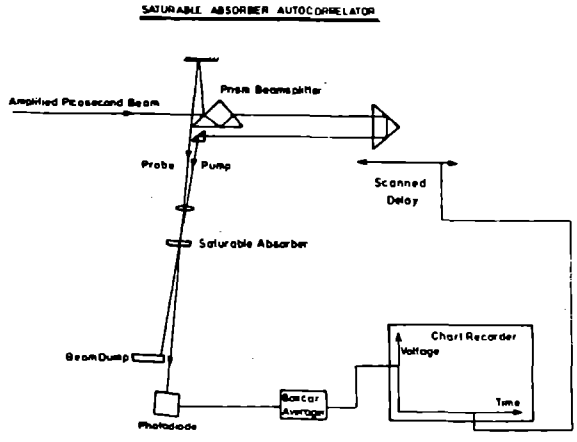

Figure 5

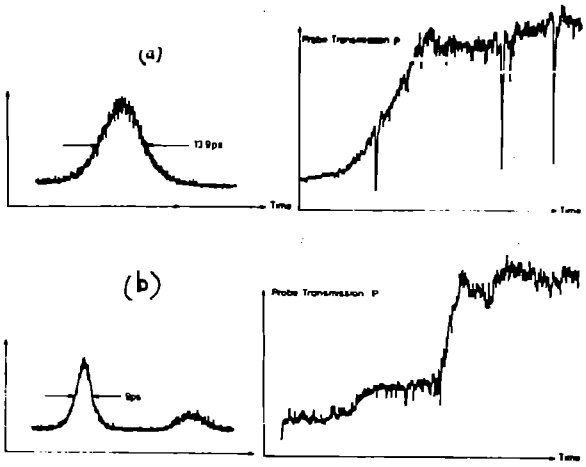

SA and SH Autocorrelation Curves
(a) Single Pulse (b) Double Pulse

Figure 6

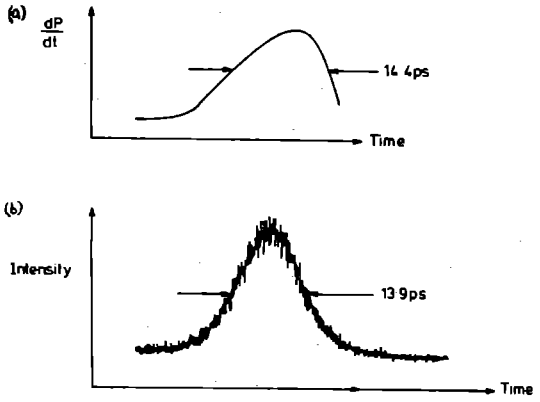

Pulse Profiles (a) Measured From SA Autocorrelator (b) Measured From SH Autocorrelator.

Figure 7

The test scheme, as shown in Figure 5, uses most of the amplified dye laser beam (pump) to saturate the absorption of the saturable absorber, thereby creating a fast shutter to enable the transmission of a second beam (probe) to be monitored as a function of time (distance).

DODC1, DQOC1 and a coloured glass filter were all assessed as possible saturable absorbers. DODC1 appeared to be the best since it had the lowest saturation fluence (1 mJ/cm^2) and the longest recovery time (> 100 ps).

Figure 6 gives examples of SA autocorrelation scans and corresponding SH autocorrelation curves for single and double pulse operation of the laser. The differential of the SA autocorrelation scan, shown in figure 7, compares quite well with the SH autocorrelation curve giving a pulse duration up to 30% more than that calculated from the SH autocorrelator. The ratio of step heights in the double pass SA autocorrelation curve is in agreement with the ratio of pulse heights in the SH autocorrelation curve, as expected.

Discussion

The technique looks promising and gave reasonable pulse length information. The following observations need attention to improve the quality of information obtainable by this technique.

i) A better SA is desirable since the substances used did not fully saturate on a ps timescale even under high fluence (we presume due to excited state absorption) and the recovery time became short with high dye concentration and heavy pumping (due probably to amplified spontaneous emission).

ii) The data was adversely affected by the high integrated energy dose (~ 10 J/cm^2) experienced by the dye during a scan. This would not of course be a problem with a single shot version of the autocorrelator.

Nonlinear Optical Measurements in a Semiconducting Polymer

K.Powell, G.Proudley

King's College London, Dept. of Physics

Introduction

Semiconducting materials with near infra-red bandgap energies have come under scrutiny by those seeking to understand and exploit nonlinear optical effects. Mechanisms for nonlinear effects are as diverse as resonant and non-resonant excitations [1], photorefractive effects [2] and thermal effects [3].

A new class of semiconductors has emerged in the last ten years which are organic polymers. Polyacetylene exemplifies this new class [4]. It is a simple conjugated 'backbone' polymer with an alternating single and double carbon-carbon bond. Polyacetylene is already known to exhibit interesting photoconduction and photoabsorptive properties [5] which involve mobile charge carriers. Electrical properties are understood in terms of mobile, charged 'solitons' which are topological unconformities capable of moving along and between polymer chains. Their role in optical effects is not so well understood although models of soliton pair generation and recombination have been proposed to explain transient absorption measurements [6].

This work is part of the continuing programme at King's to investigate optical nonlinearities in semiconducting materials which may find application in optical processing architectures. Much of the study involves the measurement of charge carrier kinetics as a key to the origin and behaviour of the nonlinear effects. Polyacetylene is investigated here using degenerate four wave mixing (DFWM) in a variable delay excite-probe arrangement. The magnitude and response time of the third order nonlinear susceptibility, subject to limitations of laser pulse duration can be measured.

Excite-probe DFWM

Figure 1 is a schematic representation of the experimental apparatus used at RAL. The laser source is a frequency doubled, mode-locked Nd:YAG which pumps a styryl-9 dye laser. The dye laser produces tunable radiation which was fixed for this experiment at 850 nm. Pulses from the dye laser are selectively amplified at a rate of 10 Hz. The final pulses were of duration 10-15 ps (FWHM) with energies of a few mJ per pulse.

Beams 1 and 2 have equalised path lengths so that pulses from these beams arrive at the sample at exactly the same time. Their interference produces a fine fringe pattern with period of 2.4 microns (beam angle ~ 10°). Any nonlinear effect in the material will cause the interference pattern to spatially modulate the permittivity forming a diffraction grating. This will diffract light from beam 3 into the path of beam 2, forming a phase conjugate of the field in beam 2. This phase conjugate beam 4 is detected at D. The relative amount of diffracted light can be measured and used to calculate the magnitude of the nonlinear coefficient:

$$|\chi^{(3)}| = \left(\frac{2\alpha^2 R}{e^{-\alpha L}\tanh(\alpha L/2)\tanh(\alpha L)}\right)^{1/2} \left(\frac{k_0\sqrt{I_3(L)I_1(0)\mu_0}}{n_0^2\sqrt{\epsilon_0}}\right)^{-1} \quad (1)$$

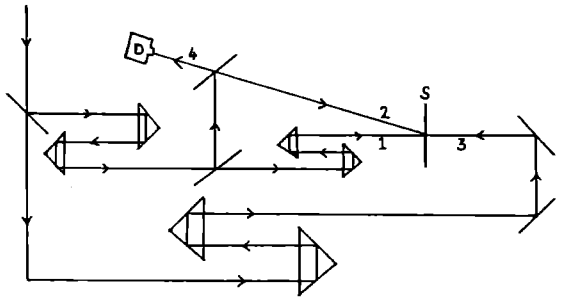

Figure 1. Optical layout (schematic).

where R is the ratio of powers in beams 4 and 2 respectively, I_1, I_3 are the respective intensities of beams 1 and 3 at the sample, α is the material's linear absorption, L is the thickness of the sample, k_0 is the wavenumber and n_0 is the refractive index. The material's nonlinear behaviour is characterised by the third order nonlinear susceptibility, $\chi^{(3)}$.

The measurement of R is made when all beam path lengths 1,2 and 3 are matched, i.e. all pulses overlap. For a nonlinear material with finite response time it may be expected that the induced change in permittivity forming the diffraction grating will remain even after the two writing pulses in beams 1 and 2 have passed. If the arrival of pulses in beam 3 is delayed by means of a path length increase then the remaining strength of this grating can be measured at that delay time. By taking seperate measurements for a series of different delay settings a picture of the response time of the grating and hence induced permittivity change can be built up in accordance with:

$$R \propto I_1(t)I_2(t)I_3(t)\int f(t')f(t-t')\,dt'$$

where f(t') is the material's temporal response function. This technique is known as excite-probe. Obviously the resolution of the technique is limited by the laser pulse duration.

Experimental results

Figure 2 shows the result of excite-probe measurements made in the manner just described. The horizontal axis is centred on a delay time Δt of zero set by delay line 1. The graph plots the relative power in beam 4.

The large coherence spike seen in figure 2 is caused by the contribution of a second grating formed between beams 1 and 3 or beams 2 and 3. The temporal width of this coherence spike is determined by the temporal coherence of the laser pulses. Amplified spontaneous emmission also contributes to this artifact, effectively synthesising a short pulse from its relatively broad bandwidth. Note that the coherence spike suggests a temporal coherence of about 0.2 ps compared with the pulse width of 10-15 ps. This means that the laser pulses were far from transform limited.

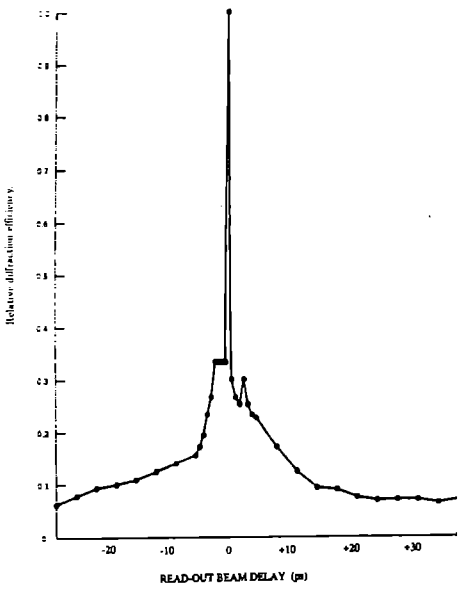

Figure 2. Excite-probe measurements with polyacetylene.

From the data in figure 2 there is little difference between the temporal response recorded and that expected from an autocorrelation/convolution of the laser pulse, suggesting that the response time of the material is of the same order or faster than the laser pulse duration. The slight asymmetry, however, about $\Delta t=0$ in figure 2 suggests a response time near to the laser pulse duration, i.e. about 10-15 ps. The limited accuracy of the measurements means that it is difficult to be more quantitative.

The magnitude of the nonlinearity is calculated from the respose at time $\Delta t = 0$ with the coherence spike removed and using equation 1. The thickness of the sample was 3.3 microns, the absorption, α, was 2288 cm^{-1} and refractive index was 2.0;

$$|\chi^{(3)}| = 1.8 \times 10^{-9} esu$$

Discussion

This experiment demonstrates that changes to the material's permittivity can be optically induced on timescales of 10-15 ps. This is too rapid a response to be associated with thermal effects (which normally operate on microsecond timescales) and must be electronic in origin. The solitonic model of nonlinear excitation predict events ranging from sub-picosecond to a few milliseconds in duration, the faster effects being due to photogenerated soliton pair recombination. Shorter optical pulses would be necessary to probe these particular events.

The magnitude of $\chi^{(3)}$ at this wavelength is considerably larger (by some two orders of magnitude) than at 1064 nm [7] which is further into the tail of the bandedge. These results are consistent with enhanced nonlinear effect as the wavelength is tuned closer to resonance with the bandedge between 700 and 800 nm.

Further experiment would reveal the relative proportions of real (refractive) and imaginary (absorptive) components of $\chi^{(3)}$. The DFWM experiments are sensitive only to the modulus of the third order susceptibility. A seperate transient absorption experiment would be necessary to allow an estimate of the imaginary component of $\chi^{(3)}$. This could be the subject of future experiments.

References

1. D.M.Pepper, *Nonlinear Optical Phase Conjugation.* Laser Handbook, 333, Elsevier Science Publishers, (1985).

2. T.J. Hall, R.Jaura, L.M.Connors, P.D.Foote, *The Photorefractive Effect: A Review.* Prog. in Quant. Elec. **10** (2) pp 77-146 (1985).

3. See for example H.J.Eichler, P.Gunter, D.W.Pohl, *Laser Induced Dynamic Gratings.* **50**, Springer series on optical physics, Springer-Verlag, (1986).

4. See for example J.C.W.Chien, *Polyacetylene, Chemistry, Physics and Material Science.* Academic press, (1984).

5. R.H.Friend et. al. *Electronic Properties of Conjugated Polymers.* Phil. Trans. R.Soc. Lond. A **314**, 37-49, (1985).

6. A.J.Heeger, D.Moses, M.Sinclair, *Semiconducting Polymers: Fast Response Nonlinear Optical Materials.* Synth. Met. **15** 95-104, (1986).

7. P.D.Foote, British Aerospace, Sowerby Research Centre, private communication.

Acknowledgements

P.D.Foote (BAe, Sowerby Research Centre) and G.McFadyen (Univesity of Manchester) for assistance with experimental work.

LASER-ANNEALING OF MAGNETO-OPTIC THIN FILMS

P W Haycock†, R H Noyau†, T Thomson*, E W Williams†, H C Patel†, X-F Zhu† , W G Stirling† and K O'Grady*

† University of Keele

* University College of North Wales, Bangor

Over the past two years we have been carrying out experiments on the nanosecond pulsed laser-annealing of thin films of Tb-Fe-Co alloy. These have been sputtered between two protective layers of silicon nitride onto glass substrates and are of the type used for erasable magneto-optic data storage media. The experiments have been performed using a Lambda-Physik FL2002 dye laser pumped by a Lumonics HyperEX 460 excimer laser at the Laser Support Facility. Anneals have been carried out at 390nm and 830nm using energy densities of 2 mJ cm^{-2} to 18 mJ cm^{-2} The sample was rastered under the beam in a variety of patterns and velocities in order to control the duration and frequency of elevated temperatures at any point on the surface.

Fairly high power anneals have led to loss of the perpendicular magnetic anisotropy of the films necessary for magneto-optic recording. This occured in samples where the transient temperature approched 830°C or above. Even in the these cases, the overall layering structure of the samples was not disturbed as determined by neutron reflectivity measurements on CRISP at ISIS. Figure 1 shows the reflectivity profiles for an as-sputtered sample and one annealed to 830°C, both originally cut from the same recording disc. The high degree of similarity between the two shows that the macroscopic layer structure has not been significantly afffected. However, in order to fit data produced by polarised neutron reflectivity fron the annealed sample a rather complex variation of composition and magnetisation through the magnetic film had to be assumed [2]. Thus the loss of perpendicular anisotropy appears in this case to be due to phase separation in the magnetic layer.

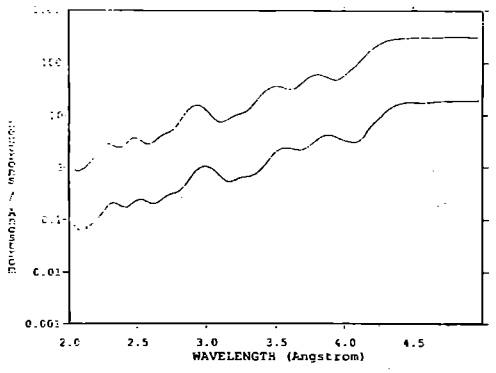

Figure 1 Neutron reflectivity profiles from an as-sputtered sample (upper) and one annealed to 830°C. The two curves have been offset for clarity.

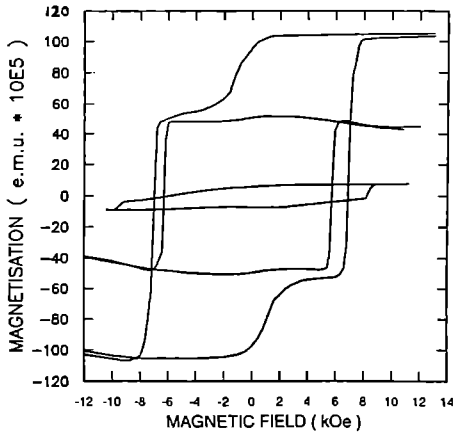

Figure 2 Hysteresis loops for an as-sputtered sample (inner) and one annealed to 230°C.

More moderate power annealing has led to a variety of modifications to the hysteresis loop. In particular, it has been found to be possible to increase both the remanent magnetisation and the coercivity by a careful choice of conditions. Figure 2 shows the hysteresis loops for an as-sputtered film and one annealed to a transient temperature of about 230°C. Although the shape of the latter loop is not suitable for optical recording, the shoulder being too close to the zero field axis, this result does show the potential of nanosecond pulsed laser-annealing for effective modification of the magnetic behaviour of rare-earth/transition-metal thin films.

Further experiments are underway on the annealed films. These include Kerr rotation, to look for improvements in the films for optical readout, and a variety of structural measurements involving X-ray and neutron scattering. EXAFS has been especially useful, revealing small differences in the short range atomic coordination which can be correlated with the values of the saturation magnetisation and coercivity.

REFERENCES

[1] P W Haycock, R H Noyau, T Thomson, G J Herdman, E W Williams and K. O'Grady, IEEE Transactions on Magnetics **26** 1921 (1990).

[2] W G Stirling and E W Williams, ISIS Annual Report 1991, RB/1764

X-ray Microscopy

R.E. Burge and A.G. Michette

Physics Dept., King's College, London

INTRODUCTION

The structure of an X-ray imaging microscope for use with an X-ray laser is shown in figure 1. Apart from the X-ray laser itself and the recording medium (S101 film) there are three main elements to the microscope: the Schwarzchild condenser, the zone plate objective and the stage which supports and positions the sample and the optics. Progress with each of these elements will be described in turn.

THE SCHWARZCHILD CONDENSER

An Ealing Electro-optic X15 Schwarzchild reflecting optic (25-0506) was coated with 50 layers of Si/Mo by the Ovonics Corp. Inc. USA, and will be referred to as SC (Schwarzchild Condenser). The Si/Mo layers were made of equal thickness. The reflectivity and bandpass of this SC were measured as a function of wavelength in the PTB laboratory at the BESSY synchrotron. The experimentally obtained reflectivity of the two-mirror system was 3±1%, with a maximum at wavelength of 23.3 nm, and a bandpass of 2.4 nm±0.1%. These are to be compared with the calculated values of 7% at a wavelength of 23 nm and a bandpass of 2.6 nm respectively.

ZONE PLATE FABRICATION

The design of the zone plate (ZP) objective is determined by the numerical aperture of the SC. These should be matched in order to optimize the efficiency of the system. The N.A. of the SC is 0.28. The N.A. of a ZP is given by the expression N.A. = R/f, where R is the ZP radius and f is the focal length. For a ZP the focal length is given by $f=2R.dR/\lambda$, where dR is the width of the outermost zone and λ is the wavelength. Thus, the N.A. for a ZP is equal to $\lambda/2dR$. This defines the required outer zone width as 42 nm with an expected resolution of 1.22 dR which is approximately 50 nm.

In order to achieve this resolution the ZP has to be fabricated in such a way that it is corrected for spherical aberration because this poses a severe problem in a high numerical aperture. This is a result of the fact that at the wavelengths involved the steep diffraction angles result in significant path differences at the optical axis between the X-rays diffracted from the outer and inner zones. Optical path analysis shows that the minimum circle of confusion which would result from an uncorrected ZP would be ≡ R/60. This would give a focal spot size of more than 0.6 micron for a ZP with a radius of 45 microns. This is 10 times worse than the diffraction limited resolution of the ZP and only 4-5 times smaller than the size of the demagnified image of the X-ray emitting source. Spherical aberration correction has been achieved by deliberately misplacing the zones in such a way as to cancel out the optical path differences between them.

A further improvement in ZP fabrication has been in the ability to build them on extremely thin substrates. These are 20 nm of Si_3N_4 or 30 nm of carbon. This results in a minimal attenuation of the X-ray flux in the ZP support.

MICROPOSITIONING STAGE

A stage has been designed and constructed which accomplishes the twin principal objectives of allowing the sample to be moved through the focal spot of the SC and also incorporates the S101 film holder and an alignment system which allows the sample and ZP to be aligned optically.

This stage incorporates a Newport 3 Axis Micro Translator (466) which has a resolution of 0.1 micron and is used to hold and position the ZP and camera. The sample stage can be moved independently of the ZP on a stage of an original design made at King's College. This sample stage has a positional resolution of approximately 1 micron along the optical axis and 5 microns at right angles to this.

SUMMARY

Significant progress has been made in the development of an imaging microscope for use with the X-ray laser. An optical system has been constructed which incorporates a well characterized Schwarzchild multilayer objective and a spherically corrected, high throughput zone plate. A micropositioning stage has been built which allows the independent positioning of the sample and zone plate with the required resolution.

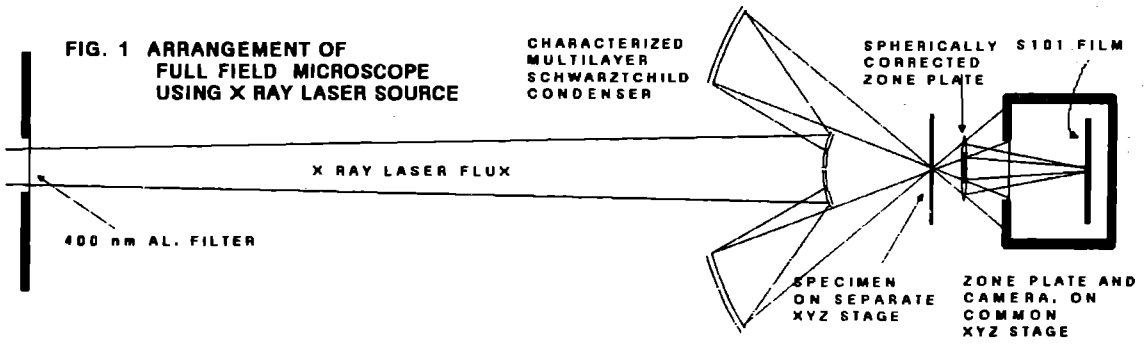

FIG. 1 ARRANGEMENT OF FULL FIELD MICROSCOPE USING X RAY LASER SOURCE

INFRA-RED STIMULATED LUMINESCENCE IN FELDSPARS: DATING ARCHAEOLOGICAL SEDIMENTS

Ian Bailiff
Luminescence Dating Laboratory
University of Durham

INTRODUCTION

Recent research has established[1] that time-dependent uv/blue luminescence may be stimulated by IR radiation (1.3-2.1 eV) in potassium feldspar previously exposed to ionizing radiation; the emission results from the eviction of trapped charge and subsequent recombination at luminescence centres. The effect (referred to as infra-red stimulated luminescence, IRSL) has also been observed in the sodic (and mixed crystals), and a number of different emission bands have been identified[2]. The initial (and integrated) emission is a function of accrued radiation dose and this property provides the basis for dating sediments using luminescence techniques[3]. There are many situations of significance in archaeology and Quaternary science where minerals within sedimentary deposits were exposed to light before burial thus zeroing the luminescence clock; after burial the minerals receive a weak radiation dose from naturally occurring radioisotopes within the burial medium. The time elapsed since the zeroing event may be obtained by determining two quantities: the accrued dose and the radiation dose-rate. A similar form of stimulated emission (requiring higher stimulation energies) has been observed in quartz; the advantage offerred by feldspar is the possibility of using simple IRED arrays as stimulation sources[4].

The potential of the method for the dating of sediments from coastal archaeological sites of the last 10,000 years is currently being examined in this laboratory in collaboration with the Sea-level Research Group of the Department of Geography. Of crucial importance in developing a dating technique based on the use of IRSL is the stability of trapped charge over long periods and identification of all charge transfer routes.

PREVIOUS WORK

The evidence gathered so far indicates that the charge carriers are located in traps associated with defects which, by correlation with thermoluminescence measurements, have thermal activation energies of ca 1.6 eV (with mean-lives at ambient temperatures $>10^7$ years) assuming first order kinetics. The stimulation spectrum for IRSL comprises three broad peaks with maxima at 1.33 (FWHM ~ 0.1 eV), 1.43 and 2.25 eV. It was initially proposed that charge carriers were evicted by photon absorption (1.33 and 1.43 eV) causing transfer to an excited state and subsequently into the conduction band by thermal assistance; the 2.25 eV absorption was assumed to correspond to a direct transition (a band at ~1.55 eV is also evident). Measurement of the variation of IRSL with sample temperature yields (by Arrhenius plot) similar evaluations of the thermal activation energy (~0.1 eV) for sodic and potassic feldspars. The ratio of optical (1.33 eV) to thermal (approx 1.5 eV) trap depth for the excited state is not consistent with expectation, being less than one. Clearly the nature of the charge transfer process requires careful examination.

THIS PROJECT

Using a tunable laser source (Ti:Sapphire), as shown in fig.1, we have investigated in more detail the wavelength dependence of infra-red stimulated luminescence (referred to as IRSL) in the range 1.8-1.35 eV. The results indicate that there is no fine structure within the broad stimulation peaks for potassic feldspar, and that the stimulation spectrum within this region

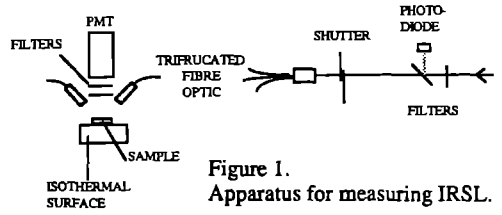

Figure 1.
Apparatus for measuring IRSL.

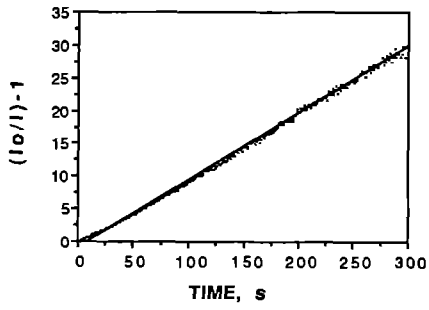

Figure 2.
Plot of IRSL vs time under continuous stimulation; I= intensity; at time t; I_o = initial intensity. During the first 30 secs the IRSL fell to 30 % of its initial value.

remains substantially unchanged at elevated temperatures (RT-100 °C). Measurements at low temperatures are about to be performed.

The IRSL decay (fig. 2) is not first order and a function of the form $1/(1+ at)$, (where a = const.; t = time), provides a reasonable first approximation for all but the initial and more rapid decay during the first 30s. Where $at>>1$, the IRSL is inversely proportional to time, which is the relationship expected for recombination by quantum mechanical tunnelling. Previous measurements have indicated that some charge is transferred via the conduction band because of the stimulation of photo-transferred TL, and there are evidently a number of escape routes, althougth the proportionality of IRSL with excitation power suggests only one optical transition for a given type of trap. If the decay follows the above function, there are important implications for dose evaluation since numerical integration must be used to obtain the total emission.

IRSL decay curves have previously been obtained using uv/blue biassed detection systems; in the example shown, the IRSL emission from albite was detected by a GaAs photo-cathode PMT after passing through a 560 nm (FWHM 15 nm) interference filter, chosen to isolate one of the two emission bands associated with IRSL from albite. The characteristics of decay are qualitatively similar to those measured by isolating the shorter wavelength emissions, suggesting similar means of charge eviction.

Measurement of IRSL at different elevated temperatures has shown that the thermal activation energy is ~0.1 eV using stimulation energies of 1.35 and 1.44 eV and ~0.03 eV for 1.55 eV stimulation, and the latter may represent a further excited level within the same trap or defect complex. Contrary to expectation the integrated IRSL was found to increase with temperature, indicating the participation of a different (eg deeper) trap. However, pulse anneal characteristics obtained for different sample measurement temperatures do not reflect the participation of a deeper trap, indicating that the original model of an optical transition to an excited state needs to be modified.

The similarity in IRSL behaviour under various stimulation and detection conditions indicates that the next step involving a search for correlation with specific centres using EPR should be fruitful.

REFERENCES

1. Hütt, G., Jaek, I., and Tchonka, J. (1988) *Quaternary Sci. Revs.*, 7, 381-385.
2. Bailiff, I.K. and Poolton, N.R.J., (1991) *Nucl. Tracks and Radiat. Measts.* In press.
3. Aitken, M.J. (1985) *Thermoluminescence dating*, Academic Press, London.
4. Poolton, N.R.J., and Bailiff, I.K. (1989) *Ancient TL*, 7(1), 18-20.

3-D PARTICLE IMAGE VELOCIMETRY

C.A. Greated

Department of Physics
University of Edinburgh, King's Buildings,
EDINBURGH. EH9 3JZ

PARTICLE IMAGE VELOCIMETRY

Particle Image Velocimentry (PIV) is a technique for measuring flow fields. A pulsed laser beam is formed into a sheet which is used to illuminate a plane in the flow. Seeding is introduced, usually in the form of smoke or fine aerosol for measurements in air, and the illuminated particles are photographed. The exposure time is so arranged that a number of images are formed on the same negative. At Edinburgh an automatic analysis system has been developed for scanning the negatives to obtain velocity vector maps of the flow. This uses the 2D correlation method, whereby the correlation is formed by two successive Fourier transforms, the first being optical and the second being digital.

PIV is now extensively used for measuring vector maps of the in-plane component of velocity. However, by using stereoscopic photography it is possible to record the positions of the tracer particles from two different standpoints. The two resulting PIV negatives can then be used to generate all three components of velocity in a plane. The object of this work has been to develop an optical technique to carry out these measurements.

It would in theory be possible to take two separate photographs using different cameras. However, in practice this presents many problems since the two negatives have to be matched precisely both in terms of magnification and alignment. We have devised a system which allows both pictures to be formed on the same negative using a single camera. As well as being simple to use this virtually eliminates the difficult alignment problems. The arrangement uses a system of two pairs of parallel mirrors and is operated just like a normal camera. It can also be easily converted back for normal 2D PIV operation.

TEST SYSTEM

In order to test the system, 3D PIV records were made of the highly 3D acoustic streaming flows which occur within a rectangular tube excited at resonance. A loudspeaker was set into one end of the tube and the other end cut off, with access for a probe microphone to monitor the pressure fluctuations. Theoretical expressions have been developed for the velocity profiles which occur in this situation.

Figure 1 shows the overall velocity vector map of the in-plane component of velocity. The characteristic cellular pattern is apparent. Figures 2, 3 and 4 show the velocity profiles across the tube for the three components. Vx is the in-plane component along the length of the tube. Theory shows that this should be parabolic and indeed this is the case. Vy is the in-plane component in the orthogonal direction which is positive on one side of the tube and negative on the other. Vz is the out-of-plane component. From a series of measurements it has been possible to deduce the full three-dimensional character of the streaming flow.

THEORY

Theoretical expressions have been derived which allow the three velocity components to be calculated from the two sets of PIV readings. These can readily be programmed into a conventional PIV analysis package to extend its capability to 3D. Expressions have also been derived for the expected measurement errors for the three components. The error in the in-plane measurement remains the same as in 2D PIV, whereas the error in the out-of-plane component is typically three greater than this.

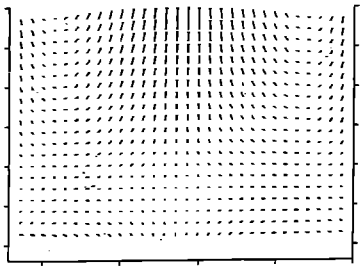

Figure 1.

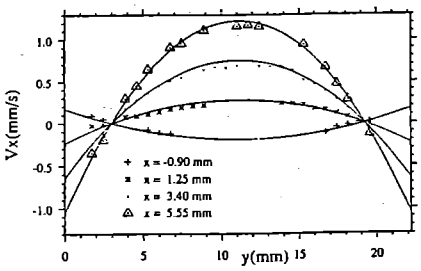

Figure 2.

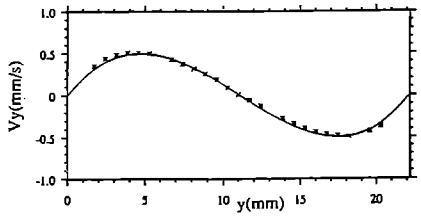

Figure 3.

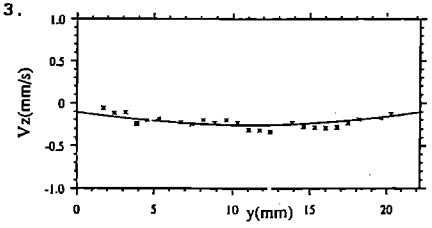

Figure 4.

REFERENCES

1. M.P. Arroyo and C.A. Greated "Stereoscopic Particle Image Velocimetry", submitted to J. of Physics.
2. M.P. Arroyo, C.A. Greated and D. Hann "A 3D PIV System and its Application to the Measurement of Acoustic Streaming", EUROMECH 1991 Delft, Images Analysis as a Measuring Technique in Flow.

LASER SUPPORT FACILITY OPERATIONS AND DEVELOPMENT

LSF APPLICATIONS STATISTICS

The LSF received 76 Applications for experimental time on the LSF picosecond, nanosecond and loan pool equipment for the period May 1990 to May 1991. This represents a 30% increase in the number of applications compared with the previous year. Approximately 90% of these experiments were approved by the LSFP and 75% of approved experiments were scheduled.

Around 70 experiments were carried out including those approved for Division Head's or unallocated time. Table 1 shows the distribution of applications by subject.

	Archaeology	Chemistry	Physics	Biology	Total
Applications	3%	54%	20%	23%	76

The distribution of application is approximately the same as previous years. The application from an archaeological research group represents a new departure for the LSF.

PICOSECOND LASER FACILITY - A J Langley and W Shaikh

Operations

A total of 12 experiments were carried out using the Spectra-Physics 10 Hz amplified picosecond pulsed laser. A broad range of science was studied including interfacial picosecond harmonic generation, photosynthesis, semiconductor carrier dynamics, multiphoton ionisation, photo-kinetic behaviour of azomethine dyes and photochromics picosecond-pulse generation of ultra-sound and pulse stretching and compression. Facility development experiments on pulse characterisation, feedback stabilisation and the generation of new wavelengths were carried out.

The Spectron cw mode-locked YAG laser and the two Spectra-Physics 3290 cavity dumped lasers were commissioned and have given reliable performance. One of the cavity dumpers is used for time-correlated single-photon counting[1]. The other cavity dumped dye laser has been set up as the picosecond source for the Cu vapour pumped amplifier experiments[2]. The pulse widths available from these systems is specified at ~5 ps. It was recently shown that by adding saturable absorber to the gain dye the pulse could be shortened to around 2.5 ps.

The Spectron 532 nm output has recently been increased to around 3w from ~1.2w with the use of a non-critically phase-matched LBO doubling crystal. This will allow synchronous pumping of three picosecond dye lasers and free the Spectra-Physics cw YAG for development work.

Picosecond Development

Feedback Stabilisation

There has been considerable interest over the past year in the reported improvement[3,4,5] in the performance of synchronously pumped dye lasers (SPDL) when a small fraction ($\sim 10^{-8}$) of the output pulse is fed back slightly ahead of the pulse circulating in the laser. This techniques was applied to the LSF SPDL in its standard single gain-jet arrangement and in hybrid mode-locked single jet and double jet configurations[6]. Feedback stabilisation was observed in all three configurations. Pulsewidth and line-width measurements and the appearance of smooth, coherence-spike free autocorrelation traces indicated the generation of near transform limited pulses. Initially no stabilisation was observed in the double jet configuration probably because in this mode of operation light coupled back is absorbed in the saturable absorber. When light was fed back via an intra cavity beam splitter, placed between the two jets, stabilisation was observed. In practise however, the most stable 'hands-off' operation was achieved with the single jet arrangement both with and without saturable absorber added to the gain dye. An advantage of feedback stabilisation and resultant narrower spectral line-width is the intensity increase (by a factor of ~2) in wavelength shifted light

generated by stimulated Raman. Over 100 μJ was generated near 700 nm using Methanol and Ethanol from ~400 μJ (3 ps) pulses. This makes possible a convenient means of generating shifted light with sufficient energy for a pump in for example pump and probe experiments. In our measurements to date it has been found that feedback has the contrary effect upon continuum generation which decreases in intensity and may have a higher threshold than with noise-burst pulses.

Picosecond Pulses at 850 nm and 425 nm

The demand from semiconductor physicists for picosecond pulses between 800-900 nm and from biologists interested in exciting 'β-carotene' near 450 nm led us to attempt to generate these wavelengths which are outside the manufacturers specifications.

The SPDL was operated at 850 nm with styryl 9 as the gain dye and produced an output of ~50 mW with ~10 ps pulses. Adding 114 mg of the saturable absorber IR140 to the SPDL gain dye the pulse lengths were reduced to 1.8 ps (0.37 nJ) per pulse (850 mW pump at 532 nm).

Amplified uncompressed pulses of ~80 μJ energy were generated in the dye amplifier using the concentration optimised dye LDS867.

The amplified pulses were frequency doubled to 425 nm with a conversion efficiency of ~20% using a type II KDP crystal cut for operation at 1064 nm.

Nanosecond Laser Facility - A W Parker

This year has seen extensive use of the nanosecond laser facilities which were rearranged and refitted early in the reported year, a total of 33 experiments have been performed by 18 different groups. The years highlights are many. A laser flash photolysis system has been developed which makes it possible to obtain photochemical transient kinetics and absorption spectra simultaneously. The equipment has been used by three groups to date, two experimental reports can be found in Section C1 and the systems description in Section C4. The laser produced plasma X-ray source (partly supported by DTI through EUREKA) using the new Questek lasers, has continued to improve, the pulsed source (100 Hz, 200 mW in 2π sr) has been put to varying uses. Kings College brought their scanning X-ray microscope from Daresbury to RAL and obtained images with exposure times of 2 to 15 minutes with better than 0.5 micron resolution. Birmingham University have also used the source for studying DNA damage by X-rays, these studies complement the groups work on DNA damage from ultra-violet light.

As with previous years spectroscopy has featured highly. Several groups have continued to use the Raman equipment on offer for both ground state and time resolved studies on photo-generated species. A rotating Raman sample cell for liquids has been produced which makes it possible to obtain resonance Raman spectra from 100 ul sample volumes at mmol dm^{-3} concentrations.

Supersonic jet spectroscopy (Oxford University) on heavy metal compounds has produced some very interesting results. The superb quality of spectra obtained will allow fundamental molecular parameters to be determined for $FeCl_2$, also InOH/D has been observed in the gas phase for the first time. Whilst involved in this work the group found it necessary to produce a optogalvanic atlas, based on a neon hollow cathode lamp, to make accurate calibration of the dye laser wavelengths and the fluorescence spectra produced. Using this system it is possible to calibrate over the wavelength range between 270 and 730 nm with an accuracy of +/- 0.05 cm^{-1}.

A fume cupboard has been installed in Laboratory C. This is mainly for the safe preparation of laser dyes but can be used by users where necessary. In the coming year the fume hoods extraction system will be connected over the Raman Triplemate spectrometer in laser laboratory B. This will allow the study of fairly toxic substances which have presented difficulties in the past.

Loan Pool Operations - M Towrie

In the past year there have been 17 chemistry based loans and 1 physics based loan. The pulsed lasers have been used in a variety of studies including the photochemical dynamics, laser ionisation and dissociation

and chemical kinetics of organic molecules, radicals and van der Waals molecules. The argon ion laser and titanium-sapphire cw lasers were used for Raman and photo-luminescence spectroscopy and for particle image velicometry.

In November the HE460 fluoride laser was converted to run with helium buffer gas, reducing its running costs by a factor of between 2 and 4. The output energy of the laser is about 120 mJ/pulse at 248 nm (KrF) and 90 mJ/193 nm (ArF) and 10 Hz operation. At <10 Hz the laser does not require water cooling or a 3Ø supply.

There have been increasing problems with some of the now aging Nd:YAG laser systems. In the coming year we hope to begin to replace them with more modern, compact systems.

References

1. S M Tavender et al, RAL report 1991.

2. M Towrie et al, RAL report 1991.

3. P Beaud, J Q Bi, W Hodel and H P Weber, Optics Comm 80, 31, (1990).

4. C J Hooker, J M D Lister, I N Ross, Optics Comm, 80, 375, (1991).

5. C J Hooker et al, RAL Report 1991.

6. A J Langley and W Shaikh, Rutherford Appleton Laboratory Report RAL-90-026.

Nanosecond Laser Flash Photolysis for the Simultaneous Capture of UV-VIS Spectra and Lifetime of Photochemical Transients

A Beeby[1], A W Parker[2] and D Phillips[1]

[1]Imperial College
[2]Rutherford Appleton Laboratory

1. Introduction

Laser flash photolysis (LFP) is a well established technique for investigating reaction intermediates from photo-initiated chemical reactions. The transient species generated from such reactions are characterised by determining their growth/decay kinetics and uv-vis spectrum. Generally detection apparatus consists of an analysing lamp and spectrometer with a fast response photo-detector. Spectra of transients are measured from the amount of absorbed analysing light after the photo-initiating laser pulse over a range of wavelengths (typically 5-10 nm steps). Once the transient spectrum has been established kinetic studies are made by tuning the spectrometer to the absorption peak and following changes in light intensity (output from photo-detector) with time.

The system developed at RAL makes it possible to simultaneously observe the transient absorption spectrum (200-800 nm) using a spectrograph and EG&G OMAIII gateable diode array detector and decay/growth kinetics at a single wavelength, using spectrometer/ photodiode or photomultiplier.

2. Apparatus

Two choices of analysing light are available, a 100 W tungsten-halogen DC lamp or a 250 W xenon arc lamp. The xenon lamp, whilst being brighter in the 200-400 nm region, suffers from two problems; (i) the very intense atomic emission lines (eg 450 nm) rapidly saturates the diode array detector (dynamic range 2^{16}). This means accumulation times for the array must be very short, and readout noise becomes a problem for absorption spectra in the weaker spectral output range leading to a low S/N ratio, (ii) the RF discharge necessary to ignite the xenon lamp has caused several failures of the sensitive computer systems and low voltage laser triggering circuits. To avoid the latter problem the lamp is currently being rehoused in an improved RF shielded box. The lamp beams are collimated (2 mm diameter) through the sample cell. The optics after the sample allows approximate F4 imaging which matches the kinetic spectrometer.

For kinetic measurements two detectors are available, (i) 25 mm^2 PIN photodiode (200 ns rise time, 400-800 nm range, response curve figure 2 or (ii) photomultiplier (Thorn EMI

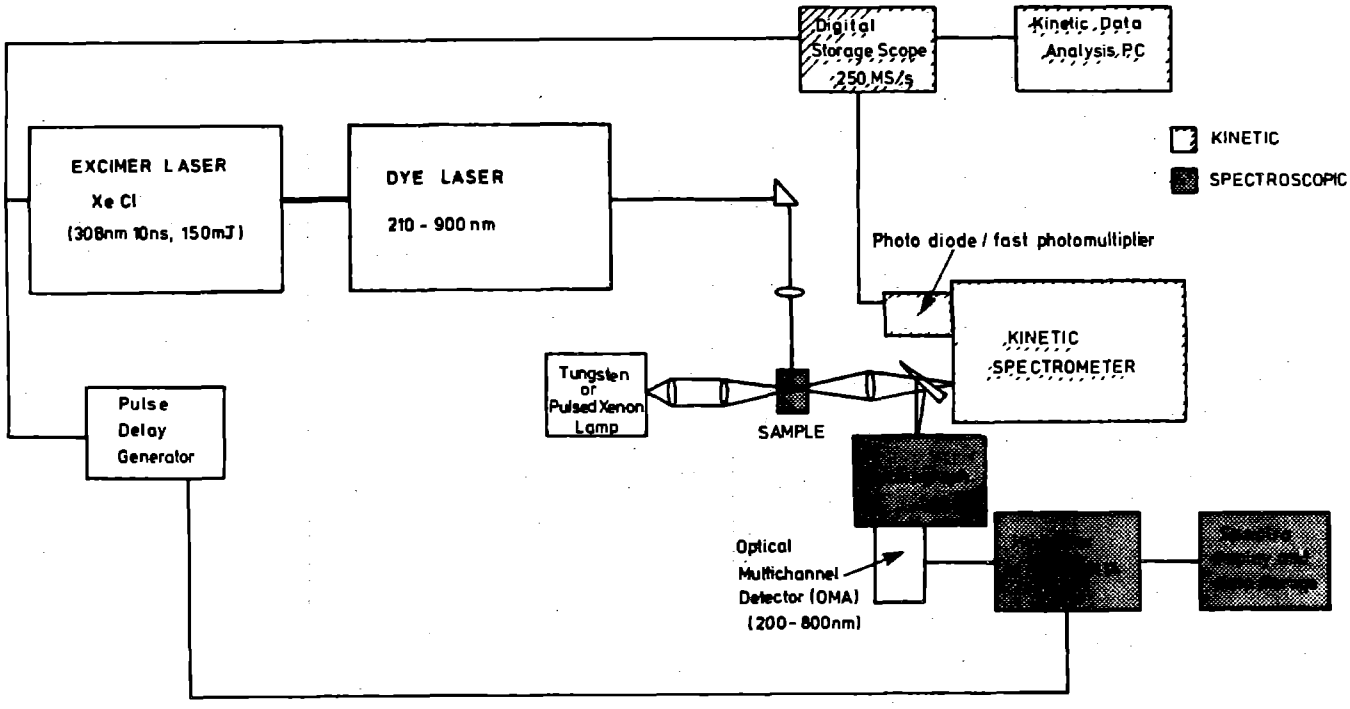

Fig.1. The nanosecond laser flash photolysis set-up for the simultaneous capture of uv-vis spectra and lifetime of photochemically produced transients.

9698QB), 50 ns rise time, 200 to 600 nm range. Transient decays are averaged using a Tektronix 2432A digital storage oscilloscope. Using a 5° wedge 4% of the analysing light is reflected in the spectrograph/diode array detector. The spectral dispersion gives a 500 nm window with a 5nm resolution. Wavelength calibration is performed using a Hg lamp placed in front of the xenon lamp, spatial positioning is crucial, or using the lamp and a number of narrow metal bandpass filters. The detector, EG&G PAR 1420 (UV) intensified diode array is run in gated mode. The width of the gate is set, using Princeton-Instruments FG-100 HV pulser, according to the transients lifetime, we have found a width equal to 1/6 of the transients lifetime to be best. Optical densities match those obtained on the kinetic system.

Synchronisation of the laser pulse to the kinetic oscilloscope and gating of the detector is performed using a Stanford Research Systems, DG535 pulser unit.

Data analysis; accumulated and stored digitised decays are transferred as ASCII files onto a PC computer and lifetimes obtained using suitable customised software (eg Lotus 123). Absorption spectra are obtained using the OMAIII dedicated software, the lamp profile P1, without the laser is measured and compared with the lamp profile with the laser P2. The absorption spectrum is calculated from $\log_{10}$ (P1/P2).

The ability to switch on (gate) the diode array detector at various time delays after the laser pulse allows the full uv-vis study of multistage reactions which produce various intermediates as the reaction progresses. To demonstrate this capability a solution of benzophenone, BP, (5×10^{-3} mol dm^{-3}) and naphthalene, N (1×10^{-4} mol dm^{-3}) in acetonitrile was pumped (308 nm, 10 ns, 4 mJ pulse). All (>99%) of the laser pulse was absorbed by BP, triplet-triplet energy transfer takes place; forming ^3N;

$$BP \xrightarrow{308\ nm} {}^1BP \xrightarrow[\text{crossing}]{\text{intersystem}} BP + N \xrightarrow[\text{Transfer}]{\text{Triplet Energy}} BP + {}^3N$$

The above reaction was followed by observing the decay of ^3BP at 530 nm and the growth/decay of ^3N at 412 nm. Maximum ^3N concentration is reached ~4 μs after the laser pulsed. The kinetics of the transients measured using the photodiode are also illustrated, see figure 3.

Another example, see Beeby et al Section C1, uses the ability to observe ground state bleaching as well as triplet states. This gives information on the concentrations of intermediates, and can be used to obtain quantum yields etc.

Other advantages of gateable multichannel detection include; (1) The ability to observe fluorescence as well as absorbance, (2) if fluorescence is a problem it can be gated out by using an appropriate time delay of the gate, (3) transient spectra obtained from a single experiment; ie, only small quantities of valuable samples are needed.

Sensitivity of the detectors has been estimated from analysis of the system noise levels. For the photodiode the noise levels are +/- 50 mV for a light intensity of 6V, this corresponds to 1×10^{-2} absorbance for a single laser shot or if averaging of 256 shots 3×10^{-4} absorbance

The diode array in its current configuration, using only 4% of the lamps output is an order of magnitude less sensitive than the photodiode. If a greater sensitivity is required, for example measurement of spectra from a single laser shot then the full beam from the lamp can be used giving a x25 increase in signal. In use the diode array stability must be carefully monitored. When cooling the reticon to its running temperature the gating system should be operating to ensure temperature locking occurs at the running temperature. Also, the high intensity of the lamp can cause considerable "after glow" of the detector, if a background or low level signal is to be measured following lamp exposure then a period of two minutes must be allowed before accumulation of low light levels.

For UV kinetic work the xenon lamp and PM tube have yet to be fully tested but we estimate absorbances of 5×10^{-2} to be measurable from a single laser shot and 1.5×10^{-3} for 256 averages.

Conclusions/Future Developments

The system is now fully operational and to date has been scheduled and used by three groups.

The system is intended to be developed further to allow measurements of quantum yields. This

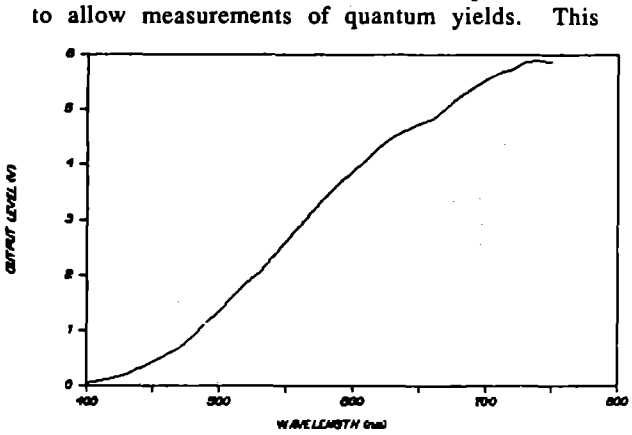

Fig.2. Combined lamp and PIN photodiode output (v) for visible wavelengths.

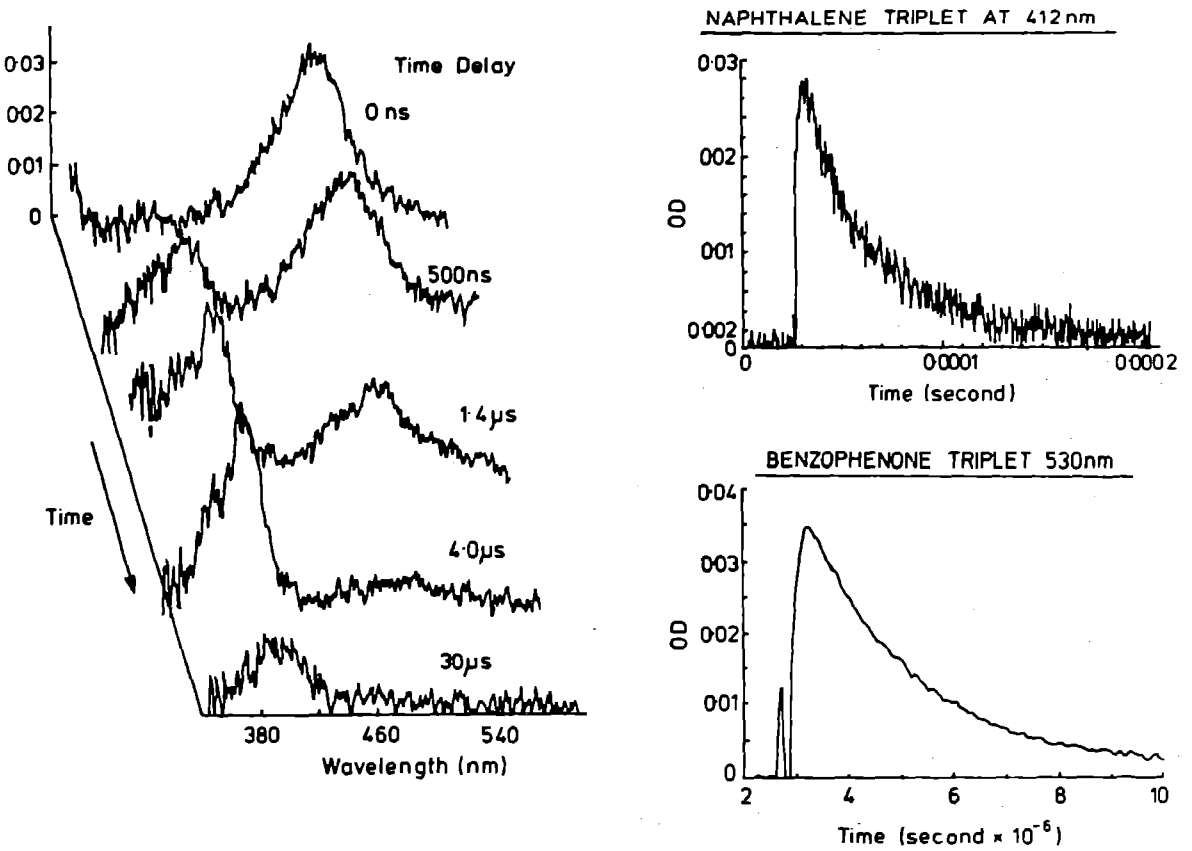

Fig.3. Time resolved spectra using the gated (50 ns gatewidth) diode array for the quenching of triplet benzophenone (530 nm) and naphthalene to form triplet napthalene (412 nm), by triplet-triplet energy transfer, time delays between the laser pulse and detector as shown.

requires careful uniform illumination of samples which will be achieved using optical fibres.

Also a near infra-red photodiode is to be added, this will enable the detection of $^1\Delta g O_2$ and other infra-red emitting species.

SIMPLE EXCIMER-DYE LASER SYSTEM FOR GENERATION OF 50 ps UV PULSES

M Steyer, I C E Turcu, I N Ross and R Kaur
Rutherford Appleton Laboratory

Introduction

We developed a picosecond excimer-dye laser system as a front end for the "Rutherford Laboratory Repetitive Laser Plasma X-ray Source". We have shown previously[1] that the efficient generation of X-rays from a commercial excimer laser focused to $\phi \sim 10$ μm on a target, requires a train of pulses ~ 100 psec long and separated by ~ 2 ns. In Ref 1 the picosecond pulse was generated with a "Distributed Feedback laser" oscillator which was very sensitive to variations in temperature and solvent concentrations. Since the picosecond system is required to work at high repetition rate in a facility environment, it should be as simple and rugged as possible.

Because our X-ray source uses a KrF amplifier, there are no special requirements on the picosecond oscillator bandwidth. Also, because of the nature of laser-plasma interaction, there is no stringent requirement on the pulse-width as long as it is $100 \leq t_p \leq 500$ psec. Therefore, we employed a simple ps generator based on a spectrally narrowed quenched dye laser system[2-4] pumped by an excimer laser, and a KrF excimer amplifier. We believe that concerning stability, ease of maintenance and compactness, this system is an interesting option as a future routine system for laser plasma generation.

Picosecond Laser System

A schematic of the ps UV system in Fig 1. An excimer laser (Questek 2440) filled with XeF generating 120 mJ, pumps the Quenched Dye Laser (QDL) and a two stage dye amplifier. The QDL consists of a 10 mm wide non-flow cell filled with a 10^{-2} M solution of Coumarin 307 in ethanol, and a back mirror tilted by approximately 0.8°. Approximately 3 mJ are selected from the excimer beam and focused onto the cell by a f = 8 cm cylindrical lens. The principle of a QDL has been described in detail by other authors[2,3]. When the dye surrounded by a low reflectivity cavity (consisting of the cell windows) is pumped appropriately above threshold lasing starts in form of distinct relaxation oscillation pulses. If properly aligned, the second cavity (consisting of the tilted 100% mirror and the front quartz-air interface) will be activated some time after the first one and will take over practically all the laser photons. Consequently, the output of the low reflectivity cavity will be quenched, and a single pulse depends on the risetime of the pump pulse, the cavity length, reflectivity of the cavity and the gain and can be as short as 30 ps[4].

Since there is no spectral restraint to the QDL, the output is broad-band (a few nm centred at ≈ 500 nm) and actually consists of a few spectral peaks arising from interference effects between the cell surfaces[5]. To allow efficient frequency conversion, the output is spectrally narrowed to ≈ 0.3 nm by a grating (2400/mm) with the pumped region in the first amplifier (10^{-3} M Coumarin 102 in Ethanol) acting as a spatial filter. It is then amplified to typically 100 μJ in the second amplifier (4 x 10^{-4} M Coumarin 307 in ethanol) and converted to ≈ 1 μJ at 248 nm in a 5 mm thick BBO crystal.

Due to the mentioned interference effects in the QDL beating of longitudinal modes occurs that leads to a random substructure of the pulse. The green pulse consists typically of a ≈ 45 ps (FWHM) pulse, which is occasionally followed by another pulse of same length after ≈ 30 ps.

The UV seed pulse is then amplified in a second excimer (Questek) spatially filtered by a pinhole of 50 μm diameter and expanded to a final cross-section of 1-1.5 cm^2 which is somewhat smaller than the available cross-section of the excimer amplifier (1 x 2 cm^2).

After the second pass, typically 15-20 mJ are available with less than 10% of the energy as Amplified Spontaneous Emission (ASE). At present the system operates at 2 Hz, however, by using a QDL cell of the flow type we intend to upgrade the system to some 50 Hz.

Conclusion

We have reported the design and implementation of a simple, rugged picosecond oscillator for the "Repetitive Laser-Plasma X-ray Source". 50 ps pulses were amplified in commercial KrF laser to 15-20 mJ/pulse. Measurements on the X-rays generated using these pulses will be reported in paper D1.4 of this annual report.

Acknowledgments

This work was partially supported by the UK Department of Trade and Industry through EUREKA European research initiative (EU213 Excimer laser project). MS was supported by a grant provided by the European Science Programme.

References

1. F O'Neill, I C E Turcu, D Xenakis and M H R Hutchinson, Appl Phys Lett 55 2603 (1989).
2. F P Schäfer, Lee Wenchong and S Szatmari, Appl Phys B32 123 (1983).
3. S Szatmari and F P Schäfer, Appl Phys 33 95 (1984).
4. B Burghardt, B Nikolaus and H Pummer, Proc SPIE 610 9 (1986).
5. Z Bor and G Szabo, Appl Phys B47 135 (1988).

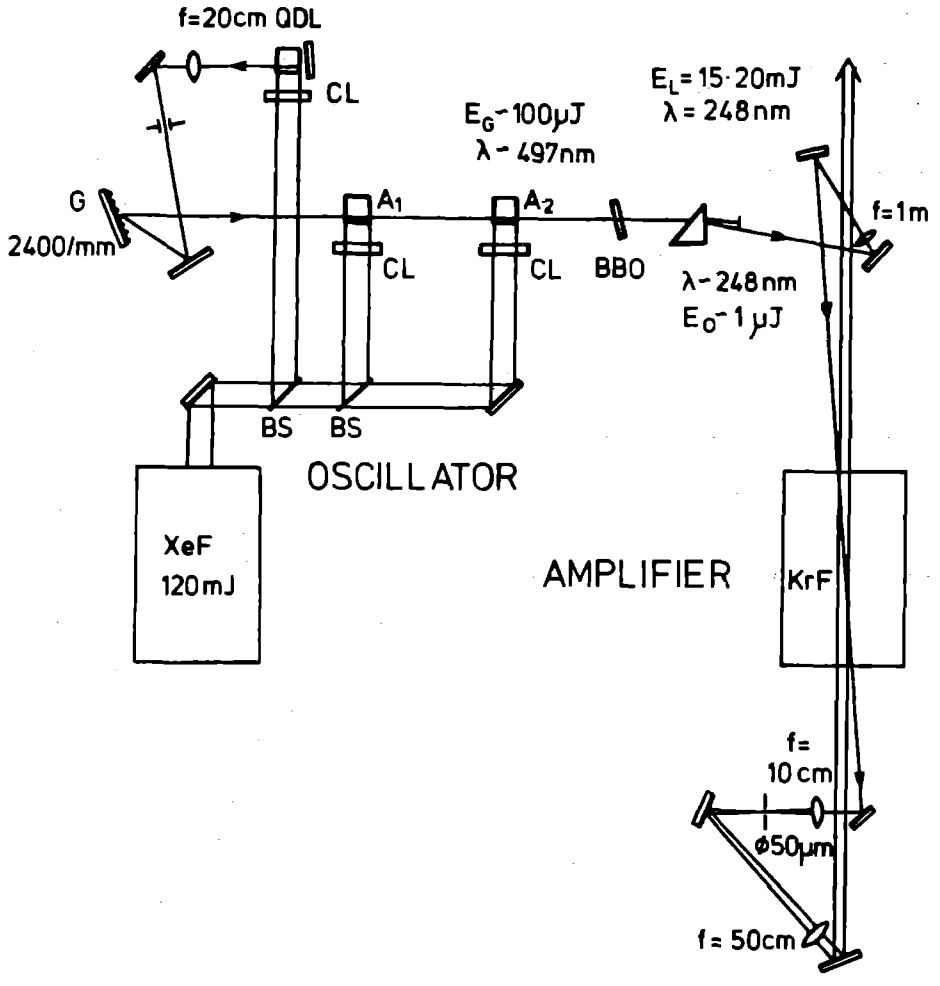

Fig 1 Excimer dye laser system for generating picosecond UV pulses.

HIGH REPETITION RATE KrF DRIVER FOR LASER-PLASMA X-RAY SOURCE

I C E Turcu, I N Ross, M C Gower, C J Reason
Rutherford Appleton Laboratory

Introduction

Plasma X-ray sources generated by low energy, repetitive KrF lasers have been used for applications such as lithography[1,2], X-ray spectroscopy[3] and the study of radiation damage to biological cells[4,5]. The advantages of using KrF lasers for laser-plasma X-ray generation are: (a) the short wavelength (λ = 249 nm) laser is absorbed efficiently in a high density plasma with potential high conversion efficiency to X-rays, (b) the gas laser operated in the oscillator-amplifier mode has near diffraction limited beam divergence and can be focused to high irradiance to generate a very bright X-ray source, (c) the KrF laser can be run at increasingly high repetition rates hence increasing the average power of the X-ray source. The main disadvantage of using KrF lasers for laser-plasma interaction is their long pulse duration (~ 20ns) which for tightly focused lasers (focal spot diameter ~ 10 μm) results in lower conversion efficiency to X-ray emission[5,6] after ~ 1 nsec. This drawback is discussed in detail and a working solution is given in Section C4.3 and D1.4. In the present section we describe the implementation of a 100 Hz KrF laser system for generation of X-rays at increased average power in an integrated laser-X-ray source-user facility. The actual X-ray source will be described in Section D1.1. Section D1.2 describes the application of the X-ray source to microscopy and Section D1.3 to sub 0.5 μm lithography.

2. Laser System

The KrF laser system consists of two commercial Questek 2440 discharge lasers[7] (rated at 40 W, 100Hz each) run as oscillator-amplifier (Fig 1). The 'Delay and Sync Unit' allows the adjustment of the delay between firing the lasers at the optimum value for amplification and then maintains the chosen delay with a shot-to-shot jitter of $\leq \pm$ 3 ns. This is achieved by receiving feedback signals from optical fibres which "see" the two laser discharges. If the laser system is switched off and fired again after an interval of time the electronics requires $\geq$ 50 pulses to stabilise the present delay. We have constructed a computer controlled fast (10 ms opening time) electronic shutter, positioned intracavity in the amplifier to protect the output coupler during these 'iteration' pulses when the amplifier runs freely. The shutter implicitly controls the laser pulses reaching the X-ray target eliminating the first poor divergence ('iteration') shots which generate enhanced target debris and no X-rays. The oscillator laser has integral unstable (U/S) resonator cavity (Fig 1). The laser system can be operated in: a) Power-Oscillator Power-Amplifier (POPA) mode when the full oscillator beam is fed through the amplifier (with no cavity) to yield pules of ~ 500 mJ energy and 22 ns duration; b) Injection-Locked U/S Resonator Amplifier (Fig 1) when the oscillator beam is restricted by ϕ = 1 mm aperture and injected through a ϕ = 1mm hole in the high reflectivity (HR) coating of the back mirror of the amplifier cavity. The amplifier output coupler can be uncoated or have an HR dot mirror. In this mode of operation the system yields pulses of ~ 350 mJ energy in τ ~ 18 ns duration.

For X-ray generation the irradiance on target should be in the region of 10^{12}-10^{13} W/cm^2 which implies that a 20 MW KrF laser should be focused to 10-40 μm. Specifically the upper irradiance (and smaller focal spot) is required for generation of $h\upsilon$ ~ 1 keV Xrays[2,6] and the lower irradiance for softer X-rays in the "water window" spectral region[8]. This condition on laser focusability deserves special attention when specifying a KrF laser system for laser-plasma X-ray generation. The beam divergence of the laser system has ben measured in the far field of a long focal length lens (f = 5 m) with a 2D diode array UV beam profiler[9]:

a FWHM beam divergence of $\approx$ 100 μrad for the injection locked U/S resonator amplifier and $\approx$ 160 μrad for the POPA configuration. In the U/S resonator amplifier mode with $E_t \approx$ 300 mJ on target, $\tau \approx$ 18 ns and a f = 9 cm lens the focal spot is 9 μm resulting in an irradiance on target $I_t \approx 2.6 \times 10^{13}$ W/cm^2. In the POPA configuration the f = 9 cm lens gives a 14 μm focal spot which for $E_t \approx$ 500 mJ and $\tau \approx$ 22 ns results in $I_t \approx 1.4 \times 10^{13}$. Even at an angle of incidence of 45° to the target normal the irradiance is 1.3 x 10^{13} W/cm^2 and 7 x 10^{12} W/cm^2 respectively. These values are adequate for $h\upsilon$ ~ keV X-ray generation in the first case and "water window" X-rays in the second.

3. Acknowledgments

We gratefully acknowledge: Mr P Gottfeldt, Mr W Lester, Mr A R Damerell, Mr K Miles, Mr D Baker and Mr D Wood (RAL) for electronic

and mechanical integration of the laser-X-ray source-user system. The SERC contribution to this work was partially supported by the UK Department of Trade and Industry through EUREKA European research initiative (EU213 excimer laser project).

4. References

1. F O'Neill, M C Gower, I C E Turcu and Y Owadano, Appl Opt 25, 464 (1986).

2. E Turcu, G Davis, M C Gower, F O'Neill and M Lawless, Microelectron Eng 6, 287 (1987).

3. M L Ginter and T J McIlrath, Appl Opt 27, 885 (1988).

4. F O'Neill, I C E Turcu, G J Tallents, J Dickerson, T Lindsay, D T Goodhead, A Stretch, C W Wharton and R A Meldrum, Proc Soc Photo-Opt Instrum Eng 1140, 232 (1989).

5. G M Davis, M C Gower, F O'Neill and I C E Turcu, Appl Phys Lett, 53 1583 (1988).

6. I C E Turcu, F O'Neill, G J Tallents, T Hannon, D Batani, A Giulietti, C W Wharton, R A Meldrum, Proc Soc Photo-Opt Instrum Eng 1278, 32 (1990).

7. Questek Inc, Manning Road, Billerica, MA 01821, USA.

8. I C E Turcu, F O'Neill, U Zammit, Y Al-Hadithi, R W Eason, A M Rogoyski, C P B Hills and A G Michette, Proc Soc Photo-Opt Instrum Eng 831, 211 (1987).

9. Exitech Limited, Hanborough Business Park, Long Hanborough, Oxford OX7 2LH, UK.

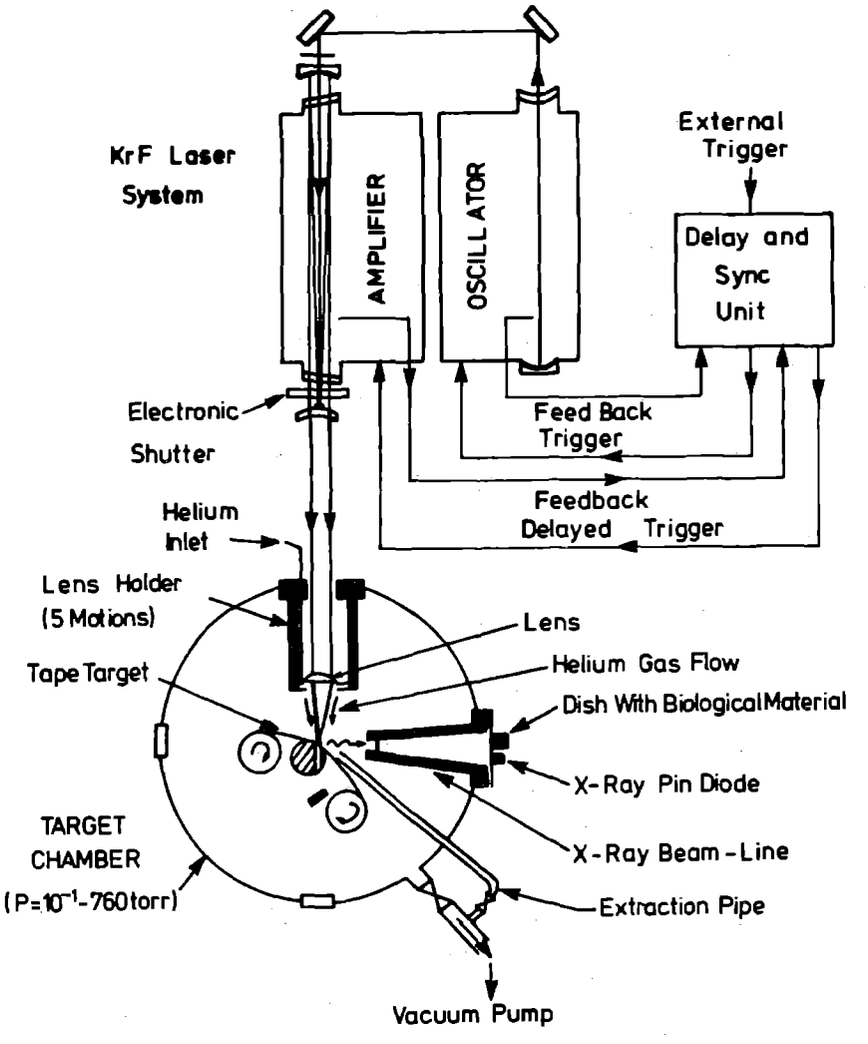

Fig. 1. 100 Hz KrF laser-plasma X-ray source.

AN ATLAS OF OPTOGALVANIC TRANSITIONS IN NEON.

S.H. Ashworth and J.M. Brown

Oxford University

Calibration is of prime importance to many laser users. The accuracy to which one wishes to know the wavelength of radiation depends, however, on the particular application. There are a number of wavemeters available for either pulsed or CW systems and accuracies of one part in 10^7 are possible. Unfortunately in our work (see Laser Excitation of Jet Cooled Molecules Formed From Involatile Solids) commercial systems have been shown to have one of two serious flaws. The most accurate wavemeter we investigated was unable to handle light below 400nm. When doubling this is not a problem as the fundamental can be used for calibration however when using, as we often do, dyes which lase around 360nm (e.g. DMQ) this wavemeter would be of no use. On the other hand one wavemeter that can handle the 360nm radiation was shown to be insufficiently accurate for our purposes as the resultant measurements were only accurate to ± 1 cm^{-1}.

Our solution to this problem was to use a secondary standard. We developed a system whereby the spectrum of neon, which is well known and accurately measured, is recorded simultaneously with our spectra. We use the optogalvanic effect in the discharge of a hollow cathode lamp to do this. When a resonance with laser radiation directed into the discharge occurs, the ionisation cross section in the plasma can change[1,2]. This causes the lamp to draw either more, or less current from the power supply to maintain equilibrium. The resultant voltage change (0.1%) can be AC coupled to either an oscilloscope or a recording device. The spectra of neon are not, unlike the case of uranium[3],directly analagous to either emission or absorption spectra. Not only can intensities be anomalous one can also observe negative signals such as those shown in Figure 1.

A second advantage of this system is that it gives a diagnostic on the performance of the laser. The specified linewidth, without intracavity etalon, for the FL3002 laser is 0.2cm^{-1}. The lines in the optogalvanic spectrum are atomic and, even at an elevated temperature in the discharge, the Doppler width is less than the laser linewidth. The width of the optogalvanic lines therefore shows how well the laser has been set up. The lines shown in Figure 1 have a full width half maximum (FWHM) of about 0.3cm^{-1}. Using this system we can now be confident that measurements of the strongest features in our spectra are accurate to ± 0.2 cm^{-1}.

The recording shown in Figure 1 is part of the work done during a Division Head's Week in order to fill in the gaps in the spectrum not covered by our other work. We will now be able to publish an atlas of optogalvanic transitions in neon. The system itself is very easy to set up and to use and has wide ranging applications. Assignment is made far more straightforward if one can match a recording with an atlas. This may be most important for regions where neon lines occur in the emission or absorption spectra of the hollow cathode lamp but the transitions do not create a change in the ionisation cross section meaning that no optogalvanic signal would be detected.

We have recorded the spectrum from around 270nm to 730nm. All that remains is to assign the new recordings and plot them in a usable form. Anyone interested in using the completed atlas should contact one of the authors at the Physical Chemistry Laboratory, South Parks Road, Oxford.

REFERENCES

1. K.C. Smyth and P.K. Schenck, *Chem. Phys. Letters*, **55**, 466 (1978)

2. D.S. King, P.K. Schenck, K.C. Smyth and J.C. Travis, *Applied Optics*,**16**, 2617 (1977)

3. R.A. Keller, R. Engelman, Jr., and B.A. Palmer, *Applied Optics*,**19**, 836 (1980)

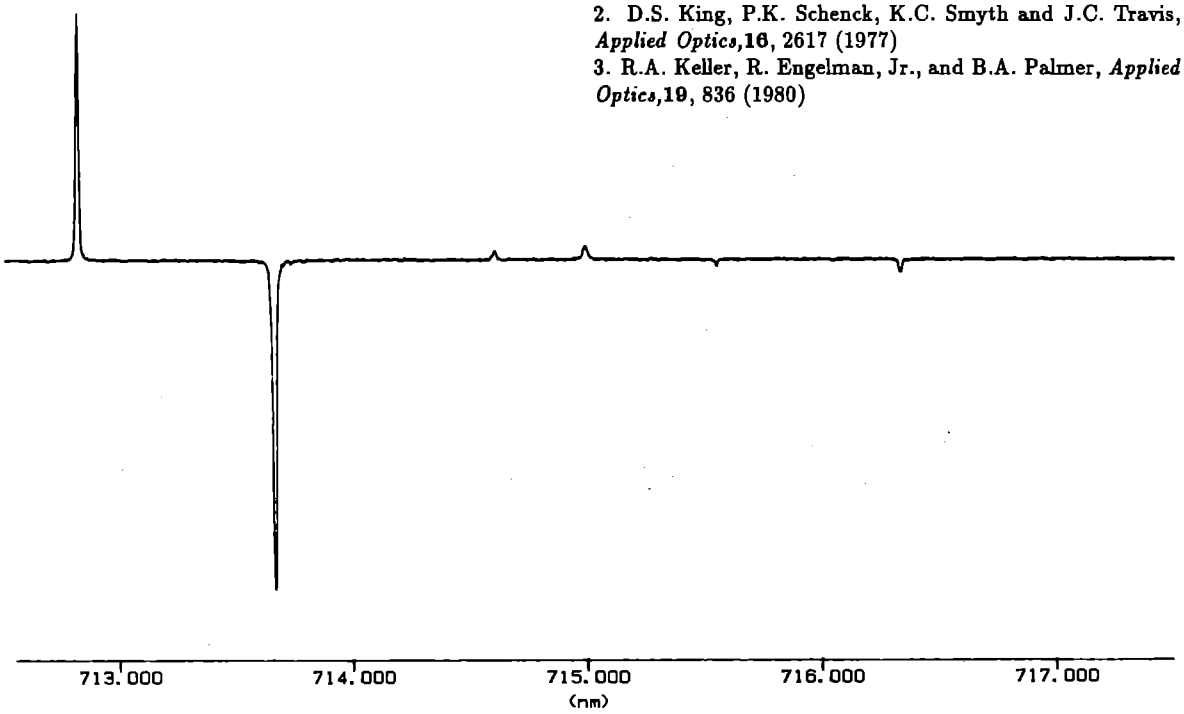

Figure 1. A portion of the optogalvanic spectrum of a neon discharge in a hollow cathode lamp. Both positive and negative signals are observed and the signal to noise ratio is excellent.

Picosecond Time-Resolved Raman Spectroscopy
A Progress Report

G J Hirst, P Matousek, P Mawson, W Toner,
M Towrie, A Parker and R Williams

Rutherford Appleton Laboratory

This short report outlines some modifications made to the Raman spectroscopy apparatus described in previous reports[1,2].

To improve the reliability and stability of the copper vapour laser the repetition rate of the system was reduced to 4.46 kHz. The resultant increase in the temporal width of the copper vapour laser pulse required the addition of a sixth stage to the dye amplifier (see Fig 1). The amplifier operates in the saturation regime (see Fig 2) where the output pulse energy is less dependent on the input pulse energy from the cavity dumper. The output pulse energy of the dye amplifier at 613 nm is 70 μJ and second harmonic conversion efficiency is 10%.

The transmission efficiency, alignment procedures and system diagnostics are at present being improved. For instance there is now a permanent on-line method for determining the zero delay position of the pump and the probe beams.

A test measurement of a Time Resolved Picosecond Resonance Raman spectrum was carried out with trans-Stilbene in n-Hexane (5×10^{-3}) M) to verify proper operation of the system under the new conditions (see Fig 3). Results are in a good agreement with work carried out by T L Gustafson et al[3].

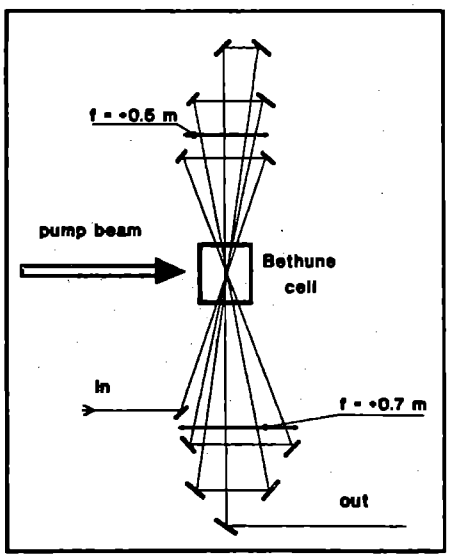

Fig.1. Schematic diagram of the 6-stage dye amplifier.

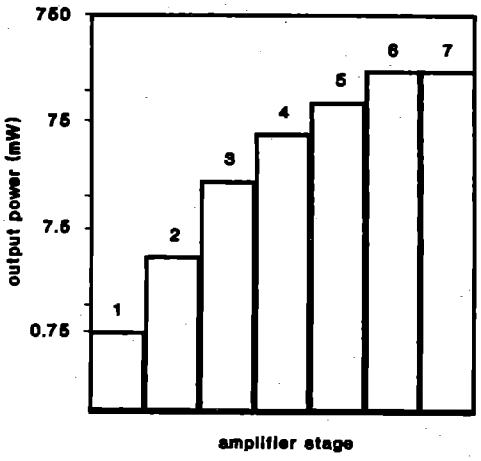

Fig.2. Output power of the dye amplifier at each amplifying stage.

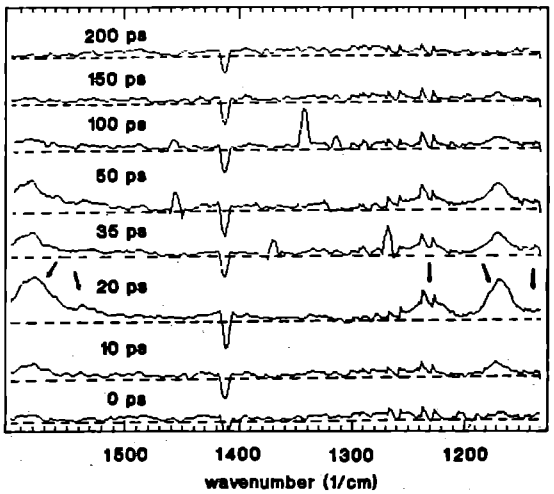

Fig.3. Transient Picosecond Raman Spectrum of trans-Stilbene in n-Hexane at various delay times between pump and probe beams.

References

1. Annual Report 1990, Rutherford Appleton Laboratory Report RAL-90-026, 1990.

2. Annual Report to the Laser Facility Committee 1989, Rutherford Appleton Laboratory Report RAL-89-045, 1989.

3. T L F Gustafson et al, Picosecond Transient Raman Spectroscopy: The photoisomerization of trans-stilbene, J Chem Phys 79 (4), 1559. (1983).

SINGLE PHOTON COUNTING

S Tavender

Rutherford Appleton Laboratory

The basic Single Photon Counting (SPC) apparatus at RAL has been described previously (ref 1). The present system (figure 1) now uses the Spectron mode-locked YAG laser pumping a Spectra Physics 3500 cavity dumper. The cavity dumper output can be frequency doubled using a KDP crystal to give excitation at UV wavelengths.

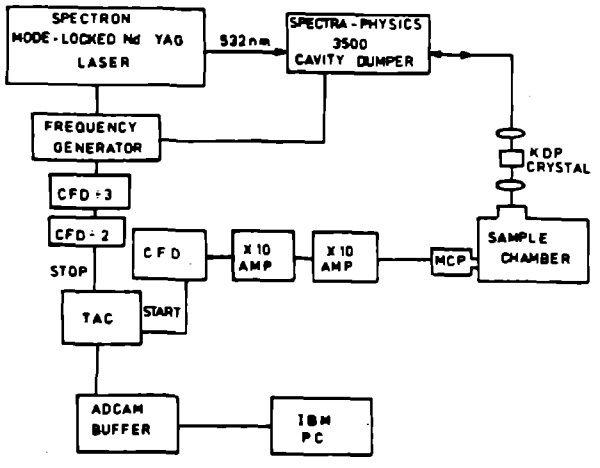

Fig. 1 SPC System.

The system now incorporates a RAL-built sample chamber (figure 2) which will allow up to 8 liquid samples to be studied in succession. Samples are mounted in an externally controlled carousel which is rotated to the desired position. Similarly, a polariser can be rotated in the emission beam to allow different emission polarisations to be studied.

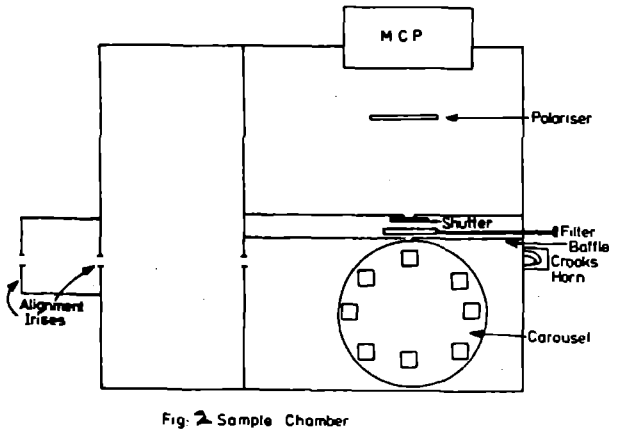

Fig. 2 Sample Chamber

Data is analysed on the Tandon PC by user programme which was written at University of Pennsylvania, USA. The program is written in c and uses a vector search to give a minimum ψ^2. Autocorrelation and residual plots are also given. Up to 3 lifetimes may be fitted simultaneously. Various standards have been used to characterise the system and curves showing the decay, fit and residuals of a sample of 2,5 diphenyloxaole (PPO) (10^{-5}M in cyclohexane undegassed) are shown (figures 3a, b). The lifetime is 1.28 ns which agrees with that in the literature (ref 2). The ψ^2 for the fit is 1.26.

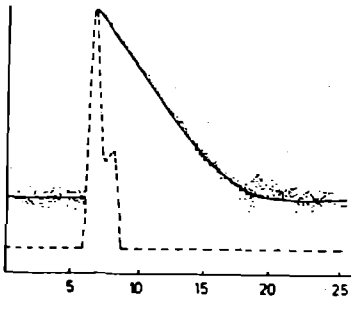

Fig 3 (a) Decay of PPO (10^{-5}M) in Cyclohexane also showing excitation curve (- - -) and fit (——)

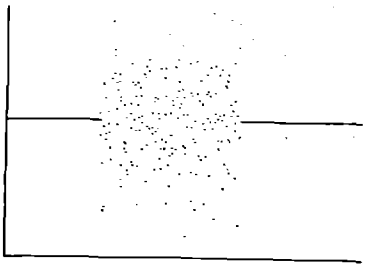

Fig. 3 (b) Residuals Plot of PPO (10^{-5}M)

The time resolution currently stands at 180 ps ± 10 ps. The microchannel plate has recently been tested in similar SPC apparatus and has given an instrument response of 60 ps. Wider band amplifiers (1-2 GHz) are currently being investigated and it is hoped these will reduce the time resolution significantly.

The system is currently working and lifetimes with sub-nanosecond components extracted.

References

1. RAL Annual Report RAL-88-042.

2. R Lampert et al, An Chem 55, 1, 1983.

SEPARATELY FUNDED PROJECTS

Introduction

This section describes the two areas of our programme which derive funding from sources other than SERC Science Board's allocation to the Central Laser Facility.

Section D1 contains all the work contributing to the EUREKA 'EU213' programme. The Central Laser Facility is a member of the 'applications' group of the 'high average power excimer laser' part of this programme, and within this group our contribution is the development of high average power laser produced X-ray sources, for which we are 50% funded by the Department of Trade and Industry. We are happy to report considerable progress in the reporting year. Notable in the area of laser development has been the installation of a short pulse oscillator providing 50 ps pulses leading to efficient ($2^1/_2$%) short pulse X-ray emission at about 1 KeV from a source size of 13 μm and providing a very clean spectrum. We are now able to operate at up to 100 Hz and an average X-ray power up to 40 mW/steradian. Interest in applications of these sources has grown considerably and we have conducted several successful demonstration experiments. In the area of X-ray high resolution lithography a resolution of 1 μm has been demonstrated and in scanning X-ray microscopy better than 0.25 μm resolution was achieved.

Section D2 contains a contribution from the work on phase conjugation. This is probably the final contribution from a long standing and productive programme which was supported over this year by an SERC research grant and conducted in association with the University of Southampton.

100 Hz KrF LASER-PLASMA X-RAY SOURCE

I C E Turcu[1], G J Tallents[2], C J Reason[1], D Batani[3], P Huntington[1]
[1]Rutherford Appleton Laboratory
[2]Dept of Physics, University of Essex
[3]Dipartimento di Fisica, Universita Statale Milano, Italy

Introduction

Plasma X-ray sources generated by low-energy, repetitive, KrF lasers have been used for applications such as X-ray lithography[1,2], X-ray spectroscopy[3] and the study of radiation damage to biological cells[4,5]. The problem of target debris was successfully improved by running the X-ray source in atmospheric pressure helium[4,5]. The source has several attractive features: (i) it is compact, (ii) it can be 'tuned' to different photon energies by changing the target material, (iii) the laser beam divergence is near diffraction limited hence the beam can be focused to a small focal spot. The last statement has two implications: a) the source has high brightness required for X-ray microscopy, b) only moderate laser energy 0.5-1.0 J/shot is required to produce keV X-rays resulting in a reduced thermal loading of X-ray windows and masks. The repetition rate of the laser used in Ref 4,5 was 5 Hz. Nevertheless the majority of applications: radiobiology, X-ray microscopy, X-ray lithography etc require high repetition rate X-ray sources to reduce the exposure time. One very important feature of KrF lasers is their operation at high average powers: indeed commercial systems to date generate in excess of 100 W and kW class system will be available in the near future. Our paper describes the operation of the laser-plasma X-ray source at repetition rates up to 100Hz and its applications. The KrF oscillator amplifier system is described in Section C4.2. The present paper describes: (a) the X-ray target chamber with tape target and helium/flow, (b) measurements on the X-ray source: size, time dependence, spectrum, average power. The use of the source for scanning X-ray microscopy (SXRM) is described in Section D1.2 and for sub 0.5 μm lithography in Section D1.3.

2. X-ray Measurements

The laser beam is focused on the target (Fig 1, Section C4.2) by an f = 9 cm aspheric singlet lens held in a special mount, described in detail in Ref 5, allowing: 5 lens motions, sealing the target chamber and producing uniform helium flow from the lens to the target. The target can be a rotating rod[4,5] or a thin (t ≈ 20 μm) tape pulled between two spools by DC motors. The tape is positioned and kept in the laser focus by a steel rod with a guiding groove and a slot behind the focus allowing the propagation of debris ejected at the back of the tape. This debris is then stopped by a shield placed behind the guide rod. The tapes used were copper (for $h\upsilon$ ~ keV X-rays) and mylar (for the "water window" X-rays). The mylar tape was a cassette player tape 'played' with the uncoated side towards the laser. The chamber contains Helium gas which does not affect the X-ray emission[5] but stops the fast ions emitted by the plasma in the forward direction. This thermalised target vapour mixed in helium gas is extracted by a pipe placed in the vicinity of the plasma (Fig 1, Section C4.2). Due to the fact that the use of helium in the target chamber is so beneficial, we report in Section D1.5 an experiment to investigate the KrF laser breakdown threshold in helium. The conclusions show that even though for an irradiance of $I = 10^{13}$ W/cm^2 breakdown occurs in helium at ~ 550 mbar, the energy loss for $I = 2 \times 10^{13}$ W/cm^2 in 1 atmosphere helium is only ~ 10% with no distortion of the laser beam.

A pinhole camera PHC with a magnification of 9 and a $\phi = 6$ μm pinhole was placed in the plane of incidence (horizontal) at 45° from the target normal (as the X-ray beam-line in Fig 1, Section C4.2). The distance between the plasma and the pinhole was 11 mm. A 0.2 μm Aluminium foil filters out the UV light. The X-ray image is obtained on Kodak 101 no screen film for the mylar tape target; and on Kodak DEF film for copper tape targets. The laser system was fired at 20 Hz but the electronic shutter was open only for a given number of shots which provided the exposure for the PHC. Fig 1a shows a PHC picture for 2 shots on the moving Cu tape target in atmospheric pressure helium. The laser system was in injection locked U/S resonator amplifier mode and the energy on target was ~ 350 mJ/pulse. The X-ray source FWHM of 13 μm is in good agreement with beam divergence measurements described in Section C4.2. Fig 1b shows a similar 2 shot image from mylar tape target in 26 torr He. The laser system was run in the POPA configuration delivering ~ 375 mJ/pulse on target (due to reduced 75% lens transmission after long exposures in the 2 week scanning X-ray microscope experiment. One notes the 39 μm FWHM image which is three times the spot size. To check this result PHC pictures were taken from mylar targets irradiated with the laser system in the injection locked U/S amplifier mode in exactly the same conditions as for the Cu targets. The measured source size

was again ~ 40 μm FWHM. Close inspection under the microscope of the PHC pictures from mylar targets shows a $\phi \sim 10$ μm blank region on the axis of the expanding plasma, as if the X-ray source consisted of a hollow cylinder. This behaviour could be explained by noting that, in the centre of the laser focal spot at irradiances on target, > 10^{13} W/cm^2 the plasma electron temperature is a few hundred ev[6] sufficient to deplete the helium-like ion population and even to fully ionise the carbon atom. Hence the "water window", carbon K-shell X-rays will be emitted at the outer regions of the focal spot where the irradiance is lower ~ 10^{12} W/cm^2. Indeed, measurements of 'water window' X-ray conversion efficiency from carbon targets[7] have shown that the emission drops for irradiances > 10^{12} W/cm^2.

We have previously reported hυ ~ keV X-ray spectra obtained with crystal spectrometers from copper[5] and steel[4] targets as well as mylar spectra[7] obtained with a grazing incidence grating spectrometer. In the present experiment we have obtained similar spectra from Cu and Fe as in Ref 4 and 5. We have also used a calibrated transmission grating spectrometer and calibrated Kodak 101 no screen X-ray film for absolute measurements of X-ray spectra from mylar targets reported in Section D1.2. It was found that ~ 3 x 10^{12} photons/sr/shot were emitted in the He_α and L_α lines each with a total "water window" emission of ~ 9 x 10^{12} photons/sr/shot.

For most measurements the X-ray source was operated at 20 Hz. In view of using the X-ray source with an STXM the laser was run at 100 Hz. A He flow of 10l/min at a pressure in the X-ray chamber of 20 torr and the mylar tape running at 4 cm/s provided stable operation for short periods of time. The histogram in Fig 2a shows the shot-to-shot variation in X-ray energy over 11 seconds - which could be sufficient to acquire 1000 pixel image on an STXM. The average X-ray power in the "water window" is ≈ 40 mW/sr and ≈ 200 mW over a 2π solid angle. For longer periods of operation the helium flow rate had to be increased to remove the debris cloud which accumulates between the target and the lens, absorbing the laser light. The accumulation of the debris cloud, before reaching the target, resulting in the cut off X-ray emission, could be observed visually as the focused laser beam becomes visible through the fluorescence and scattering it produces in the debris cloud like a searchlight scattered in the atmosphere. We call this "the searchlight effect" and its appearance signals the diminution or even termination of X-ray emission. We could run the source for long periods of time - hours - at 40 Hz with a He flow rate of 40 l/min. Using a higher flow rate was impractical without a recirculation He pump.

In view of using the X-ray source for lithography we investigated the high-repetition rate performance of the source for harder, hυ ~ 0.9 keV X-rays from silver-steel rod targets described in Ref 4. The irradiation geometry is that of Fig 1, Section C4.2 except that the tape target is replaced with a 16 mm diameter rod which rotates and translates vertically to present a new surface for each laser shot. The laser is run in the "injection locked U/S amplifier" mode for best beam divergence and is focused at 45° from target normal. The X-ray emission is measured with a PIN-XRD placed at 23 cm from the source in 1 atm of He, and filtered by 0.2 μm Al on 0.4 μm parylene (CH) and also by 2 μm mylar (CHO) which simulates the X-ray mask membrane. The PIN-XRD views the source along the target normal. The laser energy conversion efficiency to X-rays is 0.11% sr^{-1} for a laser energy on target of 280 mJ. The angular distribution was measured to follow approximately $I(\theta) \approx I_0(\cos\theta)^{1.35}$. Integrating over the angular distribution the energy conversion efficiency in 2π sr is ≈ 0.3%. The source could be operated over long periods of time at 20 Hz in atmospheric pressure helium with 20 l/min flow. When the X-ray source was operated in vacuum the signal recorded by the PIN-XRD was 1.4 times higher than in atmospheric pressure He resulting in a conversion efficiency of ≈ 0.4% into 2π sr. Fig 2b shows a histogram of the PIN-XRD signal recorded over 14 minutes with the source run in atmospheric pressure He with flow. The average X-ray power emitted is 6 mW/sr or 16 mW over 2π steradians. By increasing the He flow the repetition rate of the source can be increased and again it was limited to ~ 40 Hz for a flow rate of 40 l/min. Above this repetition rate the "searchlight" effect appeared after a short time of operation reducing the X-ray emission. Nevertheless, there should be no practical limitation to flow He at say 100-200 l/min hence allowing 100 Hz long time operation.

4. Conclusions

Utilising a modern commercial KrF excimer laser as a driver we have demonstrated that it is possible to operate a laser-plasma X-ray source at high repetition rates up to 100 Hz. The high repetition rate operation and the debris reduction can be achieved by using Helium gas as buffer and flow medium as well as thin tape target. The source was used for the first time to demonstrate a laser-plasma driven scanning transmission X-ray microscope requiring exposure times comparable with operation on SRS (Section D1.2). The source was also used to replicate with 50 nm resolution 0.3 μm structures in 1.2 μm photoresist (Section D1.3).

5. Acknowledgements

We gratefully acknowledge: Mr P Gottfeldt, Mr W Lester, Mr A R Damerell and Mr K Miles (RAL) for electronic and mechanical integration of the laser-X-ray source-user system. The SERC contribution to this work was partially supported by the UK Department of Trade and Industry through EUREKA European research initiative (EU213 excimer laser project). DB was supported by a British Council grant.

8. References

1. F O'Neill, M C Gower, I C E Turcu and Y Owadano, Appl Opt 25,464 (1986).

2. E Turcu, G Davis, M C Gower, F O'Neill and M Lawless, Microelectron Eng 6, 287 (1987).

3. M L Ginter and T J McIlrath, Appl Opt 27, 885 (1988).

4. F O'Neill, I C E Turcu, G J Tallents, J Dickerson, T Lindsay, D T Goodhead, A Stretch, C W Wharton and R A Meldrum, Proc Soc Photo-Opt Instrum Eng 1140, 232 (1989).

5. I C E Turcu, F O'Neill, G J Tallents, T Hannon, D Batani, A Giulietti, C W Wharton, R A Meldrum, Proc Soc Photo-Opt Instrum Eng 1278, 32 (1990).

6. I C E Turcu, F O'Neill, U Zammit, Y Al-Hadithi, R W Eason, A M Rogoyski, C P B Hills and A G Michette, Proc Soc Photo-Opt Instrum Eng 831, 211 (1987).

7. P D Gupta, R Popil, R Fedosejevs, A A Offenberger, D Saltzmann and C E Capjack, Appl Phys Lett 38, 103 (1986).

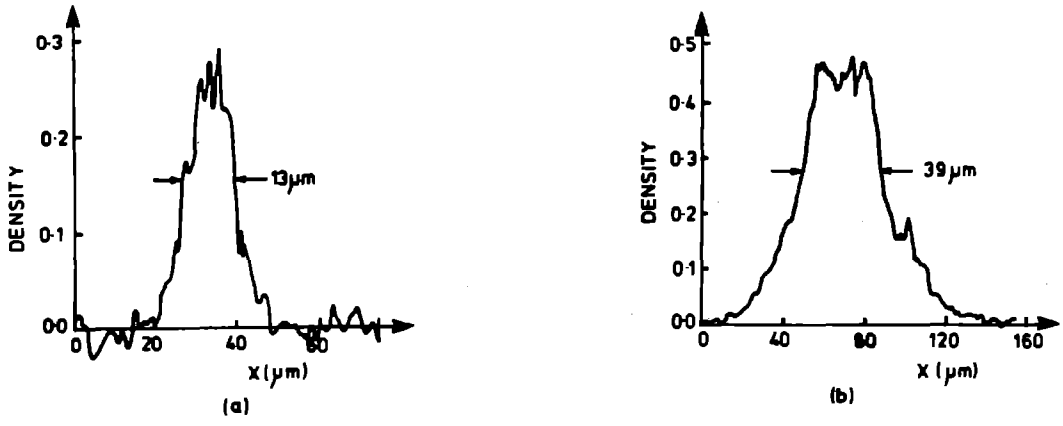

Fig 1 X-ray pinhole camera pictures of the laser-produced plasma using two shots on moving tape target: a) copper plasma, b) mylar plasma.

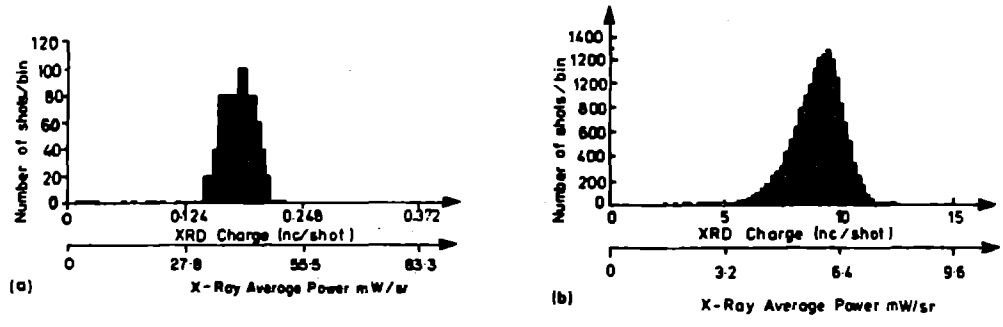

Fig 2 Histograms of X-ray signals (nC/shot) as recorded with filtered PIN-XRD: a) "water window" X-rays recorded though 0.5 μm Vanadium filter from mylar tape-target in 20 torr He with the laser in POPA mode, pulsed at 100 Hz for 11.3 sec, b) hν ~ 0.9 keV X-rays recorded through 0.2 μm Al + 0.4 μm CH + 2 μm CHO filter, from silver steel rod target in 1 atm He with laser in "Injection locked U/S amplifier" mode, pulsed at 20 Hz for 14 min. The lower axis shows signal converted to X-ray average power.

FIRST EXPERIMENTS WITH A SCANNING TRANSMISSION X-RAY MICROSCOPE ON A HIGH REPETITION RATE LASER-PLASMA SOURCE

A G Michette[1], M S Schulz[1] and I C E Turcu[2]

[1]Department of Physics, King's College London
[2]Rutherford Appleton Laboratory

INTRODUCTION

Over the past several years the development of zone-plate optics[1] and of high-brilliance synchrotron sources[2] have allowed the possibility of high-resolution (sub 0.1 μm) x-ray microscopy of both biological and non-biological material. Several x-ray microscopes are now operating in more or less routine fashion and are being used for a wide variety of applications[3]; one of these is the scanning transmission x-ray microscope (STXM) built at King's College London (KCL) and installed on the undulator beamline at the Synchrotron Radiation Source (SRS), SERC Daresbury Laboratory. The details of this microscope have been published previously[4]; briefly, a high-resolution zone plate (outermost zone width typically in the range 30-100 nm) is used to focus monochromatic radiation (at a wavelength in the range 2.3-4.4 nm, usually $\approx$3.5 nm) to a small spot the diameter of which is defined by the convolution of the demagnified exit slit of the monochromator and the outermost zone width of the zone plate. A specimen is mechanically scanned across this spot and the transmitted X rays are detected by a single-wire flow proportional counter. Images with resolutions of around 50 nm have been obtained with this instrument.

The nature of synchrotron x-ray sources means that they are expensive, remote multi-user facilities, and are therefore not suited for use with a laboratory scale x-ray microscope. For this reason, alternative sources have been under investigation, and the most promising of these for scanning x-ray microscopy is based on a high repetition rate laser-generated plasma (LGP). Previous experiments carried out at KCL[5] and at the SERC Rutherford Appleton Laboratory (RAL)[6] have established the feasibility of using such a source for x-ray microscopy, and so when the KCL/Daresbury microscope became available due to a scheduled shutdown at Daresbury the system was moved to RAL and attached to the LGP source there. This source, which uses two Questek KrF excimer lasers, was available for only two weeks, and so the experiments described here could only be preliminary.

THE SOURCE

For this experiment the two Questek 2440 lasers were used in POPA configuration: power oscillator (with integral unstable cavity) and power amplifier, as described in more detail elsewhere[6].

The laser beam, with $\approx$500 mJ per pulse, was focused by a fused silica aspheric singlet f=7 cm lens to a spot on target to give a source size of $\approx$ 20 μm. The renewable target was a 20 μm thick, 4 mm wide mylar tape (commercial cassette recorder tape with the uncoated side towards the laser) moving at up to 4 cm s^{-1} for 100 Hz laser repetition rate, driven by a commercial miniature cassette player. The tape was supported by a 16 mm diameter cylinder which kept it at focus to within $\approx \pm$10 μm. A 3 mm slot behind the laser focus allowed free expansion of debris ejected through the tape. The laser beam was incident at 45° to the normal to the cylinder in the horizontal plane, and the STXM was at 90° to the laser beam. A silicon nitride window separated the target chamber from the atmospheric environment of the microscope.

The absolute x-ray emission was measured with a calibrated, 0.25 μm thick silicon window Quantrad PIN x-ray diode (XRD) filtered by 0.5 μm vanadium on a 40% geometrical transmission mylar support grid with a 0.2 μm aluminium debris shield. The XRD was placed 23.7 cm from the source along the target normal. The signal was integrated over the pulse duration in a LeCroy ADC and averaged over many shots by a PC which also displayed the histogram of the XRD signals. For calculating the x-ray yield, the filter transmission and XRD sensitivity were calculated at 368 eV, the peak of the convolution of the (x-ray spectrum) $\otimes$ (Al + V filter transmission) $\otimes$ (sensitivity of XRD). The conversion efficiency from laser energy to water-window X rays was $\approx$0.2% sr^{-1} for the mylar tape target.

Use of 20 torr He with a flow of 10 l min^{-1} resulted in very little reduction in the x-ray signal, and no damage to the 0.2 μm Al filter placed 10 cm from the target or loss in lens transmission were observed during the experiment.

The x-ray spectrum was measured with a 44 $\times$ 44μm^2 transmission grating with period 114 nm manufactured at King's College by the contamination technique on a 100 nm thick Si_3N_4 substrate. The lines were shadowed with 30 nm of platinum. The grating was placed 10 cm from the source at 45° to the normal, behind a 0.2 μm Al filter. The spectrum was recorded over 328 shots on calibrated Kodak S101 no screen x-ray film placed 20 cm behind the grating. Preliminary calibration of the grating at the Bessy storage ring indicates a diffraction efficiency of $\approx$1%. Background subtraction and deconvolution of the x-ray film sensitivity, Al and Si_3N_4 transmission, and grating diffraction efficiency, shows that $\approx 3 \times 10^{12}$ photons sr^{-1} per shot were emitted in each of the He_α and L_α lines, with a total in the water window of $\approx 9 \times 10^{12}$ photons sr^{-1} per shot. Under the conditions used in the experiment, this should correspond to $\approx$1000 photons per pulse at the STXM detector, at a wavelength of 3.37 nm. The water-window x-ray flux measured from the transmission grating spectrum is in very good agreement with the XRD measurements.

THE DETECTOR AND IMAGE ACQUISITION

In a STXM used on a (quasi)-continuously emitting source, such as a synchrotron, a proportional counter can be used to count the number of transmitted x-ray photons. However, when a laser plasma source as described above is used the X rays arrive in pulses lasting a few nanoseconds and individual photons cannot be counted. If the counter is to be used in proportional mode a pulse height to digital converter is required. To facilitate this an in-house dual slope integrator circuit was modified and employed for this conversion. A counter pulse obtained from a preamplifier (Ortec 1421) and main amplifier (KMAC 575) had a fall time of approximately 2 μs. The dual slope integrator set with a suitable integrate time (100 μs) generated a square wave of duration equal to the time required to discharge the integrator, typically 100 μs, and this square wave was used to gate a 1 MHz photon counting circuit in the STXM.

The image acquisition system developed for use with a synchrotron source, using an IBM PC and a Microlink crate, allowed images to be obtained with a fixed dwell time per pixel. For use with the laser plasma source the

software was slightly modified so that the control computer was used to fire the laser at a given repetition rate (typically 20-40 Hz) and the data for each pixel were acquired for a set number of laser pulses.

PERFORMANCE OF THE MICROSCOPE

One problem with the detection system involved a spurious pulse picked up by the proportional counter and preamplifier when the laser fired. This was reduced but not eliminated by careful screening. However it was discovered that this pulse was bidirectional and gave rise to a negligible contribution to the charge on the integrator. The linearity of the detecting system was checked by scanning a 25 μm aperture across the edge of the target chamber exit window. The counts were plotted as a function of the unobscured area of the aperture; this plot was linear to better than 2%.

Noise arose in the images because of variation of source emission from shot to shot as well as the shot noise due to the number of photons collected during each pixel. Although the source emission was monitored it was not possible (in the time available) to modify the acquisition system to allow the effect of source emission to be removed so that only shot noise would remain. From the shot noise the number of photons per pixel could be estimated. An image of a pinhole obtained using a zone plate with 4% efficiency and one shot per pixel showed a noise which could mostly be attributed to the source and a signal compatible with that expected.

In order to obtain the position of best focus, a 3 μm pinhole was scanned across the x-ray beam. Far from the focus of the zone plate the characteristic doughnut pattern (caused because the zone plate was centrally obstructed) was observed, while near focus there was a central bright region due to the focused X rays. The position of best focus was determined by minimizing the size of this bright region. Because several x-ray lines contributed several foci should have been visible; however, the 3.37 nm line was sufficiently more intense that only its focus was obvious.

An image of a 6 μm pinhole, taken with 16 shots per pixel, was used to determine the spatial resolution of the system at a wavelength of 3.37 nm, by averaging the profile of the edge of the pinhole. The scanning step size used was 190 nm, and the averaged profile indicates a resolution of better than 0.25 μm.

FUTURE WORK

The source/microscope combination used was by no means optimized, and work in the immediate future will concentrate on rectifying this. For example, the zone plate used (with a diameter of 47 μm and an outermost zone width of 40 nm) was, due to geometrical restrictions with the system used, $\approx$ 50 cm from the source whereas the optimum distance, to fully illuminate this zone plate, is just over 11 cm. Thus an increase in the focused x-ray flux by a factor of about 20 could be gained in an optimized system. The effect of out-of-focus lines will be minimized by filters (e.g. a nitrogen buffer gas would eliminate all the radiation at wavelengths shorter than the nitrogen K edge at 3.2 nm), and the variation in source emission will be monitored using an x-ray diode and used to normalize the signal. Other laser parameters, such as energy on target, will also be varied in order to optimize the emission in particular x-ray lines.

ACKNOWLEDGEMENTS

The authors are grateful to many people at RAL and KCL for assistance with this project. In particular we wish to thank Tony Damerall (RAL) for designing the attachment of the STXM to the existing target chamber, Mike Browne (KCL) for modifying and testing the detector, Graeme Morrison (KCL) for modifying the STXM control and image acquisition software, and Guy Foster and Dean Morris (KCL) for help with running the experiments.

REFERENCES

The most up-to-date compilation of all aspects of x-ray microscopy is the proceedings of the conference XRM90, held at King's College 3-7 September 1990, to be published as *X-Ray Microscopy III* (A G Michette, G R Morrison and C J Buckley, eds), Springer Series in Optical Sciences (Springer-Verlag, Berlin, in press 1991). All the references below are from this volume.

1. Nanofabrication of zone plate lenses for high resolution x-ray microscopy, E H Anderson and D Kern;
The status of zone plate fabrication at King's College London, P S Charalambous and D Morris
2. The development of synchrotron radiation sources and x-ray microscopy at the Photon Factory, M Ando and Y Kagoshima;
Coherent radiation for x-ray imaging: the performance of the X1A beamline at the NSLS, S Lindaas, H Rarback, H Ade, C J Buckley, S Hellman, M Howells, C Jacobsen, J Kirz, I McNulty, M Oversluizen, D Shu and S Williams
3. X-ray microscopy with the Göttingen scanning x-ray microscope at 2.4 nm, B Niemann;
Following protein transport with the high resolution x-ray microscope, S S Rothman, K Goncz and B W Loo, Jr.;
Live cell specimens for x-ray microscopy, J Pine and J R Gilbert;
Investigations of wet biological specimens with the x-ray microscope at BESSY, D Rudolph, G Schneider, P Guttmann, G Schmahl, B Niemann and J Thieme;
Radiation damage studies on active myofibrils, P M Bennett, C J Buckley, G F Foster and P A F Anastasi;
Scanning transmission x-ray microscopy of hydrated mitotic chromosomes, S Williams, C Jacobsen, J Kirz, S Lamm and J Van't Hof
4. Recent progress with the King's College scanning transmission x-ray microscope, G R Morrison, M T Browne, C J Buckley, R E Burge, P S Charalambous, G F Foster, A G Michette, D Morris, J R Palmer, G E Slark, P M Bennett and P J Duke
5. A study of the feasibility of x-ray microscopy with a laser-plasma source, M S Schulz, A G Michette and R E Burge
High repetition rate laser-plasma x-ray source for microscopy, I C E Turcu, G J Tallents, M S Schulz and A G Michette

SUB 0.5 μm LITHOGRAPHY WITH HIGH REPETITON RATE KrF LASER-PLASMA X-RAY SOURCE

F Bijkerk[1], I C E Turcu[2], E Louis[1]
[1]FOM-Institute for Plasma Physics, Rijnhuizen, The Netherlands
[2]Rutherford Appleton Laboratory

Introduction

A major possible application of hυ ~ 1 keV X-rays is in replicating sub 0.5 μm structures on photoresist for microchip fabrication(1). The present X-ray source (Sections C4.2, D1.1, D1.2) was used before for lithography(2). The source was then operated in vacuum limiting the repetition rate to 2 Hz. The exposure had to be interrupted to remove the coating of the pellicle protecting the focusing lens. The present experiment brings major improvements in the following areas of the techniques:

a) the atmospheric pressure helium operation of the X-ray source reduces dramatically the target debris on the lens. The lens transmission was reduced by 24% after ~ 4 x 10^5 laser pulses on target. The helium flow removes the Fe target vapour accumulating between target and lens allowing high repetition rate operation. The present exposures were performed at 20 Hz with 20 l/min flow,

b) a further reduction of debris reaching the filter protecting the X-ray mask is achieved by choosing the X-rays emitted at 22.5° from target normal where both vapour and cluster-type debris are minimum.

The optimum exposure angle was determined where debris emission from rod targets was minimum. The debris distribution was measured by placing small fused silica plates at different angles φ in the laser plane of incidence around the plasma. For silver steel rod targets the laser was run for ~ 15 min at 20 Hz in atmospheric pressure helium and in vacuum. The transmission of the coated plates was measured in the dual beam spectrophotometer (as in ref 3) and the thickness of the deposited layer was calculated form tabulated optical constants(4). Fig 1 shows a dramatic reduction of debris by working at atmospheric pressure helium as well as peak deposition at 45° from the target normal. The debris measurements have shown that apart from these vapour-type debris there are very few cluster-type (μm size) debris which can nevertheless easily penetrate foils and have two peaks of emission: along the target normal and at 45°. The cluster debris production along the target normal - which is due to material spalated from the target by the reflected shock wave - was decreased by two orders of magnitude by using a 60 μm thick steel tape target in place of the steel rod. Not enough tape was available at the time of the experiment so that the exposures for X-ray lithography were performed using steel rods, and placing the exposure camera at the minimum debris position of 22.5° from target normal.

In the case of mylar tape targets in 20 torr Helium all the carbon debris was collected in a narrow cone of ± 10° around the target normal. The exposure apparatus in Section D1.2 (spectrometer with transmission grating or X-ray microscope with zone plate) were positioned at 45° from target normal and no damage was observed on the 0.2 μm Al fitter or the transmission grating on 0.1 μm Si_3H_4 substrate placed at 10 cm from the target over a 2 week experimental period.

The geometry of exposure is shown in Fig 2a. The exposure camera(5) is placed at 100 mm from the X-ray source. A 6 μm Be filter protects the mask from target debris and the photoresist from UV exposure. The X-ray mask(6) was a 4" x 4", 2.2 μm thick silicon membrane with sub 0.5 μm structures of Au 0.5 μm thick. Because these features are produced by electroplating, the whole membrane is coated with a thin 25-50 nm layer of Au. A 25 μm gap separates the X-ray mask from the wafer on which 1.2 μm thick photoresist was spun. We used Ray-PF (Hoechst), a novolak-based three component (3CS) positive photoresist. We have measured remaining resist film thickness (RFT) as a function of the exposure dose and established that the sensitivity of the photoresist at hυ ~ 0.9 keV (Fe L-shell) was 18 mJ/cm^2.

Fig 2b shows an X-ray image of the mask structure with 0.7 μm lines and 0.3 μm spaces etched in 1.2 μm thick photoresist. The resist pattern equals the imaged mask absorber with an accuracy of 50 nm. Since Fig 2 represents patterns replicated from the smallest structures on the masks, the resolution limit of the combination of source and resist does not yet seem to be taxed. For a full depth exposure of the masked resist a preset dose of 20 mJ/cm^2 is supplied to the resist at an average X-ray power at resist surface of ~ 5 μW/cm^2.

A large reduction in exposure time could be achieved by: a) increased laser repetition rate. Operation at ~ 200 Hz results in 10x reduction, b) increased X-ray conversion efficiency by modulating the KrF laser pulse with a

picosecond pulse-train[7] (x 10), c) thinner (1 μm) Si mask membrane (x 2) and removal of the 50 nm Au coating of the whole membrane (x 2). The resulting exposure time would be 10 seconds at 10 cm from the source in atmospheric pressure helium.

Acknowledgments

We gratefully acknowledge: Dr H Huber and Dr H Oertel of the Fraunhofer Institut für Mickrostrukturtechnick (Berlin, Germany) for the supply of X-ray masks, Dr R Dammel and G Pawlowski of Hoechst A G Corporate Research (Frankfurt, Germany) for supplying the photoresist, Dr T Blatchford from the Rutherford Appleton Laboratory (RAL, UK) and Mr J Toth (Delft Institute of Microelectronics and Submicron Technology DIMES, Delft, the Netherlands) for SEM inspection of exposed photoresist, Mr C Brown (RAL) for filter manufacture. The SERC contribution to this work was partially supported by the UK Department of Trade and Industry through EUREKA European research initiative (EU213 excimer laser project). The FOM contribution to this work was supported by the Netherlands Organisation for Scientific Research, the Netherlands Technology Foundation and the Netherlands Government in the framework of EUREKA.

References

1. A Heuberger, Microelectornic Engineering 5, 3 (1986).
2. E Turcu, G Davis, M C Gower, F O'Neill and M Lawless, Microelectron Eng 6, 287 (1987).
3. I C E Turcu, F O'Neill, G J Tallents, T Hannon, D Batani, A Giulietti, C W Wharton, R A Meldrum, Proc Soc Photo-Opt Instrum Eng 1278, 32 (1990).
4. R M A Azzam and N M Bashara, Elipsometry and polarised light, 270, North Holland, (1987).
5. F Bijkerk, G E van Dorssen, M J van der Wiel, R Dammel and J Lingnau, Microelectronic Eng 9, 121 (1989).
6. X-ray mask supplied by Dr H Huber and Dr H Oertel of the Fraunhoffer Institut für Mikrostruktur-technik (Berlin, Germany).
7. F O'Neill, I C E Turcu, D Xenakis and M H R Hutchinson, Appl Phys Lett 55, 2603 (1990).

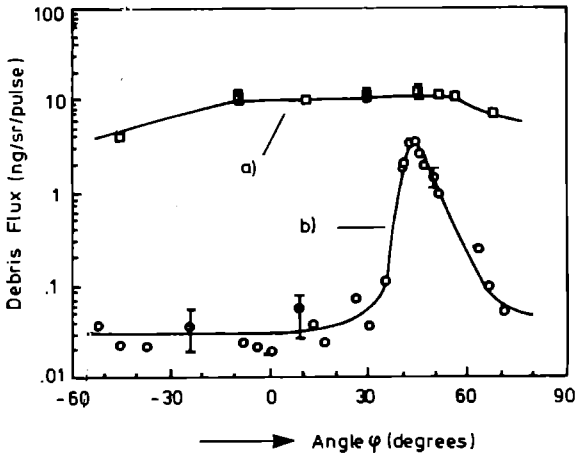

Fig. 1. Angular distribution of the flux of target debris measured in the laser plane of incidence, ϕ = 0 corresponds to the target normal. The lens is of ϕ = 45°. The chamber is: a) under vacuum and b) filled with helium at 1 atmosphere with a 10 l/min flow from the lens.

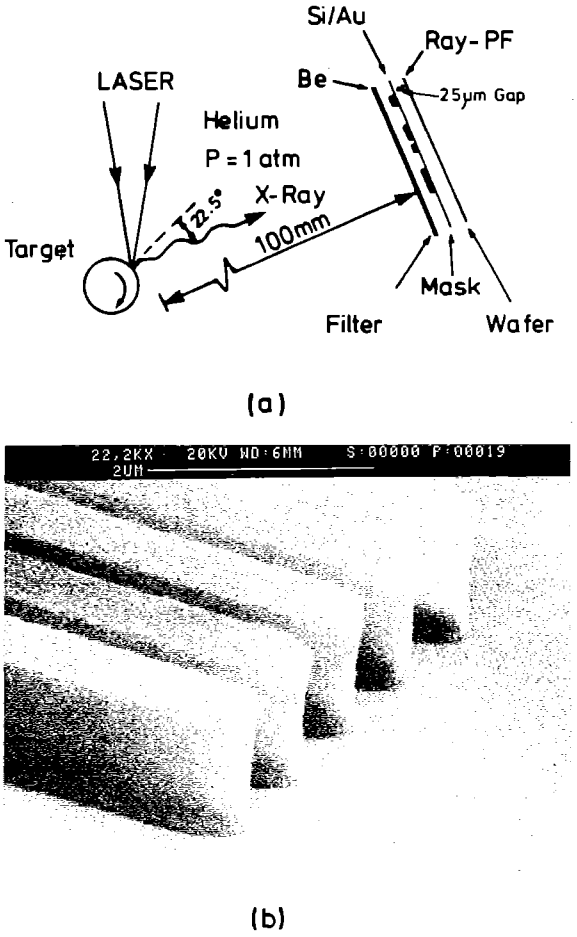

Fig. 2. Proximity X-ray lithography with a laser plasma X-ray source: a) geometry of X-ray exposure, b) X-ray image of mask structure in 1.2 μm thick photoresist.

EFFICIENT X-RAY GENERATION BY PICOSECOND KrF LASER PULSES

I C E Turcu[1], M Steyer[1], I N Ross[1], M Schulz[2], R Kaur[1],
[1]Rutherford Appleton Laboratory
[2]King's College, London

Introduction

The "Rutherford Laboratory Repetitive Laser-Plasma X-ray Source" is generating average powers of ~ 6 mW/sr of hν ~ 0.9 keV photons from iron targets and ~ 40 mW/sr of hν ~ 0.4 keV photons from mylar targets (Section D1.1). The source is driven by a 100 Hz KrF laser system generating UV pulses ~ 20 ns long focused to a focal spot of ϕ ~ 10 μm (Section C4.2). The conversion efficiency of UV energy to X-rays is limited to ~ 0.2% because the emitted X-ray pulse is very short ~ ns so that only a small fraction of the 20 ns UV pulse is used for X-ray generation[(1)]. To improve the conversion efficiency by a factor ~ 10 we have successfully used a train[(2)] of 150 ps pulses generated by injection modelocking of an excimer laser. The picosecond pulses were generated by a Distributed Feedback Dye Laser. In the present experiment we used the "Quenched Dye Laser" described in Section C4.3 as a simple, reliable system which can be run at high repetition rates. We report X-ray conversion efficiency measurements from steel, copper and mylar targets as well as spectral measurements on X-rays emitted by laser-plasma from mylar target.

X-ray Conversion Efficiency Measurements

The X-ray target chamber described in Sections C4.2 and D1.1 was used to focus 50 ps KrF pulses to focal spots of ~ 40 μm diameter with the f = 9 cm aspheric lens. (The beam divergence measurements in the far field of a f = 5 m lens have indicated that 75% of the laser energy was contained in a cone of ~ 400 μrad full angle). The max laser energy on target was ~ 17 mJ/pulse. The targets used were 20 μm thick mylar and copper tape as well as solid Silver-Steel rods. The absolute X-ray emission from the different targets was measured with calibrated 0.25 μm window silicon PIN X-ray diodes (PIN-XRD) manufactured by Quantrad (USA), placed at 23.7 cm from the X-ray source along the target normal (the laser is focused at 45° wet the target normal. For steel (hν ~ 0.9 keV)[(3)] and copper targets (hν ~ 1.2 keV)[(1)] targets the PIN-XRD was filtered with 10 μm thick beryllium filter. For the mylar target emitting "water window" X-rays (0.28 < hν < 0.53 keV) a 0.5 μm Vanadium filter was used. The measured PIN-XRD signal was converted to emitted X-ray energy by knowing the emission spectrum of each target and calculating the XRD sensitivity and the transmission of X-ray filters. The total X-ray emission was obtained by integrating over 2π steradians assuming a uniform distribution, as measured in Ref 2. The X-ray conversion efficiency is the ratio of the total X-ray emission to the laser energy deposited on target. The energy on target was varied by inserting in the KrF laser beam an attenuator cell containing NO_2 gas[(4)].

Fig 1 presents the dependence of X-ray conversion efficiency as a function of laser energy on target. The conversion efficiency for Fe targets saturates at ~ 2.5% which is an order of magnitude higher than for long (20 ns) KrF pulses.

The saturation is probably due to the fact that the KrF pulse is too short for the 36 μm focal spot. Not all the available X-ray emission volume (a cylinder of 36 μm diameter and 36 mm high) is used[(5)] because the plasma expands only ~ 5 μm in 50 ps. Nevertheless if a pulse train of such pulses is used each pulse could serve as a prepulse to enhance the X-ray emission. The Cu target efficiency follows the same feature as the Fe one. The carbon (mylar) target efficiency increases much slower with laser energy on target because the plasma temperature required for ionising carbon is much less than for Fe or Cu.

X-ray Spectrum

The spectrum of the mylar X-ray source was measured with a 44 x 44 μm^2 transmission grating manufactured in King's College London by the contamination technique on a 100 nm thick Si_3N_4 substrate. The lines spaced by 114 nm were shadowed with 30 nm of platinum. The diffraction efficiency of the grating was measured to be ~ 1% on DESY SRS (Germany). The grating was placed at 10 cm from the X-ray source at 45° wrt normal, behind an 0.2 μm Al filter. The spectrum (Fig 2) was recorded with 13.5 x 10^3 shots on mylar tape target, at a repetition rate of 2.5 Hz. This resulted in a maximum density of 3.6 on calibrated Kodak 101 no screen film placed 20 cm behind the grating. The spectrum shows remarkable resolution of all the X-ray spectral lines emitted by carbon (hydrogen and helium-like ions and oxygen (helium-like) ions. The background X-ray emission is remarkably low making this source interesting for scanning X-ray microscopy where a clean spectral X-ray line is required (Section D1.2). The brightness of the source is high. The emission at C VI L_α

line (λ = 33.7 Å) is 2.2 x 10^{11} photons/sr/Å/shot from an X-ray source of ~ 40 μm diameter.

Conclusion

In conclusion we have demonstrated high X-ray conversion efficiency and a high brightness X-ray source generated from focused 50 ps KrF laser pulses.

References

1. I C E Turcu, F O'Neill, G J Tallents, T Hannon, D Batani, A Giulietti, C W Wharton and R A Meldrum, Proc Photo Opt Instrum Eng 1278 32 (1990).
2. F O'Neill, I C E Turcu, D Xenakis and M H R Hutchinson, Appl Phys Lett 55 2603 (1989).
3. F O'Neill, I C E Turcu, G J Tallents, J Dickerson, T Lindsay, D T Goodhead, A Stretch, C W Wharton and R A Meldrum, Proc Photo-Opt Instrum Eng 1140 232 (1989).
4. I C E Turcu, F O'Neill, U Zammit, Y Al-Hadithi, R W Eason, A M Rogoyski, C P B Hills and A G Michette, Proc Photo-Opt Instrum Eng, 831 211 (1987).
5. R Kodama, T Mochizuki, K A Tanaka and C Yamanaka, Appl Phys Lett 50 720 (1987).

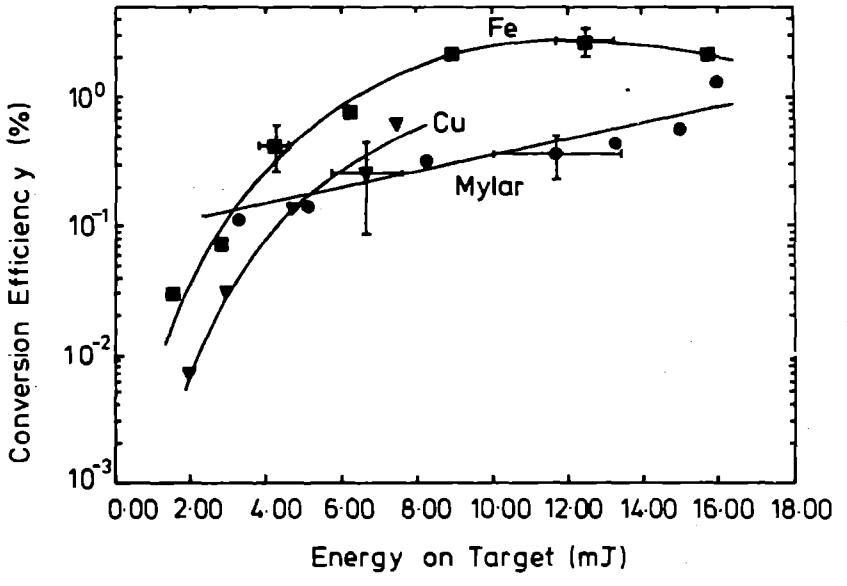

Fig 1 X-ray conversion efficiency form 50 ps KrF laser pulses.

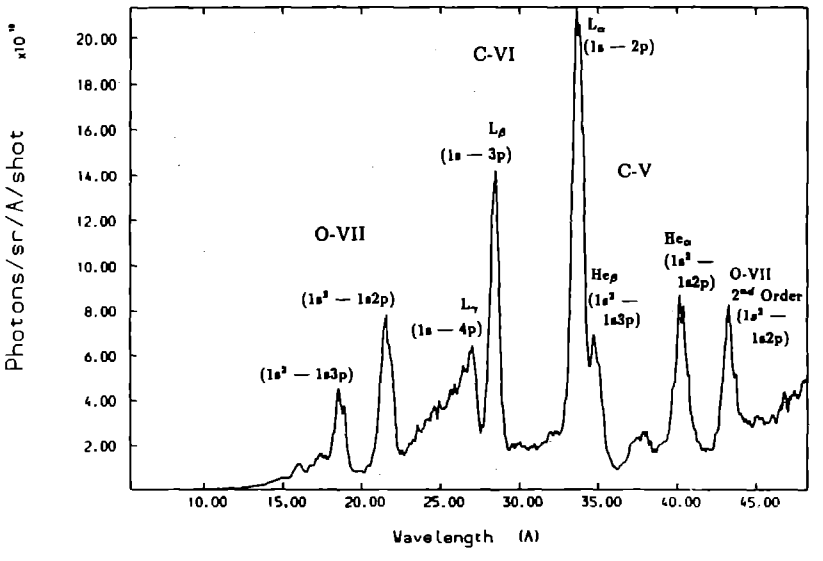

Fig 2 Laser plasma X-ray spectrum from a mylar target recorded with a 9000 lines/mm transmission grating.

MEASUREMENT ON KrF LASER BREAKDOWN THRESHOLD IN GASES

I C E Turcu, M C Gower and P Huntington
Rutherford Appleton Laboratory

Introduction

In a number of publications[1,2] and also Section D1.1, we have presented the operation of the "Rutherford Laboratory Repetitive KrF Laser-Plasma X-ray Source" and one of the remarkable features is the presence of helium gas at pressures between 20-760 torr inside the X-ray target chamber. Atmospheric pressure operation of the X-ray source reduces the target debris by two orders of magnitude[2,3] and generally, by flowing helium (as a work gas) allows the source to be run at high repetition rates hence increasing the X-ray average power generated. Ref 4 reporting KrF laser-induced breakdown threshold in gases up to an irradiance $I \sim 2 \times 10^{11}$ W/cm^2 gave an indication that at p ~ 1 atm the breakdown threshold of helium could be in the region of 10^{12}-10^{13} W/cm^2. This has justified our successful attempt of running our X-ray source in helium. In the present paper we investigate systematically the breakdown threshold of gases for KrF laser pulses focused up to irradiances of ~ 2×10^{13} W/cm^2.

Experimental Apparatus

The KrF laser system used is described in Section C4.2 and consists of an injection-locked unstable resonator KrF amplifier and KrF oscillator. The beam divergence of the system was measured in the far field of a f = 5 m lens with a 2D diode array (Exitech, UK), to be ~ 100 μrad. The pulse energy was ~ 300 mJ and pulse durations 18 ns. The laser was focused in the gas cell by an f = 9 cm fused silica aspheric singlet lens to $\phi \sim 9$ μm focal spot. The lens was fixed on an O ring in the cell wall. The chamber, Fig 1, has a transverse window through which the threshold of breakdown is determined by an observer, and a fused silica window at 18 cm from the lens and on the same axis for measurements of the transmitted KrF beam through the breakdown region. The pressure in the chamber can be varied from 10^{-2} to 3×10^3 mbar. Several research grade gases were used: Helium, Neon, Argon, Krypton and Zero grade (BOC) air. The laser energy in the focus (hence the irradiance) can be varied by an attenuator NO_2 cell[5] placed between the laser and the focusing lens. The laser energy is measured with a Gentech ED-500 energy metre and an Optical Engineering 25A power probe (Optical Engineering CA, USA). The shots with the laser energy $E_e > 50$ mJ were performed at 10 Hz and the energy was measured with the power probe while the low energy shots $E_e < 50$ mJ were measured with the Gentech which has higher sensitivity and the laser was run at 2 Hz. The two energy metres were cross-calibrated. The accuracy of the energy measurement was determined to be ± 20%. For a given laser energy the gas pressure in the cell was varied until the observer saw the threshold of the breakdown. Each measurement was repeated 2-3 times and an average value for the breakdown threshold pressure was taken. The accuracy of the measurements on the gas pressure for breakdown threshold was ± 20%.

Results and Discussion

Fig 2 shows the laser irradiance for breakdown threshold as a function of gas pressure in the cell. We note that the dependence for helium is $I \alpha P^{-1}$ which is in very good agreement with the inverse bremsstrahlung absorption process[6]. The other gases show a slightly different irradiance dependence on the power of the pressure: -1.27 for Neon, -1.36 for Argon, -1.25 for Krypton and -1.17 for Air. For these gases the absorption process is the same as for Helium but probably the electron diffusion out of the small focal volume plays an important role[6].

The data is very interesting because it shows that at λ = 248 nm the breakdown threshold for gases becomes high again after a minimum reported at λ = 350 nm[7]. The data is also in good agreement with the measurements of Ref 4 for $I \leq 10^{11}$ W/cm^2. In what the operation of the X-ray source is concerned the data shows that to avoid the breakdown at an irradiance I ~ 10^{13} W/cm^2 the pressure in the chamber should be ≤ 230 mbar. We investigated this further by measuring the laser energy transmitted through the breakdown region at helium pressure of 1 atmosphere. Only 14% of the laser energy was absorbed. Moreover looking on a fluorescent screen, at the expanded KrF beam leaving the cell at p = 1 atm, we could not observe any distortions due to transmission through the breakdown region. This small absorption and distortion of the KrF laser beam is due to the low electron density available in the atmospheric pressure Helium ~ 10^{19} electrons/cm^3 whereas the critical density for KrF radiation is ~ 10^{22} electrons/cm^3.

Acknowledgments

This work was partly supported by the Department of Trade and Industry through EUREKA European research initiative (EU213 excimer laser project).

References

1. F O'Neill, I C E Turcu, G J Tallents, J Dickerson, T Lindsay, D T Goodhead, A Stretch, C W Wharton and R A Meldrum, Proc Soc Photo-Opt Instrum Eng 1140 232 (1989).

2. I C E Turcu, F O'Neill, G J Tallents, T Hanon, D Batani, A Giulietti, C W Wharton and R A Meldrum, Proc Soc Photo-Opt Instrum Eng 1278 32 (1990).

3. I C E Turcu, A G Michette, F Bijkerk, E Louis, G J Tallents, Y Al-Hadithi and D Batani, Proc Soc Photo-Opt Instrum Eng 1503 in print (1991).

4. M C Gower, Optics Comm 36 43 (1981).

5. E Turcu, G Davis, M C Gower, F O'Neill and M Lawless, Microelectron Eng 6 287 (1987).

6. C Grey-Morgan, Sci Prog Oxf 65 31 (1978).

7. H T Busher, R G Tomlison and E K Damon, Phys Rev Lett 15 847 (1965).

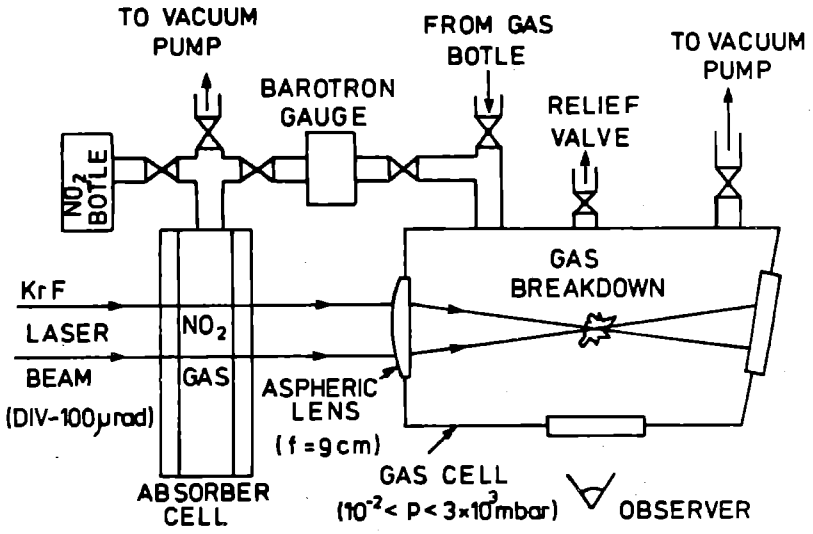

Figure 1 Apparatus for measuring laser breakdown thresholds in gases

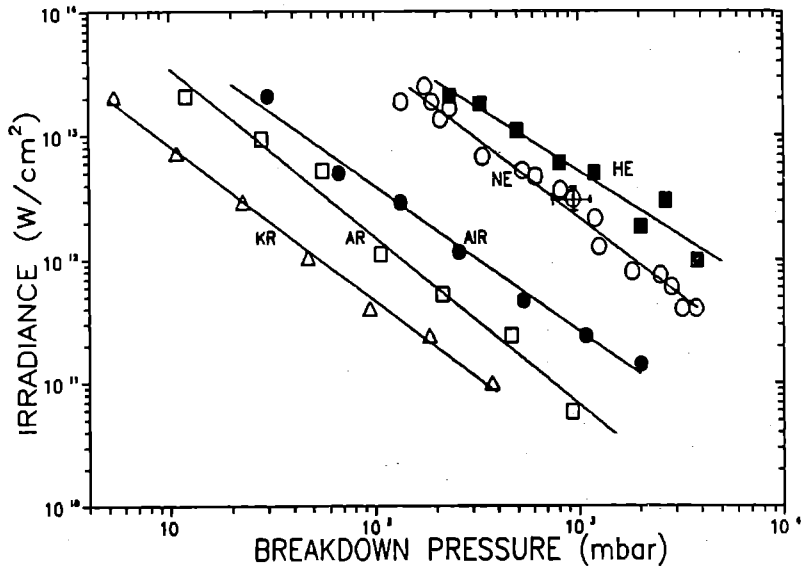

Figure 2 Breakdown threshold in gases for KrF laser

HIGH FIDELITY IMAGE AMPLIFICATION AND PHASE CONJUGATION IN PHOTOREFRACTIVE $Bi_{12}Si0_{20}$ CRYSTALS

N A Vainos and M C Gower

Rutherford Appleton Laboratory

The potential of photorefractive (PR) materials in real-time holographic applications is now well proven. However, the system performance as far as output image fidelity is concerned has hindered the development of useful devices. The factors limiting the performance are usually of fundamental nature so that the development of techniques specifically addressing the particular problem need to be found.

PR crystals with the fastest response times currently used in the visible spectral region are members of the sillenite family:

Bi_{12}[Si, Ge, Ti] 0_{20} [1]. Despite the relatively low electro-optic coefficients of these materials when compared to ferrolectric photorefractives, non-stationary grating recording techniques to enhance coupling constants and achieve high gains and phase conjugate (PC) reflectivities are now well established. These schemes employ either non-degenerate four-wave-mixing (non-DFWM) moving grating resonant recording under the application of high DC electric fields (2) or DFWM with grating recording under the application of high AC electric fields (3]. Both methods result in the enhancement of the space charge field and provide the necessary $\frac{\pi}{2}$ shift of the grating with respect to the light intensity interference pattern to achieve high diffraction efficiencies and couplings. however, because of the saturation limit of the material they inherently rely on recording holograms with large fringe spacing to produce long charge drift lengths. Furthermore, the resonance character of the process severely restricts the useful spatial frequency bandwidth around a low optimum carrier grating frequency [4,5]. Hence, the space-bandwidth product as well as the field of view of the amplified and/or conjugate image are severely restricted. The system thus becomes bandwidth limited by the amplification process.

In this work we are concerned with image fidelity of B[S,G,T]O amplifiers and conjugators under non-stationary grating recording conditions. We present for the first time to our knowledge techniques which greatly reduce some of the problems discussed above.

Moving grating resonant recording in BSO has been intensively investigated [5,6,7]. When a high DC field is applied to the crystal two beam coupling of energy between beams is produced by the imaginary part of the space charge field.

It has been shown both experimentally and theoretically that at a particular intensity, the application of an electric field determines the optimum fringe spacing for achieving the maximum gain coefficient for the material as well as the optimum velocity for the moving grating.

Under resonant recording, the grating wave vector (K) dependence of the gain coefficient (Γ) for a high applied electric field (E_0) and optimum fringe velocity takes the form (5):

$$\Gamma(K) \propto \frac{K}{1 + (K/K_{max})^2} \qquad (1)$$

The above is a highly nonlinear function of complex Lorenzian type centered at $K_{max} = (r_E\, l_E)^{-0.5}$ where the electron drift length

$$r_E = \frac{\mu E_0}{\gamma_R}$$

and tightening length

$$l_E = \frac{\varepsilon\varepsilon_0 E_0}{eN_A}$$

for a trap density N_A, recombination constant γ_R, mobility μ and static dielectric permittivity $\varepsilon\varepsilon_0$. The FWHM bandwidth of the gain in eq.(1) is

$$\Delta K_{0.5} \sim 2\sqrt{3}K_{max} \qquad (2)$$

which decreases inversely with increasing field implying that the higher the amplification the smaller the operating bandwidth.

In the simplest amplifier, two plane waves a signal S and pump P with wavevectors k_i and k_j^p respectively are mixed. In the useful linear (saturation) regime when $I_p >> I_s$ the gain will be given by

$$G(k_i, k_j^p) = \exp\,[\Gamma\,(k_i - k_j^p)l] \qquad (3)$$

where l is the interaction length.

When an arbitrary signal S is pumped by a generalised pump field P, S and P may be regarded as compositions of elementary wavefronts

$$S \sim \int s(k_i)dk_i;\ P \sim \int p(k_j^p)dk_j^p \qquad (4)$$

where the integrations are performed over the angular fields of signal and pump.

The amplified wavefront S' will be given by

$$S' \sim \iint G(k_i,k_j^p)\ s(k_i)\ dk_i dk_j^p \qquad (5)$$

For a plane pump wave eq (5) reduces to

$$S' \sim \int G(k_i)\ s(k_i)\ dk_i \qquad (6)$$

and therefore S' is severely limited by the restricted gain $G(k_i)$. The additional degree of freedom provided by eq (5) for non-plane waves can optimise the operation since it can enable the assignment of a set of elementary pump wavefronts each optimally configured to amplify a specific band of the signal field. For the experiments reported here a diverging (Gaussian) pump beam was used. The ideal choice of pump beam would have $p(k_j^p)$ = constant for all k_j^p in eq (4).

The above principle is experimentally demonstrated by the system outlined in Figure 1. An argon ion laser operating in a single longitudinal mode at λ = 514.5 nm and a single BSO crystal, with dimensions 9 mm x 8 mm x 10 mm along the [110] , [1101 , [001] directions respectively, were used. The laser beam was x10 expanded, filtered and split to provide object (signal) S and pump, P, fields. Both S and P were nominally polarised at 45° with respect to the (001) (horizontal) plane. A piezoelectrically driven mirror was used to frequency shift the pump beam P. A 4 kV DC voltage was applied to the crystal along the [110] direction. Lens Ll (f = 60 mm, F/1.2) was used to (1:1) relay the object into the crystal. An identical lens (not shown) was used to provide a diverging pump beam. The pump and signal beam divergences, $\Delta\phi$, were.both ~20° and the central Bragg angle was θ_c ~1.5°. Lens L2 (f 50 mm, F/2) imaged the output onto the camera with a ~ x3 magnification. Several pump beam intensities have been used and in each case a single optimum frequency detuning has been seen to provide the desired flat frequency response of the amplifier over all the available image field. Pump to signal beam intensity ratios were kept high at ~2000:1, and signal beam intensities as low as $60\mu W/cm^2$ were amplified with high fidelity.

Figure 2 shows a representative result using this setup. In Fig 2(a) the original image is shown recorded on Polaroid Type 55 film. In Figure 2(b) the x6 amplified image (as

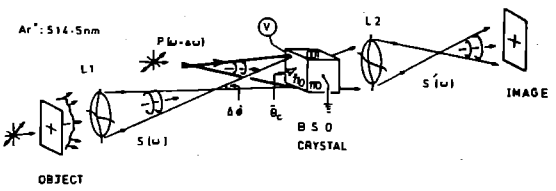

Fig 1. Schematic of the experimental arrangement used to demonstrate high fidelity image amplification.

a x1

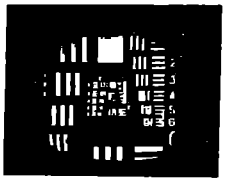

b x6

Fig 2. (a) Original image input in the amplifier. (b) x6 amplified output image.

measured with a power meter) is shown. It was recorded on the same film under the same exposure conditions. The apparent resolution is about 60*l*p/mm and densitometer measurements have verified the flat response of the system amplification over the total spatial bandwidth up to this limit. The resolution is only limited by the numerical aperture of the optical system and the recording film. The amplified beam divergence of ~20° was the same as the input.

Although in amplifiers employing plane pump beams Γ may be considered constant over the interaction length, in the present case Γ is a function of $\Delta\phi$, $\Delta\omega$, and E_0 implying that a single $\Delta\omega$ and E_0 are not appropriate for a general spatially varying grating. Experimentally it is observed that the amplifier prefers similar beam curvatures. In this case, the uniform carrier grating structure provides optimum conditions. Furthermore, for any z-axis propagation the intensity is $I_O \propto z^{-2}$, and the fringe spacing $\Lambda \propto z$, yielding a velocity [5] which is insensitive to z and therefore the maximum gain. When the curvatures are unmatched the Fresnel-zone type gratings formed result in the amplification of a narrow circular zone with a radius which is controlled by $\Delta\omega$. With this arrangement an optical filter may be constructed.

Using diverging frequency shifted mutually conjugate pump beams in the setup shown in Fig 3 we have also demonstrated high fidelity phase conjugation by non-DFWM in BSO. A poled single-domain $BaTiO_3$ crystal was used to

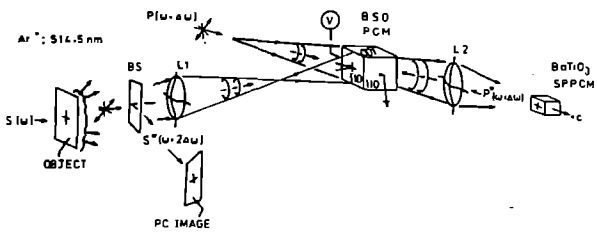

Fig 3. Schematic of the high fidelity phase conjugation system.

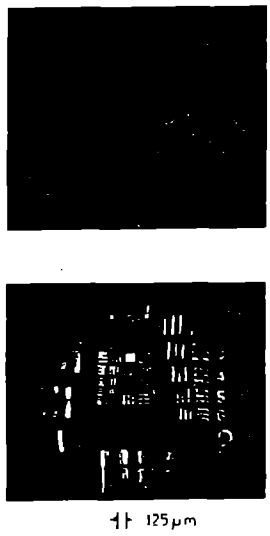

Fig 4. Images observed under (a) 'off-resonance', and (b) 'on-resonance', conditions.

provide by self-pumping a phase conjugate pair of pump beams [8] for the mixing in BSO.

The optics and geometry of the previous experiment were used here as well. After passing through the BSO crystal, the frequency shifted pump, P, was focused into the $BaTiO_3$ crystal through a $\lambda/2$-plate (not shown) used to provide the extraordinary polarisation required for self pumping in $BaTiO_3$ The PC replica of the pump, P*, was found to have the same frequency shift as P while the FWM generated PC beam, S*, had twice the shift as expected for phase matching. Polarisation control would best be provided by a Faraday rotator to obtain positive feedback [7] and high PC reflectivities in the BSO conjugator. The $BaTiO_3$ reflectivity of ~25% provides the optimum pump beam intensity ratio for high PC reflectivity. Since less than 4 kv/cm field was applied to the crystal relatively low PC reflectivities up to ~30% were obtained (reflectivities as high as 250% have been obtained using higher fields [9]).

Figure 4 shows the results of these experiments. A television system has been used here. In Fig 4(a) no PC is observed when the BSO conjugator is 'off-resonance' i.e. when the frequency shift of the pump is different from the optimum required while in Fig 4(b) a bright PC replica is obtained 'on-resonance'. It should be noted that the factors limiting the performance of this system are noise in BSO and conjugation fidelity in $BaTiO_3$.

The application of a DC field to the BSO crystal produces phase retardation on the wavefront P which affects self-pumping in the $BaTiO_3$ crystal. Nevertheless self-pumping recovers in the steady state and remains unaffected by the frequency shifts of P. Instabilities at high couplings in BSO may also affect the self pumping. However the different response times of BSO and $BaTiO_3$ are beneficial since, even at high couplings, the higher inertia of $BaTiO_3$ compensates to preserve self-pumping. In contrast, a highly unstable phase conjugator was produced when the BSO crystal was replaced by another $BaTiO_3$ crystal.

In conclusion, we have demonstrated high fidelity image amplification and phase conjugation in a BSO crystal by using diverging pump beams and non-stationary grating recording. The wide angle, large space-bandwidth product and flat frequency response operation of the present schemes may open up new ways for the development of real-time photorefractive systems for use in large scene holographic projection, information processing, and microscopy.

REFERENCES

[1] P Gunter and J-P Huignard in 'Photorefractive Materials and their Applications II, P Gunter and J-P Huignard (eds), Springer-Verlag Berlin Heidelberg (1988).

[2] J-P Huignard and A. Marrakchi, opt. Commun, 38, 249 (1981).

(31 S I Stepanov and M P Petrov, Sov Tech Phys Lett., 10, 572 (1984).

[4] S I Stepanov, K Kolikov, and M Petrov, Opt Commun, 44, 19 (1982).

[5] Ph Refregier, L Solymar, H Rajbenbach, and J-P Huignard, J Appl Phys, 58, 45 (1985).

[6] G C Valley, J Opt Soc Am.B, 1, 868 (1984).

[7] S I Stepanov and M P Petrov, in 'Photorefractive Materials and their Applications I,' P Gunter and J-P Huignard (eds) Springer-Verlag, Berlin Heidelberg (1988).

[8] J Feinberg, Opt Lett, 7, 486 (1982).

[9] H Rajbenbach, J-F Huignard and Ph Refregier, Opt Lett, 9, 558 (1984).